

---

# **ADVANCES IN CERAMICS - CHARACTERIZATION, RAW MATERIALS, PROCESSING, PROPERTIES, DEGRADATION AND HEALING**

---

Edited by **Costas Sikalidis**

**INTECHWEB.ORG**

**Advances in Ceramics - Characterization, Raw Materials,  
Processing, Properties, Degradation and Healing**

Edited by Costas Sikalidis

**Published by InTech**

Janeza Trdine 9, 51000 Rijeka, Croatia

**Copyright © 2011 InTech**

All chapters are Open Access articles distributed under the Creative Commons Non Commercial Share Alike Attribution 3.0 license, which permits to copy, distribute, transmit, and adapt the work in any medium, so long as the original work is properly cited. After this work has been published by InTech, authors have the right to republish it, in whole or part, in any publication of which they are the author, and to make other personal use of the work. Any republication, referencing or personal use of the work must explicitly identify the original source.

Statements and opinions expressed in the chapters are these of the individual contributors and not necessarily those of the editors or publisher. No responsibility is accepted for the accuracy of information contained in the published articles. The publisher assumes no responsibility for any damage or injury to persons or property arising out of the use of any materials, instructions, methods or ideas contained in the book.

**Publishing Process Manager** Nikša Mandić

**Technical Editor** Teodora Smiljanic

**Cover Designer** Jan Hyrat

**Image Copyright** Vladoleg, 2010. Used under license from Shutterstock.com

First published July, 2011

Printed in Croatia

A free online edition of this book is available at [www.intechopen.com](http://www.intechopen.com)

Additional hard copies can be obtained from [orders@intechweb.org](mailto:orders@intechweb.org)

Advances in Ceramics - Characterization, Raw Materials, Processing, Properties,  
Degradation and Healing, Edited by Costas Sikalidis

p. cm.

ISBN 978-953-307-504-4



**INTECH** OPEN ACCESS  
PUBLISHER

**INTECH** open

**free** online editions of InTech  
Books and Journals can be found at  
**[www.intechopen.com](http://www.intechopen.com)**



---

# Contents

---

## **Preface IX**

### **Part 1 Topics in Characterization Techniques and Evaluation of Advanced Ceramic Materials 1**

- Chapter 1 **On the Use of Photothermal Techniques  
as a Tool to Characterize Ceramic-Metal Materials 3**  
F. A. L. Machado, M. Filgueira,  
R. T. Faria Jr. and H. Vargas
- Chapter 2 **Spectroscopic and Dielectric Characterization  
of Plasma Sprayed Titanates 19**  
Pavel Ctibor and Josef Sedlacek
- Chapter 3 **Thermal Diffusivity of Ceramics  
During Neutron Irradiation 39**  
Masafumi Akiyoshi, Hidetsugu Tsuchida and Toyohiko Yano
- Chapter 4 **Luminescence Properties of AlN Ceramics  
and Its Potential Application for Solid State Dosimetry 59**  
Laima Trinkler and Baiba Berzina
- Chapter 5 **Non-Contact Measurements of the Apparent Density of  
Green Ceramics with Complex Shape 83**  
G.M. Revel, E.P. Tomasini, G. Pandarese and A. Cavuto
- Chapter 6 **Practical Methods for Crack Length Measurement and  
Fatigue Crack Initiation Detection Using  
Ion-Sputtered Film and Crack Growth Characteristics  
in Glass and Ceramics 103**  
Gang Deng and Tsutomu Nakanishi
- Chapter 7 **Evolution of Crystallographic Structures and Phases  
in Micropyretically Formed Boron Rich Boron Carbide –  
a New Material System 127**  
R.M. Mohanty, K. Balasubramanian and S.K. Seshadri

- Chapter 8 **Oxygen Isotope Exchange in Nanocrystal Oxides** 139  
Anatoly Fishman, Tatyana Kurennykh,  
Vladimir Vykhodets and Evgeniya Vykhodets
- Chapter 9 **Lead Free BNBT Type Ceramics:  
A Useful Material for Sensors  
and Ultrasound Applications** 165  
E. Suaste Gómez and J. J. A. Flores Cuautle
- Part 2 Topics in Characterization and Mechanical Properties  
of Conventional and Advanced Ceramic Materials** 181
- Chapter 10 **Characterization of the Firing Steps  
and Phases Formed in Mg-Zr-Containing  
Refractory Dolomitic Materials** 183  
Araceli Lavat, María Cristina Grasselli  
and Eugenia Giuliadori Lovecchio
- Chapter 11 **Characterization of Clay Ceramics  
Based on the Recycling of Industrial Residues  
– On the Use of Photothermal Techniques  
to Determine Ceramic Thermal Properties  
and Gas Emissions during the Clay Firing Process** 205  
Faria Jr. R. T., Souza V. P., Vieira C. M. F., Toledo R.,  
Monteiro S. N., Holanda J. N. F. and Vargas H.
- Chapter 12 **Mechanical Properties  
of Kaolin-Base Ceramics During Firing** 229  
Igor Štubňa, Anton Trník,  
František Chmelík and Libor Vozár
- Chapter 13 **Mechanical Properties of New Ceramic Materials  
Obtained from Granular Solid Residuals  
Coming from Mines and Diatomaceous Earth** 245  
Jaime Vite-Torres, María del Carmen Carreño de León,  
Manuel Vite-Torres and Juan Rodrigo Laguna-Camacho
- Chapter 14 **Strength of a New All-Ceramic Restorative Material  
“Turkom-Cera” Compared to Two Other Alumina-Based  
All-Ceramic Systems** 259  
Bandar M. A. AL-Makramani, Abdul A. A. Razak  
and Mohamed I. Abu-Hassan
- Chapter 15 **Physical and Metallurgical Characteristics  
of Fiber Reinforced Ceramic Matrix Composites** 281  
Zdeněk Jonšta, Evelyn A. Bolaños C.,  
Monika Hrabalová and Petr Jonšta

**Part 3 Topics in Degradation, Aging and Healing  
of Ceramic Materials 299**

- Chapter 16 **Considerations about Degradation of the Red Ceramic  
Material Manufactured with Granite Waste 301**  
Xavier Gustavo de Castro, Saboya Fernando,  
Maia Paulo Cesar de Almeida and Alexandre Jonas
- Chapter 17 **Behavior of Aging, Micro-Void, and Self-Healing  
of Glass/Ceramic Materials and Its Effect  
on Mechanical Properties 327**  
Wenning Liu, Xin Sun and Moe Khaleel
- Chapter 18 **Crack-Healing Ability of Structural Ceramics and  
Methodology to Guarantee the Reliability  
of Ceramic Components 351**  
Koji Takahashi, Kotoji Ando and Wataru Nakao



---

## Preface

---

Materials' Characterization refers to the use of external techniques aiming to better understand the structure, composition and properties of materials. In order to characterize a material what is usually needed is to determine its chemical, structural (mineralogical) and technological characteristics (determine the properties connected to the use). Characterization can take the form of actual materials testing, or analysis. Many techniques are applied today among which are: scanning and transmission electron microscopy (SEM, TEM, STEM); focused ion beam (FIB); secondary ion mass spectrometry (SIMS), and Rutherford backscattering (RBS), X-ray diffraction, reflectivity and fluorescence (XRD, XRR, XRF) including high-temperature analysis; Auger electron spectroscopy (AES), and X-ray photoelectron spectroscopy (XPS), atomic force microscopy, (AFM), Optical spectroscopy (Raman, Photoluminescence, FTIR, ellipsometry, etc.), thermal analysis (TG-DTA, DSC, etc); In addition, a great number of technological tests has been standardised to determine properties relevant to the application of each material. Furthermore, specific techniques have been developed to determine special characteristics pertinent to each material.

Some of today's most interesting research topics in materials' characterization and evaluation, included in this volume, are: the use of the non-destructive laser-induced photothermal techniques that are based on the detection of periodic thermal waves generated due to a non-radiative de-excitation, to characterize ceramic-metal materials; the use of Raman and infrared spectroscopy and near-field microwave microscopy and dielectric measurements to characterize and evaluate plasma sprayed titanates; the measurement of positron annihilation lifetime on heavily neutron irradiated ceramics to clarify changes due to neutron irradiation in thermal diffusivity one of the most important factors for a nuclear plant efficiency; the use of photoluminescence, thermoluminescence and optically stimulated luminescence methods to study of Aluminum nitride and its potential application for solid state dosimetry; the use of a newly developed non-contact method based on ultrasonic wave propagation within the material in order to measure and control the green density (which affect the shrinkage, the sintering and the mechanical properties of green and fired ceramic product) of ceramics with complex shape; the use of a newly developed method based on the application of an ion-sputtered film on a surface in order to detect fatigue crack initiation and evaluate crack growth characteristics in ceramics

and glasses; the investigation of the existence of a polytypic multi-structured boron carbide with varying B/C ratio, chemically formed through a single step solid step process using XRD, XRF and SEM techniques in order to establish the products; the investigation of oxygen isotope exchange between oxygen-containing gases  $^{18}\text{O}_2$  and  $\text{C}^{18}\text{O}_2$  and oxides examining the isotope exchange not in bulk samples but in nanoscale oxides by employing secondary ion mass spectrometry and nuclear microanalysis; the evaluation of the perovskite structure lead free BNBT type ceramics for sensors and ultrasonic applications by applying SEM and XRD techniques as well as dielectric, pyroelectric, thermal and ultrasonic measuring techniques.

The evaluation and use of local raw materials through development of new compositions for ceramics with conventional applications is of vast importance since it enforces local economies and reduces local unemployment. Raw materials and ceramic production processes, through the modification of the microstructure characteristics, directly affect all the properties of ceramics and hence the mechanical properties as compressive, tensile and shear strength, fracture toughness and ductility, hardness and abrasion resistance and elasticity/plasticity. Mechanical properties are important in structural and building ceramics, and are under consideration in development in almost all the categories of ceramic products.

Some of today's highly interesting research topics in raw materials, processes and mechanical and other properties of conventional and advanced ceramic materials, included in this volume, are: The evaluation of local raw materials for the production of  $\text{MgO-CaZrO}_3$  refractories for the cement industry by investigating the firing steps and the phases formed during firing by employing XRF, particle size analysis, BET, FTIR, XRD, SEM and EDAX techniques; the utilization of wastes and residues from steel and sanitary ware industry, as raw materials for clay based ceramics and the determination of chemical and mineralogical characteristics as well as their thermal properties using phothermal techniques and the gas emissions during firing; the study of modulus of rupture and Young's modulus of kaolin based ceramics in connection to their firing schedule; the mechanical properties of new ceramic materials obtained from granular solid residuals coming from mines and diatomaceous earth; the comparative study of the effect of special dental ceramic materials and margin design on the occlusal fracture resistance; the mechanical and other properties of advanced fiber reinforces ceramic matrix composites and the affection of the preparation techniques.

Materials in general, can be categorized as Metals, Organics (Plastics), Ceramics and Composites. Materials might be degraded by chemicals, heat, moisture, radiation, enzymatic action, mechanical wear, fatigue, creep, age etc. The environmental action, which is a combination of several of the aforementioned parameters, degrades, however to a different extent, all types of materials. Ceramics are generally considered more stable materials than others. The changes on the properties of materials with time due to interaction with air, moisture, environmental hazards etc., are often lumped together under the label "aging". The mechanisms of degradation and aging,



the effects of material's characteristics as well as the nature of the environment-material interface, the effects of degradation and aging on the material, all need to be investigated in order for degradation preventing techniques and protective ones to be developed.

A few of today's very interesting research topics on degradation, aging and healing usage of ceramic materials, included in this volume, are: the effect on artificial and natural degradation of ceramic bricks when granite waste is incorporated in the raw materials; the behavior of aging, micro-void, and self-healing of glass/ceramic materials and its effect on mechanical properties; the crack-healing ability of structural ceramics and methodology to guarantee the reliability of ceramic components.

The current book consists of eighteen chapters divided into three sections.

Section I includes nine topics in characterization techniques and evaluation of advanced ceramics dealing with newly developed photothermal, ultrasonic and ion sputtering techniques, the neutron irradiation and the properties of ceramics, the existence of a polytypic multi-structured boron carbide, the oxygen isotope exchange between gases and nanoscale oxides and the evaluation of perovskite structures ceramics for sensors and ultrasonic applications.

Section II includes six topics in raw materials, processes and mechanical and other properties of conventional and advanced ceramic materials, dealing with the evaluation of local raw materials and various types and forms of wastes for ceramics production, the effect of production parameters on ceramic properties, the evaluation of dental ceramics through application parameters and the reinforcement of ceramics by fibers.

Section III, includes three topics in degradation, aging and healing of ceramic materials, dealing with the effect of granite waste addition on artificial and natural degradation bricks, the effect of aging, micro-voids, and self-healing on mechanical properties of glass ceramics and the crack-healing ability of structural ceramics.

2011

**Constantinos A. Sikalidis**  
Department of Chemical Engineering  
Aristotle University of Thessaloniki,  
Greece



## **Part 1**

### **Topics in Characterization Techniques and Evaluation of Advanced Ceramic Materials**



# On the Use of Photothermal Techniques as a Tool to Characterize Ceramic-Metal Materials

F. A. L. Machado, M. Filgueira, R. T. Faria Jr. and H. Vargas  
*Universidade Estadual do Norte Fluminense Darcy Ribeiro, Campos dos Goytacazes-RJ  
Brazil*

## 1. Introduction

Since the discovery of the photoacoustic effect by Bell in 1881 (Bell, 1880), the so-called photoacoustic techniques have experienced great expansion. Since 1980, approximately, they have been used in a wide range of scientific areas. The photoacoustic and related photothermal techniques have proved to be a valuable tool to thermal characterization of solids, liquids and gases (Vargas & Miranda, 2003). This is one of the non-destructive laser-induced photothermal techniques that are based on the detection of periodic thermal waves generated due to a non-radiative de-excitation in the sample, which is illuminated by a chopped or pulsed optical excitation. In this chapter, thermal and structural characteristics of hardmetal (WC-10%wt Co) alloys were examined.

Hardmetal is a composite material (ceramic-metal) comprised by hard tungsten carbide – WC grains or particles, embedded into a tough binder – normally cobalt - Co (Allibert, 2001). Co percolates the WC particles, forming the WC-Co structure – the most common hardmetal alloy.

The hardmetal's formation occurs through the liquid phase sintering of the as compacted WC and Co powders, at temperatures roughly about 1400°C, in which Co spreads around WC grains and particles, enabling homogeneity, density, hardness and other desired properties.

Both phases can be modified, aiming at achieving the final desired properties (Upadhyaya, 2001). As an example, the binder phase amount is linked to the hardmetal properties, that is, as large is the Co amount, as lower is the hardness, but the fracture toughness is substantially improved.

Hardmetals present high hardness, good wear resistance, and considerable fracture toughness, allied with interesting thermal properties. These materials have been widely used in industry, due to the excellent combination among wear, impact, compressive resistance, high elastic modulus, corrosion and thermal shock resistance (Allibert, 2001; Fang *et al.*, 2009). Therefore, due to the high stability and excellent mechanical properties, their main applications includes the cutting tools in general, oil and gas well drills, forming parts – such as wire drawings tools, high energy milling components, among others (Gille *et al.*, 2002).

Thermal characterization plays an important role to qualify hardmetals, rare are the literatures with the purpose of analyzing these properties (Faria Jr. *et al.*, 2005, Kny & Neumann, 1985). This study intends to discuss the thermal behavior in six diversified WC-

10%wtCo samples (table 1), which are sintered in a not-conventional route metallurgic powder named high pressure-high temperature (HPHT), normally used to produce synthetic diamonds. For more details of HPHT see references (Faria Jr. et al., 2005, Osipov, et al., 2003).

## 2. Experimental

### 2.1 Samples

Figure 1 shows the route employed to process the hardmetal WC-10%wtCo. Commercial powders of WC and Co, mean both particle size of 5 $\mu$ m, were purchased from Derivata Ind.Com. These powder were manually mixed to perform the desired stoichiometry. The theoretical density of this hardmetal is 14.7g/cm<sup>3</sup>. Mixture was divided in samples of 1g each, approximately. Samples were put into a graphite cylinder that acts as a heater (current flow during pressing) and then assembled into a calcite capsule – responsible for the gasket formation, that ensures a good high pressure distribution into the material. Sintering treatments were carried out using a special hot press (by Ryazantyashpressmash - O138B type – 2500tons) – industrial scale, commonly used for diamonds' synthesis.

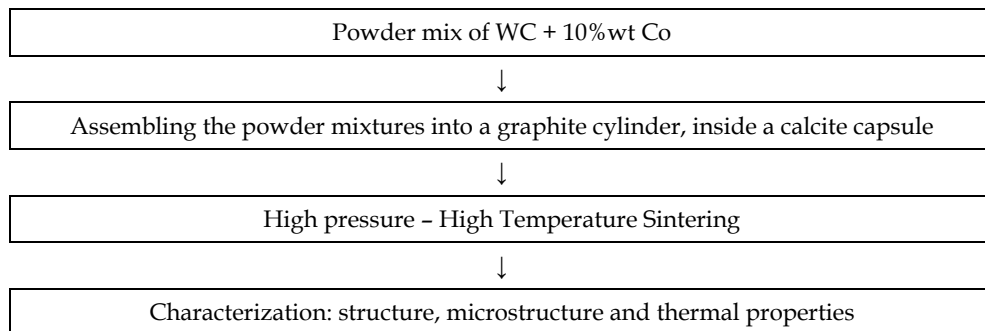


Fig. 1. Experimental flowchart for the HPHT hardmetal sintering (Rodrigues et. al, 2005)

### 2.2 Hardmetal processing

Hardmetals' processing is carried out by the conventional powder metallurgy – PM techniques, where the starting powders are blended, compacted in a determined part dimensions and geometry, and then sintered, whose objective is to acquire a product with controlled chemical composition, near net shape and mechanical properties (Borges *et al.*, 2008). Therefore, sintering is the most important processing step.

#### 2.2.1 Sintering

In this step, the compacted powders are submitted to high temperature, into a furnace. During sintering several hardmetal structural changes occurs, such as densification and grain growth.

Sintering parameters like time, temperature and environment are designed for controlling the porosity level, grain size, hardness or any other desired property.

During the sintering, the Co is the binder for the WC particles, that is, the liquid phase agent. The industrial sintering temperature ranges from 1350 to 1550°C, so that Co forms an

eutectic at about 1275°C, along with W and C – this is the so called liquid phase sintering - LPS (Allibert, 2001; Wang *et al.*, 2008).

The LPS process is divided in 3 densification stages: rearrangement, solution-precipitation and solid state sintering.

During the first stage, the compacted body behaves as a viscous solid, because the densification depends upon the liquid amount, particles' size, and solubility of the WC particles in the eutectic liquid. It forms the necks among the particles' contact points.

The solution-precipitation stage is characterized by the smaller WC particles dissolution in the liquid, which precipitates on the solid surfaces of the bigger ones. This stage enables a large densification, grains' accommodation, pores' elimination and necks' growth.

The last stage occurs when the liquid saturates. Grain growth there occurs, along with slight pore closure. It favours densification, but it is important to control the grain growth, to ensure good properties.

LPS is usually performed in furnaces with vacuum system ( $10^{-1}$  to  $10^{-2}$  mbar), or under low pressure of gas – 0,1 MPa – for example, argon. In the last case, the goal is to reduce the porosity, and to ensure an oxygen free environment (North *et al.*, 1991). It is common the use of a post-sintering process. In some cases, the use of hot isostatic pressing, at 200MPa, with the use of the same temperature and time of the previous LPS is necessary for full density.

### 2.2.2 High Pressure – High Temperature technology - HPHT

High pressure are those superior to 2 GPa, where some interesting changes in the materials' properties begin to occur, like phases transformations, electrical conductivity and others (Rodrigues, 2006). That's why this technology is widely used in the production of superhard materials.

Superhard materials (SHM) synthesis such as diamond and cubic boron nitride, for example, takes place mainly in the high pressure device (HPD), using pressures ranging from 4 to 10 GPa, and temperatures of 1200 to 2000°C. The HPD are mounted inside the working space of special hydraulic presses, employing loads of 500 to 30,000 tons.

The high pressure generation is directly linked to the presses capacity and HPD construction type. The most common types of HPD are Belt, Anvil and the Multipistons. These devices are made in hardmetal – high hardness and compression resistance, with good fracture toughness, and can be processed in relatively large parts (Rodrigues, 2006). The amount of Co in this hardmetal is 4 to 6 % in weight (Bolsaitis, 1980). Table 1 shows the sintering parameters of WC-10%wtCo samples produced by HPHT.

Number of Samples	Pressure/Temperature/Time	Number of Samples	Pressure/Temperature/Time
1	5GPa/1200°C/1min.	1	5GPa/1200°C/2min.
1	5GPa/1300°C/1min.	1	5GPa/1300°C/2min.
1	5GPa/1400°C/1min.	1	5GPa/1400°C/2min.

Table 1. Parameters sintering of samples WC-10%wtCo sintered by HPHT

Figure 2 shows a photograph of an Anvil type HPD, already installed into the press aperture. This is the HPD used to sinter the hardmetal WC-10%wtCo of this work, and it is commonly used to produce powders of diamonds and cubic boron nitride, as well as to sinter them. The HPHT sintering process may be summarized as follows: the mixture of WC and Co powders is poured into the calcite gasket – see figure 3. Alumina and graphite discs are used for thermal insulation and direct current flux, respectively. The outer polymeric ring ensures some deformation stability for the gasket. The gasket is then mounted into the HPD. This assembly is installed into the press structure – fig. 2. The press hydraulic system generates a primary pressure  $P_1$ , which raises to  $P_2$  inside the HPD – see in fig.4 the scheme of the assembly before and after pressure application. When the working pressure is reached, the electrical current system is switched on to the desired temperature inside the gasket. After the sintering time, the current is turned off, and the pressure is slowly reduced to room conditions. The HPD is removed from the press, and the sintered hardmetal sample is taken from the gasket.

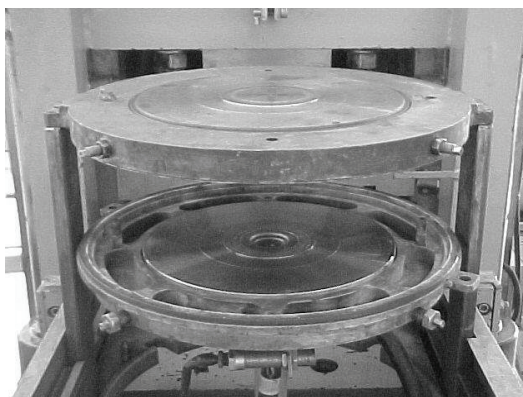


Fig. 2. Anvil type HPD



Fig. 3. Gasket with the PVC ring

Figure 4 shows, schematically, the gasket inside the HPD.



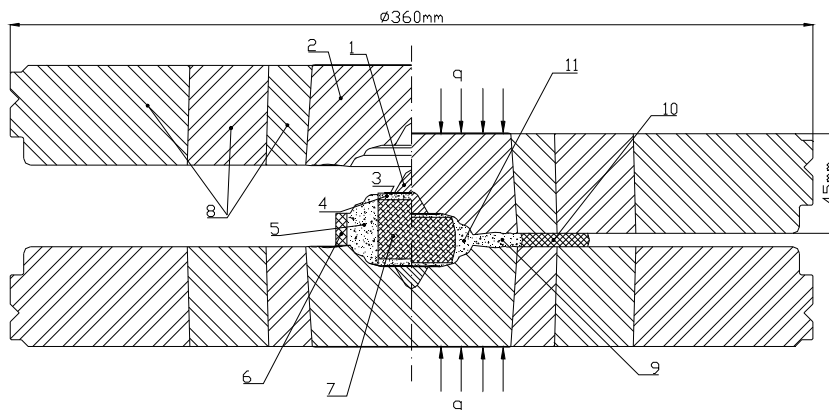


Fig. 4. Scheme of the gasket inside the HPD. (1) protective molybdenum cone; (2) anvil; (3) graphite disc; (4) alumina disc; (5) gasket prior to loading; (6) PVC ring; (7) mixed powders; (8) multi-rings; (9) gasket under loading; (10) deformed PVC ring; (11) the most deformed region of the gasket; (q) applied load

In this research, the HPHT technique was used to sinter hardmetal, aiming at the processing time reduction, and avoiding the undesirable phases formation – such as  $\eta$  phases.

### 2.3 Photothermal science

Photothermal spectroscopy can be applied to a large number of high-sensitivity methods which measure optical and thermal properties of a sample. The basis of photothermal spectroscopy is a photo-induced change in the thermal state of the sample. The nonradiative part of light energy absorbed causes the heating of the sample. This heating is responsible for the variation of temperature and thermodynamic changes in the sample. Thus, photothermal spectroscopy is based upon measurements of temperature, pressure, or density changes that occur due to optical absorption.

Generally, photothermal spectroscopy is a more direct measurement of optical absorption than are optical transmission-based spectroscopies. Sample heating is a direct consequence of optical absorption; therefore photothermal spectroscopy signals are directly dependent on light absorption. Scattering and reflection losses do not produce photothermal signals. Consequently, photothermal spectroscopy more accurately measures optical absorption in scattering solutions, in solids and at interfaces. This characteristic makes it mostly attractive for application to surface and solid absorption analysis and studies in scattering media (Bialkowski, 1996).

The indirect nature of the measurement also results in photothermal spectroscopy being more sensitive than optical absorption measured by transmission methods. For example, photothermal effects can amplify the optical signal measured. One of the factors for this amplification is the possibility to increase the power of the light source and on the optical geometry used to excite the sample. Another feature that photothermal spectroscopy is more sensitive than transmission is that the precision of the measurements is fundamentally better than that of the direct transmission method. The high sensitivity of photothermal spectroscopy methods has led to applications for analysis of low-absorbance samples (Bialkowski, 1996).

Photothermal spectroscopy is usually performed using laser light sources. Lasers can deliver high powers or pulses energies over very narrow optical bandwidths, thereby enhancing the photothermal signals.

Here, an open photoacoustic cell (OPC) in the transmission configuration (Vargas & Miranda, 1988, 2003, Bribiesca et al., 1999) is employed to evaluate thermal diffusivity and the photothermal technique of continuous investigation illumination on the sample in a vacuum (Contreras et al., 1997) is used to measure thermal capacity density.

### 2.3.1 Photoacoustical investigation – measurement of thermal diffusivity

The quantity that measures the rate of heat diffusion into a material is the thermal diffusivity ( $\alpha$ ). This property depends closely on the microstructural variations, composition and the processing conditions of the sample (Raveendranath, 2006).

The OPC technique is widely used for several applications aiming at the thermal characterization of great variety of samples such as biological liquids and colloids, plant leaves, wood (López, 1996) , two layer systems (Mansanares, 1990), semiconductors (Calderon et. al., 1997), polymers (Cella et. al., 1989), clays (Alexandre et. al., 1999, Mota et al., 2008, 2009), coating materials and so on. Figure 5 shows the schematic thermal diffusivity measurement set-up.

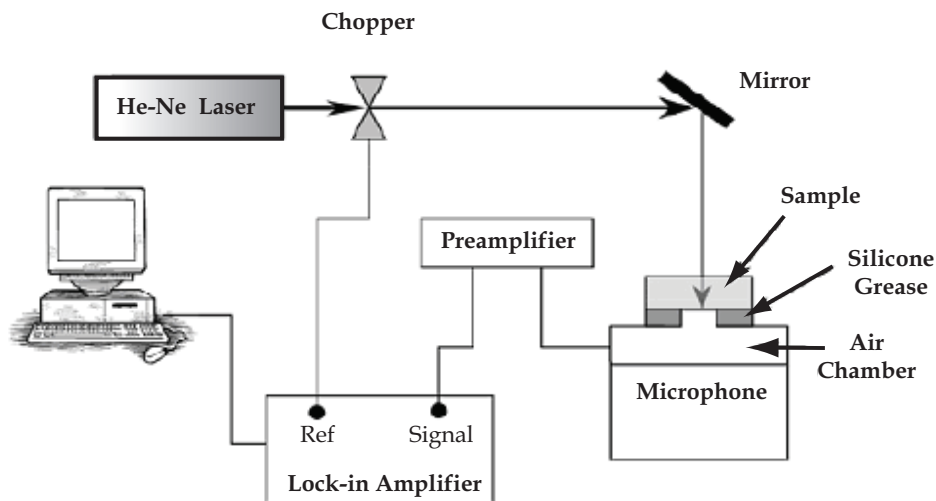


Fig. 5. Schematic measurement system of the thermal diffusivity (Yunus, 2002)

Normally, we have used a He-Ne laser (25 mW) as the excitation source. The disc sample WC-10% wt Co is mounted on the top of air chamber using vacuum grease and is illuminated on the external surface. The laser beam modulation is produced by a mechanical chopper (Stanford Research Systems SR540). The resulting PA signal is then subsequently fed into a field-effect-transistor (FET) pre-amplifier and leads directly to a "Lock-in" amplifier (Perkin Elmer Instruments mod. 5210), where it is possible to obtain the photoacoustic amplitude and the phase signal, which are recorded as a function of the

modulation frequency in an appropriate software program. The schematic cross-section of the OPC configuration is show in figure 6.

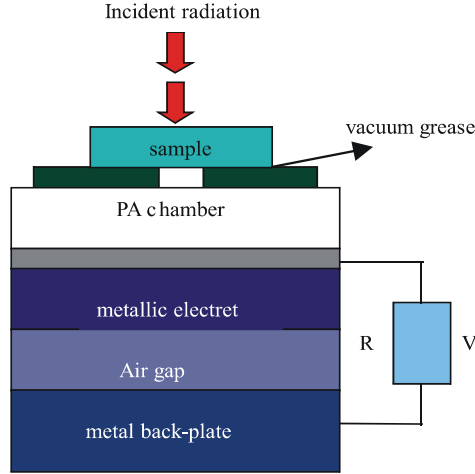


Fig. 6. Schematic design of an open photoacoustic cell (OPC)

Applying for the simple one-dimensional thermal diffusion model of Rosencwaig and Gersho (Rosencwaig & Gersho, 1976), the expression for the pressure fluctuation ( $\delta P$ ) in the air chamber is

$$\delta P = \frac{\gamma I_0 (\alpha_s \alpha_g)^{1/2}}{2\pi l_g T_0 k_s f} \frac{e^{j(\omega t - \frac{\pi}{2})}}{\sinh(\sigma_s l_s)}, \quad (1)$$

where  $\gamma$  is the air specific heat ratio,  $P_0$  the ambient pressure,  $T_0$  ambient temperature,  $I_0$  is the absorbed light intensity,  $f$  is the modulation frequency, and  $l_i$ ,  $k_i$ , and  $\alpha_i$  are the length, thermal conductivity and the thermal diffusivity of the sample respectively. Here  $i=s$  subscript denotes sample and  $g$  denotes gas medium. Also  $\sigma_s = (1+j)a_s$  where  $a_s = (\omega/2\alpha_s)^{1/2}$  is the complex thermal diffusion coefficient of the material.

If the sample is thermally thin (i.e.,  $l_s a_s \ll 1$ ), equation (2) reduces to

$$\delta P = \frac{\gamma P_0 I_0 (\alpha_s \alpha_g)^{1/2}}{(2\pi)^{3/2} l_g l_s T_0 k_s} e^{j(\omega t - 3\frac{\pi}{4})} \frac{1}{f^{3/2}} \quad (2)$$

That is, the amplitude of the PA signal decreases as  $f^{1.5}$  as one increases the modulation frequency. In contrast, at high modulation frequencies, such that the sample is thermally thick (i.e.  $l_s a_s \gg 1$ ), then

$$\delta P = \frac{\gamma P_0 I_0 (\alpha_s \alpha_g)^{1/2}}{\pi l_g T_0 k_s} e^{j(\omega t - \frac{\pi}{2} l_s a_s)} \frac{e^{-l_s} \sqrt{\frac{\pi f}{\alpha_s}}}{f} \quad (3)$$

For thermally thick samples, the amplitude of the PA signal decreases exponentially with the modulation frequency as  $(1/f) \exp(-a_s \sqrt{f})$ , where  $a_s = l_s \sqrt{\pi/\alpha_s}$ . In this case,  $\alpha$  is obtained from the experimental data fitting from the coefficient ( $a_s$ ) in the argument of the exponential ( $-a_s \sqrt{f}$ ).

When values of thermal diffusivity are determined from the amplitude data of the photoacoustical signal, we should pay attention to the microphone non-linear frequency response in relation to acoustical vibrations. Practically, all microphones present this irregularity. In our case, our microphone had a good linear frequency response above 20 Hz. In order to certify our set-up, a calibration measurement was performed. Figure 7 shows the dependence of the photoacoustical (PA) signal on the modulation frequency for the aluminium (Al) sample.

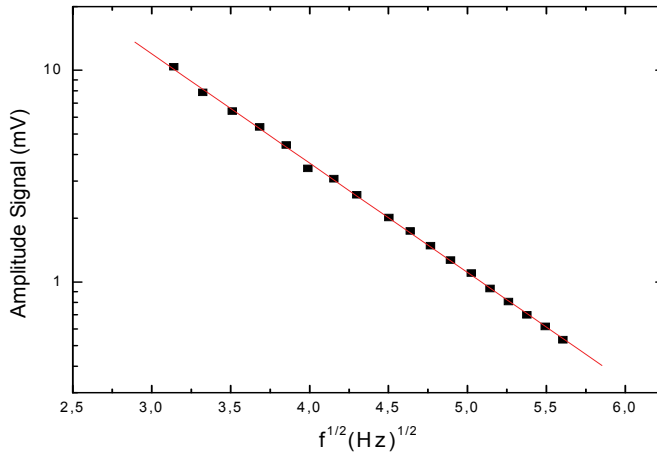


Fig. 7. Microphone output voltage as a function of the chopping frequency for the 25  $\mu\text{m}$  thick Al sample. The signal behaves roughly as  $f^{-1.5}$

For frequencies used to calibrate the thermal diffusivity measurement set, the signal exhibited a frequency dependency close to  $f^{-1.5}$ . This is the typical behaviour we would expect from the thermal diffusion model for a thermally thin sample. In fact, for a 25  $\mu\text{m}$  thick Al sample and a thermal diffusivity of  $93.28 \times 10^{-6} \text{ m}^2/\text{s}$  (Almond & Patel, 1996) the characteristic frequency  $f_c$  for the transition between the thermally thin and thick regime is about 47.5 KHz.

## 2.4 Measurement of specific heat capacity

The product of density and specific heat,  $\rho c$ , was measured using, the photothermal technique of temperature evolution induced by continuous illumination of the sample in vacuum. The surface sample is painted black and placed inside a Dewar that is subsequently vacuum-sealed. The front surface of the sample is illuminated with the He-Ne laser focused

on the sample through an optical glass window on the Dewar (figure 8). The back surface of the sample has a thin-wire T-type thermocouple. The thermocouple output is measured as in function of time by using a thermocouple monitor (model SR630 Stanford Research Systems) connected to a computer.

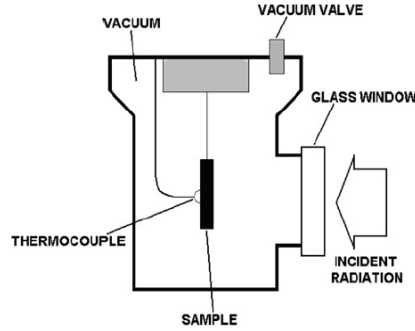


Fig. 8. Schematic measurement system of the specific thermal capacity

The temperature evolution is monitored up to reach a stationary state. Subsequently, we turn off the laser and the temperature decrease is monitored, as well. Equations 4 and 5 represent the temperature increase and temperature decrease, respectively.

$$\Delta T \uparrow = \frac{I_0}{H} (1 - e^{-t/\tau}) \quad (4)$$

$$\Delta T \downarrow = \frac{I_0}{H} e^{-t/\tau} \quad (5)$$

Finally, equations 6 and 7 present the relationship among the thermal properties. In this case, thermal diffusivity and thermal effusivity ( $e$ ) are defined as in function of thermal conductivity ( $k$ ) and specific thermal capacity ( $C$ ),  $C = \rho c$ , where  $c$  is the specific heat and  $\rho$  is the mass density.

$$k = \alpha \rho c \quad (6)$$

$$e = \sqrt{k \rho c} \quad (7)$$

Experiments concerning with thermal diffusivity, samples thickness and specific heat capacity measurements were performed five, ten and three times to produce the deviations, respectively.

### 3. Results and discussion

We show in figure 9 the XRD spectra recorded for samples HPHT sintered hardmetal samples. One can observe that there is practically no difference among the samples, only WC/Co peaks are observed and the  $\text{Co}_3\text{W}$  phase is presented in all the samples. The Rietveld analysis confirmed the  $\text{Co}_3\text{W}$  phase in low intensity for the whole samples. Figure

10 shows the Rietveld analysis for 5 GPa/1200°C/1min sample. This sample has 83,7% WC and 6.3%  $\text{Co}_3\text{W}$ .

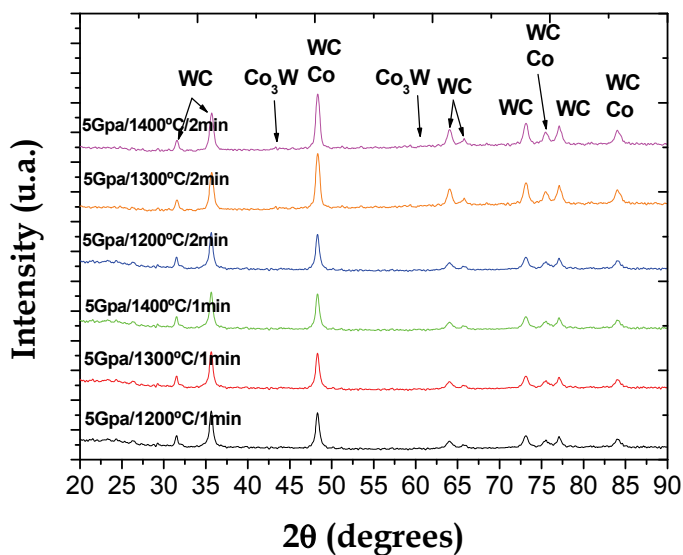


Fig. 9. X-ray diffractogram for the HPHT sintered hardmetals

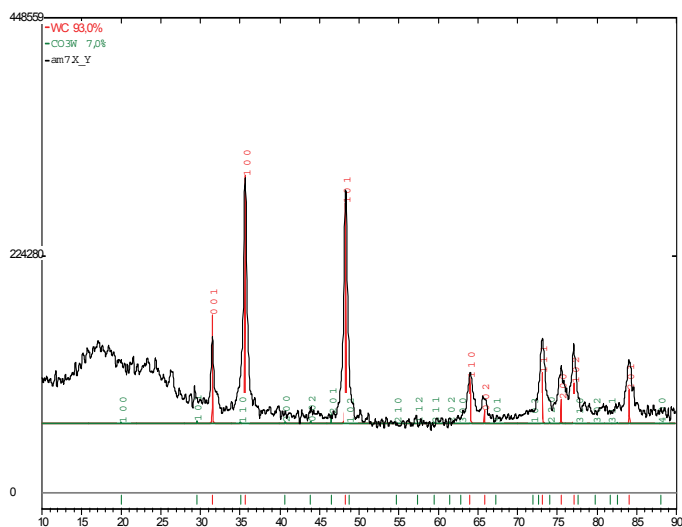


Table 2 shows the whole thermal properties reached, using our alternative method. One can see in figure 11 a typical curve for thermal diffusivity measurements for the sample subjected to 5GPa/1400°C/2min sintering conditions. It was observed that thermal diffusivity values are; in close agreement with previous works (Miranzo et al. 2002, Lauwers et al. 2001). However, the values obtained for thermal conductivity are lower when compared with other papers (Kny & Neumann, 1985, Miranzo et al., 2002).

Samples	$\alpha$ (cm <sup>2</sup> /s)	C (J/cm <sup>3</sup> K)	k (W/ m K)	e (Ws <sup>1/2</sup> cm <sup>-2</sup> K <sup>-1</sup> )
5 GPa/1200°C/1 min	0,340 ±0,005	1,0 ± 0,039	34,0 ± 0,040	0,58 ± 0,050
5 GPa/1200°C/2 min	0,380 ±0,023	1,0 ± 0,042	38,0 ± 0,050	0,62 ± 0,061
5 GPa/1300°C/1 min	0,270 ±0,046	1,0 ±0,082	27,0 ± 0,094	0,52 ± 0,107
5 GPa/1300°C/2 min	0,250 ±0,013	0,83 ± 0,020	20,7 ± 0,020	0,41 ± 0,020
5 GPa/1400°C/1 min	0,370 ±0,030	1,30 ± 0,080	48,1 ± 0,115	0,79 ± 0,156
5 GPa/1400°C/2 min	0,400 ±0,006	1,0 ± 0,041	40,0 ± 0,043	0,63 ± 0,058

Table 2. Thermal properties of WC-10%wtCo sintered by HPHT

In this case, it is desirable that, within the thermal diffusivity ( $\alpha$ ), the thermal conductivity ( $k$ ) also could have higher values, because the hard metal works in extreme stress situations, moreover, it is really important that the material reaches in a faster way its thermal balance, so increasing the useful life.

A possible justification for lower values is that in the conventional sintering route, due to the long time that is necessary firing process, metallic phases appear ( $W_3Co_3C$ ,  $Co_6W_6C$ ), which do not occur for sintering at the HPHT method. Another important factor for the low values of thermal properties is due to the not good homogeneity of the Co mixture. Although our samples present Co addition, there is phonons contribution from the phase WC heat transport. It is necessary a good crystal homogeneity for a good thermal flow, because phonons transport heat along the crystalline structure. As our HPHT samples present coalescence, porosity, phase transitions, etc, therefore phonons are easily spread out.

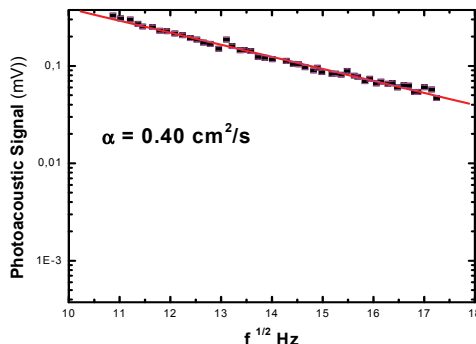


Fig. 11. Thermal diffusivity of the 5 GPa/1400°C/2 min HPHT sintered hardmetal

The samples 5GPa/1300°C/1min and 5GPa/1300°C/2min presented lower values of thermal properties due to their microstructure, which do not present a good homogeneity of the WC/Co mixture, during the whole production process. Figure 9 shows the microstructure of the sintered body 5GPa/1300°C/2min, where great cobalt lakes and a not homogeneous distribution of the Co binder are shown.

The samples sintered in 1200°C and 1400°C presented greater thermal property values. In figure 12 and figure 13 we can note the microstructure of 5GPa/1200°C/1min and 5GPa/1400°C/2min samples.

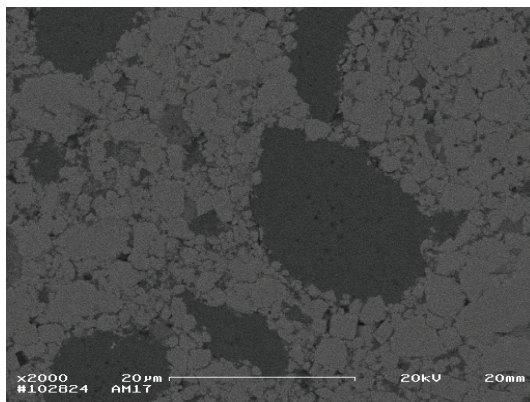


Fig. 12. Microstructure of 5GPa/1300°C/2min sintered body

The typical hardmetal microstructure can be observed, with the grain growth of some particles of WC (white), porosity (black), and cobalt distribution (dark gray). A more homogeneous microstructure in figure 14 is observed, which presents a better cobalt distribution and presents Co lakes of the order of 5 to 15 μm, while figure 13 shows Co lakes of the order of 10 to 25 μm. The presence of a slight gray phase is observed in figure 12 (with form of spots), which are uniformly distributed. We attribute to the  $\text{Co}_3\text{W}$  phase, identified in figure 9.

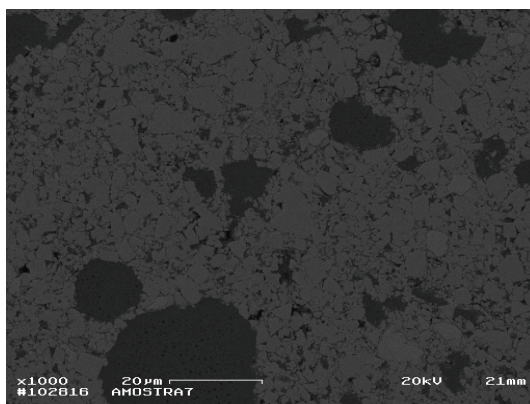


Fig. 13. Microstructure of 5 GPa/1200/1 min sintered body



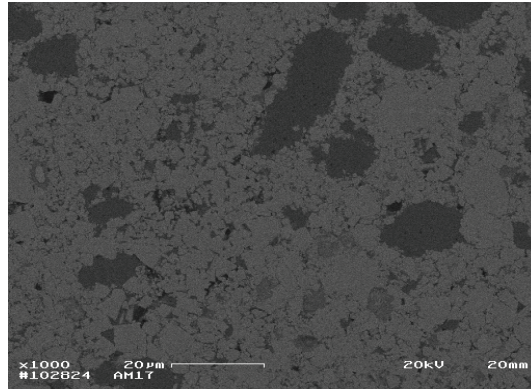


Fig. 14. Microstructure of 5 GPa/1400°C/2 min sintered body

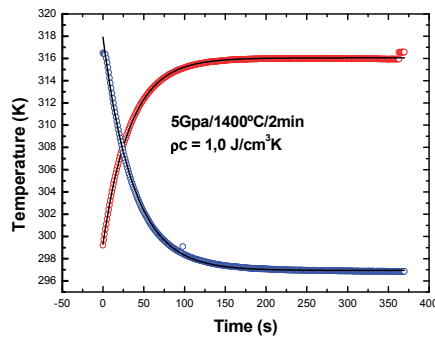


Fig. 15. Specific Heat Capacity of the 5 GPa/1400°C/2 min HPHT sintered hardmetal

The thermal energy absorption (specific heat capacity) is lower among the samples due to a not good distribution of the metal binder. Figure 15 shows a typical curve of specific heat capacity measurements in this case 5GPa/1400°C/2min sample.

The thermal effusivity was determined by  $e = \sqrt{kC}$ , which is directly influenced by the thermal conductivity and specific heat capacity. Probably, commercial hardmetals present very higher effusivity in relation to our samples. But, unfortunately, nothing can be stated, because no references were found for comparisons. We intend that these data can play an important role for this kind of material.

#### 4. Conclusions

The goal of this exploratory work was reached. The open photoacoustic cell method is very satisfactory and readily provides thermal properties measurements for hardmetals. The metallic phases ( $W_3Co_3C$ ,  $Co_6W_6C$ ) occur, normally to the conventional route, while in the HPHT process there is not enough time to produce these phases. The specific heat capacity presented lower values due to the components distribution characteristics. The cobalt binder

did not disperse homogeneously in the samples, originating large Co lakes. On the other hand the thermal diffusivity values are quite realistic to the commercial hardmetals. We can conclude that is necessary more attention to the preparation sample process, mainly in the components mixture phase. The time of the WC-Co mixture should not have been sufficient for a good cobalt distribution in the sample, which harmed the results of some thermal properties. For the first time, effusivity values were determined in relation to these materials.

Essentially, for cutting and drilling tools, thermal properties play an important role in the production process. Manipulating the powders and the sintering process, it is possible to change the thermal parameters. For instance a hardmetal under study should present low thermal effusivity, that is, the outer heat flow should be blocked. Large amount of heat into the material should be avoided. However, it should present high diffusivity, high conductivity, and high thermal capacity. This way, they should expand the time-life of the tool.

## 5. Acknowledgments

We would like to thank UENF/FAPERJ, CNPq and CAPES for the financial support.

## 6. References

- Alexandre, J., Saboya, F., Marques, B.C., Ribeiro, M.L.P., Salles, C., da Silva, M.G., Sthel, M.S., Auler, L.T., Vargas, H. (1999). Photoacoustic Thermal Characterization of Kaolinite Clays. *Analyst* Vol. 124, No 8, pp. 1209-1214.
- Allibert, C.H. (2001). Sintering features of cemented carbides WC-Co processed from fine powders. *International Journal of Refractory Metals and Hard Materials*, Vol. 19, pp. 53-61.
- Almond, D.P., Patel, P.M. (1996). *Photothermal Science and Techniques*. 1. ed. London: Chapman & Hall, 237p.
- Bell, A.G. (1880). On the production and reproduction of sound by light. *American Journal of Science*, Vol. 20, No 118, (October 1880) pp. 305-324.
- Bialkowski, S. E. (1996), *Photothermal Spectroscopy Methods for Chemical Analysis* (1<sup>st</sup> ed.), John Wiley & Sons, Inc., New York.
- Bolsaitis, P. (1980) Materials for Use in High Pressure Equipament. 1ed, Vol.1, Chapter 9 - *High Pressure Technology*. New York: Eds. Spain, I. L., Paauwe, J. 741p.
- Borges, L.H.F.; Oliveira, H.C.P.; Guimarães, R.S.; Kobayashi, T.; Filgueira, M. (2008). Pressure aided Sintering of Ultrafine Powders of WC with Addition of Co. *Materials Science Forum*. Vol. 591-593, p.308-313.
- Bribiesca, S., Equihua, R., Villaseñor, L. (1999). Photoacoustic Thermal Characterization of Electrical porcelains: Effect of Alumina Additions on thermal Diffusivity and Elastic Constants. *Journal of the European Ceramic Society*, Vol. 19, pp. 1979-1985.
- Calderon, A., Gil, J.J.A., Gurevich, G.Y., Orea, A.C., Delgadilho, I., Vargas, H., Miranda, L.C.M. (1997). Photothermal Characterization of Electrochemical Etching Processed n-Type Porous Silicon. *Physical Review Letters*. Vol. 79, pp. 5022-5025.
- Cella, N., Vargas, H., Galembeck, E., Galembeck, F., Miranda, L.C.M. (1989) Photoacoustic Monitoring of Crosslinking Reaction in Low-Density Polyethylene. *Journal Polymers Scientific Letters*, Vol 27, No 9 pp. 313-320.

- Contreras, M.E., Serrato, J., Zarate, J. (1997). Photoacoustic Thermal Characterization of Lime-Partially Stabilized Zirconia. *Journal of American Ceramics Society*, Vol. 80, No 1., pp. 245-249.
- Fang Z.Z., Wang X., Taegong Ryu, Hwang K. S., Sohn, H.Y. (2009) Synthesis, sintering, and mechanical properties of nanocrystalline cemented tungsten carbide – A review. *International Journal of Refractory Metals & Hard Materials*, 27: 288-299.
- Faria Jr., R.T., Filgueira, M., Esquef, I.A., Machado, F.A.L., Rodrigues, M.F., Bobrovitchii, G.S., Vargas, H. (2005). Thermal characterization of sintered hardmetal. *Journal of Physique IV*, Vol. 125, pp. 237-239.
- Faria Jr., R.T., Rodrigues, M.F., Esquef, I.A., Vargas, H., Filgueira, M. (2005). On the thermal characterization of a HPHT sintered WC-15% wt Co hardmetal alloy. *International Journal of Refractory Metals and Hard Materials*, Vol. 23, No 2, pp. 115-118.
- Gille, G.; Szesny, B.; Dreyer, K.; Berg, H.; Schmidt, J.; Gestrich, T.; Leitner, G. (2002) Submicron and ultrafine Grained Hardmetals for microdrills and metal cutting inserts. *International Journal of Refractory Metals & Hard Materials*. V.20, p.3-22.
- Kny, E., & Neumann, W. (1985). Einflußgroßen auf Temperatur – und Wärmeleitfähigkeit von WC-Co Hartmetallen. *High Temperatures-High Pressures*. Vol. 17, pp. 179-189.
- Lauwers B., Liu W., Eraerts W. (2002) Katholieke Universiteit Leuven, Belgium, personal communication.
- López, J.A., Limon, J.M.Y., Gil, J.J.A., Vargas, H., Silva, M.D., Miranda, L.C.M. (1996). Thermal quality and structural properties of CdZnTe. *Forest Products Journal*, Vol. 46, pp. 84-89.
- Mansanares, A.M., Bento, A.C., Vargas, H., Leite, N.F., Miranda, L.C.M. (1990). Photoacoustic measurement of the thermal properties of two-layer systems. *Physical Review B*, Vol. 42, No 1, (September, 1990), pp. 4477-4486.
- Miranzo, P., Osendi, M.I., Garcia, E., Fernandes, A.J.S., Silva, V.A., Costa, F.M., Silva, R.F. (2002). Thermal conductivity enhancement in cutting tools by chemical vapor deposition diamond coating. *Diamond and Related Materials*, Vol 11. No 3, (March, 2002) pp. 703-707.
- Mota L, Toledo R., Machado F.A.L., Holanda J.N.F., Vargas H., Faria Jr R.T. (2008). Thermal Characterisation of Red Clay from the Northern Region of Rio de Janeiro State, Brazil Using an Open Photoacoustic Cell, in Relation to Structural Changes on Firing. *Applied clay Science*. Vol 42, pp. 168-174.
- Mota, L., Toledo R, Faria Jr. R. T., da Silva E. C, Vargas H., Delgadillo-Holtfort I. (2009). Thermally treated soil clays as ceramic raw materials: Characterization by X-ray diffraction, photoacoustic spectroscopy and electron spin resonance. *Applied Clay Science*, Vol 43, pp. 243-247.
- North, B.; Pfouts, W.R.; Greenfield, M.S. (1991). Pressure Sinter and HIP on Cemented carbides. *Metal Powder Report*. PM Special Feature. p. 40-45.
- Osipov, O., Bobrovitchii, G., Filgueira, M. (2003). A contribution to the study of the diamond solid state sintering. *Cerâmica*, Vol. 49, No 311, pp. 151-157.
- Raveendranath, K., Ravi, J., Jayalekshmi, S., Rasheed, T.M.A., Nair, K.P.R. (2006). Thermal diffusivity measurement on  $\text{LiMn}_2\text{O}_4$  and its de-lithiated form ( $\lambda\text{-MnO}_2$ ) using photoacoustic technique. *Materials Science and Engineering B*, Vol. 131, (July, 2006), pp. 210-215.

- Rodrigues, M.F., Bobrovnitchii G. S., Ramalho A. M., Filgueira, M. (2005). Pressure Assisted WC-15%wtCO Sintering. *Materials Science Forum*. Vol 498-499, pp. 231-237.
- Rodrigues, M.F. (2006) *Thermobaric sintering of the WC-10%pCo alloy*, MSc Dissertation. Universidade Estadual do Norte Fluminense, Campos dos Goytacazes/RJ, Brazil, 119p. In portuguese.
- Rosencwaig, A., Gersho, A. (1976). Theory of the photoacoustic effect with solids. *Journal of Applied Physics*, Vol 47, No 1, (January, 1976) pp. 64-69.
- Upadhyaya, G.S. (2001). Materials Science of Cemented Carbides – An Overview. *Materials and Design*. v.22, p.483-489.
- Vargas, H., & Miranda, L.C.M. (1988), Photoacoustic and related Photothermal techniques *Physics Reports*, Vol. 161, pp. 43-101.
- Vargas, H., & Miranda, L.C.M. (2003), Photothermal techniques applied to thermophysical properties measurements (plenary) *Review of Scientific Instruments*, Vol. 74, No. 1, (January 2003) pp. 794-799.
- Wang, X.; Fang, Z.Z.; Sohn, H.Y. (2008). Grain growth during the early stage of sintering of nanosized WC-Co powder. *International Journal of Refractory Metals & Hard Materials*. v 26(3), p. 232-241.
- Yunus, W.M.M., Fanny, C.Y.J.; Phing, T.E.; Mohamed, S.B.; Halim, S.A. & Moskin, M.M. (2002). Thermal diffusivity measurement of Zn, Ba, V, Yand Sn doped Bi-Pb-Sr-Ca-Cu-O ceramics superconductors by photoacoustic technique. *Journal of Material Science*, Vol. 37, pp. 1055-1060.

# Spectroscopic and Dielectric Characterization of Plasma Sprayed Titanates

Pavel Ctibor<sup>1</sup> and Josef Sedlacek<sup>2</sup>

<sup>1</sup>*Institute of Plasma Physics, ASCR, v.v.i., Prague,*

<sup>2</sup>*Department of Electrotechnology, Faculty of Electrical Engineering,  
Czech Technical University, Prague  
Czech Republic*

## 1. Introduction

Synthetic perovskite  $\text{CaTiO}_3$  (CT), geikielite  $\text{MgTiO}_3$  (MT) and their mixture  $\text{MgTiO}_3\text{-CaTiO}_3$  (MCT) are materials well known and widely used as dielectrics in a sintered state. CT is high-permittivity linear dielectric material whose structure is not influenced by plasma spraying - neither chemical nor phase composition, as demonstrated earlier [Ctibor, 2003]. MT belongs to the family of low-loss microwave dielectrics and MT-CT solution is known by its temperature stability of permittivity. Namely the composition  $(\text{Mg}_{0.95}\text{Ca}_{0.05})\text{TiO}_3$  is used in connection with this feature.

In recent decades plasma spraying has become a well accepted technology as the coating method for metallic and ceramic materials and has been used in a variety of fields including electrical engineering. The coatings have lamellar character of a body formed with porosity aligned with respect to the lamellas. Spraying does not require heating of the substrate to the melting point of the deposited material.

Often the research is focused on the microstructure of plasma sprayed coatings and features like porosity, unmelted particles, cracks and residual stress. Above listed characteristics are responsible for the behavior of coatings. However in the case of titanates phenomena taking place on atomic level and single crystal cell level are also important. Raman spectroscopy, infrared spectroscopy and near-field microwave microscopy are suitable techniques for this characterization.

Ca and Mg have the same charge but different ionic radii ( $r_{\text{Ca}^{2+}} = 0.134 \text{ nm}$  and  $r_{\text{Mg}^{2+}} = 0.103 \text{ nm}$ ) [Hirata, 1996]. A mixture of CT and MT melts and forms an eutectic liquid at  $1462^\circ\text{C}$ , which, under proper solidification conditions, can be used to achieve a highly dense product. During processing presence of intermediate phases of  $\text{MgTi}_2\text{O}_5$  and  $\text{Mg}_2\text{TiO}_4$  was noted, and they were difficult to eliminate completely from the reaction products [Zhang, 2006; Zheng, 2003; Huang, 2002].

MCT exhibits differences from MT in the metal-oxygen bond lengths which are relevant to the stability of the compounds. While the infrared and Raman spectra of CT and MT have been measured [Jiang, 1998; Cavalcante, 2008], other cations at the A and/or B sites alters the vibrational properties of  $\text{ABO}_3$  studied by these spectroscopic techniques. This encourages the author to measure the Raman and infrared spectra. In the plasma sprayed MCT we have earlier recognized also  $\text{MgTi}_2\text{O}_5$  and  $\text{Mg}_2\text{TiO}_4$  phases [Ctibor, 2003].

Besides the mentioned dielectric titanate materials we have sprayed also one representative of ferroelectrics - barium titanate.  $\text{BaTiO}_3$  (BT) is an interesting multifunctional oxide that exhibits complex phase appearance. Between  $120^\circ\text{C}$  (393K) and  $1457^\circ\text{C}$  (1730K)  $\text{BaTiO}_3$  has a cubic perovskite structure that consists of corner linked oxygen octahedra containing  $\text{Ti}^{4+}$ , with  $\text{Ba}^{2+}$ . Cooling below  $120^\circ\text{C}$  results in small displacements in the positions of the cations in the unit cell resulting in polar ferroelectric phase existing in the temperature interval between  $5^\circ\text{C}$  (278K) and  $120^\circ\text{C}$  [Boutinaud, 2006].

$\text{BaTiO}_3$ , due to its high dielectric constant, is used frequently as multilayer capacitor components and sensors. However, it has been found that with respect to the electrical properties  $\text{BaTiO}_3$  in the form of thin-films does not reach the qualities of bulk material. This difference was explained by a combination of the intrinsic dead layer effect, a stress effect, an effect of the microstructure within the thin film, and an effect of the stoichiometry [Zhao, 2008]. In particular, the relative permittivity of films decreases when the film thickness is reduced [Setter, 2000]. The optimal dielectric characteristics are obtained for sintered  $\text{BaTiO}_3$ -based sample with bulk density of about  $5300 \text{ kg.m}^{-3}$  [Jin, 2003]. Any deviation from the stoichiometric Ba/Ti ratio leads to suppression of the high relative permittivity of the ferroelectric barium titanate [Mitic, 2001]. To detect the tetragonal  $\text{BaTiO}_3$  phase by X-ray diffraction, the split of peaks of (002) and (200) reflection is a well-established indication [Waser, 1999; Yu, 2009; Simon-Seveyrat, 2007].

In general there are differences of the behavior of barium titanate in the form of a single-crystal, sintered bulk material and thin film [Boutinaud, 2006; Mitic, 2001]. Plasma spraying enables to create layers with 'bulk-like' thickness but adhering on a metallic substrate of various shapes. Free-standing parts of titanate ceramics can be fabricated as well by plasma spraying [Wu, 2009].  $\text{BaTiO}_3$  itself was up to now very seldom plasma sprayed and the understanding of its behavior in the form of sprayed coating is not satisfactory. For coatings with the thickness of about  $100 \mu\text{m}$  the values of relative permittivity 50 and loss factor 0.08 were reported [Dent, 2001]. The dielectric properties of the plasma sprayed  $\text{BaTiO}_3$  were related to the degree of crystallinity [Dent, 2001]. The coatings containing more crystalline material have higher relative permittivity. The relative permittivity was affected also by cracks and splat interfaces within the coating [Dent, 2001]. The reported value of relative permittivity is however surprisingly low, because one and more orders higher values are typical for bulk  $\text{BaTiO}_3$  [Buchanan, 2004].

In frame of the presented chapter we are focused on selected aspects of the dielectric characteristics of the as-sprayed barium titanate coatings and we provide comparison of them with other plasma sprayed titanates.

## 2. Experimental

### 2.1 Feedstock materials

All materials were obtained in the form of tablets of industrial purity, produced by the sintering of micropowders. The sintering was carried out by companies Epsilon (Librice, Czech Republic), Ceramic Capacitors (Hradec Kralove, Czech Rep.) and Teceram (Hradec Kralove, Czech Rep.).

The synthetic form of perovskite  $\text{CaTiO}_3$  was produced by reactive sintering of  $\text{CaO}$  and  $\text{TiO}_2$ .  $\text{CaTiO}_3$  powder used for experiments was sintered without any additives (like  $\text{ZnO}$ ), normally used for decreasing the sintering temperature. Tablets were crushed and sieved into a powder of the correct size for spraying.  $\text{MgTiO}_3$  and MCT were sintered using  $\text{MgO}$ ,  $\text{CaCO}_3$  and  $\text{TiO}_2$ . After sieving the size distribution of the feedstocks was 63–125 microns for all three materials.

BaTiO<sub>3</sub> feedstock powder was obtained by crushing and sieving of sintered coarse agglomerates. Those agglomerates were prepared by a reactive sintering of micrometer-sized powders of BaCO<sub>3</sub> and TiO<sub>2</sub> used as starting materials. After sieving the size distribution of the BT feedstock for spraying was between 20 and 63 μm with an average at 40 μm, whereas the bulk density measured by helium pycnometry was 5721 kg.m<sup>-3</sup>.

## 2.2 Plasma spraying

The CT, MT and MCT samples were manufactured using a high throughput Water-Stabilized Plasma (WSP) spray system WSP500® at Institute of Plasma Physics (Prague, Czech Republic) at ambient atmosphere. The WSP system operates at about 160 kW arc power and can process high amounts of material. This system can be used to fabricate deposits similar but not identical to those prepared by means of conventional atmospheric plasma-spray systems based on gas-stabilized torches. As substrates flat carbon steel coupons (Euronorm S355) were used whereas the powder was fed in by compressed air through two injectors. Just before spraying, the steel was grit blasted with Al<sub>2</sub>O<sub>3</sub> with a mean diameter of 650 μm. The deposited thickness was about 1.5 mm for self-supporting deposits. Thick deposits were stripped from the substrate by a releasing agent or by thermal cycling between +200 and -70°C.

For manufacturing of BT samples a Gas-Stabilized Plasma gun (GPS) was used to perform Atmospheric Plasma Spraying (APS) process. The conventional d.c. GPS gun F4 consisted of a thoriated tungsten cathode of 10 mm in diameter with a conical tip and a copper anode/nozzle. The plasma gas mixture used was argon/hydrogen with the total flow rate 60 slm. The powder was injected perpendicularly to the plasma jet axis with argon as a carrier gas (at constant flow rate 5 slm at pressure 0.3 MPa for all spray experiments) through an injector located 3 mm downstream (called external injection) of the torch nozzle exit. The system can process 1 to 5 kg/hour of a ceramic powder. Barium titanate was sprayed at arc power around 30 kW. Spray distance was 100 mm and plasma spraying deposition time about five minutes to reach the thickness 0.9 to 1 mm. Substrates, rectangular shaped (120x20 mm<sup>2</sup>) 3 mm thick, were made of carbon steel (Euronorm S355). Just before spraying, they were grit blasted with Al<sub>2</sub>O<sub>3</sub> with a mean diameter of 400 μm. The substrates were disposed on a rotating sample holder which diameter was 90 mm. This substrate holder was rotated (tangential speed of 1 m/s) with a horizontal axis and simultaneously translated back and forth orthogonally to the plasma jet axis at a velocity of 24 mm/sec, with an excursion of 160 mm, the plasma torch being stationary.

## 2.3 Characterization techniques

X-ray diffraction (XRD) was performed as a phase identification with SIEMENS D5000™ equipment *allowed* identifying *phases* present within powders and coatings. For estimation of the crystallinity of the plasma sprayed BT coating relative peak areas have been used. These have been calculated from relative ratios of the areas of the three main peaks (101, 111 and 200) from the tetragonal titanate phase.

Raman spectra were collected by the FORAM 685 apparatus which is equipped by a 685 nm laser with output power up to 40 mW. Spectral resolution 8 cm<sup>-1</sup> and various integration times from 10 to 60 seconds were used. Raman spectroscopy of BT was performed using a Lambda Solutions P1 apparatus – laser wavelength 785 nm, objective 50 x, integration time 25 s. The surface of the coating was polished before the test.

Infrared reflective spectra of CT samples were measured by Bruker IFS 113v Fourier transform spectrometer.

Microwave microscope Agilent AFM 5400 was used for simultaneous monitoring of the surface profile by AFM and dielectric response on external field applied at resonant frequency (approx. 2.6 MHz). This relatively new technique - near-field scanning microwave microscopy (SMM) permits characterization of the effects of inhomogeneities and defects in crystals, films, and compacts on the local dielectric behavior. By moving the tip/cavity assembly over a surface, one can map the microwave cavity resonant frequency  $f_r$  and quality factor  $Q$  as a function of position and generate images of the sample. In addition to qualitative images, the microscope can provide quantitative characterization of local dielectric properties [Cheng, 2003].

The complex dielectric permittivity of CT was studied in the 440 Hz - 1 MHz frequency range and 10-270K temperature interval using HP 4192A impedance analyzer with a Leybold He-flow cryostat (operating range 5-300 K). The impedance of the cylindrical sample with Au electrodes sputtered on the cylinder ends was recorded on cooling rate of 2 K/min.

All other electric measurements were performed at room temperature. The deposits were stripped of from the substrates. The surfaces were ground after spraying to eliminate surface roughness. A thin layer of aluminum as the electrode was sputtered in a reduced pressure on the ground surface [Ctibor, 2003]. A three-electrode system was used with a guarded electrode, whereas an unguarded electrode was sputtered on the entire surface of the sample opposite side. The electric field was applied parallel with the spraying direction (i.e., perpendicular to the substrate surface). Capacity was measured in the frequency range from 120 Hz to 1 MHz using the impedance analyzer 4284A (Agilent, CA, USA). Applied voltage was 1V AC whereas the stabilized electric source was equipped with a micrometric capacitor type 16451A (Agilent, CA, USA). Relative permittivity  $\epsilon_r$  was calculated from measured capacities  $C_P$  and specimen dimensions (Eq. 1)

$$C_P = \epsilon_0 \times \epsilon_r \times 1/k \quad (1)$$

where  $\epsilon_0 = 8.854 \times 10^{-14}$  F cm<sup>-1</sup>;  $1/k$  [cm] is defined as the ratio between the guarded surface and the thickness of the sample [Morey, 2003].

This same arrangement and equipment was used for the loss factor measurement at the same frequencies as capacity.

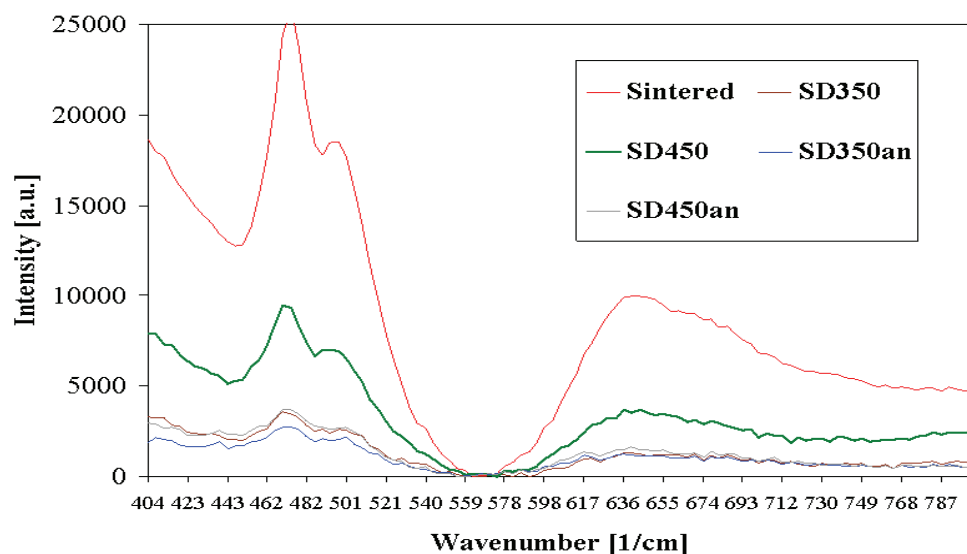
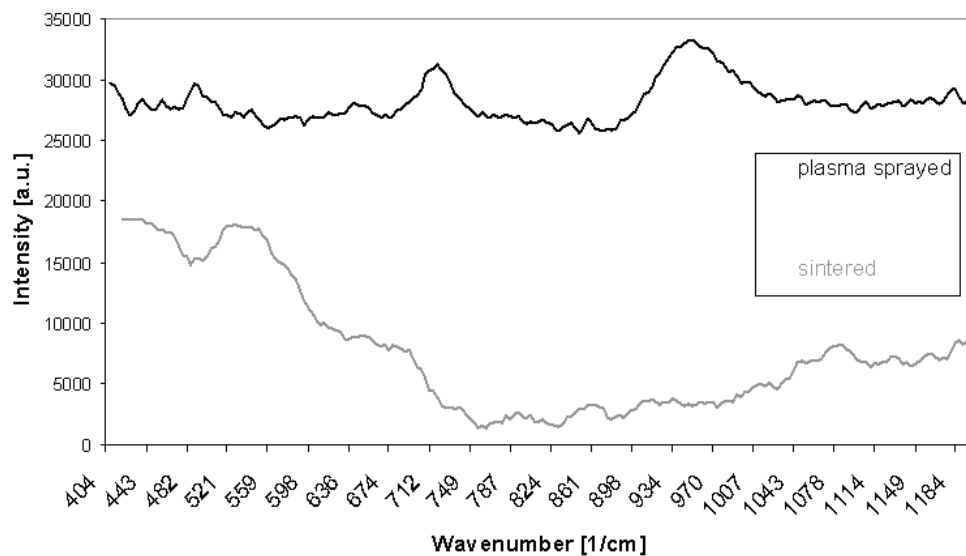
Electric resistance was measured with a special resistivity adapter - Keithley model 6105. The electric field was applied from a regulated high-voltage source and the values read by a multi-purpose electrometer (617C, Keithley Instruments, USA). The magnitude of the applied voltage was 100±2V DC. Volume resistivity was calculated from the measured resistance and specimen dimensions. Typically 4 - 5 specimens were measured and the average calculated.

### 3. Results

#### 3.1 Spectroscopic measurements

**Figure 1** shows the Raman spectra of plasma sprayed CT in comparison with the sintered sample. SD means stand-off distance, in millimeters, of the as-sprayed samples and "an" denotes annealed samples. Annealing details are given elsewhere [Ctibor, 2003].



Fig. 1. Raman spectrum of  $\text{CaTiO}_3$ Fig. 2. Raman spectrum of  $\text{MgTiO}_3$ 

The absolute values of the intensity of the reflection are associated with surface roughness and could be omitted. From the graph we see that the positions of all peaks are identical for all samples. Wavenumbers of all three main peaks observed at 471, 495, and 640  $\text{cm}^{-1}$  are in

agreement with [Cavalcante, 2008]. The bands at 471 and 495  $\text{cm}^{-1}$  are assigned to Ti-O torsional (bending or internal vibration of oxygen cage) modes [Hirata, 1996; Zheng, 2003]. The Ti-O stretching mode is centered at 640  $\text{cm}^{-1}$  [Boutinaud, 2006]. Two small peaks at about 650  $\text{cm}^{-1}$ , suggesting the simultaneous presence of  $[\text{TiO}_6]$  and  $[\text{TiO}_5]$  clusters, however in our case they are even less pronounced compare to [Cavalcante, 2008]. Also in our plasma sprayed samples incomplete organization of the  $\text{CaTiO}_3$  lattice can be attributed to the defects in the covalent bond due to the oxygen vacancies ( $\text{VO}^{\bullet\bullet}$ ) between the clusters  $[\text{TiO}_6\text{-TiO}_5\cdot\text{VO}^{\bullet\bullet}]$  as in [Cavalcante, 2008]. This is associated with slightly reducing atmosphere in the plasma stream based on H and O atoms (water stabilization).

The Raman spectrum of MT is displayed on the Fig. 2 in which the active modes at 478  $\text{cm}^{-1}$  and 501  $\text{cm}^{-1}$  [Hirata, 1996] are observed only on the coating. Next active modes are at 641 and 712  $\text{cm}^{-1}$  [Hirata, 1996] and also were detected only on the coating, whereas in the sintered sample a shoulder centered at about 530  $\text{cm}^{-1}$  is present.

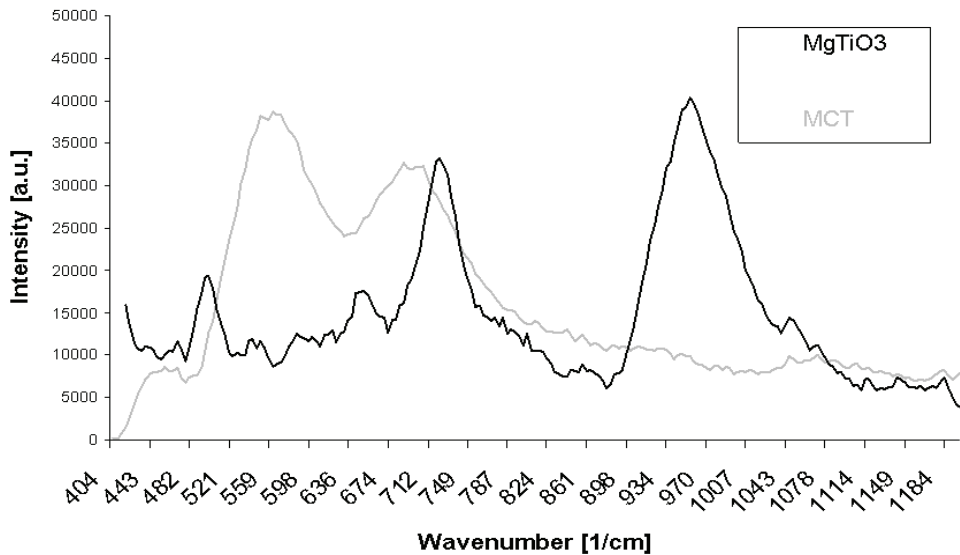


Fig. 3. Raman spectrum of MCT

The Raman spectrum of plasma sprayed MCT is displayed on the Fig. 3 in comparison with MT measured at exactly the same conditions. We can see for MCT a red shift of the peak centered at 712  $\text{cm}^{-1}$  in the case of MT. Other pronounced maximum is at 565  $\text{cm}^{-1}$ . The Raman pattern of MCT is different compare to MT and CT and moreover it is not a simple combination of both of them. This is because of  $\text{MgTi}_2\text{O}_5$  and  $\text{Mg}_2\text{TiO}_4$  origin during the spraying, as confirmed by XRD [Ctibor, 2003]. However only two phases with different relative permittivity were detected by scanning microwave microscopy, see Fig. 4, similarly as in [Zhang, 2006]. Permittivities of  $\text{MgTi}_2\text{O}_5$ ,  $\text{Mg}_2\text{TiO}_4$  and MT are very similar together and very different from CT. Figure 4 is a superposition of the AFM contact mode image (roughness) and scanning microwave microscopy capacitance mode image (colors). The image is artificially colored – blue and red zones represent different relative permittivity.

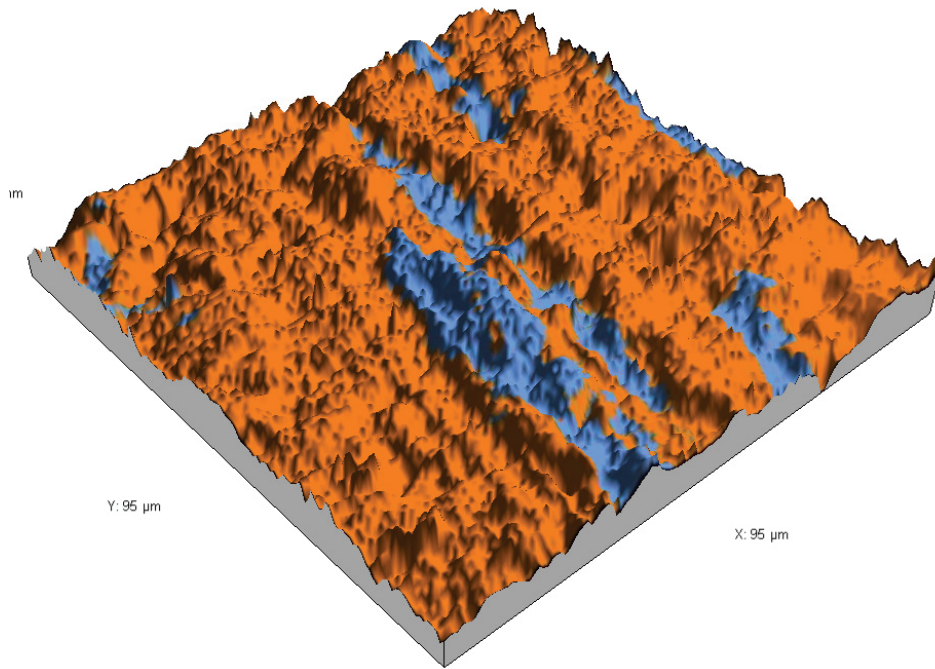


Fig. 4. Scanning microwave microscopy image of MCT as-sprayed surface (artificially colored – blue and red zones represent different relative permittivity)

CT (perovskite) is a high permittivity material  $\epsilon_r' = 170$  [Ferreira, 1997],  $\text{MgTiO}_3$  (gikielilite) has a low  $\epsilon_r' = 17$  [Zeng, 1997] and  $\text{Mg}_2\text{TiO}_4$  (qandilite) also has even lower  $\epsilon_r' = 12$  [Haefie, 1992]. However SMM setup is not able to distinguish well the two last phases [Wing, 2006], also in our Fig. 4 the blue lamellas correspond to CT, c.f. Fig. 5, and the red background to all other phases.

Raman spectrum of BT coating is displayed on Fig. 6. The spectrum with peaks at 311 and 507  $\text{cm}^{-1}$  corresponds to tetragonal phase of  $\text{BaTiO}_3$  [Souza, 2006]. At low oxygen pressure which is the condition relevant for plasma spraying, the density of oxygen vacancies is higher, and then the expansion of the lattice volume is greater [Souza, 2006]. This is why the Raman modes shift to lower frequencies: 507  $\text{cm}^{-1}$  in our case instead of 518  $\text{cm}^{-1}$  [26] or 532  $\text{cm}^{-1}$  in [Souza, 2006] for the  $A_1$  torsion mode. Raman spectrum of the long-SD coating is practically identical.

The modes further split into longitudinal (LO) and transverse (TO) components. The spectrum in Fig. 6 shows the stretching mode of  $A_1(\text{TO}_1)$ ,  $A_1(\text{TO}_2)$  and  $A_1(\text{TO}_3)$  at around 163, 259 and 507  $\text{cm}^{-1}$ , respectively [Mattsson, 2010; Guo, 2005]. The stretching mode of E ( $\text{TO}_2$ ) appeared at 311  $\text{cm}^{-1}$ , while  $A_1(\text{LO}_1)$  stretching modes at 188  $\text{cm}^{-1}$  and  $A_1(\text{LO}_2)$  at about 470  $\text{cm}^{-1}$  [Mattsson, 2010], however the last one was not very pronounced in our case. By the Raman spectroscopy presence of  $\text{TiO}_2$  in anatase form was mentioned - the peak at about 645  $\text{cm}^{-1}$  was observed in  $\text{TiO}_2$  film [Gioli, 2007] or coating [Buralcov, 2007]. Elsewhere [Ostapchuk, 2005] such a peak was shown without comments. In our case also weak peak at 631  $\text{cm}^{-1}$  was detected, which can correspond to anatase- $\text{TiO}_2$  individual phase in the  $\text{BaTiO}_3$  coating.

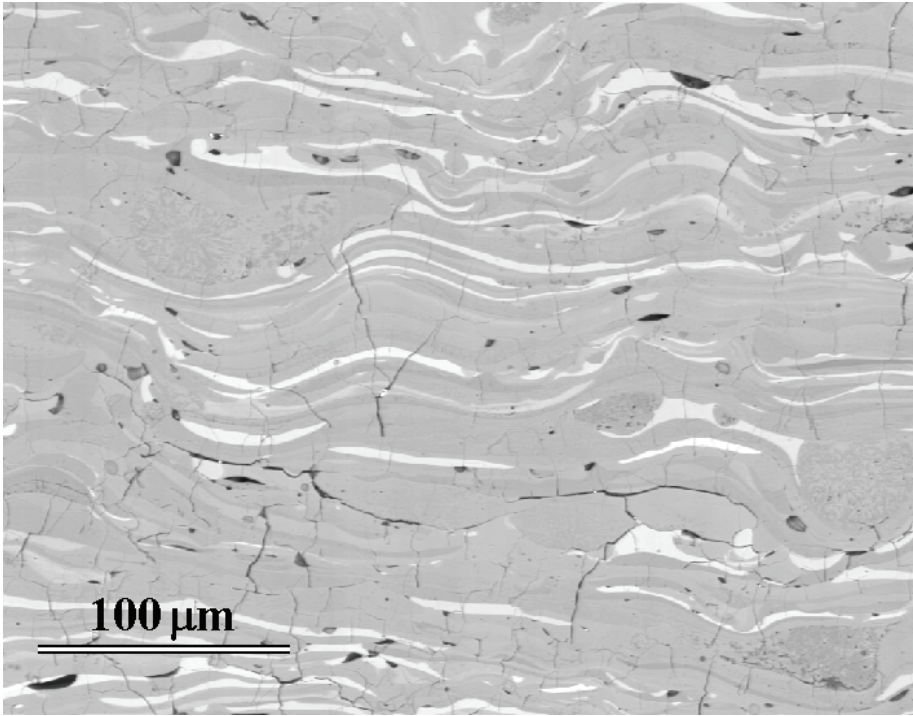


Fig. 5. SEM-BE image showing the lamellar microstructure

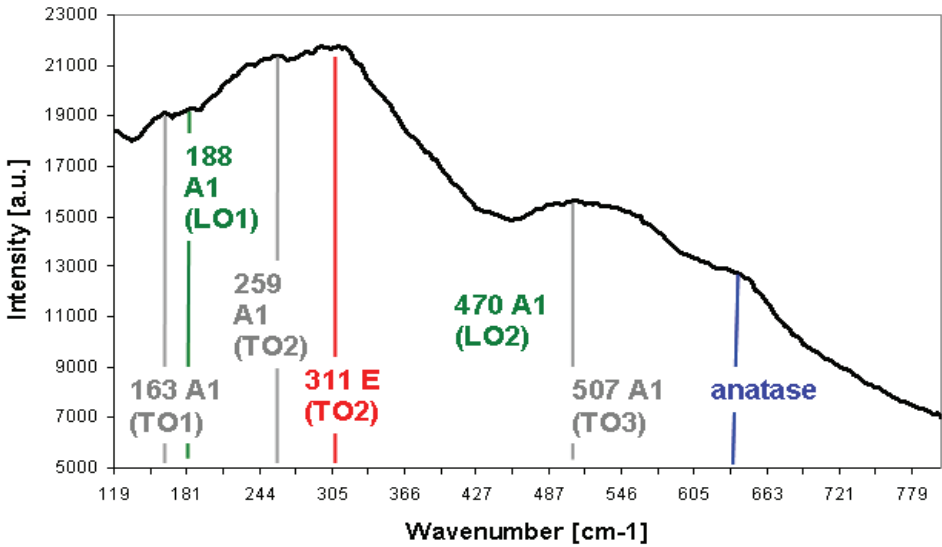


Fig. 6. Raman spectrum of plasma sprayed BaTiO<sub>3</sub>

**Figure 7** shows the infrared spectra of plasma sprayed CT in comparison with the sintered sample. The infrared-active mode at  $575\text{ cm}^{-1}$ , assigned to the Ti-O stretch, and also the mode at  $455\text{ cm}^{-1}$ , assigned to the Ti-O<sub>3</sub> torsion, are present in both samples with the same intensity. The slightly more pronounced local valley in the case of plasma sprayed sample – localized at about  $680\text{ cm}^{-1}$  is the only subtle distinction.

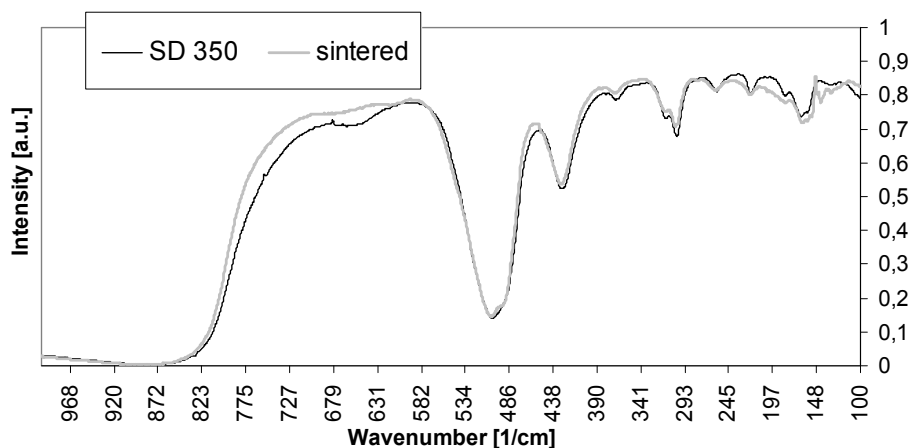


Fig. 7. Infrared spectrum of  $\text{CaTiO}_3$

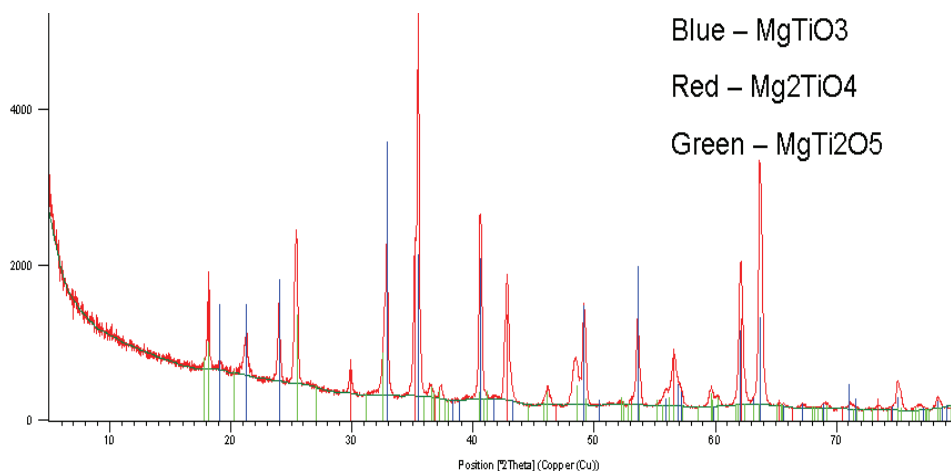


Fig. 8. XRD pattern of plasma sprayed  $\text{MgTiO}_3$

According X-ray diffraction measurement of CT coating, the phase composition is the same as in the feedstock powder – pure  $\text{CaTiO}_3$  (PDF2 card No. 00-022-0153). The XRD pattern of MT, **Fig. 8**, shows that the original metatitanate partly decomposed during the spray process on  $\text{Mg}_2\text{TiO}_4$  and  $\text{MgTi}_2\text{O}_5$ . All these components are present also in MCT coating, **Fig. 9**, whereas also  $\text{CaTiO}_3$  is present as an individual phase.

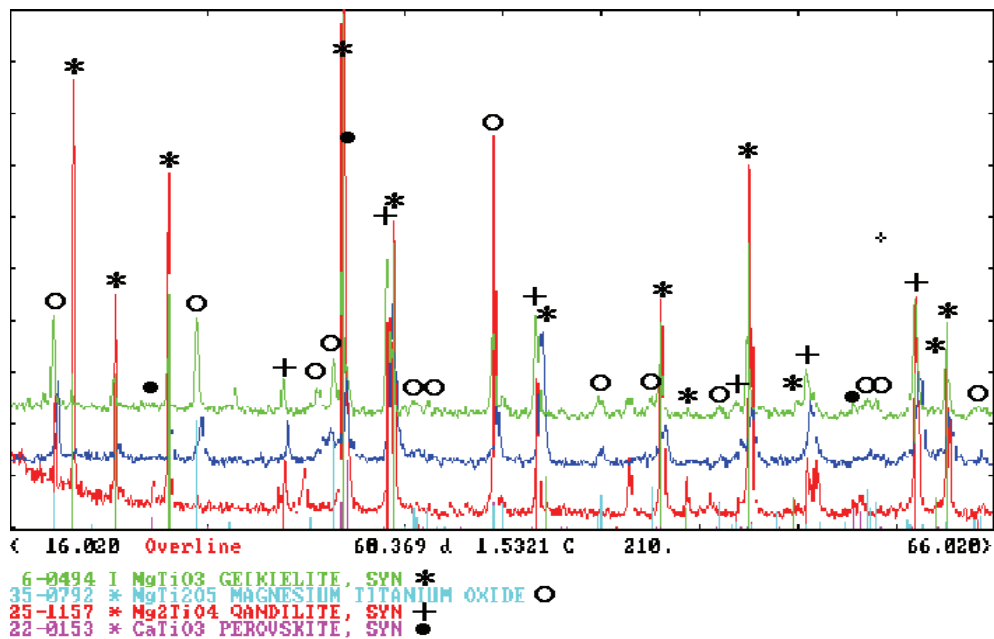


Fig. 9. XRD pattern of plasma sprayed MCT

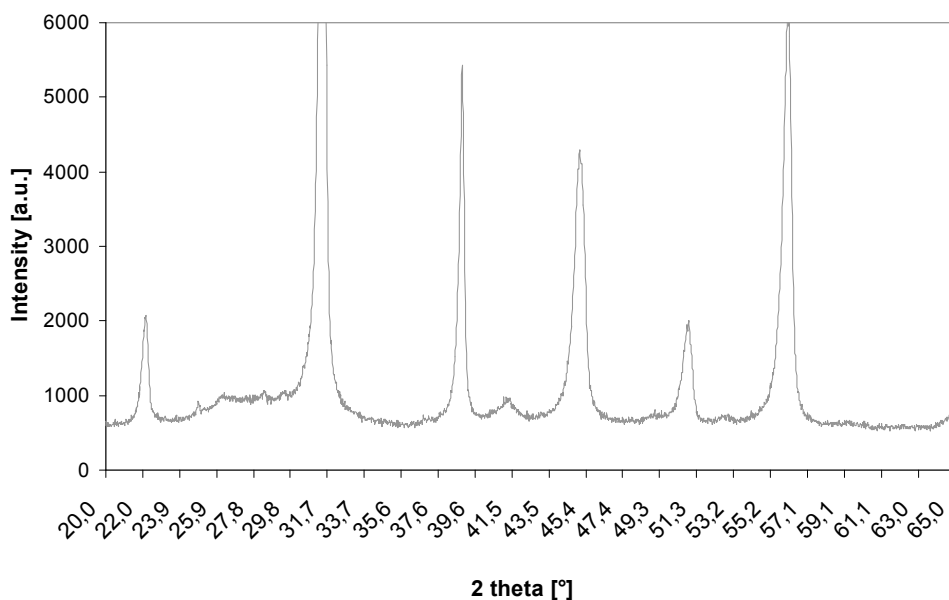


Fig. 10. XRD pattern of plasma sprayed BT coating

The XRD pattern of BT, **Fig. 10**, corresponds strictly to the tetragonal phase (PDF2 card No. 01-081-2204), which was confirmed to be the constituent of the feedstock powder as well as of the coatings. Intensity ratio of individual peaks of the feedstock as well as of the coatings is very similar to patterns reported in the literature [Wang, 2008]. In the coating, certain quantity of amorphous phase is present, manifested itself by a halo centered on  $28^\circ 2\theta$  in the pattern, and quantified as 10 %.

### 3.2 Dielectric measurements

Dielectric properties of plasma sprayed  $\text{CaTiO}_3$  between 10 K and room temperature are displayed on the **Figures 11 to 13**. The incipient ferroelectricity of CT [Lemanov, 1999; Sudheendran, 2008] is suppressed in the case of plasma sprayed coatings, see **Fig. 11**. Rather relaxor type of behavior takes place. Relaxor features are believed to be connected with a situation when more than one type of ions occupies equivalent crystallographic position. One of the most important features of relaxors is their low frequency dispersion at maximum dielectric permittivity. The other features of this include dependence of phase transition temperature on the method of its determination. The origin of such properties is probably connected with a presence of microscopic polar regions (nano-domains) in these materials [Bak, 2009]. With temperature falling down also the  $\epsilon''$  values decrease to minimum (for a given frequency), cf. **Fig. 12**.

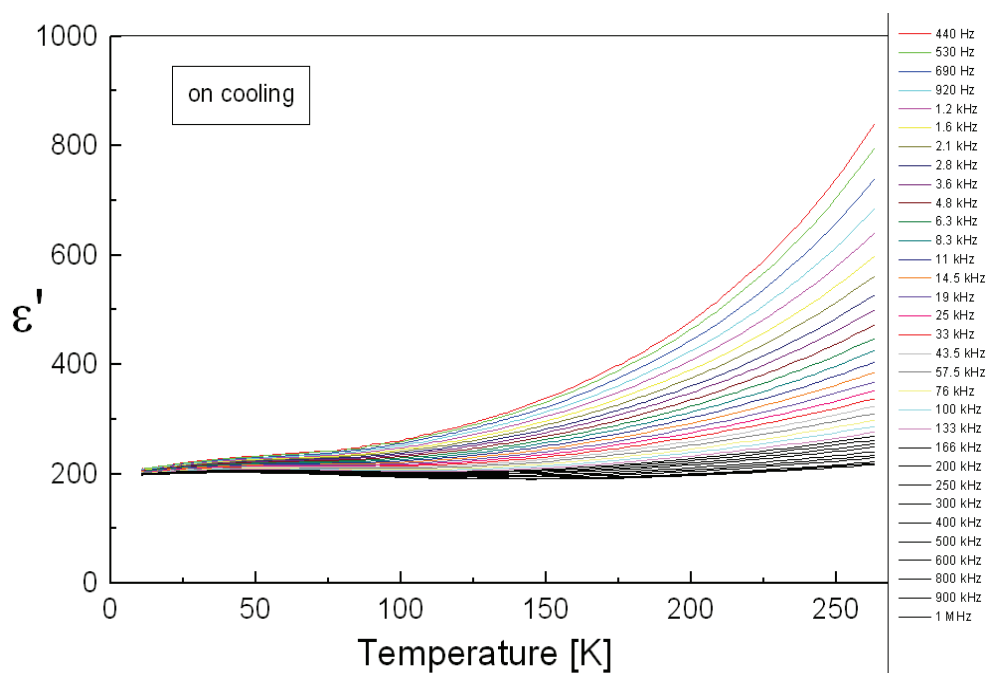


Fig. 11. Real part of permittivity of plasma sprayed  $\text{CaTiO}_3$  between 10 K and room temperature

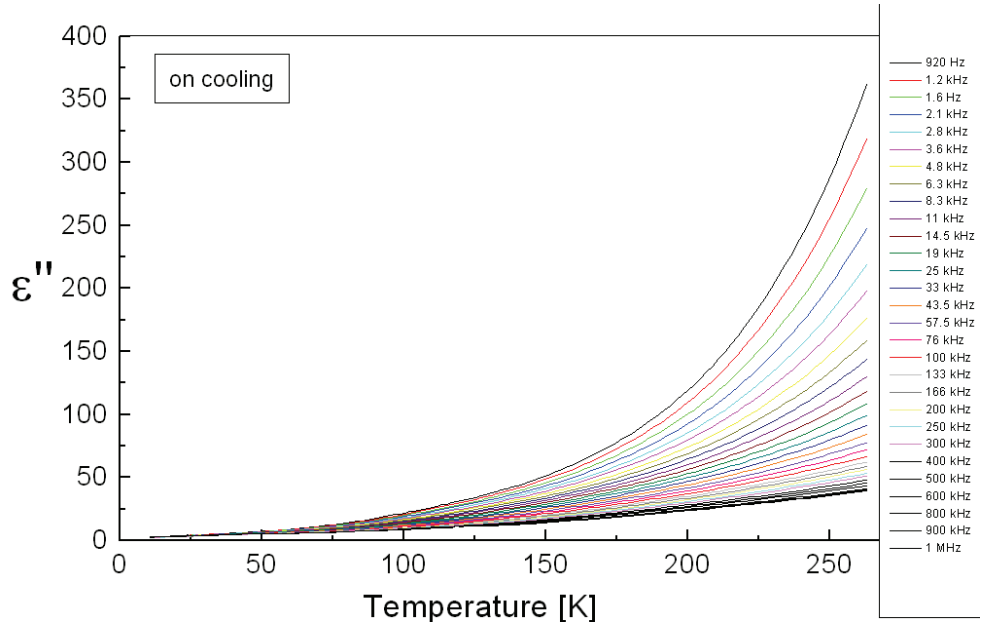


Fig. 12. Imaginary part of permittivity of plasma sprayed  $\text{CaTiO}_3$  between 10 K and room temperature

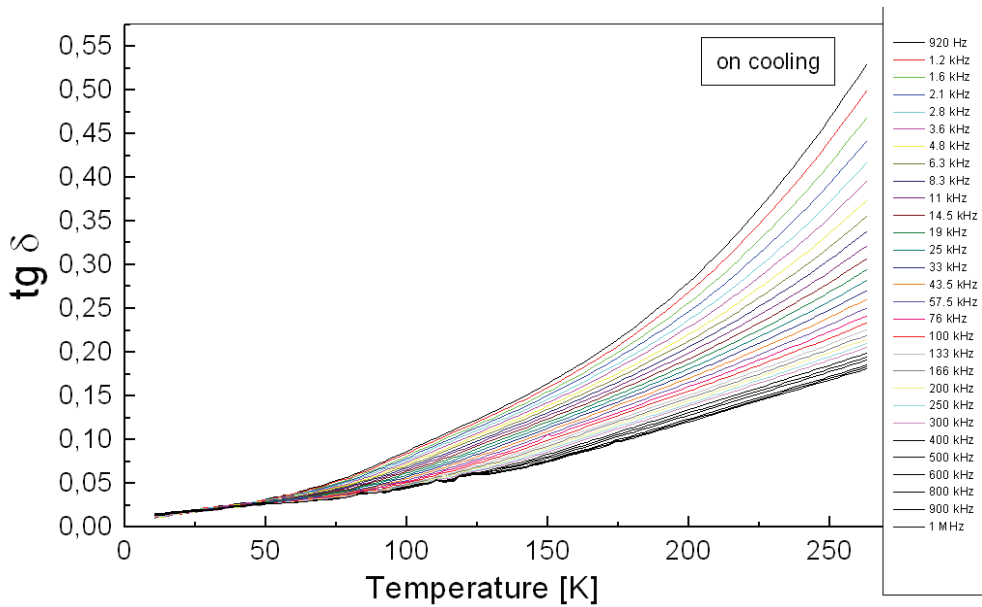


Fig. 13. Loss tangent of plasma sprayed  $\text{CaTiO}_3$  between 10 K and room temperature



In the studied frequency range, the relative permittivity of all specimens exhibits significant ionic relaxation process [Dervos, 2004]. Strong relaxation effects is shown by the  $\epsilon_r'$  reduction with the operating frequency, see Fig. 14. In Ti-based materials, the concentrations of intrinsic defects are determined by oxygen partial pressure and, additionally, variations in defect concentrations can be detected by conductivity measurements. At low oxygen partial pressures the materials show n-type conduction with oxygen vacancy as the dominant defect while at high oxygen partial pressures the materials show p-type conduction with the cation vacancy as the dominant defect. For the different materials the transition from n-type conduction to p-type conduction occurs at different oxygen partial pressures [Hu, 2011]. The partial pressure of oxygen required to reduce for example  $\text{TiO}_2$  to  $\text{Ti}_2\text{O}_3$ ,  $\text{Ti}_3\text{O}_5$  or  $\text{Ti}_4\text{O}_7$  is of the order of  $10^{-5}$  Pa at around  $2000^\circ\text{C}$ , while during plasma spraying in the air, oxygen partial pressure does not go below 1 Pa [Ctibor, 2010]. Dielectric losses of our titanate samples, namely BT and CT are however high, see Fig. 15. Electric conductivity is responsible for it with dominating contribution of dc-conductivity component. The  $\epsilon''$  dependence can be treated as typical for materials with dc-conductivity which dominates over relaxation processes [Bak, 2008].

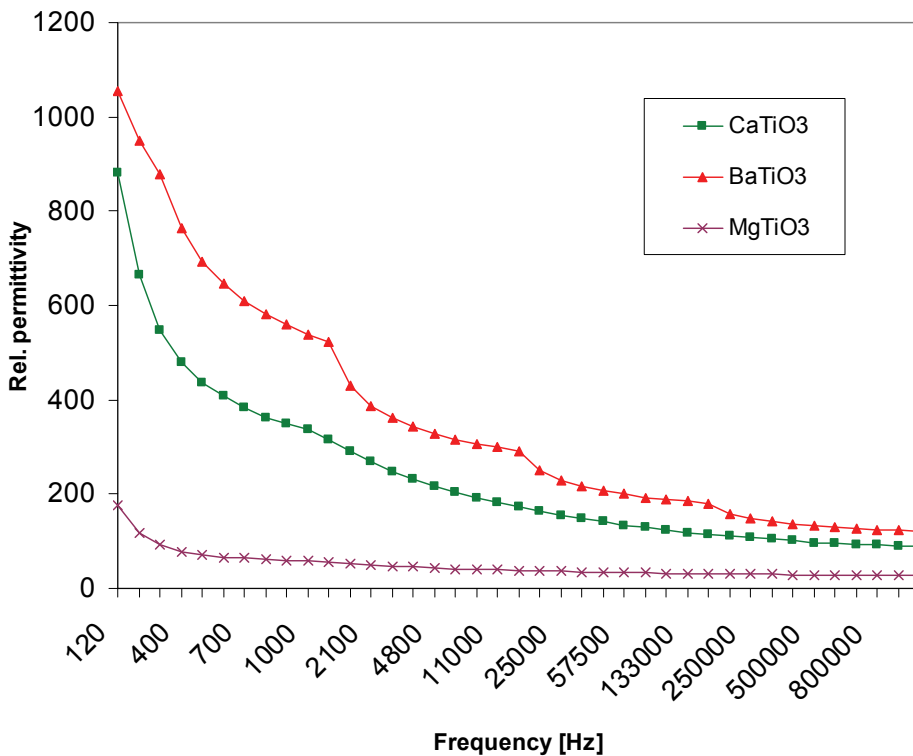


Fig. 14. Frequency dependence of the relative permittivity of plasma sprayed  $\text{BaTiO}_3$ ,  $\text{CaTiO}_3$ , and  $\text{MgTiO}_3$  at room temperature

Table 1 shows the volume resistivity and **Fig. 16** corresponding conductivity of plasma sprayed and sintered BT, CT, MT and MCT materials. We see the different values with typically several orders of magnitude lower resistivity values for plasma sprayed specimen compare to sintered materials.

Sample	BT (P)	BT (S)	CT (P)	CT (S)	MT (P)	MT (S)	MCT (P)	MCT (S)
$\rho$ [ $\Omega\text{m}$ ]	$6.08 \times 10^4$	$2.42 \times 10^9$	$7.51 \times 10^9$	$1.41 \times 10^{12}$	$1.15 \times 10^8$	$6.90 \times 10^{11}$	$1.17 \times 10^7$	$7.54 \times 10^{11}$

Table 1. Volume resistivity of studied materials (P – plasma sprayed, S – sintered)

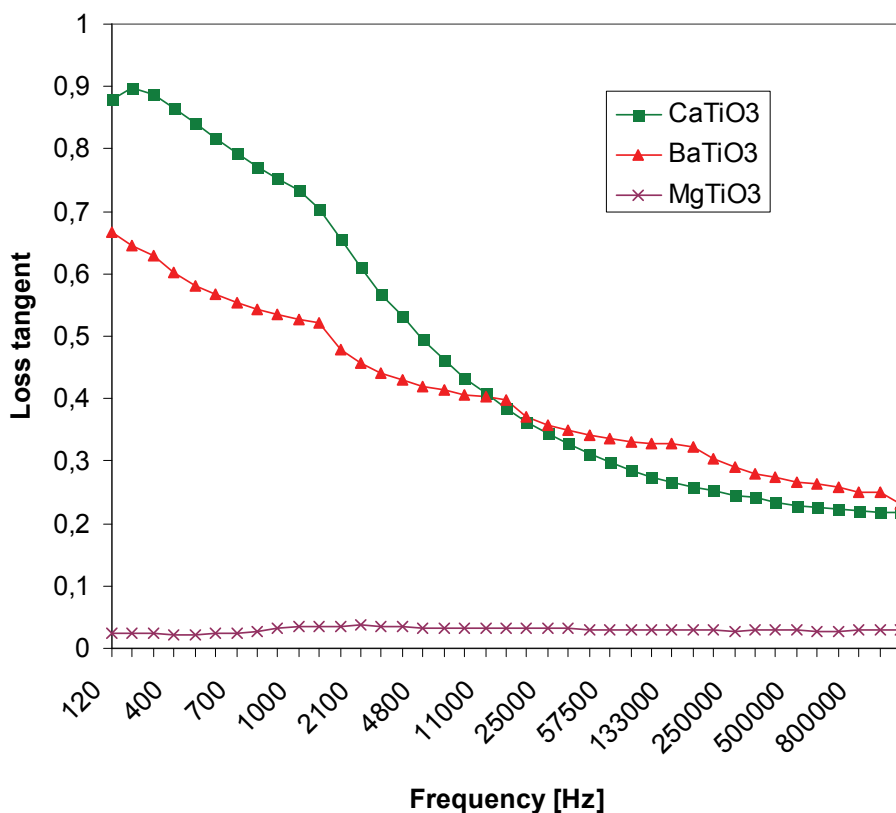


Fig. 15. Frequency dependence of the loss tangent of plasma sprayed BaTiO<sub>3</sub>, CaTiO<sub>3</sub>, and MgTiO<sub>3</sub> at room temperature

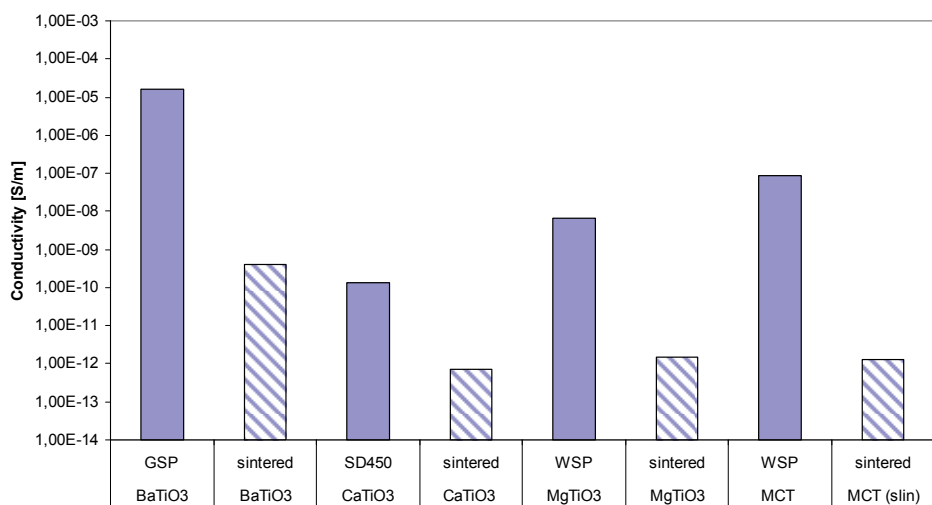


Fig. 16. Conductivity of plasma sprayed and sintered BT, CT, MT and MCT

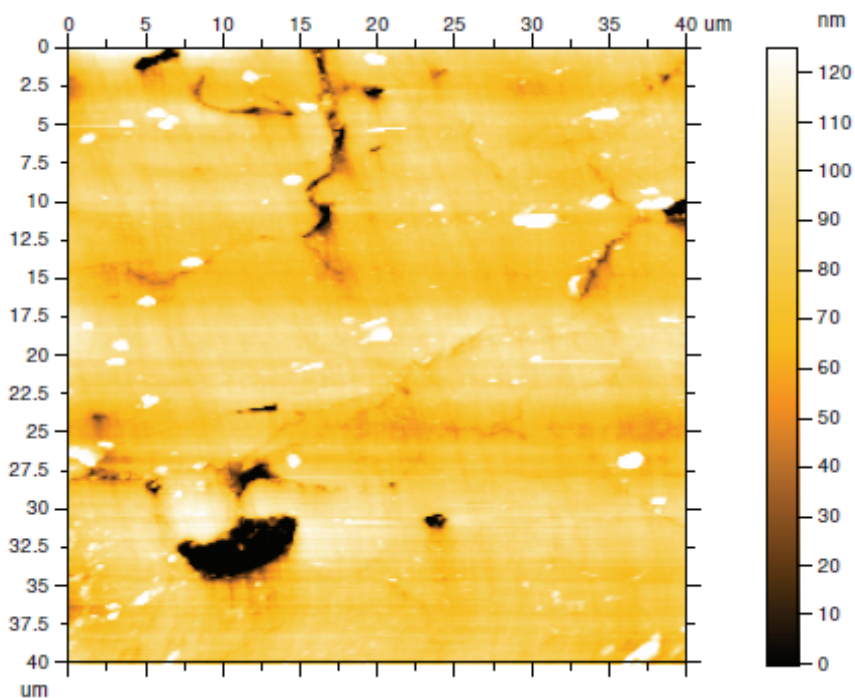


Fig. 17. AFM contact mode image of BaTiO<sub>3</sub> (in plane orientation). Roughness representation: peaks are lighter and valleys darker (black color represents pores)

### 3.3 Scanning microwave microscopy

Scanning microwave microscopy images of BT are given on **Figs. 17** and **18**. AFM images represent surface roughness. Since the surface was materialographically polished, the subtle differences in the roughness are associated with hardness of various phases. These phases are concentrated predominantly in individual lamellas, cf. MCT SEM micrograph in the **Fig. 5**. In the case of BT, the difference between lamellas is mainly in terms of Ba/Ti ratio [Ctibor 2, 2010]. Such a feature is, as expectable, more easily visible on cross sections, **Fig. 19**, then on in-plane (i.e. spray direction) sections **Fig. 18**. The lamellas, red and yellow on capacitance mode images, are more Ti-rich (higher permittivity) whereas blue areas are Ba-rich (lower permittivity). The Ba-rich phase has slightly lower hardness (hardness measured by us:  $\text{BaTiO}_3$  is about 6.5 GPa versus  $\text{TiO}_2$  about 11.0 GPa; BaO not reported as a layer). The Ba-rich phase is darker on AFM contact mode image, since it is more easily worn-out by polishing process. These “steps” on border of lamellas are about 80 nm high, see also **Fig. 20**, which height is consistent with observations made by SEM.

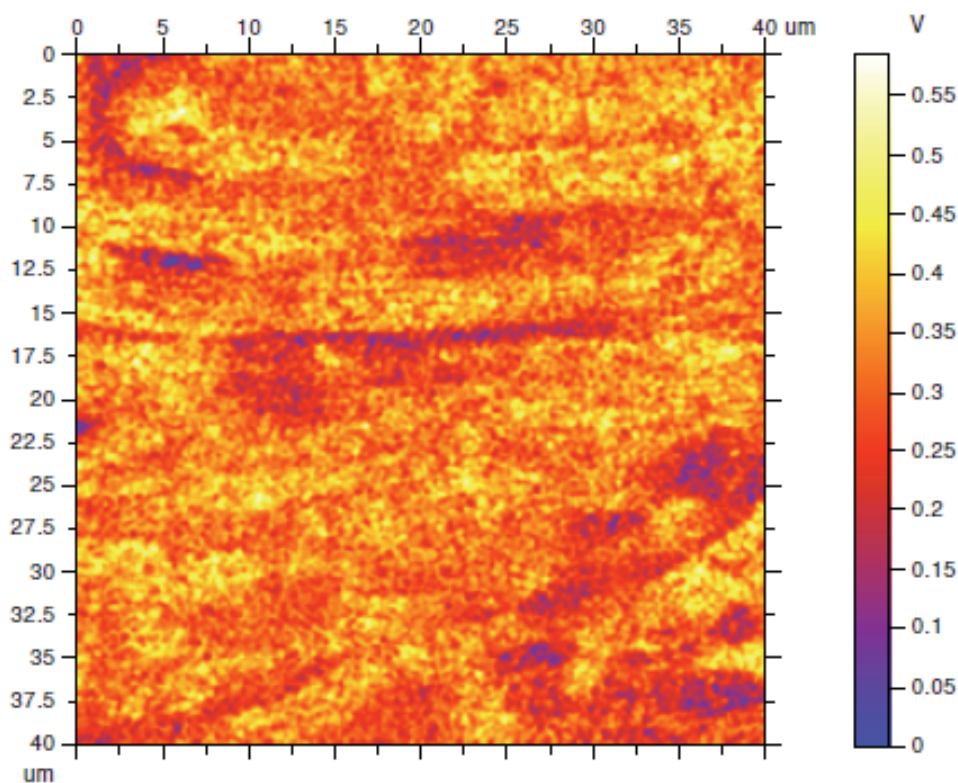


Fig. 18. Scanning microwave microscopy image of  $\text{BaTiO}_3$  (in plane orientation) - artificially colored: blue and red zones represent different relative permittivity

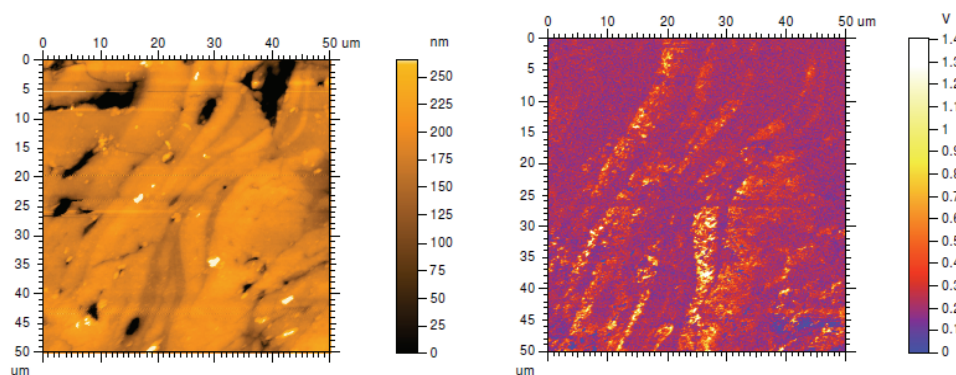


Fig. 19. AFM contact mode image of  $\text{BaTiO}_3$  (cross sectional orientation). Left: Roughness representation: peaks are lighter and valleys darker (black color represents pores). Right: Scanning microwave microscopy image of  $\text{BaTiO}_3$  (cross sectional orientation) - artificially colored: blue and red zones represent different relative permittivity

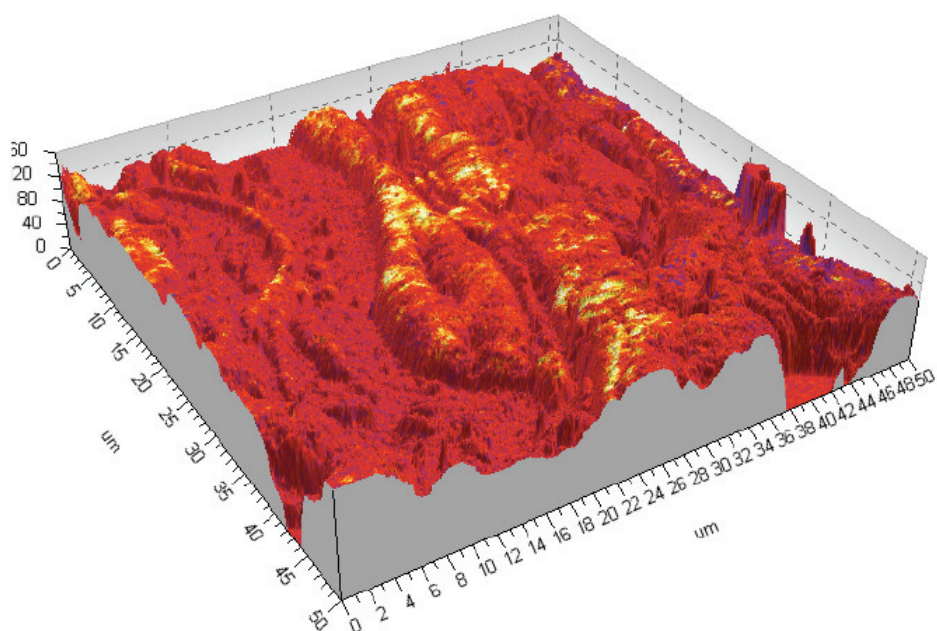


Fig. 20. Superposition of the AFM contact mode image and SMM image -  $\text{BaTiO}_3$  cross section. Hard and high-permittivity Ti-rich lamellas are yellow

#### 4. Conclusions

$\text{BaTiO}_3$ ,  $\text{CaTiO}_3$ ,  $\text{MgTiO}_3$  and a mixture of the last two materials with 5 wt.% of  $\text{CaTiO}_3$  in  $\text{MgTiO}_3$  were plasma sprayed by two complementary spray techniques. Raman and infrared

spectroscopic measurements were carried out on plasma sprayed titanates. Coating samples were tested as mono-block capacitors. Volume dc-resistivities of the materials were summarized. Microwave microscopy was used for mapping of the dielectric response of selected samples.

CaTiO<sub>3</sub> exhibits anomalous dielectric losses because of intrinsic conductivity. Relaxor type of behavior takes place at dielectric measurements, whereas dc-conductivity is responsible for the high dielectric losses. All coatings are slightly oxygen deficient – however under detection limits of XRD materials – the color of all of them is darker compare to sintered samples.

Polarization of grain boundaries combined with n-type conduction with oxygen vacancy as the dominant defect contributes to the observed pseudo-relaxor response of BaTiO<sub>3</sub> and CaTiO<sub>3</sub> to AC electric field. MgTiO<sub>3</sub> as a low-loss material has the above mentioned effects slightly suppressed and is more similar to sintered bulk. The existence of irregularities in the crystal lattice was confirmed by spectroscopic measurements. Plasma spraying of applicable ceramic dielectrics able to substitute bulk parts will need further research. In the other hand, plasma spraying, with its possibility to cover wide range of substrate materials with thick coatings having very versatile thicknesses and areas, offers promising way to future development.

## 5. Acknowledgment

The authors thank to J. Dubsky (IPP ASCR) for XRD measurements, to M. Savinov (Inst. of Physics, ASCR) for the temperature measurement of dielectric properties of CaTiO<sub>3</sub> and to V. Zelezny (Inst. of Physics, ASCR) for doing the infrared spectroscopy. Scanning microwave microscopy was done by M. Fenner (Agilent, Germany). The company ELMES, Lt.D. is acknowledged for lending of the Foram device. BaTiO<sub>3</sub> was sprayed at University of Limoges, France.

This work was supported by IPP ASCR under project AV0Z20430508.

## 6. References

- Bak W.; Starzyk, F.; Kajtoch, C. & Nogas-Cwikiel, E (2008). Elevated temperature induced dispersion phenomena in Ba<sub>1-x</sub>Na<sub>x</sub>Ti<sub>1-x</sub>Nb<sub>x</sub>O<sub>3</sub>. *Archives of Materials Science and Engineering*, Vol. 29, No. 1, pp. 5-9
- Bak W. (2009). Study of the relaxor behaviour in Ba<sub>0.68</sub>Na<sub>0.32</sub>Ti<sub>0.68</sub>Nb<sub>0.32</sub>O<sub>3</sub> ceramic. *Journal of Achievements in Materials and Manufacturing Engineering*, Vol. 37, pp. 24-27
- Boutinaud, P.; Tomasella, E.; Ennajdaoui A. & Mahiou R. (2006), Structural characterization and luminescent properties of CaTiO<sub>3</sub>:Pr<sup>3+</sup> thin films deposited by radio frequency sputtering. *Thin Solid Films*, Vol. 515, pp. 2316-2321
- Buchanan, R.C. (2004). Ceramic materials for electronics (3<sup>rd</sup> edition), M. Dekker, New York
- Burlacov, I.; Jirkovsky, J.; Kavan, L.; Ballhorn, R. & Heimann, R.B. (2007). Cold gas dynamic spraying (CGDS) of TiO<sub>2</sub> (anatase) powders onto poly(sulfone) substrates: Microstructural characterisation and photocatalytic efficiency, *Journal of Photochemistry and Photobiology A: Chemistry*, Vol. 187, pp. 285-292
- Cavalcante, L.S. et al. (2008). Synthesis, structural refinement and optical behavior of CaTiO<sub>3</sub> powders: A comparative study of processing in different furnaces. *Chemical Engineering Journal*, Vol. 143, pp. 299-307

- Ctibor, P.; Sedlacek, J.; Neufuss, K. & Chraska, P. (2003). Dielectric relaxation in calcium titanate-containing ceramics prepared by plasma spraying. *Ceramics International*, Vol. 29, pp. 955-960
- Ctibor, P. & Hrabovsky, M. (2010). Plasma sprayed TiO<sub>2</sub>: The influence of power of an electric supply on particle parameters in the flight and character of sprayed coating. *Journal of the European Ceramic Society*, Vol. 30, pp. 3131-3136
- Ctibor, P.; Ageorges, H.; Sedlacek, J. & Ctvrtlik, R. (2010). Structure and properties of plasma sprayed BaTiO<sub>3</sub> coatings, *Ceramics International*, Vol. 36, pp. 2155-2162
- Cheng H.-F. et al. (2003). Study of second-phases in Ba(Mg<sub>1/3</sub>Ta<sub>2/3</sub>)O<sub>3</sub> materials by microwave near-field microscopy. *Journal of the European Ceramic Society*, Vol. 23, pp. 2667-2670.
- Dent, A.H. et al. (2001). High velocity oxy-fuel and plasma deposition of BaTiO<sub>3</sub> and (Ba,Sr)TiO<sub>3</sub>. *Materials Science and Engineering B*, Vol. 87, pp. 23-30.
- Dervos, C.T.; Thirios, E.; Novacovich, J.; Vassiliou, P. & Skafidas, P. (2004). Permittivity properties of thermally treated TiO<sub>2</sub>. *Materials Letters*, Vol. 58, pp. 1502- 1507
- Ferreira, V. M.; Azough, F.; Freer R. & Baptista J. L. (1997). The Effect of Cr and La on MgTiO<sub>3</sub> and MgTiO<sub>3</sub>-CaTiO<sub>3</sub> Microwave Dielectric Ceramics, *Journal of Materials Research*, Vol. 12, pp. 3293-3299
- Giolli C. et al. (2007). Characterization of TiO<sub>2</sub> coatings prepared by a modified electric arc-physical vapour deposition system. *Surface & Coatings Technology*, Vol. 202, pp. 13-22
- Guo H.Z. et al. (2005). Structure dynamics of strongly reduced epitaxial BaTiO<sub>3-x</sub> studied by Raman scattering. *Journal of the European Ceramic Society*, Vol. 25, pp. 2347-2352.
- Haefie H. et al. (1992). Mg<sub>2</sub>TiO<sub>4</sub> as a novel substrate for high-temperature superconducting thin films, *Applied Physics Letters*, Vol. 61, pp. 9-19
- Hu P. et al. (2011). Influence of thermal treatments on the low frequency conductivity and microwave dielectric loss of CaTiO<sub>3</sub> ceramics, *Materials Science and Engineering B*, Vol. 176, No. 5, pp. 401-405.
- Huang, C.-L.; Pan, C.-L. & Shium S.-J. (2002). Liquid phase sintering of MgTiO<sub>3</sub>-CaTiO<sub>3</sub> microwave dielectric ceramics. *Materials Chemistry and Physics*, Vol. 78, pp. 111-115
- Hirata, T.; Ishioka K. & Kitajima M. (1996). *Journal of solid state chemistry*, Vol. 124, pp. 353-359
- Jiang, Y.; Guo, R. & Bhalla, A. S. (1998). LHPG grown crystal fibers of MgTiO<sub>3</sub>-CaTiO<sub>3</sub> eutectic system. *Journal of Physics and Chemistry of Solids*, Vol. 59, pp. 611-615
- Jin, H.Z. et al. (2003). An interfacial defect layer observed at (Ba,Sr)TiO<sub>3</sub>-Pt interface. *Thin Solid Films*, Vol. 429, pp. 282-285.
- Lemanov, V.V.; Sotnikov, A.V.; Smirnova, E.P.; Weihnacht, M. & Kunze, R. (1999). Perovskite CaTiO<sub>3</sub> as an incipient ferroelectric, *Solid State Communications*, Vol. 110, pp. 611-614
- Mattsson A. & Oesterlund L. (2010). Adsorption and photoinduced decomposition of acetone and acetic acid on anatase, brookite, and rutile TiO<sub>2</sub> nanoparticles, *Journal of Physical Chemistry*, Vol. 114 C, pp.14121-14132
- Mitic, V.V. & Mitrovic I. (2001). The influence of Nb<sub>2</sub>O<sub>5</sub> on BaTiO<sub>3</sub> ceramics dielectric properties, *Journal of the European Ceramic Society*, Vol. 21, pp. 2693-2696

- Morey, O.; Goeuriot P.; Juve D. & Treheux D. (2003). Dielectric investigations on 'MgAlON' compounds: Role of nitrogen content. *Journal of the European Ceramic Society*, Vol. 23 pp. 345-350.
- Ostapchuk T. et al. (2005). Soft-mode spectroscopy of BaTiO<sub>3</sub> thin films. *Journal of the European Ceramic Society*, Vol. 25, pp. 3063-3067
- Setter, N. & Waser, R. (2000). Electroceramic materials, *Acta Materialia*, Vol. 48, pp.151-178
- Simon-Seveyrat, L.; Hajjaji, A.; Emziane, Y.; Guiffard, B. & Guyomar, D. (2007). Re-investigation of synthesis of BaTiO<sub>3</sub> by conventional solid-state reaction and oxalate coprecipitation route for piezoelectric applications, *Ceramics International*, Vol. 33, pp. 35-40
- Souza I.A. et al. (2006). Theoretical and experimental study of disordered Ba<sub>0.4</sub> Sr<sub>0.55</sub>TiO<sub>3</sub> photoluminescence at room temperature, *Chemical Physics*, Vol. 322, pp. 343-348
- Sudheendran, K. & James Raju K.C. (2008). Temperature dependent impedance and dielectric properties of 0.7CaTiO<sub>3</sub>-0.3NdAlO<sub>3</sub> ceramics. *Indian journal of engineering & material sciences*, Vol. 15, p. 133-136
- Waser, R. (1999). Modeling of Electroceramics - Applications and Prospects, *Journal of the European Ceramic Society*, Vol. 19, pp. 655-664
- Wang, X.; Zhang, L.; Liu, H.; Zhai J. & Yao X. (2008). Dielectric nonlinear properties of BaTiO<sub>3</sub>-CaTiO<sub>3</sub>-SrTiO<sub>3</sub> ceramics near the solubility limit, *Materials Chemistry and Physics*, Vol. 112, pp. 675-678
- Wing, Z. N.; Halloran J. W.; Zhang, Q.; McGinn, P. J. (2006). Variable Dielectrics in the Calcium Magnesium Titanate System Characterized with Scanning Microwave Microscopy, *Journal of the American Ceramic Society*, Vol. 89, No. 5, pp. 1610-1614
- Wu, L. et al. (2009). Dielectric properties of barium titanate ceramics with different materials powder size, *Ceramics International*, Vol. 35, pp. 957-960
- Yu, P.; Cui, B. & Chany, Z. (2009). Preparation and characterization of Ag-doped BaTiO<sub>3</sub> based X7R ceramics, *Materials Research Bulletin*, Vol. 44 , pp. 893-897
- Zeng, J.; Wang, H.; Shang, S.; Wang, Z. & C. Lin (1997). Preparation of Textured Mg<sub>2</sub>TiO<sub>4</sub> Thin Films on Si Substrate by Atmospheric Pressure Metallorganic Chemical Vapour Deposition, *J. Mater. Sci. Mater. Electron.*, Vol. 8, pp. 159-162
- Zhao, M.H.; Bonnell, D.A. & Vohs, J.M. (2008). Effect of ferroelectric polarization on the adsorption and reaction of ethanol on BaTiO<sub>3</sub>, *Surface Science*, Vol. 602, pp. 2849-2855
- Zhang Q. & McGinn P. J. (2006). Characterization of Calcium Titanate-Magnesium Titanate Eutectic by Scanning Microwave Microscopy, *Journal of the American Ceramic Society*, Vol. 89, pp. 3817 - 3823
- Zheng, H. et al. (2003). Raman spectroscopy of B-site order-disorder in CaTiO<sub>3</sub>-based microwave ceramics. *Journal of the European Ceramic Society*, Vol. 23, pp. 2653-2659



# Thermal Diffusivity of Ceramics During Neutron Irradiation

Masafumi Akiyoshi<sup>1</sup>, Hidetsugu Tsuchida<sup>1</sup> and Toyohiko Yano<sup>2</sup>

<sup>1</sup>*Department of Nuclear Engineering, Kyoto University, Yoshida-Honmachi, Sakyo-ku, Kyoto*

<sup>2</sup>*Research Laboratory for Nuclear Reactors, Tokyo Institute of Technology, O-okayama, Meguro, Tokyo Japan*

## 1. Introduction

Several structural ceramic materials possess many superior properties for nuclear applications, such as blanket of future fusion reactor or core material of high-temperature gas cooling fission reactor for hydrogen generation, where they would be exposed to high fluence of neutrons at temperatures up to 1400 K [1–3]. High fluence of neutron irradiation introduces various changes in physical properties of the materials, especially in thermal diffusivity. Thermal diffusivity is one of the most important factors for the plant efficiency.

Thermal conductivity  $K$  (W/K·m) is obtained as  $K = \alpha C_p \rho$ , where  $C_p$  (J/K·kg) is specific heat at constant pressure and  $\rho$  (kg/m<sup>3</sup>) is density. Change in density after an irradiation is measured by linear or volume swelling, but the amount is not so large ( $< 2\%$ ), and the specific heat keep almost same after an irradiation [4]. So a change in thermal diffusivity almost represents a change in thermal conductivity.

In ceramic materials, unlike metals, heat is mainly carried by phonon. Phonon transportation is obstructed by two factors. Even in unirradiated ceramics, phonons are scattered among each other, and this phonon-phonon scattering increases with measurement temperature arise. In addition, phonon is scattered by lattice defects. This phonon-lattice scattering is decided by grain size or concentration of impurity in the case of unirradiated ceramics, but neutron irradiated material contains many lattice defects, especially vacancy scatters phonon severely. Hence, it has also been reported that neutron-irradiated specimens show severe degradation in the thermal diffusivity [5–12].

These post irradiation measurements were performed at room temperature to specimens after the irradiation. Nevertheless, it is very important to estimate the thermal diffusivity during the irradiation. But it is very difficult to measure thermal diffusivity during neutron irradiation directly. So it is required to estimate that from the post irradiation measurement, with consideration of both phonon-phonon scattering and phonon-lattice scattering.

Thermal diffusivity  $\alpha$  (m<sup>2</sup>/s) of neutron-irradiated ceramics depend on measured temperature  $T$  (K) as  $\alpha = k/T^n$ , where  $k$  is the constant that is related to the absolute value, and  $n$  is the constant that represents the state of induced defects. The  $n$  constant is usually 1 for unirradiated ceramics, but it decreased with the irradiation, so it is not easy to

estimate the thermal diffusivity at elevated temperature from the measurement at room temperature [13; 14]. In addition, to estimate the thermal diffusivity during the irradiation from the post-irradiation measurement, it must be assumed that specimens after an irradiation would retain the same amount of defects as during the irradiation. It requires quick quench of the specimens after the irradiation and that defects are stable below the irradiation temperature. In addition, the specimen during an irradiation, interstitial atoms and vacancies are created by neutron and knock-on atoms. Most of them recombine in very short time, but in bulk specimen, several numbers of defects exist along with the stable defects. These defects that exist in very short time during an irradiation are called transient defects. Neutron irradiation flux and temperature may change the number of these transient defects. To estimate the thermal diffusivity during an irradiation from the post-irradiation measurements, amount of these transient defects must be enough small. To confirm these assumption, many experiments were performed explained in three sections.

At first, degradation of thermal diffusivity with neutron irradiation dose was measured at room temperature [6; 8–10]. Around 30 dpa, the degradation was almost saturated with neutron dose, and that indicates thermal diffusivity would almost stable for very high-fluence applications.

And the next, annealing behavior showed that defects in post-irradiation specimens are stable under the irradiation temperature [5]. So, quenched defects in an irradiated specimen would keep the same amount during post-irradiation measurements operated under the irradiation temperature.

At last, transient defects are considered. Dynamic effect by transient defects during irradiation is an important issue to resolve the defect-production processes, but experimental study was very few [15–17]. Ion-beam irradiation is conventional method to investigate irradiation effects, but ion-beam induces defects in very shallow range near the surface, so the change in thermal diffusivity after an ion-beam irradiation may not be detectable. Nowadays, positron annihilation lifetime (PAL) has been measured to investigate the irradiation defects. This PAL is sensitive to distribution of vacancy-like defects, and thermal diffusivity in ceramics is also primarily controlled by the same defect. In addition, positron can probe local defects induced in small area by themselves, so defects induced by ion-beam irradiation expected to be observed with this method.

In this study, positron annihilation lifetime was measured on heavily neutron irradiated ceramics to clarify the correlation between PAL and thermal diffusivity. Several specimens showed significant change after the irradiation in PAL, but the difference in PAL and also thermal diffusivity were too small to estimate the correlation because the irradiation was too heavy and the amount of defects were almost saturated. So, electron irradiation was used to induce defect to lower dpa than the neutron irradiated specimens. From these measurements, the correlation between PAL and thermal diffusivity was suggested. And then, in-situ PAL measurements during ion-beam measurements were performed. The results were considered to deny the contribution of transient defects to thermal diffusivity.

Finally, thermal diffusivity of ceramics during the irradiation was estimated and showed almost flat profile with the irradiation temperature [13; 14].

## 2. Saturation in degradation of thermal diffusivity

In this section, degradation of thermal diffusivity measured at room temperature that depends on neutron irradiation dose and irradiation temperature is discussed.

ID	T51	T52	T53	T54	T55	T56	T57	T58	T71	T72	T73
neutron fluence ( $10^{26}$ n/m <sup>2</sup> )	2.8	5.3	3.9	7.3	4.2	8.0	3.7	6.9	0.5	1.4	0.4
irradiation temperature (K)	775	775	864	835	1004	950	1011	1039	646	668	853

Table 1. Neutron irradiation conditions

Specimens were heavily neutron-irradiated in the experimental fast reactor JOYO using CMIR-4 rig, and several specimens (T52, T54, T56 and T58) were irradiated also in CMIR-5 rig. Four kinds of materials,  $\alpha$ -Al<sub>2</sub>O<sub>3</sub>, AlN,  $\beta$ -Si<sub>3</sub>N<sub>4</sub> and  $\beta$ -SiC were enclosed in the same capsule. Irradiation conditions for each specimen are listed in Table 1, and additional details for several specimen are listed in Table 2. The dimensions of the specimens were 3 mm diameter and 0.5 mm height for T5x specimens and 10 mm diameter and 2 mm height for T7x specimens.

Thermal diffusivity was measured by the laser flash method with the  $t_{1/2}$  analysis [18] using a specially ordered ULVAC TC-7000 that can measure  $\phi 3 \text{ mm} \times 0.5 \text{ mm}$  (T5x) specimens. The measurements were performed at room temperature. Specimens were coated by a carbon spray and baked on a hot plate at about 373 K before the measurement to reduce translucence of AlN and  $\alpha$ -Al<sub>2</sub>O<sub>3</sub> and to equalize the temperature on the surface of specimen.

Figs. 1a to 1d show the thermal diffusivity measured at room temperature for each material depend on neutron-irradiation dose. These results showed that  $\beta$ -Si<sub>3</sub>N<sub>4</sub> specimens maintained the highest thermal diffusivity after neutron irradiation, compared to  $\alpha$ -Al<sub>2</sub>O<sub>3</sub>, AlN and even  $\beta$ -SiC. In Figs. 1, number in parentheses under a specimen ID shows the irradiation temperature (K). Specimens were separated into two groups by irradiated temperature, and specimens irradiated at relatively high temperature (950-1039 K) are shown with open symbols, while solid symbols represent lower temperatures (646-864 K). With this grouping, the data shows that the dose dependence of thermal diffusivity saturated near  $3 \times 10^{26} \text{ n/m}^2$  for all materials here.

After the saturation with neutron dose, thermal diffusivity was simply determined by the irradiation temperature. That is, thermal diffusivity measured at room temperature after an irradiation increased slightly with the irradiation temperature rose.

Figs. 2a to 2d show the relationship of thermal diffusivity measured at room temperature after an irradiation and the irradiation temperature for each material. In this figure, a number in parentheses under a specimen ID gives the neutron fluence ( $10^{26} \text{ n/m}^2$ ). It is easy to see that T7x specimens with solid symbols showed higher thermal diffusivity than the other specimens irradiated more than  $3 \times 10^{26} \text{ n/m}^2$  presented with open symbols. This verifies that T7x specimens were not saturated with the neutron fluence, while T5x specimens irradiated more than  $3 \times 10^{26} \text{ n/m}^2$  reached saturation and the thermal diffusivity was determined only by the irradiation temperature.

In Figs. 1c and 1d, the T71 specimens showed relatively low thermal diffusivity at that neutron dose. T71 specimens were irradiated at 646 K and the microstructure of a  $\beta$ -Si<sub>3</sub>N<sub>4</sub> specimen was observed by HREM [19]. It showed that the T71  $\beta$ -Si<sub>3</sub>N<sub>4</sub> specimen contained no obvious interstitial dislocation loops but poorly defined clusters or small rudiment of loops, while the T72 specimen irradiated at 668 K contained clear dislocation loops. In addition, the annealing behavior of swelling and thermal diffusivity in T71  $\beta$ -Si<sub>3</sub>N<sub>4</sub> specimens was obviously different from that in T72 or T73 specimens [8; 19]. The behavior showed that at 646 K interstitial atoms were not enough mobile to create interstitial dislocation loops or to annihilate with non-neighboring vacancies, therefore many isolated interstitial atoms and vacancies remain. This difference in microstructure of irradiation induced defects caused lower thermal diffusivity of T71 specimen than the other specimens. This also caused

material	$\alpha$ -Al <sub>2</sub> O <sub>3</sub>	AlN	$\beta$ -Si <sub>3</sub> N <sub>4</sub>	$\beta$ -SiC
manufacturer	Nippon Steel	Tokuyama	Nippon Steel	Nippon Steel
product name	NSAR	Super Shapal	NS101	SiC
raw material	$\alpha$ -Al <sub>2</sub> O <sub>3</sub> 100wt%	AlN (unknown)	$\beta$ -Si <sub>3</sub> N <sub>4</sub> > 88wt% Y <sub>2</sub> O <sub>3</sub> < 10wt% ZrSi <sub>2</sub> < 2wt%	$\beta$ -SiC > 99wt% Al <sub>2</sub> O <sub>3</sub> < 1wt%
sintering method	pressureless	pressureless	hot-press	hot-press
thermal diffusivity (10 <sup>-4</sup> m <sup>2</sup> /s)	0.118	0.991	0.250	0.410
density (10 <sup>3</sup> kg/m <sup>3</sup> )	3.96	3.25	3.33	3.20
specific heat (10 <sup>3</sup> J/kg·K)	0.789	0.738	0.636	0.697
thermal conductivity (W/m·K)	36.9	238	53.0	91.4

Table 2. Properties of specimens for neutron irradiation

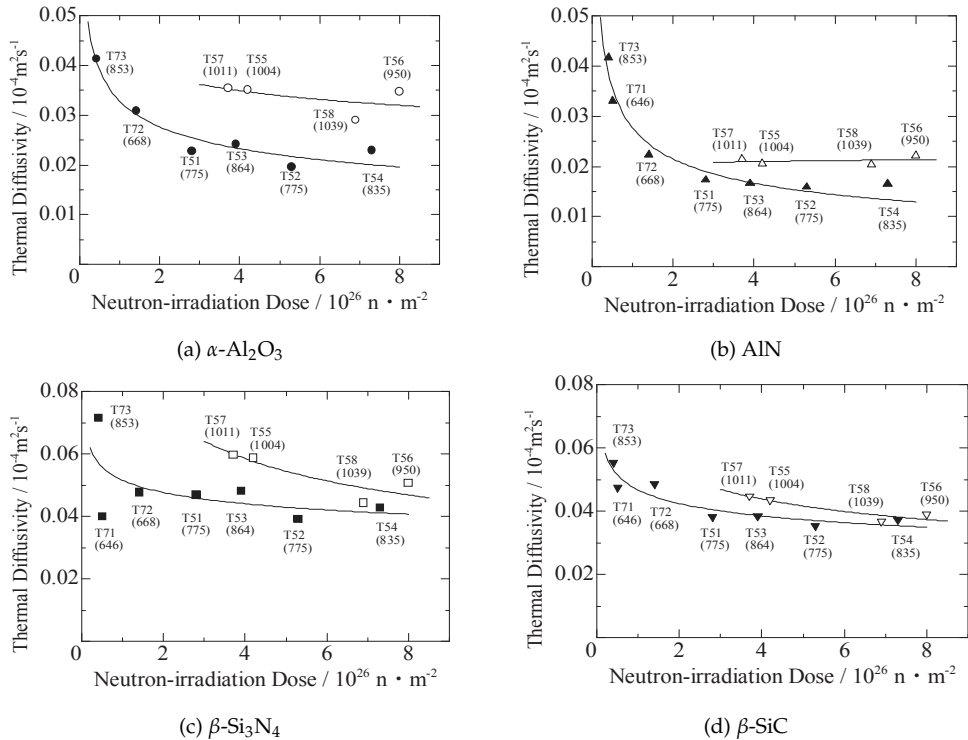


Fig. 1. The dose dependence of thermal diffusivity for each material. A number in parentheses under a specimen ID gives the irradiation temperature (K). Specimens they were irradiated at relatively high temperatures are shown by open symbols, and irradiated at lower temperatures shown by solid symbols.

significant difference in swelling behavior, and the T71  $\alpha$ -Al<sub>2</sub>O<sub>3</sub> specimen was hardly cracked and thermal diffusivity could not be measured.

In ceramic materials, the thermal diffusivity is proportional to the mean free path of phonons. This mean free path can be heavily affected by irradiation induced defects, especially vacancies. The mean free path of phonons after irradiation ( $\lambda_I$ ) is given as  $1/\lambda_I = 1/\lambda_0 + 1/\lambda_d$  where  $\lambda_0$  is for non-irradiated material and  $\lambda_d$  is related to the irradiation induced defect. Experimentally,  $\lambda_0$  and  $\lambda_I$  were obtained from measured thermal diffusivity before and after irradiation, with the expression  $\alpha = \frac{1}{3}\mu\lambda$  [4]. In this expression,  $\mu$  (m/s) represent the mean speed of phonon, and it was calculated from  $\mu = \sqrt{E/\rho}$  where  $E$  (Pa) is the Young's modulus and  $\rho$  (kg/m<sup>3</sup>) is the density.

The  $\lambda_0$ , reflect the thermal diffusivity of non-irradiated specimen, is affected by many factors, such as grain shape, grain boundary structure, impurities or sintering agents. However, these effects are insignificant in irradiated materials, because dimensions of these defects are far large compared to that of irradiation defects.

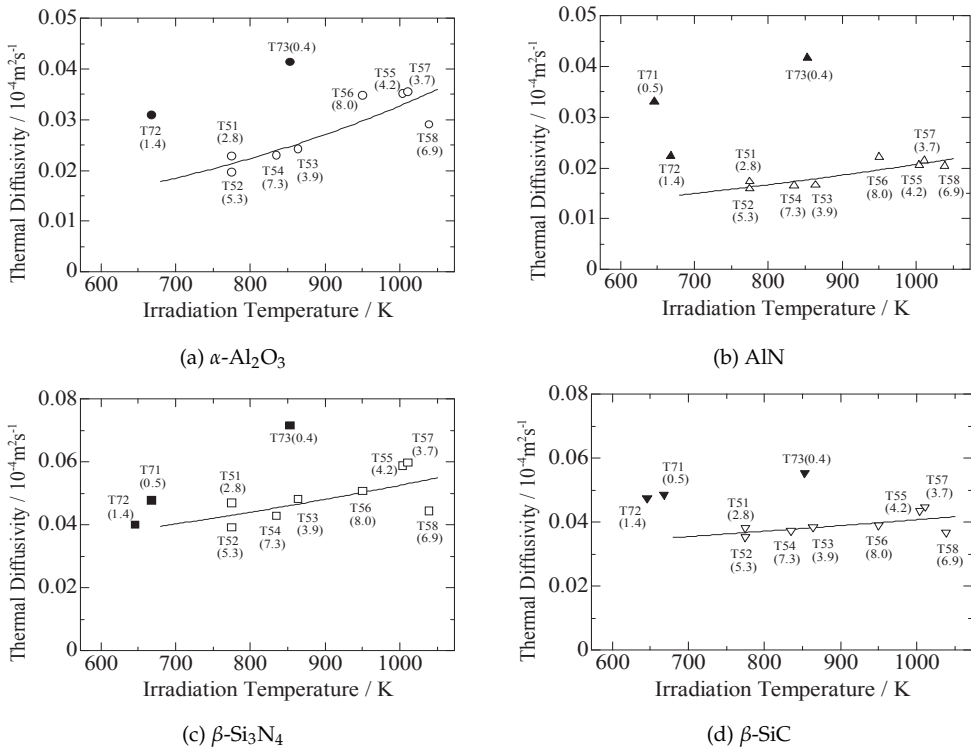


Fig. 2. Dependence of thermal diffusivity on irradiation temperature for each material. A number in parentheses under a specimen ID gives the neutron fluence (10<sup>26</sup> n/m<sup>2</sup>). Specimens they were irradiated to relatively high neutron fluences (> 3 × 10<sup>26</sup> n/m<sup>2</sup>) are shown with open symbols, and to lower fluences shown with solid symbols.

### 3. Annealing behavior after the irradiation

In this section, annealing behavior was studied to make sure that defects in irradiated specimen keeps the same amount during post-irradiation measurements operated under the irradiation temperature.

The neutron-irradiation conditions for ceramic specimens are the same in the previous section (Table 1). Thermal diffusivity was measured by the same method in the previous section, too. Isochronal annealing was conducted every 100 K up to 1773 K in a vacuum of  $< 1$  Pa ( $< 1273$  K) or  $< 10^{-4}$  Pa (1373-1773 K). Specimens were annealed for 1 h at an objective temperature. After the annealing, specimens were cooled in the furnace, and each measurement was performed at room temperature.

Figs. 3a to 3h show recovery behavior of thermal diffusivity by isochronal annealing in neutron-irradiated ceramics. From the limitation of space, irradiation condition of T51 ( $2.8 \times 10^{26}$  n/m<sup>2</sup>, 775 K) and T57 ( $3.7 \times 10^{26}$  n/m<sup>2</sup>, 1011 K) are mentioned here.

Figs. 3a and 3b show recovery behavior in  $\alpha$ -Al<sub>2</sub>O<sub>3</sub>. The recovery started around the irradiation temperature along with parabolic curves, and then it changed to linearly around 1423 K. This moderation at high temperature may cause saturation of recovery. After the annealing of 1773 K, the thermal diffusivity was recovered to about 80% of non-irradiated Al<sub>2</sub>O<sub>3</sub>. From the microstructure observation of neutron-irradiated  $\alpha$ -Al<sub>2</sub>O<sub>3</sub> with TEM, both interstitial atom and vacancy have enough mobility to make interstitial dislocation loops or voids at least above 775 K while the recovery started above 1073 K in T57. The temperature on which the recovery started rose with the irradiation temperature, and in Fig. 3a recovery started around 973 K. It is thought that activation energy to recombine of interstitial loops and vacancies changes with size of loops, and the size changed with the irradiation temperature. The linear recovery at higher temperature is usually solved with sintering-like process that dissolve voids and micro cracks.

Figs. 3c and 3d show recovery behavior in AlN. In both Fig. 3c and Fig. 3d, the recovery of thermal diffusivity started around 1173 K. Above the temperature, mobility of vacancy is seemed to be enough to annihilate with interstitial loops. Unlike  $\alpha$ -Al<sub>2</sub>O<sub>3</sub> formed by ionic bond, AlN,  $\beta$ -Si<sub>3</sub>N<sub>4</sub> and  $\beta$ -SiC are formed by covalent bond, and vacancies are not mobile at relatively low temperature (below 1173 K) while interstitial atoms enough mobile to gather interstitial dislocation loops around 573 K.

Figs. 3e and 3f show recovery behavior in  $\beta$ -Si<sub>3</sub>N<sub>4</sub>. In the  $\beta$ -Si<sub>3</sub>N<sub>4</sub> that was irradiated to high dose, nano-partition structure was formed [20], and it restricted growth of loops, so interstitial atoms lost sink and recombined with vacancies. The fast recovery above 1273 K is interpreted that vacancies were enough mobile above 1273 K to recombine with small loops. But obvious length or density change of loops and also formation of voids were not observed by TEM in specimens annealed to 1773 K. In Fig. 3f thermal diffusivity was recovered a little around 773 K, that was lower than the irradiation temperature. This problem was discussed with  $\beta$ -SiC described below. All specimens in this study showed recovery from the same temperature of 673-773 K, and it was considered to be the threshold where interstitial atoms get mobile and recombine with vacancies.

Figs. 3g and 3h show recovery behavior in  $\beta$ -SiC. It is well known that  $\beta$ -SiC showed linear recovery in swelling from an irradiation temperature, and with annealing to 1773 K, swelling was recovered completely [21; 22]. Several interstitial atoms on the edge of dislocation loops separate from the edge and growth to larger loops or recombine with vacancies. A stability of an interstitial dislocation loop is decided by the size of the loop, and a distribution of the size was determined by irradiation temperature. It may cause the recovery from the

irradiation temperature. However, Fig. 3h shows a recovery in thermal diffusivity started below the irradiation temperature. Most possible reason is that the sample was irradiated lower temperature than the nominal irradiation temperature while the reactor was shutting down and suffered remarkable effect. It was reported that the JOYO fast reactor have high neutron flux of  $5 \times 10^{19} \text{ n/m}^2\cdot\text{s}$  near the core that gives about  $2 \times 10^{24} \text{ n/m}^2$  ( 0.2 dpa ) within 12 h. This neutron flux might get smaller during the shut down the reactor, but even neutron flux of  $1 \times 10^{23} \text{ n/m}^2$  ( 0.01 dpa ) gives enough degradation in thermal diffusivity examined with electron irradiation described in the next section. All  $\beta$ -SiC specimens in this study showed recovery from 673-773 K, and it was explained that interstitial atoms get mobile and recombine with vacancies, same as in  $\beta$ -Si<sub>3</sub>N<sub>4</sub>. Further more, Fig. 3h shows change of trend around the nominal irradiation temperature, which signifies the sample was surely irradiated at the temperature for most of the irradiation term.

It is concluded that the number of vacancies induced by neutron irradiation keeps almost same amount below the irradiation temperature.  $\alpha$ -Al<sub>2</sub>O<sub>3</sub> and AlN showed no recovery below 973 K even irradiated lower temperature. It can be said in other word, the temperature where recovery of thermal diffusivity start did not depend on the irradiation temperature.  $\beta$ -Si<sub>3</sub>N<sub>4</sub> and  $\beta$ -SiC showed a little recovery below the irradiation temperature, but it may arose from the shutting down process of the irradiation, and at least, defects were not recovered below 673 K.

#### 4. Estimation an amount of transient defects during irradiation

In this section, amount of transient defects during irradiation was estimated from positron annihilation lifetime.

Nowadays, positron annihilation lifetime ( PAL ) has been widely used for many material studies to investigate the distribution of defects. Both PAL and thermal diffusivity are sensitive to distribution of vacancy-like defects, but the correlation was not clarified.

In this section, at first, PAL in neutron irradiated specimen was measured to clarify the correlation with thermal diffusivity. Several specimens showed significant change on PAL after the neutron irradiation, but the difference in PAL and also thermal diffusivity between irradiated specimens was too small to estimate the correlation, because the irradiation was too heavy and the amount of defects were almost saturated. So next, high-energy electron irradiation was performed to induce defect to lower dpa than the neutron irradiated specimens. From these measurements, the correlation between PAL and thermal diffusivity was suggested.

After that, in-situ PAL measurement during ion-beam irradiation was challenged to estimate the amount of transient defects during irradiation.

##### 4.1 Correlation between positron annihilation lifetime and thermal diffusivity

Electron irradiations were performed using 30 MeV electron linac in Kyoto University Research Reactor Institute. The beam current was 110-170  $\mu\text{A}$  in 2 cm<sup>2</sup> in average. The range of 30 MeV electron was about 5 cm in ceramics, and the defects were induced equally all over the  $\phi 3 \times 0.5 \text{ mm}$  specimens. The specimens were irradiated at 300-310 K in cooling water and the electron irradiation dose was  $1.3-3.0 \times 10^{24} \text{ e/m}^2$  that correspond to  $0.93-2.1 \times 10^{-2} \text{ dpa}$ . Detail of irradiation conditions were listed in Table 3.

The specimens prepared for the electron irradiations were different from the neutron irradiations. The specimens for neutron-irradiation were quite unique products looking for liquid-metal cooling fast reactor. But the number of non-irradiated specimens was limited

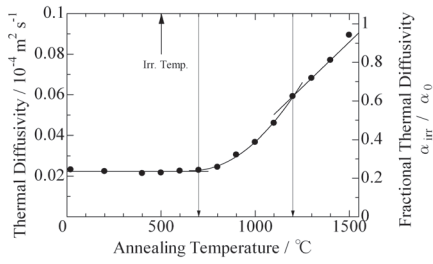
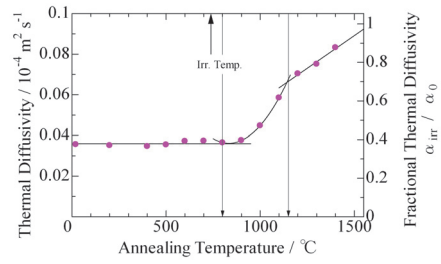
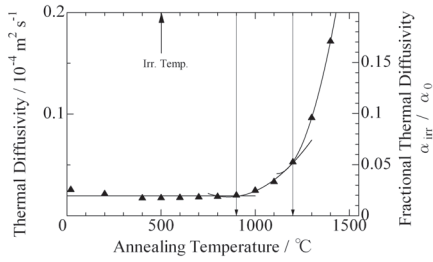
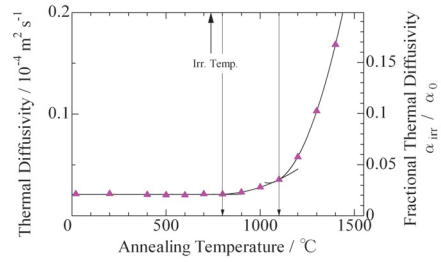
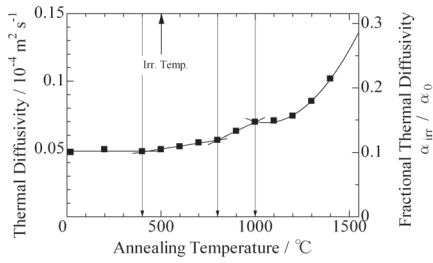
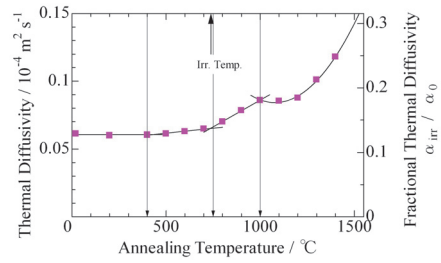
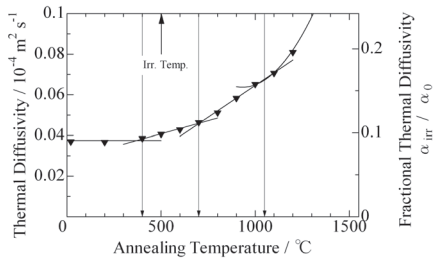
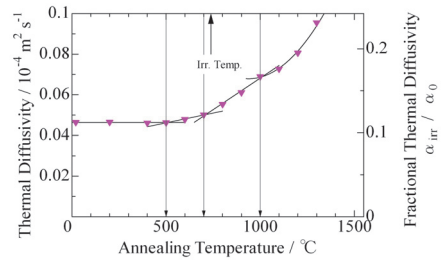
(a)  $\alpha$ -Al<sub>2</sub>O<sub>3</sub> T51 (2.8 × 10<sup>26</sup> n/m<sup>2</sup>, 775 K)(b)  $\alpha$ -Al<sub>2</sub>O<sub>3</sub> T57 (3.7 × 10<sup>26</sup> n/m<sup>2</sup>, 1011 K)(c) AlN T51 (2.8 × 10<sup>26</sup> n/m<sup>2</sup>, 775 K)(d) AlN T57 (3.7 × 10<sup>26</sup> n/m<sup>2</sup>, 1011 K)(e)  $\beta$ -Si<sub>3</sub>N<sub>4</sub> T51 (2.8 × 10<sup>26</sup> n/m<sup>2</sup>, 775 K)(f)  $\beta$ -Si<sub>3</sub>N<sub>4</sub> T57 (3.7 × 10<sup>26</sup> n/m<sup>2</sup>, 1011 K)(g)  $\beta$ -SiC T51 (2.8 × 10<sup>26</sup> n/m<sup>2</sup>, 775 K)(h)  $\beta$ -SiC T57 (3.7 × 10<sup>26</sup> n/m<sup>2</sup>, 1011 K)

Fig. 3. Recovery behavior of thermal diffusivity by isochronal annealing in neutron-irradiated ceramics



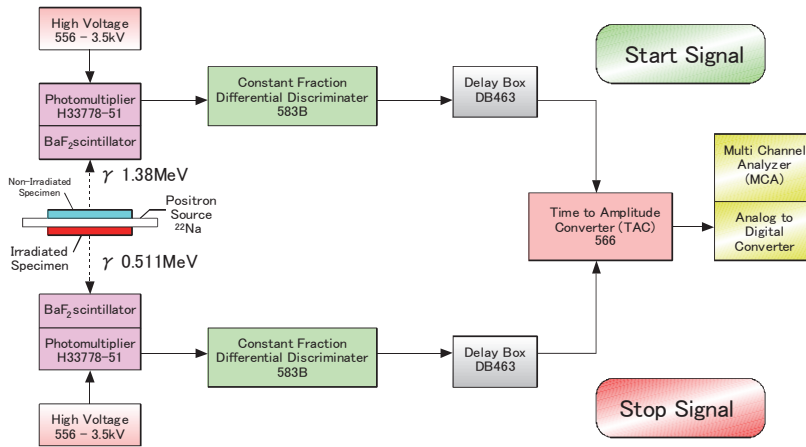


Fig. 4. Conventional  $\gamma$ - $\gamma$  coincidence circuit-diagram to measure PAL in specimen after an irradiation

and the detail was not publicized, so in this study, specimens for electron irradiation were supplied from the market. Properties of these specimens were listed in Table 4.

Positron annihilation lifetime was measured by conventional  $\gamma$  -  $\gamma$  fast coincidence method, and the circuit-diagram is shown in fig. 4. Our facility allows only sealed  $^{22}\text{Na}$  source, and the diameter of irradiated specimens were only 3 mm. So, the PAL measurements were performed with specially ordered  $^{22}\text{Na}$  1 MBq positron source that have active diameter of 1 mm sealed by  $12.7\ \mu\text{m}$  Ti foil. The positron from  $^{22}\text{Na}$  have an energy 0.55 MeV in maximum that reaches 0.5 mm in ceramics, but the average range was  $100\ \mu\text{m}$ . The measurements were performed at room temperature.

In addition, a positron source is put between two specimens at ordinary setup. However, only one disk was prepared for each irradiation condition in this study, so a non-irradiated

ID	KURL0708	KURL0801	KURL0802
electron fluence [ $\text{e}/\text{m}^2$ ]	$1.5 \times 10^{24}$	$1.3 \times 10^{24}$	$3.0 \times 10^{24}$
irradiation dose [dpa]	$1.0 \times 10^{-2}$	$0.93 \times 10^{-2}$	$2.1 \times 10^{-2}$
irradiation temperature [K]	300	310	310

Table 3. Electron irradiation conditions

material	$\alpha\text{-Al}_2\text{O}_3$	AlN	$\beta\text{-Si}_3\text{N}_4$	$\beta\text{-SiC}$
manufacturer	Toray	Tokuyama	Toray	Bridgestone
product name	A-999	SH-30	SN	PB-S
sintering method	pressureless	pressureless	hot-press	hot-press
thermal diffusivity [ $10^{-4}\ \text{m}^2/\text{s}$ ]	0.122	0.744	0.110	1.07
density [ $10^3\ \text{kg}/\text{m}^3$ ]	3.9	3.34	3.2	3.15
thermal conductivity [ $\text{W}/\text{m}\cdot\text{K}$ ]	38	174	25	230
volume resistivity [ $\Omega\cdot\text{cm}$ ]	$> 10^{14}$	$8.4 \times 10^{13}$	$> 10^{14}$	$2.0 \times 10^{-2}$

Table 4. Properties of specimens for electron irradiation

specimen was located at the other side of an irradiated specimen. This treatment may change intensity of long lifetime component, but not change bulk and long lifetime itself.

The obtained PAL spectrum was analyzed with PALSfit program [23], with resolution FWHM about 300 ps at first and improved gradually to 230 ps at last. The analyzed positron lifetimes are described as  $\tau_1$ : short lifetime and  $\tau_2$ : long lifetime, and  $I_i$  are the intensities for each components. The average positron lifetime  $\langle\tau\rangle$  is obtained as  $\langle\tau\rangle = \tau_1 I_1 + \tau_2 I_2$ . In this study, source component that represent annihilation of positron in Ti foil was not resolved since the PAL of Ti was measured as  $\tau_1$ : 136 ps (97 %),  $\tau_2$ : 447 ps (3 %) and  $\langle\tau\rangle$ : 145 ps that is very close to the PAL in ceramics. So only two components were guessed in the analysis.

Electron irradiated ceramics to doses of 0.01-0.02 dpa showed distinct changes in thermal diffusivity.  $\alpha$ -Al<sub>2</sub>O<sub>3</sub> and  $\beta$ -Si<sub>3</sub>N<sub>4</sub> showed rather low thermal diffusivity before the irradiation ( about  $0.11 \times 10^{-4} \text{ m}^2/\text{s}$  ), and it showed small degradation to  $0.08 \times 10^{-4} \text{ m}^2/\text{s}$ . On the other hand, thermal diffusivity of non-irradiated AlN and  $\beta$ -SiC were 0.73 and  $0.95 \times 10^{-4} \text{ m}^2/\text{s}$ , and they decreased to 0.46-0.65 and  $0.23-0.40 \times 10^{-4} \text{ m}^2/\text{s}$  for each.

PAL measurements were performed on neutron irradiated specimens at first, and then on electron irradiated specimens mentioned above. The correlation between thermal diffusivity and PAL is presented in Fig. 5.

Neutron and also electron irradiated  $\alpha$ -Al<sub>2</sub>O<sub>3</sub> showed obvious increment in  $\langle\tau\rangle$  with degradation of thermal diffusivity as shown in Fig. 5a. In this study, electron irradiated  $\alpha$ -Al<sub>2</sub>O<sub>3</sub> showed relatively small change in thermal diffusivity, but large change in PAL at the dose of 0.01-0.02 dpa. It is said that PAL detect vacancy-like defects in crystal more sensitive than thermal diffusivity at early stage of irradiation.

AlN in Fig. 5b showed almost the same feature in Al<sub>2</sub>O<sub>3</sub>. This result shows  $\langle\tau\rangle$  was saturated in early stage of irradiation, too. Heavily neutron irradiated AlN showed almost same thermal diffusivity and PAL, but electron irradiated AlN showed correlation between thermal diffusivity and PAL. Kanechika et al. reported similar correlation even in non-irradiated specimens sintered in different conditions [24].

However in Fig. 5c,  $\beta$ -Si<sub>3</sub>N<sub>4</sub> specimens showed no increment or rather decrement in  $\langle\tau\rangle$  with degradation of thermal diffusivity. In addition, average lifetime of non-irradiated  $\beta$ -Si<sub>3</sub>N<sub>4</sub> prepared for neutron irradiation was  $216 \pm 8$  ps and for electron irradiation was  $226 \pm 2$  ps, which is larger than any other ceramics in this work (about 150 ps). This result is considered to arise from large barrel structure surrounded by six SiN<sub>4</sub> tetrahedron that penetrate the crystal perpendicular to the (0001) plane. Neutron irradiated  $\beta$ -Si<sub>3</sub>N<sub>4</sub> contained larger 'peanuts' like structures [25; 26], but the fraction in the crystal was small. It is considered that most positron annihilated in this large empty structure and showed long lifetime, so small number of vacancies did not affect the PAL in irradiated  $\beta$ -Si<sub>3</sub>N<sub>4</sub>.

$\beta$ -SiC showed also almost no change after the neutron irradiation in Fig. 5d, but the electron irradiated specimens prepared from 'pure- $\beta$ ' SiC ( Bridgestone ) showed a little increment. However, many works reported change of PAL in SiC irradiated by electron or ion beam [27-33]. Kawasuso et al. reported that electron irradiated n-type (nitrogen-doped) 6H-SiC showed obvious change in  $\langle\tau\rangle$  ( 143 ps to 178 ps ), while p-type (aluminum-doped) 6H-SiC showed almost no change ( 136 ps to 138 ps ) [33]. The specimen was irradiated with 3 MeV electron to a fluence of  $1 \times 10^{17} \text{ e}^-/\text{cm}^2$ , that correspond to about  $4 \times 10^{-6}$  dpa. And also Henry et al. reported 6H-SiC that was irradiated by 12 MeV proton up to  $4 \times 10^{15}$  showed same tendency [29]. In this work,  $\beta$ -SiC specimens used for neutron irradiation were sintered with 1% Al<sub>2</sub>O<sub>3</sub>, so it was possible that the crystal contains several aluminum that makes the specimens p-type. On the other hand,  $\beta$ -SiC specimens for electron irradiation were sintered

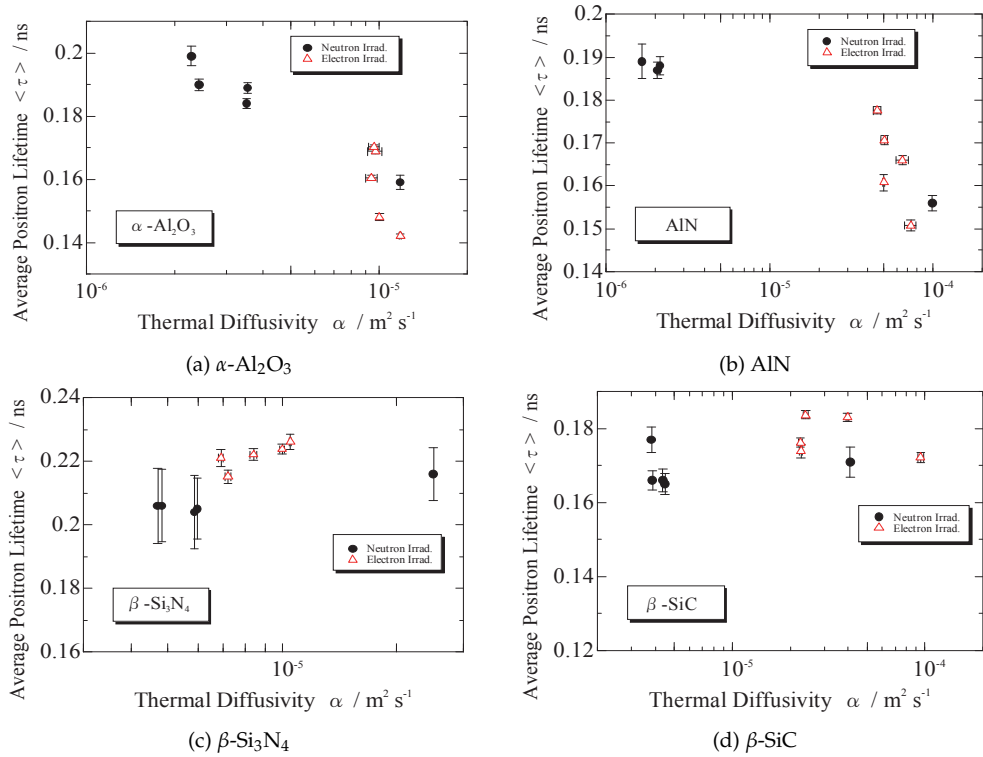


Fig. 5. Change of average positron lifetime  $\langle \tau \rangle$  in neutron irradiated ceramics compared with thermal diffusivity

without any sintering additive, and electron irradiated specimen showed a little increment in PAL, but the change was very small and the relation between thermal diffusivity and the PAL was not sure.

From these result, 30 MeV electron irradiation and PAL measurement is good combination to investigate the distribution of defects in several materials. Using KURRI-Linac, irradiation at elevated temperature ( up to 1400 K ) is available, and it may give many contributions to clarify the behavior of defect. Anyway, thermal diffusivity has some correlation with positron annihilation lifetime, at least  $\alpha$ -Al<sub>2</sub>O<sub>3</sub> and AlN.

#### 4.2 In-situ PAL measurement during ion-beam irradiation

It was concluded that  $\alpha$ -Al<sub>2</sub>O<sub>3</sub> and AlN showed some correlation between thermal diffusivity and PAL measured after the irradiation. And then, in-situ PAL measurement during ion-beam irradiation is examined to clarify the amount of transient defects is enough small.

To execute in-situ measurement during ion-beam irradiation, conventional  $\gamma - \gamma$  coincidence system ( Fig. 4 ) can not be applied, because this system requires symmetrical specimen and detector arrangement to create start and stop signal, and they obstructs ion-beam irradiation. In this study, asymmetric  $\beta - \gamma$  coincidence system was applied using avalanche photodiode ( APD ) for a device to detect a positron and give a start pulse ( Fig. 6 ). Usually APD is used to detect photon and the crystal is rather thick, but in this system positron penetrates the crystal

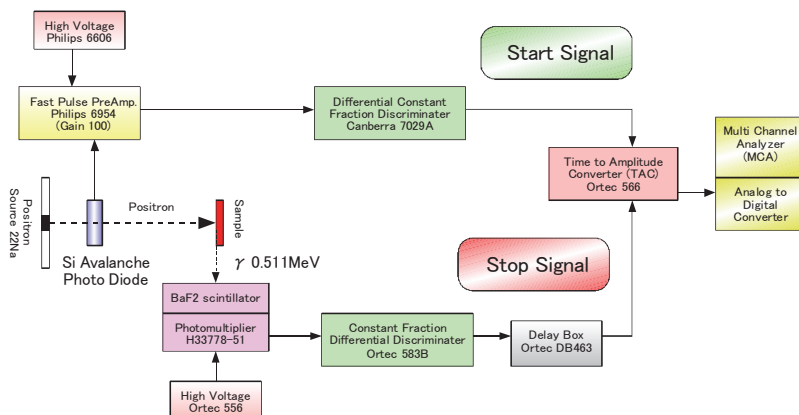


Fig. 6. Circuit-diagram using  $\beta$ - $\gamma$  coincidence for in-situ PAL measurement during ion-beam irradiation

to reach a specimen, so the thickness of Si in the APD was  $110\text{ }\mu\text{m}$  in the size of  $5\times 5\text{ mm}^2$  (EG & G Optoelectronics, C30626-CD2274). The pulse height from APD is fixed by energy of incident positron, and that enables to select the depth where the positron was injected and annihilate. Ion-beam irradiation induces defects within very shallow range, so the pulse from APD is selected by Constant Fraction Differential Discriminator (CFDD) to match the defect induced area and positron annihilation area. Positron source in this measurement was  $^{68}\text{Ge}$  that irradiate almost no  $\gamma$ -ray when a positron is projected unlike  $^{22}\text{Na}$ . The positron source was arranged crossly at the same side of the specimen irradiated by ion-beam.

At first, PAL in a specimen before irradiation was measured at room temperature. Then the specimen was irradiated by ion-beam and in-situ PAL measurement was performed during the irradiation. Ion-beam irradiation was conducted by  $2.0\text{ MeV H}^+$  with a flux of  $1.2\times 10^{16}\text{ ion/m}^2\cdot\text{s}$  using a Van de Graaff accelerator in Radiation Laboratory, Uji, Kyoto University. The irradiation and measurement was operated for  $6\times 10^4\text{ sec}$ , to a fluence of  $7\times 10^{20}\text{ ion/m}^2$  that corresponds to  $5.8\times 10^{-2}\text{ dpa}$ . After the irradiation, PAL was measured again.

The obtained in-situ PAL spectrums are shown in Figs. 7a to 7d. In Fig. 7a, spectrum illustrated by solid dot represents the specimen before the irradiation, and the spectrum after and during the irradiation showed larger intensity around 1-1.5 ns. This difference represents that this measurement can detect the static defects remain after the irradiation. On the other hand, because of the limitation of resolution and S/N ratio, certain lifetime was not analyzed, but it is said that difference between after and during the irradiation was not larger than the difference between before and after the irradiation of  $5.8\times 10^{-2}\text{ dpa}$ . AlN showed almost same tendency in Fig. 7b.

Fig. 7c and 7d shows the in-situ PAL spectrum in  $\beta$ - $\text{Si}_3\text{N}_4$  and  $\beta$ -SiC, respectively. Difference between the spectrum before, during and after the irradiation was not detected, and also  $\beta$ - $\text{Si}_3\text{N}_4$  showed same tendency. Just as the case of neutron-irradiated specimen, these spectrums showed that even static defects were not detected by positron annihilation measurement. Anyway, to evaluate the transient defects, more fine examination is expected in future work.

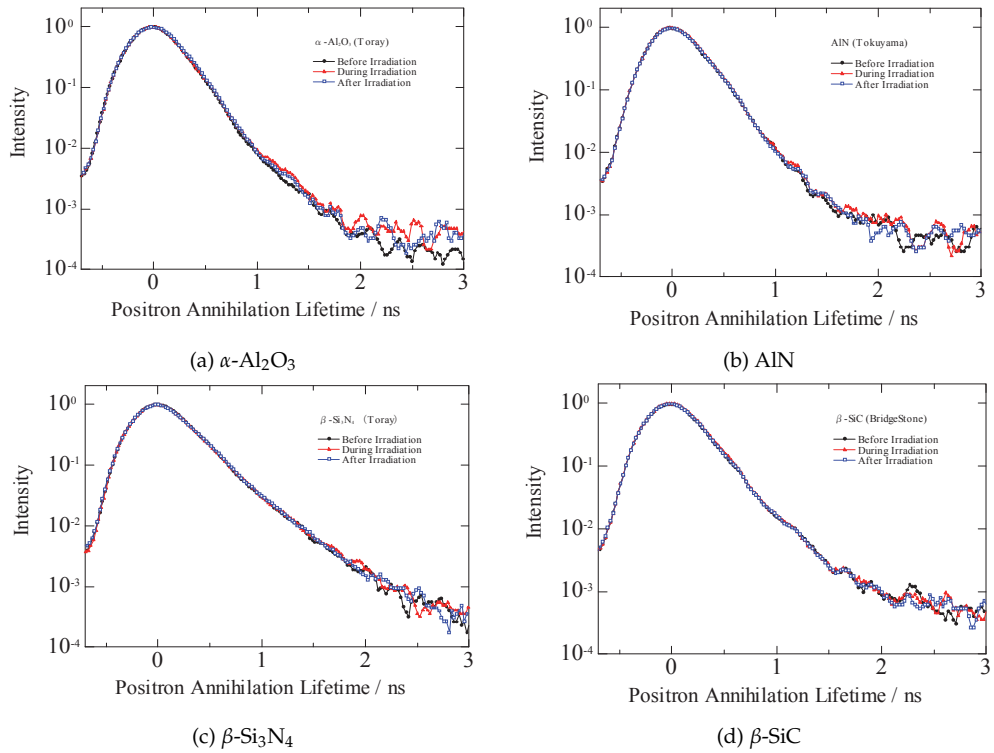


Fig. 7. PAL spectrum change among before, during and after ion-beam irradiation. Ion-beam irradiation was performed by 2.0 MeV  $H^+$  with a flux of  $1.2 \times 10^{16}$  ion/m<sup>2</sup>·s.

In addition, defect induced rate was discussed to evaluate the transient defect. In the specimen during irradiation, the interstitial atoms and vacancies are created by neutron irradiation, and subsequently, most of them recombine in a very short time. Neutron irradiation flux changes the amount of transient defects before recombination. In this study, the neutron irradiation dose of specimens irradiated in CMIR-4 rig reached 42 dpa ( T55 ), that is said in other word, each atom was displaced 42 times during 176 days, and is calculated as  $2.8 \times 10^{-6}$  dpa/s. It indicates that the ratio of the transient defects that scatters phonon between the static defects is very small. During the in-situ PAL measurement above, the displacement ratio was calculated as  $9.2 \times 10^{-7}$  dpa/s. This rate is a little smaller than the ratio in the fast reactor JOYO, but enough larger than the ratio in Japan Material Testing Reactor, JMTR,  $9.2 \times 10^{-7}$  dpa/s. Dynamic effect by transient defects during irradiation is an important issue to resolve the defect-production processes [34], but the amount of transient defects is supposed too small to produce significant effect on thermal diffusivity.

## 5. Estimation of thermal diffusivity at the neutron irradiation temperature

In this section, thermal diffusivity during the irradiation was estimated from the post irradiation measurements. Thermal diffusivity  $\alpha$  (m<sup>2</sup>/s) of neutron-irradiated ceramics depend on measured temperature  $T$  (K) as  $\alpha = k/T^n$ . We assumed three assumptions, that is

- 1) Degradation of thermal diffusivity with irradiation is almost saturated above 30 dpa
- 2) Defects are stable until annealed above the irradiation temperature
- 3) Post-irradiated specimens kept the same amount of defects as during the irradiation.

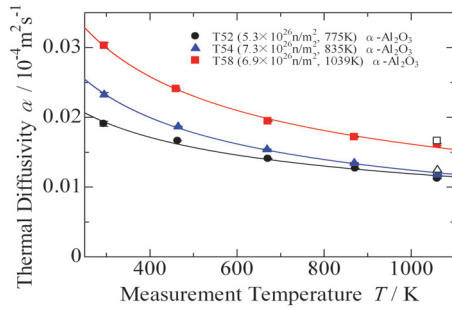
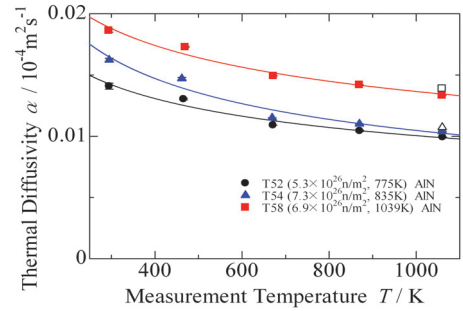
Each assumption was confirmed in sections above. Then, thermal diffusivity at the irradiation temperature represents the thermal diffusivity during the irradiation. The  $n$  parameter in the equation  $\alpha = k/T^n$  is 1 for non-irradiated ceramics, but after the irradiation, this  $n$  parameter decreased, so it is not easy to estimate the thermal diffusivity at elevated temperature from the measurement at room temperature.

In this section, thermal diffusivity was measured by the laser-flash method using specially ordered measurement system that can measure  $\phi 3$  mm disk at high (up to 1723 K) and low (100-473 K) temperature (ULVAC-RIKO Inc. TC-7000H/L Special), and was analyzed with the  $t_{1/2}$  method. All the specimens were coated by graphite spray and baked on a hot plate at about 373 K to avoid transmission of laser flash. Measurements at elevated temperatures were performed for T52, T54, and T58 specimens using SiC furnace of TC-7000H system from room temperature to 1073 K, and a rapid increment of temperature after a laser flash was measured by IR sensor. After the measurement at 1073 K, all specimens showed recovery in thermal diffusivity at room temperature. Heavily-neutron irradiated specimen is very precious, and to avoid annealing effect even to the specimen irradiated relatively low temperature, measurements at low temperature were performed. After a laser flash, a rapid increment of temperature on the other surface of a specimen was measured by  $\phi 0.05$  mm K-type thermocouple, because an intensity of IR from the cold surface is too small to measure with IR sensor. Thermocouple was attached on a surface of specimen using electroconductive epoxy (Circuit works CW2400) below 373 K to avoid annealing. Measurements at low temperature were carried out in He atmosphere ( $< 10^4$  Pa), and a cryostat was cooled by liquid nitrogen. Measurements were taken at every 20 K from 123 K to 413 K.

Figs. 8 show thermal diffusivity of neutron-irradiated ceramics measured at room temperature to 1073 K. Open symbols at 1073 K represent as-measured values that contain annealing recovery. So, the thermal diffusivity at 1073 K plotted with solid symbols was modified via  $\alpha_{1073} \times \alpha_0 / \alpha_{an}$  where  $\alpha_{1073}$  is the thermal diffusivity measured at 1073 K (plotted with open symbols),  $\alpha_0$  is measured at room temperature before annealing and  $\alpha_{an}$  is measure at room temperature again after annealing to 1073 K. In addition, Figs. 9 show thermal diffusivity of neutron-irradiated ceramics measured at 123-413 K. From these measurements,  $n$  parameter was obtained. And then the thermal diffusivity at irradiation temperature,  $\alpha_{irr}$ , was estimated as  $\alpha_{irr} = \alpha_{300} (300/T_{irr})^n$  where  $T_{irr}$  represent the irradiation temperature and  $\alpha_{300}$  the thermal diffusivity at 300 K measured by infrared sensor.

Finally, Figs. 10 show the estimated thermal diffusivity during the irradiation,  $\alpha_{irr}$ , plotted with the irradiation temperature  $T_{irr}$ . For each material,  $\alpha_{irr}$  was distributed in same line except T7x specimens. The T7x specimens were irradiated to  $0.4-1.4 \times 10^{26}$  n/m<sup>2</sup> and the degradation of thermal diffusivity was not saturated with neutron dose, on the other hand, the T5x specimens were irradiated to  $2.8-8 \times 10^{26}$  n/m<sup>2</sup> and saturated. It is expected that specimens irradiated more than  $3 \times 10^{26}$  n/m<sup>2</sup> at the irradiated temperature of T7x,  $\alpha_{irr}$  may be distributed in the same line.

Estimated thermal diffusivities during the irradiation were almost independent on the irradiation temperature within the range of 775-1039 K, i.e.,  $1.5, 1.3, 2.7, 2.3 \times 10^{-6}$  m<sup>2</sup>/s for  $\alpha$ -Al<sub>2</sub>O<sub>3</sub>, AlN,  $\beta$ -Si<sub>3</sub>N<sub>4</sub> and  $\beta$ -SiC, respectively.  $\beta$ -Si<sub>3</sub>N<sub>4</sub> kept highest thermal diffusivity during irradiation rather than the SiC. But in range of lower and higher irradiation temperature, behavior of defects basically different, and this flat profile may be changed at that range.

(a)  $\alpha$ -Al<sub>2</sub>O<sub>3</sub>

(b) AlN

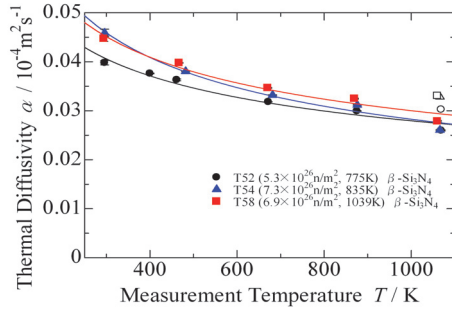
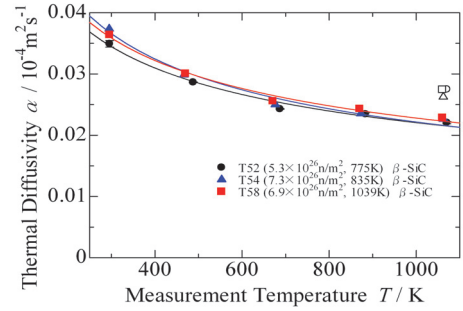
(c)  $\beta$ -Si<sub>3</sub>N<sub>4</sub>(d)  $\beta$ -SiC

Fig. 8. Thermal diffusivity of neutron-irradiated ceramics measured at room temperature to 1073 K. Open symbols at 1073 K represent as measured values that contain annealing recovery, and the corrected values were plotted with solid symbols.

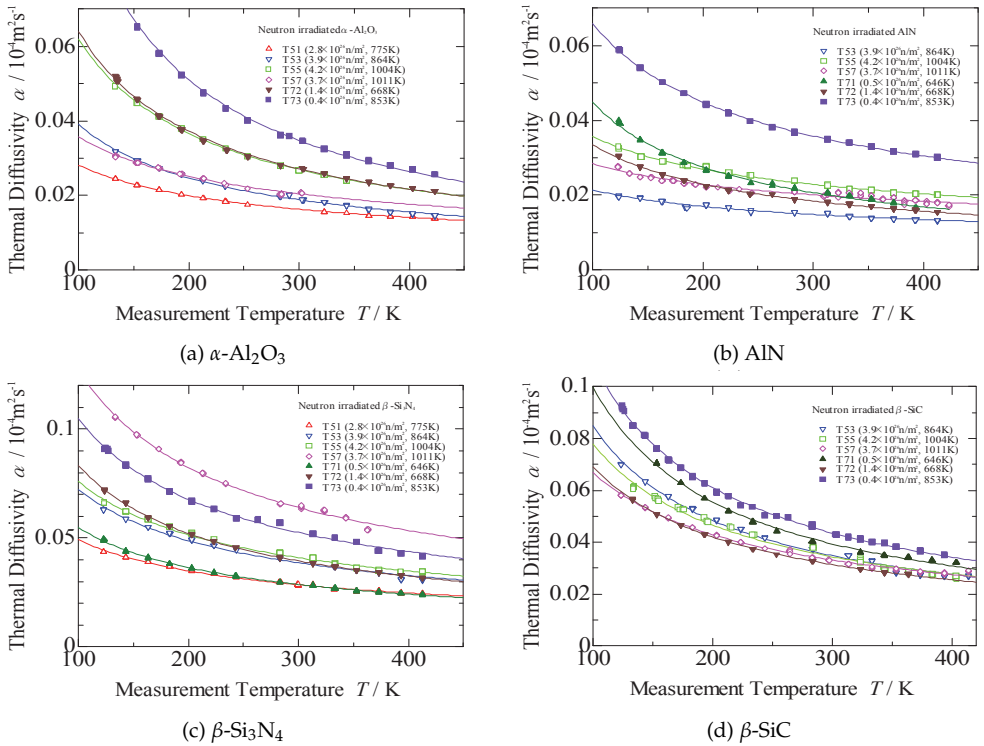


Fig. 9. Thermal diffusivity of neutron-irradiated ceramics measured at 123-413 K.



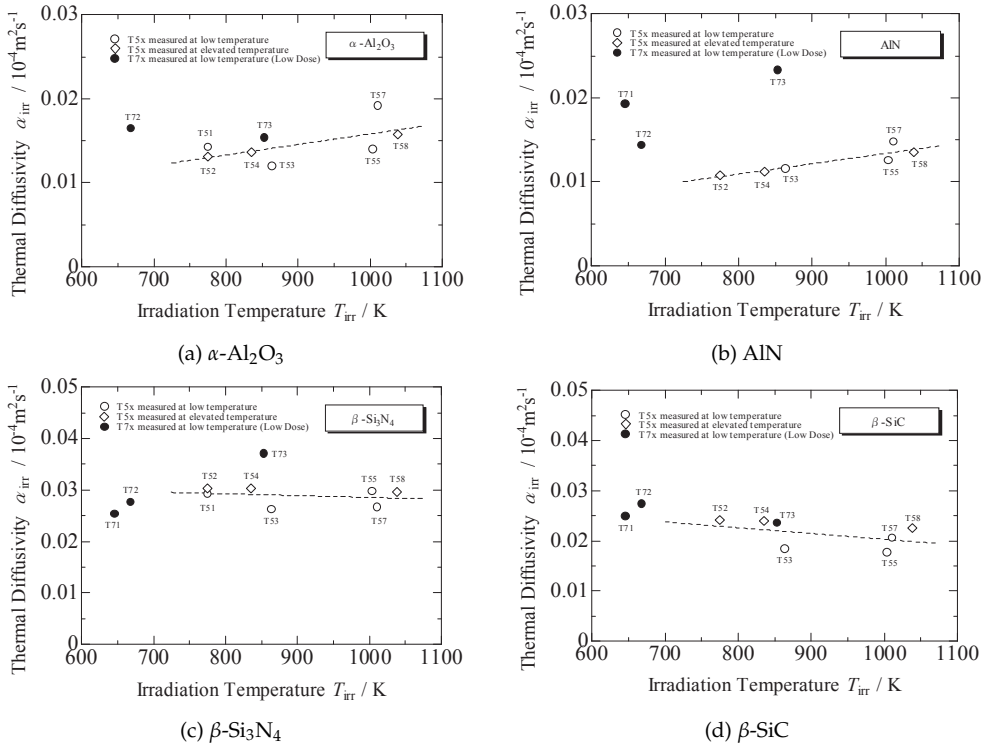


Fig. 10. Estimated thermal diffusivity of neutron-irradiated ceramics during the irradiation.

## 6. References

- [1] Y. Katoh, L.L. Snead, C.H. Henager Jr., A. Hasegawa, A. Kohyama, B. Riccardi, and H. Hegeman. Current status and critical issues for development of SiC composites for fusion applications. *Journal of Nuclear Materials*, Vol. 367-370, pp. 659–671, 2007.
- [2] T. Hino, E. Hayashishita, T. Yamada, X. Liu, A. Kohyama, Y. Yamauchi, Y. Hirohata, and Y. Nobuta. Progress of plasma surface interaction study on low activation materials. *Fusion Engineering and Design*, Vol. 81, pp. 181–186, 2 2006.
- [3] R. Andreani, E. Diegele, R. Laesser, and B. van der Schaaf. The European integrated materials and technology programme in fusion. *Journal of Nuclear Materials*, Vol. 329-333, pp. 20–30, 2004.
- [4] J.C. Corelli, J. Hoole, J. Lazzaro, and C.W. Lee. Mechanical, thermal, and microstructural properties of neutron-irradiated SiC. *Journal of the American Ceramic Society*, Vol. 66, No. 7, pp. 529–538, July 1983.
- [5] M. Akiyoshi and T. Yano. Neutron-Irradiation Effect in Ceramics Evaluated from Macroscopic Property Changes in As-irradiated and Annealed Specimens. *Progress in Nuclear Energy*, Vol. 50, pp. 567–574, 2008.
- [6] M. Akiyoshi, T. Yano, Y. Tachi, and H. Nakano. Saturation in degradation of thermal diffusivity of neutron-irradiated ceramics at  $3 \times 10^{26} \text{ n/m}^2$ . *Journal of Nuclear Materials*, Vol. 367-370, pp. 1023–1027, 2007.
- [7] L. L. Snead, T. Nozawa, Y. Katoh, T. Byun, S. Kondo, and D. A. Petti. Handbook of SiC properties for fuel performance modeling. *Journal of Nuclear Materials*, Vol. 371, pp. 329–377, 2007.
- [8] M. Akiyoshi, K. Ichikawa, T. Donomae, and T. Yano. Macroscopic properties and microstructure changes of heavily neutron-irradiated  $\beta\text{-Si}_3\text{N}_4$  by annealing. *Journal of Nuclear Materials*, Vol. 307-311, pp. 1305–1309, 2002.
- [9] T. Yano, M. Akiyoshi, K. Ichikawa, Y. Tachi, and Y. Iseki. Physical property change of heavily-neutron-irradiated  $\text{Si}_3\text{N}_4$  and SiC by thermal annealing. *Journal of Nuclear Materials*, Vol. 289, pp. 102–109, 2001.
- [10] T. Yano, K. Ichikawa, M. Akiyoshi, and Y. Tachi. Neutron irradiation damage in aluminum oxide and nitride ceramics up to a fluence of  $4.2 \times 10^{26} \text{ n/m}^2$ . *Journal of Nuclear Materials*, Vol. 283-287, pp. 947–951, 2000.
- [11] C. Hazelton, J. Rice, L.L. Snead, and S.J. Zinkle. Effect of neutron radiation on the dielectric, mechanical and thermal properties of ceramics for rf transmission windows. *Journal of Nuclear Materials*, Vol. 253, pp. 190–195, 1998.
- [12] M. Rohde and B. Schulz. The effect of the exposure to different irradiation sources on the thermal conductivity of  $\text{Al}_2\text{O}_3$ . *Journal of Nuclear Materials*, Vol. 173, pp. 289–293, 1990.
- [13] M. Akiyoshi. Thermal diffusivity of ceramics at the neutron irradiation temperature estimated from post-irradiation measurements at 123–413 K. *Journal of Nuclear Materials*, Vol. 386-388, pp. 303–306, 2009.
- [14] M. Akiyoshi, I. Takagi, T. Yano, N. Akasaka, and Y. Tachi. Thermal conductivity of ceramics during irradiation. *Fusion Engineering Design*, Vol. 81, pp. 321–325, 2006.
- [15] K. Abe, A. Kohyama, C. Namba, F. W. Wiffen, and R. H. Jones. Neutron irradiation experiments for fusion reactor materials through JUPITER program. *Journal of Nuclear Materials*, Vol. 258-263, No. Part2, pp. 2075–2078, 1998.
- [16] L.L. Snead, R. Yamada, K. Noda, Y. Katoh, S.J. Zinkle, W.S. Eatherly, and A.L. Qualls. In situ thermal conductivity measurement of ceramics in a fast neutron environment. *Journal of Nuclear Materials*, Vol. 283-287, pp. 545–550, 2000.

- [17] K. Yasuda, K. Tanaka, M. Shimada, T. Yamamoto, S. Matsumura, and C. Kinoshita. Influence of an electric field on the microstructure evolution of ion-irradiated alumina. *Journal of Nuclear Materials*, Vol. 329-333, pp. 1451–1455, 2004.
- [18] W.J. Parker, R.J. Jenkins, C.P. Butler, and G. L. Abbott. Flash method of determining thermal diffusivity, heat capacity, and thermal conductivity. *Journal of Applied Physics*, pp. 1679–1684, 1961.
- [19] M. Akiyoshi, N. Akasaka, Y. Tachi, and T. Yano. Interstitial atom behavior in neutron-irradiated beta-silicon nitride. *Journal of the Ceramic Society of Japan*, Vol. 112, No. 5, pp. 1490–1494, 2004.
- [20] M. Akiyoshi, N. Akasaka, Y. Tachi, and T. Yano. Relation between macroscopic length change and the crystal structure in heavily neutron-irradiated ceramics. *Journal of Nuclear Materials*, Vol. 329-333, pp. 1466–1470, 2004.
- [21] H. Miyazaki, T. Suzuki, T. Yano, and T. Iseki. Effect of thermal annealing on the macroscopic dimension and lattice parameter of heavily neutron-irradiated silicon carbide. *Journal of Nuclear Science and Technology*, Vol. 29, No. 7, pp. 656–663, July 1992.
- [22] T. Yano, K. Sasaki, T. Maruyama, T. Iseki, M. Ito, and S. Onose. A step-heating dilatometry method to measure the change in length due to annealing of a SiC temperature monitor. *Nuclear Technology*, Vol. 93, pp. 412–415, March 1991.
- [23] P. Kirkegaard, J.V. Olsen, M. Eldrup, and N.J. Pedersen. Palsfit: A computer program for analysing positron lifetime spectra. Technical report, RisøDTU, February 2009. Risø-R-1652, ISBN 978-87-550-3691-8.
- [24] Y. Kanechika, M. Azuma, and H. Fukushima. Optimum sintering conditions for optical properties of translucent aluminum nitride ceramics. *Chinese Science Bulletin*, Vol. 54, No. 5, pp. 842–845, 2009.
- [25] M. Akiyoshi, T. Yano, and M. Jenkins. A new type of defect on {11 $\bar{2}$ 0} planes in  $\beta$ -Si<sub>3</sub>N<sub>4</sub> produced by neutron irradiation. *Philosophical Magazine Letters*, Vol. 81, No. 4, pp. 251–258, 2001.
- [26] M. Akiyoshi and T. Yano. Connection structures between type-I and type-II defect in neutron irradiated  $\beta$ -Si<sub>3</sub>N<sub>4</sub>. *Journal of Electron Microscopy*, Vol. 52, pp. 267–275, 2003.
- [27] Q. Xu, T. Yoshiie, and M. Okada. Positron annihilation of vacancy-type defects in neutron-irradiated 4H-SiC. *Journal of Nuclear Materials*, Vol. 386-388, pp. 169–172, 2009.
- [28] S. Dannefaer and D. Kerr. Positron annihilation investigation of electron irradiation-produced defects in 6H-SiC. *Diamond and Related Materials*, Vol. 13, No. 1, pp. 157–165, 2004.
- [29] L. Henry, MF. Barthe, C. Corbel, P. Desgardin, G. Blondiaux, S. Arpiainen, and L. Liskay. Silicon vacancy-type defects in as-received and 12-MeV proton-irradiated 6H-SiC studied by positron annihilation spectroscopy. *Physical Review B*, Vol. 67, No. 11, p. 115210, 2003.
- [30] A. Polity, S. Huth, and M. Lausmann. Defect characterization in electron-irradiated 6H-SiC by positron annihilation. *Physical Review B*, Vol. 59, No. 16, pp. 10603–10606, 1999.
- [31] A. Kawasuso, H. Itoh, N. Morishita, M. Yoshikawa, T. Ohshima, I. Nashiyama, S. Okada, H. Okumura, and S. Yoshida. Silicon vacancies in 3C-SiC observed by positron lifetime and electron spin resonance. *Applied Physics A - Materials Science & Processing*, Vol. 67, No. 2, pp. 209–212, 1998.

- [32] A. Kawasuso, H. Itoh, T. Ohshima, K. Abe, and S. Okada. Vacancy production by 3 MeV electron irradiation in 6H-SiC studied by positron lifetime spectroscopy. *Journal of Applied Physics*, Vol. 82, No. 7, pp. 3232–3238, 1997.
- [33] A. Kawasuso, H. Itoh, S. Okada, and H. Okumura. Annealing processes of vacancy-type defects in electron-irradiated and as-grown 6H-SiC studied by positron lifetime spectroscopy. *Journal of Applied Physics*, Vol. 80, No. 10, pp. 5639–5645, 1996.
- [34] T. Iwai, Y. Ito, and M. Koshimizu. Vacancy-type defect production in iron under ion beam irradiation investigated with positron beam Doppler broadening technique. *Journal of Nuclear Materials*, Vol. 329-333 Part2, pp. 963–966, 2004.

# Luminescence Properties of AlN Ceramics and Its Potential Application for Solid State Dosimetry

Laima Trinkler and Baiba Berzina

*Institute of Solid State Physics, University of Latvia  
Latvia*

## 1. Introduction

Aluminum nitride (AlN) is a wide band material ( $E_g = 6.2$  eV) with a wurtzite structure. It has already found practical application in microelectronics as substrate, insulator and packaging material due to combination of the uppermost qualities, such as high thermal conductivity, good dielectric properties and thermal expansion coefficient comparable with that of silicon. There are different modifications of the material used for application and investigation purposes: single crystal, powder, nanostructures, thin films and so on. AlN ceramics is one of them, it is easy to produce and to handle, thereat in the form of ceramics AlN maintains the main properties of the material.

The objective of the study is investigation of luminescence properties of AlN ceramics including elucidation of luminescence centers and mechanisms as well as estimation of potential application of the material in the field of solid state dosimetry. This chapter is based on our papers devoted to luminescent and dosimetric properties of AlN ceramics published in 1998-2009 and quite recent measurements performed at low temperatures.

## 2. Experimental details

### 2.1 Samples of AlN ceramics

Samples of high-density AlN ceramics were obtained in Institute of Inorganic Chemistry, Riga Technical University, Latvia (Palcevskis et al., 1997; 1999). AlN powder with specific surface area in the range 20-40 m<sup>2</sup>/g and Y<sub>2</sub>O<sub>3</sub> powder (30 m<sup>2</sup>/g), both produced by plasma synthesis, were used for production of ceramics. Directly after synthesis AlN powders were kept in organic solvent. AlN and Y<sub>2</sub>O<sub>3</sub> powders (2-9 wt.%) were mixed in organic media. Then powder mixtures were dried and pressed in cylinders (12 mm in diameter) at 200 MPa. After burning out organic components in vacuum at 500 °C cylinders were embedded into alumina crucibles and placed in a tungsten resistance furnace. The sintering was carried out in nitrogen atmosphere (0.12 MPa) at temperature 1600-1800 °C during 300-900 min. The produced polycrystalline ceramic cylinders were sliced into 1 mm thick tablets, suitable for optical measurements.

Sintered samples were characterized by the producers as follows (Palcevskis et al., 1999). Size of polycrystalline grains is around 4 μm. Depending on sintering conditions

(temperature and time) density varies from 3.2 to 3.4 g/cm<sup>3</sup> and thermal conductivity – from 80 to 260 W/mK. AlN grains constitute more than 90% of the volume of the sintered samples; the rest volume belongs to secondary phases: Y<sub>4</sub>Al<sub>2</sub>O<sub>9</sub>, AlYO<sub>3</sub> and Y<sub>3</sub>Al<sub>5</sub>O<sub>12</sub>. Though nominally pure, AlN always contains oxygen impurity as a natural dopant, which substitutes nitrogen in regular lattice sites and forms oxygen-related defects of various types. The total oxygen content in the studied AlN ceramic samples determined by the neutral activation analysis is from 0.1 to 0.7 wt.%. Alongside with oxygen impurity aluminum vacancies are generating for maintenance of charge balance. Besides there are detected other uncontrolled impurities of small concentration (< 1000 ppb) such as Fe, Cr, Ni and Zr. The further spectral measurements have proved the presence of Mn impurity, too. Oxygen and other impurities contribute to luminescence properties of the material. In some of experiments we used AlN ceramics samples subjected to oxygen ion implantation. This procedure was done in Taiwan National University with doses 10<sup>14</sup> and 10<sup>15</sup> ion/cm<sup>2</sup>.

## 2.2 Methods of photoluminescence, thermoluminescence and optically stimulated luminescence

Luminescence properties of AlN ceramics were studied using methods of photoluminescence (PL), thermoluminescence (TL) and optically stimulated luminescence (OSL). Photoluminescence is luminescence of material revealed under irradiation with ultraviolet (UV) or visible light. We have used such characteristics of PL as emission spectra obtained under irradiation with a fixed wavelength from UV region and excitation spectra – dependence of luminescence intensity at a fixed emission wavelength upon the varied wavelength of excitation light.

Irradiation of wide band gap materials with UV light and ionizing radiation results not only in immediate response in the form of luminescence but also in ionization – transfer of previously bound charge carriers (electrons and holes) into the conduction band. After relaxation charge carriers can be trapped on trapping centers. Trapping levels remain occupied until supply of additional stimulation energy in the form of heat or light (visible or infrared) releases charge carriers, which can participate in further retrapping or recombination processes with light emission. Such light emission is called TL or OSL depending on type of stimulation energy supplied.

Optically stimulated luminescence is characterized with OSL emission spectra – dependence of emission intensity versus emission wavelength at fixed irradiation wavelength (energy) and dose, OSL excitation spectra – dependence of emission intensity of irradiation wavelength or energy at fixed emission and stimulation wavelength and OSL stimulation spectra – dependence of emission intensity on wavelength of stimulation light at fixed emission and irradiation wavelength. TL is characterized with TL glow curves – dependence of TL emission intensity on heating temperature, TL emission spectra – dependence of emission intensity versus emission wavelength at fixed irradiation wavelength (energy) and dose, TL excitation spectra – dependence of emission intensity of irradiation wavelength or energy at fixed emission wavelength.

## 2.3 Equipment

Experiments on PL and OSL as well as some TL experiments in the 0-300 °C temperature range were carried out in Institute of Solid State Physics, University of Latvia, Latvia, using an experimental setup for spectroscopic measurements. The setup was equipped with a

deuterium lamp LDD-400 as a source of UV light and a grating monochromator MDR-2 (LOMO) in the excitation channel. The luminescence signal was analyzed either with a prism monochromator SPM-2 (Carl Zeiss Jena) and detected with photo multiplier tubes H7468-03, H7468-20 (Hamamatsu) and FEU-100 (earlier experiments), or with a grating monochromator SR-303i-B (Shamrock) equipped with a CCD camera DV420-BU2. For low temperature measurements samples were inserted into a closed cycle helium refrigerator (Janis) providing stable temperatures in the 8-325 K range. TL measurements were done using a small home-made oven with linear heating up to 300 °C, used as a sample holder in the experimental setup for spectral measurements.

Beta, gamma, X-ray and UV light induced TL and partly OSL measurements were fulfilled in Riso National Laboratory, Denmark, using the available equipment: Riso model TL/OSL readers with linear planchet heating and Alnor Dosacus TLD reader, operating with hot nitrogen heating. For most of irradiations a  $^{90}\text{Y}/^{90}\text{Sr}$  beta source build in the Riso TL reader and a  $^{60}\text{Co}$  standard gamma calibration facility were used. UV irradiation was performed with a metal halide lamp Sol-2 (K.Honley GmbH), which simulates a solar spectrum at ground level from 300 nm upwards.

Some of TL measurements were done in University of Nice-Sophia Antipolis, LPES-CRESA, France, using a home-made TL reader with linear heating and an optical multichannel analyzer (Princeton Instruments). UV irradiation was carried out with a deuterium lamp (50W) with attached interference filters.

### 3. Photoluminescence properties of AlN ceramics

Luminescence spectra of AlN were studied using different excitation types; however, excitation with UV light, producing photoluminescence, appeared to be the most informative. PL emission of AlN ceramics was observed in the 300-1100 nm region, which is spectral area of luminescence of defect centers. It contains several emission bands, and for each of them excitation spectrum was measured. Excitation spectra were measured beginning from the fundamental absorption edge (in other words band-to-band transition area) at 200 nm and up to 600 nm. The luminescence region of exciton emission (below 250 nm) is not available with the equipment used and will not be discussed here.

The general view of PL emission spectrum could be illustrated by our recent results on PL measurements of AlN ceramics fulfilled in the 8-300 K temperature range. The following emission bands can be distinguished in the PL spectra at 300 K in Fig.1, a.: a broad UV-blue band in the 300-500 nm region, a narrower band at 600 nm and minor bands at 700 nm and 1000 nm. At low temperature the composition of PL spectrum remains the same, except for emergence of an additional minor band at 500 nm, while relative intensity of emission bands under different excitation wavelengths changes, see Fig.1, b. Contribution of individual bands varies from sample to sample and depends on composition and sintering conditions of ceramics. Let us discuss properties and origin of individual bands.

#### 3.1 Oxygen-related emission

The main attention should be devoted to the broad complex UV-blue band. It is composed of two subbands – those at 400 and 480 nm each of them having its own excitation spectrum. As it is seen from Fig.2. taken from (Berzina et al., 2009), 400 nm emission band has excitation band at 240-250 nm, while 480 nm emission band has excitation band centered at 280-290 nm; both of them are excited also in the fundamental absorption edge at 200-220 nm.

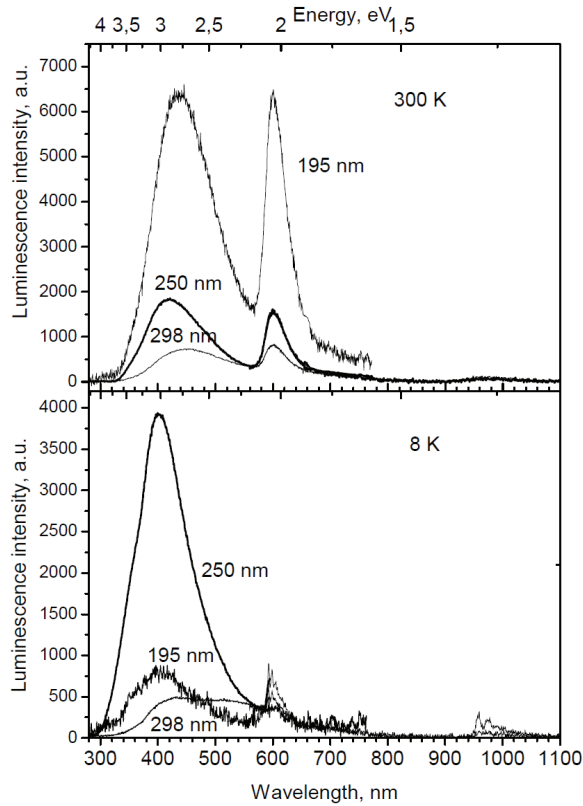


Fig. 1. PL spectra of AlN ceramics at 300 and 8 K, excitation wavelengths shown on the graph

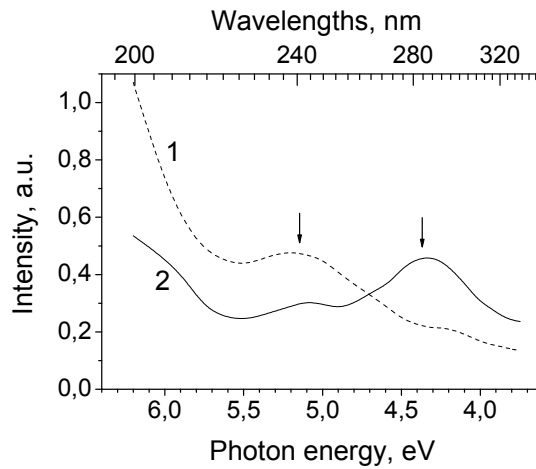


Fig. 2. Excitation spectra of 400 nm (1) and 480 nm (2) emission bands of AlN ceramics at 300 K



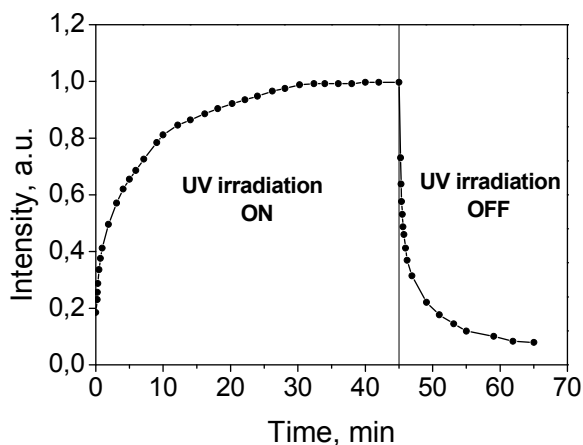


Fig. 3. Time dependence of intensity of the UV-blue emission at start and stop of UV irradiation at 300 K

It was observed in (Berzina et al., 2001) that intensity of the UV-blue emission band depends upon duration of the continuous UV irradiation. As seen from Fig.3, at the beginning of the UV irradiation with 245 nm it is low, and then gradually increases until reaching saturation level after approximately 30 min. After ceasing of UV irradiation the gradually decreasing afterglow emission is observed for several minutes. In the same time position of the maximum of emission band shifts to the longer wavelengths.

Many publications are devoted to elucidating the origin of luminescence centers responsible for the UV-blue band. In (Slack, 1973; Youngman & Harris, 1990 and Harris et al., 1990) it was shown that this band is connected with emission of oxygen-related defects. Later our works (Trinkler et al, 1998, 2001a, 2003, 2005, 2007a, 2007b) have shown that this band is revealed also in TL and OSL emission spectra. Presence of the emission band in PL, TL and OSL as well as afterglow emission and time characteristics of its intensity speak in favor in its recombination character. The nature of the 400 nm subband was determined by the EPR and ENDOR studies (Schweizer et al, 2000) as recombination luminescence of two defect centers: a donor - ( $O_N-v_{Al}$ ) - a complex defect center formed by an oxygen ion substituting for nitrogen ion  $O_N$  in a regular site and a neighboring aluminum vacancy  $v_{Al}$  and an acceptor - another closely situated oxygen ion  $O_N$ .

The luminescence mechanism responsible for the 400 nm emission band in AlN ceramics, was formulated in papers (Berzina et al., 2002, 2009). The corresponding energy band diagram is shown in Fig. 5. According to it the ( $v_{Al}-O_N$ ) center forms its energy level within the band gap above the valence band (level 5). Irradiation of AlN with 245 nm light from the own absorption band ( $h\nu_{def}$ ) results in its excitation (level 6). The excited state is situated close to the bottom of the conduction band resulting in ionization of the ( $v_{Al}-O_N$ ) center and an electron transfer into the conduction band. An electron from the conduction band can be captured by one of numerous electron traps (levels from 7 up to 11). One of them is an  $O_N$  defect (level 7) - a close neighbour of the ionized ( $v_{Al}-O_N$ ) center. Recombination of the ( $v_{Al}-O_N$ )<sup>+</sup> and ( $O_N$ )<sup>-</sup> centers with emission of a light quantum ( $h\nu_{lum}$ ) results in appearance of the 400 nm emission band.

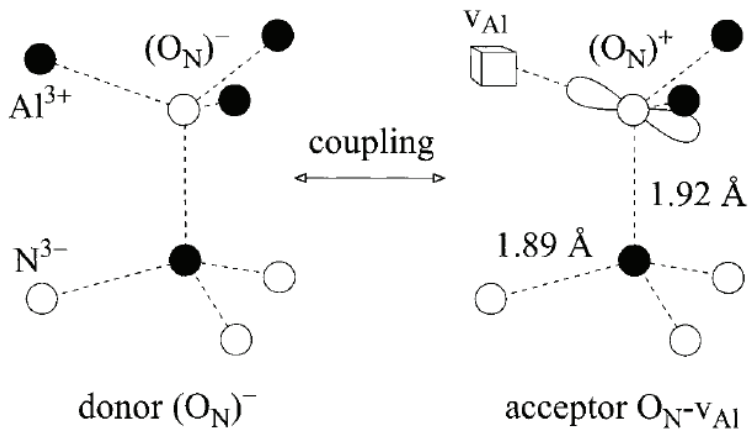


Fig. 4. Model of the coupled donor and acceptor pairs in AlN ceramics (Schweizer et al., 2000)

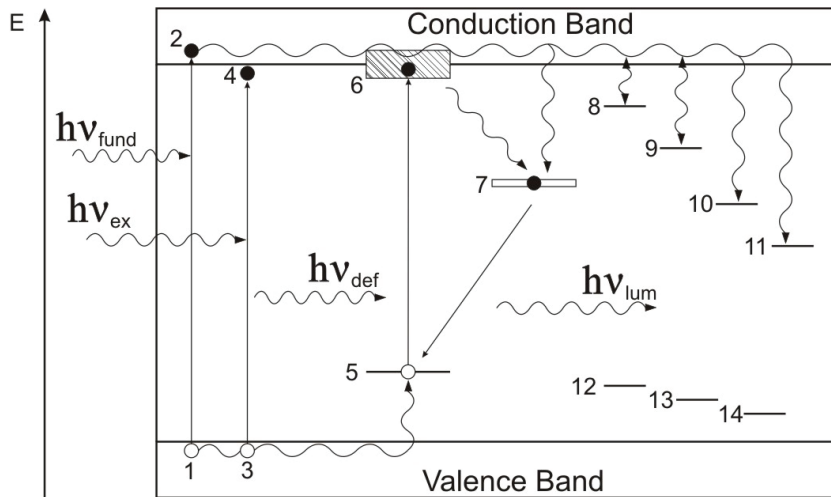


Fig. 5. Energy band diagram of AlN (Berzina et al., 2009). Explanation is given in the text

An electron from the conduction band can be repeatedly recaptured and released by trapping centers, before finally being trapped by  $O_N$  defect, thus causing delay of emission rise under continuous excitation with 245 nm, shown in Fig.3.

The similar recombination process can occur under irradiation with light from the fundamental absorption edge region, corresponding to electron-hole pair ( $hv_{fund}$ ) or exciton ( $hv_{ex}$ ) generation. In this case energy is transferred from host lattice to oxygen-related defects resulting in formation of  $(V_{Al}-O_N)^+$  and  $(O_N)^-$  centers and 400 nm emission.

The 480 nm subband is also connected with oxygen impurity, which most probably is a part of a complex defect. Tentatively 480 nm emission is ascribed to recombination luminescence with participation of  $(V_{Al}-2O_N)$  center (Nappe et al., 2009 and references therein). Such centers are comprised of two close oxygen ions substituting for nitride ion and an aluminum

vacancy. In the energy band diagram the corresponding level is not shown, though it is clear that it should be located a little higher than that of ( $v_{\text{Al}}\text{-O}_{\text{N}}$ ) center and participate in similar processes. Our studies of nanostructured AlN (Berzina et al., 2009 and references therein) have shown that contribution of the 480 nm into the total UV-blue emission increases when size of AlN grains diminishes, and hence, specific surface area expands. It allows supposing that these oxygen-related defects responsible for the 480 nm emission band are located mainly on surface. Besides, the relative increase of the 480 nm band was observed in the samples of AlN ceramics after implantation of oxygen ions (Trinkler et al. 2007a, 2007b). Ion implantation causes damage of the surface layers of AlN and increases oxygen concentration, thus making generation of ( $v_{\text{Al}}\text{-2O}_{\text{N}}$ ) center more probable compared to untreated samples.

### 3.2 Manganese-related emission

The 600 nm band was observed in PL, afterglow and TL emission spectra of all studied samples of AlN ceramics. Our high resolution measurements, illustrated by Fig. 6 show the presence of fine structure, which can be distinguished at room temperature (RT) and becomes more clearly seen at low temperature. This fine structure is characterized with equidistant peaks with separation energy around 20 meV. This emission band usually is interpreted as luminescence of tetravalent manganese ion  $\text{Mn}^{4+}$  substituting for Al ion, and equidistant peaks are ascribed to phonon replicas. For the first time this band was observed and interpreted in (Karel et al., 1966) and later studied in other works (Benabdesselam et al., 1995). However, some authors (Miyajima et al., 2006) basing on the results of X-ray absorption fine structure measurements, state that this band is caused by Mn ion having charge between +2 and +3. Other interpretations of the band ascribed to intrinsic defects of AlN are also found in literature, for example, defects formed from nitrogen vacancies ( $v_{\text{N}}$ ) and excess Al (Sarua et al., 2003).

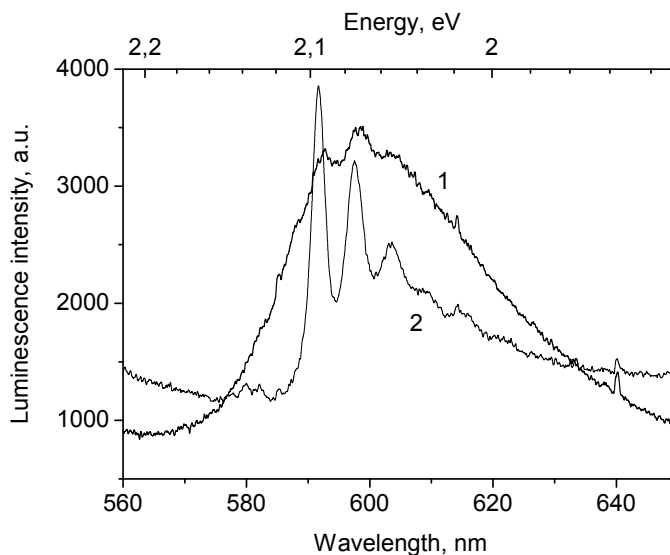


Fig. 6. 600 nm emission band of AlN ceramics measured under excitation wavelength 243 nm at temperature 300 K (1) and 8 K (2)

Excitation spectrum of this emission band is shown in Fig. 7. together with that of 400 nm band. Besides the fundamental absorption edge at 200 nm two excitation bands at 255 and 400 nm are observed. The latter excitation band covers the spectral region of the UV-blue emission band; this results in reabsorption and conversion of UV light into red light. Presence of the 600 nm band in afterglow and TL emission spectra confirms that the corresponding luminescence centre also participates in recombination process.

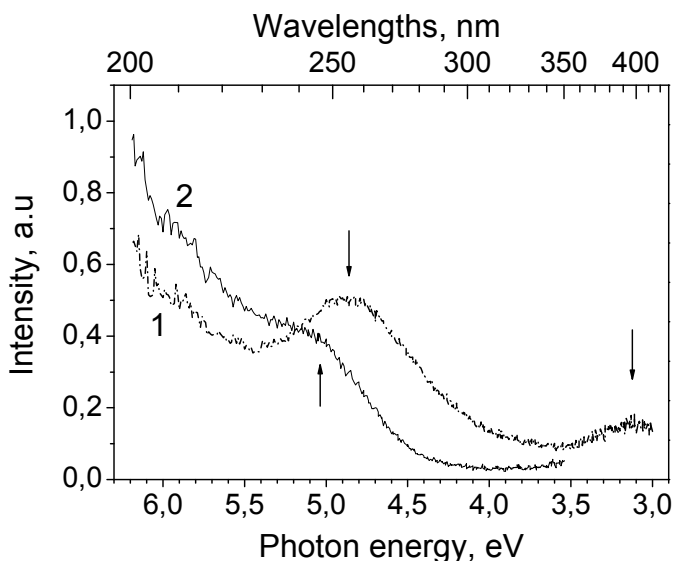


Fig. 7. Excitation spectra of 600 nm band (1) and 400 nm band (2) of AlN ceramics at 300 K

### 3.3 Other minor PL bands

Other PL luminescence bands observed in AlN ceramics are connected with other uncontrolled impurities. They are the following: a minor band at 700 nm, excited at 280 and 400 nm excitation bands and tentatively ascribed to chromium impurity (Nappe et al., 2011 and references therein) and an infrared band around 1000 nm, connected with iron impurity. At low temperatures the 1000 nm emission band reveals fine structure seen at Fig.1, which is explained as 3d-3d transition  ${}^4T_1(G) \rightarrow {}^6A_1(S)$  of  $Fe^{3+}$  ion substituting for Al in a regular site and its phonon replicas (Baur et al., 1994).

Summarising the data on PL of AlN ceramics, a conclusion can be drawn that the observed spectral properties of this material are determined by presence of uncontrolled impurities - oxygen, manganese, iron and probably chromium, which form luminescence centres taking part in inter-center and recombination luminescence.

## 4. AlN ceramics as potential material for solid state dosimetry

There is a number of materials widely used for TL dosimetry as thermoluminescence detectors (TLD) of ionizing radiation, such as  $LiF:Mg,Ti$ ;  $LiF:Mg,Cu,P$  and  $Al_2O_3:C$ .  $Al_2O_3:C$

is used also as an effective OSL dosimeter of UV light. Nevertheless a search for new prospective dosimetric materials continues. One of such new dosimetric materials could become AlN ceramics due to its properties revealed under exposure to ionizing radiation and UV light.

As it has been already mentioned irradiation of AlN ceramics causes not only the immediate response to irradiation in luminescence form, but also provides the delayed response in the form of optically and thermally stimulated luminescence. Both TL and OSL processes may be applied in dosimetry for recovering the received radiation dose. Processes of stimulated luminescence in AlN have been studied already before our works (Tale et al., 1982; Benabdesselam et al., 1995). Our studies of the processes of storage and release of radiation induced luminescence signal in AlN ceramics began in 90<sup>th</sup> and continues up to now. We have found that AlN ceramics is sensitive both to ionizing radiation and UV light, producing TL and OSL response in each case. Properties revealed by AlN ceramics after preliminary irradiation with ionizing radiation (X,  $\beta$ ,  $\gamma$  rays) and UV light are similar, but they have also some differences. They will be discussed individually according to irradiation type.

#### **4.1 Stimulated luminescence processes induced by ionizing radiation**

##### **4.1.1 Thermoluminescence induced by ionizing radiation**

There are several important TL characteristics of material, which determine possibility of its practical application in the area of solid state dosimetry: intensity of TL signal (or in other words sensitivity of material to irradiation), characteristics of TL glow curve, TL emission spectrum, need for additional treatment for use and reuse of a sample, linearity of the dose response, stability of the stored signal and others.

TL properties of AlN ceramics induced by ionizing radiation were studied in comparison with other widely known TLD using the same experimental conditions and irradiation doses (Trinkler et al., 1998). Particularly, it was found that AlN ceramics exhibits amazingly high TL sensitivity. Thus, after irradiation with beta rays (<sup>90</sup>Sr/<sup>90</sup>Y beta source) for a typical routine read out procedure with the Riso TL reader using a heating rate 10 °C/s the ratio of the TL lightsum (sum of recorded electronic counts) per unit detector mass and radiation dose constitutes 54:27:7:1 for AlN ceramic sample, LiF:Mg,Cu,P, Al<sub>2</sub>O<sub>3</sub>:C and LiF:Mg,Ti, respectively, see Fig.8.

The TL glow curve of AlN ceramics is characterized with one intensive broad peak extending up to 500 °C, see Fig.8, curve 1. The thermal position of the peak maximum varies from 200 to 300 °C depending on heating rate. No difference in glow curve was observed whether beta particles,  $\gamma$ -rays or X-rays were used for irradiation. The TL signal is completely erased during a single reading using a heating temperature up to 500 °C. Thus no additional annealing or other procedure is necessary for re-use of the sample. A repeatability test showed that reduction of sensitivity after 10 successive irradiation-TL reading cycles was less than 1 %.

Dose response curve of AlN ceramics was measured in dose range  $5 \cdot 10^{-3}$  -  $5 \cdot 10^{-2}$  mGy (irradiation with <sup>60</sup>Co source) in comparison with other mentioned TLD. The curves shown in Fig.9 were obtained by Alnor TL reader using a nitrogen temperature of 300 °C for all samples except for LiF:Mg,Cu,P, which was heated up to 260 °C. AlN ceramics sample revealed linear dose response in the range of five orders of magnitude, like other acknowledged TLD materials, which must be confessed as a very good result.

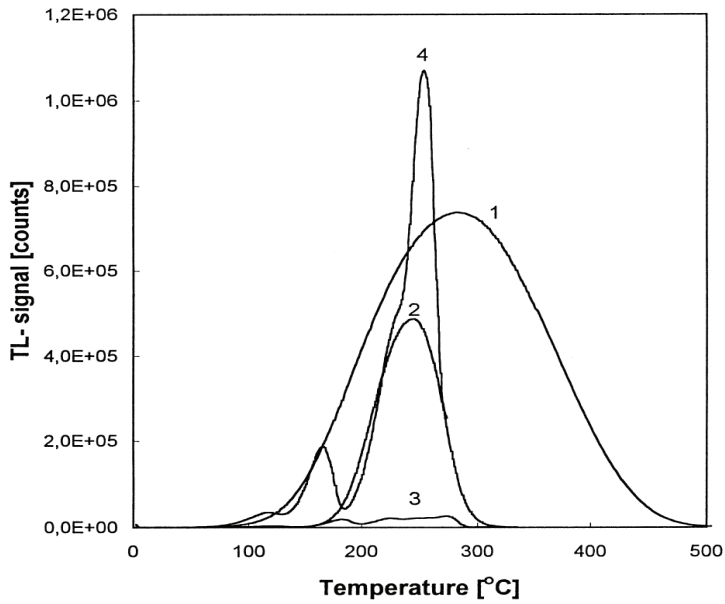


Fig. 8. Glow curves of different types of TL dosimeters irradiated with 28 mGy beta radiation: 1 – AlN ceramics; 2 -  $\text{Al}_2\text{O}_3\text{:C}$ ; 3 -  $\text{LiF:Mg,Ti}$ , 4 -  $\text{LiF:Mg,Cu,P}$  (Trinkler et al, 1998)

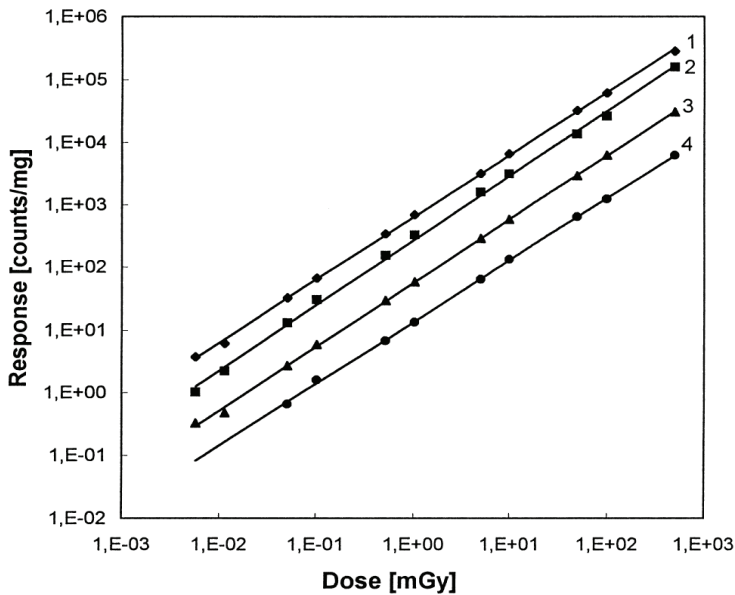


Fig. 9. Gamma ray ( $^{60}\text{Co}$ ) dose response of AlN ceramics (1),  $\text{LiF:Mg,Cu,P}$  (2),  $\text{Al}_2\text{O}_3\text{:C}$  (3) and  $\text{LiF:Mg,Ti}$  (4) obtained with Alnor hot-nitrogen heated TL reader

TL emission detection region was limited by spectral region of 300-500 nm, in order to discriminate thermal glow emission of the heater, which is observed at high temperatures in the red region. In the same time it is an optimal spectral region for detection with usual photoelectron tubes and other light detectors. In this spectral range AlN emission was observed with a maximum position around 400 nm, which shifted to longer wavelengths with rise of heating temperature. The observed emission corresponds to UV-blue luminescence band of AlN, which is ascribed to oxygen-related defects. Other luminescence bands of AlN ceramics can not be observed in these experimental conditions.

Influence of heating rate on TL signal for AlN ceramics was measured for heating rates from 0.5 to 20 °C/s in comparison with TLD  $\text{Al}_2\text{O}_3\text{:C}$ , whose response is critically sensitive to heating rate, hampering routine reading measurements of this TLD and resulting in uncertainty in the dose measurements if significant fluctuations of heating rate occur. Contrary to  $\text{Al}_2\text{O}_3\text{:C}$ , TL response of AlN sample shows only a small influence on heating rate, as it is illustrated in Fig.10.

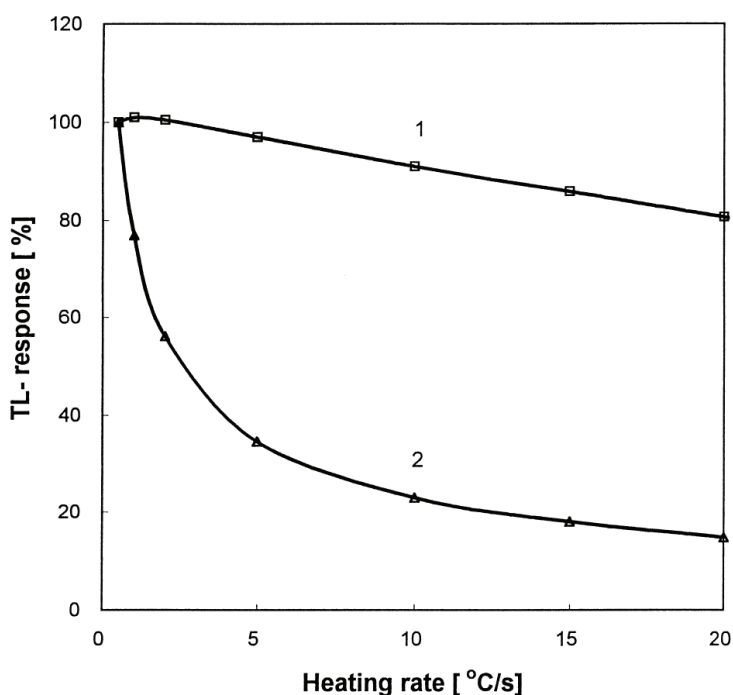


Fig. 10. Influence of heating rate on the TL response of AlN ceramics (1) and  $\text{Al}_2\text{O}_3\text{:C}$  (2) irradiated with 28 mGy beta radiation

Considerable fading of the TL signal was observed for AlN ceramics sample on storage at RT. Change of TL glow curve on storage at RT during 114 hours is illustrated in Fig.10. The TL signal is decreasing mainly due to disappearance of the low temperature part of the glow curve, but the high temperature part is also decreasing considerably. Different pre-heat procedures were tried varying preheat temperature and duration: as a result the fading rate

was decreased but not eliminated. However, at the same time the TL yield was essentially reduced by this procedure.

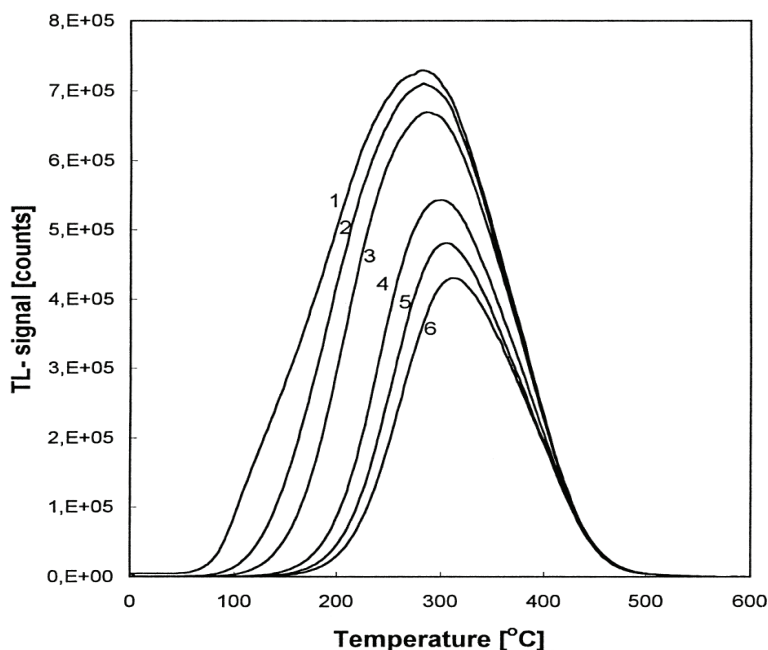


Fig. 11. TL glow curves of AlN samples recorded for different storage periods at RT after irradiation with 42 mGy beta radiation: just after irradiation (1); after a storage period of 0.17 (2); 1 (3); 24 (4); 72 (5) and 114 (6) hours

Neither the pre-irradiation with high dose (1 kGy of  $^{60}\text{Co}$  gamma irradiation) with subsequent annealing nor a special procedure of very slow annealing (1 °C/min) resulted in improvement of fading characteristics of AlN ceramics. The pronounced fading of the TL signal in AlN ceramics is a serious obstacle for its application as TLD material.

Sample No	Sintering time (min)	Sintering temperature (°C)	TL response after irradiation (counts.mg <sup>-1</sup> )	TL response after 17 h (counts.mg <sup>-1</sup> )	Fading (%)	TL peak position (°C)
612	210	1645	1334	920	32	380
592	210	1705	13053	7826	40	310
572	210	1745	27673	14639	47	260
552	210	1780	36165	18160	50	250
541	120	1780	32252	15240	53	250
511	40	1780	12601	3238	74	210

Table 1. Influence of sintering conditions of AlN ceramics on TL properties. The TL response is measured immediately after and 17 h after irradiation with 1.7 R X-rays



An attempt was made to study the effect of ceramics sintering conditions on the fading rate (Trinkler et al., 1999). Samples under investigation were produced from the same initial material varying sintering temperature and time. The results of the study are summarized in Table 1. It was found that rise of the sintering temperature leads to the strong increase of the TL yield and also to a shift of the TL peak position to lower temperature with increasing fading rate. An increase of sintering time at constant sintering temperature also causes a rise of the TL yield, but in this case the thermal peak shifts to higher temperature, and hence, the fading rate decreases. The reasons why the TL peak shifts may be explained by generation of oxygen-related defects of different types, whose balance depends on sintering conditions. The optimal sintering conditions are found using the lowest sintering temperature and the longest sintering time, but even this procedure does not eliminate completely fading of the TL signal.

#### **4.1.2 Optically stimulated luminescence induced by ionizing radiation**

Optically stimulated luminescence is detected as a pulse of luminescence light decaying in time under continuous exposure of stimulation light. An OSL signal bleaches because stimulation light empties trapping levels. Typical OSL decay curve of AlN contains an intensive fast component and a weak slow component. Each of them has its own specific fading rate, fast component fades faster. Intensity of OSL is characterized with a lightsum – integral of electronic counts detected during a pulse up to its complete depletion. The following characteristics of OSL are important for characterization of material and estimation of its potential application as an OSL dosimeter: OSL emission spectrum, OSL stimulation spectrum; linearity of dose response, fading of the stored signal and others.

OSL induced by ionizing radiation in AlN ceramics (Trinkler et al., 1999) was studied using Riso TL/OSL reader, which is not designed for spectral measurements, but at the same time allows comparison of TL and OSL properties of material under the same conditions. Irradiation was performed with beta source, while stimulation was done by infrared and blue light sources, all sources integrated in the reader. Luminescence was recorded in the 300-500 nm range, corresponding to oxygen-related luminescence of AlN.

It was found that OSL sensitivity to ionizing radiation is approximately 40 times lower than TL sensitivity after the same beta dose. Not all the light yield produced by the irradiation can be released by optical stimulation: after the complete optical bleaching a residual TL signal was observed in the 300-500 °C temperature region. Study of the preheat influence showed that OSL is much more sensitive to preheat treatments than TL: after a preheat up to 150 °C during 300 s only 10% of OSL yield is left compared to 65% of TL yield in the same conditions.

The OSL decay curve induced by ionizing radiation has a dominating fast component, and its fading rate is high. It was found that OSL fading characteristics are worse than those of TL: after 150 hours of storage at room temperature only 10% of the initial OSL response is left compared with 45% of the TL response.

All the above mentioned results show that only a part of the light yield produced by ionizing radiation can be released by optical stimulation. The light-sensitive part of the stored signal can be ascribed to the trapping of the charge carriers in the shallowest trap levels located in the band gap of AlN, while the rest part of the stored signal is more stable due to trapping of charge carriers on deeper levels, which can be emptied only by heating up to sufficiently high temperatures.

It may be concluded that AlN can not be recommended for use as OSL detector of ionizing radiation because a typical OSL response is much weaker and more unstable than the TL response for the same dose.

## 4.2 Stimulated processes induced by UV light

Detection of UV radiation doses is an important area of dosimetry. UV radiation usually is divided into three spectral regions namely: UV-C (shorter than 280 nm), UV-B (280-315 nm) and UV-A (315-400 nm). Radiation of UV-C region is used in industry for characterization of materials and products and in disinfection procedures due to its bactericidal effect. UV-B region corresponds to the part of the spectral distribution of the Sun's rays reaching ground level and which is potentially harmful to human beings and other organisms. Uncontrolled exposure of naked human bodies to Sun rays from UV-A region also can cause some problems. Monitoring of UV light intensity and measuring of UV doses is important in all of these regions.

A number of our works is devoted to UV light induced stimulated processes in AlN ceramics (Trinkler et al., 2000, 2001b, 2002). It was found that this material is extremely sensitive to UV radiation producing high response both in TL and OSL. Some experiments were done in comparison with dosimetric material  $\text{Al}_2\text{O}_3\text{:C}$ , commonly used for UV dose measurements (Akselrod et al., 1990). We have measured full spectral characteristics of UV light induced TL and OSL processes: excitation spectra, emission spectra and stimulation spectra (for OSL), as well as TL glow curves, including 8-300 K temperature region.

### 4.2.1 Properties of UV light induced TL and OSL compared to those induced by ionizing radiation

A study was done when TL and OSL measurements were performed with AlN ceramics and  $\text{Al}_2\text{O}_3\text{:C}$  dosimeter in the same conditions after exposition to ionizing radiation and UV light, simultaneously comparing sensitivity of materials to radiation exposure and effects of different type of radiation on both materials (Trinkler et al., 2000). For this study the Sol-2 lamp in combination with interference filters was used as a UV light source, while TL and OSL response was measured with Riso TL/OSL reader.

The most attractive feature of AlN ceramics is the very high sensitivity to UV radiation, which is demonstrated by Fig.12. The TL response from AlN ceramics irradiated by beta particles is about 20 times higher than that of  $\text{Al}_2\text{O}_3\text{:C}$  (curves 1 and 3) and about 6000 times higher in the case of UV irradiation with wavelength 350 nm (curves 2 and 4). On this figure for the used TL yield scale the curve 4 is undistinguishable from the temperature axis. TL signal from the UV dosed AlN ceramics is characterized with a very broad and structureless glow curve (curve 2) with a maximum around 320 °C, which is significantly higher than that for beta irradiated AlN, corresponding to 230 °C (curve 1). A lower fading rate of the integrated TL signal was observed for AlN samples exposed to UV light (40 % fading over 24 h storage) than for samples exposed to beta radiation (66 % fading). This is explained by the shift of the TL curve to the higher temperature.

The TL response of AlN ceramics to UV radiant exposure was obtained by varying both the irradiation time and the irradiance, changing the distance between the sample and the excitation lamp and using sieve filters of different density. Figure 13 shows a linear relationship between the TL yield and UV radiant exposure over at least five decades. The

deviation from the linear slope observed at the highest UV doses is explained by fading effects, due to the relatively long irradiation times required.

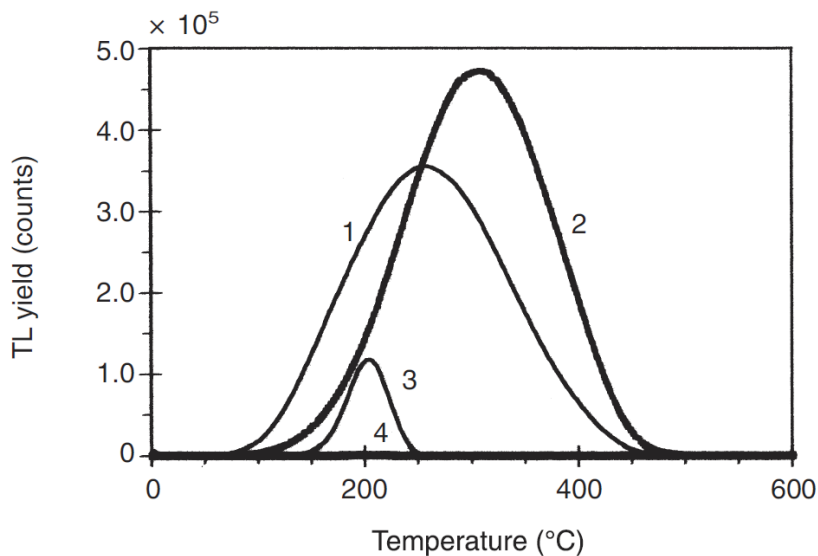


Fig. 12. TL curves obtained from AlN ceramics and  $\text{Al}_2\text{O}_3\text{:C}$  after irradiation with 100 mGy beta dose (1 and 3) and 1 min exposure to UV light produced by the lamp Sol 2 and using an interference filter with peak transmission at 350 nm

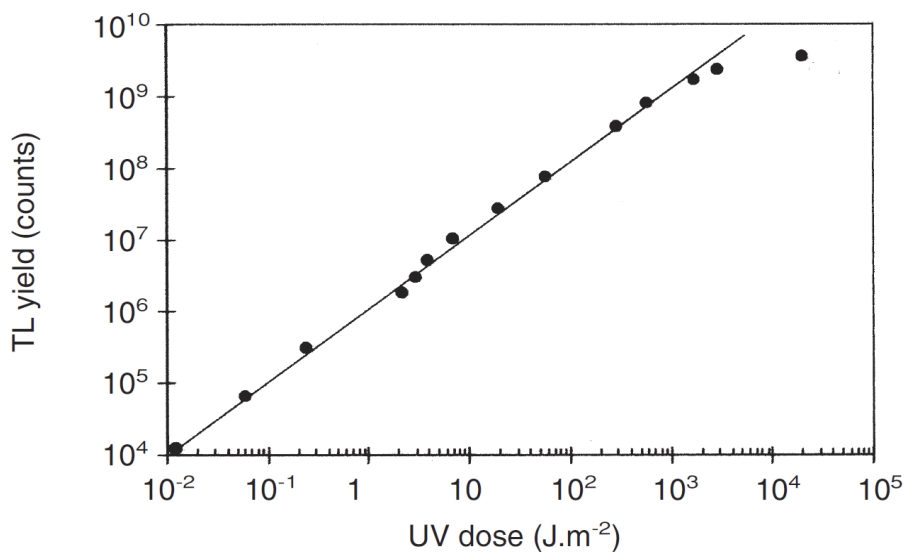


Fig. 13. UV light dose dependence of AlN

The OSL decay curves obtained from AlN and Al<sub>2</sub>O<sub>3</sub>:C after both beta and UV radiation are shown in Fig.14. In contrast to Al<sub>2</sub>O<sub>3</sub>:C showing the same shape of decay curves for both type of irradiation (curves 3 and 4), AlN ceramics has two different decay curves: an intensive fast component that dominates in beta-induced OSL (curve 1) and a slow component, which dominates in UV-induced OSL (curve 2). Although the initial OSL intensity of the AlN sample is significantly higher than that of Al<sub>2</sub>O<sub>3</sub>:C when exposed to beta radiation, this very fast AlN component yields less signal. Alternatively, when irradiating AlN with UV light of 350 nm, its OSL signal is about 60 times higher than that of Al<sub>2</sub>O<sub>3</sub>:C. Ratio of the UV light induced TL and OSL signals from AlN and Al<sub>2</sub>O<sub>3</sub>:C depends on the wavelength of UV irradiation, because each of the materials has its own spectral sensitivity, revealed by TL and OSL excitation spectrum. Thus at irradiation 200-230 nm corresponding to the highest sensitivity of Al<sub>2</sub>O<sub>3</sub>:C is the OSL response of this material is higher than that from AlN, at other wavelength it is lower.

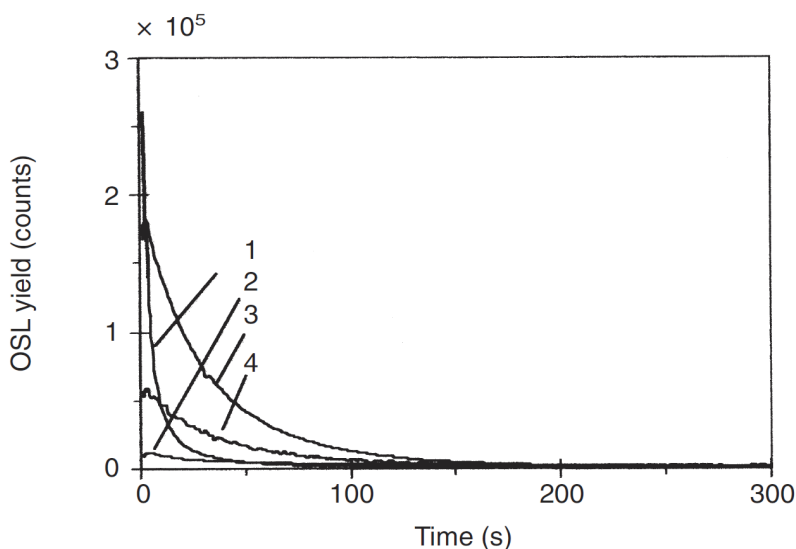


Fig. 14. OSL decay curves obtained from AlN ceramics and Al<sub>2</sub>O<sub>3</sub>:C after irradiation with 100 mGy beta dose (1 and 3) and 1 min exposure to UV light produced by the lamp Sol 2 and using an interference filter with peak transmission at 350 nm. Stimulation was performed with 470 nm light. Curve 4 is multiplied by a factor of 100

The initial part of the OSL pulse, which consists mainly of the fast component, fades faster during the storage of the dosed sample than the tail of the pulse, consisting of the slow component. That is why the fading effect is higher for the beta induced OSL, which has a dominant fast component of the decay curve: only 10% of the initial response is left after 24 hours of storage. The effect of fading is less pronounced for UV induced OSL having a dominant slow component: 45% of the initial response is left after 24 h.

The properties observed in the UV induced AlN samples such as the peaking of the TL glow curve at a higher temperature, absence of an intensive fast component of the OSL decay curve, lower fading rate of both the TL and OSL signals, assume that the UV radiation

induced stimulated luminescence involves a larger part of deep traps compared to those created by beta radiation. The deeper traps need higher energy for depopulation. The OSL response dose dependence taken as OSL yield versus UV irradiation time up to 60 min deviates from a linear slope. This is explained by fading of the OSL signal during irradiation and insufficient OSL readout time for the higher doses.

#### 4.2.2 Spectral characteristics of UV induced TL and OSL

Spectral sensitivity of AlN ceramics was determined from excitation spectrum of TL and OSL, which appeared to be similar and covering almost the whole UV region from 200 to 350 nm, with maximum effect at 240-270 nm, corresponding to absorption of oxygen-related centers. This characteristic for OSL process is shown on Fig. 15, curve 1 (Trinkler et al, 2002).

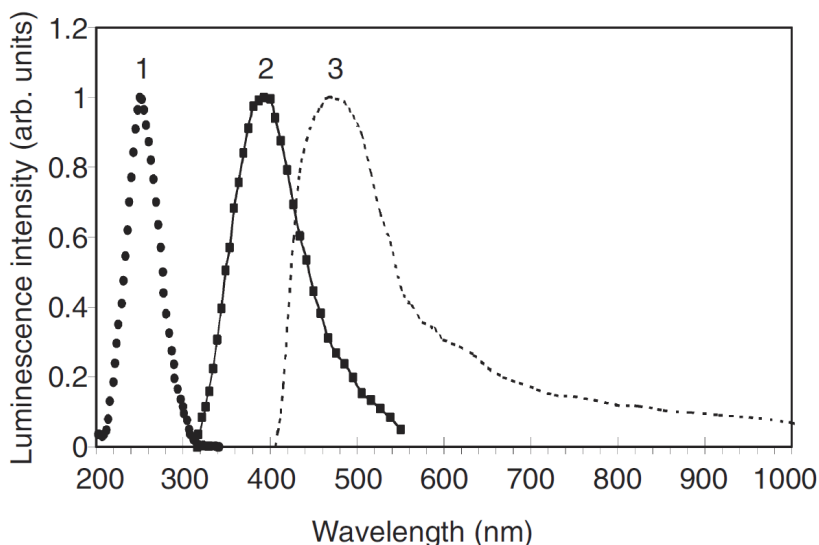


Fig. 15. Spectral characteristics of UV light induced OSL of AlN ceramics: OSL excitation spectrum (1), OSL emission spectrum (2), OSL stimulation spectrum (3)

It is remarkable that spectral sensitivity of AlN is similar with spectral sensitivity of human skin in the 280-340 nm range (see Fig.16), which corresponds to UV-B region of Solar emission potentially dangerous for human beings. This property makes AlN ceramics useful for application as material for personal UV dosimeter.

OSL emission spectrum is presented with the same UV-blue band as PL band ascribed to oxygen-related centers, as it is seen from Fig. 15, curve 2. In order to separate emission and stimulation light the detection region is limited and nothing could be said about presence of long wavelength bands in OSL emission. TL emission spectrum shown on Fig. 17. (Trinkler et al., 2003) also has the same UV-blue band, whose intensity and position of maximum shifts depending on excitation wavelength. Besides, it contains also 600 nm band. TL and OSL emission spectra fall into the 300-600 nm range, which is suitable for detection with common light detectors.

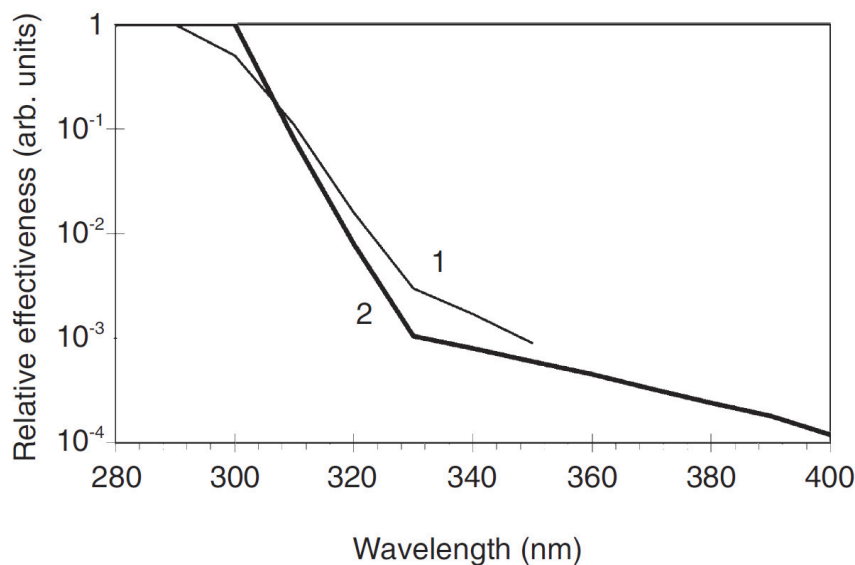


Fig. 16. Comparison of OSL excitation spectrum of AlN ceramics (1) with action spectrum of human erythema (2) (CIE Research Note, 1987)

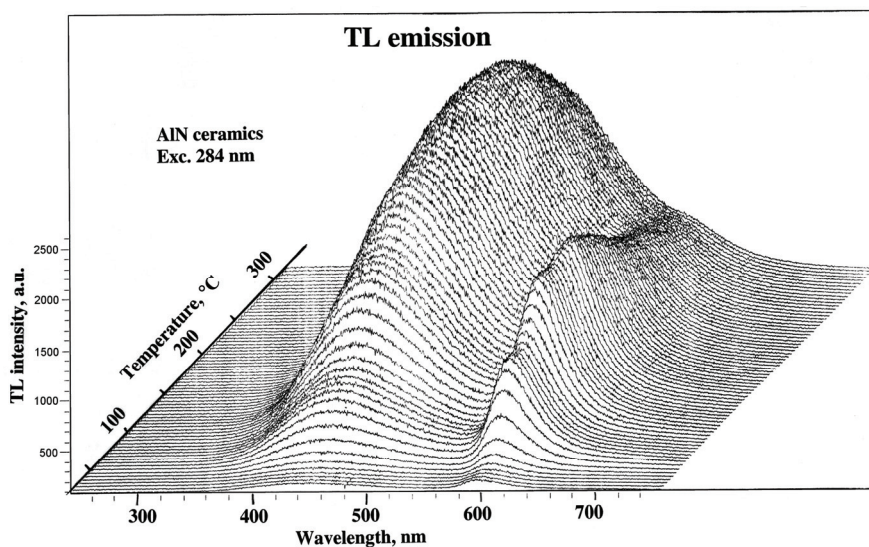


Fig. 17. 3D image of UV light induced (excitation 284 nm) TL emission from AlN ceramics

OSL is characterized also by stimulation spectrum, determined by energy levels of trapping centres, emptied during optical stimulation. For AlN ceramics it extends from 400 up to 1000 nm with an expressed maximum at 500 nm, see Fig.15, curve 3. Large spectral interval and

complex structure of the OSL emission spectrum means that numerous different trap levels participate in the stimulated luminescence process. Most of halogen and incandescent lamps with continuous distribution of emission in combination with glass filters as well as monochromatic LEDs and lasers are suitable for use as stimulation sources of OSL from AlN ceramics.

### 4.2.3 Use of 480 nm emission band for UV induced TL and OSL

It has been shown already that the oxygen-related UV-blue PL emission band contains two subbands around 400 and 480 nm, each subband having its own excitation spectrum, as shown in Fig.18, curves 1 and 2. The same emission bands at 400 and 480 nm can be distinguished also in TL and OSL emission spectra. Similarly to PL case, each of these bands is characterised with a distinct shape of TL or OSL excitation spectra. The case of TL excitation spectra recording emission at 400 and 480 nm is shown in Fig. 18 (curves 3 and 4). The results on TL and OSL experiments mentioned in previous sections were obtained selecting either the 400 nm emission band or the whole UV-blue band. However, it appeared that selection of the 480 nm for detection of stimulated emission results in better parameters of the TL and OSL processes (Trinkler et al, 2007a, 2007b).

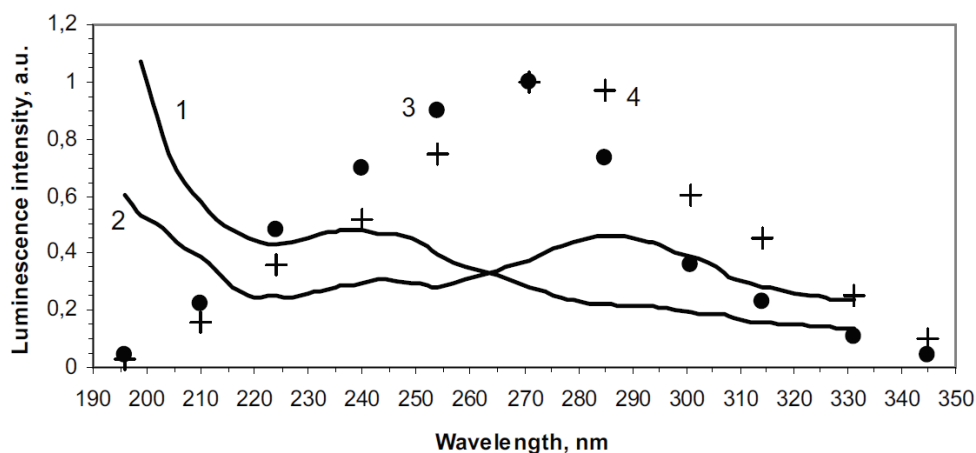


Fig. 18. Excitation spectrum of PL (1, 2) and TL (3, 4) of AlN ceramics recording emission at 400 nm (1, 3) and 480 nm (2, 4)

It was found that intensity and shape of TL curves measured in the same conditions depend on the selected excitation and emission wavelength. Two peaks are distinguished in TL curves: those at 80 and 220 °C (see Fig.19). The low temperature peak is better pronounced selecting 400 nm emission under irradiation in its characteristic excitation band (curve 1), while the high temperature peak appears for selection of 480 nm emission after excitation in the long wavelength region (curve 4). Other curves (2 and 3) contain both peaks due to overlapping of the emission bands. The higher temperature of the TL glow peak implies the lower fading rate of the stored signal. Indeed, measurement of TL signal after one hour of storage had shown 50 % of the initial yield of the TL response at 400 nm emission excited at 245 nm contrary to 80 % of that for 480 nm emission excited at 315 nm.

Correlation of emission bands with the definite TL glow peaks speaks in favor of pair distribution of trap centers and recombination centers, as it was approved already for  $(V_{Al}-O_N)^+$  and  $(O_N)^-$  centers, responsible for the 400 nm band. The trap centers responsible for the 480 nm emission evidently are more stable, than those participating in the 400 nm emission, and the corresponding TL and OSL signal fades slower. Similar effect was observed for the OSL process (Trinkler et al., 2007b): after one hour storage selection of the 480 nm band provided 40% of the initial value of the OSL yield versus 18 % for selection of 400 nm band.

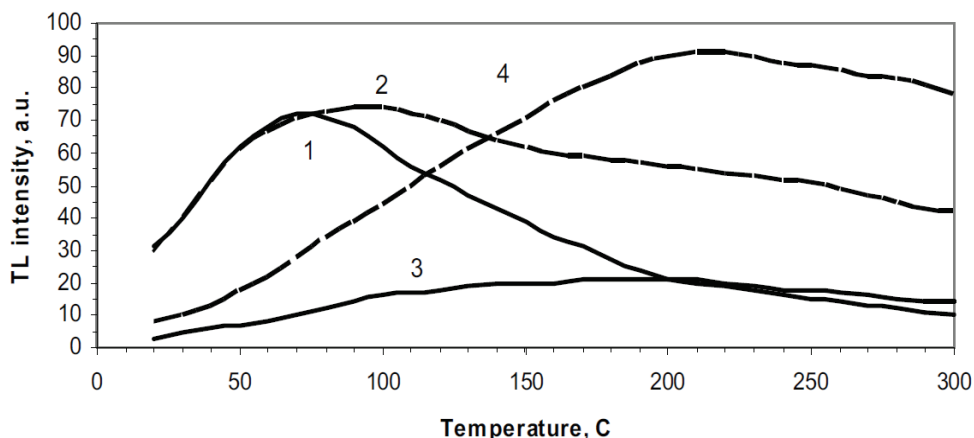


Fig. 19. TL curves of AlN ceramics after UV light irradiation at 245 nm (1, 2) and 315 nm (3, 4) detecting emission at 400 nm (1, 3) and 480 nm (2, 4)

We have done a special study of stimulated processes in AlN ceramics subjected to ion implantation with oxygen ions. It was found that after such treatment relative contribution of the 480 nm band into the total emission spectrum increases. In the same time this procedure provides very little improvement in the intensity and stability of the OSL signal, but gives some improvements of the dosimetric characteristics for TL.

From the results obtained it follows that for UV dosimetry applications it is better to use the 480 nm emission band, since the response signal is more stable than that for the 400 nm band and its excitation spectrum falls in the UV-B region, which is the detection range of practical interest. Comparing different types of dosimetric applications of AlN ceramics it should be recognized that OSL method is less suitable because of a higher rate of decrease of the signal at room temperature.

#### 4.2.4 TL in the low temperature region

Recently we have done experiments on TL measurements of AlN ceramics at low temperature. The sample was irradiated with UV light of different wavelengths at 8 K. TL signal was recorded during heating of the sample up to 300 K. Two glow curves corresponding to the main oxygen-related bands are shown in Fig. 20.

The common feature of all glow peaks is a peak at 60 K, at further rise of temperature behavior of glow curves is different until 270 K, when both curves begin to rise. This rise is the beginning of the main TL peaks, whose maxima were observed at 80 °C (353 K) for 400 nm emission band and 220 °C (493 K) for 480 nm emission band. It means that room



temperature 20 °C (293 K) is sufficiently high to start the spontaneous thermoluminescence process without any external heating. This process will continue until complete depletion of the trapped charge carriers. Storage of the dosed samples at room temperature will lead to the fading of the stored TL and OSL signal.

Thermal region of the main peaks is determined by the set of trapping centres present in AlN ceramics. The fading problem could be solved if the dosed AlN samples are stored at reduced temperature (around 250-260 K). Another way to eliminate fading is to introduce impurities providing deep trapping levels in the energy band diagram of AlN, which are stable at room temperatures. Further practical studies of this phenomenon are planned.

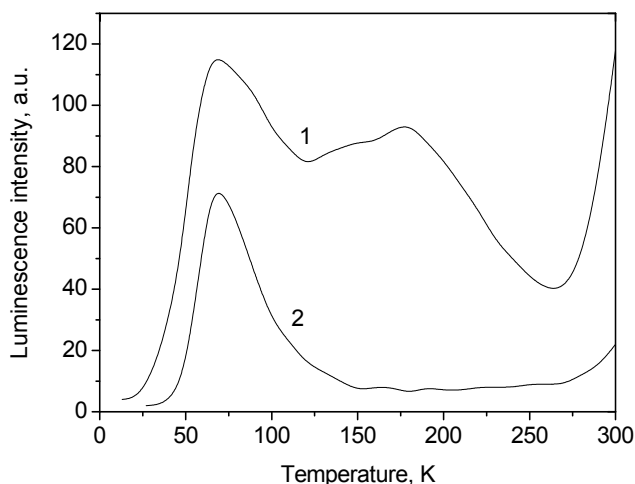


Fig. 20. TL glow curves of AlN irradiated at 8K: (1) excitation 243 nm, emission 400 nm, (2) excitation 298 nm, emission 500 nm

## 5. Conclusions

AlN ceramics is a wide-gap material whose spectral properties are determined by presence of uncontrolled impurities and intrinsic defects, the main role played by oxygen-related defects. The fulfilled investigations show that AlN ceramics is a material, highly sensitive to irradiation with both ionizing radiation and UV light. The dose of the obtained irradiation can be retrieved using TL and OSL method. In many aspects AlN ceramics outperforms other actually used TL and OSL dosimeters. However, this material has an important drawback, hampering its practical application in dosimetry area – it is high fading rate of the signal during storage at room temperature.

Different measures have been tried to diminish the effect of TL or OSL signal fading, such as optimization of ceramics sintering conditions, use of preheat procedure, detection of the definite emission band (480 nm) and oxygen ion implantation. These measures helped to slow down, but not to eliminate the fading process, which is determined by intrinsic properties of AlN ceramics. That is why at present AlN is not offered for practical

application in the area of solid state dosimetry. The further studies of this potentially perspective material are planned.

## 6. Acknowledgement

This work was supported by ERAF Project 2010/0204/2DP/2.1.1.2.0/10/APIA/VIAA/010.

## 7. References

- Akselrod, M.S.; Kortov, V.S.; Kravetsky, D.J. & Gotlib, V.I. (1990). High sensitive thermoluminescence anion-defective  $\text{Al}_2\text{O}_3:\text{C}$  single crystal detector. *Radiation Protection dosimetry*, Vol 32, Nos. 1-4, (April 1990), pp. 15-29, ISSN: 0144-8420
- Baur, J.; Maier, K.; Kunzer, M.; Kaufman, U. & Schneider, J. (1995). Determination of the GaN/AlN band discontinuities via (-/0) acceptor level of iron. *Materials Science and Engineering B*, Vol. 29, No. 1-3, (January 1995), pp. 61-64; ISSN: 0921-5107
- Benabdesselam, M.; Iacconi, P.; Lapraz, D.; Grosseau, P. & Guilhot, B. (1995). Thermoluminescence of AlN – Influence of synthesis processes. *J. Phys. Chem.*, Vol. 99, No. 25, (June 1995), pp. 10319-10323, ISSN: 1089-5639
- Berzina, B.; Trinkler, L.; Sils, J. & Palcevskis, E. (2001). Oxygen-related defects and energy accumulation in aluminum nitride ceramis. *Rad. Eff. & Def. In Solids*, Vol. 156, No.1, (January 2001), pp. 241-247, ISSN: 1029-4953
- Berzina, B.; Trinkler, L.; Sils, J. & Atobe, K. (2002). Luminescence mechanisms of oxygen-related defects in AlN. *Rad. Eff. & Def. In Solids*, Vol. 157, No. 6-12, pp. 1089-1092, (January 2001), ISSN: 1029-4953
- Berzina, B.; Trinkler, L.; Jakimovica, D.; Korsaks, V.; Grabis, J.; Steins, I.; Palcevskis, E.; Belluci, S.; Chen, L.—Ch.; Chattopadhyay, S. & Chen K.-H. (2009). Spectral characterisation of bulk and nanostructured aluminum nitride. *Journal of Nanophotonics*, Vol. 3, 031950, (December 2009), pp. 1-16, ISSN: 1934-2608
- CIE (International Commission on Illumination) Research Note (1987). A reference action spectrum for ultraviolet induced erythema in human skin. *CIE Journal* Vo. 6, No. 1, (January 1987), pp. 17-22; ISSN: 0252-9246
- Harris, R.A.; Youngman, R.A. & Teller, R.G. (1990). On the nature of the oxygen-related defects in in aluminum nitride. *J. Mater. Res.*, Vol. 5, No. 8, (August 1990), pp. 1763-1773, ISSN: 2044-5326
- Karel, F.; Pastrnak, J.; Hejduk, J. & Losik, V. (1966). Fine structure of emission spectra of the red AlN:Mn luminescence. *phys. stat. sol. (b)*, Vol. 15, No. 2, (February 1966), pp. 693-699, ISSN: 0370-1972
- Miyajima, T.; Kudo, Y.; Uruga, T. & Hara, K. (2006). Analysis of the local structure of AlN:Mn using X-ray absorption fine structure measurements. *phys. stat. sol. (c)*, Vol.3, No. 6, (May 2006), pp. 1742-1745, ISSN: 1862-6351
- Nappe, J.C.; Grosseau, Ph.; Benabdesselam, M., Beauvy, M. & Guilhot, B. (2009). Characterization of aluminum nitride material under swift heavy ion irradiations. Proceedings of the 11 th ECERS conference, 2009. *11th International Conference and Exhibition of the European Ceramic Society*, pp. 1105-1108, ISBN:9788360958544, Cracow, Poland, May 21-25, 2009
- Nappe, J.C.; Benabdesselam, M.; Grosseau, Ph. & Guilhot, B. (2011). Effect of swift heavy ion irradiations in polycrystalline aluminum nitride. *Nuclear Instruments and Methods in*

- Physics Research Section B: Beam Interactions with Materials and Atoms*, Vol. 269, No. 2, (February 2011), pp. 100-104; ISSN: 0168-583X
- Palcevskis, E. ; Berzina, B. ; Trinkler, L. ; Ulmanis, U. & Mironova-Ulmane, N. (1999). Ceramics from fine plasma processed AlN powder, sintering and properties. *Latvian Journal of Physics and Technical Sciences*, No.1, (February 1999), pp. 34-51, ISSN: 0868-8257
- Palcevskis, E. ; Jakobsen, L. ; Trinklere, L. & Ulmanis, U. (1997) . Ceramics from fine plasma-processed AlN powder. *Key Engineering Materials*, Vols. 132-136, (1997), pp. 185-188, ISSN: 1662-9795
- Sarua, A.; Rajasingam, S.; Kuball, M.; Garro, N.; Sancho, O.; Cros, A.; Cantarero, A.; Olguin, D.; Liu, B.; Zhuang, D. & Edgar, J. (2003). Effect of impurities on Raman and photoluminescence spectra of AlN bulk crystals. *Materials Research Society Symposium – Proceedings*, 798, (May 2003), pp. 297-302, ISSN: 0272-9172
- Schweizer, S.; Rogulis, U.; Spaeth, J.-M.; Trinkler, L. & Berzina, B. (2000). Investigation of oxygen-related luminescence centres in AlN ceramics. *phys. stat. sol. (b)*, Vol. 219, No. 1, (January 2000), pp. 171-180, ISSN: 0370-1972
- Slack, G.A. (1973). Nonmetallic crystals with high thermal conductivity. *J. Chem. Phys. Solids*, Vol. 34, No. 2, (February 1973), pp. 321-335, ISSN : 0022-3697
- Tale, I. & Rosa, J. (1984). Fractional glow technique spectroscopy of traps in heavily doped AlN:O. *phys. stat. sol.(a)*, Vol. 86, No.1, (January 1984), pp. 319-326, ISSN: 0031-8965
- Trinkler, L.; Christensen, P.; Larsen, N.A. & Berzina, B. (1998). Thermoluminescence properties of AlN ceramics. *Rad. Meas.*, Vol. 29, (May 1998), No. 3-4, ISSN: 1350-4487
- Trinkler, L. ; Bos, A.J.J. ; Winkelman, A.J.M. ; Christensen, P. ; Agersnap Larsen, N. & Berzina, B. (1999). Thermally and optically stimulated luminescence of AlN-Y<sub>2</sub>O<sub>3</sub> ceramics after ionising irradiation. *Radiation Protection Dosimetry*, Vol. 84, Nos. 1-4, (August 1999), pp. 207-210, ISSN: 0144-8420
- Trinkler, L.; Botter-Jensen, L.; Christensen, P. & Berzina, B. (2000). Studies of aluminium nitride ceramics for application in UV dosimetry. *Radiation Protection Dosimetry*, Vol. 92, No. 4, (March 2000), pp. 299-306, ISSN: 0144-8420
- Trinkler, L. & Berzina, B. (2001a). Radiation induced recombination processes in AlN ceramics. *J. Phys. : Condens. Matter*, Vol. 13, (September 2001), pp. 8931-8938 ; ISSN: 0953-8984
- Trinkler, L. ; Botter-Jensen, L. ; Christensen, P. & Berzina, B. (2001b). Stimulated luminescence of AlN ceramics induced by ultraviolet radiation. *Rad. Meas.*, Vol. 33, No. 5, (October 2001), pp.731-735, ISSN: 1350-4487
- Trinkler, L. ; Botter-Jensen, L. & Berzina, B. (2002). Aluminium nitride ceramics: a potential dosimeter material. *Radiation Protection Dosimetry*, Vol. 100, Nos. 1-4, (April 2002), pp. 313-316, ISSN: 0144-8420
- Trinkler, L. ; Berzina, B. & Benadbesselam, M. (2003). Use of AlN ceramics in ultraviolet radiation dosimetry. *Proceedings of SPIE* Vol. 5123, (November 2003), pp. 49-54, ISSN: 0277-786X
- Trinkler, L. ; Berzina, B. ; Shi, S. C. ; Chen, L.-Ch. ; Benabdesselam, M. & Iacconi, P. (2005). UV lighth induced luminescence processes in AlN nanotips and ceramics. *phys. stat. sol. (c)*, Vol. 2, No. 1, (January 2005), pp. 334-338, ISSN: 1862-6351

- Trinkler, L.; Berzina, B.; Auzina, A.; Benabdesselam, M. & Iacconi, P. (2007a). UV light energy storage and thermoluminescence in AlN ceramics. *phys. stat. sol. (c)*, Vol. 4, No. 3, (March 2007), pp. 1032-1035, ISSN: 1862-6351
- Trinkler, L.; Berzina, B.; Auzina, A.; Benabdesselam, M. & Iacconi, P. (2007b). Use of aluminum nitride for UV radiation dosimetry. *Nuclear Instr. And Methods in Physics Research A*, Vol. 580, (May 2007), pp. 354-357, ISSN: 0168-9002
- Youngman, R.A. & Harris, J.H. (1990). Luminescence studies of oxygen-related defects in aluminum nitride. *J. Am. Ceram. Soc.*, Vol. 73, No. 11, (November 1990), ISSN: 0002-7820

# Non-Contact Measurements of the Apparent Density of Green Ceramics with Complex Shape

G.M. Revel, E.P. Tomasini, G. Pandarese and A. Cavuto  
*Università Politecnica delle Marche, Dipartimento di Meccanica, Ancona  
Italia*

## 1. Introduction

The apparent density (or, as often reported in the technical literature, the bulk density) of green ceramic tiles is a fundamental parameter for the quality of final products. In fact, the apparent density determines the entity of the dimensional shrinkage of the ceramic body during firing and is proportional to the mechanical resistance.

In industrial production an irregular shrinkage can be responsible for example for non-planar tiles or residual strengths. Measuring the apparent density allows to control this parameter to limit the production waste and increase the quality of the final product. The apparent density, in the ceramic industries, can be currently measured off-line [Standard UNI EN 1097 - 3, (1999)], and the most used method is generally the hydrostatic weighting in a mercury bath on a small sample [Pei et al, (1999)]. This technique has a limit on the control sample and a continuous mercury use is dangerous for the human health. This, together with ISO 14000 Standard application, poses severe limitations to the use of mercury in Europe, in the United States and other countries. So new methods have been developed to measure the bulk density of ceramic tiles. Some are based on the gas laws utilizing air pressure to determine test specimen volume in a measuring chamber [Dietrich, (1999)], whilst more recent ones are based on X-ray absorption [Amorós et al, (2010)]. The first is a destructive and discrete method, so it is not suitable for on-line application. The second is accurate and non-destructive, but can be expensive and X-ray devices still have some acceptance problems in industry.

In this chapter an innovative method for non-contact measurement of the apparent density of green ceramics is presented, which is also suitable to be used during production. This method, previously developed by the authors, is based on ultrasonic wave propagation within the material. The waves are generated and received by dedicated air-coupled probes. The time of flight is measured in transmission mode on the tile together with the thickness. The thickness can be derived by the ultrasonic signals or, if higher accuracy is required on complex shapes, by a laser triangulation sensor. The velocity of the ultrasound wave can be calculated by these measurements and it is proportional to the apparent density. The conversion factor between velocity and apparent density is evaluated by a calibration procedure with a reference method of known uncertainty (e.g. mercury bath).

The chapter not only summarizes the research steps performed in this field in the last 10 years for measurements both at the laboratory and industrial level, but also presents a new challenging application to pieces with complex shapes.

## 2. Bulk density and ultrasonic propagation

The ultrasound propagation is the physical phenomenon on which the theory for measurement of the apparent density in green ceramics is founded. A probe generates a ultrasound wave that propagates in the medium with a characteristic velocity so the time of flight, given a certain length of the propagation path, can be measured.

In a solid material longitudinal and transversal waves can be propagated. In an isotropic material, the relationships between longitudinal (oscillation along the propagation direction) waves velocity  $v$  and transversal (oscillation orthogonal to the propagation direction) waves velocity  $v_t$  with the elasticity properties of the material are given by [Krautkramer et al, (1983)]:

$$v = \sqrt{\frac{E}{\rho} \cdot \frac{(1 - \mu)}{(1 + \mu) \cdot (1 - 2\mu)}} \quad (1)$$

$$v_t = \sqrt{\frac{E}{\rho} \cdot \frac{1}{2(1 + \mu)}} = \sqrt{\frac{G}{\rho}} \quad (2)$$

where  $E$  is the Young's modulus,  $G$  is the elasticity tangential modulus,  $\mu$  is the Poisson coefficient and  $\rho$  is the bulk density of the material. For a porous body, like a green tile (isotropic in first approximation, as obtained by powder compaction), there are many theoretical models linking the elastic properties with porosity and consequently with the apparent density [Wachtman, (1996)]. Commonly for ceramic bodies, the empiric Spriggs model is used [Spriggs, (1961)], which states that Young's and elasticity tangential modules exponentially decrease with porosity  $p$ . Porosity can be defined as:

$$p = \frac{\rho_s - \rho}{\rho_s} = \frac{V_a - V_s}{V_a} \quad (3)$$

where  $V_a$  is the apparent (bulk) volume of the body gross open and closed pores, considered as the total volume in the macroscopic external surface of the body, i.e. in its envelope and  $V_s$  is the effective volume of the body net of the closed and open pores;  $\rho_s$  is the average actual density. So the Spriggs model can be written as:

$$E = E_0 e^{-bp} \quad (4)$$

$$G = G_0 e^{-bp} \quad (5)$$

where  $E_0$  and  $G_0$  are the values at null porosity ( $p=0$ ,  $\rho=\rho_s$ ), and  $b$  is a parameter to be experimentally determined, which can differ by some percentage between equations (4) and (5), but it is normally  $b=4,0 - 4,5$  when  $p=0 - 40\%$ .

In this approach only the longitudinal waves velocity is considered, because the  $v_t$  is not easily measurable in the industrial application. This is supported by the assumption that the Poisson coefficient is invariant with the apparent density [Revel, (2007)]. The longitudinal waves velocity, like those propagated by a non contact ultrasound probe, are measured

orthogonally to the sample surface and the relationship linking the velocity  $v$  and the apparent density  $\rho$  is obtained by (Eq. 1), (Eq. 3) and (Eq. 4):

$$v = \sqrt{\frac{E_0 e^{-b\left(1-\frac{\rho}{\rho_s}\right)}}{\rho} \cdot \frac{(1-\mu)}{(1+\mu)(1-2\mu)}} \quad (6)$$

In Fig. 1 (a) the function of (Eq. 6) is plotted for typical values (e.g. [Wachtman, (1996)]) for ceramic green tiles ( $E_0 = 6$  GPa,  $b = 4$ ,  $\mu = 0,2$ ,  $\rho_s = 2,600$  g/cm<sup>3</sup>) obtained by traditional mix of raw materials (clays, feldspars, etc.) and with a fixed constant humidity content.

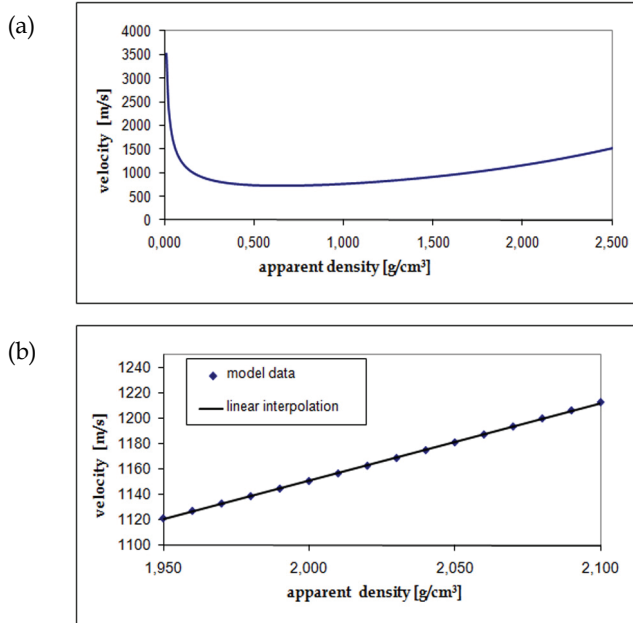


Fig. 1. (a) Plot of the longitudinal waves velocity  $v$  in function of the apparent density ( $E_0 = 6$  GPa,  $b = 4$ ,  $\mu = 0,2$ ,  $\rho_s = 2,600$  g/cm<sup>3</sup>); (b) Zoom of the diagram in a typical range of industrial interest with relative interpolating straight line

The graphic shows that, increasing the apparent density up to porosity values lower than 60 % (i.e. about  $\rho > 1,000$  g/cm<sup>3</sup>), the longitudinal waves velocity tends to increase with an almost linear trend. If a typical range of apparent density of industrial interest for green tiles is considered (Fig. 1 (b)), with a good approximation the model can be considered as linear. In fact the discrepancies between the model's data and their linear interpolation is always lower than 2 m/s (i.e. lower than 0,2 %).

In [Revel, (2007)] the results of a parametric analysis of (Eq. 6) with the variation of  $E_0$ ,  $b$  and  $\mu$  was presented. This analysis clearly showed that the uncertainty on the model parameters can generate significant uncertainty on the results of the correlation between velocity and apparent density. On the contrary the discrepancies caused by the linearization seem to be always very low.

Ultrasound measurements are usually performed with contact probes using film of gel, oil or water as coupling media. This set-up is capable of guaranteeing high signal-to-noise ratio, thanks to the reduced attenuation at the interfaces.

In the case of non contact inspection (air-coupled probes), the propagation path is more complex and the attenuation significantly higher. The energy of the signal that passes through the material in this case is very limited, due to the high difference between the acoustic impedance of the air and of the solid material. In fact, if an ultrasonic wave is propagating from a medium with acoustic impedance  $Z_1$  to another medium with acoustic impedance  $Z_2$ , the reflected signal energy will be proportional to the difference between  $Z_1$  and  $Z_2$ . This is quantified by the coefficients of reflection  $R$  and transmission  $T$  of the sound pressure, defined as:

$$R = \frac{P_r}{P_i} = \left( \frac{Z_2 - Z_1}{Z_2 + Z_1} \right) \quad (7)$$

$$T = \frac{P_t}{P_i} = \left( \frac{2Z_2}{Z_2 + Z_1} \right) \quad (8)$$

where  $P_t$ ,  $P_r$  and  $P_i$  are sound pressures of the reflected, transmitted and incident waves respectively (Fig. 2).

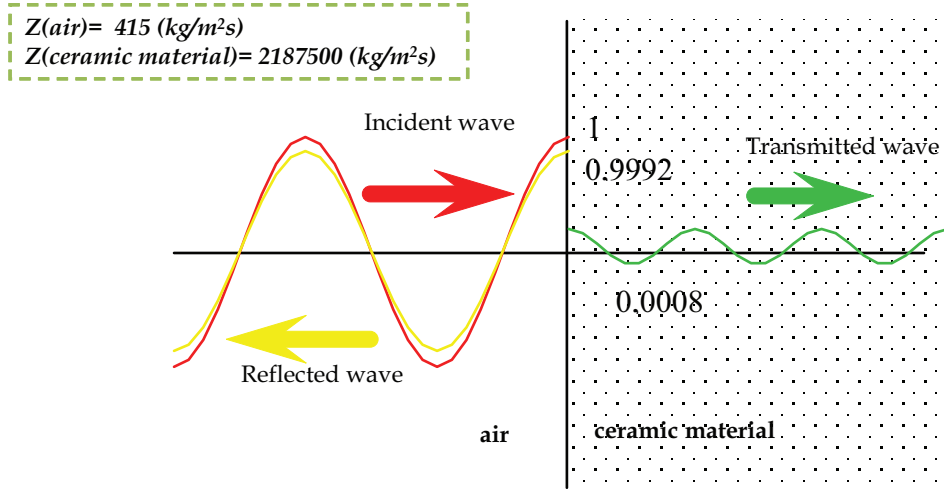


Fig. 2. Scheme of Transmission and Reflection energy: air-ceramic material

In terms of energy, these coefficients become:

$$\bar{R} = \left( \frac{Z_2 - Z_1}{Z_2 + Z_1} \right)^2 \quad (9)$$



$$\bar{T} = \frac{4Z_2Z_1}{(Z_2 + Z_1)^2} \quad (10)$$

As depicted in Fig. 2, if we consider the energy transmitted at a single interface between air and ceramic, this is in the order of about 0,1 %. If multiple reflections are used for time of flight measurement, the wave goes through the interfaces several times, thus creating a dramatic signal attenuation of several order of magnitudes.

Therefore air-coupled ultrasonic techniques require proper signal conditioning (filtering, averaging, signal enhancement, etc.) and measurement set-up to reach an acceptable signal-to-noise ratio (> 20 dB).

On the other hand, this technique offers several advantages:

- possibility of measurement on moving objects or with moving probes;
- easy set-up of a scanning system;
- no contamination of the samples with coupling medium;
- the total production can be inspected with reduced testing time.

### 3. The measurement method - laboratory tests

According to velocity theory the propagation velocity is proportional to the apparent density  $\rho$ . Once the speed is measured, (Eq. 6) could allow to determine  $\rho$ , nevertheless it would be also necessary to know  $E_0$ ,  $b$ ,  $\mu$  and  $\rho_s$ . Considering that these parameters change by tile typology (body, raw materials, etc.), that their measure is very complex and uncertain and that this uncertainty can reduce the accuracy in the apparent density determination, it is not here suggested to use (Eq. 6) to measure  $\rho$ , whilst a more practical approach is proposed.

In the proposed measurement method the time of flight of ultrasound waves is firstly measured with non contact probes in transmission configuration through the tile. The scheme of this measurement method is showed in Fig. 3.

The times of flight are measured with cross-correlation algorithms between the excitation signal of the transmission probe and the received signal.

As shown in Fig. 3 (b),  $t_c$  is the time of flight of the wave from probe to probe through the tile, while  $t_m$  is the propagation time inside the material. A typical cross-correlation signal measured on a green tile is showed in Fig. 3 (c),  $t_c$  is represented by the first peak, while the difference in the time axis between the first and second peak represents  $2t_m$ .

From the time of flight measured in air  $t_a$ , if the distance  $D$  between probes is known, the propagation velocity can be achieved.

In this first approach the distance among the probes membranes  $D$  (= 100 mm in this case) has to be measured using a calliper. It follows that the ultrasound measurement method consists in two steps: (a) measure of the time of flight  $t_a$  of the ultrasound wave in air in the environmental condition of use; (b) measure of the time of flight of the ultrasound wave through the tile body  $t_c$  (where  $t_c < t_a$ ) where, through the measurement of the arrival time of the second echo, it is possible to know also the time of propagation  $t_m$ . These steps are repeated every time a tile passes through the probes during the production.

From the measure in air the propagation velocity of sound in air in the application environmental condition can be derived:

$$v_a = \frac{D}{t_a} \quad (11)$$

It is necessary to often repeat this measure because, as well known, the sound velocity  $v_a$  changes in environmental condition mainly in function of temperature and humidity. For example with a temperature of 20 °C and with relative humidity of 50 % there is a speed of 344 m/s.

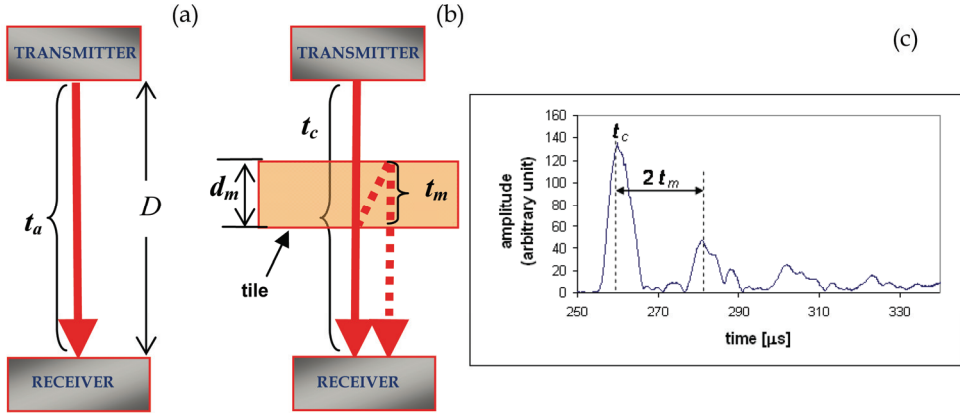


Fig. 3. Scheme of the measurement method: (a) Measurement in air; (b) Measurement on the tile; (c) Example of cross-correlation signal measured on a tile (amplitude in arbitrary unit)

In literature there are many formulas for the sound velocity estimation, for example one can be approximated from [Cramer, (1993)]:

$$v_a(T, \theta) = (331,5 + 0,59 \times T[^\circ\text{C}]) \left( 1 + 0,004 \frac{\theta[\%]}{100} \right) \quad (12)$$

where  $T$  is the air temperature and  $\theta$  the relative humidity.

Nevertheless in order to avoid the measurement of temperature and humidity, it is better to compensate this effect by directly measuring  $v_a$ , especially in the production line where it is not possible to take under control the environmental conditions.

By the measurement of  $t_c$  and  $t_m$  the average thickness of the tile in the area of the ultrasonic beam (about 1 cm<sup>2</sup>) can be obtained

$$d_m = D - v_a(t_c - t_m) \quad (13)$$

and in the end the propagation velocity of longitudinal waves as:

$$v = \frac{d_m}{t_m} \quad (14)$$

Considering that in the range of interest Eq. 6 can be considered as linear with an error lower than 0,2 %, it is proposed to determine a linear experimental correlation between

velocity and apparent density. This relationship can be obtained by an experimental calibration procedure to be carried out with a reference method of known uncertainty, such as the one based on mercury.

The Fig. 4 provides an example of correlation diagram, which can be later used to determine the apparent density of unknown samples, once measured the propagation velocity.

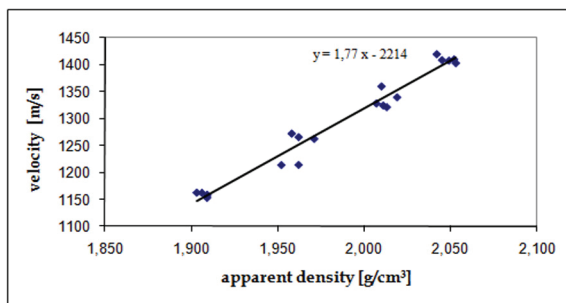


Fig. 4. Correlation diagram (with relative straight fitting line) between longitudinal wave velocity and apparent density measured on green ceramic tiles

In reality also the humidity content has an influence on the propagation velocity, but this effect is considered negligible when measurements are performed on dried tiles or on tiles with constant humidity level. A preliminary attempt to deal with the humidity influence on such ultrasonic measurements has been presented in [Cantavella et al., (2006)]. The problem of moisture influence in on-line measurements has been tackled by the authors in [Revel et al., (2009)] and [Rivola et al., (2007)] and will be discussed in the next chapter.

The experimental apparatus used in the first investigations was based on piezoelectric probes [Bhardwaj, (2002)] with a membrane diameter of 12,5 mm working at around 1 MHz. Air coupled piezoelectric probes have usually a dedicated layer of low impedance material (porous plastic, pressed fibres, polymers, etc. depending on the specific patent) placed between the piezoelectric crystal and the air, in order to reduce the impedance difference between emitting element and air.

Green ceramic tiles having flat faces on both sides, produced in laboratory, have to be used as calibration samples. The planarity of the sides allows to have a higher SNR because the grid in the rear side of the tile represents a modifying input for the ultrasound measurement, caused by the effects of diffraction and thickness variations. In addition, the samples are dried in order to avoid any effect due to moisture. For the calibration of Fig. 4, 20 samples of known density (5 samples for 4 different pressing levels) were used. The propagation velocity was measured in a point of each sample with 200 averages on the signal. It is worth to underline that the determined parameters are valid only for ceramic green tiles with body and raw materials used for the calibration samples. In industrial field, it is necessary to repeat the calibration with every change of body. Examples of correlation diagrams achieved for 3 different kinds of clay and body are reported in Fig. 5, showing the possibility of generalizing the method.

Therefore measurement of the apparent density with the proposed method consists of 3 main steps (once fixed and measured the distance  $D$  between the probes):

**Step 1.** times of flight measurement.

**Step 2.** estimation of the longitudinal waves velocity through.

**Step 3.** experimental correlation between velocity and apparent density through calibration.

In each step there are uncertainty components which could be generated and propagated up to the final results. In order to optimize the measurement process, it is necessary to determine the weight of each uncertainty source on the final results. This has been addressed in detail in [Revel, (2007)] where it is shown that the method guarantees an uncertainty below  $\pm 0,009 \text{ g/cm}^3$ .

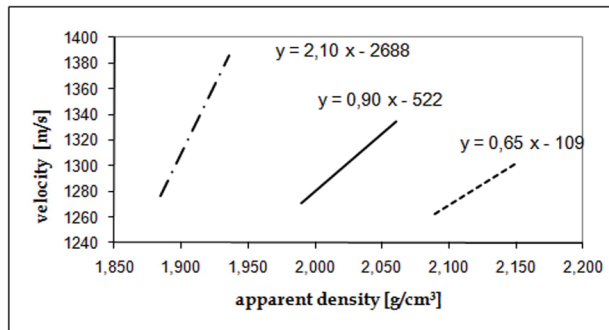


Fig. 5. Examples of correlation diagrams achieved on green tiles with different raw materials and body

#### 4. Industrial application

After some years of research in the EU funded project SENSOCER techniques based on non-contact ultrasonic probes have been developed to properly measure the bulk density of ceramic tiles directly on the line after pressing. These systems are based on air-coupled electro-capacitive transducers and laser triangulation sensors for the detection of the thickness. They have recently demonstrated enough accuracy for industrial applications (repeatability below  $0,01 \text{ g/cm}^3$ ) [Revel at al, (2009)] and are being now exploited in an industrialisation phase, after application of an international patent [Rivola at al, (2007)]. The measurement apparatus is conceived to monitor both the average production value and the spatial distribution of the bulk density and takes into account the effect of moisture content on the measurement accuracy.

The on-line system is a development of the basic one described in the previous Par. 3 for laboratory tests [Revel, (2007)], upgraded for further improvement of accuracy and flexibility. It is constituted by electro-capacitive transducers and a couple of laser triangulation sensors. The electro-capacitive transducers, specifically developed for the application, are driven by a Metalscan ultrasonic board and have an active area diameter of 20 mm and a working frequency of 190 kHz. They have been chosen for this application because of their high sensitivity, in particular in the low frequency range. They are set in a through-transmission configuration for measuring the time of flight of the ultrasonic signal through the tile, while the laser triangulation systems, M7L/10-B24 produced by MEL, measure the tile thickness. Thanks to these devices, it is possible to evaluate the ultrasound velocity  $v$  in the green ceramic tiles, using equation 14.

The main difference with respect to the method in Par. 3 is that the thickness is independently measured (by the laser probes) and it is not derived using the same ultrasonic signals. From one side, this makes the system more expensive and complicated, but on the other hand the accuracy is improved. Therefore, if the basic system was already able to guarantee an uncertainty in the order of  $\pm 0,009-0,01 \text{ g/cm}^3$ , here the performances are better (uncertainty in the order of  $\pm 0,006-0,007 \text{ g/cm}^3$ , having an accuracy on the measurement of the thickness of  $\pm 0,02 \text{ mm}$ ). In addition, since the thickness has not to be measured by ultrasounds, a lower frequency can be used (190 kHz), allowing lower attenuation in air and thus higher *signal-to-noise* ratio (30 – 34 dB in this work with 200 averages for each acquisition). This solution showed to be the best one also for the application on complex shapes as will be reported in next Par. 5.

In the production line there is very few time for the measurement and for a good calibration it is important to measure the real produced tiles. So the linear correlation between apparent density and velocity, at the production moisture level, has been estimated using samples taken directly from the line at 3 different density levels (achieved with 3 different pressure levels varying about 70 bar above and below the normal press operating conditions, of 444 bar).

Concerning the effect of the moisture on the ultrasound measurements, it is known that moisture decreases the propagation velocity [Cantavella at al, (2006)], so also the influence of this parameter was evaluated to guarantee the required uncertainty (max  $\pm 0,009-0,01 \text{ g/cm}^3$ ).

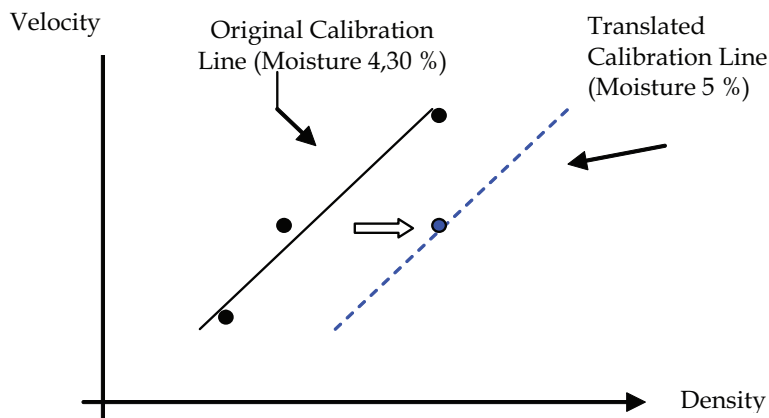


Fig. 6. Adjustment of the calibration line to different moisture values

An extensive sensitivity analysis performed during the SENSOCER project demonstrated that, on average, humidity variations higher than 0,3 % can cause a deviation in apparent density measurements in the order of  $0,005 \text{ g/cm}^3$ . To deal with this problem, two methods have been implemented and tested. In the first one, the results of continuous humidity measurements using an IR probe serve as a correction factor when evaluating the density readings. Long on-line observations showed, however, that in many cases the variations are lower than 0,3 % for many hours. Thus a second method, simpler and cheaper but less accurate, has been introduced. Here, the moisture content is manually measured by an

operator on the line (e.g. every hour, as standard practice already is in industry) and, when the moisture level varies more than 0,3 %, a new calibration point has to be measured by the mercury reference method and used to rigidly translate the calibration line. In fact, it has been demonstrated that, for moisture variations in the order of 0,5–1 %, the slope of the calibration line does not significantly change (effects in the order of 0,001 g/cm<sup>3</sup>).

A last important point of the on-line measurement system is that the probes have been mounted on an automatic scanning system. This system is capable of translating together the ultrasonic and the laser probes along the direction perpendicular to the tile motion. This system, coupled with an additional control device suitable to stop the tiles in different positions along the line, allows to scan the apparent density values over different areas of the produced tiles. An average trend of the density spatial distribution can be thus finally achieved and used to predict and correct the differential shrinkage in the different zones.

#### 4.1 Results of on-line test

A schematic presentation of the installation in the on-line ceramic factory (for details see [Revel et al, (2009)]) is shown in Fig. 7 (a). The system is located between the press and the dryer, taking up less than 1 m of the production line. Both the signals coming from the ultrasonic device and the laser triangulation systems are acquired and processed with an industrial PC and visualized in real-time together with the current density value.

Fig. 8 (a) shows the moving head, holding both the non-contact ultrasonic transducers and the laser triangulation sensors. A general view of the scanning system with remote PLC control can be seen in Fig. 8 (b). This positioning system, perfectly integrated with the production line process, has been specially developed as a reference system for the test: the direction of the product flow is labeled as Y axis, while the X axis is the perpendicular one.

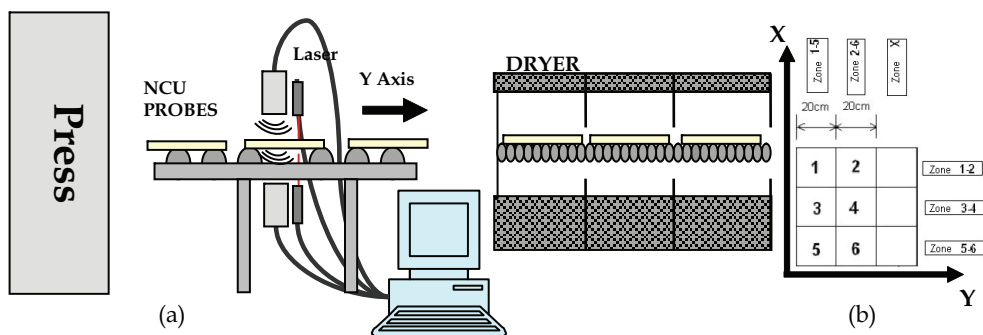


Fig. 7. (a) Schematic drawing of the on-line installation; (b) Reference system for the inspected tile zones

The measurement procedure is as follows: one measurement is performed per tile, each time in a different position, until all the defined areas are covered. Then a new scanning cycle is started. In practice, if 9 areas have to be measured, 9 tiles are required to pass along the line. In this way, a large data set is obtained from which it is possible to derive: a) information on

the average density of the products; b) information on the average spatial density distribution.



Fig. 8. (a) Head with the sensor holder; (b) Support for on-line positioning

Averaging (both the mean value and spatial distribution) ensures that corrective action on the press is taken only in the event of systematic problems (e.g. wear of a die, non-uniformity in powder loading, significant variations in powder moisture, etc.) and not due to local or instantaneous deviations of the measured values.

The results obtained from measurements on a  $60\text{ cm} \times 60\text{ cm}$  format with a regular rectangular grid on the back are shown. The tile surface is divided into 9 square areas of  $20\text{ cm} \times 20\text{ cm}$ . For the sake of better clarity, the combinations of the areas along the X or Y axis are defined as zones and marked with the number of the first and last included areas (Fig. 7 (b)). For these tests, only 6 areas have been monitored, neglecting the last zone of the tile (zone X), thus reducing the necessary production controller modifications to a minimum.

In order to simulate a production variation, the pressure was increased by 60 bar.

The interval where the pressure has been varied (from tile 24 to tile 40) was detected by the system in its whole duration, with an increase in the average apparent density of about  $0,016\text{ g/cm}^3$ . Some few samples have been taken from the line and measured with the mercury-based method, which revealed a maximum deviation of about  $0,005\text{ g/cm}^3$ . In order to confirm the possibility of predicting variations in the tile dimensions (calibre) after firing, i.e. dimensional shrinkage, each single measured tile was marked and its dimensions after firing were measured.

Fig. 9 (b) illustrates the calibre trend measured along Zone 5–6 for the same tiles, whose apparent density measurements on the Area 5 are plotted in Fig. 9 (a). The trend clearly confirms the behaviour expected from the ultrasonic measurements: the increase in pressure generates higher density and, consequently, larger tile dimensions. In addition, it is possible to note that in both the apparent density and the calibre measurements there is a correlated drift: in fact, their average values at the beginning and at the end of the interval considered seem to increase, probably due to a variation in the moisture content.

The Fig. 9 (a) shows also the relative moving average used to highlight the trends on the single investigated area (with a delay of some samples, due to the algorithm itself). This drift is thus well predicted by the proposed method.

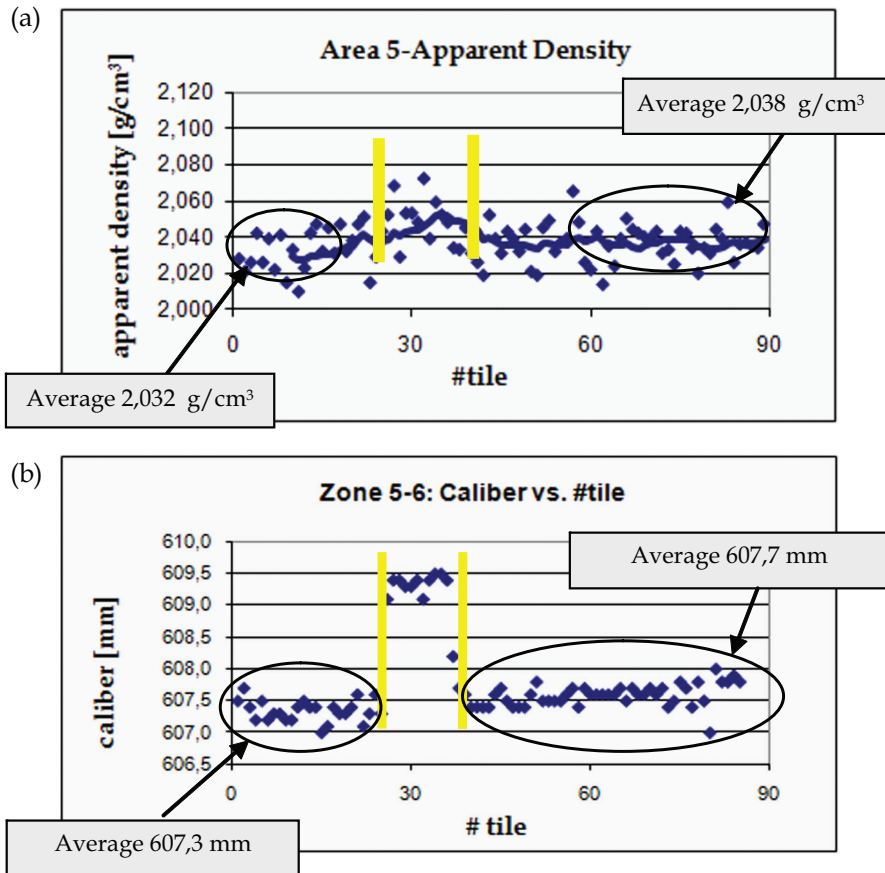


Fig. 9. (a) On-line apparent density measurement for Area 5 in consecutive tiles: the continuous lines represent the interpolation curve obtained with a moving average evaluated on 10 samples; (b) Tile dimension (caliber) trend along Zone 5-6 (measured after firing)

## 5. Advanced application on complex shapes

An additional new goal for the developed non-contact measurement techniques is to inspect also ceramic bodies with complex shape. In tile industry this is becoming of wide interest, due to potential irregular compaction achieved by new production processes.

Here therefore a feasibility study of the method applicability on tiles with high thickness variation and irregular superficial profile (see Fig. 10) is approached. The test has been focused on the central part of the tile, which presents relevant thickness variations higher than a normal tile. The monitoring of the central part is an important achievement, as this is the part with lower strength section: a strong density gradient here is reflected in dimensional and angular problems also in the other 3D parts.



This study was performed in laboratory using the low-frequency electro-capacitive ultrasonic probes (working frequency 190 kHz) interfaced with a dedicated acquisition board, plugged into a PCI slot of a personal computer.

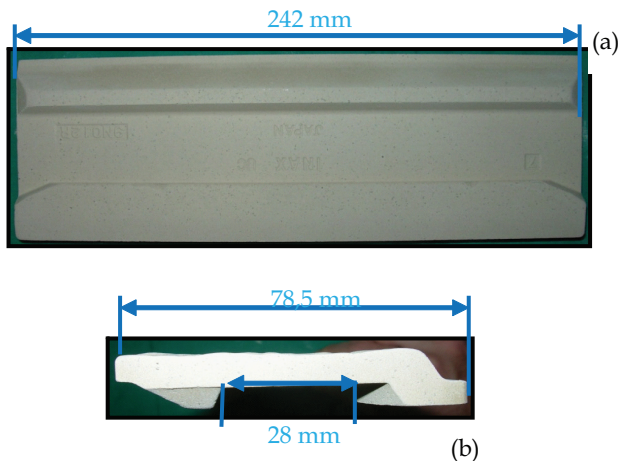


Fig. 10. Tile: (a) Bottom view; (b) Lateral view

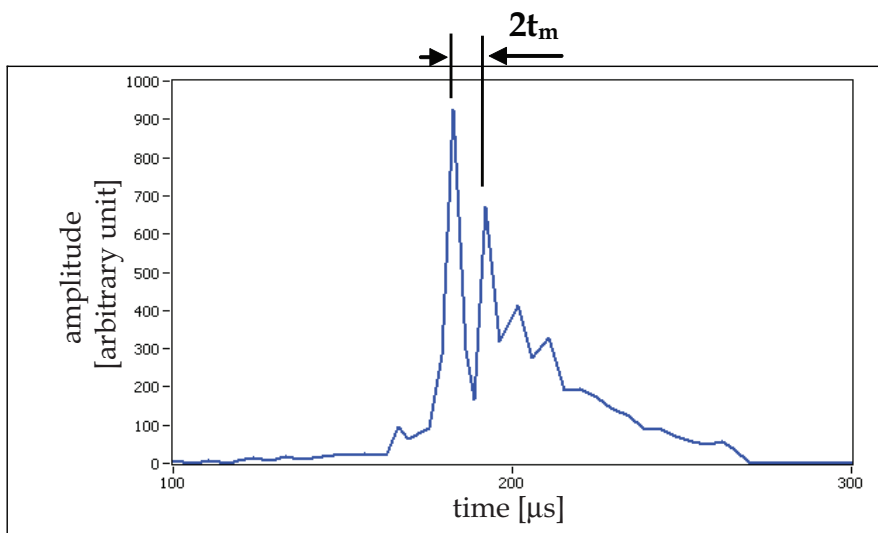


Fig. 11. Waveform of cross-correlation between signal in air and signal through the material

Following the developed procedure, firstly the time of flight  $t_a$  of the ultrasound wave in air in the environmental condition of use is measured by acquisition with no samples between the probes. Then the time of flight in the material  $t_m$  is measured with cross-correlation algorithms between the signal in air without sample and the signal with the sample between

the probes (300 averages for each acquisition). An example of cross-correlation signal is shown in Fig. 11, demonstrating the good quality of the measurements. The thickness was independently measured with two laser triangulation sensors (Laser Mel M5L, resolution 6  $\mu\text{m}$  and laser Keyence LC-2100, resolution 0,5  $\mu\text{m}$ ).

The system was calibrated with four laboratory planar samples at know density (referred to mercury bath measurements performed by the tile manufacturer). The samples had different compaction and were manufactured using same batch composition of the production tiles. For each calibration sample, time of flight and thickness were measured. Fig. 12 shows the achieved calibration line, i.e. the relationship between velocity and bulk density.

After calibration, the system was applied on the real tiles firstly in laboratory conditions and then in simulated on-line tests.

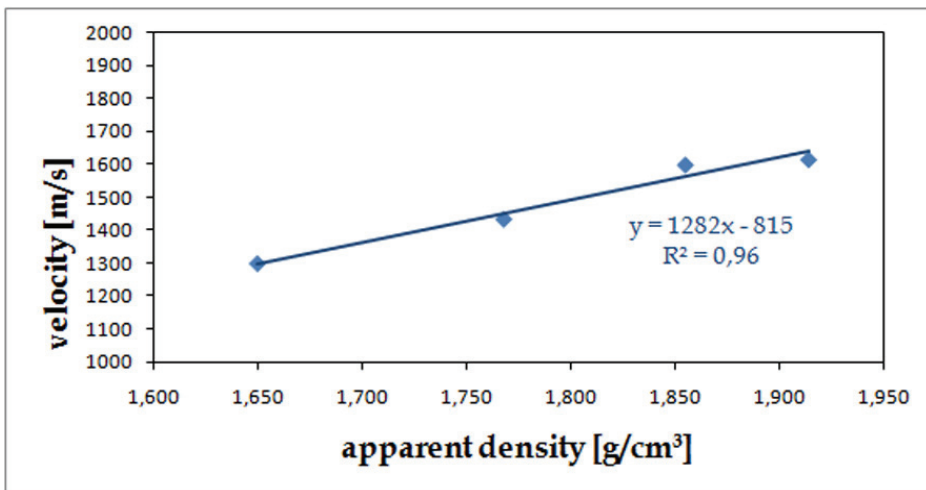


Fig. 12. Calibration line

### 5.1 Test in laboratory conditions

To verify the calibration line and the measurement system on the real tile with complex shape, tests were performed on the central portion of the tile using a manual planar scanning system for transducers. The analyzed portion was divided in 3 zones (Fig. 13 (a)), each having dimensions of 24x32 mm, thus comparable with the diameter of the ultrasonic transducer. In each area the propagation velocity was measured using an average thickness for each of them. The average thickness was evaluated by measuring 5 points taken randomly within each area.

Using the calibration line shown in Fig. 12, once velocity is measured, a density value can be estimated for each zone. In order to have a reference for the achieved values, the 3 areas have been cut and for each of them bulk density was measured with hydrostatic buoyancy method with the samples sealed by wax. This method has a lower accuracy (about  $\pm 0,01 \text{ g}/\text{cm}^3$ ) with respect to the mercury bath (about  $\pm 0,002 \text{ g}/\text{cm}^3$ ), but it was the only one available in our lab. Comparison results are reported in Table 1: it is shown that the growing

density trend is well detected, even if the thickness variations are relevant, with an average discrepancy of about  $0,024 \text{ g/cm}^3$ . This discrepancy is slightly higher than expected, but this can be also due to the lower accuracy of the hydrostatic buoyancy method used as reference.

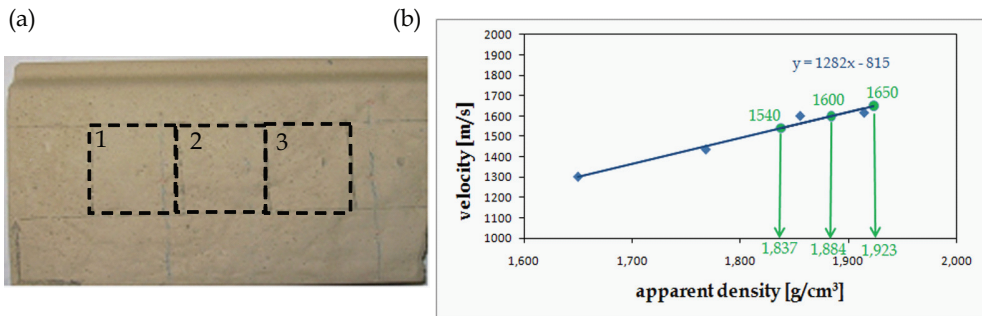


Fig. 13. (a) The 3 investigated areas; (b) Bulk density measured by calibration line (green values)

Zone	Average Thickness (mm)	Velocity (m/s)	Apparent density Ultrasonic method/buoyancy method ( $\text{g/cm}^3$ )	$\Delta$ ( $\text{g/cm}^3$ )	$\Delta$ (%)
1	8,74	1540	1,837/1,807	0,030	1,7
2	8,52	1600	1,884/1,856	0,028	1,5
3	7,85	1650	1,923/1,908	0,015	0,8

Table 1. Measurement results on the 3 considered zones

## 5.2 Tests in simulated on-line conditions

In order to simulate on-line measurements, an automatic planar scanning system was used to move the ultrasonic and laser triangulation transducers with a 1 mm step while the tile was at rest (Fig. 14). So in this case the probes are moved, but in a real on-line installation it could be possible to use the tile movement to acquire thickness and density profiles.

Whilst the density measurements in Par. 5.1 are related to an area of  $24 \times 32 \text{ mm}$ , here the density profile is measured along a longitudinal section of the tile using a new approach. Fig. 15 shows the measured thickness profile and morphological reconstruction of the tile.

The tile thickness profile seems to be quite irregular with maximum deviations up to 3 mm. This probably can also lead to expect bulk density and compaction variations along the profile. There construction of the propagation velocity profile was made along the same longitudinal section in the middle of the tile, where the time of flight was measured. The

edges with variable thickness were not considered, as it was assessed that here ultrasound beam propagation is complex and depends on the size of the probes, incidence angle and scattering phenomena.

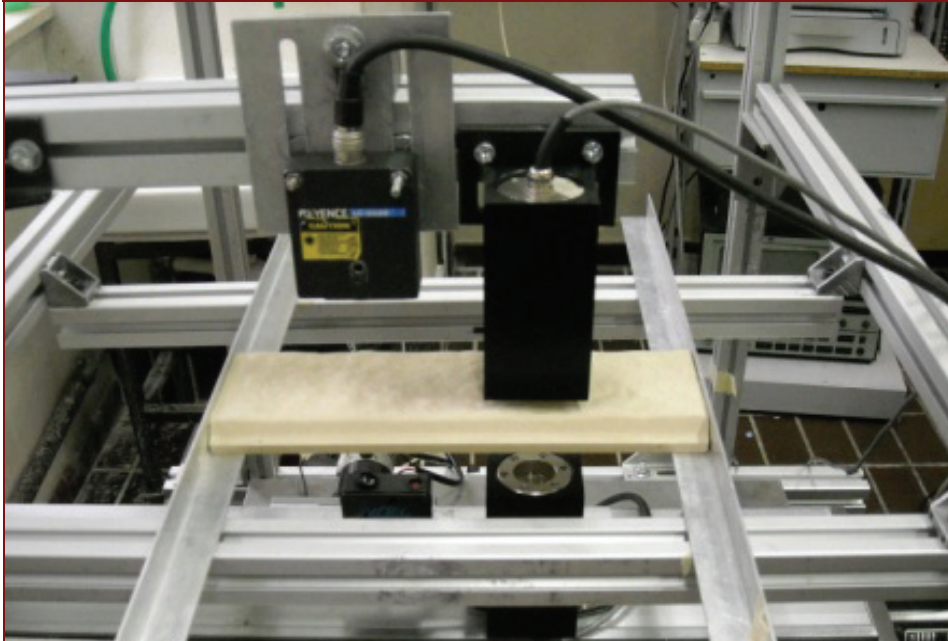


Fig. 14. The scanning system with ultrasonic and laser triangulation transducers

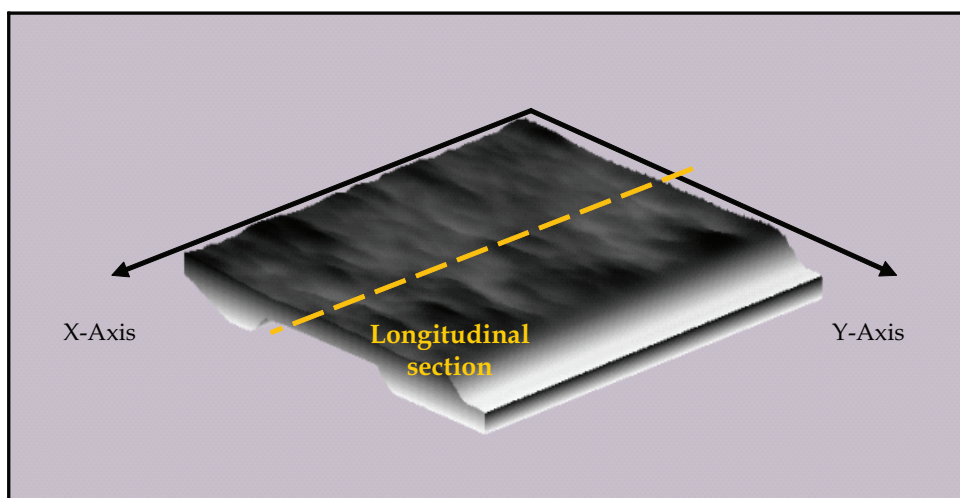
It is worth noting that, whilst thickness measurements by triangulation laser systems are punctual, the times of flight are measured in an area as large as the beam size (about 20 mm). So, even if also the ultrasonic probes are moved by the scanning system at steps of 1 mm, there is the need to define which thickness value has to be associated to the times of flight measured at each different step. It is clear that it has no sense to associate to the measurements performed at one position the single thickness value measured by the laser on the same ultrasonic probe axis position.

As a consequence, it has been decided that, in order to take into account an average thickness within the beam area, a moving average algorithm was adopted: the idea is that, from one position to the next one, the average thickness value is updated discarding the first value (now outside the beam area) and considering the new last value (just entered in the beam area).

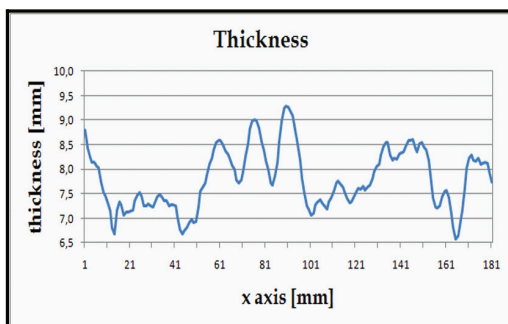
Fig. 16 shows respectively: the raw data of the thickness profile along the longitudinal section indicated in Fig. 15 (a) and the relative moving average; the times of flight along the same section and, finally, the velocity/density along the longitudinal section calculated from the "moving average" thickness. As an example of the adopted procedure the first time of flight value is measured with the ultrasonic probe axis placed in  $x = 10$  mm. At this value, the moving average thickness value computed with the first 20 sample (i.e.  $x = 20$  mm in Fig. 16 (a)) is associated to estimate velocity and density. The use of the moving average

allows to achieve a sort of continuous bulk density profile (with 1 mm spatial resolution), which can be useful to evaluate undesired trends. It is clear that, from one point to the other, many information are overlapping. So, it could also be useful to estimate average values for larger areas (e.g. 20 mm as the beam size): this can be easily done from the measured data and results are reported in the same graph of Fig. 16 (c). On these values also error bars with amplitude proportional to the uncertainty estimated in previous Paragraphs are reported.

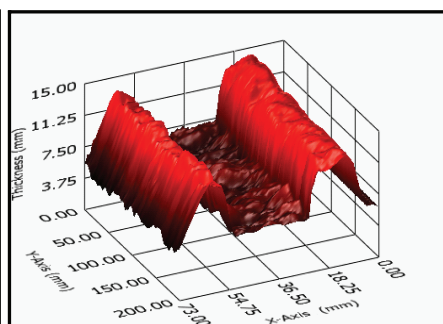
Measured density distribution seems to be coherent with the sample values measured in Par. 5.1. In addition it can be noted that thickness and density profiles tends to have inversely proportional trends, which is coherent with the compaction process, thus demonstrating the feasibility of the proposed measurements.



(a)



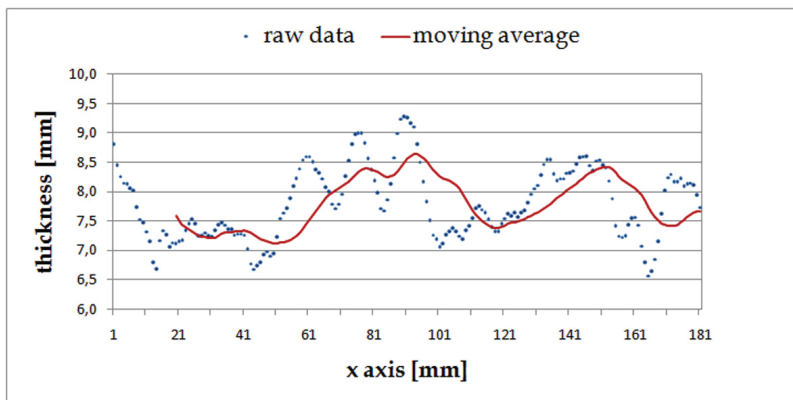
(b)



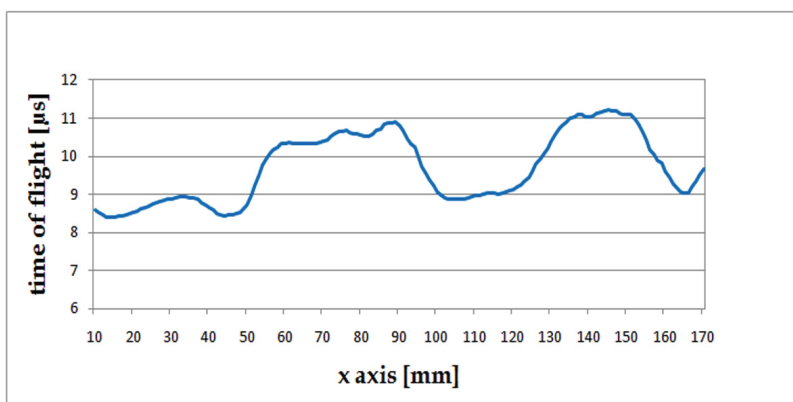
(c)

Fig. 15. (a) Morphological reconstruction of the tile; (b) Thickness profile along the longitudinal section; (c) Tile thickness distribution

(a)



(b)



(c)

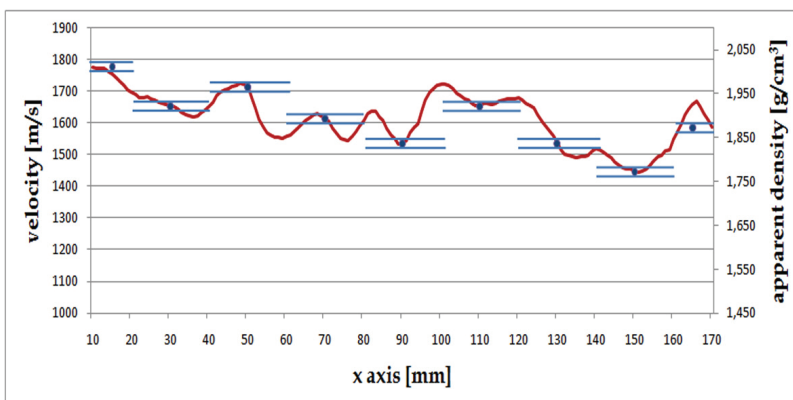


Fig. 16. Diagrams of: (a) Thickness (raw data and moving average); (b) times of flight and (c) velocity/density estimated with "moving average" thickness, with discrete average values computed on 20 mm lengths superimposed

## 6. Conclusion

This Chapter has shown the complete development of the non-contact ultrasonic method for the laboratory and on-line measurement of apparent density on green ceramic tiles. The research was developed in several years and the outcomes have been protected by an international patent. Both the basics of the method and experimental set-ups for laboratory and on-line applications are described, showing that the system is capable of tracking average production values and spatial distribution of apparent density with the industrially required accuracy ( $\max \pm 0,01 \text{ g/cm}^3$ ).

An original application on green ceramics with complex shape has been also developed and presented. The results showed the feasibility of measuring on parts with irregular thickness variations up to 3 mm. However the method can be further developed to determine the density values even at the edges of the tile where the profile is curve. The main objective will be to implement dedicated post-processing algorithms to identify and isolate the portions of the measurement signals related to the different paths of the ultrasound wave in the tile.

## 7. Acknowledgments

The research has been partly funded by the EU project SENSOCER. The authors would like to thank the company SACMI for the cooperation in the on-line implementation of the prototype. In addition they would like to thank INAX Corporation for the samples with complex shape.

## 8. References

- Amorós, J.L.; Boix, J.; Llorens, D.; Mallol, G.; Fuentes, I. & Feliu, C. (2010). Non-destructive Measurement Of Bulk Density Distribution In Large-Sized Ceramic Tiles. *Journal of the European Ceramic Society*, 30, pp. 2927–2936, Available online at [www.sciencedirect.com](http://www.sciencedirect.com), 12 March 2010
- Bhardwaj, M.C. (2002). High Transduction Piezoelectric Transducers And Introduction Of Non-Contact Analysis, In: *Chapter of Encyclopedia of Smart Materials*, Wiley, J.A. Harvey, (Ed), New York, ISBN 0-471-17780-6
- Cantavella, V.; Llorens, D.; Mezquita, A.; Moltò, C.; Bhardwaj, M. C.; Vilanova, P.; Ferrando, J. & Maldonado-Zagal, S. (2006). Use of ultrasound techniques to measure green tile bulk density and optimise the pressing process, *Proceedings of QUALICER 2006*, Vol. 2, P.BC – 161, ISBN 84-95931-21-4
- Cramer, O. (1993). The variation Of The Specific Heat Ratio And The Speed Of Sound In Air With Temperature, Pressure, Humidity, And CO<sub>2</sub> Concentration, *J. Acoust. Soc. Am.*, 93(5) pp. 2510-2616, ISSN 0001-4966
- Dietrich, E. (1999) *New Measurement Principle for Determining Bulk Density*, EP 0936451.
- Krautkramer, J. & Krautkramer, H. (1983). *Ultrasonic Testing of Materials*, Springer-Verlag, ISBN 3-540-11733-4
- Pei, P.; Minor, D. & Onoda, G. (1999). Laboratory Techniques For Bulk Density Measurement, In: *Advances Process Measurements For The Ceramic Industry*, A. Jyllavenkatesa and G. Onoda, (Ed). 293-306, Westerville, OH, ISBN 1574980866.

- Revel, G.M. (2007). Measurement Of The Apparent Volumic Mass Of Green Ceramic Tiles By A Non-Contact Ultrasonic Method, *Experimental Mechanics* 47 pp. 637-648
- Revel, G.M.; Pietroni, P.; Tomasini, E.P.; Pandarese, G. & Cocquio, A. (2009). On-Line Measurement of Green Tiles Apparent Density: Industrial Implementation and Test of an Ultrasonic-Based System, *Tile&Brik International Manual 2009* pp. 42-46. ISSN 0938-9806
- Rivola, P.; Cocquio, A.; Tomasini, E.P.; Revel, G.M.; Pietroni, P. & Pandarese, G. (2007). A Process For Manufacturing Ceramic Tiles, WO2007093481AL - 2007
- Spriggs, R.M. (1961). Expression for Effect of Porosity on Elastic Modulus of Polycrystalline Refractory Materials, particularly Aluminium Oxide, *J. Am. Ceram. Soc.*, Vol. 45, 94, , ISSN 0002-7820
- Standard UNI EN 1097 - 3: (1999), *Determinazione della massa volumica in mucchio e dei vuoti intergranulari*, ICS 91.100.15
- Wachtman, J.B. (1996). Mechanical Properties of Ceramics, *John Wiley & Sons Inc.*, ISBN: 0-471-13316-7



# **Practical Methods for Crack Length Measurement and Fatigue Crack Initiation Detection Using Ion-Sputtered Film and Crack Growth Characteristics in Glass and Ceramics**

Gang Deng<sup>1,2</sup> and Tsutomu Nakanishi<sup>1</sup>

<sup>1</sup>*Faculty of Engineering, University of Miyazaki,*

<sup>2</sup>*State Key Lab of Mechanical Transmission, Chongqing University*

<sup>1</sup>*Japan*

<sup>2</sup>*China*

## **1. Introduction**

A crack length measurement method is very important in the investigation of the fatigue crack growth characteristics of a material and in the evaluation of the fatigue strength of a machine element. Many crack length measurement methods have been proposed. Brown et al. (1966) and Nishitani et al. (1985) measured crack length through the changes in the displacement and compliance of the test piece. Ashida et al. (1996) and Nakai et al. (1989) investigated the changes in electrical properties around a crack during its growth. Lee et al. (1985) and JSME (1986) recommended estimating the crack length from the opening or closing displacement of a crack. In addition, crack length can also be measured by using an optical microscope, an optical grid technology (Bucci et al., 1972, Maustz et al., 1976, James et al., 1981), an acoustic emission method (Masuyama et al., 1994) and an ultrasonic method (Shimada et al., 1983). However, the methods proposed up to now require specific measuring apparatuses and complex calculation processes for crack length, and are applicable to long cracks several millimeters in length, not to small cracks shorter than 1mm in length or cracks with a high growth rate. In addition to the above-mentioned methods, a thin metal film, such as a crack gauge (e.g., KV-25B manufactured by Kyowa Co.), has been used for crack length measurement and fatigue crack initiation detection in some machine elements, such as gears, where cracks are up to several millimeters in length (Deng et al., 1991). Since this metal film is formed on a plastic base film with a thickness of about several tens of micrometers, there is a relatively large error between the actual and measured crack lengths. Increasing the measurement accuracy of the film can only be achieved by decreasing the thicknesses of the metal and plastic base films.

An ion-sputtering device, widely used in a scanning electron microscopy system, is a coating device used to form a nanoscale-thickness metal film on a surface. In this chapter, we introduce methods for crack length measurement using an ion-sputtered film, which are considered as ideal and practical methods applicable to micro-cracks or small cracks in glass

and ceramics as well as metals. The measurement principle and measuring system are very simple. As an application of the ion-sputtered film to crack length measurement, cracks in soda-lime glass and alumina ceramics were measured and the microcrack growth characteristics of these materials were clarified. In addition, an ion-sputtered film was also applied to the detection of fatigue crack initiation, and a very small crack that initiated from the notch surface of the acrylic test piece during the fatigue test was detected..

## 2. Crack length measurement using grid pattern ion-sputtered film

### 2.1 Measurement principle

Conductive films have been used for crack length measurement. Ogawa et al. (1991a, 1991b) and Nakamura et al. (1993) utilized carbon films to measure the crack length on ceramic surfaces, but their methods are not widely used because the presented relationship between crack length and the resistance of the film is applicable only to the film of specific dimensions. A crack gauge is also a sensor for measuring crack length and has been used to measure the crack length of gears (Deng et al., 1991), but the measurement precision is not satisfied owing to the thickness of the gauge.

An ion-sputtering device, as shown in Figure 1, is commonly used to fabricate a conductive with a thickness of several tens of nanometers. The application of an ion-sputtered film to crack length measurement would contribute to increasing the crack length measurement precision.



Fig. 1. Ion-sputtering device

The electrical resistance  $R$  of a conductive film is expressed by

$$R = \rho \frac{l}{wt} \quad (1)$$

where  $l$ ,  $w$  and  $t$  are the length, width and thickness of the film, respectively.  $\rho$  is the specific resistance of the film material. However, expression (1) is applicable only to a film with a simple shape. If there is a crack of length  $a$  across the film, attention should be paid on the fact that the electrical resistance cannot be calculated simply by substituting the width  $w$  of expression (1) with the residual width  $w-a$ ; the theoretical expression for the electric resistance of a cracked film is nearly impossible. However, if the length of the film is very large compared with the width of the film, indicating that the shape of the film is similar to

that of a grid whose length  $l$  is very larger than its width  $w$ , the electric resistance will not change before the crack entirely cuts off the film; the electric resistance is expressed by the following expression (Ogawa et al., 1991a).

$$R = \begin{cases} \text{constant} & a \neq w \\ \infty & a = w \end{cases} \quad (2)$$

Thus, at the instant when a crack grows across the film with a grid shape, the electric resistance of the film will increase to infinity and the complex calculation of the electric resistance of the ion-sputtered film with a crack can be avoided; referring to the crack gauge, a grid pattern ion-sputtered film should be available for crack length measurement (Deng et al., 2006). The electric resistance of the grid pattern ion-sputtered film will increase owing to crack growth, crack length can be determined by counting the number of the increasing steps in the electric resistance and measuring the positions of the grids after or before an experiment.

## 2.2 Bending test piece and crack length measurement

To investigate the precision of the crack length measurement method using a grid pattern ion-sputtered film, three-point bending fatigue tests for acrylic test pieces were performed. Figure 2 shows the loading method, the test piece and the grid pattern ion-sputtered film. In the experiment, first, a notch was introduced into the test piece to easily introduce the fatigue crack from the notch under a cyclic load. The crack growth experiment was performed under a cyclic load for a slow crack growth. The thickness of the grid pattern ion-sputtered film was about 10nm, the grid width was 0.2mm, and the interval between two grids was 0.1mm. The supporting span was 80mm, and the width and thickness of the test piece were 20mm and 10mm, respectively. The cyclic load was a sine wave of 10Hz and the load ratio ( $P_{min}/P_{max}$ ) was approximately 0.02. A very simple measurement system used for recording the electrical resistance, which consists of a DC power source, a variable resistor and a voltmeter, is shown in Figure 3. The supply voltage was approximately 1-2V, the supply voltage and variable resistor were adjusted for a current below 100mA. The voltage on the film during the fatigue test was recorded by a data recorder. The sampling speed for the voltage was 80Hz.

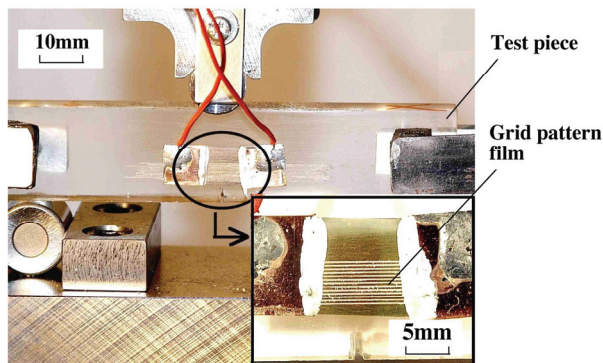


Fig. 2. Test piece and grid pattern ion-sputtered film

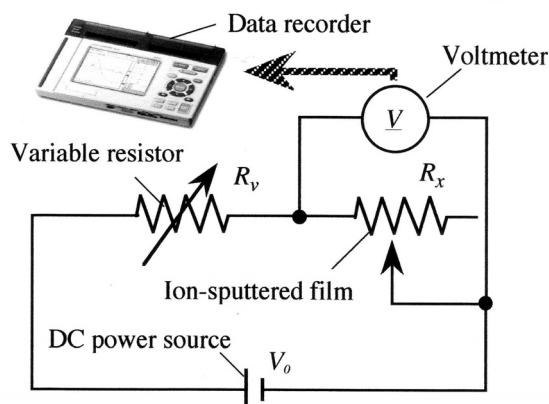


Fig. 3. Measurement system for the electrical resistance of ion-sputtered film

### 2.3 Precision of crack length measurement with grid pattern ion-sputtered film

The change in the voltage of the grid pattern film during crack propagation is shown in Figure 4. Although fluctuations in voltage signals due to the deformation of the film and the sampling error were observed, a distinct staircase pattern was recorded for the electric resistance. Considering the characteristic of the electric resistance change for a cracked grid as expressed in expression (2), the increasing step in Figure 4 shows the instant of grid snapping. From the positions of the grids that can be measured with an optical microscope before or after an experiment with a very high precision, the crack length at the instant of the increasing step can be accurately estimated. The precision of this method depends on the film thickness and the speed of the measuring system in response to the crack growth. Since the recorded signal upturns vertically and the film is extremely thin, this method can intermittently measure cracks with a very high precision at the instant of grid snapping.

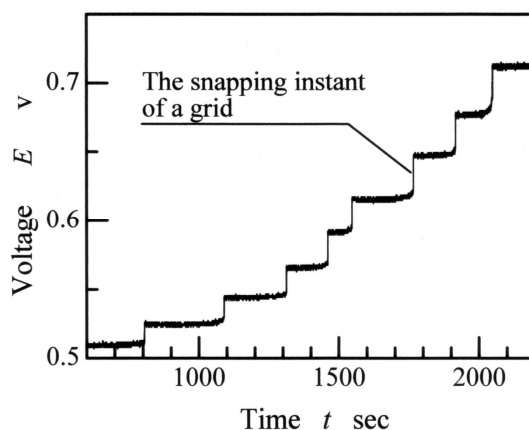


Fig. 4. Change in voltage of grid pattern film during crack propagation

For the application of the crack length measurement method using a grid pattern film to a rapidly growing crack, a fine-pitch grid pattern ion-sputtered film is desirable. Scribing the film using a sharp scriber tip, as shown in Figure 5, can produce grids of  $25\mu\text{m}$  width and  $50\mu\text{m}$  pitch. A film with 40 grids was fabricated and applied to a fatigue test. The change in the voltage of the film during crack propagation is shown in Figure 6, and 40 steps are identified clearly, indicating that 40 points of crack length can be obtained. Tokunaga et al. (2007) have succeeded in fabricating a grid pattern film using an excimer laser micromachining technology where the grid width is about  $13\mu\text{m}$  and the pitch is  $20\mu\text{m}$  for the measurement of cracks in ceramics.

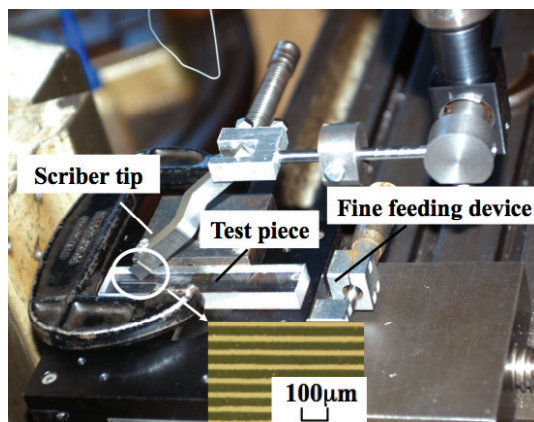


Fig. 5. Fabrication of fine grid film using scriber tip

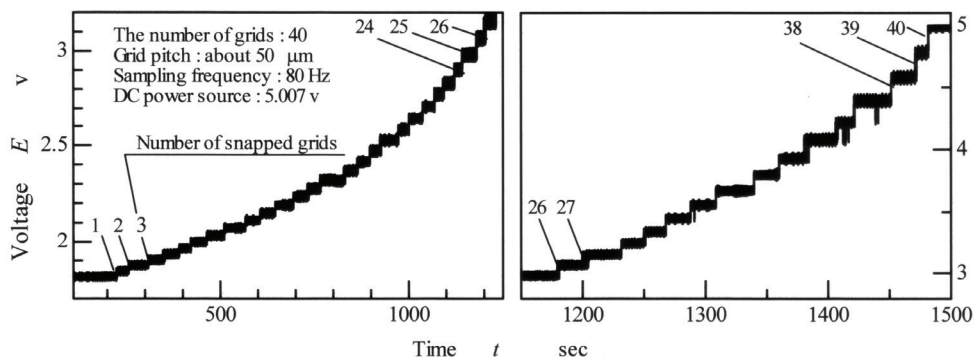


Fig. 6. Change in voltage of fine grid pattern film during crack propagation

### 3. Crack length measurement using rectangular ion-sputtered film

Although the grid pattern ion-sputtered film can measure crack length with a high precision, the crack length cannot be determined continuously. In addition, an isolation film is necessary for the application of the grid pattern film to a conductive surface; the

formation of the grid pattern without destroying the isolation film would be very difficult. Thus, for measuring the crack length continuously and applying the ion-sputtered film to a conductive surface, such as a metal surface, a rectangular ion-sputtered film is desirable.

### 3.1 Calculation of electric resistance of cracked metal film

In the case of a cracked film under electric potential difference, the feature of electron flow around the crack, which is similar to that of stress concentration, is shown in Figure 7, and the electric resistance calculation becomes very complex. Ogawa et al. (1991a, 1991b) calculated the electric resistance of an across-cracked carbon film by FEM analysis and presented an approximating formula for the electric resistance of a regulated film where the crack length is in the range of  $0.2-0.8w$  ( $w$  is the film width along the crack growth direction). Generally, the film width is several millimeters; thus, it is difficult to calculate the electric resistance of a film with a micro-crack shorter than 1mm using Ogawa's formula.

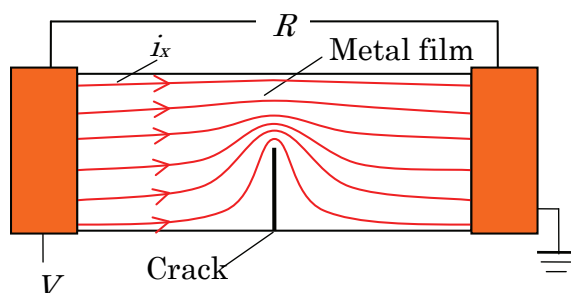


Fig. 7. Electron flows around crack

Electrothermal FEM is a practical method for calculating the electric resistance of the film with a crack (Deng et al., 2007). For example, when the mesh of a rectangular metal film and the boundary condition, shown in Figure 8, are prepared, the current density  $i_x$  of each element can be obtained by FEM analysis. The total current in the  $x$  direction can be calculated by integrating the current of each element, and the electric resistance can be obtained through the total current and electric potential difference on the basis of the law of ohm. The effect of the element size in FEM analysis on the calculation precision was investigated. Figure 9 shows the relationship between the calculated electric resistance and the number of elements for FEM analysis. Under the conditions that the length  $l$  of the film is 20.8mm, the width  $w$  of the film is 10.4mm and the crack length  $a$  is  $0.4w$ , the electric resistance approaches a constant value when the number of elements is more than 5000. It is strongly recommended that the change in the calculated electric resistance with the increase in the number of elements should be investigated, and that an appropriate number of elements should be chosen. Many software programs, such as ANSYS and Marc, are available for electrothermal analysis.

Figure 10 indicates the electric resistance of a cracked ion-sputtered film on an acrylic piece, where crack length was measured using an optical microscope. The difference between the electric resistances obtained by measurement and FEM analysis is only 2-3%; thus, it can be considered that the electric resistance of a cracked film is calculated correctly by FEM analysis.

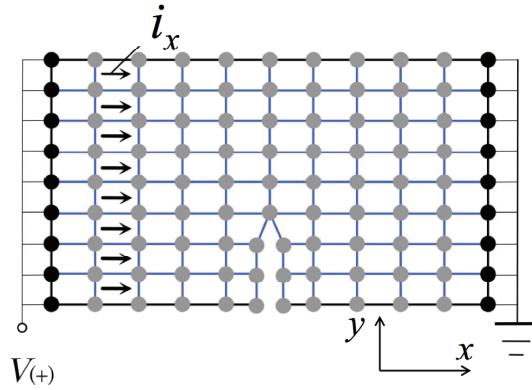


Fig. 8. Mesh of cracked film and boundary condition for electro-thermal FEM analysis

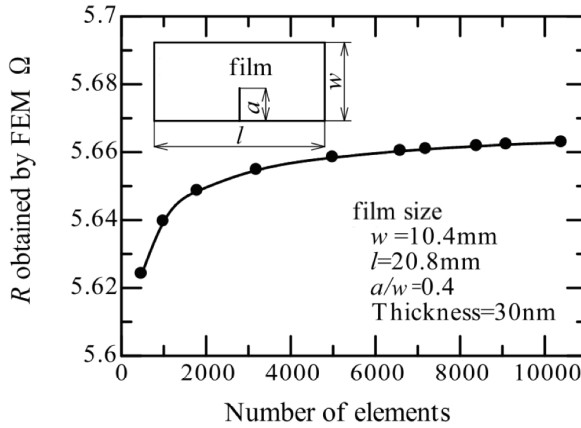


Fig. 9. Electric resistance value obtained under different number of elements

Despite the many approaches that can be used to find the expression for the relationship between the electric resistance and the crack length from 0 to the film width, a satisfactory expression was not obtained. Finally, considering practicability, the following expression is introduced to show the relationship in the crack length range from 0 to a portion of the film width.

$$R = R_0 + ca^b \quad (3)$$

Here,  $R$  ( $\Omega$ ) is the electric resistance of the cracked film,  $a$  is the crack length (mm),  $R_0$  ( $\Omega$ ) is the electric resistance when  $a=0$ , and  $c$  and  $b$  are constants. Many calculations were carried out to determine the values of  $b$  for the various dimensions of the films. The results of the calculations revealed that  $b$  depends on the shape of the film. Figure 11 shows the values of  $b$  at different ratios of the film length  $l$  to the film width  $w$ . In the  $l/w$  range from 2.0 to 3.5, constant  $b$  is approximately equal to 2.268 on average.

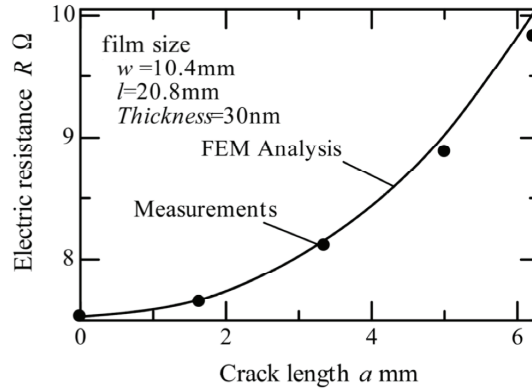


Fig. 10. Electric resistance obtained by measurement and FEM analysis

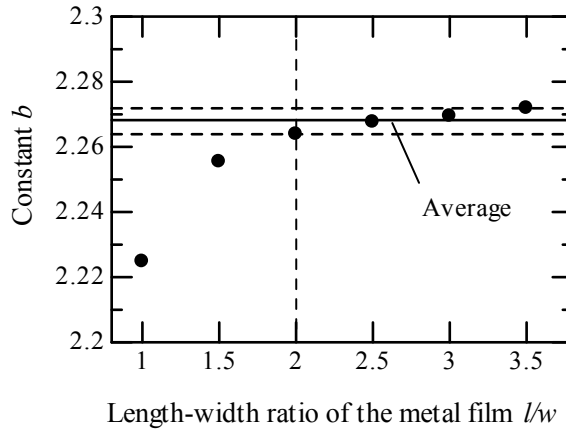


Fig. 11. Values of  $b$  under different shape of the film

On the other hands,  $c$  can be determined by stopping the experiment before the crack entirely cuts off the film, measuring the crack length  $a_e$  using an optical microscope, and substituting the electric resistance  $R_e$  and crack length  $a_e$  into expression (3). Several ion-sputtered films were used to verify the accuracy of expression (3). On the basis of the good agreement between the crack length estimated with expression (3) and measured using an optical microscope, the following expression is considered practical for estimating the electric resistance of a cracked film.

$$R = R_0 + ca^{2.268} \quad (0 \leq a \leq 0.6w, 2.0 \leq \frac{l}{w} \leq 3.5) \quad (4)$$

However, the physical meaning of expression (4) has not yet been clarified, and such an expression is only a curve-fitting formula and should be applicable to the condition shown in expression (4). Although this approximating expression can calculate the electric



resistance of a cracked film in a specific crack length range, it is better to carry out FEM analysis for a good precision in the electric resistance calculation if a FEM software program is available; the necessary physical and electrical properties for FEM analysis can be obtained by using the initial electric resistance and dimensions of the film.

### 3.2 Crack length measurement using rectangular ion-sputtered film

Three-point bending tests were performed for acrylic test pieces, whose crack lengths were measured using a microscope and ion-sputtered films. The test piece were 100mm in length, 10mm in depth, and 20mm in height, and the supporting span in the tests was 80mm. A V-notch was introduced into the middle of the supporting span. The load ratio  $P_{\min}/P_{\max}$  was 0.02 and the load frequency was 10Hz. The experimental method and an ion-sputtered film on a test piece are shown in Figure 12. All tests were stopped when the crack grew to about  $0.6w$  ( $w$ : film width) for the determination of the constant  $c$  in expression (4).

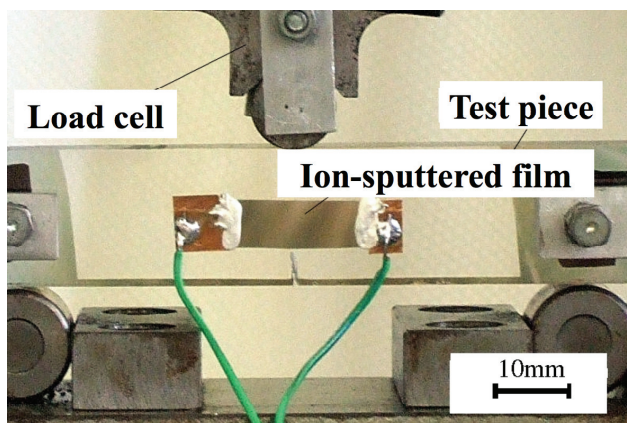


Fig. 12. Rectangular ion-sputtered film on acrylic test piece

The comparison of the crack lengths measured using an optical microscope and an ion-sputtered film is shown in Figure 13. The crack lengths are in very good agreement. Their maximum difference is 0.113mm and their average is only 0.051mm. A relatively large crack length difference occurs when the cracks are very short. This difference is considered to be due to the interruption of the experiment and taking off the test pieces from test rig for crack length measurement using an optical microscope that leads to the changes in the electrical environmental conditions around the test pieces. Although the precision of this rectangle is not as high as that of a grid pattern film, it is greatly higher than that of a commercial crack gauge (Deng et al., 1991). Therefore, a rectangular ion-sputtered film can be used to measure crack length continuously; short cracks or cracks with high growth rate, such as those in glass and ceramics, might be measurable by using a high-frequency sampling system.

## 4. Evaluation of crack growth characteristics of glass and ceramics based on crack length measurement using ion-sputtered film

It is known that fatigue failures also occur in structure components made of glass and ceramics under a constant load or a dynamic load (Hoshide, 1994). Since a small crack will

grow more unstably and crack growth rate may increase more markedly within a small stress intensity factor range in brittle materials than in ductile metals, the understanding of the small crack growth characteristics in brittle materials, such as glass and ceramics, is very important for the prediction of the residual life. Many researches have been performed to clarify the relationship between the crack growth rate and the stress intensity factor for glass and ceramics using fatigue tests (Wakai et al., 1986, Takahashi et al., 1991, Sawaki et al., 1992, Aze et al., 2002, Yoda, 1989, Kimura et al., 1987). However, most of these researches used standard test pieces, such as compact test pieces or double-torsion test pieces, where the crack length is usually over several millimeters; thus, the crack growth characteristics known up to now are considered appropriately restricted to the large cracks that are impractical in the structure components made of glass and ceramics. For investigating the growth characteristics of a small crack with a length shorter than 1mm in glass and ceramics, a high-precision and high-speed crack length measurement method is necessary. Other methods, such as microscopy observation, the compliance method, the opening displacement method and the estimation methods based on the changes in electric properties around the crack are not applicable. However, the presented crack length measurement method using an ion-sputtered film makes it possible to measure the crack growing in glass and ceramics, since the ion-sputtered film is extremely thin that its electric resistance may change owing to a small increase in crack length, and a high-speed sample system is used for recording the electric resistance of the film.

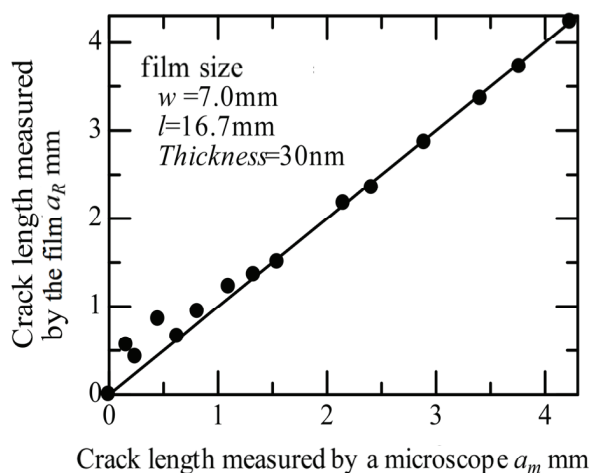


Fig. 13. Comparison of crack length obtained by microscope and ion-sputtered film

In this section, a concrete example of the application of a rectangular ion-sputtered film to clarifying small crack growth characteristics, namely, the relationship between the crack growth rate and the stress intensity factor, in soda-lime glass and alumina ceramics is discussed in detail.

#### 4.1 Four-point bending test piece and fatigue test method

Four-point bending fatigue tests were performed under a constant load. The test pieces were made of soda-lime glass and alumina ceramics. The main chemical components and typical

properties of the materials are shown in Table 1. The dimensions of the test pieces are shown in Figure 14. The test piece of soda-lime glass is 100mm long, 12mm wide ( $B$ ) and 9.6mm thick ( $W$ ), and the test piece of alumina ceramics is 100mm long, 12mm wide and 10mm thick. A precrack was introduced at the center of the lower surface of the test piece using a diamond indenter, and the ion-sputtered film was prepared traversing the crack growth directions. The film  $w$  and  $l$ , precrack length  $c_0$ , and distance  $s$  were measured using an optical microscope before the fatigue tests. The measurement error in the electric resistance of the cracked film was about 2-3% for the film of  $l/w=2.0$  based on the results mentioned in section 3.1.

Material	Soda-lime glass		Alumina ceramics	
Main components    wt%	SiO <sub>2</sub>	72.0	Al <sub>2</sub> O <sub>3</sub>	99.5
	CaO	10.0		
	Na <sub>2</sub> O	14.0		
Grain size        μm	Amorphia		10	
Young's modulus   GPa	71.6		363	
Bending strength   MPa	49.0		441	

Table 1. Main chemical components and properties of the test materials

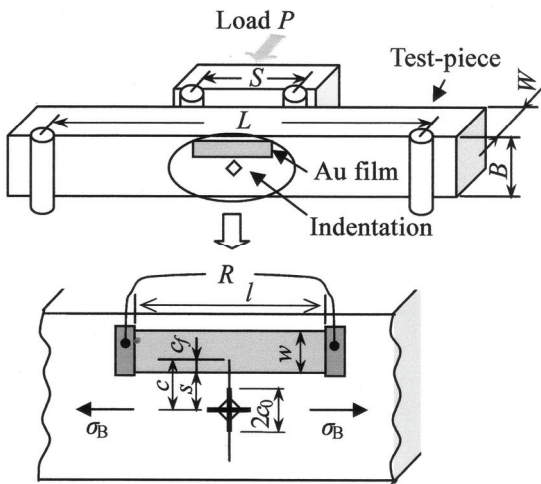


Fig. 14. Dimensions of four-point bending test piece

Static fatigue crack growth can be observed in glass and ceramic materials owing to stress corrosion. A constant load was applied to the test piece in this experiment. The loading and supporting methods are shown in Figure 14. The upper loading span ( $S$ ) and lower supporting span ( $L$ ) are 30mm and 90mm for the soda-lime glass, and 10mm and 25mm for

the alumina ceramics, respectively. The simple system shown in Figure 3 was used to record the voltage on the ion-sputtered film, and the electric resistance of the film was calculated with the voltage and the set values of the other components in the measurement system. Since the crack grew at a high speed in glass and ceramics under a constant load, the recording frequency was 125kHz; thus, the crack length could be measured nearly continuously.

#### 4.2 Calculation of stress intensity factor for surface crack and crack growth rate

A surface crack from a diamond indenter pit takes the shape of a semi-ellipse as shown in Figure 15. The stress intensity factor varies with the position at the edge of a crack. The maximum stress intensity factor at point A, which is used in the following discussion, is expressed as below (Kunio et al., 1984),

$$K_I = \frac{3.3P(L-S)\sqrt{\pi c(a_0/c_0)}}{2BW^2\sqrt{1+1.46(a_0/c_0)^{1.65}}} \quad (5)$$

here,  $P$ ,  $S$ ,  $L$ ,  $W$ ,  $B$ ,  $a_0$ , and  $c_0$  are the load, upper loading span, lower supporting span, test piece thickness, test piece width, initial crack length in the depth direction, and initial surface crack length, respectively. In expression (5), the crack length  $a$ , as shown in Figure 15, is substituted by  $c(a_0/c_0)$  on the basis of the assumption that the aspect ratio  $\lambda$ , defined as the ratio of the crack length (depth)  $a$  to the surface crack length  $c$  namely,  $\lambda=a/c$ , is a constant during crack propagation. The aspect ratio  $\lambda$  can be obtained using the initial crack length  $a_0$  and  $c_0$  measured in the break section after the fatigue test using an optical microscope, and  $c$  is the surface crack length measured using the ion-sputtered film.

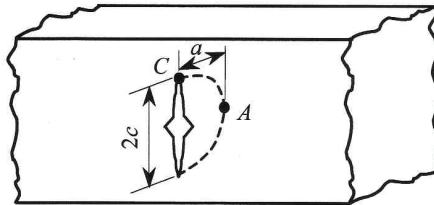


Fig. 15. Semi-ellipse surface crack

The surface crack length was derived from the electric resistance of the film based on the relationship between the crack length and the electric resistance of the ion-sputtered film obtained through the above-mentioned FEM analysis. To remove the effects of the sampling errors included in the electric resistance of the ion-sputtered film, as shown in Figure 16, on the surface crack length, the simple moving average method was used to obtain a smooth relationship between the surface crack length and the loading time, as shown in Figure 17. On the basis of the assumption that the aspect ratio  $\lambda$  is constant during crack propagation, the crack length  $a$  in the depth direction of the test piece was measured as the product of the surface crack length  $c$  multiplied by the aspect ratio  $\lambda$ , namely  $a=c \cdot \lambda$ , and then, the crack growth rate  $da/dt$  was determined by differentiating the relationship between the crack length  $a$  and the loading time  $t$ .

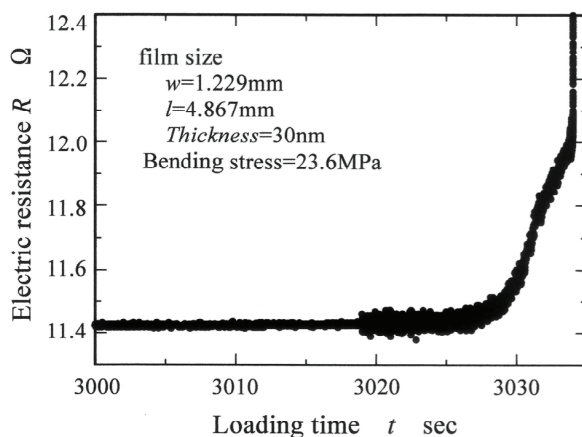


Fig. 16. Electric resistance of the ion-sputtered film during fatigue test for soda-lime Glass

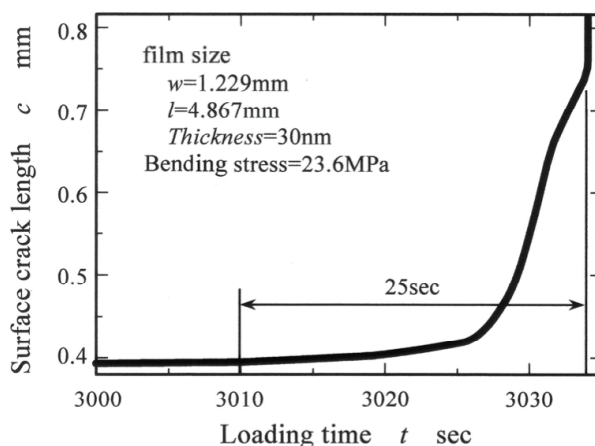


Fig. 17. Crack growth during fatigue test for soda-lime glass

#### 4.3 Crack growth characteristics of soda-lime glass

The growth of a surface crack in the soda-lime glass test piece is shown in Figure 17. Fracture occurred when the crack length reached about 0.8mm; thus, the critical or unstable crack growth is expected to start from a small crack under a constant load. Moreover, crack growth time was about 25sec from the total fatigue time of about 3,040sec; the crack growth stage occupied less than 1% of the entire fatigue process.

Figure 18 shows the relationship between the crack growth rate and the stress intensity factor for the soda-lime glass under the bending stress of 22.8 and 23.6MPa. It has been very difficult up to now to measure the growth rate of a small crack, particularly the low and high (unstable) growth rates in brittle materials. In this experiment, since the ion-sputtered film can measure a small crack with high precision, and the sampling frequency of the

measurement systems is so high that the surface crack can be measured almost continuously, a complete relationship including the three regions of crack growth was obtained successfully. In the stress intensity range from 0.45 to 0.85 MPa·m<sup>1/2</sup>, the crack growth rate changed from very low to very high in the soda-lime glass; thus, the unstable crack growth occurs easily in the soda-lime glass under a constant load.

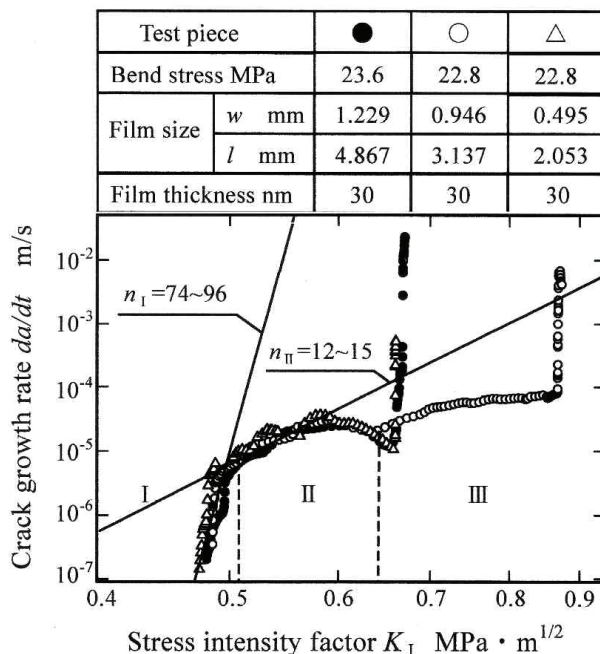


Fig. 18. Crack growth characteristics in soda-lime glass

On the basis of the Paris law indicating that the crack growth rate is proportional to the  $n$ th power of the stress intensity factor, that is  $\frac{da}{dt} = cK_I^n$ , the constant  $n$  was determined to range from 74 to 96 in region I, and from 12 to 15 in region II for the soda-lime glass. Yoda (1989) and Wiederhorn (1967) obtained  $n$  values ranging from 10 to 16 in the region of the crack growth rate from  $1 \times 10^{-6}$  to  $1 \times 10^{-4}$ , which agree with those obtained in region II of this experiment. The results of this experiment consequently clarify the crack growth characteristics of the soda-lime glass not only in region II but also in regions I and III; the crack length measurement method using a rectangular ion-sputtered film might be practical for investigating the crack growth characteristics of brittle materials, such as soda-lime glass.

#### 4.4 Crack growth characteristics of alumina ceramics

The surface crack lengths measured during the test for alumina ceramics are shown in Figure 19. Brittle fracture occurred when the crack length reached about 0.55mm; thus, the critical or unstable crack growth is expected to start from a small crack under a constant

load. Moreover, crack growth time was about 130sec from the total fatigue time of about 15,760sec; the crack growth stage occupied less than 1% of the entire fatigue process.

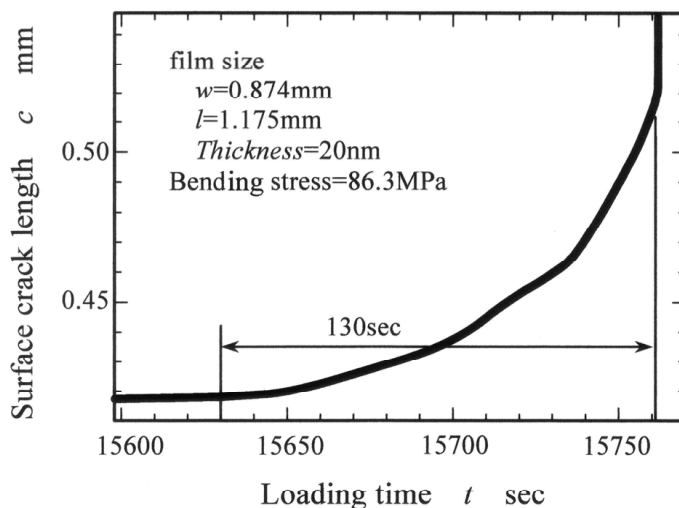


Fig. 19. Crack growth during fatigue test for alumina ceramics

Figure 20 shows the relationship between the crack growth rate and the stress intensity factor for the alumina ceramics under the bending stress of 86.3MPa. The surface crack length was also measured almost continuously, resulting in the successful determination of a complete relationship in the three regions of crack growth. The stress intensity factors range where the crack growth rate changes from low to high (unstable) in the alumina ceramics is very small (about 0.2 to 0.4  $\text{MPa}\cdot\text{m}^{1/2}$ ), which is similar to that of soda-lime glass; thus, the unstable crack growth occurs easily under a constant load. On the basis of the fact that the stress intensity factor for the crack growth in alumina ceramics is much higher than that in the soda-lime glass, alumina ceramics are considered to have a much higher fatigue strength than soda-lime glass.

Considering that the  $n$  values range from 530 to 580 in region I, and from 17 to 25 in region II for the alumina ceramics, the crack growth rate increases markedly owing to the small increase in stress intensity factor, particularly in region I. The  $n$  values obtained by Wakai et al. (1986) using double-torsion test pieces range from 84 to 130 in the crack growth rate range of  $2\times 10^{-7}$  to  $1\times 10^{-3}$ , which is different from those obtained in this experiment. Considering that the crack lengths in this experiment are below 1mm, much shorter than those in the experiments of Wakai et al., the difference in  $n$  might be due to the fact that the crack growth characteristics depend on crack length.

The circle in region II in Figure 20 also indicates a decrease in crack growth rate. The shapes of the surface cracks in the soda-lime glass and alumina ceramics are observed using a microscope and shown in Figure 21. The crack grew linearly in the soda-lime glass but meandered in the alumina ceramics. Since the ion-sputtered film can only measure the crack length in the traversing direction of the film, the meandering of the crack would be seen as a decrease in crack growth rate.



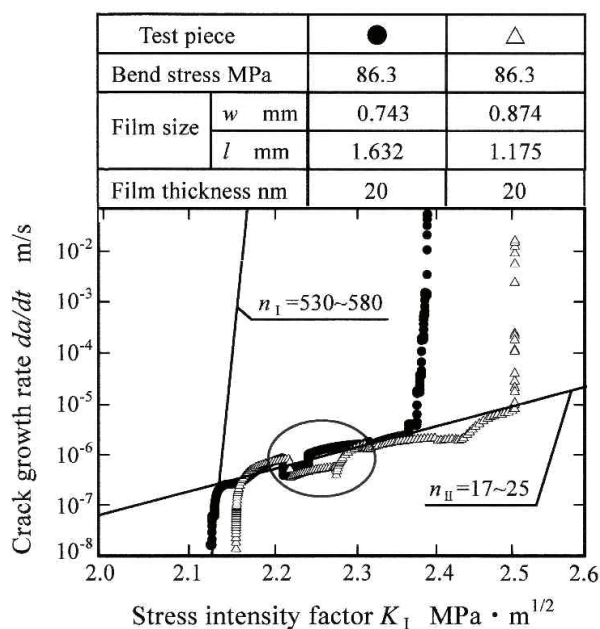


Fig. 20. Crack growth characteristics in alumina ceramics

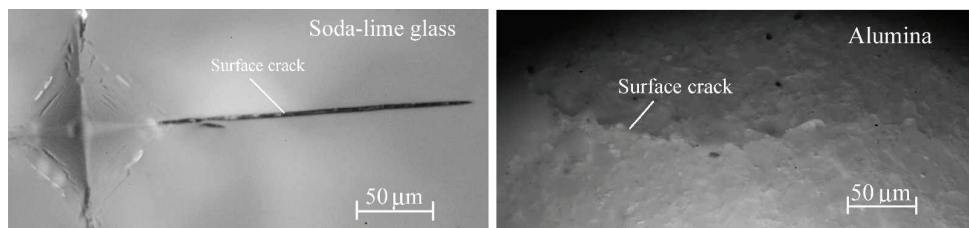


Fig. 21. Appearances of surface cracks in soda-lime glass and alumina ceramics

## 5. Application of crack length measurement using ion-sputtered film to metal surface

Ion-sputtered films can also be applied to crack length measurement for a metal surface if an insulating film could be fabricated between an ion-sputtered film and a metal surface. The insulating film should be as thin as possible for a high measurement precision. Many methods, such as the vacuum evaporation of silicon and glass, spray pyrolysis using ZnO, painting with quick-drying glue (Krazy Glue) and varnishing using an insulating spray paint, have been used to fabricate a thin insulating film on a steel surface. The method of varnishing using an insulating spray paint was selected finally for the high insulating resistance, thinness and fabrication convenience. The spray paint used in this experiment is the coating agent AY-302 (Sunhayato Co., Tokyo, Japan), which is commonly used in the insulation of printed circuit boards. The main component of the coating agent is polyvinyl



resin. Wiping the steel surface with absorbent cotton wetted with the coating agent produces a good-quality and thin isolating film of about 1-2 $\mu$ m thickness. The insulating electric resistance between the ion-sputtered film and the steel surface was measured; its value was as high as several hundreds of ohm for an ion-sputtered film of about 5mm $\times$ 10mm.

A sectional view of the insulating film, the ion-sputtered film and the wiring method used for the crack length measurement on a steel test piece are shown in Figure 22. The insulating film should be fabricated after the setting of the terminal and wiring, and the ion-sputtered film should be fabricated immediately before the experiment.

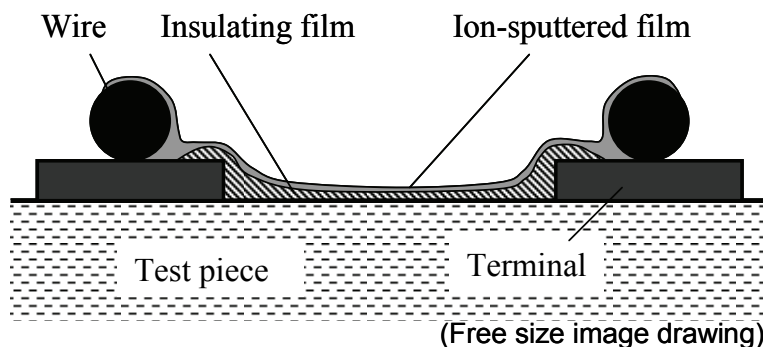


Fig. 22. Method applying ion-sputtered film to metal surface

## 6. Fatigue crack initiation detection method using ion-sputtered film

Many studies have been performed on the detection method for fatigue crack initiation that is very important in the evaluation of fatigue strength. Makabe et al. (1992, 1994a, 1994b) used a strain waveform for the detection of a fatigue crack with a length of 0.5 to 1mm on a round test piece with a small hemispherical pit. Katayama et al. (1996) and Lee et al. (2002) detected crack initiation using an AC potential method on a sharply notched test piece. Tohmyoh et al. (2001) detected the fatigue crack initiation of a test piece with a surface slit during rotating bending tests using surface SH (shear-horizontal) waves. Papazian et al. (2007) and Zilberstein et al. (2001, 2003, 2005) performed many studies on the application of a meandering winding magnetometer array sensor, ultrasonic techniques and an electrochemical fatigue sensor for the detection of crack initiation for many different types of fatigue test pieces. In addition to the above-mentioned methods, since the ion-sputtered film is very thin, a very short crack can change the electric resistance of the ion-sputtered film; thus, the ion-sputtered film would be practical for detecting the instant of fatigue crack initiation during a fatigue test.

### 6.1 Principle of fatigue crack initiation detection method

The ion-sputtered film is as thin as several tens of nanometers; thus, a small surface crack is expected to crack the film and change the electric resistance of the film, as shown in Figure 23. The starting point of the increase in electric resistance corresponds to the instant of crack initiation.

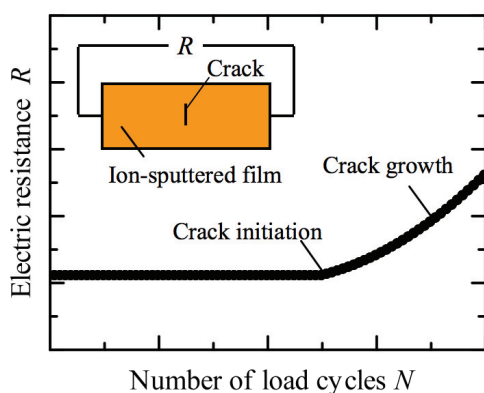


Fig. 23. Change in electric resistance of ion-sputtered film due to crack initiation and crack growth

## 6.2 Test piece for fatigue crack initiation detection

Three-point bending fatigue tests were performed to investigate the effectiveness of the ion-sputtered film in crack initiation detection. Considering that the crack initiates from stress concentration regions in machine elements, such as shafts and gears, and the convenience of fabricating an ion-sputtered film, the notch in the test piece should be round instead of being V- or U-shaped. The notches of the test pieces were in the shape shown in Figure 24, and crowned so that the crack could initiate at their centers. The test pieces were 100mm long, 10mm thick and 20mm high, and the supporting span in the tests was 80mm. The radius of the round notch was 4mm, the depth of the notch top  $T$  was about 5mm and the crowning radius  $R$  was about 5mm.

The test pieces were made of acrylic. The ion-sputtered film was formed on the notch surface. The length of the film in the direction of the test piece length was about 10mm, and the width and the thickness of the film were about 5mm and 10-50nm, respectively. The initial electric resistance of the film was lower than 20ohm. As shown in Figure 3, the system was used to record the voltage on the ion-sputtered film.

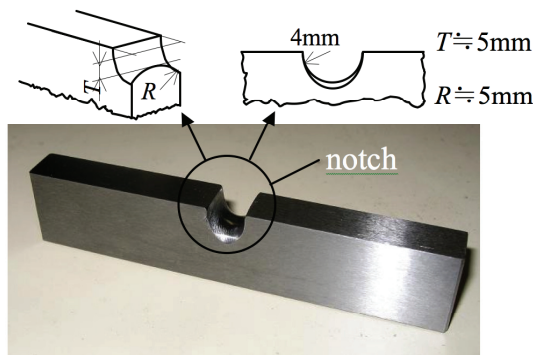


Fig. 24. Test piece for crack initiation detection test

### 6.3 Durability of ion-sputtered film

Whether the change in electric resistance or physical damage to the film occurs during the fatigue test before crack initiation was investigated to confirm the suitability of the film. The film was subjected to an endurance test under a light load without fatigue breaks. Figure 25 shows the electric resistance of the film during the test. It is obvious that no physical damage occurred in the film during the test, although a slow decrease in the electric resistance of about 0.5ohm was observed under load cycles of  $1 \times 10^7$  (about 90hr). Gradual changes in electric resistance also occurred during some of the subsequent experiments; the reasons for these changes have not yet been clarified. However, considering that the film was made of pure gold (Au) without deteriorations of material properties due to chemical reactions under these test conditions, and that the changes were much slower than that due to crack initiation, the gradual changes might be caused by some unknown environmental factors or the electric shifts of the apparatuses in the measurement system. On the basis of the above-mentioned results, the gradual changes are considered not so severe that the judgment of crack initiation is prevented.

### 6.4 Change in electric resistance due to crack initiation

The electric resistance of the ion-sputtered film on an acrylic test piece during the fatigue test is shown in Figure 26. The maximum load was 400N, the loading frequency was 10Hz and the film thickness was about 30nm. The experiment was stopped manually after recognizing a rapid increase in voltage signal on the monitor of the data recorder. Figure 26 clearly shows an increase in the electric resistance of the film, indicating crack initiation. Despite the fact that gradual changes in the electric resistance of the film sometimes occur, as shown in Figure 25, the increase in electric resistance due to crack initiation is clear compared with the gradual changes shown in Figure 25, and the crack initiation point can be confirmed from Figure 26 by observing the upward tendency of the electric resistance. The point where the electric resistance leaves the extension line of the mean electric resistance is considered to be the start point of crack initiation. The notch after the experiment is shown in Figure 27, and a very small round crack, the crack in the primary stage of fatigue, can be observed clearly.

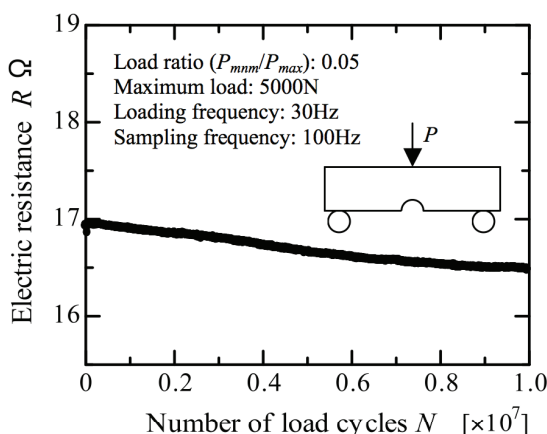


Fig. 25. Electric resistance of ion-sputtered film during the test without crack initiation

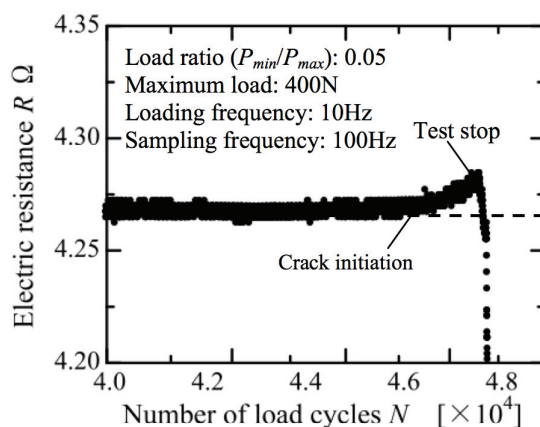


Fig. 26. Change in electric resistance of ion-sputtered film when fatigue crack initiation

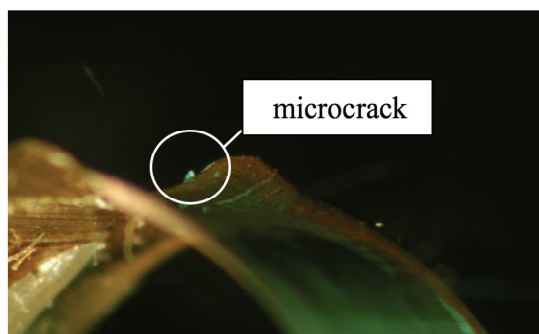


Fig. 27. View of micro-crack initiated on notch surface

### 6.5 Shape of detected crack in primary stage of fatigue

A small sample around the notch was quarried out from the test piece to determine the crack front shape. The sample was cut bit by bit from the side using a milling machine. The depth of the sample  $d$  and the crack length  $a$  on the side surface were measured using a micrometer and an optical microscope, respectively. The shape of the crack front is shown in Figure 28. It can be seen that the shape of the crack front is approximately half an ellipse, the length of the crack on the notch surface is about 0.35mm and the maximum depth is about 0.2mm. The half ellipse shape indicates that the crack is in the primary stage of fatigue. It is slightly difficult to say that the crack shown in Figure 28 is the just-initiated crack since the dimensions of the crack are rather large. The large dimensions are due to the time lag between the judgment of crack initiation from the change in electric resistance and the termination of the test, not due to the sensitivity of the ion-sputtered film because the measurement error of the film is as small as 0.068mm (Deng et al., 2007). From the change in the electric resistance of the ion-sputtered film and the shape of the detected crack shown in

Figures 26, 27 and 28, it can be concluded that the ion-sputtered film can be used to detect the initiation of a fatigue crack. Considering the convenience to prepare the detecting system, this method is simple and practical for monitoring fatigue crack initiation.

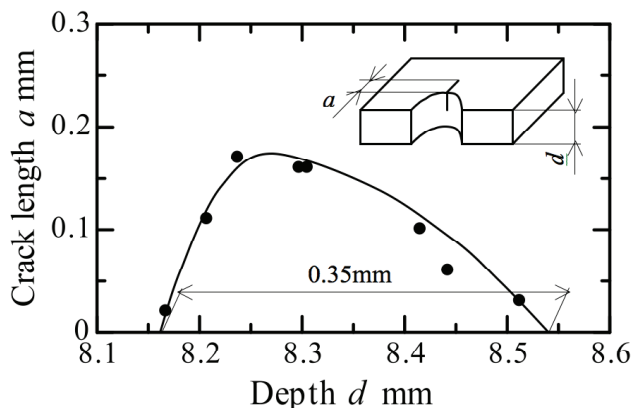


Fig. 28. Shape of crack initiated in acrylic test piece

## 7. Conclusions

The methods for crack length measurement and fatigue crack initiation detection using an ion-sputtered film based on the changes in the electric resistance of the film due to crack growth or crack initiation are presented. On the basis of that the experimental results of crack length measurement and crack initiation detection, and considering the convenience to prepare the measurement and monitoring systems, the presented methods are very practical for investigating crack growth characteristics and crack initiation life.

One of the crack length measurement methods is the use of a grid pattern ion-sputtered film, which is similar to a crack gauge. Since the electric resistance of the film changes only at the point when a grid is entirely snapped by a crack, the calculation of the electric resistance is not necessary, the crack length can be obtained by counting the number of increasing steps in the recorded electric resistance and measuring the positions of the grids. Because the thickness of the ion-sputtered film is only several tens of nanometers, the change in the electric resistance of the film due to grid snapping is more immediate than that of the commercial crack gauge. Grid pattern ion-sputtered films were applied to the crack length measurement for a three-point bending test piece. Very obvious staircase changes in the electric resistance of the film were recorded.

Another crack length measurement method is the use of a rectangular ion-sputtered film, which can measure crack length continuously. The relationship between the electric resistance of the film and crack length is obtained by electrothermal FEM analysis, and an approximate expression is proposed to calculate the electric resistance of a cracked film using the results of electrothermal FEM analysis. Since the film is extremely thin, it is very sensitive to the increase in the length of a small crack and practical for investigating a small crack with high growth rate. As the application of the crack length measurement method using a rectangular ion-sputtered film, cracks in soda-lime glass and alumina ceramics were

measured and the crack growth characteristics in these materials were clarified continuously from the crack growth region I to the crack growth region III.

In addition to crack length measurement, an ion-sputtered film can also be applied to the detection of fatigue crack initiation, which is a very important technique for evaluating the fatigue strength of a material. Since the film is extremely thin and can be fabricated directly on a surface, a very small crack can change its electric resistance. As an attempt to confirm the fatigue crack initiation life, an ion-sputtered film was formed on the round notch surface of a three-point bending acrylic test piece; a very small crack that initiated from the notch surface during the fatigue test was detected. From the change in the electric resistance of the ion-sputtered film during the test and the shape of the detected crack, it can be concluded that the ion-sputtered film can be used to detect the initiation of a fatigue crack.

## 8. References

- Ashida, U., Ishihara, T., Fujihara, H. & Tobita, H. (1996). Automatic Measurement of Fatigue Crack Length by a D.C. Electrical Potential Difference Method, *Journal of The Kansai Society of Naval Architects (in Japanese)*, 225, 181-185
- Aze, A.D., Chevalier, J., Fantozzi, G., Schehl, M. & Torrecillas, R. (2002). Crack Growth Resistance of Alumina, Zirconia and Zirconia Toughened Alumina Ceramics for Joint Prostheses, *Biomaterials*, Vol.23, No.3, 937-945
- Brown, T.F. & Srawley, J.E. (1966). In Plane Strain Crack Toughness Testing of High Strength Metallic Materials, *ASTM STP410*
- Bucci, R.J., Paris, P.C., Hertzberg, R.W., Schmidt, R.A. & Anderson, A.F. (1972). Fatigue Threshold Crack Propagation in Air and Dry Argon for a Ti-6Al-4V Alloy, *ASTM STP513*, 125-140
- Deng, G., Inoue, K., Takatsu, N. & Kato, M. (1991). Evaluation of the Strength of Carburized Spur Gear Teeth Based on Fracture Mechanics, *Trans. Jpn. Soc. Mech. Eng. (in Japanese)*, C-57-535, 909-913
- Deng, D., Tokunaga, H., Daniel-Redda, T., Ikeda, K., Nakanishi, T. & Kaizu, K. (2006). Crack Length Measurement with an Ion Sputtered Film, *Trans. Jpn. Soc. Mech. Eng. (in Japanese)*, 72-715, 997-1002
- Deng, D., Nasu, K., Kuroia, S. & Nakanishi, T. (2007). Crack Length Measurement with an Ion Sputtered metal Film, *Trans. Jpn. Soc. Mech. Eng. (in Japanese)*, 73-727, 849-854
- Hoshide T. (1994). Fatigue in Ceramics I, *Journal of The Society of Materials Science*, Vol.43, No.490, 902-908
- James, L.A. (1981). Specimen Size Considerations in Fatigue Crack Growth Rate Testing, *ASTM STP738*, 45-57
- JSME (1986). JSME Standard, *Jpn. Soc. Mech. Eng.*, S-001, 8-9
- Katayama, Y., Sakane, M. & Ohnami, M. (1996). Surface Crack Detection by A. C. Potential Drop Method; Experiment and FEM Considerations, *Trans. Jpn. Soc. Mech. Eng. (in Japanese)*, Vol.62-602, 2216-2223
- Kimura, Y., Yamamoto, S., Sekiya, M. & Kunio, T. (1987). Crack Growth Characteristics of Vickers Indented Glass Plate Specimen in Water, *Journal of The Society of Materials Science*, Vol.36, No.401, 160-165
- Kunio, T., Nakazawa, K., Hayashi, I. & Okamura, H. (1984). (*Methods for Fracture Mechanics*), (*in Japanese*) , 251-252

- Lee, J.H. & Kobayashi, H. (1985). Detection and Closure Measurement of Short Fatigue Crack Initiated at Notch Root, *Trans. Jpn. Soc. Mech. Eng. (in Japanese)*, A-51-461, 142-147
- Lee, Y. & Sakane, M. (2002). Multiple Surface Crack Detection Using A. C. Potential Drop Method, *Trans. Jpn. Soc. Mech. Eng. (in Japanese)*, Vol.68-672, 1220-1227
- Makabe, C., Nishida, S., Kaneshiro, H. & Tamaki, S., (1992). Method of Detecting Fatigue Crack Initiation through Analysis of Strain Waveform, *Trans. Jpn. Soc. Mech. Eng. (in Japanese)*, Vol.58-551, 1191-1195
- Makabe, C., Kaneshiro, H., Nishida, S. & Urashima, C. (1994a). Detection of 1mm Fatigue Crack Initiation Using Strain Waveform, *Journal of engineering Materials and technology, Trans. of ASME*, Vol.116, 483-487
- Makabe, C., Nishida, S., Urashim, C. & Kaneshiro, H. (1994b). Detection of Fatigue Crack Initiation under a Random Load, *Trans. Jpn. Soc. Mech. Eng. (in Japanese)*, Vol.60-576, 1753-1760
- Masuyama, T., Inoue, K. & Kato, M. (1994). Acoustic Emission during Fatigue Crack Growth in Carburized Gear Tooth, *Trans. Jpn. Soc. Mech. Eng. (in Japanese)*, C-60-575, 2456-2461
- Mautz, J. & Weiss, V. (1976). Mean Stress and Environmental Effects on Near Threshold Fatigue Crack Growth, *ASTM STP601*, 154-168
- Nakai, Y., Akagi, H., Kitamura, Y. & Ohji, K. (1989). Measurement of Short Surface Crack Length by an AC Potential Method, *Trans. Jpn. Soc. Mech. Eng. (in Japanese)*, A-55-511, 543-548
- Nakamura, M., Saitoh, K., Ikeyama, M., Kozuka, T. & Shigematsu, I. (1993). A Study on the Utilization of an Electro-Conductive Surface Layer on a  $\text{Si}_3\text{N}_4$  Ceramic Formed by Ion Implantation as a Crack Gage and a Strain Gage, *Journal of the Ceramic Society of Japan (in Japanese)*, 101-1, 139-142
- Nishitani, H. & Chen, D. (1985). A Consideration on the Unloading Elastic Compliance Method, *Trans. Jpn. Soc. Mech. Eng. (in Japanese)*, A-51-465, 1436-1441
- Ogawa, T. & Suresh, S. (1991a). Surface Film Technique for Crack Length Measurement in Nonconductive Brittle Materials: Calibration and Evaluation, *Engineering Fracture Mechanics*, Vol.39-4, 629-640
- Ogawa, T. (1991b) Fracture Resistance Curve and Fatigue Crack Growth in Polycrystalline Magnesia, *Trans. Jpn. Soc. Mech. Eng. (in Japanese)*, A-57-535, 492-499
- Papazian, J. M., Nardiello, J., Silberstein, R., Welsh, G., Grundy, D., Craven, C., Evans, L., Goldfine, N., Michaels, J.E., Michaels, T.E., Li, Y. & Laird, C. (2007). Sensors for Monitoring Early Stage Fatigue Cracking, *International Journal of Fatigue*, Vol.29, 1668-1680
- Sawaki, Y., Nagase, Y., Yoshida, H., Inoue, A. & Fujiwara, T. (1992). Crack Propagation Behaviour in Alumina Ceramics under Static and Cyclic Loading, *Trans. Jpn. Soc. Mech. Eng., Series A*, Vol.58, No.552, 1333-1338
- Shimada, H. & Date, K. (1983). Crack Depth Measurement with High Accuracy by Ultrasonics, *The Iron and Steel Institute of Japan (in Japanese)*, 69-2, 196-202
- Takahashi, M. & Mutoh, Y. (1991). Static and Cyclic Fatigue Crack Growth in Several Ceramic Materials, *Trans. Jpn. Soc. Mech. Eng., Series A*, Vol.57, No.543, 2615-2621

- Tohmyoh, H., Ochi, Y. & Matsumura, T. (2001). Study on Detection and Quantitative Evaluation of Fatigue Cracks Using Surface SH Waves, *Trans. Jpn. Soc. Mech. Eng. (in Japanese)*, Vol.67-661, 1508-1513
- Tokunaga H., Ikeda K., Kaizu K. & Kinishita H. (2007). Micro-Crack Length Measurement Method in Ceramics by Using Grid Pattern Metal Film, *CD Proceedings of International Conference an Advanced Experimental Mechanics 2007*, 1-5
- Wakai, F., Sakuramoto, H., Sakaguchi, S. & Matsuno, Y. (1986). Evaluation of Crack Propagation in Ceramics by Double-Torsion, *Journal of The Society of Materials Science*, Vol.35, No.395, 898-903
- Wiederhorn, S. M. (1967). Influences of Water Vapor on Crack Propagation in Soda-lime Glass, *Journal of American Ceramics Society*, 50(8), 407-414
- Yoda, M. (1989). Subcritical Crack Growth Characteristics of Soda-Lime Glass Evaluated from CT Specimen and Bend Specimen with Small Indented Crack, *Journal of the Ceramic Society of Japan*, Vol.97, No.9, 960-964
- Zilberstein, V., Schlicker, D., Walrath, K., Weiss, V. & Goldfine N. (2001). MWM Eddy Current Sensors for Monitoring of Crack Initiation and Growth During Fatigue Tests and In Service, *International Journal of Fatigue*, Vol.23, S477-S485
- Zilberstein, V., Walrath, K., Grundy, D., Schlicker, D., Goldfine, N., Abramovici, E. & Yentzer, T. (2003). MWM Eddy-current Arrays for Crack Initiation and Growth Monitoring, *International Journal of Fatigue*, Vol.25, 1147-1155
- Zilberstein, V., Grundy, D., Weiss, V., Goldfine N., Abramovici, E., Newman, J. & Yentzer, T. (2005). Early Detection and Monitoring of Fatigue in High Strength Steels With MWM-Arrays, *International Journal of Fatigue*, Vol.27, 1644-1652



# Evolution of Crystallographic Structures and Phases in Micropyretically Formed Boron Rich Boron Carbide – a New Material System

R.M. Mohanty, K. Balasubramanian and S.K. Seshadri  
*NonFerrous Materials Technology development Centre,  
 Kanchanbagh, Hyderabad  
 India*

## 1. Introduction

The 'boron- carbon system' is a typical representative of hard refractory nonmetallic low Z-ceramic. Among various boron to carbon stoichiometry, the ratio higher than 2, are known as boron carbides. These offer many attractive advantage compared to any commercially available hard materials [1-2]. Beside the powder forms, the sintered shapes find wide spread application in ballistic, biomedical application and component engineering. In principle the binary B-C system exist with a number of stable and metastable configurations [3]. Many classical and non classical processes have been considered [4 -12] for producing boron carbides. Among them the researchers have reported on existence of rhombohedral boron carbide with stoichiometry ratio (B/C) near to 4:1. The widely adopted carbothermal process requires rapid heating of all particle separately and individually up to temperature range 2473K to 2773K to achieve significant conversion of input material in 5 hours to 24 hours. In almost all carbothermal processes it is reported to have agglomerated carbon rich boron carbide with boron value up to 78.8%. As per the literature surveys, hardly any systematic investigation has been reported for existence of multiple phases in a single step solid state processing path. It is possible that selection or tailoring of properties for particular use can be made on basis of different stoichiometric phases of boron carbide [13]. The presence of boron rich boron carbide can compensate the boron loss during boron carbide based solid body formation processes and thus preserves or improves the functional requirement. 'Vapor deposition' and 'boron doping' processes are the well studied processing methods which have confirmed the 'non stoichiometric existence of boron carbides' [3, 14,15]. With reference to above facts the research article discusses the structure and analytical development of many phases of boron carbide formed in a ' $B_2O_3$  - Mg - C' micropyretic process with bulk boron to carbon ratio as 5.042:1[16].

### 1.1 Crystal structure and stoichiometry

In variety of boron based systems, the structure of low boron containing systems are determined by the metal lattices or semi metallic lattices. For boron-rich compounds, the

structures are determined by their boron atoms which form covalent boron-boron lattices [17]. In these systems the non stoichiometry phenomenon arises from the existence of a broad free energy minimum in the free energy vs. composition diagram. This is facilitated either by the defects in boron chains or because of vacancies in the covalent lattices with a slight shift in lattice spacing [18-19]. The presence of these non-stoichiometric phases complicates the crystal structure elucidation. Different modifications of elementary boron and numerous compounds of it belonging to boron rich lattices exhibit a close similarity in their structures. The structure consisting of complicated three dimensional network of B12 or B11C (in case of B-C system) icosahedra or related aggregates of atoms as essential common structural elements. The structure of rhombohedral boron carbide is a modification of alpha-B12 structure [20 -21]. In general the structure of B-C system is an arrangement of regular do-decahedrons at the nodes of a rhombohedral Bravais lattice (R-3M space group) as shown in Fig.1.

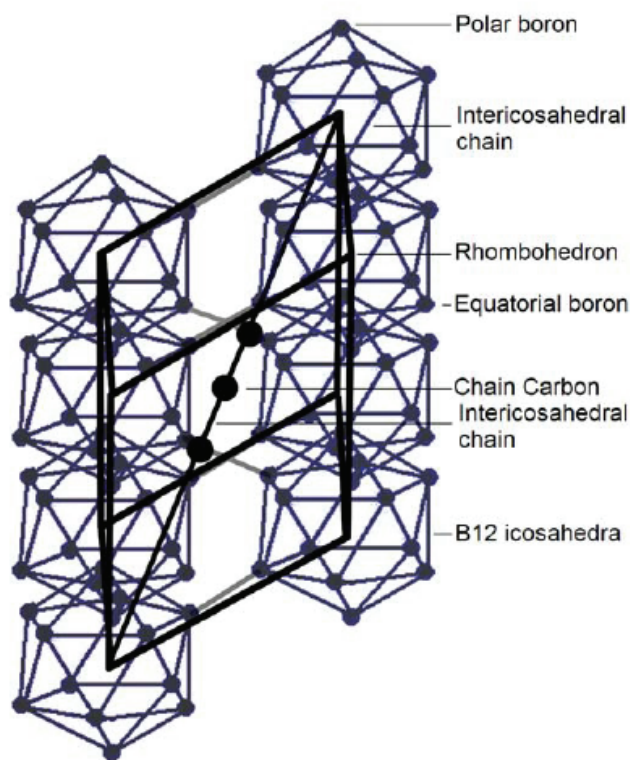


Fig. 1. Rhombohedral crystal structure of a stoichiometric boron carbide , B<sub>4</sub>C

The boron rich icosahedral structures reside at the vertices of a rhombohedron. Four sites are available for a total of 15 'B and C' atoms in the crystal structure. Thus the B and C atoms can interchange each other within both icosahedral and inter icosahedral atom chains. This constitutes the basis for the large homogeneity range for B-C system. Mostly the C-atoms are

along the diagonal of the rhombohedron forming the inter-icosahedral chains in chain configuration. The widely studied three carbon atoms as in  $B_{12}C_3$  along the intericosahedral chain can be substituted all or in parts by vacancies or several types of atoms, thus forming the boron rich and carbon rich end of the stoichiometry [22]. The case of tetragonal structural unit for boron carbides is little different. It consists of four boron icosahedra in a tetragonal arrangement with two carbon atom and the two remaining boron atoms occupying inter-icosahedral sites.

## 2. Experimental

A thermal explosion process mode was used to form boron carbide using stoichiometric amount of high pure boron oxide with excess carbon and magnesium considering  $B_4C$  as the expected product [16]. The input material were mixed in a high energy planetary ball mill, cold compacted and heat treated in presence of positive non-oxidizing gas pressure. The chemically purified products were collected and characterized in as formed as well as in crushed condition. The characterization techniques like X-ray diffraction (Cu anode), X-ray fluorescence techniques along with scanning electron microscopy were used to establish the products. The XRD pattern for the multi phases was compared with a high pure boron carbide standard with B/C ratio as 4:1. The diffraction patterns were recorded using Bragg - Brentano geometry at the room temperature over the angular range  $8^\circ$  to  $90^\circ$  in the step of  $0.002^\circ$  with 2 second as step time. A number of secondary experiments, graphical simulation and calculations were performed to confirm the presence of poly crystalline phases. These were carried out especially where the percentages of phases were less and when the pattern breaking was critical because of peak over laps, experimental, compositional, structural, machinery and algorithms limitations [23]. Lattice constants were calculated from the peak positions in the XRD profiles using peaks existing up to  $50^\circ$  of two theta values.

## 3. Result and discussion

The effect of an limited penetrable boundary material such as carbon, on the reaction dynamics of a double species (B-C) reaction process in the low exothermic B-O-Mg-C system with diffusive reactants were studied [24]. The SEM micrographs showing the as formed and as chemically purified powders have been presented in the Fig.2. The purity was more than 99.97% with boron to carbon ratio determined as 5.042 [16]. The observed x-ray diffraction pattern has been shown in Figure-3 with a comparative account with a standard obtained by thermally and chemically purifying a commercially available  $B_4C$ . As observed in the Fig.3 a number of new peaks were found compared to the  $B_4C$  standard.

**Phase detection and quantification:** In case of XRD analysis of rhombohedral boron carbides the strong (021) Debye ring is ideally located in between  $36.764^\circ$  to  $38.116^\circ$  and the ring (104) from  $34.0760^\circ$  to  $35.284^\circ$  of 2-theta values. The relative peak positions of boron carbides depend on the carbon contents [25]. Beside this fact, the data analysis of a multi phase pattern is always a complicated process. It happens specially in presence of factors like peak overlaps, continuous back grounds, variation in fixing of peak parameters, fixed algorithm, absorption, porosity, axial divergence of beam, radiation types, alignment problems, disorders, crystallinity, sample preparation, grain size and its uniformity [22, 25]. Such a problem becomes critical when the structural variation are narrow as found in r-boron carbides. Considering the above discussed factors, during subsequent approaches and

by search-match comparison with JCPDS-ICDD data the determined phases were as  $B_{13}C_2$ ,  $B_{48}B_2C_2$ ,  $B_{41.11}C_{4.45}$ ,  $B_{12}C_3$ ,  $B_8C$ ,  $B(T)$  and  $B(Rh)$  with JCPDS cards numbers as 33-0225, 71-1107, 71-0363, 35-0798, 26-0232, 31-0206 and 78-1571 respectively. The phases were quantified in a semi quantitative manner using the combination of normalized RIR method [26], integrated intensities and mass absorption ratios. Through the semi-quantitative analysis give theoretically exact result, there are several source of as- discussed errors which prohibit an accurate result. However in any case the result is at least approximately correct [Philips electronic publication, Nov 2001]. Stepwise standard workouts were carried out to confirm the accuracy of the quantification [27].

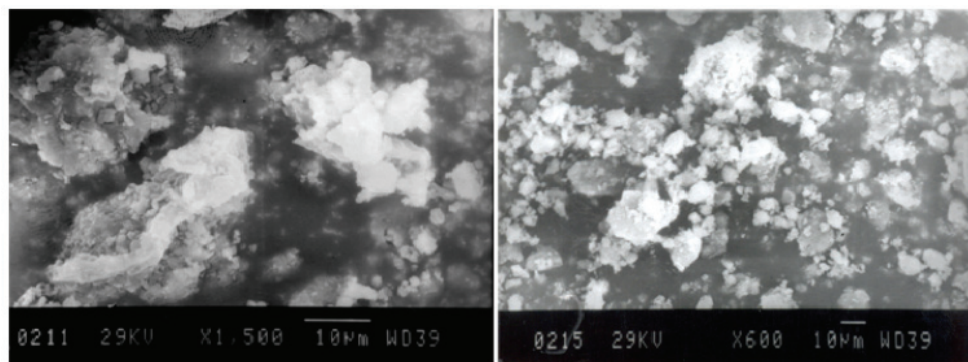


Fig. 2. SEM micrograph of (a) as formed product (b) the chemically purified product

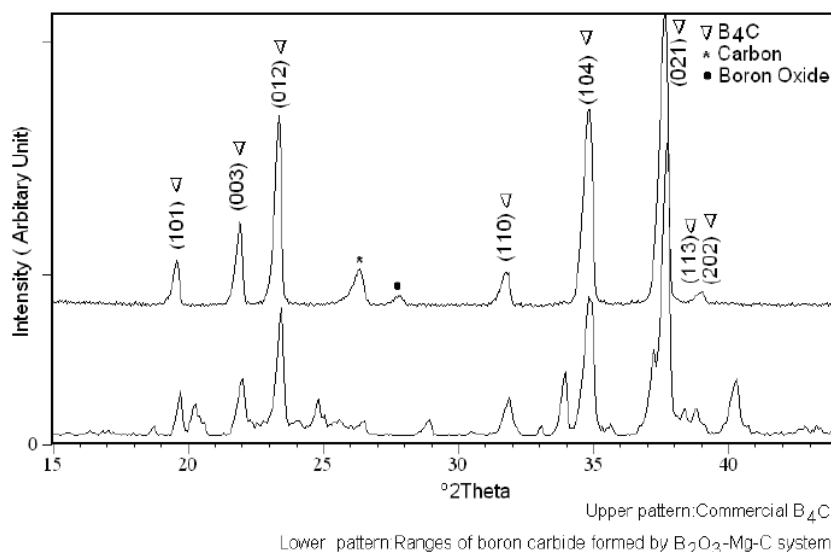


Fig. 3. XRD peak comparison of a carbothermal and the micropyrretic BC product

In this study, the peak shapes were determined using individual intensity convolution and peak shape functions (mainly a set of Psedo-Voigt functions). The intensity of boron rich

peaks were found to be weak in compared to carbon rich boron carbides which have also been confirmed by a work of Disbudak and Silvestre et al. [28]. A variation in peak positions as observed for various rhombohedral boron carbides are explained to be the substitution of a carbon atom by a boron atom in the inter or intra icosahedrons [19,21,22,28]. The phase detection has also been confirmed by a multiphase simulation programme and the results have been represented by Fig. 4.

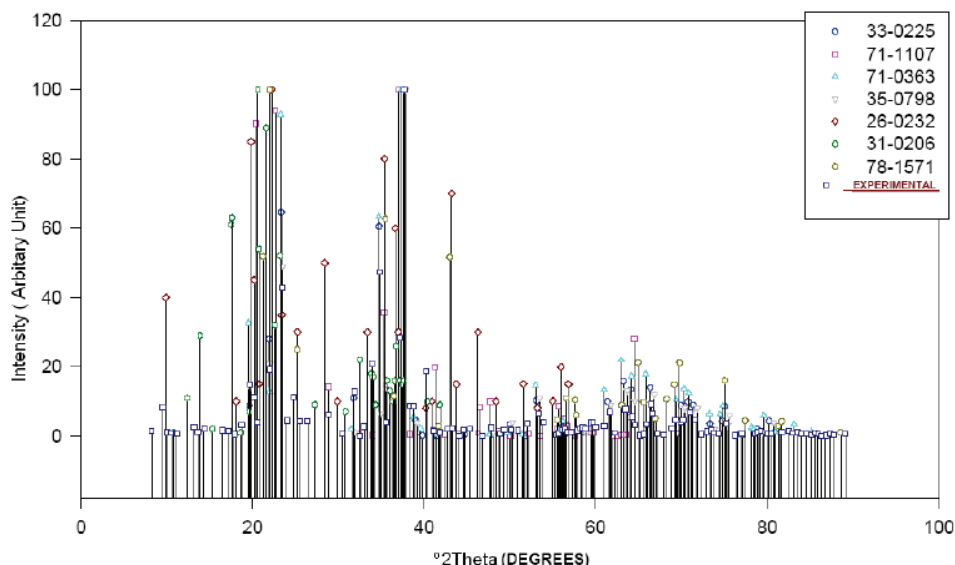


Fig. 4. Overlapped graph of experimental and simulated stick patterns

### 3.1 Structure estimation

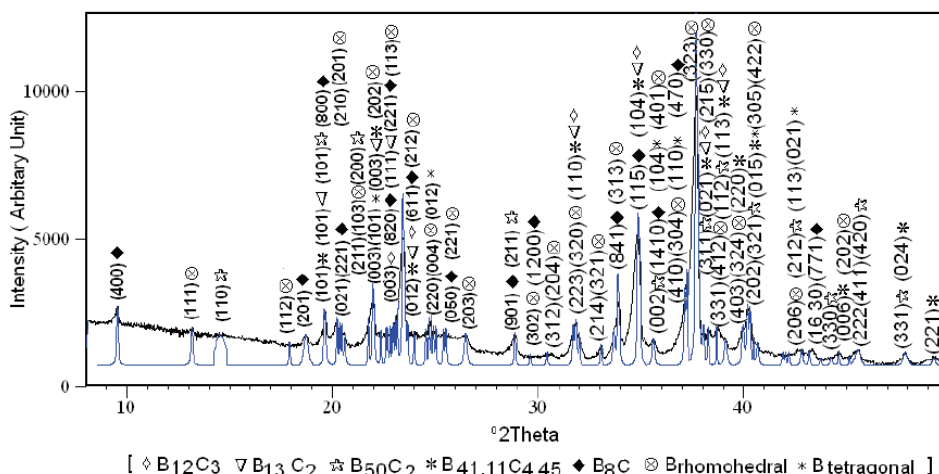


Fig. 5. Selected range of the multiphase, ab-initio indexed pattern

The classical ways to obtain accurate unit cell parameters are full pattern decomposition and full profile based Rietveld refinement [29]. Since some of the parameter required for a Rietveld refinement are not known for the nonstoichiometric phases, the experimental pattern [8° to 90° range, 0.002° step size] was structurally analyzed by defining the ab initio indexing to the determined 2-theta peak positions within 8° to 50° range (Fig.5). In total 42 peaks were used to find best lattice parameter sets for the multi phase pattern. The results were summarized as in the table-1 and table-2 which predict the existence of both tetragonal and rhombohedral borons along with rhombohedral, tetragonal and orthorhombic phases for boron carbides.

Phases	Major2θ (ideal)	Major2θ(Observed)	(hkl)	Obs. Intensity	Calculated BxCy	Mass absorption coefficient	Space Group	SemiQ (%)
$B_{12}C_3$	37.819°	37.747°	(021)	130.22	$B_4C_4$	3.589	R-3M	52.59
$B_{13}C_2$	37.604°	37.677°	(021)	114.29	$B_{6.5}C$	3.416	R-3M	42.41
$B_{48}B_2C_2$	37.059°	37.136°	(311)	32.12	$B_{25}C$	3.165	$P4_2/nmm$	02.30
$B_{41.11}C_{4.48}$	37.324°	37.324°	(021)	29.23	$B_{9.24}C$	3.320	R-3M	01.40
$B_3C$	22.206°	22.013°	(820)	58.49	$B_8C$	3.354	$P222_1$	00.80
$B_{(T)}$	22.579°	22.590°	(221)	11.90	-	3.06	$P4_1$	rest
$B_{(Rb)}$	21.982°	22.020°	(101)	29.54	-	3.06	R-3M	rest

Table 1. Observed experimental values with standard available values for the multiphase pattern

### 3.2 Explanation to observed result

Most of the reported solid state processes [10,12,30] produce single phase boron carbide. The discussed experimentation process is initially a solid state process. With increase of temperature the ( $B_2O_3$ -C-Mg) system with high carbon acts like a 'colloidal system'. Local melting in the vicinity of the reacting species has an appreciable effect on the equilibrium interfacial concentrations and the diffusion co-efficient in contacting phases. The decrease in the exothermicity because of presence of low melting glassy  $B_2O_3$ , is adequately compensated by the external heating. The excess external heat sustained the reactive process to attain the adiabatic temperature and the colloidal condition assisted in suppression of initial reduction products like  $B_2O_3$  and thus the other sub oxides or gaseous species [31]. These along with the prevailing reaction conditions in the "high pressure changed environment" prevented the formation of 'MgC<sub>2</sub> or MgB<sub>2</sub>'. As a result, the expected reactive interactions were achieved. The products were mostly B-C and Mg-O based compounds. Presence of carbon as buffer reduced the formation of MgO<sub>2</sub>, Mg<sub>2</sub>B<sub>2</sub>O<sub>6</sub> with a self adjustment to CO activity in the closed furnace environment.

Phases	$a_{\text{exp}}(a_{\text{estab}}) \text{ \AA}$	$b_{\text{exp}}(b_{\text{estab}}) \text{ \AA}$	$C_{\text{exp}}(C_{\text{estab}}) \text{ \AA}$	$\alpha (^{\circ})$	$\beta (^{\circ})$	$\gamma (^{\circ})$	Synd.FOM	Sp.gr. sym.	$V_{\text{exp}}(V_{\text{estab}})(\text{\AA}^3)$	Data type
$B_{12}C_3$	5.616(2) [5.6003(5)]	5.616(2) [5.6003(5)]	12.129(8) [12.086(2)]	90 90 120 90 90 120			28.905 [58]	R-3M(166)H R-3M(166)H	331.291 [328.270]	Experimental 1984,Exper.
$B_{13}C_2$	5.877(4) [5.633]	5.877(4) [5.633]	12.17(1) [12.164]	90 90 120 90 90 120			12.1365 [103]	R-3M(166)H R-3M(166)H	364.017 334.260	Experimental 1980, Calcu.
$B_{49}B_2C_2$	8.770(7) [8.722]	7.241(7) [8.722]	6.176(6) [5.080]	90 90 90 90 90 90			13 5.701	$P4_2/nmm(134)$ $P4_2/nmm(134)$	392.250 386.450	Experimental 1997,Calcu..
$B_{41.11}C_{4.45}$	5.211(4) [5.672]	4.847 [5.672]	8.962(9) [12.1428]	90 90 112.06 90 90 120			23.000 -	R-3M(166)H R-3M(166)H	211.000 338.320	Experimental 1997,Calcu..
$B_8C$	20.809 [35.909]	4.503(3) [17.653]	4.109 [5.094]	90 90 90 90 90 90			14 2	$222_1(17)$ -	386.66 3229.09	Experimental Single crystal
$B_{(I)}$	9.443(9) [10.140]	9.443(9) [10.140]	8.322(7) [14.170]	90 90 90 90 90 90			5.744 73	$P4_1(76)$ $P4_1(76)$	749.954 1456.95	Experimental Calculated.
$B_{(Rb)}$	3.2776 [4.927(3)]	3.2776 [4.927(3)]	36.38 [12.564(7)]	90 90 120 - - -			9.9937 7.745428	R-3 M(166)H R-3 M(166)H	336.8905 264.13	Experimental Calculated.

Notation : \*exp.(experimental finding) \*estb.(established value from literatures) \* FOM (Figure of merit) \*Calcu.(Calculated)

Table 2. Crystal structure values as deduced from the indexed peaks in the multi-phase pattern

Considering the experimental results and the above analysis, a non-equilibrium mechanism is proposed. The global behavior of such a process depends on limiting factors like, the number of particles that interact locally in a single step and the dynamics of the reacting phases. Considering the report of combustion process achievements ( maximum adiabatic temperature, combustion propagation rate, rate of heating, and thermal gradient ) and the behavior of inputs, the phase formation in the process is proposed to have occurred in a non isothermal condition with existence of normal diffusive to ballistic diffusive behaviors. The diffusion length, inter effect of particles growth were found to be less and the MgO growth is not determined to be higher [figure-2]. Considering the above discussions, ignoring the Langmuir adsorption and basing on Fick's second law, a self consistent equation is defined for the process as

$$\frac{\partial \bar{\rho}_r}{\partial t} = D_T \nabla^2 \bar{\rho}_r - 2k \cdot \bar{\rho}_r^2$$

where  $k$  represents the slower kinetic term,  $D_T$  as diffusion constant at corresponding temperature,  $\bar{\rho}_r$  is the average density of reacting phases and  $\frac{\partial \bar{\rho}_r}{\partial t}$  is the rate of decay of

reacting phases. Under present condition the product phase concentration is dependent more on the mean free path rather on ' $k$ ' or ' $D_T$ '. Since the spatial dimension of the process path is low i.e. two dimensional, at any time, reacting phases those are close to each other react at a faster rate compared to widely separated one. This explains the formation of 'mix phases' with the importance of process input homogeneity. The limit to achieve theoretical yield value is much dependent on 'before process interaction homogeneity'. Thus the



possibilities associated with a simple type of propagating 'non equilibrium heat wave' is generalized as in the Fig.6.

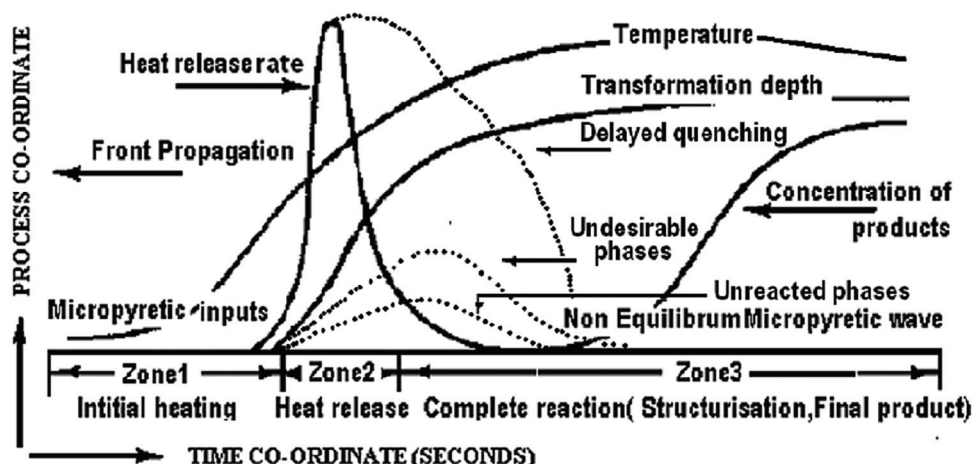


Fig. 6. A typical presentation of associated non equilibrium micropyretric wave

The multiphase boron carbides formation can be explained in the following ways. Above 1400°C with relatively longer reaction time, the formation of  $\beta$ -rhombohedral boron or the tetragonal elementary boron is possible with a three dimensional net work of B12 clusters [32]. Among them  $\beta$ -rhombohedral boron is more stable but its survival as an elementary phase depends on the existing high temperature thermodynamics. The formation of both type borons as found in this study also supported by an earlier published work [32]. Concerning the formation of tetragonal boron, as per Gmelin et al carbon helps in stabilizing the tetragonal boron [33]. In this current high pressure experiment carbon was one of the excessive input. The diffusion of boron and carbon to one another crystal lattices are also possible. However the diffusion length is limited by the involved high temperature kinetics. Again reports of C.E. Lowell et al reveal the maximum solubility of B in C(gr) as 2.35 at% at 2350°C if interstitial formation is neglected [34]. Boron has a diffusivity of  $2.028 \times 10^{-11} \text{ m}^2/\text{sec}$  for others lattices at 1000°C. The phase formation results along with the predictions of mentioned literatures favour the formation of B-C lattice on carbon particle with diffusion of C into the developing B-lattice. Thus in boron rich boron carbides the primary bonding is B-B. The arrangement of boron structures depending on its relative activity in a compound can be summarized as in Fig.7.

Earlier the formation of tetragonal boron carbide with less than 10% C-content had been reported by CLJ Adkins and other [35]. As per them this occurs mostly under carbon depletion conditions compared to that exist for the rhombohedral form. The presence of the tetragonal boron, short processing time [Fig. 6], the time based consumption of carbon along with the high diffusion coefficient of boron indicate tetragonal boron carbide is a modification of tetragonal boron. And the conversion process is a consecutive process. The relative percentage of its formation is affected by the prevailing heating conditions in the furnace and the reactants homogeneity. According to Aselage et al. the thermodynamic instability of pure  $\beta$ -rhombohedral boron allows the formation low C-



rhombohedral boron carbide. This supports the experimental result of getting a range of rhombohedral boron carbides and also may be an out come of increased chemical potential of B or reduced chemical potential of C. The presences of larger unit cell of boron carbides suggest the reduced carbon concentration. A comparative study of  $\beta$  - rhombohedral boron and boron carbide spectra with different C-concentration has been reported by Tallant et al. [37]. The main structural difference in-between them is the presence of a CBC linear chain in the boron carbides [26,38,39]. Like boron, rhombohedral boron carbide also has a crystalline icosahedral appearance with B<sub>12</sub> cluster as a part of its structure. Thus the above evidences and all results favour the formation of B-C system from elementary boron.

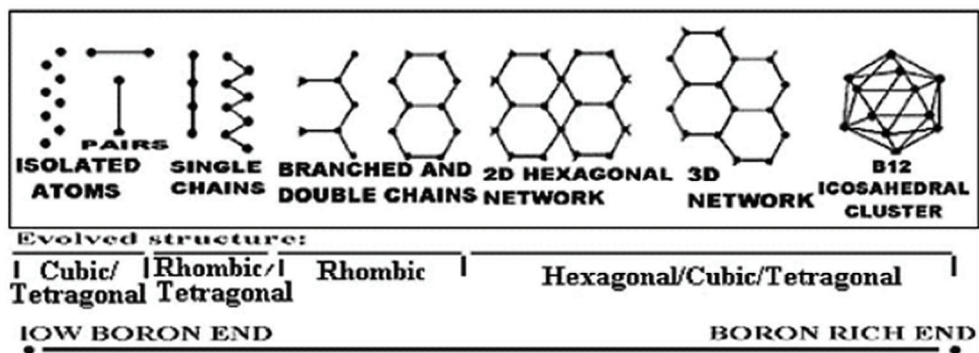


Fig. 7. Relative prediction of structural development in boron based system

#### 4. Conclusion

Experimental data obtained during the investigation and subsequent analysis predict the existence of a range of boron carbides and borons like  $B_{13}C_2$ ,  $B_{48}B_2C_2$ ,  $B_{41.1}C_{4.45}$ ,  $B_{12}C_3$ ,  $B_8C$ , B(T) and B (Rh) in the single step solid state process. The other findings of the study are summarized as

1. Both 'rhomohedral and tetragonal' boron are formed as in-situ reactive products.
2. The nature and the stability of this insitu boron decide the type of boron carbide thus formed. In other word, varying multiple heat waves as obtained in the micropyretic process and the prevailing reaction conditions like steady heat wave formation, vortex detachment or quenching (heat flow stability), coupling between the pressure wave and combustion assist the formation of the boron carbides with varying crystallographic structures.
3. Absence of carbon rich boron carbide shows the diffusion of boron to carbon lattice is limited and even show at high temperatures.
4. Tetragonal boron carbide forms under carbon depletion condition with availability of tetragonal borons.
5. Thermodynamic and kinetic instability of pure rhombohedral borons leads to the formation of low carbon boron carbides. The existence of a range of rhombohedral boron carbide is a out come of either the increased chemical potential of r- boron or the decreased chemical potential of the carbon in the local chemical environment.

6. The foamy and less agglomerated crude products obtained from the reactive process indicate the existence of high reaction rate and low partial surface energy. And the reaction mechanics of the process enables the obtaining of both equilibrium and non equilibrium boron based powders of high purity with a low micron size good particle dispersity.
7. Type and quantity of insitu boron controls the percentage and structure formation of boron carbides.

## 5. References

- [1] Knoch, H, Steinmann, D., Ceramic bearings and abrasion resistant components from silicon nitride, silicon carbide and boron carbide, *Metall* (J. South African Institute of Mining and Metallurgy) 43/3(1989), 250-254,
- [2] Umeda, K., Enomoto, Y., Mitsui, A., Mannami, K., Tribological properties of boron carbide, *Japanese J. tribology*, 40/2(1995), 53-64.
- [3] Nihara, K, Nakahira, A, Hirai, H. The effect of stoichiometry on mechanical properties of boron carbide, *Commn.Am.Cer.soc*, 67(1984), C13-14.
- [4] Sinha A, Mahata, T, Sharma, B .P., Carbothermal route for preparation of boron carbide powder from boric acid-citric acid gel precursor, *J.Nuc.materials*, 301(2002) ,165-169.
- [5] Thevenot, F, Boron carbide- A comprehensive review, *J.Europ.Cer. Soc*, 6 (1990), 205-207.
- [6] Weimer, A.W., Moore, W. G., Roach, R. P., Hitt, J .E., Dixit, R.S., Pratsinis S.E., Kinetics of Carbothermal reduction synthesis of boron carbide, *Al Che.Journal* 37 (1991), 759.
- [7] Freire Jr, F.L., Reigada , D.C., Priolli, R, Boron carbide and boron-carbon nitride films deposited by DC sputtering, *Phys.state.Soc.A* (2001), 1871.
- [8] Radev, D.D., Boron Carbide, Part 1: Synthesis of Powders, *Metall*, 51/10 (1997), 564-567.
- [9] Goller, G., Toy, C., Tekin, A., Gupta, C.K., The production of boron carbide by carbothermic reduction, *High temp.Mat.Procs*, 15/1-2 (1996), 117-122.
- [10] Sung-won Jo , Lee, G ., Moon , J ., Kim, Y ., On the formation of MoSi<sub>2</sub> by self-propagating high-temperature synthesis, *J.Mat.Sc.Lett*, 19 (2000), 951-954.
- [11] Mierze Jewska, S., Niemyski, J. J, Formation of Group- IVb Carbides, *J.less common metals*, 8(1965), 368
- [12] Junga, C.H., Leeb, M. J., Kima, C. J., Preparation of carbon- free B<sub>4</sub>C powder from B<sub>2</sub>O<sub>3</sub> oxide by carbothermal reduction process, *Mat.Lett*, 58(2004), 609-614.
- [13] Dobrova, M B, Kozynkin, B. I., Kalvgin, V. I., Agafonov, A .V., Fadeev , A. A., Sidorenko, E. S., Optimizing neutron detection with semiconducting Boroncarbide, *J.Adv.Mater*, 11(1994), 69-73.
- [14] Ploog, K., Gasphasenabscheidung von binären Bor - Kohlenstoff -Phasen bei Substrattemperaturen von 900 bis 1800 °C I. Tetragonales und orthorhombisches Borcarbide. *J.less common metals* 5/1 (1974), 115-130.
- [15] Sezer, A.O., Brand, J.J., Chemical vapor deposition of boron carbide, *Mater. Sci. Eng*, B79 (2001), 191-202.

- [16] Mohanty, R.M., Balasubramanian, K., Seshadri, S.K., Multiphase formation of boron carbide in B<sub>2</sub>O<sub>3</sub>-Mg-C based micropyretic process, *J. alloys compd*, 441 (2007), 85-93.
- [17] Samsonov, G.V., Serebryakova, T.I., Boron compounds with group VI elements, *Sov.Powder Metall.Met.Ceramic* (English trans.)17/2 (1978) 116-120
- [18] Mc Colm, I.C., Ceramic Science for materials technologist, Leonard Hill, London (1983), 330-343.
- [19] Schwarzkoff, P., Kieffer, R., Refractory hardmetals (1953), Mac Millan.
- [20] Lazzari, R., Vast, N., Besson, J. M., Baroni, S., Corso, A.D., Atomic structure and vibrational properties of icosahedral B<sub>4</sub>C boron carbide, *Phys. Review Lett.* 83/16 (1999), 3230.
- [21] Fujimori, M., Nakata, T., Nakayama, T., Nishibori, E., Kimura, K., Takata, M., Sakata, M., Peculiar covalent bonds in  $\alpha$ -Rhombohedral Boron, *Phys.Rev.lett* 82 (1999), 4452-4455.
- [22] Samsonov, G. V., Vinitskii, I. M., *Handbook of refractory compounds*, Plenum press (1980), New York.
- [23] Suematsu, H., Kitajima, K., Ruiz, J., Kobayshi, K., Takeda, T., Shimdo, D., Suzuki, T., Jiang, W., Yatsui, K., Thermoelectric properties of crystallized boron carbide thin films prepared by ion-beam evaporation, *Thin solid films*, 407 (2002), 133.
- [24] Lowell C E, Solid Solution of Boron in Graphite. *J. Am. Ceram. Soc.* 50 (1967), 142-144.
- [25] Chung, F.H., Quantitative interpretation of X-ray diffraction patterns: I. Matrix-flushing method of quantitative, *J.App.Cryst.* 7 (1974), 513-519.
- [26] Synder, R.L., The use of reference intensity ratios in X-ray quantitative analysis, *Powdiff.* 7 (1992), 186-193.
- [27] Conde, O., J Silvestre, A., Oliveira, J .C., Influence of carbon content on the crystallographic structure of boron carbide, *Surf. Coat. Technol.* 125 (2000), 141.
- [28] Silvestre, A.J., Santoss, M.J., Conde, O., The Role of Carbon Precursor on boron carbide Synthesis by Laser-CVD, *Key Eng. Mater* 56 (2002), 230-232.
- [29] Stoto, N.H., Zuppiroli, L. Swelling and microcrackin of boron carbide subjected to fast neutron irradiations, *J.App. Phys.* 68/7 (1990). 3198.
- [30] Bougoin, M., Thevenot, F., Synthèse et caracterisation de ceramiques denses en carbure de bore, *J.Less Common.Metals*, 114(1985), 257-271.
- [31] Southard, J.C., Thermodynamic of boron compounds, *J. Am. Chem. Soc.* 63(1941), 3147.
- [32] Vandenbulcke, L., Vuillard, G., Polymorphism in boron deposited by the H<sub>2</sub> reduction of BC<sub>13</sub>, *J.Less.Commo.met.* 67(1979) p65.
- [33] Gmelin, Boron (System No.13) Supliment Vol.2, Unidentified publication, 1981
- [34] Lowell, C.E., Solid solution of boron in Graphite, *J.Am. Ceram. Soc.*, 50 (1967), 142-144.
- [35] Adkins, C.L.J., Cambell, A.M., Headley, T.J., Synthesis of high temperature materials, VCH Publishers, New York (1990.) 391-398,
- [36] Aselage, T.L., Van Deusen, S.B., Morosin, B., Solution growth, structure and composition of boron carbide crystals, *J.Less. Comm. Metals.* 166/1(1990), 29-44.
- [37] Tallant D, Aselage, T, Cambell, A, Emin D., Boron carbide structure by Raman spectroscopy, *Physical Rev.B* 8 (1989), 5649.

- [38] R.M. Mohanty, K. Balasubramanian, Boron Rich Boron Carbide: An Emerging High Performance Material, *Progress in High Temperature Ceramics* (ISBN: 0-87849-361-1) KEMV395, pages 125-142, Trans Tech Publications Inc., Switzerland 2009.
- [39] R.M. Mohanty, K. Balasubramanian , P.Horidoss, S.K. Seshadri , Compositional and structural variations in solid state formed boron carbide, *Recent advances in composite materials* (Intelligent, smart, Sustainable & Infrastructural Materials) (ISBN:81-8424-175-5) pages 580-586, Allied Publisher Limited, 2007.

# Oxygen Isotope Exchange in Nanocrystal Oxides

Anatoly Fishman<sup>1</sup>, Tatyana Kurennykh<sup>2</sup>,  
Vladimir Vykhodets<sup>2</sup> and Evgeniya Vykhodets<sup>3</sup>

<sup>1</sup>*Institute of Metallurgy, Ural Division, Russian Academy of Sciences,*

<sup>2</sup>*Institute of Metal Physics, Ural Division, Russian Academy of Sciences,*

<sup>3</sup>*Ural Federal University, Yekaterinburg  
Russia*

## 1. Introduction

The subject of investigation in this work is oxygen isotope exchange (OIE) between oxides and oxygen-containing gases  $^{18}\text{O}_2$  and  $\text{C}^{18}\text{O}_2$ . OIE studies yield information about the rate of processes on the gas – solid interface and oxygen self-diffusion in oxides. In turn, the surface processes can involve some elementary stages, in particular, physical and chemical adsorption. Several types of diffusion processes can be observed also inside oxides, for example, volume and grain boundary diffusion. OIE investigations are of much practical interest, for example, in connection with the problems of catalytic oxidation of metals and development of materials for chemical and electrochemical devices (fuel cells, electrolyzers, sensors, hydrogen storage devices, devices for separation of gas and isotope mixtures, etc.). Two experimental approaches to OIE examination are known. The pioneer approach was based on measurements of the isotope composition of a gas mixture interacting with oxide. In the alternative approach developed in the last decades, the isotope composition of the oxygen subsystem of oxides was measured, which was studied usually by secondary ion mass spectrometry (SIMS) and nuclear microanalysis (NRA). The present work is devoted to the examination of the isotope composition of solid-state samples. The overwhelming majority of studies by means of this approach were performed on bulk samples. A distinguishing feature of this work is its orientation toward isotope exchange examination in nanoscale oxides. As will be shown below, this results in novel or supplementary data on the surface reaction rates during isotope exchange and the rates of diffusion processes in oxides. Moreover, the investigations into oxygen isotope exchange in oxide nanomaterials are of great practical importance. It is not improbable that the use of nanomaterials may lead to favorable changes in the functional properties of oxides when it is necessary to increase the quantity of absorbed gas or to increase rates of gas absorption or extraction etc.

## 2. Investigations on bulk samples

Most often, OIE studies on bulk samples involve isothermal annealing of samples in oxygen (or other oxygen-containing gas) enriched with  $^{18}\text{O}$  isotope and measurement of

concentration profiles (depth distribution) of  $^{18}\text{O}$  tracers in the sample. In case of bulk diffusion described by one value of oxygen self-diffusion coefficient  $D$ , the concentration profile  $C(x,t)$  is described by the expression (Ruiz & Kilner, 1997)

$$C(x,t) - C_G = C_S^{\max} \left[ \operatorname{erfc}(Z) - \exp(Hx + H^2Dt) \operatorname{erfc}\left(Z + \frac{Hx}{2Z}\right) \right], \quad Z = \frac{x}{2\sqrt{Dt}}, \quad (1)$$

where  $H$  is a parameter characterizing the surface energy barrier;  $C_S^{\max}$  is the maximal permissible concentration of  $^{18}\text{O}$  atoms on the surface of a sample;  $t$  is the diffusion annealing time;  $C_G$  is the concentration of  $^{18}\text{O}$  in a sample prior to annealing. According to (Ruiz & Kilner, 1997), the parameter  $H$  in expression (1) is connected with the parameter  $k$  characterizing the surface reaction rate during isotope exchange by the relation

$$k = HD. \quad (2)$$

It is seen from expressions (1)-(2) that OIE studies on bulk samples provide measurements both of diffusion coefficients  $D$  and surface reaction rates  $k$ .

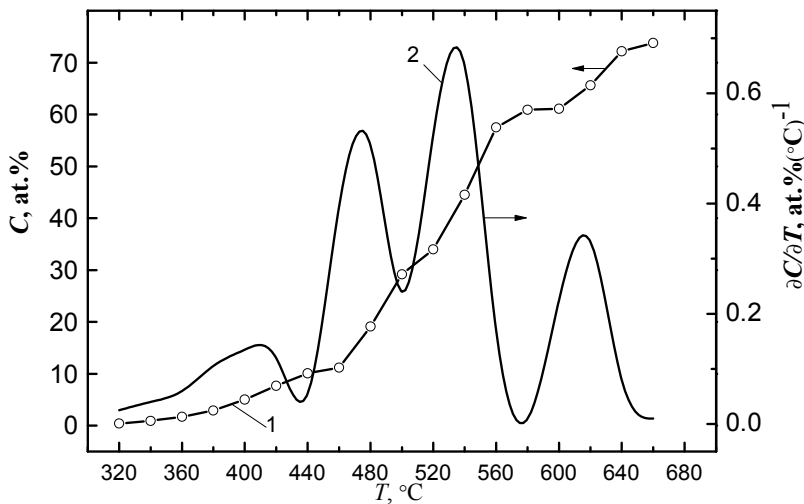


Fig. 1. Temperature dependence of concentration  $C$  and derivative  $\partial C/\partial T$  during step-wise isochronous annealing of  $\text{YBa}_2\text{Cu}_3\text{O}_{7-\delta}$  (Vykhodets et al., 1994). The concentration is given in percents of the number of positions in the oxygen sublattice of the oxide

For strongly anisotropic diffusion systems (HTSC oxides and other oxides with complicated crystal structure and chemical composition), a different route of OIE experiments can be chosen. In some works, step-wise isochronous annealing of samples was carried out in oxygen enriched with  $^{18}\text{O}$  isotopes. The isochronous annealing conditions can be selected such that the systems with strong anisotropy of oxygen diffusion coefficients can exhibit a

site-plane effect. It consists in successive substitution of  $^{18}\text{O}$  atoms for crystallographic oxygen planes or positions occupied by  $^{16}\text{O}$  atoms before annealing.

By way of example, Fig. 1 demonstrates the isochronous-annealing curve  $C(T)$  and its derivative  $\partial C/\partial T$  characterizing the variation in  $^{18}\text{O}$  isotope concentration  $C$  in  $\text{YBa}_2\text{Cu}_3\text{O}_{7-\delta}$  samples as a function of experiment temperature  $T$  (Vykhodets et al., 1994). The results displayed in Fig. 1 show that there are several types of energetically non-equivalent sites for oxygen atoms in the oxide lattice.

The data on the site -plane effect make it possible to obtain information about the fraction of each type of sites in the oxygen subsystem of the oxide, to estimate the activation energy and the frequency factor for oxygen atom transition from one site to another, as well as to examine the effect of phase transformations in oxides on the distribution of oxygen atoms in the lattice sites, etc.

### 3. Investigations on nanocrystalline powders

The concentration profiles of  $^{18}\text{O}$  atoms in a nanoparticle can not be determined experimentally since neither SIMS nor NRA methods ensure the locality of measurements commensurable with the size of nanopowder particles. Therefore, in our OIE studies on nanopowders we measured the average concentration of  $^{18}\text{O}$  atoms in a large assembly of powder particles (Gizhevskii et al, 2008); the same assembly was annealed in oxygen enriched with  $^{18}\text{O}$  isotopes. In view of the destructive character of SIMS measurements, this technique can scarcely be used to determine the average oxygen isotope concentration in powders. Here, the NRA method, which permits measurement of  $^{18}\text{O}$  and  $^{16}\text{O}$  atom concentration in the depth to several microns without sample failure, is certainly advantageous.

At first, we shall consider the isotope exchange model, in which only oxygen ions from the external atomic layer of the oxide particle participate. Let only  $^{18}\text{O}_2$  molecules be present in the gaseous phase, while the oxide particle contains no  $^{18}\text{O}$  atoms at all in the start time. In that case, the differential equation for isotope exchange has the form

$$dN_{18} = N_{16}\Gamma dt \quad , \quad (3)$$

where  $dN_{18}$  is the number of  $^{18}\text{O}$  atoms that entered into the oxide during time  $dt$ ;  $N_{16}$  is the number of  $^{16}\text{O}$  atoms located in the instant time  $t$  on the surface of the oxide atomic layer;  $\Gamma$  is the frequency, with which  $^{16}\text{O}$  atom in the oxide surface atomic layer is replaced by  $^{18}\text{O}$  atom. Generally, this parameter is a function of the annealing temperature and the pressure in the gaseous phase. During isotope exchange, when neither oxidation nor reduction of the oxide take place, for the numbers of atoms  $^{16}\text{O}$  and  $^{18}\text{O}$  the relation  $N_{16} + N_{18} = \text{const}$  is fulfilled. Then equation (3) for spherical particles is solved as

$$C(t) = C_0 \frac{3\Delta}{r} (1 - \exp(-\Gamma t)) \quad , \quad (4)$$

where  $C(t)$  is the average concentration of  $^{18}\text{O}$  atoms in the oxide;  $\Delta$  is the monolayer thickness in the oxide;  $r$  is the particle radius;  $C_0$  is the atomic concentration of oxygen in the oxide. For arbitrarily shaped particles it is easy to obtain an analogous "relaxation"-type dependence

$$C(t) = C_0 S \rho \Delta (1 - \exp(-\Gamma t)) , \quad (5)$$

where  $S$  is the powder specific surface determined usually with the BET technique and  $\rho$  is the oxide density. Frequency  $\Gamma$  measured in OIE experiments on oxide powders is an analogue of the parameter  $k$  in formula (2). Based on the results (Vykhodets et al., 2000), it is possible to establish a correlation between  $\Gamma$  and  $k$

$$k = l\Gamma , \quad (6)$$

where  $l$  is an atomic jump distance.

A fundamentally different "diffusion" model for the description of OIE (Gizhevskii et al, 2008) is used for processes characterized by the very high surface reaction rate and by comparatively slow volume diffusion of oxygen in the oxide particle. Here, for spherically shaped particles it is easy to obtain

$$C(t) = C_0 \left( 1 - \frac{3\Delta}{r} \right) \left( 1 - \frac{6}{\pi^2} \sum_{s=1}^{\infty} \frac{1}{s^2} \exp \left( - \left( \frac{s\pi}{r} \right)^2 Dt \right) \right) + C_0 \frac{3\Delta}{r} . \quad (7)$$

Finally, the OIE model version providing for simultaneous implementation of the relaxation and diffusion mechanisms (Gizhevskii et al, 2008) was considered. In this case, the  $C(t)$  dependence is found by numerical calculations.

Expressions for relaxation-type isotope exchange analogous with (4)-(5) will be valid not only at very slow oxygen diffusion in oxide, when a typical diffusion length is  $(Dt)^{1/2} < d$  ( $d$  is the oxide particle size). It can be shown (Fishman et al, 2009) that they are correct also at very fast diffusion when  $(Dt)^{1/2} \gg d$ . In that case, all oxygen ions of the oxide particle take part in isotope exchange, and the concentration of  $^{18}\text{O}$  atoms becomes similar in the bulk of the particle more quickly than it grows on the boundary with the gaseous phase. Here we have

$$C(t) = C_0 [1 - \exp\{-(3\Delta / r)\Gamma t\}] \quad (8)$$

or

$$C(t) = C_0 [1 - \exp\{-(S\rho\Delta)\Gamma t\}] . \quad (9)$$

From the aforesaid it is seen that the examination of isotope exchange on nanopowders may give data on their dimensional characteristics. Otherwise, the information received from isotope exchange studies on powders and bulk samples is in many respects analogous. This concerns both the diffusion characteristics of oxide materials and the processes on the surface of oxides.

OIE studies on nanopowders attract particular interest since they permit measuring low  $D$  values. Analysis of expression (7) shows that diffusion coefficients of oxygen tracers as small as  $10^{-23}$  -  $10^{-24}$  m<sup>2</sup>/s or even lower can be measured in such studies. This level of measurements is due to the small size of the powder nanoparticles, and is not typical of OIE investigations on bulk samples.

Expressions (4),(7),(8) are written for spherically shaped particles with a single value of the particle radius  $r$ . Certainly, for real powders, dimension distribution of powder particles



should be taken in account (Fishman et al, 2009). Corresponding relaxation-type dependences for an assembly of different-size particles can be easily obtained. For example, for  $(Dt)^{1/2} \ll d$  we have

$$C(t) = C_0 3\Delta \left[ 1 - \exp\{-\Gamma t\} \right] \sum_i r_i^2 / \sum_i r_i^3, \quad (10)$$

and for  $(Dt)^{1/2} \gg d$

$$C(t) = C_0 \sum_i r_i^3 \left[ 1 - \exp\{-(3\Delta / r_i) \Gamma t\} \right] / \sum_i r_i^3. \quad (11)$$

The expediency and informativity of experimental studies of isotope exchange on nanopowders is not a trivial problem. First, there may be an unacceptable diversity of annealing conditions for individual particles contained in the powder assembly. Agglomeration of powders aggravates the situation. Second, analysis of expressions (10)-(11) shows that the presence in a nanopowder of large, for example, micron-size particles will result in a very strong decrease in the  $^{18}\text{O}$  concentration as compared with that for a powder containing no large particles. Even with a small part of large particles, isotope exchange experiments may turn out senseless since the experimental data on  $C(t)$  will characterize to a greater extent the isotope exchange on large particles rather than the assembly of particles. Virtually, this means that the considered technique will be effective only for nanopowders with a narrow size distribution function of powder particles.

Taking into consideration the above observations, in this work we devote much attention to the optimization of the technique for experimental studies on nanopowders, in particular, we examine powders obtained by different technologies and analyze the quantitative correspondence between the theoretical and experimental  $C(t)$  values.

#### 4. Oxygen isotope exchange with oxide powders

In this work we present OIE data for oxide nanopowders produced by mechanoactivation (grinding), laser sputtering of a ceramic target, and electrical explosion of wire. In some cases, comparative studies on micropowders were also performed. These technologies are characterized by the following features. The powders obtained by laser sputtering of a ceramic target or by electrical explosion of wire are traditional nanopowders with particles ranging within the nanoscale interval. For the nanopowders produced by grinding, the term *nanopowder* is not conventional. The size of their particles is usually within the micron range. At the same time, such powders have also nanoscale characteristics: the average size of X-ray coherent scattering domains is often of the order of 10 nm.

##### 4.1 Oxygen isotope exchange with oxide powders $\text{LaMnO}_{3+\delta}$

The oxide  $\text{LaMnO}_{3+\delta}$  is a convenient model object for optimization of the OIE technique (Gizhevskii et al, 2008) on nanopowders. In practice, there often occurs uncontrolled doping and diffusion characteristics of oxides are known to be extremely sensitive to the presents of impurities. Naturally, such materials are difficult to be analyzed. At the same time, nonisovalent doping of the cationic sublattice of  $\text{LaMnO}_{3+\delta}$  does not lead to the formation of structural vacancies in the oxygen sublattice and oxygen volume diffusion coefficients

change only slightly in this oxide (Fishman et al., 2003). Probably, this effect is connected to variable valence of manganese ions ( $\text{Mn}^{2+}$ ,  $\text{Mn}^{3+}$ ,  $\text{Mn}^{4+}$ ).

The micropowder  $\text{LaMnO}_{3+\delta}$  was synthesized by the standard ceramic technology from oxides  $\text{La}_2\text{O}_3$  and  $\text{Mn}_3\text{O}_4$ . A single-phase manganite powder with the orthorhombic crystal lattice and the particle size of about several microns was obtained. A FRITSCH planetary ball monomill was used to produce a nanostructured material from the initial powder. The grinding was in air in ethyl alcohol. Zirconium dioxide grinding balls and cups were used. The time of grinding was 13 h. According to X-ray diffraction results, the ground powder had an orthorhombic modification with the average coherent scattering domains of about 15 nm.

Isothermal annealings of nano- and micropowders were carried out in oxygen enriched by 80% with  $^{18}\text{O}$  isotope. Oxygen pressure was 0.26 atm. The change in the isotope composition of the gaseous atmosphere during annealing was negligible. Previously, stabilization annealings of the powders had been performed in air at the same temperatures as in oxygen containing tracer atoms. Their duration was approximately the same as the maximal time of annealing in  $^{18}\text{O}_2$ . The annealings were carried out in a quartz tube. The temperature of samples was measured with a chromel-alumel thermocouple with an accuracy of  $2^\circ\text{C}$ .

The concentration of  $^{18}\text{O}$  in the samples was determined with NRA using a 2 MV Van de Graaff accelerator (reaction  $^{18}\text{O}(\text{p}, \alpha)^{15}\text{N}$ ), the incident beam energy being 762 keV. The sample plane surface was mounted perpendicular to the incident beam axis. The acceptance angle of the nuclear reaction products was  $160^\circ$ . The energy spectra of the reaction products were registered with a silicon surface barrier detector of 10 mm in diameter. The diameter of the primary proton beam was from 1 to 2 mm. The number of incident beam particles reaching the sample was measured with an accuracy of  $\sim 1\%$  using a secondary monitor. For control by means of reaction  $^{16}\text{O}(\text{d}, \text{p})^{17}\text{O}^*$  when the incident beam particle energy is 900 keV, the content of  $^{16}\text{O}$  isotopes in samples was measured. The total oxygen concentration in all the samples was the same to within several percents.

The concentration of  $^{18}\text{O}$  and  $^{16}\text{O}$  isotopes was measured immediately on powders. For this purpose, the powder particles were pressed into a plate of indium. As a result, a layer containing only particles of oxide with thickness large than  $2\text{ }\mu\text{m}$  was formed on the plate of indium. Nondestructive analysis by means of the NRA technique was performed to the depth of about  $2\text{ }\mu\text{m}$ . In the test experiments the spectra of reaction products  $^{16}\text{O}(\text{d}, \text{p})^{17}\text{O}^*$  and  $^{18}\text{O}(\text{p}, \alpha)^{15}\text{N}$  for a bulk oxide and for powders, which were not annealed in the atmosphere of tracer atoms, did not differ within experimental error. The concentration profiles were calculated using the stopping power data for the examined samples (Vykhodets et al., 1987).

Experimental and calculated  $C(t)$  dependences for the ground powder  $\text{LaMnO}_{3+\delta}$  are given in Fig. 2. In our model calculations we considered several OIE scenarios for systems with low oxygen volume diffusion coefficients. In particular, the experimental data were processed using relaxation (4) and diffusion (7) expressions, as well as different powder particle size distribution functions. We also considered models for simultaneous realization of relaxation and diffusion mechanisms. For numerical calculations, corrections were introduced to expressions (4) and (7), which are due to the experimental conditions: presence of  $^{18}\text{O}$  atoms in powders before annealing and value of gas enrichment with  $^{18}\text{O}$  atoms. A similar correction of theoretical expressions for  $C(t)$  was made while processing the experimental data for other oxides.

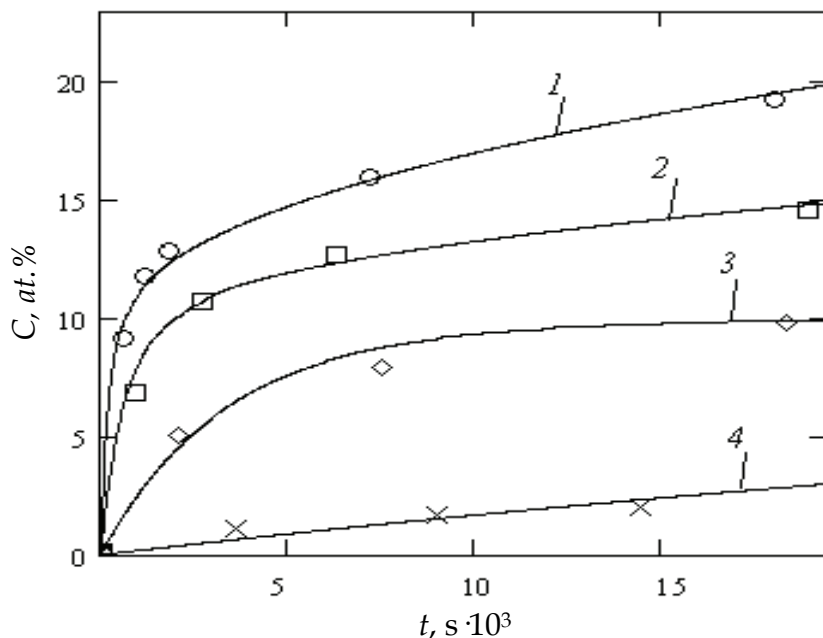


Fig. 2.  $C(t)$  dependences for ground powder  $\text{LaMnO}_{3+\delta}$  (Gizhevskii et al, 2008): 1 – 560°C; 2 – 500°C; 3 – 400°C; 4 – 300°C. Dots – experimental data; lines – calculation in the model for simultaneous realization of relaxation and diffusion mechanisms. Calculated curve parameters: 560°C –  $\Gamma = 5.17 \cdot 10^{-3} \text{ s}^{-1}$ ,  $D = 1.35 \cdot 10^{-23} \text{ m}^2/\text{s}$ ; 500°C –  $\Gamma = 1.70 \cdot 10^{-3} \text{ s}^{-1}$ ,  $D = 3.55 \cdot 10^{-24} \text{ m}^2/\text{s}$ ; 400°C –  $\Gamma = 3.07 \cdot 10^{-4} \text{ s}^{-1}$ ; 300°C –  $\Gamma = 1.93 \cdot 10^{-5} \text{ s}^{-1}$ . At 400 and 300°C, the diffusion contribution to the calculated dependences was negligibly small. In the calculations,  $r = 7.5 \text{ nm}$  and  $\Delta = 0.5 \text{ nm}$  were assumed

It turned out that the experimental dependences  $C(t)$  are not described in terms of diffusion theoretical models assuming no surface energy barrier during isotope exchange. In relaxation models, satisfactory fit with experimental data was shown only for low temperatures (300 and 400°C). For elevated temperatures (500 and 560°C), the best fit with experimental data was achieved in the model for simultaneous relaxation and diffusion. The caption to Fig. 2 contains the values of isotope exchange frequencies  $\Gamma$  and oxygen volume diffusion coefficients  $D$ , which provide satisfactory fit with experimental dependences  $C(t)$ . The temperature dependence of frequency  $\Gamma$  (see Fig. 7) can be described with the Arrhenius expression for the frequency factor  $\Gamma_0 = (0.97 \cdot 10^3 \pm 0.70 \cdot 10^3) \text{ s}^{-1}$  and the activation energy  $E = (0.88 \pm 0.07) \text{ eV}$ .

The results presented in Fig. 2 showed that the technique for OIE examination on oxide nanopowders proposed in work (Gizhevskii et al, 2008) is consistent. It furnishes information about nanopowder dimensional characteristics, reaction rates on the oxide particles surface during isotope exchange, and oxygen volume diffusion coefficients in oxides. The reliability of the technique is supported by the following facts. The best possible

fit with the experimental dependences  $C(t)$  was provided by the nanoparticle radius  $r = 7.5$  nm, which is close to the experimentally determined average radius of the X-ray coherent scattering domain for the examined powder (6.5 nm). Thus, the main dimensional parameter of the powder responsible for the isotope exchange rate became apparent, namely, the size of the X-ray coherent scattering domains. The difference between 6.5 and 7.5 nm is not fundamental since the notion of the monolayer thickness is not strictly defined; in fact, it is a parameter of theory. The value  $\Delta = 0.5$  nm was assumed by the authors merely by tradition. For example, in the grain boundary diffusion studies, exactly this value was postulated for the grain boundary width. The oxygen volume diffusion coefficients (see caption to Fig. 2) obtained from  $C(t)$  dependences processing also proved to be quite reasonable. For strontium-doped  $\text{LaMnO}_{3+\delta}$ -based perovskites, experimental oxygen volume diffusion coefficients are available in the literature for higher temperatures (Carter et al. 1992; De Souza et al. 2000; Fishman et al., 2003; Routbort et al., 1997). Strontium was not found to have any profound effect on the volume diffusion coefficients of tracer oxygen atoms (Fishman et al., 2003). Extrapolated diffusion coefficient values ranged from  $1 \cdot 10^{-24}$  to  $6 \cdot 10^{-24}$   $\text{m}^2/\text{s}$  (for  $500^\circ\text{C}$ ) and from  $1.6 \cdot 10^{-22}$  to  $3.2 \cdot 10^{-23}$   $\text{m}^2/\text{s}$  (for  $560^\circ\text{C}$ ) (see Fig.5). The values obtained in this work (see Fig. 5 and caption to Fig. 2) are within the above-mentioned intervals.

From Fig. 2 it is seen that the calculated and experimental dependences  $C(t)$  agree to a high accuracy. This finding is important in two respects. First, it reveals that the size distribution function of powder particle was rather narrow when the grinding technology was used. Second, it shows that the differences in annealing conditions in  $^{18}\text{O}_2$  for individual particles contained in the powder assembly were insignificant. Therefore, the same technology was applied in experiments with other powders.

From general considerations it was obvious that the value of frequency  $\Gamma$  should depend on the oxide type and the kind of oxygen-containing molecules in the gaseous phase. For the theoretical parameter  $\Delta$ , the presence or absence of such dependence is not trivial. Therefore, we compared OIE kinetics for  $\text{LaMnO}_{3+\delta}$  nanopowders annealed in  $^{18}\text{O}_2$  and  $\text{C}^{18}\text{O}_2$ . The degree of carbon dioxide enrichment with  $^{18}\text{O}$  isotopes was 90%; the pressures of oxygen and carbon dioxide during annealing were similar. The  $C(t)$  data for  $400^\circ\text{C}$  obtained during annealing in  $\text{C}^{18}\text{O}_2$  were satisfactorily described by expression (4), while the concentrations of  $^{18}\text{O}$  isotopes in the powder were from 1.5 to 2 times higher than those in oxygen. It was also found that the values of  $\Gamma$  and  $\Delta$  increased when  $^{18}\text{O}_2$  was replaced by  $\text{C}^{18}\text{O}_2$ . The corresponding values were  $3.07 \cdot 10^{-4}$  and  $6.4 \cdot 10^{-4}$   $\text{s}^{-1}$  for  $\Gamma$  and 0.5 and 0.66 nm for  $\Delta$ . The question why the surface layer thickness  $\Delta$  varies when the kind of the oxygen-containing molecule of the gaseous phase is changed calls for further research.

Figure 3 demonstrates experimental  $C(t)$  dependences for  $\text{LaMnO}_{3+\delta}$  micropowder. They do not differ qualitatively from those for the nanopowder (Fig. 2) and can be also used to receive the information about surface reaction rates and oxygen diffusion coefficients in oxide. It is seen from comparison of the data in Figs. 2 and 3 that the dimensional factor showed up very vividly: the concentrations of  $^{18}\text{O}$  isotopes in the micropowder were tens times lower. Evidently, the  $C(t)$  dependences for nanopowders are more convenient for theoretical analysis than the data for micropowders. In case of nanopowders, a better accuracy of analysis results is achieved. Besides, for microparticles, the particle spherical shape approximation and, consequently, the self-diffusion equation may turn out unsatisfactory.

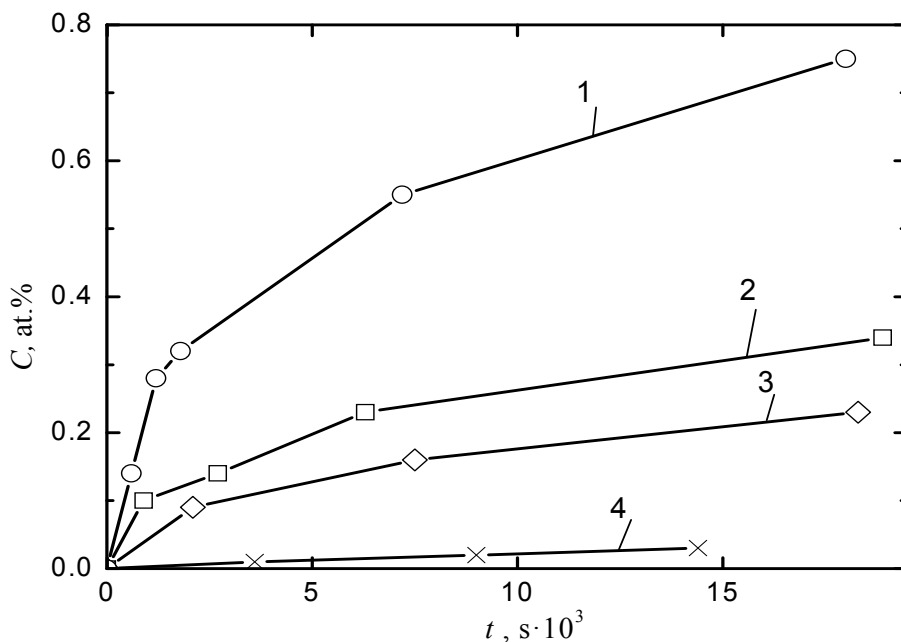


Fig. 3. Experimental dependences  $C(t)$  for  $\text{LaMnO}_{3+\delta}$  micropowder: 1 – 560°C; 2 – 500°C; 3 – 400°C; 4 – 300°C

#### 4.2 Oxygen isotope exchange with $\alpha\text{-Mn}_2\text{O}_3$ oxide powders

Manganese oxides are technically important and scientifically interesting materials. However, for these species, as far as we know, there is no information about OIE, oxygen diffusion coefficients, and surface reaction rates in the interaction with gaseous oxygen. Therefore, in this work we carried out appropriate studies on  $\alpha\text{-Mn}_2\text{O}_3$  oxide powders produced by mechanoactivation.

A planetary mill AGO-2 was used to prepare  $\text{Mn}_2\text{O}_3$  powders. Nanoscale domains were formed for a much shorter period of time than in the FRITSCH monomill: the grinding time for the examined samples was 60 s. The average particle size during grinding decreased insignificantly: from 1026 to 344 nm. The corresponding data were obtained by method of dynamic light scattering using a laser analyzer. X-ray diffraction studies showed that the phase composition of the ground powder remained unchanged upon heating in air to 950°C. The difference between  $\text{LaMnO}_{3+\delta}$  and  $\alpha\text{-Mn}_2\text{O}_3$  powders produced by mechanoactivation consisted in a pronounced enhancement of the average size of domains with an increase in temperature. In the temperature range from 300 to 700°C the radius varied from 16 to 35 nm (Petrova et al., 2010). We used these data as reference points in analysis of OIE results. At the same time, it was taken into account that sizes of coherent scattering domains during OIE investigations could differ from those established in work (Petrova et al., 2010) owing to different temperatures and duration of heating.

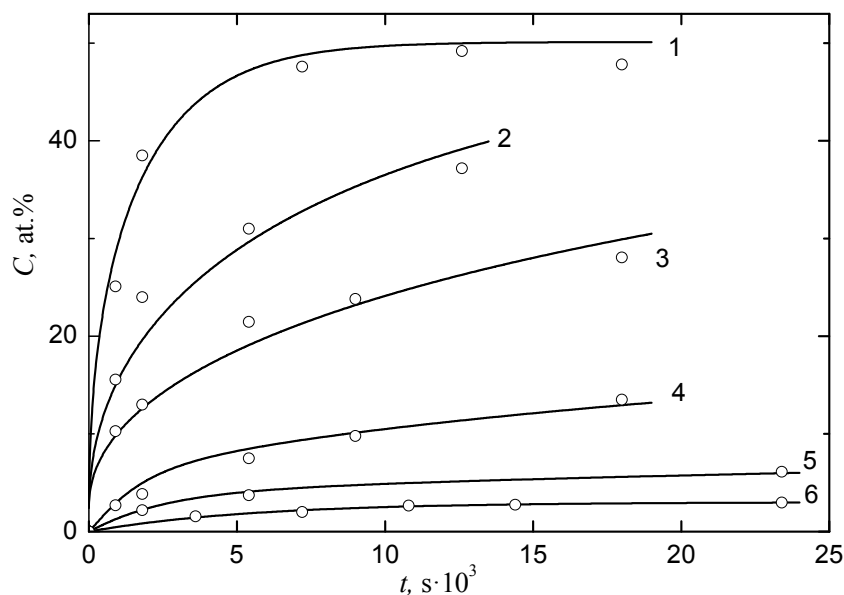


Fig. 4.  $C(t)$  dependences for ground powder  $\alpha\text{-Mn}_2\text{O}_3$ : 1, 2, 3, 4, 5, and 6 – results for 700, 550, 500, 400, 350, and 300°C, respectively. Dots – experimental data. Lines – calculation with expression (7) for curves 1, 2, and 3; with expression (4) for curve 6; and in the model for simultaneous relaxation and diffusion for curves 4 and 5. Calculated curve parameters:  $D = 0.5 \cdot 10^{-19}$ ,  $0.7 \cdot 10^{-20}$ ,  $1.7 \cdot 10^{-21}$ ,  $1.5 \cdot 10^{-22}$ , and  $1.5 \cdot 10^{-23}$   $\text{m}^2/\text{s}$  for 700, 550, 500, 400, and 350°C, respectively;  $\Gamma = 0.9 \cdot 10^{-3}$ ,  $5.0 \cdot 10^{-4}$ , and  $1.8 \cdot 10^{-4}$  for 400, 350, and 300°C, respectively; nanoparticle radii  $r = 34$ , 30, 27, 26, 25, and 24 nm for 700, 550, 500, 400, 350, and 300°C, respectively.  $\Delta = 0.5$  nm was assumed in the calculations

Experimental and calculated  $C(t)$  dependences for the ground powder  $\alpha\text{-Mn}_2\text{O}_3$  are depicted in Fig. 4. On the whole, the isotope exchange features for  $\text{LaMnO}_{3+\delta}$  and  $\alpha\text{-Mn}_2\text{O}_3$  powders prepared by grinding were analogous. This showed up first of all in the fact that the dimensional parameter of the powder responsible for the isotope exchange rate was the X-ray coherent scattering domain radius. However, the OIE parameters for these oxide powders differed drastically. So, at similar temperatures the frequencies  $\Gamma$  (see captions to Figs. 2 and 4) for  $\alpha\text{-Mn}_2\text{O}_3$  were three to ten times higher than for  $\text{LaMnO}_{3+\delta}$ . Even more dramatic differences were observed for the oxygen volume diffusion coefficients  $D$  (see Fig. 5). The data on oxygen diffusion coefficients in manganese oxides were obtained for the first time and can be commented in the following way. The measurement error shown in Fig. 5 was  $\sim 50\%$ ; it was due mainly to the uncertainty in the powder nanoparticle size in our experiments. We believe that the diffusion coefficient measurement error can be reduced several times if the nanoparticle radius is determined upon each isothermal annealing in gaseous oxygen. Thus, the technique employed can probably provide precision measurements of low values of oxygen volume diffusion in oxides. Of importance is the

following finding. The least typical diffusion length  $(Dt)^{1/2}$  in our experiments was about 0.1 nm. This level of measurements can hardly be achieved with other techniques based on concentration profile measurements of light element atoms in solids. Based on the obtained results, we suppose that the use of oxide nanopowders in diffusion experiments will allow one to make a qualitative leap in oxygen diffusion coefficient measurements in oxides.

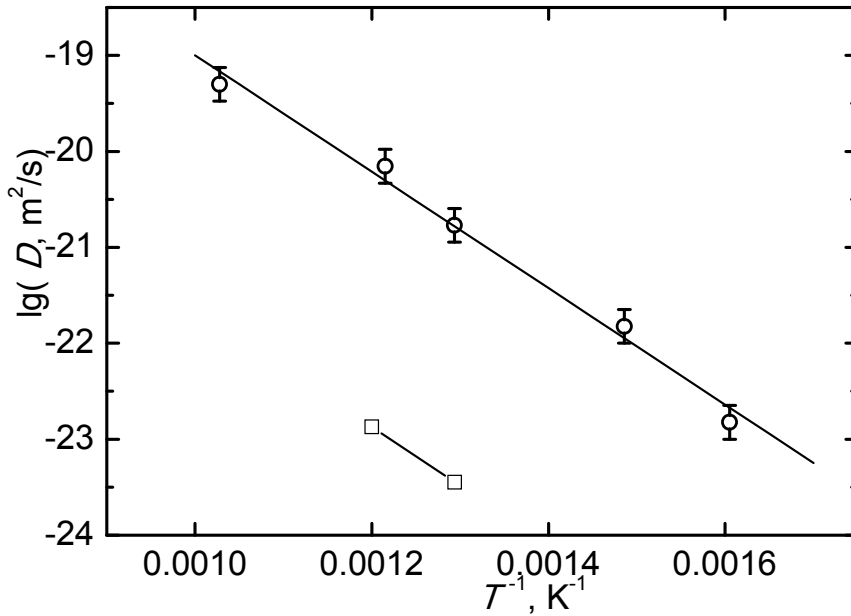


Fig. 5. Temperature dependence of volume diffusion coefficients  $D$  in  $\alpha\text{-Mn}_2\text{O}_3$  (circles) and  $\text{LaMnO}_{3+\delta}$  (squares)

The oxygen diffusion activation energy in  $\alpha\text{-Mn}_2\text{O}_3$  was  $(1.20 \pm 0.08)$  eV. For oxygen diffusion in oxides, this value is typical of oxygen ion migration energy. When oxygen diffusion was due to structural vacancies in the oxygen sublattice of the oxide, approximately the same value was observed also for the volume oxygen diffusion activation energy. For example, in yttrium-stabilized cubic zirconium oxides, oxygen diffusion activation energies were found (Solmon et al., 1995; Brossmann et al., 2004) to be 1.23 and 1.11 eV, respectively. The pre-exponential factor in the temperature versus diffusion coefficient dependence for  $\alpha\text{-Mn}_2\text{O}_3$  turned out to be very low, namely,  $D_0 \approx 10^{-13}$  m<sup>2</sup>/s. On the basis of this result, the structural oxygen vacancy concentration  $c_v$  in the examined manganese oxide can be estimated (Shewmon, 1989) as  $c_v \approx D_0/a^2\nu \approx 10^{-6}$  ( $a$  – oxide crystal lattice parameter,  $\nu$  – oxygen ion vibration frequency in the lattice).

In the temperature range 350 – 700°C in  $\alpha\text{-Mn}_2\text{O}_3$  oxide containing no structural vacancies in the oxygen sublattice, the oxygen diffusion coefficients will be evidently much smaller than those established by the authors, since in oxides without structural vacancies the diffusion activation energy is approximately equal to the sum of migration energy and vacancy formation energy. We don't know any literature data on oxygen vacancy formation energies in manganese oxides.

### 4.3 Oxygen isotope exchange with cubic zirconium oxide powders

In this section, as distinct from 4.1 and 4.2, we shall consider OIE for gaseous oxygen with an oxide characterized by very fast oxygen volume diffusion coefficients. The condition  $(Dt)^{1/2} \gg d$  ( $d$  is the particle linear size) corresponding to such species is fulfilled for many oxides containing structural vacancies in the oxygen sublattice.

OIE studies (Fishman et al., 2009) were performed on yttrium-stabilized cubic zirconium oxide YSZ containing 9 mol. % of  $Y_2O_3$ . It can be shown that the condition  $(Dt)^{1/2} \gg d$  at the minimal isothermal annealing experiment time ( $t \approx 10^3$  s) is met not only for nano-, but also for micropowders of this oxide in a wide range of experimental conditions. For example, at 500°C the oxygen diffusion coefficient value is  $5.9 \cdot 10^{-13}$  m<sup>2</sup>/c (Solmon et al., 1995) and the typical diffusion length  $(Dt)^{1/2}$  is 24  $\mu$ m. Since at  $(Dt)^{1/2} \gg d$  all oxygen ions of the oxide particle take part in isotope exchange, the concentrations of <sup>18</sup>O isotopes in the YSZ oxide upon annealing were higher than for  $LaMnO_{3+\delta}$ . This allowed us to carry out high-accuracy OIE studies on YSZ oxide powders.

YSZ micropowder was produced by coprecipitation of components. For better particle size homogeneity, it was calcined at 1100°C in air for 3 h. The powder specific surface was 2.15 and 0.64 m<sup>2</sup>/g before and after calcination, respectively. Figure 6 displays the experimental and calculated with eq. (9)  $C(t)$  dependences for YSZ micropowder. In the calculations we postulated that  $\Delta = 0.5$  nm, as in the case of  $LaMnO_{3+\delta}$ . The experimental and theoretical  $C(t)$  dependences are seen to be in reasonable agreement.

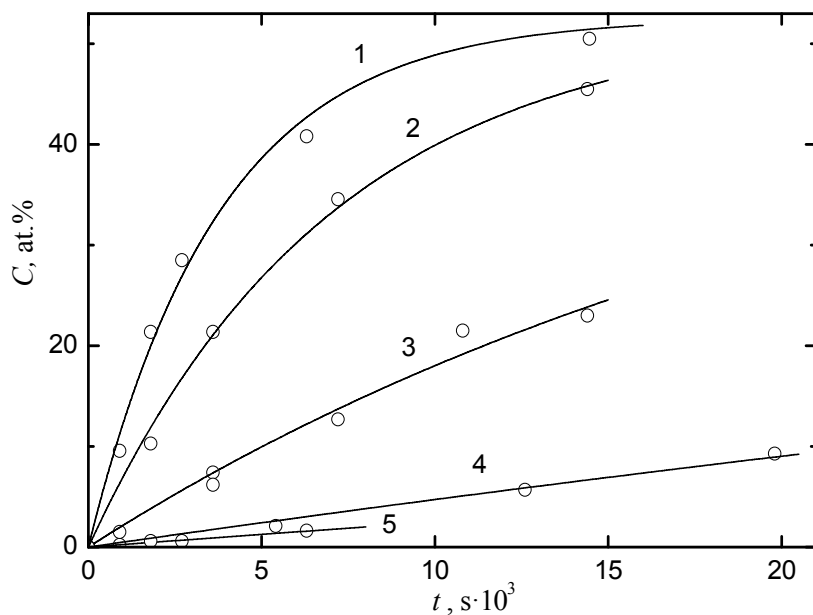


Fig. 6.  $C(t)$  dependences for calcined YSZ micropowder. Dots – experiment. Curves – calculation with equation (9). 1, 2, 3, 4, 5 – results at 800, 700, 600, 500, and 450°C, respectively



The temperature versus frequency  $\Gamma$  dependence is presented in Fig. 7. The frequency factor  $\Gamma_0 = 0.84 \cdot 10^3 \text{ s}^{-1}$  and the activation energy  $E = 0.79 \text{ eV}$  correspond to this dependence  $\Gamma(T)$ . The mean-square error in their determination was 60 and 4%, respectively. These results for the YSZ powder can be compared with the literature data (Manning et al., 1997) obtained in concentration profile measurements for  $^{18}\text{O}$  tracer atoms in bulk samples (see eqs. (1)-(2)). These data are also given in Fig. 7 (triangles). In study (Manning et al., 1997), the surface reaction rate was described using the parameter  $k$ .  $\Gamma$  was calculated on the basis of  $k$  values with eq. (6) at  $l = 2 \cdot 10^{-10} \text{ m}$ . The good agreement of  $\Gamma$  data for the micropowder and the bulk sample of YSZ is indicative of the reliability of the results obtained in works (Fishman et al. 2009; Manning et al., 1997).

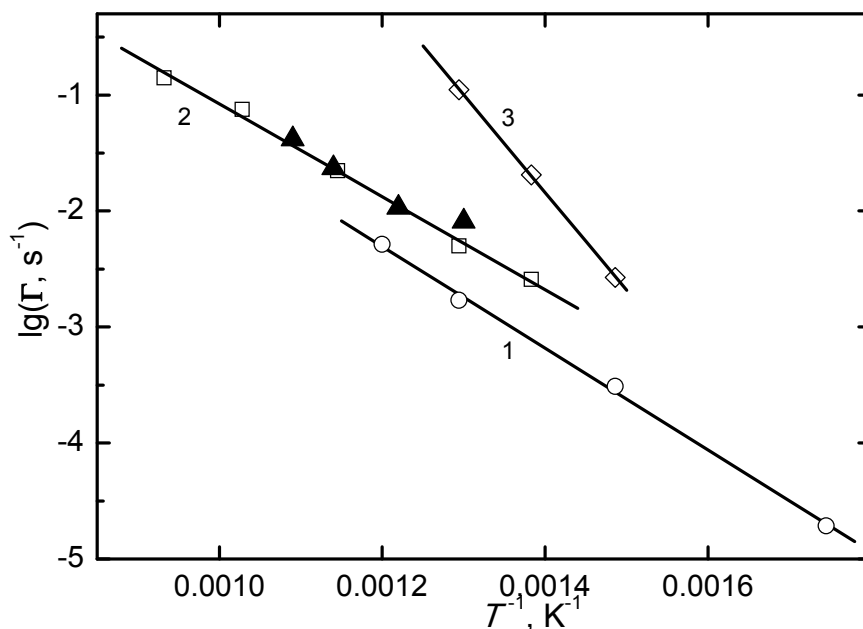


Fig. 7. Temperature dependence of exchange frequency  $\Gamma$  for  $\text{LaMnO}_{3+\delta}$  nanopowder (line 1), YSZ micropowder (line 2), and nanoboundaries of  $\text{LaMnO}_{3+\delta}$  (line 3). Triangles – data of work (Manning et al., 1997) for a bulk YSZ sample

Attention is drawn to the very low values of the frequency factor  $\Gamma_0$  in the temperature versus  $\Gamma$  dependence, which are about  $10^3 \text{ s}^{-1}$  for  $\text{LaMnO}_{3+\delta}$  and YSZ oxides. Almost the same frequency factor values were obtained also for bulk samples of other oxides:  $\text{La}_{0.8}\text{Sr}_{0.2}\text{MnO}_{3+\delta}$  (De Souza et al., 1999),  $\text{La}_{0.8}\text{Sr}_{0.2}\text{Mn}_{1-y}\text{Co}_y\text{O}_{3\pm\delta}$  (De Souza & Kilner, 1998),  $\text{La}_{1-x}\text{Sr}_x\text{YMnO}_{3-\delta}$  (Ruiz-Trejo & Kilner, 1997). These values are by several orders of magnitude smaller than other frequencies characterizing the examined systems. So, the vibration frequency of light atoms in solids is  $\geq 10^{12} \text{ s}^{-1}$ , whereas the frequency of gaseous molecule collisions with solid particle atoms during isotope exchange is about  $10^9 \text{ s}^{-1}$ . Such a considerable discrepancy in the characteristic frequency values points to a very low concentration of active centers on the surface of oxides participating in isotope exchange.

Their identification is of current importance. Moreover, such discrepancies in the characteristic frequency values may be due to the existence of several isotope exchange mechanisms, instead of only one mechanism of dissociation adsorption – desorption (Odzaki, 1979).

The YSZ nanopowder containing 9.5 mol. %  $\text{Y}_2\text{O}_3$  was produced by laser sputtering of a ceramic target (Ivanov et al., 2006). It was subjected to sedimentation in isopropyl alcohol to remove particles with diameter of 200 nm or larger from the powder. The specific surface of the nanopowder was  $(58.6 \pm 0.4) \text{ m}^2/\text{g}$ . Upon annealings at  $500^\circ\text{C}$ , it decreased to  $(53.3 \pm 0.8) \text{ m}^2/\text{g}$ , which is likely to be connected with agglomeration of smaller particles.

The experimental and calculated  $C(t)$  dependences for the YSZ nanopowder are exhibited in Fig. 8 (Fishman et al., 2009). Comparing the experimental data in Figs. 6 and 8 we see that the nanopowder is characterized by higher  $^{18}\text{O}$  isotope concentrations, which were also observed for other oxides. The calculated curve 2 in Fig. 8 was plotted with expression (11). In the calculations we used powder particle size distribution established by transmission electron microscopy (Ivanov et al., 2006); it was narrow with the width of about 13 nm and had a maximum at the particle diameter of 11 nm. It was also assumed that the isotope exchange frequencies  $\Gamma$  are not different for nano- and micropowders. From Fig. 8 it is seen that the calculated (curve 2) and experimental  $C(t)$  dependences do not agree with each other. At the same time, the powder specific surface calculated with the above nanopowder particle size distribution ( $58.1 \text{ m}^2/\text{g}$ ) practically coincided with its experimental value ( $58.6 \text{ m}^2/\text{g}$ ). The agreement between theoretical and experimental  $C(t)$  results was not improved when possible changes in the frequency  $\Gamma$  in going from micro- to nanopowder were taken into account. The experimental  $C(t)$  dependence was not at all described by theoretical expressions supposing a narrow powder particle size distribution.

It was suggested on the basis of these results that the discrepancy in the calculated and experimental  $C(t)$  data is due to the existence of large particles in the nanopowder, which were not presented in the size distribution function of powder particles obtained with transmission electron microscopy. The corresponding calculation had an evaluating character, where all large particles were postulated to have a spherical shape and similar size. The calculations showed that a satisfactory fit between calculated and experimental  $C(t)$  dependences can be achieved within this model. Figure 8 (curve 1) demonstrates one of the model versions postulating the presence of particles with radius 130 nm in the nanopowder. Their part in the total number of particles was estimated to be 0.0003. A similar satisfactory agreement between calculated and experimental  $C(t)$  data was achieved for large particle radii ranging from 100 to 130 nm. However, this interpretation of the experimental  $C(t)$  data was in conflict with the specific surface experimental data. It was calculated that the nanopowder containing particles with a 130 nm radius would have the specific surface  $20.4 \text{ m}^2/\text{g}$  if the part of large particles is 0.0003 (the experimental value being  $53.3 \text{ m}^2/\text{g}$ ).

The problems of interpretation of experimental data on specific surface for nanopowders produced by laser sputtering of a ceramic target were also known earlier. They manifested themselves in the following result: the specific surface of sedimentated and non-sedimentated powders were virtually the same according to numerous studies. For example, in work (Kotov et. al., 2004) the specific surface of sedimentated and non-sedimentated  $\text{Ce}_{0.78}\text{Gd}_{0.22}\text{O}_{2-8}$  nanopowder was found to be 57 and  $56 \text{ m}^2/\text{g}$ , respectively, though the non-sedimentated powder contained to 8 mass % of large particles. Such results

are usually explained in the following way: during sedimentation both large and finest particles are removed. However, this explanation seems doubtful. Some estimations show that small differences in the specific surface for sedimentated and non-sedimentated powders can occur only in the case of multi-layer coating of large particles with nanoparticles. According to the available data, less than one nanoparticle layer on large particles was usually registered on photographs.

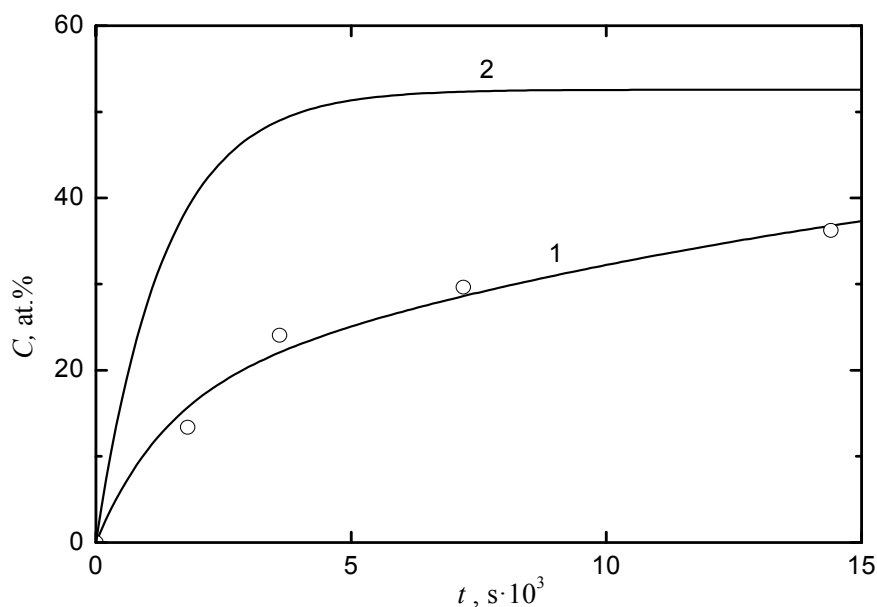


Fig. 8.  $C(t)$  dependences for the YSZ nanopowder at 500°C. Dots – experiment; curves 1 and 2 – calculation with equation (11). Curve 2 – calculation with the particle size distribution function obtained by transmission electron microscopy. Curve 1 – calculation with the particle size distribution function obtained by transmission electron microscopy and supplemented by the presence of particles with the radius of 130 nm

It can be supposed as an alternative that large YSZ particles appearing during laser sputtering of a ceramic target are conglomerates of usual nanoparticles. When the BET technique is used, nitrogen molecules penetrate into the space between nanoparticles contained in large particles. That is why the specific surface values for non-sedimentated and sedimentated nanoparticles are almost the same. At the same time, the presence of large particles in nanopowder was reliably established with the OIE technique. These findings show that the OIE technique can yield supplementary (as compared with the BET method) information about the dimensional characteristics of powders and is very sensitive to the presence of small amounts of large particles in nanopowder, which lie beyond the main peak of the size distribution function of powder particles. According to these results, the expected sensitivity of the isotope exchange technique is about 0.01% of the number of particles.

#### 4.4 Oxygen isotope exchange with aluminum oxide nanopowders

In this section we consider OIE in nanopowders produced by electrical explosion of wire. The powders were sedimentated in isopropyl alcohol. The sedimentation regime provided removal of particles with diameter greater than 200 nm from the powder. The main characteristics of the powders are listed in the Table 1.

$S, \text{m}^2/\text{g}$	$d_{\text{BET}}, \text{nm}$	$\gamma\text{-Al}_2\text{O}_3/\delta\text{-Al}_2\text{O}_3$	$d_x, \text{nm}$	$d_p, \text{nm}$	$\Theta, \text{nm}$
23.2	73	30/70	18.5	16	19
38.3	45	40/60	17	17	24
41.7	40	15/85	21	-	-
84	20.5	53/47	21	13	13

Table 1. Characteristics of aluminum oxide powders

The values of specific surface  $S$  were determined with the BET method; the nanoparticle diameter  $d_{\text{BET}}$  was calculated with the expression  $d_{\text{BET}} = 6/S\rho$ , where  $\rho$  is the calculated density for the crystalline component of the powder. X-ray phase analysis data showed that all the powders contained two crystalline phases:  $\gamma\text{-Al}_2\text{O}_3$  and  $\delta\text{-Al}_2\text{O}_3$ . The ratios of their mass fractions are presented in the Table 1. X-ray powder diffraction patterns were also indicative of an amorphous component; however, its amount in the powders could not be determined. The tabulated sizes  $d_x$  of X-ray coherent scattering domains characterize the  $\delta\text{-Al}_2\text{O}_3$  phase. The size distribution functions of powder particle were determined using transmission electron microscopy. All the distributions featured a narrow peak; its widths  $\Theta$  and the most probable particle diameters  $d_p$  are also listed in the Table 1.

As is seen from the Table 1, the aluminum oxide nanopowders are much more complicated objects than those examined in sections 4.1, 4.2, and 4.3. Since the OIE technique for nanopowders made a good showing in the case of relatively simple oxide systems (see the above sections), it is interesting to apply this method to more complicated species. The major task in this section was to estimate the sensitivity of the OIE technique to the multi-phase state of nanopowders and, in particular, to the presence of an amorphous phase.

$C(t)$  dependences at 500°C for OIE of aluminum oxide nanopowders with  $^{18}\text{O}_2$  are depicted in Fig. 9. For one of the oxides (with specific surface of 41.7  $\text{m}^2/\text{g}$ ), investigations were also performed for a powder, which was not exposed to preliminary stabilization annealing in air. In this case, the concentrations  $C(t)$  were appreciably higher than for the stabilized powder. This finding points to a nonstoichiometric chemical composition of the aluminum oxide powders produced by electric explosion of wire. Such peculiarities of nanooxides can be easily revealed with the NRA method.

The  $C(t)$  dependences in Fig. 9 differ from those for other nanopowders in appreciably lower  $^{18}\text{O}$  concentrations. This hampered experimental studies of IOE kinetics at temperatures, for which the nanoparticle agglomeration effect can be disregarded. For this reason, the main body of OIE data for aluminum oxides was obtained with the use of carbon dioxide  $\text{CO}_2$  enriched with  $^{18}\text{O}$  isotopes, rather than with gaseous oxygen. As was shown in section 4.1, replacement of  $^{18}\text{O}_2$  by  $\text{C}^{18}\text{O}_2$  led to an increase in the  $^{18}\text{O}$  isotope concentration in  $\text{LaMnO}_{3+\delta}$  powders. The same effect is also observed for aluminum oxide nanopowders, which

permitted us to perform  $C(t)$  dependence measurements in the temperature range from 500 to 1000°C. Figure 10 shows  $C(t)$  dependences for the powder with specific surface 38.3 m<sup>2</sup>/g. For other powders,  $C(t)$  dependences were analogous, namely, the concentration of <sup>18</sup>O isotopes in the powders increased with the time and temperature of annealing and powder specific surface.

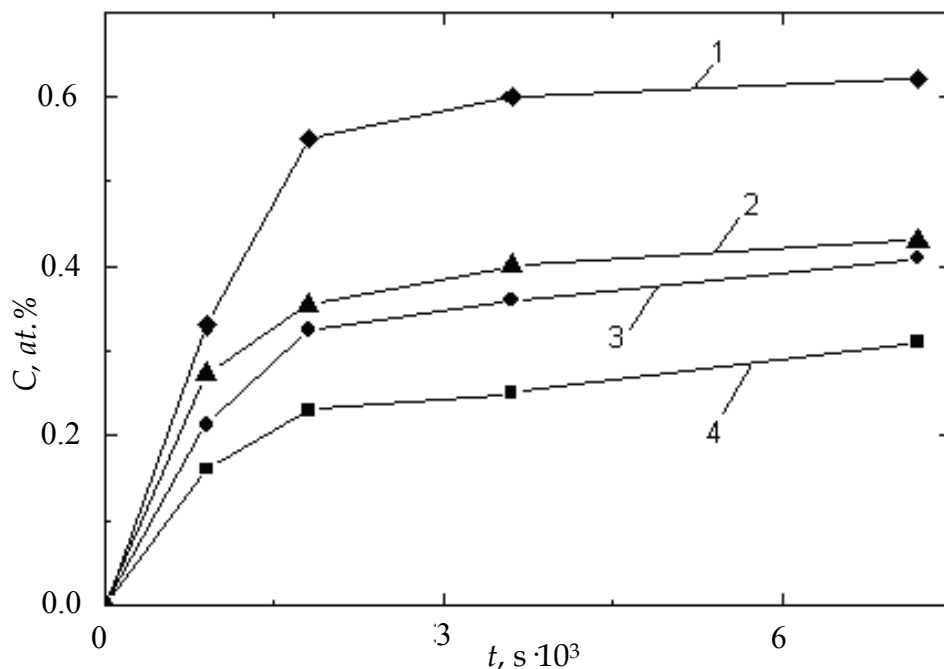


Fig. 9. Experimental  $C(t)$  dependences for aluminum oxide nanopowders at 500°C. 1,3,4 – results for powders with specific surface 84, 41.7, and 23.2 m<sup>2</sup>/g, respectively. 2 – results for the powder, which was not exposed to preliminary stabilization annealing in air, its specific surface is 41.7 m<sup>2</sup>/g

Figure 11 demonstrates several  $C(S)$  dependences of <sup>18</sup>O isotope concentration versus the powder specific surface  $S$ . For each dependence, the time and temperature of annealing in the atmosphere of tracer atoms were constant. All the  $C(S)$  dependences, including those not given in Fig. 11, were linear. As is seen in Fig. 11, for the systems powder - <sup>18</sup>O<sub>2</sub> they are fulfilled to a very high accuracy, while for the systems powder - C<sup>18</sup>O<sub>2</sub> a more considerable deviation from the linear dependences is observed. Thus, it can be stated quite definitely that for multiphase oxide powders the concentration of <sup>18</sup>O isotopes during isotope exchange is also a linear function of the powder specific surface. Note that at 500°C the extrapolation of  $C(S)$  dependences to the region  $S \rightarrow 0$  gives values  $C(S \rightarrow 0) \neq 0$ . This is likely to be due to oxygen diffusion in nanopowders. This peculiarity of  $C(S)$  dependences can be used for the estimation of oxygen diffusion coefficients in aluminum oxides at 500°C.

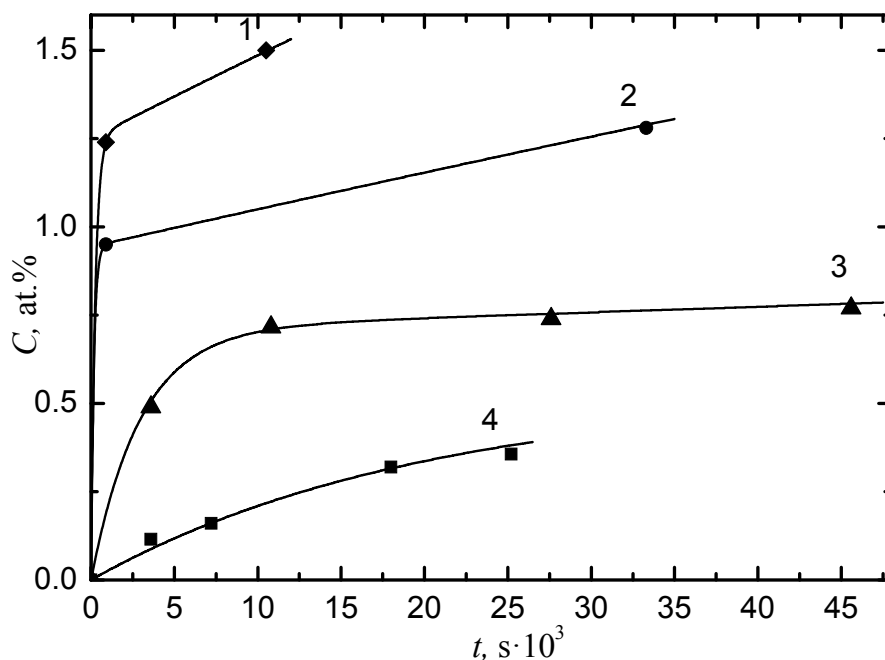


Fig. 10.  $C(t)$  dependences for aluminum oxide nanopowder during annealing in carbon dioxide enriched with  $^{18}\text{O}$  isotopes. Dots – experimental data. 1,2,3,4 – results for 500, 400, 200, and  $100^\circ\text{C}$ , respectively. Curves – calculation with equation (14). Calculated curve parameters:  $\Delta_2 = 0.66$  nm,  $\alpha_1 = 0.13$ ,  $\Gamma_1 = 5.0 \cdot 10^{-5}$ ,  $3.4 \cdot 10^{-4}$ ,  $6.0 \cdot 10^{-3}$ , and  $1.0 \cdot 10^{-2}$   $\text{s}^{-1}$ ,  $\Gamma_2 = 2.5 \cdot 10^{-8}$ ,  $3 \cdot 10^{-7}$ ,  $2.6 \cdot 10^{-6}$ , and  $0.57 \cdot 10^{-5}$   $\text{s}^{-1}$ ,  $\Delta_1 = 0.66$ ,  $0.88$ ,  $1.17$ , and  $1.55$  nm at 100, 200, 400, and  $500^\circ\text{C}$ , respectively

Thus, some OIE regularities for single- and multi-phase oxide nanopowders were found to be of the same type. This is true for linear  $C(S)$  dependences and the effect of the oxygen-containing gas type on  $^{18}\text{O}$  isotope concentrations. At the same time, multi-phase aluminum oxide powders exhibited some features that distinguished them from other examined systems, namely, the aforementioned low level of  $^{18}\text{O}$  isotope concentrations in powders upon annealing in  $^{18}\text{O}_2$ . When the gaseous atmosphere was changed to  $\text{C}^{18}\text{O}_2$ , the concentrations of  $^{18}\text{O}$  isotopes increased, but still remained low as compared with those for oxide powders earlier considered. Moreover, the  $C(t)$  concentrations for aluminum oxides powders were also unusual (see Fig. 10). They were described neither by relaxation-type expressions (4)-(5), nor by the model for simultaneous relaxation and diffusion. The same is true of the attempts to explain the experimental  $C(t)$  data by the presence of larger particles in aluminum oxide powders, which are not present in the main peak of size distribution function of powder particles.

No strict theoretical description of  $C(t)$  data could be given for aluminum oxides since IOE in amorphous oxide phases has not been studied at all. Therefore let us analyze  $C(t)$  dependences in a crude model, which allows for the multi-phase character of aluminum oxide powders and, especially, for the presence of an amorphous phase in them. For this

phase we postulate that the number of oxygen ions participating in isotope exchange between the amorphous phase and the gaseous atmosphere increases with temperature. It means that parameter  $\Delta$  in eqs. (4)-(5) for the amorphous phase increases with temperature too. We shall also restrict our analysis to the model considering only two – amorphous and crystalline – phases. True, X-ray structural analysis revealed the existence of two crystalline phases:  $\gamma$ - $\text{Al}_2\text{O}_3$  and  $\delta$ - $\text{Al}_2\text{O}_3$ . However, the approximation proposed for aluminum oxide powders may be acceptable since no noticeable distinctions were observed in the  $C(t)$  dependences for powders with close specific surface values (38.3 and 41.7  $\text{m}^2/\text{g}$ ) and with drastically different volumes of  $\gamma$ - $\text{Al}_2\text{O}_3$  and  $\delta$ - $\text{Al}_2\text{O}_3$  phases (see the Table 1). Assume that the oxygen diffusion rate in oxide particles is negligibly small (at least for  $T < 500^\circ\text{C}$ ).

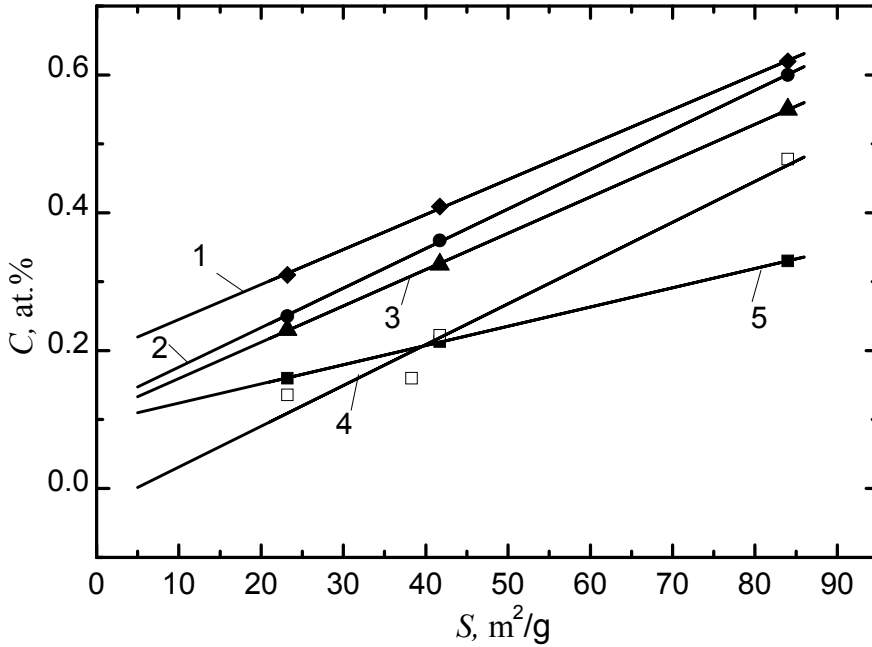


Fig. 11. Average  $^{18}\text{O}$  isotope concentration  $C$  in aluminum oxide nanopowders as a function of the powders specific surface  $S$  during annealing in oxygen and carbon dioxide enriched with  $^{18}\text{O}$  isotopes. Annealing conditions: 1,2,3,4 – annealing in  $^{18}\text{O}_2$  at  $500^\circ\text{C}$  for 120, 60, 30 and 15 min., respectively; 5 – annealing in  $\text{C}^{18}\text{O}_2$  at  $100^\circ\text{C}$  for 120 min

In terms of the above approximations, the expression for  $C(t)$  is a sum of relaxation-type contributions (see eq. (5)) from amorphous and crystalline powder components

$$C(t) = C_0 S [\alpha_1 \rho_1 \Delta_1 (1 - \exp(-\Gamma_1 t)) + \alpha_2 \rho_2 \Delta_2 (1 - \exp(-\Gamma_2 t))] , \quad (12)$$

where indexes 1 and 2 relate to the oxide powder amorphous and crystalline phases, respectively;  $\alpha_{1,2}$  – parts of these phases in the total surface area of the powder ( $\alpha_1 + \alpha_2 = 1$ ). The results of  $C(t)$  calculations with eq. (14) are given as solid lines in Fig. 10. The values of parameters  $\alpha_i$ ,  $\Delta_1$ ,  $\Delta_2$ ,  $\Gamma_1$ , and  $\Gamma_2$  are presented in the caption. In the calculations we also took

into consideration that the densities of the aluminum oxide amorphous phase, the  $\gamma$ - $\text{Al}_2\text{O}_3$  phase and the  $\delta$ - $\text{Al}_2\text{O}_3$  phase are 3.0, 3.35 and 3.62 g/cm<sup>3</sup>, respectively.

It is seen that the "two-phase" model easily provides a satisfactory description of experimental  $C(t)$  dependences during isotope exchange for a powder with specific surface 38.3 m<sup>2</sup>/g at all temperatures. Such a satisfactory description should be obtained also for powders with other specific surface values (all model parameters being the same) owing to the linear dependence  $C(S)$ . No special problems are expected also in the description of  $C(t)$  dependences for isotope exchange in aluminum oxides -  $^{18}\text{O}_2$  systems by means of eq. (12). However, the hypothesis that the number of oxygen ions in the amorphous phase surface layer participating in isotope exchange depends on the annealing temperature requires special experimental verification.

Thus, the studies of aluminum oxide powders with complex phase compositions showed that the OIE technique is very sensitive not only to the particle size of nanopowders, but probably to the presence of an amorphous phase in them.

## 5. Oxygen grain boundary diffusion and oxygen isotope exchange in nanocrystalline oxide $\text{LaMnO}_{3+\delta}$

Grain boundary diffusion in metal oxides is a poorly studied phenomenon and the data from different authors are controversial. In some of the most reliable works, the presence of enhanced diffusion at the grain boundaries is questioned (Kaur et al., 1995). At the same time, this fact has been reliably determined for metallic systems. The question of the possible common properties of the grain boundary diffusion for oxides and metals is still open. New experimental data on the coefficients of grain boundary diffusion in oxides attract the interest of theoreticians due to the specific properties of the grain boundaries in ionic compounds; in particular, these boundaries are charged. The investigations under consideration are of an applied interest, because metal oxides are widely used as functional materials in applications. The coefficients of the grain boundary diffusion determine the stability of the properties of polycrystalline materials. Presently, most researchers explain this inadequate situation with the diffusion data for oxides citing methodological reasons. It is difficult to obtain correct results primarily because of the strong influence of impurities in the oxides (Kaur et al., 1995). Control of the purity and stoichiometry of a material, especially near grain boundaries, is a complicated problem. In this connection, the study (Vykhodets et al., 2008) dealt with the problem of obtaining correct data on grain boundary diffusion in oxides.

The measurements were carried out for  $\text{LaMnO}_{3+\delta}$  oxide. This is a suitable model object, because it does not have structural vacancies in the oxygen sublattice. Similar systems are characterized by low values of the volume diffusion coefficients of oxygen  $D$ . This facilitates the choice of the annealing regimes for which the contribution of the grain boundary diffusion to the formation of the concentration profiles for the tracer atoms will be determinative. The research was focused on the realization of two kinetic regimes: the B type, when the grain boundary diffusion and volume diffusion take place simultaneously; and the C type, when the diffusion of the tracer atoms into the bulk of grains is negligible. Such an approach allows one to determine two parameters characterizing grain boundary diffusion: the diffusion coefficient for grain boundaries  $D_{\text{GB}}$  and the boundary width  $\delta$  (Kaur et al., 1995).



The research was carried out for nanocrystalline samples. For them, the conditions to obtain reliable results are more favorable due to the presence of the branching net of the boundaries, which enhances the contribution of the grain boundary diffusion to the diffusion flux. Besides, the nanocrystalline samples were prepared with the method in which the time of the nanostructure formation is very short. This requirement is fulfilled by the shockwave loading method (Kozlov et al., 1997) using explosives. In this case, it is expected that the doping of the nanograin boundaries is weak or absent. The initial material for the shockwave method is a coarse-grained powder of  $\text{LaMnO}_{3+\delta}$  with 15–30- $\mu\text{m}$  grains. According to the results of x-ray diffraction analysis, the material obtained after an explosion was nanocrystalline with an average particle size of 41 nm. These characteristics did not change after further diffraction annealing. Samples 3-mm-thick with an area of 1  $\text{cm}^2$  were cut out of this material. Mechanical operations of cutting, polishing, etc., were not performed to avoid the surface contamination of the samples. The scanning electron microscopy investigation of the fractured surface of the samples revealed that the main element of the microstructure of the samples under consideration is a crystallite with an average size of 3  $\mu\text{m}$ . The distance between the crystallites was very large (submicron); as a result,  $^{18}\text{O}_2$  molecules penetrate freely into the space between the crystallites during annealing. This feature was taken into account in mathematical treatment of  $C(x)$  profiles.

The results presented in Fig. 2 allow one to choose the optimal conditions for the diffusion annealing of compact samples. At 500°C, the C and B kinetic types are expected for  $t \leq 1$  h and for a few hours, respectively. The concentration of  $^{18}\text{O}$  atoms near the surface of the samples should be less than  $(3/2)C_0\Delta/r$  in the C regime and about or larger than this value in the B regime. This estimate was obtained by taking into account that, in contrast to an insulated nanoparticle, one boundary inside the massive sample simultaneously belongs to two particles. Similarly, the optimal conditions of annealing were also determined for other temperatures. Diffusion annealings were performed at 500, 450, and 400°C for  $\sim 1$ , 4, and 26 h, respectively, to realize the C type kinetics. At 500°C, diffusion annealings for  $\sim 4$  and 8 h oriented to the B type kinetics were carried out.

The concentration profiles  $C(x,t)$  of  $^{18}\text{O}$  atoms for bulk samples (some of them are shown in Fig. 12) were determined with the NRA method, the measurement conditions being the same as for powders (see section 4.1). The concentration profiles were characterized by the presence of background concentration  $C_{PH}(t)$ . It appears due to the free penetration of  $^{18}\text{O}$  molecules into the space between crystallites during annealing. It is easy to show that the following relation should be fulfilled in this case:  $N(t)/C_{PH}(t) = n/4$ ,

where  $N(t) = \int_0^\infty dx (C(x,t) - C_{PH}(t))$ ,  $n$  is the linear size of a crystallite. The experimental value

of  $N(t)/C_{PH}(t)$  for  $\sim 1$ -, 4-, and 8-h annealing did not differ within the statistical error ( $\sim 6\%$ ) and the average value of the parameter  $n$  was approximately 3  $\mu\text{m}$ . This value is in agreement with the results of the investigations of the microstructure of the samples. Thus, there is good reason to believe that the difference profiles  $(C(x,t) - C_{PH})$  were due to diffusion into crystallites of size  $\sim 3$   $\mu\text{m}$ , which, in their turn, have a nanocrystalline structure.

In  $C(x,t)$  profiles processing, expression (1) was used for the C regime. Here, the volume diffusion coefficient  $D$  was replaced by the grain boundary diffusion coefficient  $D_{GB}$  and it

was assumed that  $C_S^{\max} = 3C_0\Delta/2r = 1.75$  at. %. For the B regime, the following expression (Kaur et al., 1995) was used for  $C(x,t)$  profiles processing:

$$D_{GB}\delta = 1.332(D/t)^{1/2} (\partial \ln C(x)/\partial x)^{-2}, \quad (13)$$

where  $\delta$  is the grain boundary width. Expression (13) satisfactorily describes the corresponding experimental data within measurement error.

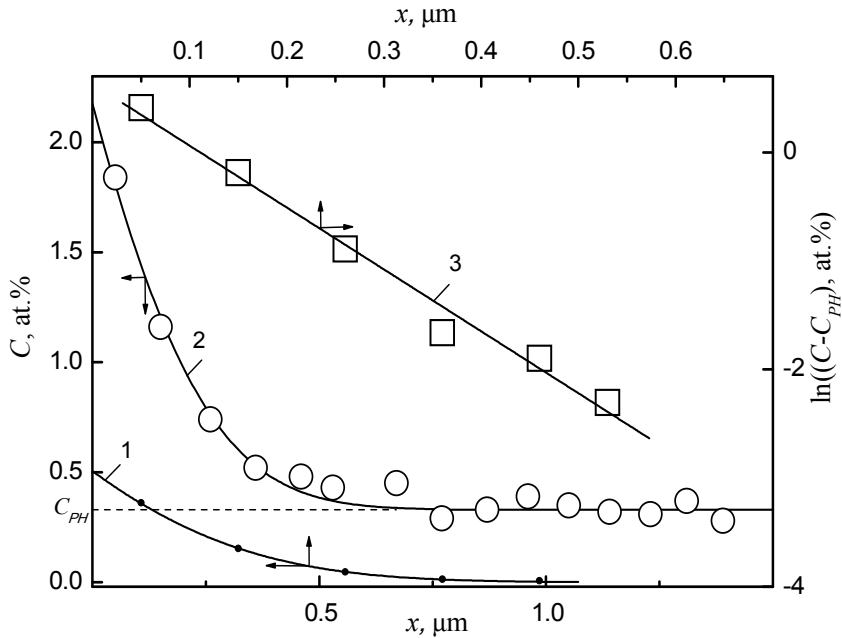


Fig. 12. Concentration profiles of  $^{18}\text{O}$  atoms in  $\text{LaMnO}_{3+\delta}$  nanocrystal: 1 -  $400^\circ\text{C}$ ,  $t = 26$  h, curve – calculation by eq. (3), background  $C_{PH}$  is deducted; 2 -  $500^\circ\text{C}$ ,  $t = 4$  h 11 min., curve – experimental dependence; 3 -  $500^\circ\text{C}$ ,  $t = 8$  h 12 min.; dots – experiment

Figure 13 shows the results of temperature versus grain boundary diffusion coefficients studies. The grain boundary diffusion activation energy  $Q_{GB}$  was found to be 1.95 eV. Using the data of study (De Souza et al., 2000) for volume diffusion activation energy  $Q_V$  we find  $Q_{GB} \approx 0.7Q_V$ . Such a relationship is typical of metallic systems for vacancy-type diffusion (Kaur et al., 1995). Thus, no qualitative differences in the diffusion behavior for oxide and metallic systems were established.

A value of 0.044 nm was found for boundary width  $\delta$ . It is an order of magnitude larger than the value  $\delta \approx 0.5$  nm obtained in all of the correct experiments on grain boundary diffusion. Note that using eq. (13) one can only determine an effective thickness of the boundary,  $\delta$ , disregarding its structure and, correspondingly, diffusion inhomogeneity. For an inhomogeneous boundary with the mixing of tracer atoms between intervals with strong disordering (dislocation cores) and with a weakly distorted lattice, the  $\ln C(x)$  dependence is

linear (Kondrat'ev & Trakhtenberg, 1986), as in the case of the homogeneous boundary. The left-hand side of Eq. (13) is reduced to the form  $D_{GB}\delta p$ , where  $p$  is the volume fraction of the trajectories with a high diffusion permeability. It is seen that the  $\delta$  value for  $p \ll 1$  is strongly underestimated. We can point out some reasons why the structural inhomogeneity of the boundaries was manifested in our experiments. This can be associated with a specific type of nanoboundaries formed in a brittle material after shock loading and with a short diffusion length  $(Dt)^{1/2}$ , which was on the order of the atomic size in our experiments.

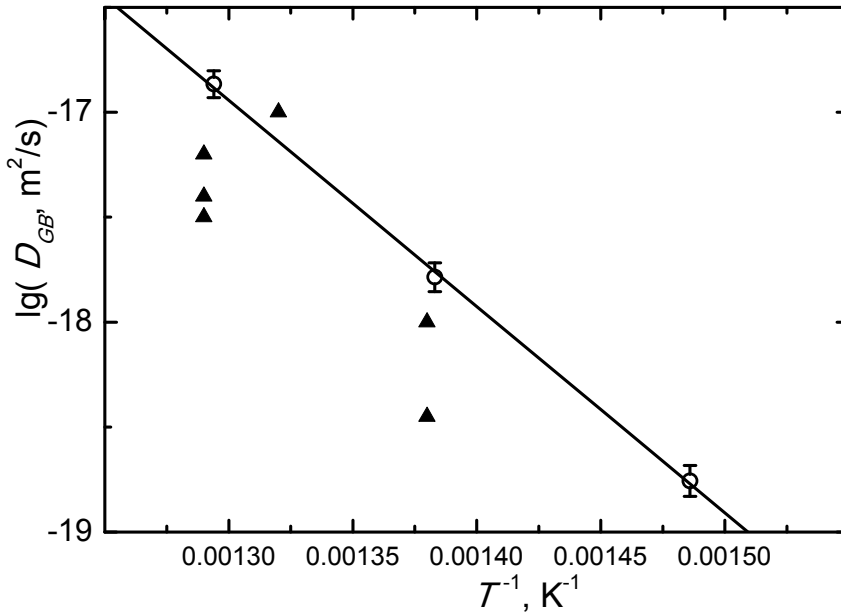


Fig. 13. Temperature dependence of grain boundary diffusion coefficients  $D_{GB}$  in  $LaMnO_{3+\delta}$  nanocrystal. Triangles – results of work (Brossmann et al., 2004) for  $ZrO_2$  nanocrystal

We know only one work (Brossmann et al., 2004) devoted to oxygen grain boundary diffusion in oxide nanocrystalline. This study was performed on a high-purity oxide  $ZrO_2$ . The  $ZrO_2$  nanocrystalline was produced by sintering of oxide nanoparticles with the average nanograin size 100 nm. Diffusion was examined with the use of the B type kinetics; the grain boundary width value  $\delta = 0.5$  nm was postulated for determination of grain boundary diffusion coefficients  $D_{GB}$ . The value of  $Q_{GB} = 1.95$  eV obtained in work (Brossmann et al., 2004) coincided with the result of study (Vykhodets et al., 2008). In both works, enhanced grain boundary diffusion was registered. The  $D_{GB}$  values from work (Brossmann et al., 2004) are given in Fig. 13 for comparison. The oxygen grain boundary diffusion coefficient in  $ZrO_2$  and  $LaMnO_{3+\delta}$  nanocrystallines are seen to be very similar. This coincidence of the results reported in the two works (Brossmann et al., 2004; Vykhodets et al., 2008) is considered to be accidental; nevertheless, we draw attention to these facts. Thus, an important finding for the diffusion theory has been obtained in the above studies, namely, no qualitative differences in volume and grain boundary diffusion were found for oxide and metal systems. Note that both studies were performed on nanocrystallines; besides, systematic measurement errors

due to uncontrolled doping of oxide grain boundaries with impurities were probably excluded.

As was mentioned above, the grain boundary diffusion coefficients  $D_{GB}$  in study (Vykhodets et al., 2008) at 500, 450, and 400°C were determined with the use of the C type kinetics, i.e. in the absence of oxygen volume diffusion. By means of expressions (1), (2), and (6) we calculated for the same temperature the parameters  $H$ ,  $k$ , and  $\Gamma$  characterizing the surface energy barrier during isotope exchange of gaseous oxygen with  $\text{LaMnO}_{3+\delta}$  oxide nanoboundaries (Fishman et al., 2010). The results for  $\Gamma$  are given in Fig. 7. As in section 4.3, the  $k$  values were recalculated in  $\Gamma$  using expression (6) at  $l = 2 \cdot 10^{-10}$  m. Figure 7 shows a great difference in the frequency factor  $\Gamma_0$  and activation energy  $E$  values in the temperature versus  $\Gamma$  dependence, which were obtained, respectively, for the nanograin boundary and the regular lattice of  $\text{LaMnO}_{3+\delta}$ . The difference is almost 7 orders of magnitude for  $\Gamma_0$  ( $0.9 \cdot 10^{10}$  and  $0.97 \cdot 10^3 \text{ s}^{-1}$ ) and 2 times for  $E$  (1.67 and 0.88 eV). In our opinion, such a dramatic difference in  $\Gamma_0$  and  $E$  parameters for the nanograin boundary and the regular lattice of one and the same oxide is difficult to understand from the isotope exchange mechanism only. Competing mechanisms can take place simultaneously, and, depending on the relationship between the system parameters, one or another mechanism will prevail. A similar situation happens, for example, in studies of diffusion in solids, when volume and grain boundary diffusion occur simultaneously. For such objects, the contributions from volume and grain boundary diffusion to the mass transfer rate will depend on the experiment conditions; as a result, drastically different values of effective diffusion coefficients, activation energies, and frequency factors in the temperature dependence  $D$  can be obtained.

## 6. Conclusion

In the studies presented here it was shown that the OIE parameters are sensitive to the dimensional characteristics of oxide powders. Therefore, the approach based on OIE examination shows promise for receiving the information about the size of nanopowder particles. Similar data are obtained with other techniques (electron microscopy, X-ray diffraction, specific surface measurement, dynamic light scattering by means of a laser analyzer etc.); in this respect, the OIE technique has an important specific feature. In addition to the conventional methods, it makes it possible to determine the stoichiometry of oxide powders, is sensitive to chemical activity of powders and, probably, to the presence of amorphous phases and very small amounts of larger particles in nanopowders. These peculiarities of the considered technique are of great interest both for theory and practice, since all existing technologies for nanopowder synthesis lead to the formation of non-equilibrium materials and assemblies consisting of particles with different sizes and shapes. Moreover, when the OIE technique is used on nanopowders, very low oxygen volume diffusion coefficient values can be measured as compared with traditional approaches. The application of the OIE technique for bulk nanocrystalline samples also holds much promise. Already in several works it was shown that considerable progress can be achieved with the use of this technique in the examination of oxygen grain boundary diffusion in oxides.

## 7. Acknowledgment

This work was supported by RFBR (grant 10-03-96016-p\_ural\_a and grant 09-03-00335\_a), the Program of fundamental research of Presidium of Russian Academy of Sciences N 27

"Foundations of fundamental research of nanotechnology and nanomaterials" and the Federal Target Program "Scientific and scientific-pedagogical staff of innovation Russia (contract 02,740. 11.0641).

## 8. References

- Brossmann, U. et al. (2004), Oxygen diffusion in nanocrystalline  $\text{ZrO}_2$ , *Rev. Adv. Mater. Sci.*, Vol. 6, p. 7-11, ISSN 1605-8127
- Carter, S. et al. (1992), Oxygen transport in selected nonstoichiometric perovskite structure oxides, *Solid State Ionics*, Vol. 53-56, p. 597-605, ISSN 0167-2738
- De Souza, R.A. & Kilner, J.A. (1998), Oxygen transport in  $\text{La}_{1-x}\text{Sr}_x\text{Mn}_{1-y}\text{Co}_y\text{O}_{3\pm\delta}$  perovskites - Part I. Oxygen tracer diffusion, *Solid State Ionics*, Vol. 106, p.175-187, ISSN 0167-2738
- De Souza, R.A. et al. (2000), A SIMS study of oxygen tracer diffusion and surface exchange in  $\text{La}_{0.8}\text{Sr}_{0.2}\text{MnO}_{3+\delta}$ , *Materials Letters*, Vol. 43, p. 43-52, ISSN 0167-577X
- Fishman, A.Ya. et al. (2003), Diffusion in concentrated Jahn-Teller systems, *Advances in quantum chemistry*, Vol. 44, p.497- 509, ISBN: 0-12-034844-6, ISSN 0065-3276
- Fishman, A.Ya. et al. (2009), Oxygen isotope exchange in nanocrystal oxides *Journal of NanoResearch*, Vol.7, p. 33-41, ISSN 1662-5250
- Fishman, A.Ya. et al. (2010), Isotope Exchange between Gaseous Oxygen and Nano-Grain Boundary of  $\text{LaMnO}_{3+\delta}$  Oxide, *Defect and Diffusion Forum*, Vol. 297-301,p. 1301-1305, ISSN 1012-0386.
- Gizhevskii, B.A. et al, (2008), Oxygen Isotope Exchange Between the Gaseous Phase Enriched with the  $^{18}\text{O}$  Isotope and Nanocrystal Oxides  $\text{LaMnO}_{3+\delta}$  Obtained By Severe Plastic Deformations, *Defect and Diffusion Forum*, Vol.273-276, p.233-238, ISSN 1012-0386
- Ivanov, M.A. et al. (2006), Formation of a thin-layer electrolyte for SOFC by magnetic pulse compaction of tapes cast of nanopowders, *Journal of Power Sources*, Vol. 159, p. 605-612, ISSN 0378-7753
- Kaur, Y et al. (1995), *Fundamentals of Grain and Interphase Boundary Diffusion* (3rd ed.) Wiley, ISBN 978-0-471-93819-4, New York, USA
- Kondrat'ev, V.V. & Trakhtenberg, I. Sh. (1986), Grain-boundary diffusion of atoms in a model of structurally heterogeneous boundary, *The Phys. Metal & Metallogr.*, Vol. 2, p. 434-441, ISSN 0031-918X
- Kotov, Yu.A. et. al. (2004), Characteristics of nanopowders produced by vaporation  $\text{CeO}_2/\text{Gd}_2\text{O}_3$  emission targets repetitively pulsed  $\text{CO}_2$  laser, *Journal of Technical Physics*, Vol. 74, N3, p.72-77, ISSN 0044-4510
- Kozlov, E. A. et al. (1997), Patent of Russian Federation No. 2124716, December 24, 1997
- Manning, P.S. et al. (1997), The kinetics of oxygen transport in 9.5 mol % single crystal yttria stabilized zirconia, *Solid State Ionics*, Vol. 100, p. 1-10, ISSN 0167-2738
- Odzaki, A. (1978), *Isotopic studies of heterogeneous catalysis*, Acad.Press, ISBN 0125319509, New York, USA
- Routbort, J.L. et al. (1997), Diffusion-controlled creep in mixed-conducting oxides, *Def. and Dif. Forum*, Vol. 143-147, p.1201-1205, ISSN 1012-0386
- Ruiz-Trejo, E. & Kilner, J.A. (1997), Oxygen diffusion and proton conduction in  $\text{La}_{1-x}\text{Sr}_x\text{YO}_{3-\delta}$ , *Solid State Ionics*, Vol. 97, N 1-4. - P. 529-534, ISSN 0167-2738

- Petrova, S.A. et al. (2010), Phase states of mechanoactivated manganese oxides, *Proceedings of the Ninth Israeli - Russia Bi-National Workshop 2010 "The optimization of composition, structure and properties of metals, oxides, composites, nano and amorphous materials"*, p. 138-152, Belokurikha, Russia, July 25-30, 2010
- Shewmon, P. (1989), *Diffusion in solids* (2nd ed.) The Minerals, Metals & Materials Society, ISBN 0-87339-105-5, Warrendale, PA, USA
- Solmon, H. et al. (1995), Ionic transport properties of yttria-doped zirconia, *Solid State Phenomena*, Vol. 41, p.103 – 112, ISSN 1012-0394
- Vykhodets, V.B. et al. (1987), Oxygen diffusion in  $\alpha$ -Ti. II. The calculation of the concentration profile of impurities in the nuclear microanalysis, *The Phys. Metal & Metallogr.*, Vol.64, p.920-923, ISSN 0031-918X
- Vykhodets, V.B. et al. (1994), Potential barriers in the migration of tracer oxygen atoms in the  $\text{YBa}_2\text{Cu}_3\text{O}_{7-\delta}$  lattice, *JETP*, Vol.106, N2(8), p.648-662, ISSN 0044-4510
- Vykhodets, V. B. et al. (2000), Atomic structure and diffusion properties superanizotropnyh systems, *Journal of Solid State Physics*, Vol.42, N4, p.595-601, ISSN 0367-3294
- Vykhodets, V.B. et al. (2008), Grain Boundary Self-Diffusion of Tracer  $^{18}\text{O}$  Atoms in Nanocrystalline Oxide  $\text{LaMnO}_{3+\delta}$ , *JETP Letters*, Vol. 87, No. 2, pp. 115-119, ISSN 0370-274X

# Lead Free BNT Type Ceramics: A Useful Material for Sensors and Ultrasound Applications

E. Suaste Gómez and J. J. A. Flores Cuautle

*Centro de Investigación y de Estudios Avanzados del Instituto Politécnico Nacional  
México*

## 1. Introduction

Ferroelectric, piezoelectric and pyroelectric materials, belong to the family called smart materials and have been extensively studied for several years, not only because they have interesting physical phenomena but also because it can be used in wide variety of applications in the most diverse fields, ranging from the automotive industry as temperature or pressure sensors, even in scientific circles as polarizers or light waveguide modulators (Moulson and Herbert, 2003).

Among the smart materials most widely used are those based on combinations of lead titanate ( $\text{PbTiO}_3$ ) and lead zirconate ( $\text{PbZrO}_3$ ), leading to the formation of so-called lead zirconate-titanate (PZT), PZTs for many years has been that present the best piezoelectric and pyroelectric characteristics, however due to environmental efforts in different countries are doing, such as the Directive of the European Parliament and the Council on restriction of the use of certain hazardous substances in electrical and electronic equipment, and the restriction of hazardous substances in the USA, it is necessary to enforce research in order to find materials to replace the PZTs.

There are no materials that display the excellent characteristics that PZT presents that is why in order to replace PZT system it is necessary to divide applications and develop materials which suite for each application. Several lead free materials have been studied as possible replaces for PZT; barium titanate  $\text{BaTiO}_3$  (BIT) is one of the most studied ferroelectric oxide with perovskite structure, it has been used in piezoelectric applications such as sonar due to its high electromechanical coupling factor, however BIT has low Curie temperature ( $T_c = 120^\circ \text{C}$ ), (Jaffe, 1971).

Potassium niobate  $\text{KNbO}_3$  is another lead free ferroelectric material with high  $T_c$  ( $425^\circ \text{C}$ ) but to obtain dense ceramic body requires long soaking time (Jaeger & Egerton, 1962). The bismuth sodium titanate ( $\text{Bi}_{0.5}\text{Na}_{0.5}\text{TiO}_3$ ) (BNT) is an excellent candidate for use in lead-free ferroelectric ceramics because BNT is strongly ferroelectric and has a high Curie temperature ( $T_c = 320^\circ \text{C}$ ) (Smollenky et al., 1961; Buhrer, 1962). However data on BNT properties are scarce due to the difficulty in poling process for these ceramics. Recently BNT-based solid solutions which can be poled easily have been studied (Takenaka et al., 1989, 1991; Sasaki et al., 1999; Rajeev & Dwiwedi, 2005).

Lately  $(\text{Bi}_{0.5}\text{Na}_{0.5})_{0.935}\text{Ba}_{0.065}\text{TiO}_3$  ferroelectric ceramics have been developed (Suaste et al., 2008), this type of ceramics present high  $T_c$ , high dielectric constant at this point, excellent density, pyroelectric coefficient at room temperature (RT) near to lead titanate, thermal properties at RT near to those of BIT, in addition this type of ceramics present photovoltaic response not only to a visible light but also to near UV light, these characteristics joining with its lead free composition makes this material an option of choice to develop sensors and actuators. In this chapter we describe the development, electrical and thermal characterization of  $(\text{Bi}_{0.5}\text{Na}_{0.5})_{0.935}\text{Ba}_{0.065}\text{TiO}_3$  (Gonzalez & Suaste, 2009, Flores et al., 2009), and at the same time present an ultrasound application for this material.

## 2. Fabrication

To ensure that the perovskite structure is stable, we must consider the size of the ionic radii of the cations that constitute such structure, which is expressed in the so-called tolerance factor  $t$ , the tolerance factor is given by the equation 1

$$t = \frac{R_A + R_o}{\sqrt{2}(R_B + R_o)} \quad (1)$$

Where  $R_A$  is the divalent cation ionic radius for our formulation this site is occupied by bismuth (Bi), sodium (Na) and barium (Ba),  $R_B$  is the ionic radius of tetravalent cation titanium (Ti) and  $R_O$  is the ionic radius of oxygen, the tetragonal structure is ensured with  $t$  values between 0.77 and 0.99, in the case of a cubic structure this factor takes a value of 1, for our ceramic  $t$  has a value of 0.84.

Starting from the formulation  $(\text{Bi}_{0.5}\text{Na}_{0.5})_{1-x}\text{Ba}_x\text{TiO}_3$  is necessary to calculate the value of  $x$ , this is done taking into account two main points: the first is to ensure that the final compound is in the interest region in its phase diagram, the second is to find the  $x$  value that makes calculations easier, in our case  $x$  has a value of 0.065.

Ceramic samples were prepared by a conventional solid state reaction, reagent-grade powders of oxides and carbonates with 99+% purity of  $\text{Bi}_2\text{O}_3$ ,  $\text{NaCO}_3$ ,  $\text{BaCO}_3$ , and  $\text{TiO}_2$  were used as starting raw materials. These materials were weighted in appropriate portions, mixed and calcined at 800° C during one hour, after calcining the ceramic powders were grounded, milled and pressed into disks of 10 mm in diameter and about 1.9 mm in thickness. These disks were sintered at 1200° C for one hour in air. Once samples were sintered, fired-on silver paste was used as electrodes in order to measure their electric properties. Finally, the samples were poled at 60° C in a silicone oil bath by applying a dc electric field of 3 kV/mm for 1 hour.

## 3. Characterization

### 3.1 Structure characterization

In order to verify the ceramic structure a SEM micrograph with a magnification of 5000X and resolution of 1 micrometer was taken. Ceramic density was measured by the Archimedes method the average density was 5.6 g/cm<sup>3</sup>. Figure 1 shows a SEM image of BNBT ceramic taken at 5000X with a 1 µm scale bar, micrograph shows that the ceramic has a compact structure with few impurities that do not affect the ceramic behaviour, compact structure joins to ceramic density of 5.6 g/cm<sup>3</sup> pointed out that this material may be optimal for transducers. The crystal structure of the ceramics was examined by the use of X-ray



diffractometer, as Fig 2 shows, XRD pattern is in agreement with the reported literature (Rajeev & Dviwedi, 2005; Weihua et. al., 2008).

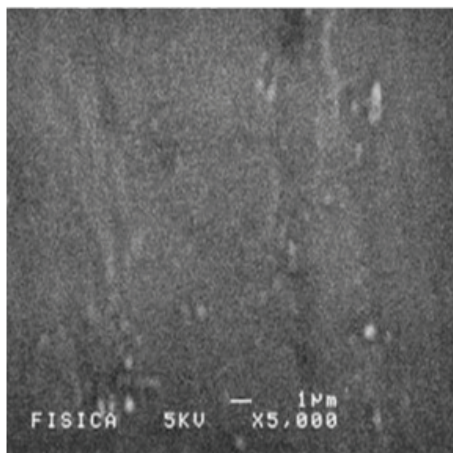


Fig. 1. Piezoelectric ceramic SEM image taken at 5000X and 1µm scale bar

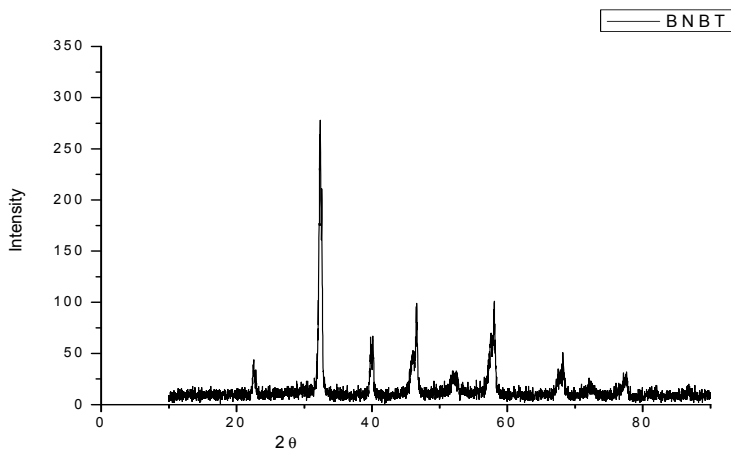


Fig. 2. XRD pattern of the ceramic specimen

### 3.2 Electrical characterization

The dielectric constant was determined by the capacitance measure. Samples were heated at a rate of 5 °C/min, until 600° C while the capacitance was measured at 1 kHz with a Beckman LM22A RLC bridge. The dielectric constant was then determined by expression (2):

$$\varepsilon = \frac{Cl}{\varepsilon_0 A} \quad (2)$$

Where  $C$  is the capacitance in  $F$ ,  $l$  is the sample thickness in  $m$ ,  $A$  the sample area in  $m^2$  and  $\epsilon_0$  the vacuum permittivity  $=8.85 \times 10^{-12} F/m$ .

The resonance frequency was determined by the transmission method described by the IRE Standards [IRE Standard on piezoelectric crystals, 1961], the experimental setup consist in a voltage divisor formed by ceramic and one load resistance fed by a signal generator, an oscilloscope was connected to the resistance as Fig 3 shows. A frequency sweep was performed; the resonance frequency is then presented as an increase in signal amplitude, this is due to the ceramic impedance is minimum at this point consequently current trough circuit is maximum, in the same way the antiresonance frequency was found. These frequencies were also measured with an Agilent E4411B spectrum analyzer

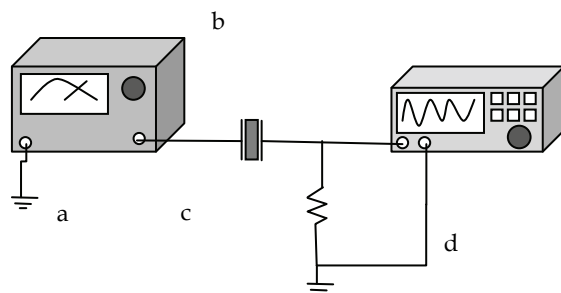


Fig. 3. Experimental setup used to get resonance and antiresonance frequency, a) generator, b) piezoelectric ceramic, c) load resistance and, d) oscilloscope

Coupling factor  $k_p$  was obtained by using IRE Standard [IRE Standard on piezoelectric crystals, 1961], which relates resonance and antiresonance frequency in form of the equation 3

$$k_p = \frac{f_a - f_r}{f_r} \quad (3)$$

Where  $f_r$  = resonance frequency  
 $f_a$  = antiresonance frequency

For the thickness coupling factor  $k_t$  the Onoes method was used (Onoe & Tiersen, 1963). The method involves to find the fundamental resonance frequency and the first four harmonics, divide each of the harmonic frequencies between the fundamental and seek the coefficients obtained in the table given by Onoe.

The dielectric constant was determined using equation 2; Fig 4 shows the dielectric constant dependence with the temperature.  $T_c$  occurs at  $425^\circ C$  that is a relatively high temperature for ceramics, at this temperature dielectric constant reach its maximum value  $\epsilon = 4429$ , a large value compared with other lead free ceramics.

As previously was mentioned the resonance frequency depends on the ceramic thickness, Fig 5 shows the resonance spectrum ranging from 100 Hz until 15 MHz for a BNBT ceramic with 1.9 mm thickness taken with a spectrum analyzer, theoretical frequency resonance was calculated by the use of equation 4 (Efimovich, 1964)

$$f = \frac{c}{\lambda} \quad (4)$$

Where  $c$  is the phase velocity and  $\lambda = 2l$  with  $l$  ceramic thickness, in order to find phase velocity the equation 5 was use (Efimovich, 1964)

$$c = \frac{1}{\sqrt{s\rho}} \quad (5)$$

where  $s$  is the elastic constant and  $\rho$  ceramic density, for this type of ceramics  $s = 8.59 \times 10^{12} m^2 N^{-1}$  and  $\rho = 5.6 \times 10^3 kg m^{-3}$  (Takenaka et al., 1991; Suaste et al., 2008), theoretical resonance frequency was 1.2 MHz which is near to the measurement frequency as it can be seen in Fig 5.

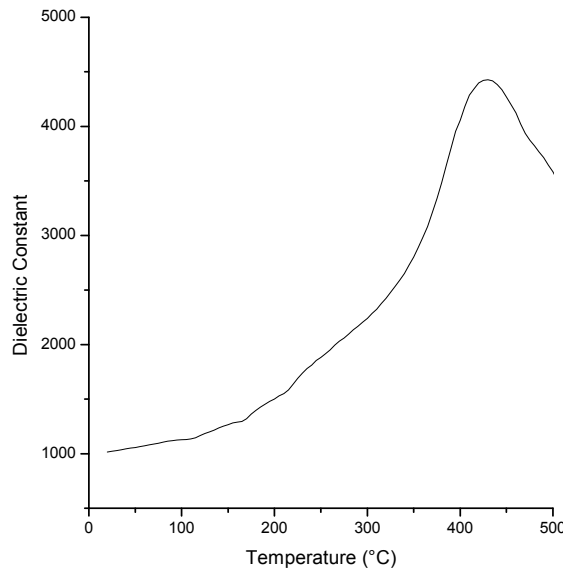


Fig. 4. Dielectric constant characterised by temperature for BNBT ceramics. The Curie temperature is reached at 425°C

The electromechanical coupling factors  $k_p$  and  $k_t$  were measure for some samples, the average values were:  $k_p=6.68$  and  $k_t=0.588$ .

Pyroelectric coefficient ( $P_i$ ) was found by the used of Byer and Roundy method, the ceramic was placed into a programmable oven and temperature was increased gradually, the electrodes were connected to a resistance and voltage drop on the resistance was measured with a high sensibility multimeter (Byer & Roundy, 1972); for pyroelectric detectors the relationship between pyroelectric coefficient and permittivity is calculated with the expression 6 (Liu et at., 1975)

$$\frac{p_i}{\sqrt{\epsilon}} \quad (6)$$

where  $p_i$  is the pyroelectric coefficient and  $\epsilon$  is the permittivity, for many pyroelectric materials, the ratio  $P_i/\sqrt{\epsilon}$  tends to be constant and has a value of  $(3.0 \pm 1.0) \times 10^{-9} CK^{-1}cm^{-2}$  (Liu et al., 1975) and is an indicator of how good pyroelectric detector is the material, Table 1 shows permittivity, pyroelectric coefficient and this ratio for BNBT ceramic as well as BIT in order to compare it.

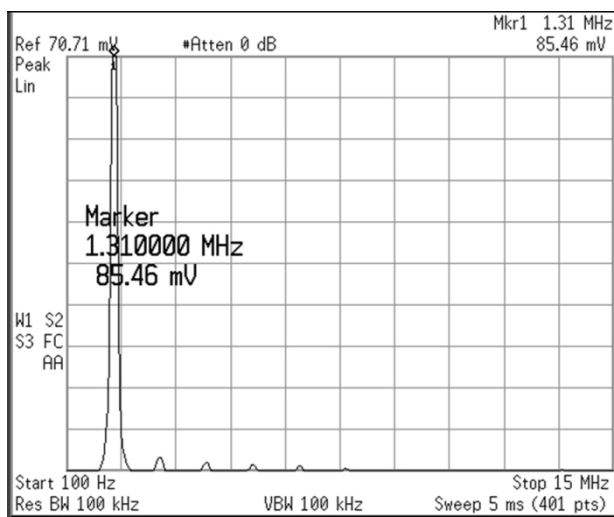


Fig. 5. Resonant frequency (1.31 MHz) of a piezoelectric ceramic with a 1.9 mm thickness in a logarithmic scale

Material	$\epsilon$	$P_i$ ( $10^{-9}CK^{-1}cm^{-2}$ )	$P_i/\sqrt{\epsilon}$ ( $10^{-9}CK^{-1}cm^{-2}$ )
BaTiO <sub>3</sub>	160	20	1.58
(Bi <sub>0.5</sub> Na <sub>0.5</sub> ) <sub>0.935</sub> Ba <sub>0.065</sub> TiO <sub>3</sub>	1185	49.6	1.44

Table 1. Room temperature dielectric constant, pyroelectric coefficient and the relationship for pyroelectric detectors of BNBT and BaTiO<sub>3</sub> (Lines & Glass, 1979; Suaste et al., 2008)

### 3.3 Optical characterization

In order to probe the ceramic response to the ultraviolet light, ceramic was submitted to a frequency modulated UV light, while the voltage response was monitoring. The experimental setup consist in a UV lamp with an illuminance of 1 lux and peaks at 365 nm, 404 nm and, 436 nm wave-length, a mechanical chopper modulates the light at a 22 Hz frequency and this modulated light was coupled to the ceramic by the use of an optic fiber to one side with electrical transparent contact made with indium oxide, by the use of a tuned amplifier and oscilloscope ceramic signal was obtained, experimental setup is show in Fig 6.

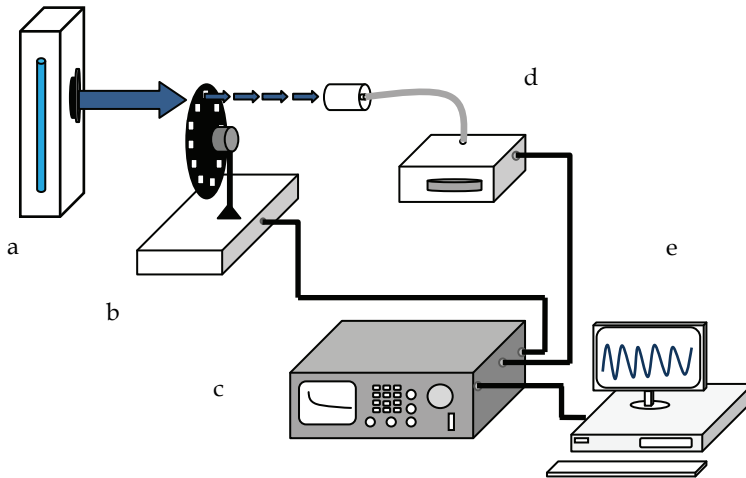


Fig. 6. Experimental setup used to obtain ceramic response to UV light at different temperatures, a) UV lamp, b) chopper, c) tuned amplifier, d) BNBT ceramic, e) personal computer

Photovoltaic BNBT ceramic response when is stimulated with visible light was found (Suaste & Gonzalez, 2009), by the ceramic stimulation with near UV light it was probed that ceramic presents electrical response to near UV light range as Fig 7 shows.

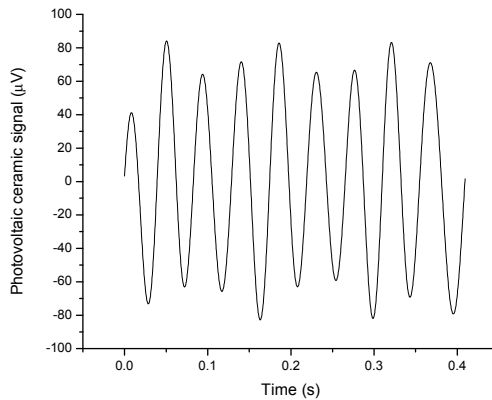


Fig. 7. Photovoltaic ceramic signal under near UV light stimulation

### 3.4 Thermal characterization

It is well known that thermal diffusivity is a physical quantity extremely sensitive to the composition and structure of materials (Rosencwaig, 1980; Calderon et al., 1997), and also depends on the processing conditions, is why it was done a measure of this physical quantity as well as thermal effusivity.

The measurements of thermal characteristics were performed using the open photoacoustic cell (OPC) (Marquezini et al., 1991; Cruz et al., 1996) and inverse photopyroelectric (IPPE) techniques (Caerels et al., 1998). The experimental setup employed to obtain the sample thermal diffusivity ( $\alpha$ ) consisted of 100mW argon (Ar) laser whose light beam was mechanically modulated with a chopper and focused into the sample as shown in Fig 8. The sample (e) was fixed with vacuum grease (f) upon the inlet of an electret microphone formed by g-j sections as shown. The microphone output signal was amplified by a lock-in amplifier (c) and the amplitude and phase were measured as function of light modulation frequency.

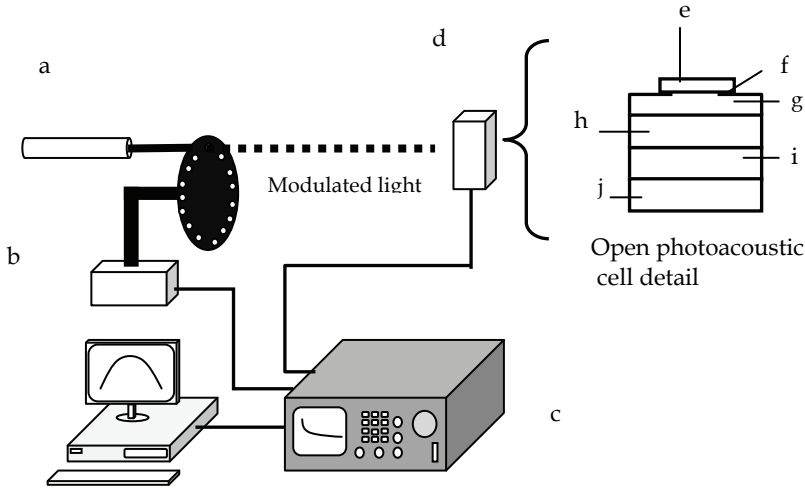


Fig. 8. OPC experimental setup a) Laser, b) chopper, c) lock-in amplifier, d) open photoacoustic cell, e) ceramic sample, f) vacuum grease, g) photoacoustic chamber, h) metalized electret diaphragm, i) air gap, j) metallic back plate

The theoretical expression (7) for the OPC in the heat transmission configuration, for optically opaque and thermally thick samples (i.e.  $l_s a_s \gg 1$ , where  $l_s$  is the sample thickness and  $a_s = \sqrt{\pi f / \alpha_s}$ ), used to fit the experimental values is (Marquezini et al., 1991):

$$V_{OPC} = V_0 \frac{j\omega RC}{1 + j\omega RC} \frac{I_0 \exp(-l_s \sigma_s) \exp(j\omega t)}{T_0 l_g \sigma_g k_s \sigma_s} \quad (7)$$

Where  $V_{OPC}$  is the OPC voltage obtained from the electret microphone,  $RC$  is the time constant of the microphone,  $l_s$  is the sample thickness,  $\omega$  is the modulation frequency in  $rad/s$ ,  $\sigma_i = (i + j)\sqrt{\pi f / \alpha_i}$ , with  $j = \sqrt{-1}$  and  $\alpha_i$  is the thermal diffusivity of medium  $i$ , with  $i=g, s$  (gas and sample respectively).

In order to obtain the thermal effusivity the experimental setup showed in Fig 9 was used which consists of a Helium-Neon (He-Ne) laser whose light beam was modulated by an acousto-optic modulator. The sample was fixed with thermal grease upon the pyroelectric detector. The pyroelectric signal was amplified with a lock-in amplifier and the amplitude and phase were measured as a function of  $f$ .

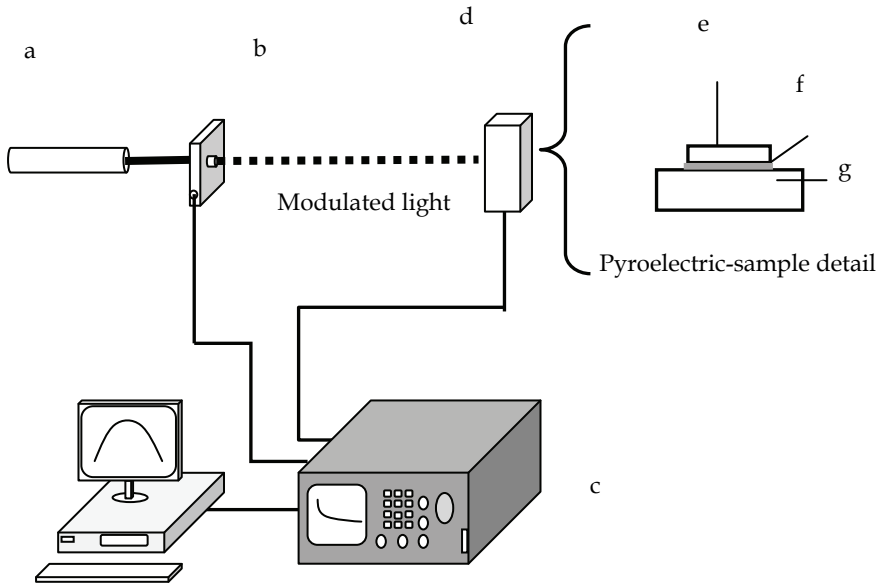


Fig. 9. Experimental setup used to obtain the IPPE signal a) Laser, b) acousto-optic modulator, c) pyroelectric-sample, d) lock-in amplifier, e) sample, f) thermal grease, g) pyroelectric sensor

For the IPPE geometry, when is assumed a thermally thick sample, the theoretical expression (8) used to fit the experimental data is (Glorieux & Thoen, 1998):

$$\theta(\omega) = \frac{(1 - e^{\sigma_p l_p})(1 + b) + (e^{-\sigma_p l_p} - 1)(1 - b)}{(1 + b)^2 e^{\sigma_p l_p} - (1 - b)^2 e^{-\sigma_p l_p}} \quad (8)$$

Where  $\theta(\omega)$  is the pyroelectric detector output signal  $l_p$  is the pyroelectric thickness,  $b = e_s/e_p$  with  $e_s$  and  $e_p$ , the thermal effusivities for sample and pyroelectric respectively.

Substances with high thermal diffusivity rapidly adjust their temperature to that of their surroundings because they conduct heat quickly in comparison to their volumetric heat capacity that means that do not require much energy from their surroundings to reach thermal equilibrium (Eckert, 1987), materials with high thermal diffusivity are suitable to be use in the pyroelectric detectors, table 2 shows thermal diffusivity and thermal effusivity values for BNBT ceramics as well as BIT thermal values for comparison porpoises (He Yi, 2004; Flores et al., 2008).

Material	$\alpha$ (cm <sup>2</sup> s <sup>-1</sup> )	$e$ (Ws <sup>1/2</sup> cm <sup>-1</sup> K <sup>-1</sup> )
BaTiO <sub>3</sub>	0.0103	0.2623
(Bi <sub>0.5</sub> Na <sub>0.5</sub> ) <sub>0.935</sub> Ba <sub>0.065</sub> TiO <sub>3</sub>	0.0154	0.277

Table 2. Room temperature thermal difussivity ( $\alpha$ ) and thermal effusivity ( $e$ ) of BNBT and BaTiO<sub>3</sub> ceramic materials

#### 4. Ultrasound application

An array of eight ultrasonic transducers was made in octagon form in order to be able for scan, from different ways, the object under study. The ultrasonic chamber design is as follows: a dielectric layer is placed at the top of the transducer, next is the ceramic with its respective electric contact immediately other ceramic without poling is using as backing material finally the transducer cover is put, Fig 10 shows a octagon schematic and a ultrasonic transducer detail, this design was repeated in everyone of the sides of the octagon. The distance between transducers is 120mm.

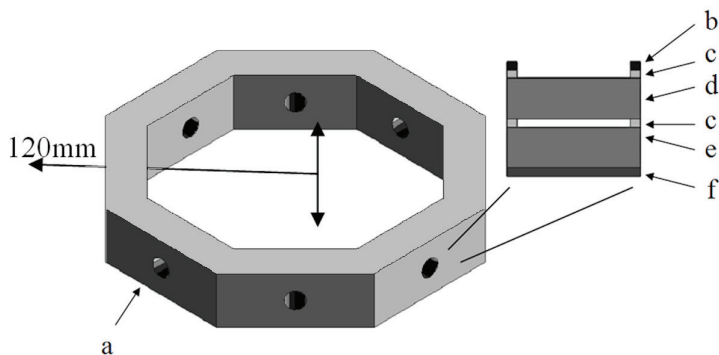


Fig. 10. Ultrasonic octagon schematic representation and ultrasonic transducer detail, a) ultrasonic transducer, b) isolating material, c) electrode, d) Piezoelectric ceramic, e) ceramic as backing, f) cover

A control circuit was design in order to get a electrical signal for be applied to the ceramic, this circuit has three parts: short pulses generator made with a microcontroller, a preamplifier and a power amplifier; microcontroller provides a pulses train with eight pulses and 5V amplitude, the preamplifier increases this signal to 12V amplitude and finally, the power amplifier give us a signal with 160V amplitude, Fig 11 shows circuit control schematic diagram.

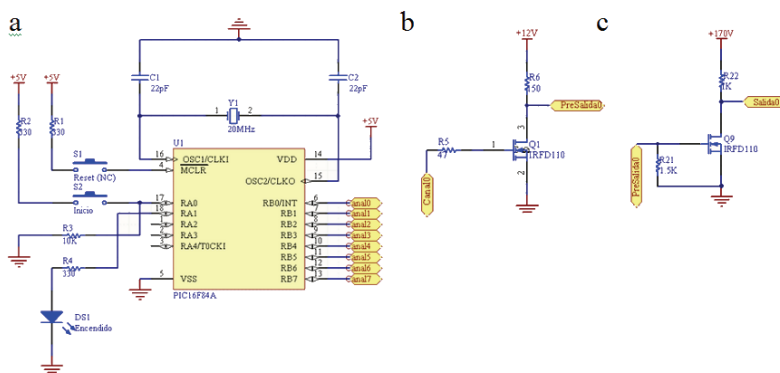


Fig. 11. Schematic design of circuit control, a) microcontroller, b) preamplifier, and c) power amplifier



Function probes were made by applying a pulse train signal with amplitude of 160 V peak to peak and 555 kHz of frequency, (as Fig 12 shown); to one of the transducers (Tx) while monitoring the response by other ceramic of the array (Rx). The transmission medium was air, water, iron, and human leg.

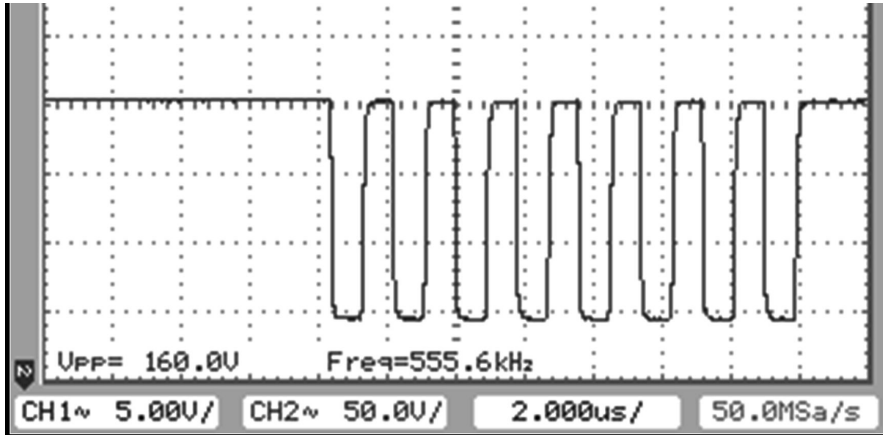


Fig. 12. Excitation signal applied to the piezoelectric ceramic

An aluminum transducer was made following the design showed in Fig 10, the final transducer is illustrated in Fig 13, at left is possible to see the complete transducer, at right a transducer detail in which is possible to see electrical contacts, acoustic isolation and spring to maintain all components in its respective place.

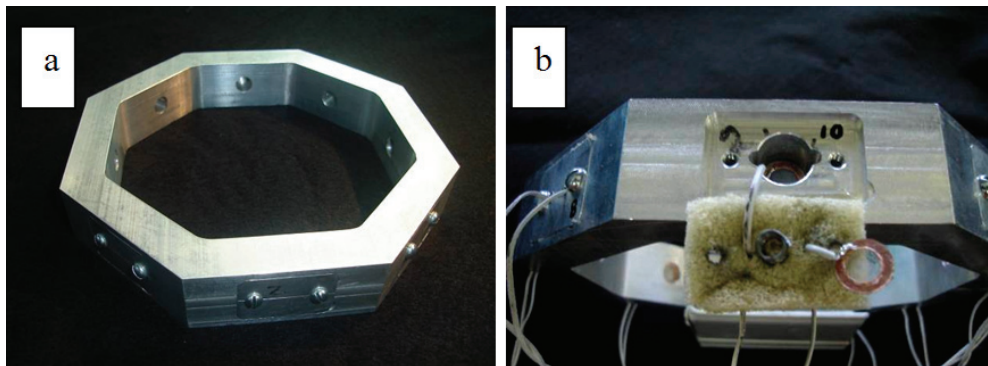


Fig. 13. a) Octagon for the ceramics and b) ultrasound transducer detail

Several materials were occupied to fill the transducer cavity in order to probe the ceramic emission and reception when the ultrasonic signal pass thought mediums with different densities, Fig 14 shows the experimental setup for ultrasound transmission in which is possible to see the octagon containing jelly while ultrasound pulse is applied.

Table 3 shows amplitude signals in an octagon array when a ceramic acts as emitter, and other ceramic in the opposite side acts as receiver, the array was filled with

different propagation mediums, table also shows medium density as well as acoustic impedance.

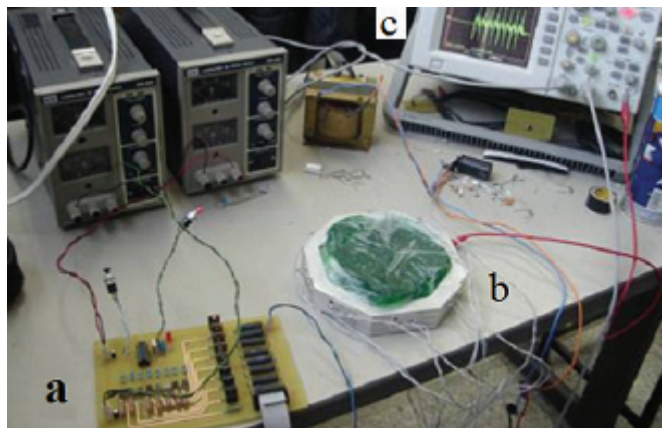


Fig. 14. Experimental setup use for ultrasound transmission, a) circuit control, b) octagon containing jelly and, c) signal obtained

Transmission medium	Signal Amplitude (V)	Density (kg/m <sup>3</sup> )	Acoustic Impedance (kg/m <sup>2</sup> s)
Air	1.54	1.3	446
Water	1.8	1000	1.493x10 <sup>6</sup>
Iron	1.2	1380	2.036x10 <sup>6</sup>
Human Leg	0.8	1070	1.62 x10 <sup>6</sup>

Table 3. Signal amplitude obtained with different transmission medium

The transmitter was excited with a 160 V p-p signal and opposite side ceramic was used as receiver, different propagation mediums were placed filling the octagonal array, differences among signals gotten can be shown in Fig 15, attenuation in the received signal give us an idea of the density of propagation medium, it can be seen that amplitude and signal form are different. This is useful at the processing signal.

Signal showed in Fig 15 were digital processed and its spectral content were obtained as shown in Fig 16, spectra by each transmission medium was obtained by get the FFT of signals received. Differences in spectral content are due to medium scattering properties, for a solid and homogeneous transmission medium as iron the frequency spectrum contains only frequency components near to the excitation frequency that are reflected as one principal lobe in its spectrum as Fig 16c shows, for those materials with high scatter properties (human leg in our case), spectrum has more frequencies which can be seen as many peaks in frequency spectrum, as in Fig 16d case.

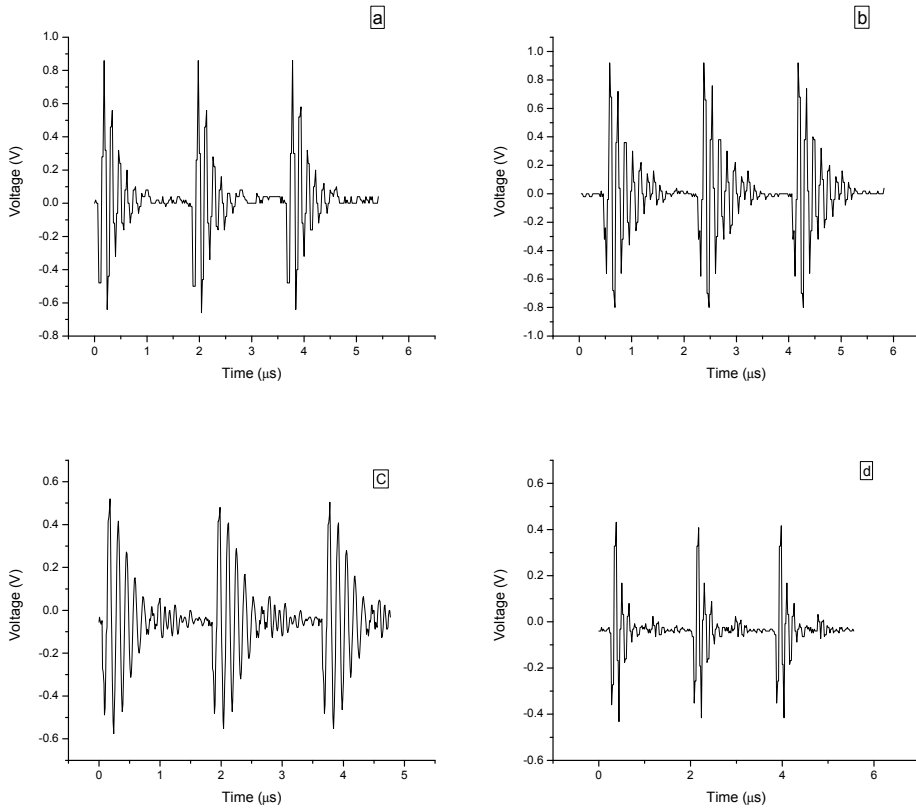


Fig. 15. Signals from octagon with different transmission medium, a) air, b) water, c) iron, and d) leg

#### 4. Conclusions

Ceramics with formulation  $(\text{Bi}_{0.5}\text{Na}_{0.5})_{0.935}\text{Ba}_{0.065}\text{TiO}_3$  were obtained, electrical, thermal and optical characterization was made, a transducer based on this material was design and an application on ultrasound field was proposed. The ceramic properties were measured in order to characterize the piezoelectric ceramic.

SEM micrographs join with ceramic density revels compact structure that makes this ceramic suitable for develop ultrasound transducers and piezoelectric devices. This ceramic presents similar characteristics, as high  $T_c$  425°C, high resonance frequency, that PZT shows, so it is an excellent candidate to substitute those ceramics made with lead, thermal properties are similar to BIT, XRD pattern is in agreement with the literature.

It was probed that ceramic presents electrical response when it is stimulated with light with length wave ranging from near UV to visible light, further probes need to be made to determine if this type of ceramics not only have electrical response under the stimulation of near UV but also in far UV.

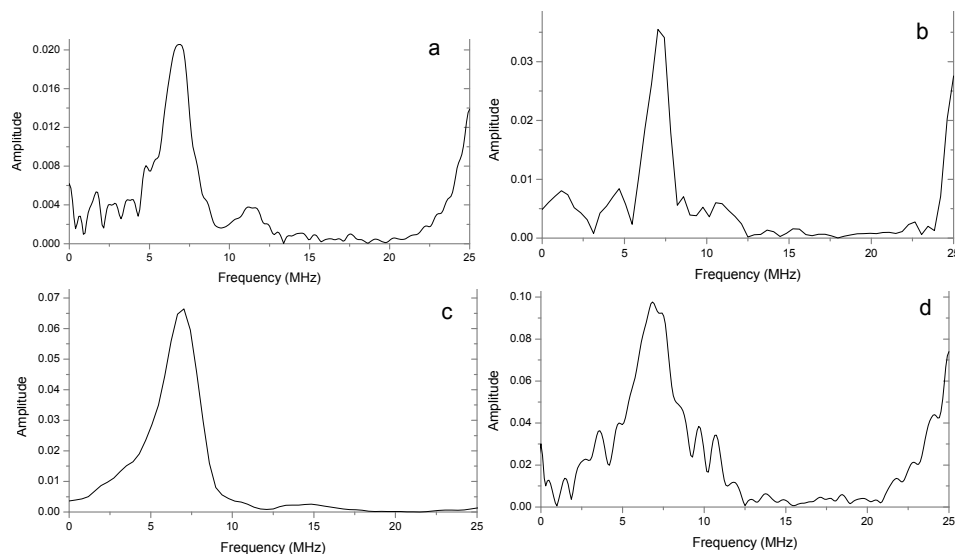


Fig. 16. Frequency spectrums obtained from signals received by Rx with different transmission medium, a) air, b) water, c) iron, and d) leg

Signals by the ceramic transducer acting as transmitter and receiver were obtained and differences in amplitude and form were found this is useful at the processing signal moment. Amplitude signals were in 0.8 and 2 V peak to peak range, this make easier detection and signal processing and make possible the use of this ceramic in pulse-echo mode A detection.

Since iron acoustic impedance is similar that Tx, coupling impedance is good as its frequency spectra shows, whereas frequency spectra is different for each transmission medium that means an advantage for the image reconstruction.

This ceramic kind avoid environment contamination by the lead use and this first probes show its response in an ultrasound application.

For further work, some other electric and thermal characteristics of this material will be study in order to make a full characterization of BNBT ceramic. Also, the relaxor properties and its effect on the target application are going to be investigated.

## 5. References

- Buhrer C. F. (1962). Some properties of bismuth perovskites, *Journal of Chemical Physics* 36, 798-803, 0021-9606
- Byer R. L., Roundy C. B. (1972). Pyroelectric coefficient direct measurement technique and application to a NSEC response time detector, *IEEE Trans sonics & ultrasound*, 19, 333-338, 0018-9537
- Caerels J., Glorieux C., and Thoen J. (1998). Absolute values of specific heat capacity and thermal conductivity of liquids from different modes of operation of a simple photopyroelectric setup, *review of scientific instruments*, 69(6), 2452-2458, 10897623

- Calderon A., Alvarado Gil J. J., Gurevich Y. G., Cruz Orea A., Delgadillo I., Vargas H., Miranda L. C. M. (1997). Photothermal Characterization of Electrochemical Etching Processed n-Type Porous Silicon, *Physics Review Letters*, 79, 5022 – 5025, 0031-9007
- Cruz-Orea A., Delgadillo I., Vargas H., Pichardo J. L., Alvarado-Gil J. J., Miranda L. C. M. (1996). On the Use of the Photoacoustic Technique for the Measurements of the Thermomechanical Properties of Semiconductor Two-Layers Systems, *Solid State Communications*, 100(12), 855-859, 0038-1098
- Eckert E. R. G. (1987). *Analysis of heat and mass transfer*, Hemisphere, Pub. Corp., 0070189250
- Efimovich I. (1964). *Ultrasound physical, chemical, and biological effects*, Consultants Bureau, New York
- Flores-Cuautle J. J. A., Cruz-Orea A., and Suaste-Gomez E. (2008). Determination of Thermal Diffusivity and Thermal Effusivity of the  $(\text{Bi}_{0.5}\text{Na}_{0.5})_{0.935}\text{Ba}_{0.065}\text{TiO}_3$  Ferroelectric Ceramics by Photothermal Techniques, *Ferroelectric Letters*, 35, 136-143, 0731-5171
- He Yi (2004). Heat capacity, thermal conductivity, and thermal expansion of barium titanate-based ceramics, *Thermochimica acta*, 419, 135-141, 0040-6031
- IRE Standard on piezoelectric crystals: Measurements of piezoelectric ceramics. 1961. *IRE Proceedings*, 1161-1169
- Jaeger R E and Egerton L. (1962). Hot Pressing of Potassium-Sodium Niobates. *Journal of American Ceramics Society*, 962, 45, 209-213, 1551-2916
- Jaffe B., Cook W. R., Jaffe H. (1971). *Piezoelectric Ceramics*, Academic Press, 1878907107, London
- Lines M. E., and Glass A. M. (1979). *Principles and applications of ferroelectrics and related materials*, Clarendon Press, 0-19-852003-4, Oxford
- Liu S. T., Zook J. D., and Long D. (1975). Relationships between pyroelectric and ferroelectric parameters, *Ferroelectrics*, 9, 39-43, 0015-0193
- Marquezini M. V., Cella N., Manzanares A. M., Vargas H., and Miranda L. C. M., (1991). Open photoacoustic cell spectroscopy, *Measurement Science and Technology*, 2. 396–401, 0957-0233
- Onoe M., Thiersen H. F. (1963). Shift in the location of resonance frequencies caused by large electromechanical coupling in thickness-mode resonator, *Journal of acoustical society of America*, 35(1), 0001-4966
- Rajeev Ranjan R., and Dwiwedi A., (2005). Structure and dielectric properties of  $(\text{Na}_{0.50}\text{Bi}_{0.50})_{1-x}\text{Ba}_x\text{TiO}_3$ :  $0 \leq x \leq 0.10$ . *Solid State Communications*, 135(6), 394–399, 0038-1098
- Rodríguez-Ruiz R., Gonzalez-Ballesteros R., Flores-Cuautle J. J. A., and Suaste-Gomez E. (2008). Determination of the Pyroelectric Coefficient of the  $(\text{Bi}_{0.5}\text{Na}_{0.5})_{0.935}\text{Ba}_{0.065}\text{TiO}_3$ , *Ferroelectrics* 368, 216-223, 0015-0193
- Rosencwaig A. (1980). *Photoacoustic and Photoacoustic spectroscopy*, John Wiley & sons Inc., 0894644505, New York
- Sasaki A., Chiba T., Mamiya Y., and Otsuki E. (1999). Dielectric and Piezoelectric Properties of  $(\text{Bi}_{0.5}\text{Na}_{0.5})\text{TiO}_3$ – $(\text{Bi}_{0.5}\text{K}_{0.5})\text{TiO}_3$  Systems, *Japan Journal of Applied Physics*, 38(9B), 5564–5567, 0021-4922
- Smollenky G. A., Isupov V. A., Agranovkaya A. I., and Krainik N. N. (1961). New Ferroelectrics of complex composition. *Soviet Physics Solid State*, 2, 2651-2654, 0038-5654

- Suaste-Gómez E. & González-Moran C. O. (2009). Photovoltaic Effect of Lead-Free Piezoelectric Ceramics,  $(\text{Bi}_{0.5}\text{Na}_{0.5})_{0.935}\text{Ba}_{0.065}\text{TiO}_3$  and  $\text{Pb}_{0.88}(\text{Ln})_{0.08}\text{Ti}_{0.98}\text{Mn}_{0.02}\text{O}_3$  (Ln = La, Eu), *Ferroelectrics*, 386, 70-76, 0015-0193
- Takenaka T., Maruyama K. I., and Sakata K. (1991).  $(\text{Bi}_{0.5}\text{Na}_{0.5})\text{TiO}_3$ - $\text{BaTiO}_3$  System for Lead-Free Piezoelectric Ceramic, *Japan Journal of Applied Physics* 30(9B), 2236-2239, 0021-4922
- Takenaka T., Sakata K., and Toda K. (1989). Acoustic Wave Characteristics of Lead-Free  $(\text{Bi}_{1/2}\text{Na}_{1/2})_{0.99}\text{Ca}_{0.01}\text{TiO}_3$  Piezoelectric Ceramic, *Japan Journal of Applied Physics* 28(28-2), 59-62, 0021-4922
- Uchino K. (2000). *Ferroelectric Devices*, Marcel Dekker, Inc., New York, United States
- Weihua Liu, Qing Xu, Wen Chen, Min Chen and Bokhee Kim (2008). Structure and electrical properties of  $(\text{Na}_{0.5}\text{Bi}_{0.5})_{0.94}\text{Ba}_{0.06}\text{TiO}_3$  ceramic with 0.5 wt% of MnO, *Journal of Wuhan University of Technology-Mater. Sci. Ed.* 23(4), 499-502, 1000-2413

## **Part 2**

### **Topics in Characterization and Mechanical Properties of Conventional and Advanced Ceramic Materials**





# Characterization of the Firing Steps and Phases Formed in Mg-Zr-Containing Refractory Dolomitic Materials

Araceli Lavat, María Cristina Grasselli and Eugenia Giuliodori Lovecchio  
*Facultad de Ingeniería, U.N.C.P.B.A.  
Argentina*

## 1. Introduction

The production of cement clinker is one of the most important industrial processes at world scale. Many technological innovations have been developed in order to increase the production at a lower cost, having in mind that the materials are exposed to severe operational conditions. The fabrication process of modern Portland clinker basically involves the firing at around 1500°C of limestone- $\text{CaCO}_3$  accompanied by silica- $\text{SiO}_2$  sources such as clays, sand, iron ore, shale, fly ashes and slags. The final product is a synthetic mineral called clinker which is basically formed by four crystalline phases: alite ( $\text{Ca}_3\text{SiO}_5$ ), belite ( $\beta\text{-Ca}_2\text{SiO}_4$ ), tricalcium aluminate ( $\text{Ca}_3\text{Al}_2\text{O}_6$ ) and ferrite ( $\text{Ca}_2(\text{Al}_x\text{Fe}_{2-x})_2\text{O}_5$ ); and other minor common components. Therefore the process involves aggressive basic environments and atmospheres, with high alkali and sulphur contents, that can strongly modify the microstructure and phase composition of the refractories of the kilns work zone (Kingery et al., 1976).

On the other hand, over the last decades the substitution of fossil fuels for alternative or industrial wastes; such as rubber, used tires, fly ashes, among others; has affected drastically the useful life and performance of the refractory bricks which coat the rotary kilns. Nowadays the burning zone of the kilns is exposed to alkali salts, chlorine, sulphur oxides, proceeding from industrial by products or hazardous products of animal origin, that enhance the corrosion process of the kilns refractory. This technological problem is the reason for focussing in the development of new suitable refractories. Improvements have been made by using higher purity raw materials; however there are economic limits and therefore other more sustainable alternatives are necessarily searched.

According to the modern tendencies in refractories the improvements in the thermal, chemical and mechanical properties of refractories are related to the optimization of the matrix, through the careful design of the mixture of the phases and the microstructural characteristics. As it is well known the performance of these structural parts is a function of the grain material, the nature of the bonding phase, and the distribution and shape of grains and pores. The increase in the proportion of "direct" bonding between refractory aggregate grains is very important. Furthermore the microstructural bonding is the main attribute for an adequate refractory matrix because it contributes to the resistance by the combination of rigidity and sufficient structural flexibility in order to prevent the formation of cracks and disintegration of the hot phase.

The periclase-MgO has excellent refractory properties due to the high melting point (2800°C), strongly basic, without being toxic and good corrosion resistance. All these characteristics have determined the importance of this material as refractory in the cement industry, during the last 65 years. Notwithstanding its use has been limited in rotary kilns due to low thermal shock resistance (Kingery et al., 1976).

In fired magnesia-based bricks, the low-melting bond phases are silicates which melting ranges are a function of the molar ratio of CaO to SiO<sub>2</sub>. Silicate-bonded magnesia chromite contain magnesia (MgO) and chromite ((Mg,Fe)(Cr,Al)<sub>2</sub>O<sub>4</sub>) grains with silicates at the grain boundaries. In this system the “direct” attachment of magnesia to chromite occurs without any interrupting film of silicate. These materials show a high resistance to a wide variety of slag and stability under vacuum at high temperature (Goto&Lee, 1995; Qotaibi et al., 1998). Although magnesia-chrome refractory has excellent thermo-mechanical characteristics, the use of these materials has been restrained in many countries due to environmental considerations and governmental regulations concerning the chrome-wastes that they generate and because of their dangerousness. The environmental protection is due to the carcinogenic issues related to hexavalent chromium (CrO<sub>4</sub><sup>2-</sup>). In view of these refractories wastes with more than 5 mg/l of Cr are forbidden in Europe and USA (Obregón et al., 2011).

Containing chrome-free materials in clinker kilns has been one of the most important challenges in cement industry. In some years later the addition of MgAl<sub>2</sub>O<sub>4</sub>-spinel to MgO was a possible alternative for refractories with a significant improvement of the thermo-mechanical properties of magnesia material. The spinel mixed oxide is very attractive as refractory material in heavy industries because it exhibits an unusual combination of properties: high melting point (2135°C), low thermal expansion, considerable hardness, high resistance to chemical attack, favourable chemical stability, and good thermal spalling (Domanski et al., 2004). Based on their properties these materials are being used for lining by glass, cement and siderurgy industries.

Magnesia-spinel refractories are usually prepared by sintering from high alumina cement and synthetic MgAl<sub>2</sub>O<sub>4</sub>-spinel. However, at present, the cost of the sintered and electrofused spinels has limited their applications. Consequently, in view of the irreplaceable character of such materials in the industry, alternative routes focused on the synthesis of this kind of refractories, by a more economic procedure, have been developed. In this way the preparation of calcium aluminate cements containing MgAl<sub>2</sub>O<sub>4</sub>-spinel using appropriate mixtures of active alumina and dolomite from Spain and Egypt has been reported (De Aza et al., 2003; Khalil et al., 2001). On the other hand, it has been described, recently, a similar way of synthesis using a dolomitic raw material from Argentina, and the  $\alpha$  and  $\gamma$  polymorphs of alumina, commercially available. (Lavat & Grasselli, 2007; Lavat et al., 2009). According to these results, independently of the type of alumina used, a mixed phase product consisting of spinel, as a major phase, accompanied by CaAl<sub>2</sub>O<sub>4</sub> (CA) and CaAl<sub>4</sub>O<sub>7</sub> (CA<sub>2</sub>), as secondary phases, was obtained. In addition, it was found that the formation of spinel phase at lower temperature is favoured by  $\gamma$ -Al<sub>2</sub>O<sub>3</sub>.

Although these materials are conventionally applied refractories, their composition is not adequate, from the thermodynamic point of view, as they would form liquids at low temperature ( $\approx$ 1400°C) when combined with the components of cement, as can be recognized from the phase equilibrium diagram in the system Al<sub>2</sub>O<sub>3</sub>-CaO-MgO-SiO<sub>2</sub> (Obregón et al., 2011). Furthermore, magnesia-spinel refractories present relatively low

corrosion resistance under the work conditions in the cement kilns, developing hot points. In the beginning of the corrosion process the liquid phase of clinker penetrates inside the substrates through open porosity and grain boundaries.

It is in this context that, in recent years, the calcium zirconate ( $\text{CaZrO}_3$ )-magnesium oxide ( $\text{MgO}$ ) composite material is an interesting alternative for replacing the  $\text{MgAl}_2\text{O}_4$ - $\text{MgO}$  system, which has become important for the development of cement industry, due to their enhanced refractoriness (Contreras et al., 2005). On the other hand  $\text{CaZrO}_3$ - $\text{MgO}$  is relevant, from the environmental point of view, because it is an ecological alternative for the development of cement industry, due to the fact that non dangerous wastes are generated. In particular  $\text{CaZrO}_3$  is a phase of high melting point ( $\approx 2340^\circ\text{C}$ ), without polymorphic transformations, which is compatible with  $\text{MgO}$  and Portland cement silicates, very resistant to the penetration of fluxes from the clinker (Obregón et al., 2011).

In this system, a so-called elastic direct bond between  $\text{MgO}$  and  $\text{CaZrO}_3$  has been reported. Due to this bonding formation and the high refractoriness of  $\text{CaZrO}_3$ , the  $\text{MgO}$ - $\text{CaZrO}_3$  composite materials are characterized by a high hot mechanical resistance and an excellent corrosion resistance against alkaline, earth alkaline oxides and basic slag (Serena et al., 2004). Moreover from the analysis of the *post-mortem* bricks conformed from the above mentioned materials, it was demonstrated a higher corrosion resistance than in  $\text{MgO}$ -chrome or  $\text{MgO}$ -spinel refractories (Rodríguez-Galicia et al., 2007).

On the other hand,  $\text{MgO}$ - $\text{CaZrO}_3$  composite refractories also can be synthesized from low cost raw materials, as dolomite, by mixing this mineral with the adequate stoichiometric amount of commercial zirconium sources, using a conventional solid-state reaction (Serena et al., 2005; Suzuki et al., 2000). Dolomite ores are available around the world and Zr occurs widely over the earth crust, but not in very concentrated deposits; as the major minerals are baddeleyite- $\text{ZrO}_2$  and zircon-  $\text{ZrSiO}_4$ . Undoubtedly, this seems an attractive route for the production at low cost of the Mg-Zr-based high temperature structural material.

Considering that the most important dolomite mineral resources in Argentina are located in Olavarría District, close to cement plants, and in order to advance in the feasibility of application of these potentially useful raw materials, our investigation has been extended to the preparation of  $\text{MgO}$ - $\text{CaZrO}_3$  refractories for the cement industry.

In order to establish the most adequate synthesis condition for the composite refractory materials, two batches, containing commercial grade zirconia- $\text{ZrO}_2$  and zircon- $\text{ZrSiO}_4$ , labeled D-Z and D-ZS, respectively, with the appropriate amount of the dolomitic ore (D), were prepared. The thermal and structural changes which take place during the firing of the batches up to  $1400^\circ\text{C}$  were studied by the combination of diffractometric and infrared spectroscopy data, at the most remarkable reaction steps. The microstructures of the final products of each specimen were also analyzed.

## 2. Experimental procedure

### 2.1 Materials characterization

The starting materials employed in this investigation were a commercially available zirconia (CF-Plus, Z-Tech) and industrial grade zircon (Kreutzonit), which were mixed with the adequate molar ratio of a dolomitic mineral ore supplied by Polysan S.A. Company (Polysan M. R., Sierras Bayas, Bs. As., Argentina). A sieved dolomite fraction  $\leq 125\mu\text{m}$  was characterized from its chemical, mineralogical and grain size properties.

The chemical composition was determined by X-ray fluorescence wavelength dispersive technique. The automatic fusion with lithium tetraborate was applied as preparation sample method. Reference certificated materials were used for calibration.

The particle size analysis was determined by laser granulometry, in wet suspensions with isopropyl alcohol, using a Malvern-Mastersizer-S apparatus. The chemical composition, mean particle size "d" and specific surface area "S" results of samples are given in Table 1.

Composition	Raw Materials		
	Zirconia	Zircon	Dolomite
SiO <sub>2</sub>	0,90	33	6,56
ZrO <sub>2</sub>	96,7	64	-
Al <sub>2</sub> O <sub>3</sub>	0,20	-	1,47
Fe <sub>2</sub> O <sub>3</sub>	0,05	<0,10	1,63
TiO <sub>2</sub>	0,10	<0,15	0,11
P <sub>2</sub> O <sub>5</sub>	-	-	0,03
MnO	-	-	0,08
CaO	0,05	-	29,60
MgO	0,01	-	17,83
Na <sub>2</sub> O	0,05	-	<0,01
K <sub>2</sub> O	-	-	0,43
SO <sub>3</sub>	-	-	<0,01
HfO <sub>2</sub>	1,90	2,5	-
Y <sub>2</sub> O <sub>3</sub>	0,15	-	-
U	0,025	-	-
Th	0,01	-	-
L.O.I. 1000 °C	-	-	42,07
d (µm)	13,00	1,61	24,27
S (m <sup>2</sup> /g)	31,7	11,1	2,4
L.O.I.: Loss on ignition			

Table 1. Chemical composition (in oxides, wt %. L.I., loss on ignition) and textural properties

The surface area was determined by the BET method through the N<sub>2</sub> adsorption technique at 77 K, using a Quantachrome Nova 1200e pore size and surface area analyzer.

Finely ground polycrystalline samples were mineralogical analysed by FTIR vibrational spectroscopy and X-ray diffraction. The XRD measurements were carried out with an automated PW model 3710 Philips diffractometer, with graphite monochromated Cu K $\alpha$  radiation. Phase identification analysis was carried out by comparing the respective powder X-ray diffraction patterns with standard database stated by JCPDF and the bibliography information available in the literature. Table 2 shows the PDF records for every material under study together with the formula, name, symbol and main reflections used in this work.

PDF N°	Formula, name	Symbol	d ( Å )
36-0426	CaMg(CO <sub>3</sub> ) <sub>2</sub> , Dolomite	D	2,8880
05-0586	CaCO <sub>3</sub> , Calcite	C	3,0350
33-1161	SiO <sub>2</sub> , Quartz	Q	3,3420
37-1484	ZrO <sub>2</sub> , Monoclinic Zirconia	m-Z, m- ZrO <sub>2</sub>	3,1640
34-0104	HfO <sub>2</sub> , Hafnium oxide	m-HfO <sub>2</sub>	3,1470
37-1497	CaO, Lime	CaO	2,4058
44-1481	Ca(OH) <sub>2</sub> , Portlandite	CH	2,6270
04-0829	MgO, Periclase	M	2,1060
35-0790	CaZrO <sub>3</sub> , Calcium zirconate	CZ	2,8340
36-1473	CaHfO <sub>3</sub> , Ca, Hf oxide	CHf	2,8230
26-0341	(Zr,Ca)O <sub>2</sub> (ss), (ss:solid solution) stabilized zirconia	Z*	2,9610
21-1152	MgAl <sub>2</sub> O <sub>4</sub> , Spinel	E	2,4370
33-0302	Ca <sub>2</sub> SiO <sub>4</sub> , Larnite	β-C <sub>2</sub> S	2,7830
06-0266	ZrSiO <sub>4</sub> , Zircon	ZS	3,3020
42-1164	ZrO <sub>2</sub> , Tetragonal Zirconia	t-Z, t- ZrO <sub>2</sub>	2,9950
31-0298	Ca <sub>2</sub> SiO <sub>4</sub> , Calcium silicate	CS	2,7960
35-0591	Ca <sub>3</sub> Mg(SiO <sub>4</sub> ) <sub>2</sub> ; Ca,Mg Silicate	CMS	2,6865
41-0185	Mg <sub>2</sub> Zr <sub>5</sub> O <sub>12</sub> ; Zr,Mg oxide	MZO	1,7850

Table 2. Nomenclature, PDF No. and principal diffraction lines of the phases under analysis

The FTIR spectra were measured using a Nicolet-Magna 550 FTIR instrument, with CsI optics applying the KBr “pellets” technique and software OMNIC 3.1. Spectra interpretation was based on published data and FTIR spectra of Minerals Library Software.

The microstructure of the materials was obtained by scanning electron microscopy (SEM) using a Microscope Jeol JSM-6460LV. The X-ray microanalysis was performed by an EDAX Genesis XM4 - Sys 60, equipped with an EDAX mod EDAM IV multichannel analyzer, with Zaffire Si(Li) detector and a ultra thin Be window and software EDAX Genesis versión 5.11

## 2.2 Samples preparation

Two batches of refractories, labelled D-Z and D-ZS; as already stated, were synthesized in view of the respective phase diagram. Firstly considering the ZrO<sub>2</sub>-MgO-CaO ternary system phase diagram (Serena et al., 2005), as well as the chemical composition of raw materials detailed in Table 1, equimolar mixtures of dolomite and zirconia were prepared in order to obtain the refractory material of nominal composition MgO-CaZrO<sub>3</sub>. After that, according to the ZrO<sub>2</sub>-MgO-CaO-SiO<sub>2</sub> quaternary system phase diagram (Rodríguez-Galicia et al., 2005), a mixture containing 78% dolomite with industrial zircon was also manufactured.

The mixtures were dry-homogenized. Half of them were submitted to conventional ceramic procedure by solid state reaction at high temperatures with intermediate grindings. The rest

was pressed at approximately 200 MPa and the “pellets” were thermally treated simultaneously with the powdered sample preparation. Although both alternatives were carried out for purposes of comparison, the latter procedure is more feasible at an industrial level. Firing was carried out in a muffle furnace under atmospheric condition.

To stabilize the ceramic bond, the materials were kept at intermediate temperatures for 1 hour and at the highest temperature for several hours. The samples treated at the various temperatures, in the thermal interval, were mineralogical characterized applying the same methodology as described for raw materials. Based on these results, the optimum temperatures for the in-situ generation of phases were established.

### 3. Results and discussion

#### 3.1 Raw materials characterization

According to the chemical analysis of raw materials given on Table 1, it may be seen that the major impurities of the dolomitic source under study are  $\text{SiO}_2$ ,  $\text{Fe}_2\text{O}_3$  and  $\text{K}_2\text{O}$ , bearing a higher  $\text{SiO}_2$  content than those used by other researchers which are around 0,02-0,5 weight % (De Aza et al., 2003; Khalil et al., 2001). The presence of these impurities is related to the geological origin of  $\text{CaMg}(\text{CO}_3)_2$  ores. The most important dolomite mineral resources in Argentina, comprises an igneous-metamorphic basement covered by Neoproterozoic sedimentary rocks. These dolostones are characterized by abundant dolomite and low proportions of calcite. Quartz, illite and feldspar are the most common impurities of carbonates fraction. Calcite cements are included in voids and veins and quartz generally is present as silt-sized clasts dispersed in the dolomite matrix, as well as multi-generational cement inside voids. Occasionally silica is present as fine chert (amorphous silica), which fills voids or replaces carbonate. The mineralogical composition estimated by XRD is: dolomite 75-95%, calcite 1-5%, quartz and chert 1-15%, clay minerals <2% and feldspar <1% (Gómez Peral, 2007).

The weight loss of around 40% is compatible with the release of gaseous  $\text{CO}_2$ . Meanwhile, the mean size particle of the dolomitic mineral, measured by laser granulometry, is  $24,27 \mu\text{m}$  and the surface area is  $2,4 \text{ m}^2/\text{g}$ .

On the other hand, the chemical composition of Zr-sources was also analyzed. In the case of zirconia, the main impurity  $\text{HfO}_2$  is normally present in this mineral due to the extremely difficult separation of Zr from Hf. The reason for this is the similarity between the crystal chemistry of Zr(IV) and Hf(IV) which ionic radios are identical. In the light of the chemical similarity between Zr and Hf which is well exemplified in their geochemistry, for Hf is found in nature in all zirconium minerals in the range of a fraction of a percentage of the Zr content (Cotton & Wilkinson, 1988). The amounts of the rest of the elements are negligible. The well-known mechanical and electronic properties of  $\text{ZrO}_2$ -materials based on total or partially stabilized cubic or tetragonal zirconia have led to their widespread use as structural materials, solid-state electrolytes, catalytic support, and thermal barrier coatings (Serena et al., 2005).

As can be seen, according to the chemical composition, commercial zircon is very pure. The impurities in natural zircon powder limit its applications, especially for high temperature uses (Popa et al., 2006). Notwithstanding the presence of a certain amount of Hf in zircon, as in zirconia, should not be unexpected.  $\text{ZrSiO}_4$  is commonly used in the pigment industry in the production of glazes and pigments due to their high thermal and chemical stability, as well as for its low thermal expansion coefficient and low thermal conductivity. Zircon sands

are widespread geological occurrence, as a common accessory mineral of igneous rocks and sediments. In technical applications is more advantageous in comparison with  $\text{ZrO}_2$  because this oxide is obtained by a complex and expensive process from zircon sands (Ozel & Turan, 2007).

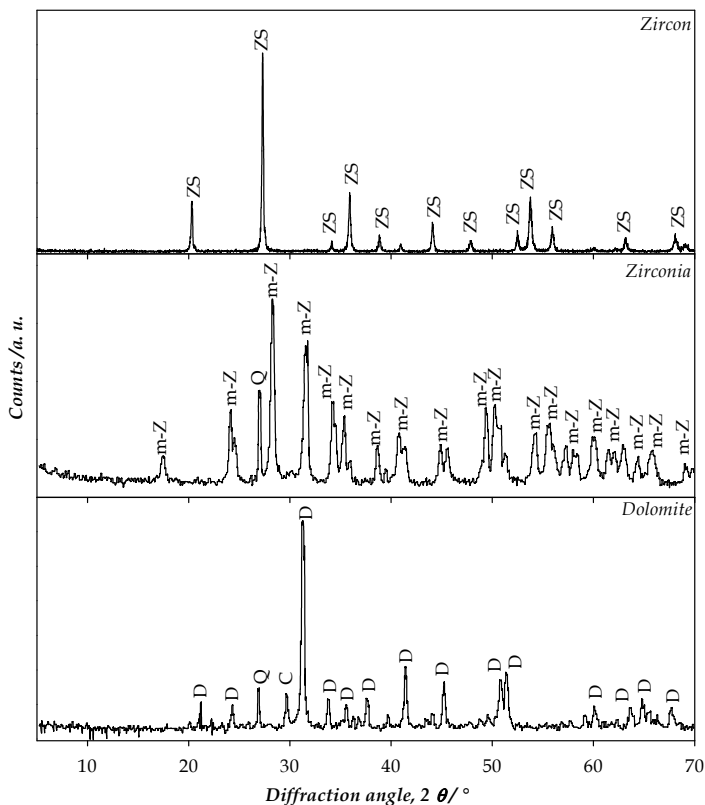


Fig. 1. Minerals characterization of raw materials, XRD patterns

Regarding the particle size and surface properties of both Zr materials, these display lower particle sizes and appreciable higher specific surface than natural dolomite, which should be beneficial for the reactivity of both solids.

In order to analyze the mineralogical composition, the XRD patterns of all the raw materials were registered. The diffractograms are depicted in Fig. 1. In addition, the PDF records for raw materials, as well as the files belonging to the rest of the phases under analysis, are detailed in Table 2, as already stated.

Based on this analysis, it is concluded that the dolomite sample also contains subordinate amounts of calcite (C) and quartz (Q) but in a lesser extent, in accordance with the chemical composition. Quartz is, of course, of almost universal occurrence in dolostones, at least in trace amounts, the enhanced intensity is due to an orientation effect.

In the case of zirconia it is mainly monoclinic zirconium oxide ( $\text{m-ZrO}_2$ ) and presents quartz as impurity. The quartz presence is consistent with the small amount of  $\text{SiO}_2$ , which was

determined by chemical analysis, in both raw materials, as detailed in Table 1. The presence of  $\text{HfO}_2$  could not be determined by DRX because its diffraction pattern is superimposed with the  $\text{m-ZrO}_2$  which possesses an identical crystal cell.

Regarding the XRD pattern of Zircon, the presence of  $\text{ZrSiO}_4$  as a pure phase, is confirmed, in accordance with the chemical analysis.

To complete the analysis of the mineral phases present in the raw material the measurement of the vibrational spectra was registered. The FTIR spectral patterns are shown in Fig.2.

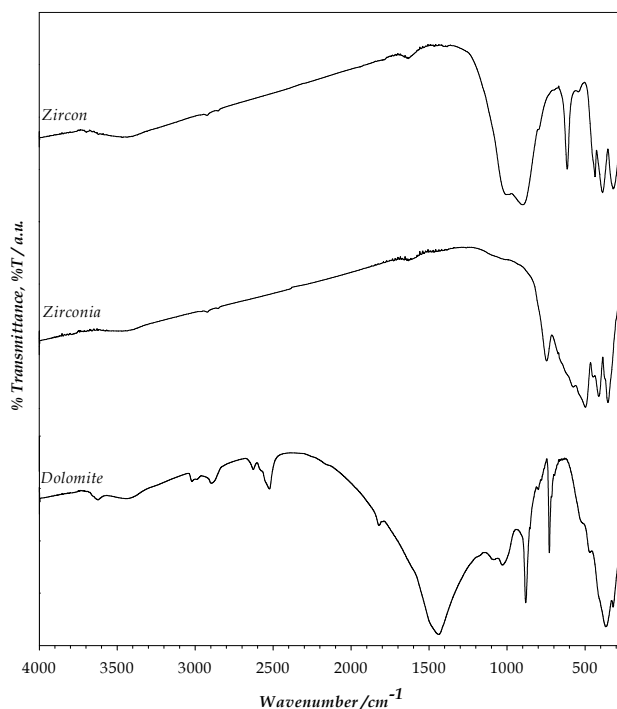


Fig. 2. FTIR of starting materials

Dolomite, which has a calcite-type structure, shows its overall bands among which the diagnostic ones are at 1443, 882 and 728  $\text{cm}^{-1}$  belonging to  $\text{CO}_3^{2-}$  anion, are present, as can be seen in Fig.2. The positions are shifted to higher frequency due to the smaller size of  $\text{Mg(II)}$  in comparison with  $\text{Ca(II)}$ . Despite the structural differences, calcite bands are not seen because they are located at similar frequencies as dolomite bands (1428, 878 and 714  $\text{cm}^{-1}$ ) and therefore overlapped with the broad bands of this predominant mineral. Although quartz is a minor constituent, it can clearly be identified by the bands located at 1144 and 1085  $\text{cm}^{-1}$ , which are attributed to  $\text{SiO}_4$  group vibrations (Wilson, 1987).

The zirconia spectrum, depicted in Fig.2, indicates the presence of isostructural  $\text{ZrO}_2$  and  $\text{HfO}_2$ , both having a monoclinic structure, with contributions to the bands attributed to Zr-O and Hf-O vibrations from the  $\text{ZrO}_7$  ( $\text{HfO}_7$ ) units. The six characteristic bands of zirconium oxide can be seen located at: 722, 574, 490, 409, 343 and 258  $\text{cm}^{-1}$ . A unique  $\text{HfO}_2$  band can be observed at 752  $\text{cm}^{-1}$ , the remaining bands (635, 600, 512, 410, 343, 324 and 255  $\text{cm}^{-1}$ )



belonging to this oxide are hidden behind those of zirconium oxide (Neumayer & Cartier, 2001). These features are in accordance to the low proportion of  $\text{HfO}_2$  present in the raw material, as already discussed.

The  $\text{SiO}_4$  group vibrations belonging to quartz are observed at 1144 and 1085  $\text{cm}^{-1}$ , as in dolomite. However, these are weak; corroborating that amount of quartz present in zirconia is lower than in dolomite, in accordance with the chemical analysis (see Table 1). The additional weak absorptions, centered in 3400  $\text{cm}^{-1}$ , 1630  $\text{cm}^{-1}$  and 1575  $\text{cm}^{-1}$  are assigned to O-H, H-O-H and M-OH (M is Zr or Hf) vibrations respectively, which are attributed to absorbed water to these metal oxides (Neumayer & Cartier, 2001).

Regarding the spectrum of zircon, it may be interpreted based on its structure which is formed by chains of alternating edge-sharing  $\text{SiO}_4$  tetrahedra and  $\text{ZrO}_8$  triangular dodecahedra, running parallel to the c-axis. The spectrum depicted in Fig. 2 exhibit the diagnostic bands of  $\text{ZrSiO}_4$ . The main infrared absorptions observed at 1005 and 900  $\text{cm}^{-1}$ , belong to Si-O stretching vibrations, with the deformational mode of  $\text{SiO}_4$  unit at 435 and 387  $\text{cm}^{-1}$ ; the sharp band observed at 613  $\text{cm}^{-1}$  are associated to Zr-O bonds of  $\text{ZrO}_8$  units (Ozel & Turan, 2007). In addition, the weak absorptions bands located at 3000-2900  $\text{cm}^{-1}$  and at 1630  $\text{cm}^{-1}$  are due to hydroxyl ion impurities in zircon and deformation of the HOH bonds, respectively (Dawson et al., 1971).

### 3.2 Evolution of the phases on heating, for D-Z specimens

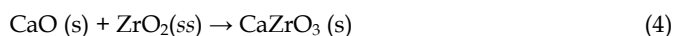
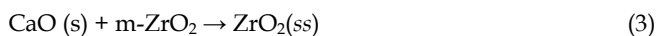
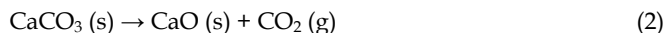
For the detailed analysis of the phase changes during the preparation of the D-Z refractory, in every thermal step; the relative intensity of the characteristic peaks of each crystalline compound expected to appear was measured, within the temperature range from ambient to 1400°C. The instrumental conditions were maintained constant in order to obtain the comparison of the same XRD characteristic lines by using “batch program” analysis in PC-APD software (version 3.6). With the same aim a standard procedure was adopted for the preparation of the test specimens as in other related works (Aras, 2004). The typical reflections selected to carry out the analysis are detailed in Table 2. The FTIR spectra measurements were carried out in order to study the structural changes and the formation of the new bonds during the reactions. The microstructure of the final product obtained was evaluated by SEM-EDX analysis.

#### 3.2.1 Evolution of the phases D-Z on heating by X-Ray diffraction

The XRD patterns belonging to the different heating temperatures selected to represent the phase evolution upon calcinations, for the batches labelled D-Z, after heating at 1000, 1150 and 1400°C, are shown in Fig.3.

From X-ray diffraction analysis of the most relevant reaction steps, it was possible to establish that no dolomite is detected after the calcination at 1000°C, in accordance with equation 1, whereas the peak of calcite persists, suggesting that equation 2 has not been completed. At the same time, the main peaks belonging to m- $\text{ZrO}_2$  are still present. The new phases resulting from the thermal decomposition of dolomite and subsequent reaction with zirconia, as  $\text{CaZrO}_3$  and  $\text{MgO}$ , were clearly detected, as well as the presence of zirconia, labeled  $\text{ZrO}_2(\text{ss})$ , with cubic structure. The typical diffraction lines of both zirconia polymorphs are distinguishable by XRD measurements, accurately, as can be seen from the data available in Table 2. This allows to confirm the formation of a solid solution of  $(\text{Zr,Ca})\text{O}_2$ , commonly called stabilized zirconia, by the solid state reaction between  $\text{CaO}$  and

m-ZrO<sub>2</sub>, with improved mechanical properties. In summary, these results allow affirming that, after the thermal treatment at 1000 °C, the following reactions have occurred:



Despite CaO peaks are absent, giving support to equations 3 and 4, the presence of free lime is discussed later, when FTIR results are analyzed. On the other hand the diffractions belonging to SiO<sub>2</sub>, as quartz, accompanying the dolomitic source, remained constant.

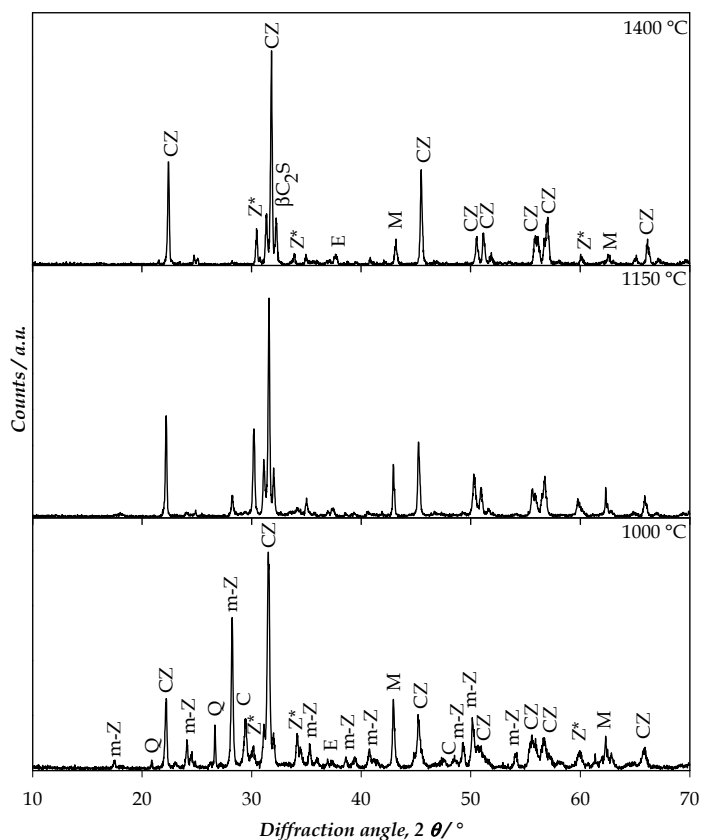
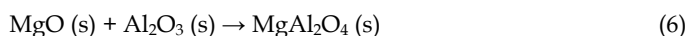
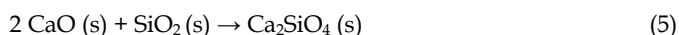


Fig. 3. XRD patterns of sample D-Z, at different firing temperatures

At 1150 °C, the main features observed in the patterns are that the diffraction lines from calcite and quartz disappeared, and instead some new lines belonging to dicalcium silicate,

$\text{Ca}_2\text{SiO}_4$ , labeled  $\beta\text{-C}_2\text{S}$ , and the spinel phase  $\text{MgAl}_2\text{O}_4$  appear, at this temperature. The presence of  $\beta\text{-C}_2\text{S}$  is attributed to the solid state reaction involving  $\text{SiO}_2$  from quartz, and  $\text{CaO}$  available, in accordance with equation 5. The formation of the mixed oxide  $\text{MgAl}_2\text{O}_4$ , belonging to the spinel structure, in a minor extent, is supported by the appearance of its main peak as a weak signal. This compound is a consequence of the reaction between free  $\text{MgO}$  and  $\text{Al}_2\text{O}_3$  (see equation 6), consistent with the low amount of aluminum oxide, determined by X-ray fluorescence in the raw material (see Table 1). Spinel formation was observed at the same temperature in the previous research, involving the reaction between the dolomitic resource and alumina, in the synthesis of  $\text{MgAl}_2\text{O}_4$ -spinel-containing refractory cements (Lavati & Grasselli, 2007; Lavati et al., 2010). Concerning the peaks belonging to  $\text{m-ZrO}_2$ , these remained but with considerable low intensity. According to these results the following reactions are proposed, after this thermal step:



When the temperature reaches  $1400^\circ\text{C}$ ,  $\text{m-ZrO}_2$  is not present and simultaneously all the phases formed by the preceding reactions (labeled as CZ, M,  $\text{ZrO}_2 \text{(ss)}$ , E and  $\beta\text{-C}_2\text{S}$  in Fig.3), are maintained with increased intensity.

Concerning the presence of a minor amount of  $\text{HfO}_2$  in zirconia, the XRD measurements do not recognize the formation of  $\text{CaHfO}_3$ , as the resulting compound from the reaction of available  $\text{CaO}$  and  $\text{HfO}_2$ , because the characteristic lines of this solid lay in the same diffraction angle value than the analogous Zr compound, due to the identical crystal sizes. The same consideration has been already reported (Zoz & Karaulov, 1991).

For more detailed information, the XRD main diffraction intensities of every component detected in the patterns is plotted against temperature as depicted in Fig. 4. When there is an overlap of the main peaks for two phases, the second reflection reported in Table 2 was also used. As can be seen in this figure, a sharp decrease is observed in dolomite peaks down to  $900^\circ\text{C}$  whereas the rest of the accompanying mineral, as calcite and quartz, as well as zirconia, decline more slowly until around  $1100^\circ\text{C}$  and the latter is observable down to  $1200^\circ\text{C}$ . These features account for an early temperature of reaction of dolomite and simultaneously the maintenance of zirconia in the original monoclinic structure, in this thermal range.

Regarding the phases formed upon firing, the growth of peak intensities of all the products,  $\text{CaZrO}_3$ ,  $\text{ZrO}_2 \text{(ss)}$ ,  $\text{MgO}$ ,  $\beta\text{-C}_2\text{S}$  and  $\text{MgAl}_2\text{O}_4$ , is observable over  $1100^\circ\text{C}$ . This indicates that the reactions proceed more straightforward over this temperature. Furthermore, as shown in the same figure, a sharp increase is observed in the XRD counts for all components around  $1150^\circ\text{C}$  and  $1300^\circ\text{C}$ , more markedly in the major components. These features could be attributed to many effects, such as degree of crystallinity, changes in the size of crystals, due to firing, and also with crystal preferential orientation. Nevertheless the general trends of the evolution of the all phases are similar and consequently it may be infer that the rate of formation of the products is similar. A resembling profile has been observed during the preparation of spinel-containing refractory cements, which shows a maximum assignable to the porosity and small grain size of the crystalline phases formed during the reaction (De Aza et al., 2003).

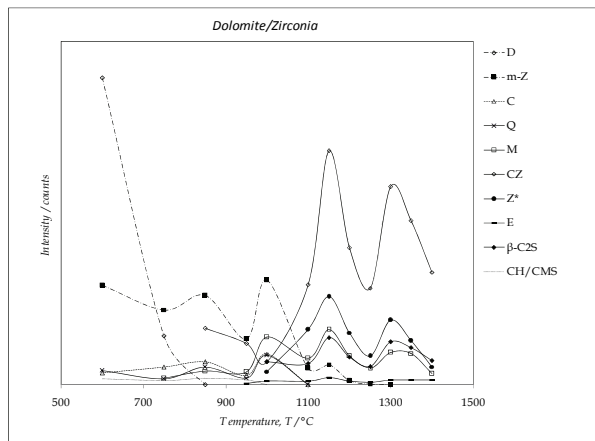


Fig. 4. Evolution of phases during firing for specimen D-Z

The amount of the major phase formed,  $\text{CaZrO}_3$ , ( $A_{CZ}$ , in percent), can be estimated from XRD measurements using the following expression, and nomenclature detailed in Table 2:

$$A_{CZ} = [I_{CZ} / (I_{CZ} + I_M + I_{Z^*} + I_{\beta\text{-C}_2\text{S}} + I_E)] \times 100 \quad (7)$$

Where  $I_i$  is the integrated intensity of the characteristic diffraction of each phase. A similar methodology was employed in another work (Domanski et al., 2004).

According to this semi-quantitative analysis the proportion of the major phase  $\text{CaZrO}_3$  in the final mixture, at  $1400^\circ\text{C}$ , is 66 %. Whereas the amounts of rest of the components, estimated by the same calculation, are:  $\text{ZrO}_2(\text{ss})$ , 10,5%;  $\text{MgO}$ , 6,6%;  $\beta\text{-C}_2\text{S}$ , 14% and  $\text{MgAl}_2\text{O}_4$ , 2,8%. As can be seen, the amount of  $\beta\text{-C}_2\text{S}$  is not negligible, in consistence with the relatively high content of  $\text{SiO}_2$  found in local dolomite, in comparison with the amount reported for the same mineral in other countries. However the global composition is suitable for refractory purposes. Finally, no vitreous components are observed in the material.

### 3.2.2 FTIR spectra analysis of specimen D-Z, during firing

The FTIR vibrational spectra depicted in Fig. 5 are suitable to complement XRD information in order to get a more accurate composition of phases at each thermal step during the synthesis of  $\text{MgO-CaZrO}_3$ -containing refractory material. The advantage of using IR spectra is the sensibility and that even amorphous materials can be identified.

According to Fig. 5, after the thermal step at  $950^\circ\text{C}$ , the significant bands located at  $1443$  y  $882\text{ cm}^{-1}$  due to the  $\text{CO}_3^{2-}$  anion, characteristic of dolomite, are observed (Wilson, 1987). It would be necessary to indicate that the characteristic diffraction line of dolomite could not be ascertained by XRD analysis, at this temperature, as already discussed. However, due to the higher sensibility of the spectroscopic technique, these bands are still observed.

In the spectrum of the sample treated  $1000^\circ\text{C}$ , the carbonate anion absorptions show a displacement to a lower frequency region, lying at  $1428$  and  $878\text{ cm}^{-1}$ , which are assignable to calcite. Calcite bands are persistent in the spectrum up to  $1150^\circ\text{C}$ . These results corroborate the calcite formation at  $1000^\circ\text{C}$ , detected from XRD analysis, as a result of the

partial decomposition of dolomite (see equation 1). In addition, according to this technique, the persistence of calcite is ascertained up to 1150°C.

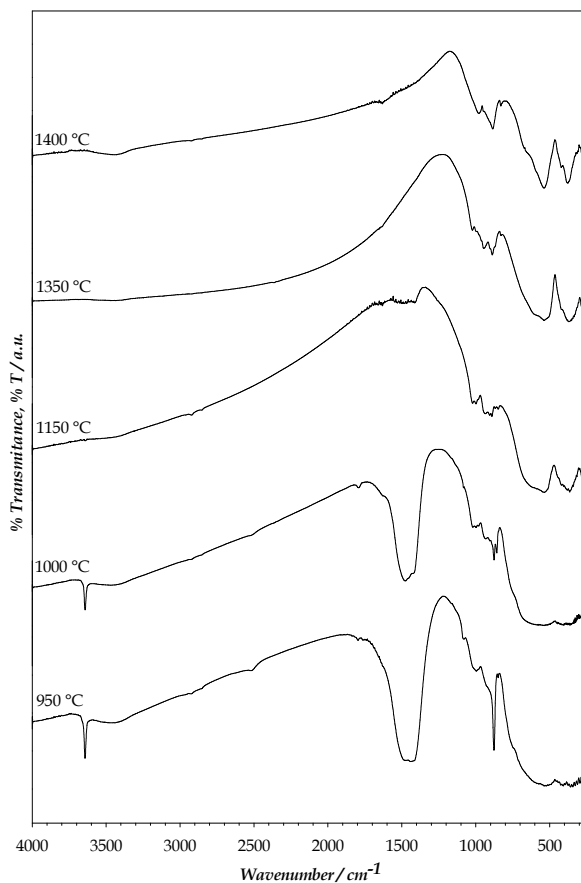


Fig. 5. FTIR spectra of D-Z specimens treated in the thermal range 950-1400 °C

At the same time, when the spectra of the samples fired over 750°C were analyzed, the presence of portlandite- $\text{Ca}(\text{OH})_2$ , could be ascertained by the sharp absorption located at 3643  $\text{cm}^{-1}$ , assigned to O-H stretching vibration belonging to calcium hydroxide. This band becomes weaker as temperature increases, until it disappears completely at 1000°C. This spectroscopic evidence is in agreement with the presence of free lime- $\text{CaO}$  (see equation 2), since this highly reactive oxide forms portlandite, as a consequence of its ease to react with the atmospheric humidity (Lavati & Grasselli, 2007). However, the characteristic XRD lines belonging to portlandite were not observed due to their superposition with the ones of the other compounds XRD diffractograms, especially with those of zirconia; or furthermore due to the poorly crystallized nature of this solid.

The  $\text{CaZrO}_3$  is an extremely ionic solid which belongs to the perovskite structure, with orthorhombic symmetry (Orera et al., 1998; Prasanth et al., 2008). The infrared active (IR)

modes are somewhat similar to that of the cubic perovskite. These modes can be described; in decreasing frequency order, as: Stretching of Ca-O ( $550\text{ cm}^{-1}$ ), stretching of Zr-O ( $400\text{ cm}^{-1}$ ) and stretching of Ca-Zr ( $150\text{ cm}^{-1}$ ). Consequently, the signals located at  $550$  and  $400\text{ cm}^{-1}$  which are diagnostic of this phase, are detected from  $1100^\circ\text{C}$ . As the temperature increases these bands become better resolved, in consistence with increasingly calcium zirconate that is formed, as can be seen in the spectrum of the material treated at  $1400^\circ\text{C}$ .

This technique neither is suitable to corroborate the formation of  $\text{CaHfO}_3$ , because its bands are located in the same region than the bands associated to  $\text{CaZrO}_3$ . Nevertheless it can be affirmed that  $\text{HfO}_2$  has reacted due to the fact that its band located at  $752\text{ cm}^{-1}$  has disappeared. For this reason, the formation of  $\text{CaHfO}_3$  could be supported (Zoz\_ & Karaulov, 1991).

Monoclinic  $\text{ZrO}_2$  and  $\text{CaZrO}_3$  phases absorb in the same spectral region due to their similarities in coordination number and bonding characteristics. However, regarding Zr-O vibrations belonging to zirconia, these frequencies are observed at  $574$  and  $490\text{ cm}^{-1}$ , in the spectra of samples treated below to  $1350^\circ\text{C}$ .

The absorptions located between  $910\text{--}880\text{ cm}^{-1}$  and at  $980\text{ cm}^{-1}$ , are attributed to Si-O symmetric and asymmetric stretching, respectively; which are the typical vibrational modes of the silicate moieties forming the structure of the phase  $\beta\text{-C}_2\text{S}$  (Gou et al., 2005). These bands are observed, in samples submitted to calcination over  $1000^\circ\text{C}$ , and subsequently its definition improves, as a consequence of bond reinforcing with the temperature increases.

The existence of MgO is supported by the presence of a shoulder at  $671\text{ cm}^{-1}$  in the spectra registered for of all the materials obtained over  $750^\circ\text{C}$ . This frequency is assigned to the stretching of the bonds Mg-O forming the MgO ionic crystal (Singh & Upadhyaya, 1972).

On the other hand, the weak absorptions remaining in the spectrum of the end products calcined at  $1400^\circ\text{C}$ , located at  $3400$ ,  $1630$  and  $1575\text{ cm}^{-1}$ , are due to the presence of adsorbed moisture in the samples. In the same way as in zirconia these signals are assigned to O-H, H-O-H, and M-OH vibrations, respectively (Prasanth et al., 2008).

The spectral features of the samples are maintained, showing the maximum definition when the end products are formed, in the final thermal treatment at  $1400^\circ\text{C}$ . Finally, it should be remarked that the FTIR spectra are in full agreement with XRD results. Moreover, the subtle details due to the formation of the new bonds were determined using the spectroscopic tool. Accordingly, the optimal temperature for the refractory material process seems to be  $1400^\circ\text{C}$ .

### 3.2.3 Microstructure of the material D-Z

In Fig. 6 is presented a SEM micrograph of the bulk porous composite refractory material. The SEM image illustrated in this figure shows a homogenous microstructure consisting of dense rounded borders grains. This morphology should be attributed to the high temperature of synthesis which allows the grain growth and a reduction of porosity. Upon magnification, some degree of inhomogeneity is detected; since over the dark background some clear and smaller particles are observed on the surface. This feature is attributable to the mixed phase system, as determined by the combination of XRD and FTIR measurements.

A careful inspection of the X-ray microanalysis of both regions allows confirming that they differ slightly in the chemical composition. The atomic analysis of the darker particles with block like appearance and some cracks on its surface is composed mainly by Zr and Ca, with a minor amount of Mg and Si, compatible mostly with the presence of  $\text{CaZrO}_3$ ,  $\text{ZrO}_2$ , MgO

and  $\text{Ca}_2\text{SiO}_4$ . On the other hand, in the X-ray microanalysis of the dispersed clear particles, a very low percentage of Al atoms were also identified, it would be attributed to the presence of the spinel  $\text{MgAl}_2\text{O}_4$  phase. Moreover these results are in fair agreement with the global composition estimated from XRD analysis. The elemental compositions measured during the scanning of the surface are similar, suggesting that the components are uniformly distributed in the microstructure.

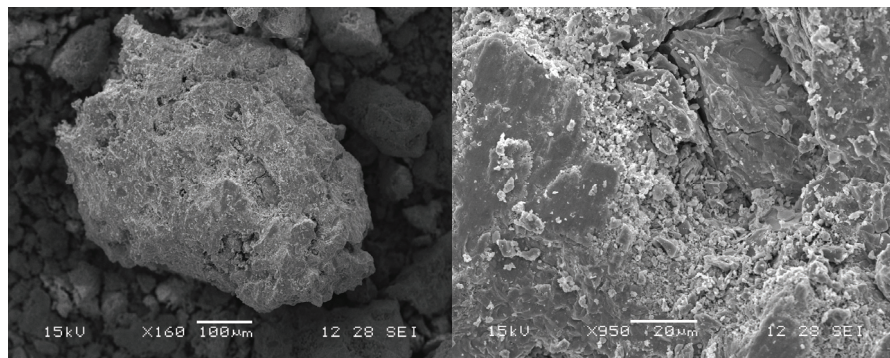


Fig. 6. SEM micrograph of sample D-Z treated at 1400°C, (left, 160x and right, 950x)

### 3.3 Formation of refractories from Dolomite-ZrSiO<sub>3</sub> mixtures, D-ZS

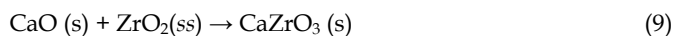
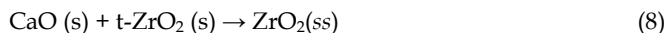
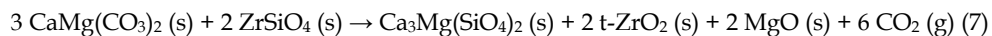
The behavior of the different batches submitted to firing up to 1350°C, labelled D-ZS, was evaluated by using the combination of spectroscopic FTIR technique and XRD analysis; using a similar procedure to that described for D-Z specimens. The microstructure of the resulting material was also analyzed.

#### 3.3.1 Evolution of the phases D-ZS on heating by X-Ray diffraction

Some of the XRD patterns belonging to the most relevant heating temperatures are illustrated in Fig. 7. A detailed analysis of the diffractometric results suggests that at 350°C, only the diffractions belonging to the minerals composing the starting materials, such as dolomite, calcite, quartz and zircon, appear; suggesting that no chemical solid state reactions have occurred yet.

When the batch is submitted to calcination at 850°C, both carbonate minerals, dolomite and calcite, are no longer observable, whereas quartz and zircon persist. Simultaneously new lines assigned to  $\text{MgO}$ ,  $\text{t-ZrO}_2$ ,  $\text{ZrO}_2(\text{ss})$ ,  $\text{CaZrO}_3$ ,  $\text{Ca}_3\text{Mg}(\text{SiO}_4)_2$  and  $\text{Ca}_2\text{SiO}_4$ , are detected as the result of the apparently complete transformation of the dolomitic raw mineral in the products of the reaction with zircon. The tetragonal polymorph of  $\text{ZrO}_2$ , which is the thermodynamically stable structure in the phase diagram (Rodríguez et al., 2002) is recognizable. The  $\text{CaO}$  generated simultaneously, seems to be partly as portlandite- $\text{Ca}(\text{OH})_2$  due to its ease to hydration by air moisture. Whereas the remaining  $\text{CaO}$ , along with some  $\text{MgO}$  react with zircon and quartz giving rise to  $\text{CaZrO}_3$ ,  $\text{Ca}$  silicate and also the calcium-magnesium silicate already mentioned. A remarkable increase of the characteristic peak of  $\text{CaZrO}_3$  is observed over 950°C. In coincidence, the presence of the as called spinel  $\text{MgAl}_2\text{O}_4$  phase is detected (see equation 6).  $\text{CaZrO}_3$  keep growing to become the major phase at 1050 °C and at this temperature the apparition of the mixed oxide formulated  $\text{Mg}_2\text{Zr}_5\text{O}_{12}$  is

observed. Consequently, these phases seem to be the result of a series of reactions which could be interpreted as follows:



The peaks of Portlandite, quartz and zircon become not observable at 1000, 1150 and 1200 °C, respectively; whereas the signal belonging to the t-ZrO<sub>2</sub> polymorph diminishes until disappearance at 1300°C.

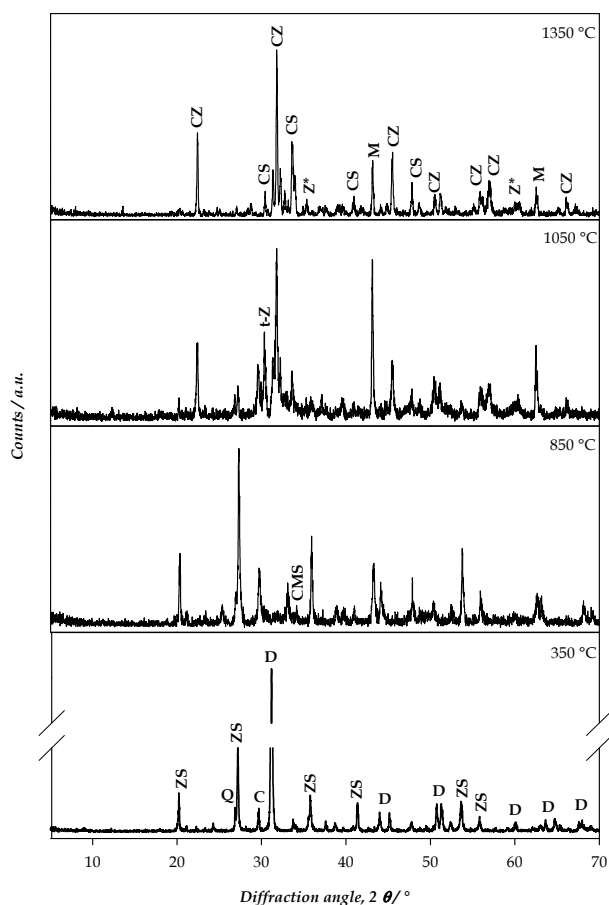


Fig. 7. XRD patterns of sample D-ZS, at different firing temperatures



The compound  $\text{Ca}_3\text{Mg}(\text{SiO}_4)_2$  persists until  $1050^\circ\text{C}$ , and then it decomposes upon firing giving rise to  $\text{Ca}_2\text{SiO}_4$  which is a more stable silicate phase. This result is supported by thermodynamic calculations which establishes a reaction mechanism according to which  $\text{Ca}_3\text{Mg}(\text{SiO}_4)_2$  appears as the first phase during the reaction (Rodríguez et al., 2002). It is in this context that the reaction was proposed. Furthermore the coexistence of both silicates, in equilibrium, in the range  $850\text{--}1100^\circ\text{C}$  is valid. On the other hand, since this reaction demands  $\text{CaO}$  to proceed, this suggests that its hydroxide should be present in the mixture ; although it is undetectable by XRD, probably due to superposition with the peaks of other compounds, especially that of calcium silicate, or due to low crystallinity.

The specimen treated at  $1350^\circ\text{C}$  is mainly constituted by  $\text{CaZrO}_3$ ,  $\text{CaSiO}_4$  and  $\text{MgO}$ . A semi-quantitative XRD analysis of the phases present was carried out by taking into account the peak intensities obtained by XRD data with the appropriate software, as already described. The amount of the components in the mixed phase is estimated in the proportion 47: 20: 16 %, respectively. The compounds  $\text{Mg}_2\text{Zr}_5\text{O}_{12}$ ,  $\text{ZrO}_2(\text{ss})$  and the so-called spinel phase  $\text{MgAl}_2\text{O}_4$  were detected as minor components. The cubic calcium partially stabilized zirconia is present in the final product, as the result of incorporation of  $\text{Ca}(\text{II})$  ions to the crystal lattice of  $\text{t-ZrO}_2$ .

A careful analysis of the evolution of the different phases with the temperature in the range  $350\text{--}1350^\circ\text{C}$ , was studied. The peak intensities found for each compound at the main temperatures of synthesis are depicted in Fig. 8.

According to the plotted XRD data of raw minerals, dolomite and calcite show a complete transformation at  $850^\circ\text{C}$ . Whereas quartz and zircon behave as thermally resistant phases, with a marked decrease over  $850^\circ\text{C}$ , due to the reaction with the oxides  $\text{CaO}$  and  $\text{MgO}$ , released by the dolomitic material, until disappearance around  $1150^\circ\text{C}$  and  $1200^\circ\text{C}$ , respectively.

In addition to this, the complex interplay of reactions between raw materials and fired products formed during the intermediate steps, justify the trends observed for the phases formed upon calcinations. Nevertheless, the XRD intensities profiles observed suggest that the products formed,  $\text{CaZrO}_3$ ,  $\text{Ca}_2\text{SiO}_4$  and  $\text{MgO}$ , grow uniformly when the calcination temperature rises. The compounds  $\text{t-ZrO}_2$  and  $\text{Ca}_3\text{Mg}(\text{SiO}_4)_2$  are transitory phases formed.

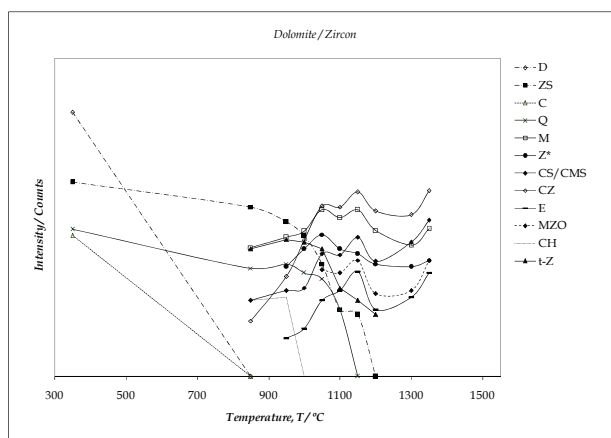


Fig. 8. Evolution of phases, during firing, for D-ZS specimens

### 3.3.2 FTIR analysis of D-ZS samples, treated in the thermal range 350-1350 °C

The FTIR spectra of the specimens are in full agreement with the XRD results. In addition, some other evidences, regarding phases not so clearly detected by X-ray diffraction, could be ascertained. The IR data of the calcined samples at different temperatures were analyzed. The spectral patterns of most representative firing steps may be seen in Fig. 9.

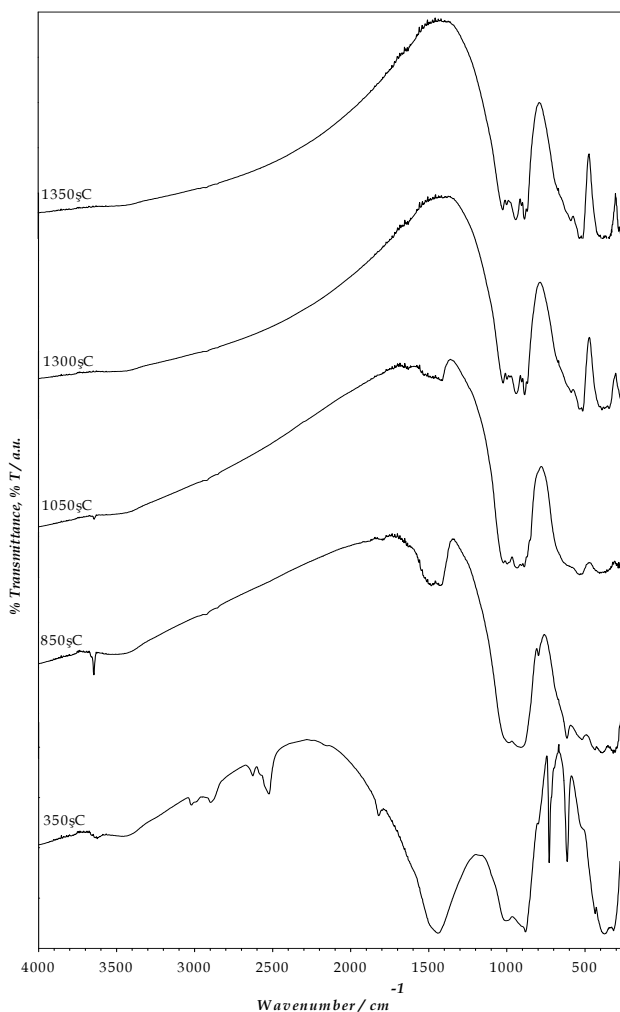


Fig. 9. Spectral FTIR patterns of D-ZS, between 350 and 1350 °C

Up to 350°C no significant changes are observed in the IR spectra, in comparison with the spectral patterns of the reactants. During the thermal treatment from 850°C to 1050°C, the bands assigned to dolomite are detected, which disappeared totally at 1300 °C. This spectral evidence allows determining accurately the end of the decomposition of this mineral that could not be ascertained through XRD analysis.

The sharp and low intensity signal at  $3643\text{ cm}^{-1}$ , attributed to the vibration of the bond Ca-OH, is diagnostic to identify hydrated CaO. This signal is observed over  $750^\circ\text{C}$  then it weakens as temperature increases being observable until  $1200^\circ\text{C}$ .

The characteristic bands of  $\text{CaZrO}_3$  are detectable from  $850^\circ\text{C}$ , showing enhanced definition as temperature rises up to  $1350^\circ\text{C}$ , due to the increase in the formation of Ca-O-Zr bonds.

On the other hand the typical vibrations belonging to the Si-O-Si bonds of silicates are detected at  $850^\circ\text{C}$ , confirming the proposed reactions. Nevertheless it is difficult to assign unambiguously this vibration to distinguish between  $\text{Ca}_3\text{Mg}(\text{SiO}_4)_2$  and  $\text{Ca}_2\text{SiO}_4$ .

Despite Zr-O vibrations belonging to zircon and zirconia, absorb in a similar spectral region, due to the similar coordination and bonding; the typical  $\text{ZrO}_2$  absorption located at  $574$  and  $490\text{ cm}^{-1}$ , are present until  $1300^\circ\text{C}$ .

MgO could be observable through the shoulder at  $671\text{ cm}^{-1}$ , in the low energy region in the spectra of the specimens treated over  $1200^\circ\text{C}$ .

### 3.3.3 Microstructure of the material D-ZS

Concerning the morphology of the material D-ZS obtained at  $1350^\circ\text{C}$ , which can be seen in Fig. 10, the formation of a bulk porous microstructure is observable, with a quite different microstructure in comparison with the D-Z specimen.

Indeed the refractory obtained from the D-ZS batch seems to be more porous and smaller in the size of the grains than the D-Z batch; and also in contrast with this material, in the case of D-ZS a very well developed three dimensional network microstructure was observed for this composite material. This feature is probably due to the liberation of  $\text{CO}_2$ , through the silicate network, that forms a homogeneous open pore structure.

The analysis of the backscattering image shows that the grains with bright contrast are belonging to the Zr-compounds; whereas those with dark contrast should be mainly attributed to MgO and  $\text{Ca}_2\text{SiO}_4$ . Moreover it is clearly observed that the grains are connected to each other via thick necks, suggesting that in this composite the Zr-phases have a “direct” bond to the other components, with good mechanical integrity. In addition the X-ray microanalysis is in fair agreement with the global composition, estimated from XRD data.

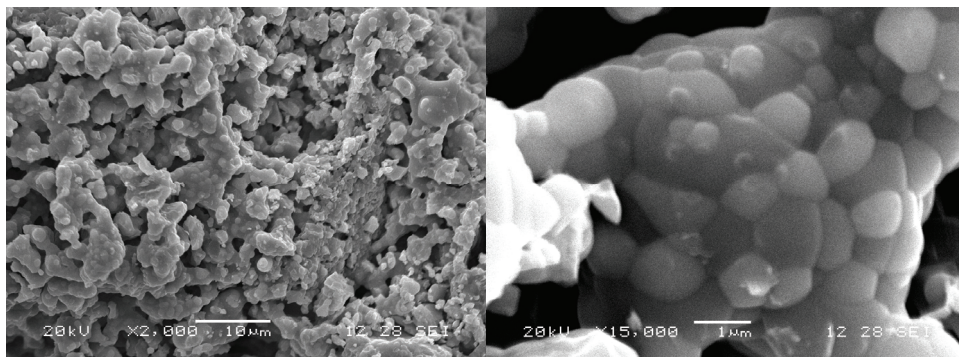


Fig. 10. SEM micrograph of D-ZS materials obtained at  $1350^\circ\text{C}$  The backscattering image is shown on the right

#### 4. Conclusions

Dolomites from Olavarría have got mineralogical, chemical, granulometric, and specific surface characteristics that make them appropriate to obtain MgO-CaZrO<sub>3</sub> refractory materials manufacture by a simple processing at high temperature by solid-state reaction.

The process used in this study is very cost-effective because of the use of a natural ore and commercial grade zirconium sources.

The phases formed during the refractory material synthesis could be well characterized, structurally and spectroscopically, by combination of XRD and FTIR techniques.

The final composition is dependent of the Zr-sources. When ZrO<sub>s</sub> is employed the preparation optimal temperature can be estimated at 1400°C and the main co-products are ZrO<sub>2</sub>(ss), the spinel MgAl<sub>2</sub>O<sub>4</sub> and β-CS<sub>2</sub>. When ZrSiO<sub>4</sub> is used the principal co-product is Ca<sub>2</sub>SiO<sub>4</sub>, accompanying by ZrO<sub>2</sub>(ss), the spinel MgAl<sub>2</sub>O<sub>4</sub> and the mixed oxide Mg<sub>2</sub>Zr<sub>5</sub>O<sub>12</sub>, in a minor proportion. The final product is formed at 1350 °C.

Despite the high quartz-SiO<sub>2</sub> content of Argentine dolostones, in comparison with the dolomitic mineralogy of other deposits in the world, the composition of phases and the microstructures achieved meet the requirements for cement kiln refractories.

The morphology of the samples shows that the Zr-phases are well dispersed within the composite matrix. In addition, in the powdered specimen obtained using zircon the “direct” bonding of the compounds could be confirmed.

#### 5. References

- Aras, A. (2004). The change of phases composition in kaolinite- and illite-rich clay-based ceramic bodies. *Appl. Clay Sci.*, Vol.24, No.3-4, (February 2004), pp.257-269, ISSN 0169-1317
- Contreras, J. E.; Castillo, G.A.;Rodríguez, E.A.;Das, T.K. & Guzmán, A.M. (2005). Microstructure and properties of hercynite-magnesia-calcium zirconate refractory mixtures. *Mater. Charact.*, Vol. 54, No.4-5, (May 2005), pp. 354-359, ISSN 1044-5803
- Cotton, F. A. & Wilkinson, G. (1988). *Advanced Inorganic Chemistry* (5<sup>th</sup> Edition), John Wiley & Sons, ISBN 0-471-84997-9, United States of America
- Dawson, P.; Hargreave M. M. & Wilkinson, G. R. (1971). The vibrational spectrum of zircon (ZrSiO<sub>4</sub>). *J. Phys. C: Solid State Phys.*, Vol. 4, No.2, (February 1971), pp. 240-256, ISSN 0022-3719
- De Aza, A. H.; Pena, P.; Rodríguez, M. A.; Torrecillas, R. 6 de Aza, S. (2003). New spinel-containing refractory cements. *J. Eur. Ceram. Soc.*, Vol.23, No.5, (April 2003), pp. 737-744, ISSN 0955-2219
- Domanski, D.; Urretavizcaya, G.; Castro, F. J. & Gennari, F. C. (2004). Mechanochemical Synthesis of Magnesium Aluminate Spinel Powder at Room Temperature. *J. Am. Ceram. Soc.*, Vol. 87, No.11, (November 2004), pp. 2020-2024, ISSN 0002-7820
- Gómez Peral, L. E., Poiré, D. G., Strauss, H. & Zimmermann, U., (2007). Chemostratigraphy and diagenetic constraints on Neoproterozoic carbonate successions from the Sierras Bayas Group, Tandilia System, Argentina. *Chem. Geol.* Vol.237, No.1-2, (February 2007), pp. 109-128, ISSN 0009-2541
- Gou, Z.; Chang, J. & Zhai, W. (2005). Preparation and characterization of novel bioactive dicalcium silicate ceramics. *J. Eur. Ceram. Soc.*, Vol.25, No.9, (June 2005), pp. 1507-1514, ISSN 0955-2219

- Goto, K. & Lee, W. (1995). The "Direct Bond" in Magnesia Chromite and Magnesia Spinel Refractories. *J. Am. Ceram. Soc.*, Vol. 78, No.7, (July 1995), pp. 1753-1760, ISSN 0002-7820
- Khalil, N M. A.; El-Hemaly, S. A. S. & Girgis, L. G. (2001). Aluminous cements containing magnesium aluminate spinel from Egyptian dolomite. *Ceram. Int.*, Vol.27, No.8, pp. 865-873, ISSN 0272-8842
- Kingery, W. D.; Bowen, H. K. & Uhlmann, D.R. (1976). *Introduction to ceramics* (2<sup>nd</sup> Edition), John Wiley & Sons, Inc., ISBN 0-471-47860-1, United States of America.
- Lavat, A. E. & Grasselli, M. C. (2007). Phase evolution during preparation of spinel-containing refractory cements from argentine dolomite. *Adv. In Tech. of Mat. and Mat. Proc. J. (ATM)*, Vol. 9 No. 1, pp. 103-108, ISSN 1440-0731
- Lavat, A. E.; Grasselli, M. C. & Giuliodori Lovecchio, E. (2010). Effect of alpha and gamma polymorphs of alumina on the preparation of MgAl<sub>2</sub>O<sub>4</sub> spinel-containing refractory cements. *Ceram. Int.*, Vol. 36, No.1, (January 2010), pp. 15-21, ISSN 0272-8842
- Neumayer D. A. & Cartier, E. (2001). Materials characterization of ZrO<sub>2</sub>- SiO<sub>2</sub> and HfO<sub>2</sub>- SiO<sub>2</sub> binary oxides deposited by chemical solution deposition. *J. Appl. Phys.*, Vol 90, No. 4, (August 2001), pp. 1801-1808, ISSN 0021-8979
- Obregón, A.; Rodríguez-Galicia, J. L., López-Cuevas, J., Pena, P. & Baudín, C. (2011). MgO-CaZrO<sub>3</sub>-based refractories for cement kilns. *J. Eur. Ceram. Soc.*, Vol.31, No.1-2, (January-February 2011), pp. 61-74, ISSN 0955-2219
- Orera, V. M.; Pecharromán, C.; Peña, J. I.; Merino, R. I. & Serna, C. J. (1998). Vibrational spectroscopy of CaZrO<sub>3</sub> single crystals. *J. Phys.: Condens. Matter*, Vol. 10, No.3, (August 1998), pp. 7501-7510, ISSN 0953-8984
- Ozel, E & Turan, S. (2007). Production of coloured zircon pigments from zircon. *J. Eur. Ceram. Soc.*, Vol. 27, No.2-3, pp. 1751-1757, ISSN 0955-2219
- Popa, M.; Kakihana, M.; Yoshimura, M. & Calderón-Moreno; J.M. (2006). Zircon formation from amorphous powder and melt in the silica-rich region of the alumina-silica-zirconia system. *J. Non-Cryst. Solids*, Vol. 352, No.52-54, (December 2006), pp. 5663-5669, ISSN 0022-3093
- Prasanth, C.S.; Padma Kumar, H.; Pazhani, R.; Solomon, S.; Thomas, J. K. (2008). Synthesis, characterization and microwave dielectric properties of nanocrystalline CaZrO<sub>3</sub> ceramics. *J. Alloys Compd.*, Vol. 464, No.1-2, (September 2008), pp. 306-309, ISSN 0925-8388
- Qotaibi, Z.; Diouri, A.; Boukhari, A.; Taibi, M. & Aride, J. (1998). Analysis of magnesia chrome refractories weared in a rotary cement kiln. *Ann. Chim. Sci. Mat.*, Vol.23, No.1-2, (January-February 1998), pp. 169-172, ISSN 01551-9107
- Rodríguez, J. L. , De Aza, A. H.; Pena, P.; Campo, J.; Convert, P. & Turrillas, X. (2002). Study of Zircon-Dolomite monitored by neutron thermodiffractometry. *J. Solid State Chem.*, Vol. 166, No.2, (July 2002), pp. 426-433, ISSN 0022-4596
- Rodríguez-Galicia, J. L.; Fernández-Arguijo, B.; Rendón-Ángeles, J. C.; Pena, P.; Valle-Fuentes, J. F. & López-Cuevas, J. (2005). Reaction sintering of Mexican dolomite. *Bol. Soc. Esp. Ceram. V.*, Vol. 44 No.4, (July-August 2005), pp. 245-250, ISSN 0366-3175
- Rodríguez-Galicia, J.L.; De Aza, A.H.; Rendón-Ángeles, J.C. & Pena, P. (2007). The mechanism of corrosion of MgO-CaZrO<sub>3</sub>-calcium silicate materials by cement clinker. *J. Eur. Ceram. Soc.*, Vol. 27, No1, pp. 79-89, ISSN 0955-2219

- Serena, S.; Sainz, M.A. & Caballero, A. (2004). Corrosion behavior of MgO/CaZrO<sub>3</sub> refractory matrix by clinker. *J. Eur. Ceram. Soc.*, Vol. 24, No.8, (July 2004), pp. 2399-2406, ISSN 0955-2219
- Serena, S.; Sainz, M.A. & Caballero, A. (2005). Thermodynamic assessment of the system ZrO<sub>2</sub>-CaO-MgO using new experimental results Calculation of the isoplethal section MgO-CaO-ZrO<sub>2</sub>. *J. Eur. Ceram. Soc.*, Vol. 25, No.5, (February 2005), pp. 681-693, ISSN 0955-2219
- Singh, R. K. & Upadhyaya, K. S. (1972). Crystal dynamics of magnesium oxide. *Phys. Rev. B*, Vol. 6, No. 4, (August 1972), pp. 1589-1596, ISSN 1098-0121
- Suzuki, Y.; Morgan, P.E.D & Ohji, T. (2000). New uniformly porous CaZrO<sub>3</sub>/MgO composites with three- dimensional network structure from natural dolomite. *J. Am. Ceram. Soc.*, Vol. 83, No. 8, (August 2000), pp. 2091-2093, ISSN 0002-7820
- Wilson, M. J. (1987). A handbook of determinative methods in clay mineralogy. Blackie & Son Ltd. Place, ISBN 0-412-00901-3
- Zoz, E. I. & Karaulov, A. G. (1991). Comparative study of the solid solutions in the ZrO<sub>2</sub>-HfO<sub>2</sub>-MgO(CaO) systems. *Refract. Ind. Ceram.*, Vol. 32, No.3 (March 1991), pp. 109-112, ISSN 0034-3102

# Characterization of Clay Ceramics Based on the Recycling of Industrial Residues – On the Use of Photothermal Techniques to Determine Ceramic Thermal Properties and Gas Emissions during the Clay Firing Process

Faria Jr. R. T.<sup>1</sup>, Souza V. P.<sup>1</sup>, Vieira C. M. F.<sup>2</sup>, Toledo R.<sup>1</sup>,  
Monteiro S. N.<sup>2</sup>, Holanda J. N. F.<sup>2</sup> and Vargas H.<sup>1</sup>  
*Universidade Estadual do Norte Fluminense Darcy Ribeiro – UENF*  
<sup>1</sup>*Laboratório de Ciências Físicas,*  
<sup>2</sup>*Laboratório de Materiais Avançados,*  
*Parque Califórnia, Campos dos Goytacazes, RJ*  
*Brasil*

## 1. Introduction

Since Sumerians about 4000 - 3000 BC had created ceramics (Heydorn *et al.*, 1989), the ceramic production has worldwide increased, but the methodology has not suffered substantial evolution in relation to the ancient process. Research work continues to a better understanding of the processes involved and tailoring the desired properties of the final product. The most of ceramists has just worried up with the morphological, physical and structural quality of their products (Okada *et al.*, 1986; Dubois *et al.*, 1995; Nastro *et al.*, 2006). However, one of the main ceramics features was not yet well concerned by the community, that is, its thermal behaviour. Urban buildings of equatorial and tropical countries are often subjected to constant solar radiation. Thus, thermal properties play a significant role in the quality of end-products. A better indoor ambient of the houses should be ever pursued. While technological properties of those materials are frequently found in the literature, information about the thermophysical characteristics of red ceramics is very scarce (Alexandre *et al.*, 1999).

In the early eighties, a new physical device to generate and detect thermal waves was proposed (Vargas and Miranda, 1988). It has been widely used in last few years as a tool to measure the thermal properties of a large range of materials (Marín *et al.*, 2002; Faria *et al.*, 2005). The photoacoustic (PA) technique via OPC (an open photoacoustic cell) is used to evaluate the thermal diffusivity, an important parameter that determines the light-to-heat conversion efficiency, and furthermore, it allows us to study how heat diffuses through the sample (Perondi and Miranda, 1987). The thermal diffusivity is an intrinsic property of matter. Moreover, it is dependent upon the effects of composition and microstructural variables, as well as processing conditions. Thermal properties are very sensitive to

amorphous-crystalline phase transitions of clays heated above 900 °C, typical temperatures applied in the manufacturing process of ceramic materials.

Clay deposit areas have a high economic potential, and soil mineralogical composition, plasticity and porosity are fundamental properties for industrial applications. The resulting ceramic products present a network of capillary pores that vary according to the firing cycle. Important ceramic properties such as hardness, water absorption, gas permeability, shrinkage, density, thermal properties, gas emission as well as the vitrification temperature range are intrinsically correlated to the porous system (Rice and Dekker, 1998).

In addition, the whole world presently draws increasing attention to the environment, requiring the adjustment of industrial activities according to laws and norms that rule the sector. Thus, increasing environmental problems related to climate changes and pollution are going attention and raising special concern regarding to the dispersal of industrial wastes. As a consequence, the society is demanding not only actions towards waste reduction but also measures for redirecting or post-using wastes mainly those of industrial origin. Most of the residues generating in the production process is normally handled by land disposal in certain areas, thus recycling of these residues may produce the value-added products and prevent environmental deterioration. As solid wastes are becoming a matter of increase world concern due to their amount as well as difficulty and cost of final disposal, ceramic products can well supply as matrices for industrial residues incorporation such as giving an option for the solid waste disposal with a possible increase in the properties of the clay ceramic products. The incorporation of wastes from several industrial activities is a technological alternative to reduce the environmental impact due to their indiscriminate disposal. One such a measure is the waste incorporation into intensive-produced clay ceramics like bricks and tiles (Parsons *et al.*, 1997). This incorporation is now a common practice and benefits both, the industry that generates the waste and the ceramic industry that saves on the clay, which is its basic raw material. In some cases the incorporation also improves the properties of the ceramic product (Oliveira and Holanda, 2004).

Research works on the structural and physical changes that wastes, mainly industrially produced, cause to the final ceramic product has been rapidly expanding in these last two decades. See, for instance references in (Vieira and Monteiro, 2009). In spite of these examples of a continuous effort to incorporate wastes into clay ceramic motivated by technical and economical advantages, environmental issues are still a matter of concern. The firing stage during the clay ceramic process can promote the elimination of potentially toxic constituents present in the solid residues through their volatilization. However, the gas emission due to the clay firing process and its related atmospheric pollution may be enhanced as a consequence of an incorporated waste (Souza *et al.*, 2008). It is known that the firing of clay ceramics in conventional furnaces using fuels such as wood, charcoal, heavy oil and natural gas generates appreciable amounts of gaseous components, mainly carbon dioxide (CO<sub>2</sub>), carbon monoxide (CO) and methane (CH<sub>4</sub>). Additionally to the atmospheric pollution, these gas sets could be harmful to the human health and can corrode equipments (Morgan, 1993).

Works on the effect of gas emission caused by the firing of clay ceramics incorporated with industrial wastes are practically inexistent. Therefore one of the mean objectives of this chapter was to investigate the gas emission resulting from the firing of clay ceramics incorporated with different industrial residues. Here, slag type of waste from steel refining operation and sanitary ware mass wastes were the selected residues.



In order to show methodologies to characterize ceramics here depicted, the samples under study were clay from Rio de Janeiro state and from São Paulo state. Firstly, the raw materials without residues is presented and throughout characterized. In a second stage, the aggregation of the residues is pointed out. Characterizations are performed and compared with the clays without residues.

## 2. Ceramic samples

Clayey soils from two sites of the Southeast Brazilian region were studied for the production of red ceramics. The samples preparation was pointed out in the following.

### 2.1 Kaolinite clay from Rio de Janeiro state (CG clay)

The raw material was collected from a quaternary sedimentary basin situated in Campos dos Goytacazes, from a layer localized between 0.30 m and 1.80 m below the surface, where large clay deposits are quarried as raw material for red bricks and tiles. About 20 kg of material collected in situ were dried, grounded, and passed through a sequence of sieves yielding a homogeneous powder with particle size smaller than 75  $\mu\text{m}$ , corresponding to 95 % of the original mass.

For technological measurements, a quantity of the powder was mixed with water and then extruded at 36 MPa into a rectangular prismatic mould with a 20x10 mm cross-section, cut into bars 100 mm long which were left drying in air for two weeks at room temperature. Before the firing process, the samples were subjected to an additional drying cycle in an oven at  $(110 \pm 5\text{ }^{\circ}\text{C})$  for 24 hours. Then, the sample weight and dimensions were measured just before starting the firing process. X-ray diffraction measurements were done on the same samples used for technological measurements.

To simulate the continuous sintering process of the ceramic material up to 1200  $^{\circ}\text{C}$ , and to accompany the changes that occur, 13 thermal treatment steps were chosen, each step being denoted  $T_F$  henceforth. For firing temperatures up to 600  $^{\circ}\text{C}$  the heating rate was set to 2  $^{\circ}\text{C}/\text{min}$ . Once the desired  $T_F$  was reached, the sample was left at constant temperature for 3 hours, and then cooled down to room temperature at a rate of 1.5  $^{\circ}\text{C}/\text{min}$ . For  $T_F$  above 600  $^{\circ}\text{C}$ , the heating cycle was such that the sample was heated at a rate of 2  $^{\circ}\text{C}/\text{min}$  up to 600  $^{\circ}\text{C}$ , left at this temperature for one hour, and then heated at a rate of 10  $^{\circ}\text{C}/\text{min}$  up to the selected firing temperature, where it was left for 3 hours before cooling down to room temperature at a rate of 1.5  $^{\circ}\text{C}/\text{min}$ .

To perform the thermal characterization the raw material was passed through a sieve with nominal aperture of 75  $\mu\text{m}$  (mesh 200 ASTM). In order to prepare the samples for analysis, a press (SHIMADZU) was used. 90 mg of each sample was weighed and submitted to a 9 tonne pressure for 10 minutes, using disc samples with 10 mm diameter and a thickness between 200  $\mu\text{m}$  and 500  $\mu\text{m}$ . After that, the samples were fired in a furnace (MAITEC 12 kW/32 A) at six different temperature steps, ranging from 900 to 1100  $^{\circ}\text{C}$ .

Finally, to analyse the gas emissions from the CG clay and its residue, rectangular 114.5 x 25.4 x 10 mm samples with 8 % of humidity were 20 MPa moldpress by mixing the clay with different amounts of 5 and 10 wt% of steel slag. Samples of pure clay were also considered for comparison. All samples were initially dried at 110  $^{\circ}\text{C}$  in a laboratory stove and then fired in a continuous way, from room temperature to a maximum of 1100  $^{\circ}\text{C}$ , inside a tubular model FT-1200 BI, MAITEC electrical furnace. The firing was conducted at a heating rate of 2  $^{\circ}\text{C}/\text{min}$  from RT to 500  $^{\circ}\text{C}$  and 4  $^{\circ}\text{C}/\text{min}$  between 500 and 1100  $^{\circ}\text{C}$ .

## 2.2 Illitic clay from São Paulo state (J clay)

The raw material was collected from a neocenozoic sedimentary soil placed in Jundiá city, 60 km far from São Paulo city in São Paulo state. The preparation process was similar to the sample of Campos dos Goytacazes for both applications. However, the J clays do not have such plasticity as CG clays. According to their chemical properties (sub-section 3.1), they can be considered fluxes clays mainly by the alkaline elements ( $K_2O$ ,  $CaO$  and  $MgO$ ), which are responsible for the ceramic sintering. The value of  $K_2O$  comes from the mineral illite, while  $CaO + MgO$  are linked with calcite and dolomite minerals.  $Al_2O_3$  is related mainly to the kaolinite mineral.

## 3. Characterization by X-Ray

The chemical composition and crystalline phases of the raw material with and without residues and only of the residues were presented. The microstructure of the samples as in function of the firing temperature was represented by X-ray diffractions.

### 3.1 Energy dispersive X-Ray fluorescence

Using X-ray fluorescence spectrometry methods described in previous work Mota *et al.*, 2008), the percentual contribution of the main oxides present in our material was determined.

The chemical characterizations were obtained by energy dispersive X-ray spectroscopy (EDS), using a SHIMADZU equipment. The resulting values of this quantitative analysis from CG clay and its steel slag residue and from J clay and its sanitary ware mass residue are shown in Table 1 and Table 2, respectively.

Observing Table 1 and Table 2 we can classify CG clay as kaolinite-based clay (higher  $Al_2O_3$ ) and J clay as illitic-based clay (higher fluxes oxides), as explained in the previous section. In addition to  $SiO_2$  and  $Al_2O_3$ , there are considerable amounts of  $Fe_2O_3$ ,  $K_2O$  and  $TiO_2$ , which is favourable for red ceramics production. Iron oxide accounts for the bodies' red pigmentation after firing.

Oxides in wt%	CG Clay	Steel slag residue
$SiO_2$	46.42	10.29
$Al_2O_3$	27.90	21.5
$MnO$	0.11	5.40
$MgO$	0.71	10.33
$CaO$	0.22	45.10
$Na_2O$	0.36	-
$K_2O$	1.67	-
$TiO_2$	1.32	0.34
$Fe_2O_3$	9.10	*
$P_2O_5$	-	1.85
$SO_3$	-	0.54
$SrO$		0.18
$LoI$	11.96	12.96
* Total Fe from the residue (%) - 23.62		

Table 1. Chemical composition of the CG clay and steel slag (% in weight). The slag predominantly is formed by composites of Ca, Al, Fe, Mg and Si

Oxides in wt%	J Clay	Sanitary ware mass residue
SiO <sub>2</sub>	59.61	64.8
Al <sub>2</sub> O <sub>3</sub>	21.19	21.5
MnO	0.05	0.06
MgO	1.07	0.78
CaO	0.33	0.32
Na <sub>2</sub> O	0.12	0.51
K <sub>2</sub> O	2.33	2.53
TiO <sub>2</sub>	0.94	0.89
Cr <sub>2</sub> O <sub>3</sub>	-	0.05
P <sub>2</sub> O <sub>5</sub>	0.13	0.13
SO <sub>3</sub>	-	0.06
Fe <sub>2</sub> O <sub>3</sub>	5.45	5.96
ZnO	-	0.03
ZrO <sub>2</sub>	-	0.13
LoI	9.28	2.25

Table 2. Chemical composition of the J clay and the sanitary ware mass residue (wt.%). The residue is a silt-clay with very low plasticity which should enhance the structural quality of the ceramic

### 3.2 X-Ray diffraction

The X-ray diffraction experiments were performed at room temperature Using the Co-K $\alpha$  or Cu-K $\alpha$  radiation of a Seifert URD65 diffractometer, equipped with a diffracted beam graphite monochromator. The CG clay diffractograms were obtained from 3 to 50° using the Co-K $\alpha$ , while the slag steel residue from 3 to 70°. The J clay diffractograms were obtained from 3 to 75° with step sizes of 0.03° and accumulation time of 3 s. From the diffractograms the sample crystallinities were determined as the ratio between the integrated intensity of the sharp diffraction peaks to the total area of the diffraction pattern, which includes the non-coherent intensity. The CG clay sample was thoroughly analysed as in function of the firing temperature, whereas the J clay was just analysed the 110 °C sample.

Fig. 1 shows the XRD patterns as a function of the firing temperature TF. A quantitative phase analysis was performed for the natural powdered soils of Campos dos Goytacazes using the Rietveld refinement method (Manhães *et al.*, 2002). The Rietveld analysis was performed considering the angular range 10° < 2 $\theta$  < 70°, thus not taking into account the illite phase due to its peak shape. Kaolinite is the main crystalline phase with 86% mass fraction, followed by quartz (5%), anatase (5%) and gibbsite (4%).

The diffractograms of the samples treated up to 400 °C show a similar mineral composition with kaolinite as the major phase. Between 400 and 500 °C the kaolinite dehydroxylation occurs, with the transformation to a non-crystalline phase, metakaolin: Al<sub>2</sub>Si<sub>2</sub>O<sub>5</sub>(OH)<sub>4</sub> → Al<sub>2</sub>Si<sub>2</sub>O<sub>7</sub>+2H<sub>2</sub>O↑. The other crystalline phases (illite and quartz) remain unchanged up to 900 °C. For this temperature range no more organic material is present in the amorphous component. . The main crystalline phases present in our non-treated samples were kaolinite (Al<sub>2</sub>Si<sub>2</sub>O<sub>5</sub>(OH)<sub>4</sub>), quartz (SiO<sub>2</sub>), anatase (TiO<sub>2</sub>), gibbsite (Al(OH)<sub>3</sub>), goethite (FeO(OH)) and illite ((K,H<sub>3</sub>O)Al<sub>2</sub>Si<sub>3</sub>AlO<sub>10</sub>(OH<sub>2</sub>)), while the sinterized samples showed the presence of

mullite ( $\text{Al}_6\text{Si}_2\text{O}_{13}$ ), cristobalite ( $\text{SiO}_2$ ) and hematite ( $\text{Fe}_2\text{O}_3$ ). Quantitative phase analysis using the Rietveld refinement method showed that kaolinite is the main crystalline phase responding for approximately 86 wt. %.

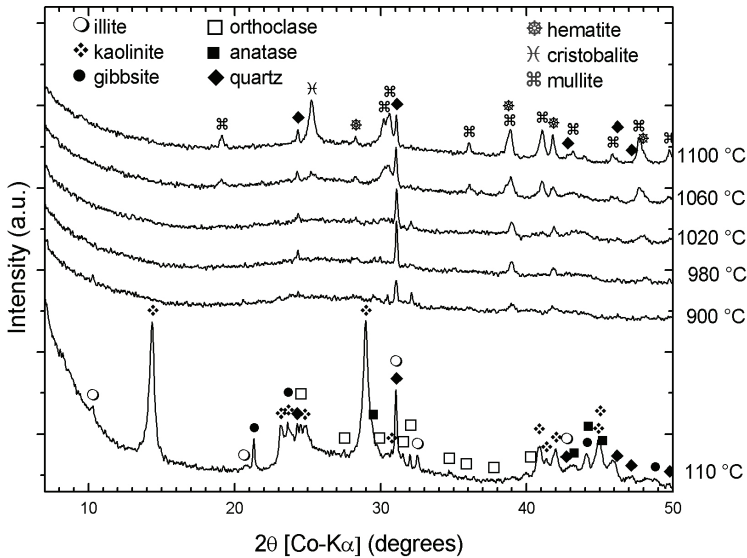


Fig. 1. X-Ray diffractograms of CG clay as in function of firing temperature

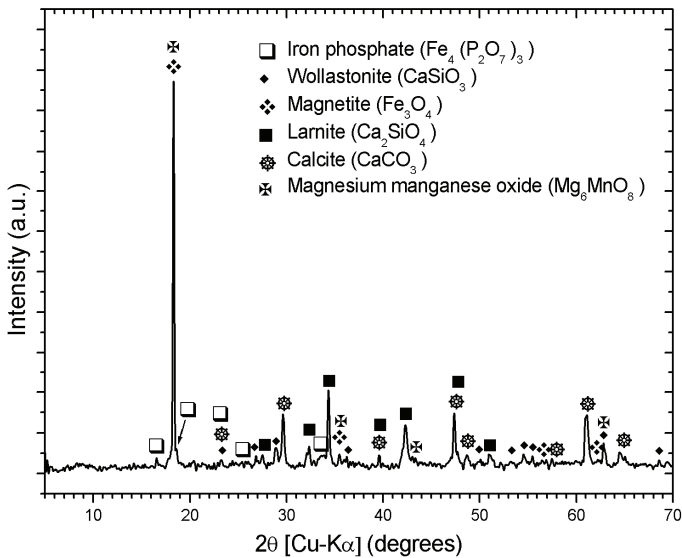


Fig. 2. Steel slag residue as processed diffractogram

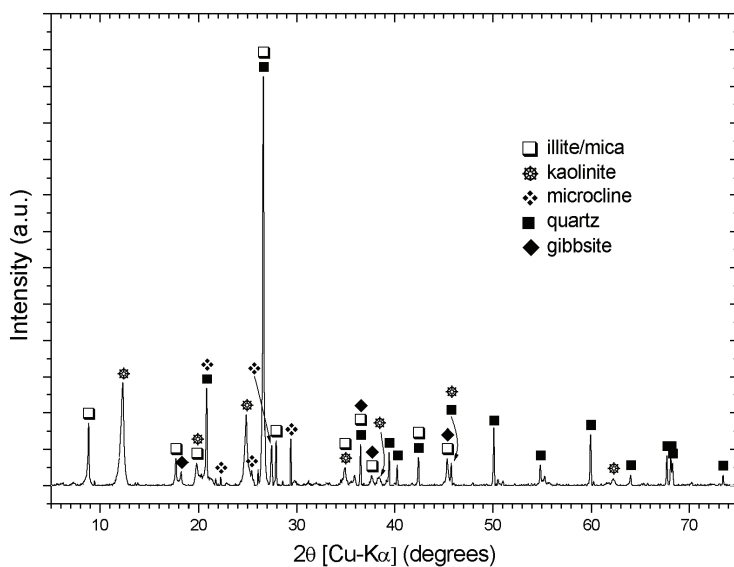


Fig. 3. X-ray diffractogram of J clay at room temperature

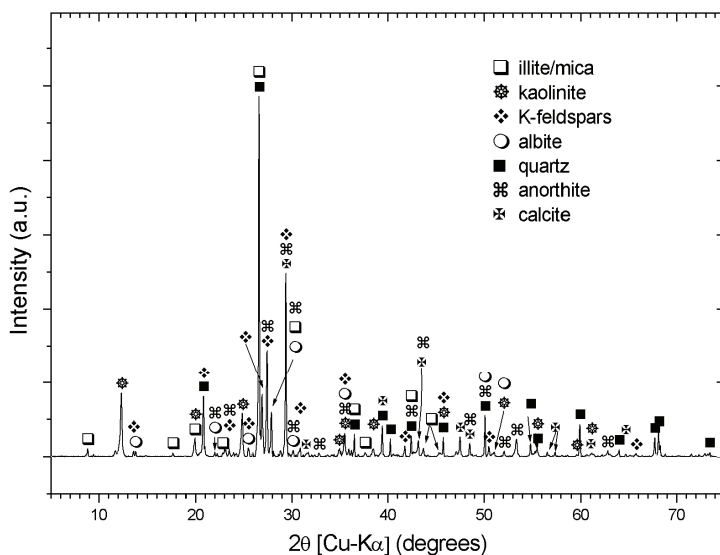


Fig. 4. X-ray diffractogram of the sanitary ware mass residue

Fig. 2 shows the X-rays diffraction pattern of the steel residues. In the respective figure the predominantly formed crystalline phases of Ca and Fe had been identified to associate diffraction peaks. The rich phases in calcium (Ca) are silicates and the calcite. On the other

hand, iron (Fe) is present in the form of magnetite and iron phosphate. Diffraction peaks of the magnesium manganese oxide were identified. In accordance to Fig. 2, Ca is present in the wollastonite ( $\text{CaSiO}_3$ ) and larnite ( $\text{Ca}_2\text{SiO}_4$ ) form and also as carbonate (calcite –  $\text{CaCO}_3$ ). Mg and Mn are presented as magnesium manganese oxide ( $\text{Mg}_6\text{MnO}_8$ ), while Fe is given in form of magnetite ( $\text{Fe}_3\text{O}_4$ ).

Fig. 3 shows the XRD patterns of the J clay raw material. This diffractogram indicates the presence of a micaceous mineral, quartz, microcline, gibbsite and kaolinite.

Fig. 4 points out the sanitary ware mass diffractogram, which shows the presence of micaceous material, albite, anorthite, k-feldspars, clay minerals, quartz, and calcite. We observed a variety of flux materials. Feldspars and microcline are sources of alkaline flux materials, such as  $\text{K}_2\text{O}$  and  $\text{Na}_2\text{O}$ , which make possible the formation of a liquid phase above 700 °C (Reed, 1976). The fluxing capacity of this residue, which is associated with lower porosity after firing, is also confirm by the presence of  $\text{K}_2\text{O}$  and  $\text{Na}_2\text{O}$  containing minerals. Then, the sanitary ware mass is the source of  $\text{K}_2\text{O}$  and  $\text{Na}_2\text{O}$ , which act as fluxes to improve the sintering process.

## 4. Technological essays

### 4.1 Density and porosity measurements

The samples dimension and mass were measured before and after each firing cycle so that the volumetric shrinkage and bulk densities could be straightforwardly determined.

Between 500 and 1200 °C, the porosity measurement consisted in measuring first the mass of the dry sample after firing at temperature  $T_F$ , denoted henceforth as  $m_{TF}$ , then two water-saturated sample masses: one, denoted as  $m_i$ , inside water after 2 h boiling, the other, denoted as  $m_o$ , outside taking care to remove the excess water from the sample surfaces. The sample open porosity was obtained as the ratio  $(m_o - m_{TF}) / (m_o - m_i)$ .

For samples that undergone heat treatments at 110, 300 and 400 °C, we have adopted the conventional pycnometer method, the reason for this being that these samples usually exhibit larger porosity and lower particle cohesion than those treated at higher temperatures. In this way, we have avoided eventual sample disintegration due to prolonged water immersion.

### 4.2 Mechanical testing

The flexural rupture tension of our samples was determined by a universal testing machine using the three-point loading test with a crosshead speed of 0.1 mm/min, designed following the ABNT standard procedure<sup>17</sup>, method equivalent to ASTM C67. The bending strength was calculated from the breaking load using the relation  $BS = 3PL/2bd^2$ , where  $P$  is maximum load,  $L$  is the distance between the supports of the beam,  $b$  is the brick average width and  $d$  is the brick average depth.

Figure 5 indicates that after 1000 °C the open porosity decreases abruptly from 39.6 % to 5.6 %, while the volumetric shrinkage and the bending strength both exhibit a large increase from 16.8 % to 40.0 % and from 9.0 MPa to 25.2 MPa, respectively. These results together with the X-ray diffraction data indicate that these changes are associated with recrystallization and sintering processes setting in between 1000 and 1200°C with the formation of mullite, cristobalite, and hematite phases, with great improvement of the ceramic properties. To further strength this aspect we present in Fig. 6 the correlations of the sample density, bending strength and volumetric shrinkage with the sample crystallinity, in

the temperature range above 1000 °C. The solid lines in this figure correspond to the data linear regression. These results indicate that, indeed, these physical properties are all well correlated with the crystallinity changes taking place in our sample in this temperature interval.

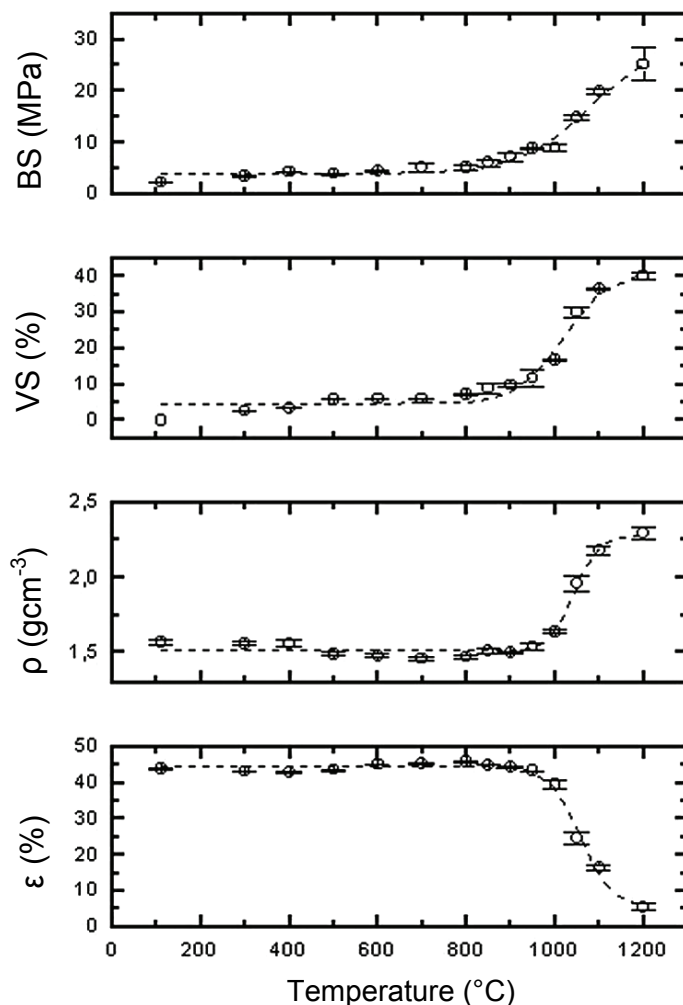


Fig. 5. The dashed lines in the bending strength, volumetric shrinkage, density and porosity plots correspond to the data fitting using a logistic function (Eq. 1)

In Fig. 5 we present the evolution of the technological properties (bending strength (BS), volumetric shrinkage (VS), bulk density ( $\rho$ ) and open porosity ( $\epsilon$ )) as a function of the firing temperature. In order to single out the temperature point at which the phase transitions taking place in our sample affect most the corresponding physical properties we have performed a fitting of our data to a logistic curve of the following form,

$$f(T) = A + B \frac{\exp((T - T_0) / \Delta T)}{1 + \exp((T - T_0) / \Delta T)}, \quad (1)$$

where  $A$ ,  $B$ ,  $T_0$  and  $\Delta T$  are all adjustable parameters. The dashed lines Fig. 5 correspond to this logistic data fitting. In Eq. 1,  $T_0$  indicates the point at which the transition occurs whereas  $\Delta T$  gives us an idea of how wide this transition is. The resulting values obtained from this data fitting procedure for the parameters  $T_0$  and  $\Delta T$  are summarized in Table 3.

Data	$T_0$ (°C)	$\Delta T$ (°C)
Open Porosity ( $\epsilon$ )	1057.03	35.62
Bulk Density ( $\rho$ )	1042.57	28.00
Volumetric Shrinkage (VS)	1021.61	52.68
Bending Strength (BS)	1079.97	80.39

Table 3. Values of the data fitting parameters characterizing the temperature and its excursion where the main changes of the physical properties of our samples occur

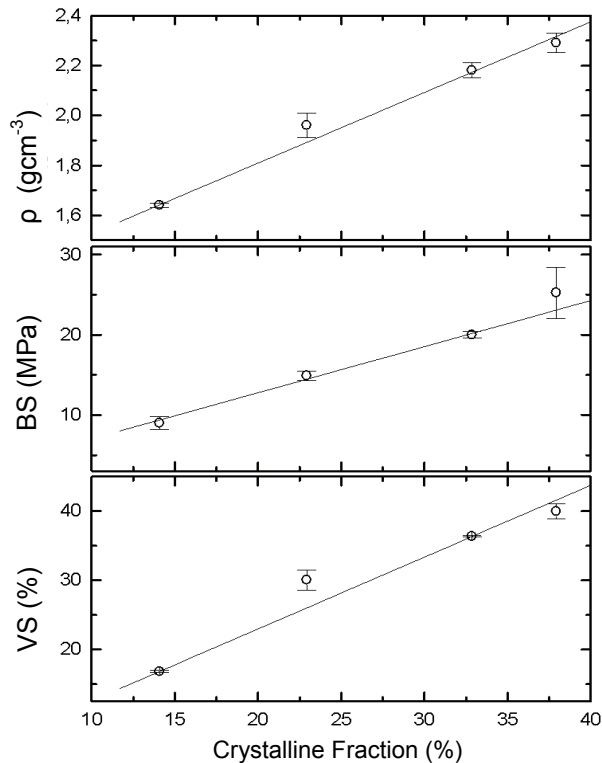


Fig. 6. Correlations of the sample density, bending strength and volumetric shrinkage with the sample crystallinity, in the temperature range above 1000 °C. The solid lines correspond to the data linear regression



The data shown in Fig. 6 also suggest some other interesting correlations among the different measured physical properties. For instance, the changes in bending strength and the volumetric shrinkage, as well as those of the porosity and density, seem to be well correlated.

We present in Figs. 7 and 8 the correlations between these physical properties. The straight lines in these figures correspond to the data linear regression. It follows from Fig. 6 that the bending strength and the volumetric shrinkage are well correlated up to 1050 °C, at which point a sharp discontinuity in the correlation takes place.

As to the correlation between the sample porosity and density, shown in Fig. 5, the same behaviour is observed, that is, a good correlation among these properties up to 1050 °C followed by a sharp discontinuity at this temperature. These critical transitions taking place around 1050 °C, are in good agreement with the values found from the logistic data fitting for  $T_0$ , as shown in Table 3, as well as with the argument presented above indicating that a sintering process is set in around this temperature.

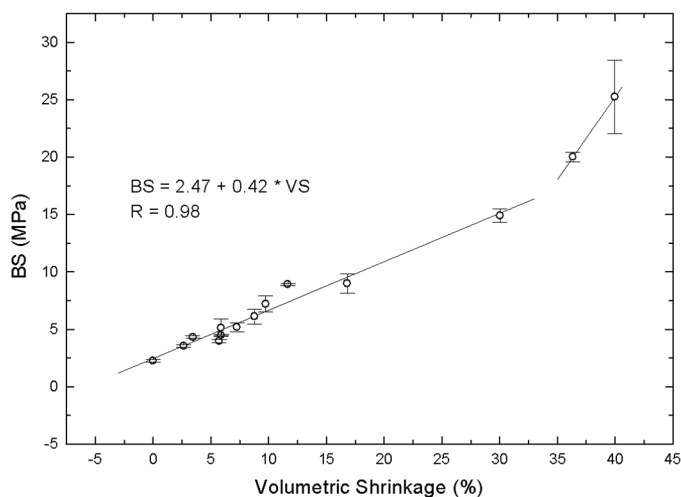


Fig. 7. Correlation between the bending strength and the volumetric shrinkage. The straight lines correspond to the data linear regression

The phase transformations from X-ray diffraction data are well known. Up to 400 °C the dominant phase transformations are due to intense dehydroxylation processes of components, such as gibbsite and goethite, with kaolinite remaining as the major mineral phase. Between 400 and 500 °C, we observed a reduction in crystalline fraction, due the transformation of kaolinite to a noncrystalline phase, metakaolinite ( $\text{Al}_2\text{Si}_2\text{O}_5(\text{OH})_4 \rightarrow \text{Al}_2\text{Si}_2\text{O}_7 + 2\text{H}_2\text{O}$ ) took place, while the other crystalline phases (quartz, anatase and illite) remained unchanged up to 900 °C. Heat treatments above 1000 °C cause new structural changes with the formation of mullite, cristobalite, and hematite phases, among others.

Considering the technological measurements of the J clay and the sanitary ware mass residue, Table 4 presents the technological properties of volumetric shrinkage, bending

strength and water absorption for the product fired at 980 °C, considered the best temperature for commercial purposes.

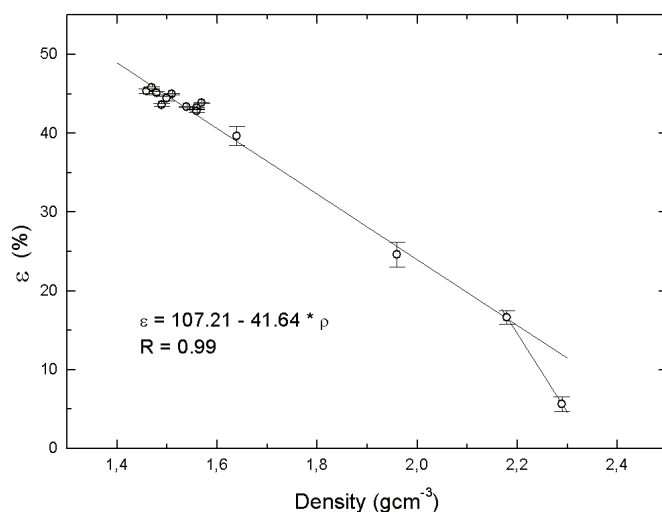


Fig. 8. Correlation between the samples porosity and density. The straight lines correspond to the data linear regression

Sample	Volumetric Shrinkage (%)	Bending Strength (MPa)	Water Absorption (%)
J Clay	2.1	3.3	20.3
J Clay 30	1.5	2.6	20.9

Table 4. Technological properties of end-product ceramic (~980 °C) without residue (J clay) and with 30 wt.% of sanitary ware residue (J Clay 30)

Comparing the Kaolinitic CG clay and the illitic J clay, we noted that the volumetric shrinkage value of J clay is half of the value of CG clay. In this case, J clay has advantages for the ceramic serial production in relation to dimensions uniformity. On the other side, CG clay presents a double value of bending strength, in relation to the J clay, i. e., more resistant pieces are shaped.

## 5. Thermal characterisation of CG and J clays using photothermal techniques, in relation to structural changes on firing

By analysing the thermal properties, some information can be collected from the material. In the following, we define the thermal properties and point out the values and their correlations with the sample microstructure.

Thermal diffusivity, a particular property that evaluates the heat propagation behaviour within the sample, is quite sensitive to the material structure as well as preparation and sintering conditions.

When values of thermal diffusivity ( $\alpha$ ) are evaluated from the amplitude data of the photoacoustic signal, we should pay attention to the microphone non-linear frequency response in relation to acoustic vibrations. Practically, all microphones present this irregularity. In our case, our microphone had a good linear frequency response above 20 Hz. In order to certify our set-up, a calibration measurement was performed. Figure 9 shows the dependence of the photoacoustical (PA) signal on the modulation frequency for the aluminium (Al) sample.

For frequencies used in this work, the signal exhibited a frequency dependency close to  $f^{-1.5}$ . This is the typical behaviour we would expect from the thermal diffusion model for a thermally thin sample. In fact, for a 25  $\mu\text{m}$  thick Al sample and a thermal diffusivity of  $93.28 \times 10^{-6} \text{ m}^2/\text{s}$  (Almond and Patel, 1996) the characteristic frequency  $f_c$  for the transition between the thermally thin and thick regime is about 47.5 kHz.

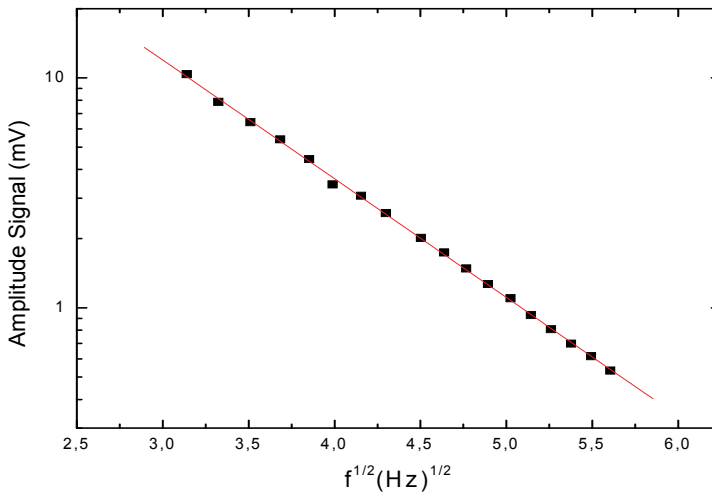


Fig. 9. Microphone output voltage as a function of the chopping frequency for the 25  $\mu\text{m}$  thick Al sample. The signal behaves roughly as  $f^{-1.5}$

The thermal conductivity ( $\kappa$ ) is associated with thermal conduction, which is the phenomenon where the heat is carried from regions of high temperature to regions of low temperature in a material.

The thermal effusivity ( $\epsilon$ ) denotes the material thermal impedance and is a measurement of the heat energy stored in a solid per degree of temperature rise from the start of a surface heating process (Marín *et al.*, 2002).

Here, thermal conductivity and thermal effusivity are reached applying the following expressions:

$$k = \alpha \rho c \quad (2)$$

$$\varepsilon = \sqrt{k\rho c} \quad (3)$$

Experiments concerning with thermal diffusivity, samples thickness and specific heat capacity measurements were performed five, ten and three times to produce the deviations, respectively.

### 5.1 Thermal diffusivity measurement

The thermal diffusivity experimental set-up is shown in Fig. 10. The sample is mounted directly onto a commercial electret microphone (Omnidirectional back electret condenser microphone cartridge, model WM-61A - Panasonic), fixed with a silicone grease, illuminated by the light beam from a He-Ne laser (Unilaser mod. 025) and modulated with a mechanical chopper (EG&G Instruments mod. 651), before it reaches the sample's surface. It consists of an OPC configuration in the sense that the sample is placed on top of the detection set-up itself (Vargas and Miranda, 1988). As a result of the periodic sample heating by modulated light absorption, the pressure inside the cell oscillates at the chopping frequency and can be detected by the microphone. The resulting PA signal is then subsequently fed into a field-effect-transistor (FET) pre-amplifier and leads directly to a "Lock-in" amplifier (Perkin Elmer Instruments mod. 5210), where it is possible to obtain the photoacoustic amplitude and the phase signal, which are recorded as a function of the modulation frequency in an appropriate software program.

According to the model proposed by (Rosencwaig and Gersho, 1976) for thermal diffusion, the equation that leads us to the pressure fluctuation ( $\delta P$ ) in the air chamber is

$$\delta P = \frac{\gamma P_0 I_0 (\alpha_g \alpha_s)^{1/2} \exp j(\omega t - \pi/2)}{2\pi l_g T_0 k_s f \sinh(\sigma_s l_s)}, \quad (4)$$

where  $\gamma$  is the air specific heat ratio,  $P_0$  the ambient pressure,  $T_0$  ambient temperature,  $I_0$  is the absorbed light intensity,  $f$  is the modulation frequency, and  $l_i$ ,  $k_i$  and  $\alpha_i$  are the length, thermal conductivity and the thermal diffusivity of the sample, respectively. Here, the subscripts denote the absorbing samples (s) and the gas (g) media, respectively, and  $\sigma_i = (1 + j)\alpha_i$ , is the complex thermal diffusion coefficient of  $i$  medium. It is assumed in the Eq. 4 that the sample is optically opaque  $l_\beta \ll l_s$ , where  $l_\beta$  is the optical penetration depth. For thermally thin sample  $\mu_s > l_s$ ;  $f < f_c$ , where  $\mu_s$  is the thermal diffusion length and  $f_c = \alpha/l_s^2$  is the cut-off frequency, Eq. 4 reduces to

$$\delta P = \frac{\gamma P_0 I_0 (\alpha_g)^{1/2} \alpha_s \exp j(\omega t - 3\pi/4)}{2\pi^{3/2} T_0 l_g l_s k_s f^{3/2}} \quad (5)$$

Here, the amplitude of the PA signal decreases as  $f^{-1.5}$ . On the other hand, at modulation frequencies above  $f_c$ , the sample is regarded as thermally thick and the corresponding equation is

$$\delta P = \frac{\gamma P_0 I_0 (\alpha_g \alpha_s)^{1/2} \exp -l_s \sqrt{\pi f / \alpha_s}}{\pi l_g T_0 k_s f} \exp j(\omega t - \pi/2 - l_s \alpha_s) \quad (6)$$

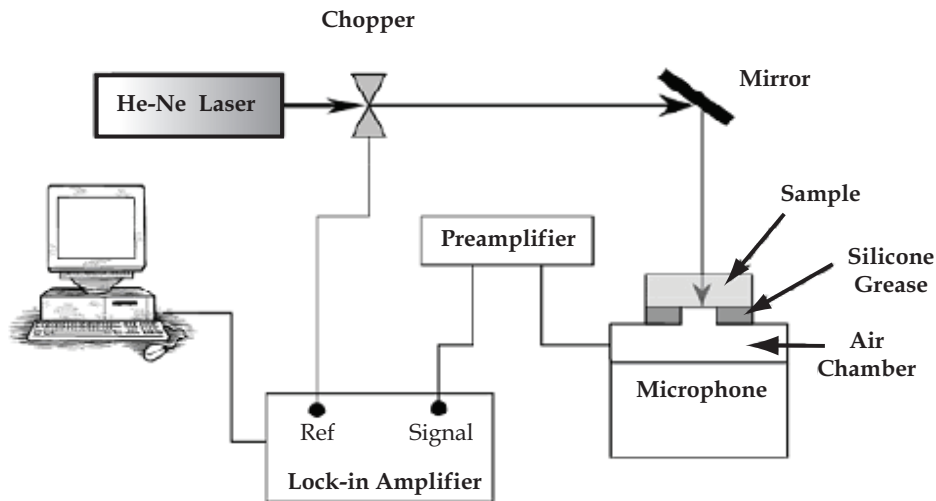


Fig. 10. Experimental arrangement for the thermal diffusivity measurements following (Yunus *et al.*, 2002)

The amplitude of the PA signal for a thermally thick sample decreases exponentially with the modulation frequency as  $S_{PA} \propto 1/f \exp(-b\sqrt{f})$ , where  $b = l_s \sqrt{\pi/\alpha_s}$ . In this case,  $\alpha_s$  is obtained from the experimental data fitting from the parameter  $b$ .

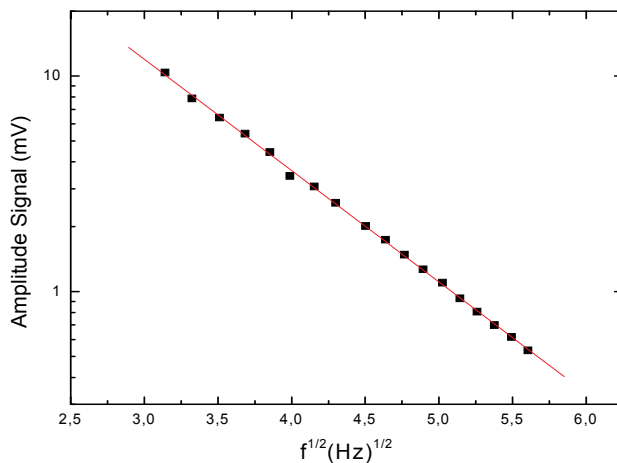


Fig. 11. Photoacoustic signal amplitude measurements as a function of the frequency square root for the 900 °C sample, together with the theoretical line

Taking values of thermal diffusivity from the literature, the cut-off frequency  $f_c$  is about 5.87 Hz, i.e. the frequency domain is regarded as thermally thick. As an example, Fig. 11 shows one of our sets of experimental points and the theoretical line for the 900 °C sample.

## 5.2 Specific heat capacity measurement

Specific heat capacity illustrates how a material can store large amount of heat, without suffering drastic temperature changes. The specific heat capacity ( $\rho c$ ) was measured using the photothermal technique of temperature evolution induced by continuous illumination of the sample in vacuum. The sample surface was painted black to make the parameter characterising the radiative properties of the surface equals to unit ( $\epsilon = 1$ ) and placed inside a Dewar, which is subsequently vacuum-sealed, As shown in Fig. 12. The front surface was illuminated by the He-Ne laser focused on the sample through an optical glass window on the Dewar. On the sample backside was connected a thin-wire T-type thermocouple. The thermocouple output was measured as a function of time by using a thermocouple monitor (Model SR630, Stanford Research Systems) attached to a computer. Care has been taken to prevent the heating light from reaching the thermocouple. Since the sample thicknesses, typically of the order of micrometers was much smaller than their widths (e.g., 10 mm), the simple one-dimensional heat diffusion equation with radiation losses can be applied to our experiment (Mansanares *et al.*, 1990).

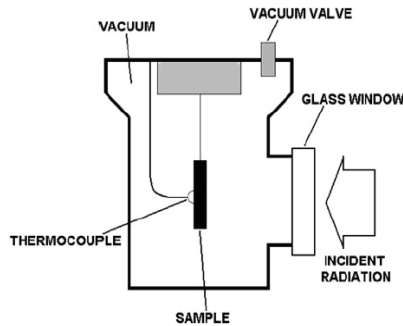


Fig. 12. Experimental arrangement for the specific heat capacity measurements

The temperature evolution was monitored from the ambient temperature up to the sample temperature saturation, obeying Eq. 7 and then the light was turned off and the temperature variation recorded until it reached the ambient temperature again (Eq. 8).

$$\Delta T \uparrow = \frac{I_0}{H} (1 - \exp(-t / \tau)) \quad (7)$$

$$\Delta T \downarrow = \frac{I_0}{H} \exp(-t / \tau) \quad (8)$$

Here,  $I_0$  is the incident light intensity,  $\tau = l\rho c / 2H$  is the thermal relaxation time,  $H = 4\sigma T_0^3$  is the heat transfer coefficient, where  $\sigma$  is the Stefan-Boltzmann constant,  $T_0$  is the ambient temperature and  $t$  is the time variable (Mota *et al.*, 2008).

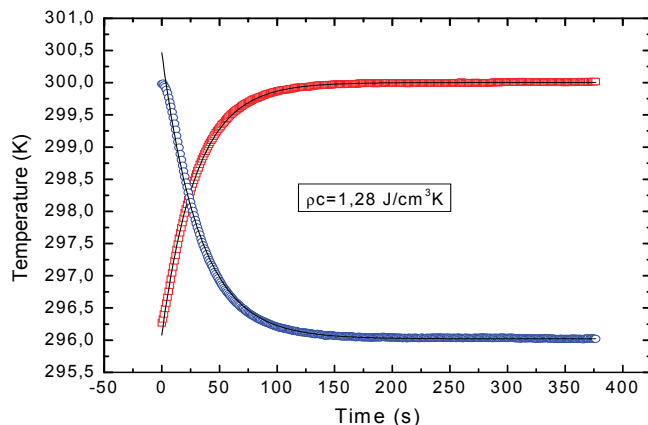


Fig. 13. Experimental data and theoretical lines of rising (square) and decreasing (circle) temperatures as a function of time for the 1060 °C sample

As an example, Fig. 13 shows the experimental data (open symbols) and theoretical lines for the 1060 °C sample (CG clay).

### 5.3 Results and discussion

Results of measurements of the thermal properties from CG clay are shown in Table 5 as a function of firing temperature.

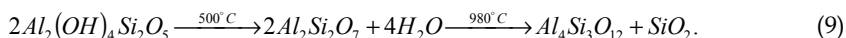
Temperature (°C)	Thickness (μm)	Thermal diffusivity (cm <sup>2</sup> /s)	Specific heat capacity (J/cm <sup>3</sup> K)	Thermal conductivity (W/cmK)	Thermal effusivity (Ws <sup>1/2</sup> /cm <sup>2</sup> K)
900	275±1.56%	0.012±2.58%	1.367±4.13%	0.016	0.148
950	273±3.58%	0.025±4.96%	1.064±3.08%	0.027	0.168
980	419±0.61%	0.012±2.99%	1.178±3.64%	0.014	0.129
1020	323±1.41%	0.021±2.16%	1.201±1.34%	0.025	0.174
1060	330±0.63%	0.031±0.22%	1.141±2.14%	0.035	0.200
1100	323±1.56%	0.013±2.58%	1.067±1.37%	0.014	0.122

Table 5. Thermal properties values and samples thickness as a function of firing temperature with its standard deviation

Thermal diffusivity values ranged from 0.0016 to 0.0063 cm<sup>2</sup>/s and are in close agreement with the literature (Alexandre *et al.*, 1999; García *et al.*, 2002). Table 5 presents values for specific heat capacity that were around 1.0 (J/cm<sup>3</sup>K). Thus, we can infer that thermal conductivity and effusivity tend to follow the thermal diffusivity profile in relation to the firing temperature. Moreover, for this kind of material, thermal properties are strongly dependent on the material microstructure.

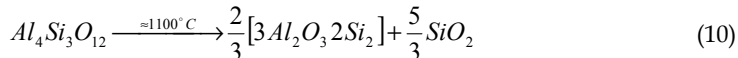
In relation to the structure, Fig. 1 shows the evolution of the X-ray diffraction patterns as a function of firing temperature. For natural clay the diffractogram reveals predominant phases of kaolinite, quartz and small amounts of gibbsite, illite, orthoclase and anatase. Following the treatment at 900 °C, illite, quartz, anatase and orthoclase remain unchanged and a hematite phase is revealed. Treatments at 950 °C or higher cause sample recrystallization in the Al-Si spinel (Okada *et al.*, 1986) and a liquid phase formation. Data clearly show the evolution of mullite and cristobalite in samples over the temperatures 1060 °C and 1100 °C.

Analysing the thermal diffusivity and the diffractograms, we can explain that the lower diffusivity value in 980 °C and 1020 °C is possibly due to the Al-Si rearrangements, owing to a crystallization process followed by a lattice formation (Okada *et al.*, 1986), according to



Equation 9 shows kaolinite  $2Al_2(OH)_4Si_2O_5$  evolution, which reaches the spinel phase  $Al_4Si_3O_{12} + SiO_2$  formation, with an intermediate phase, namely metakaolin  $2Al_2Si_2O_7 + 4H_2O$ . The high diffusivity value at 1060 °C could possibly be connected to the liquid phase formation within the beginning of the vitreous phase. The heat can be transported easier in this kind of phases than through the clay mineral grains. In support of this explanation for the highest thermal diffusivity, we note the clear modification of structure shown to occur above 1060 °C.

At 1100 °C, the thermal diffusivity decreases as explained by the reaction.



Through sintering at this temperature, formation of mullite  $\frac{2}{3}[3Al_2O_3 \cdot 2Si_2]$  and cristobalite  $\frac{5}{3}SiO_2$  starts from the spinel phase  $Al_4Si_3O_{12}$ , as reported by references in (Okada *et al.*, 1986). We suggest that there is a reduction of liquid phase and pores, with the formation of cristobalite, which probably is responsible for the thermal diffusivity decay.

Summarizing, the red clay from Campos dos Goytacazes-RJ region are used mainly for bricks and roofing tiles. In general, ceramic plants fire their products at temperatures below 900 °C. In the raw state the red clay, as shown in Fig. 1, is composed of a high proportion of kaolinite clay mineral besides accessory minerals including oxy-hydroxide, illite, quartz, and anatase. In this case sintering is dominated by particle-to-particle contact mainly of metakaolinite platelets, resulting in a more open structure and also ceramic products of low quality. High porosity results in a lower thermal diffusivity and thermal conductivity. On the other hand, the sintering accelerates above 950 °C with drastic microstructural changes due to the formation of a vitreous phase, resulting in better densification behaviour of the red clay. As a consequence, the thermal diffusivity increases abruptly. However, a decrease in the thermal diffusivity occurred between 1060 °C – 1100 °C. This is due mainly to formation of mullite, which is characterized by a high proportion of oxygen vacancies that lead to low thermal diffusivity. It will be reasonable then to consider that the optimum firing temperature range for the studied red clay is above 950 °C.



Temperature (°C)	Thermal diffusivity (cm <sup>2</sup> /s)	Specific heat capacity (J/cm <sup>3</sup> K)	Thermal conductivity (W/cm K)	Thermal effusivity (Ws <sup>1/2</sup> /cm <sup>2</sup> k)
900	0.003 ± 0.0004	0.61 ± 0.11	<b>0.002 ± 0.00</b>	0.034 ± 0.0013
950	0.005 ± 0.0000	0.83 ± 0.02	<b>0.004 ± 0.00</b>	0.061 ± 0.0005
1000	0.007 ± 0.0000	0.82 ± 0.13	<b>0.006 ± 0.00</b>	0.072 ± 0.0008
1050	0.004 ± 0.0000	0.92 ± 0.09	<b>0.004 ± 0.00</b>	0.061 ± 0.0001
1100	0.004 ± 0.0002	0.67 ± 0.11	<b>0.003 ± 0.01</b>	0.045 ± 0.0010

Table 6. Thermal properties of the J clay as in function of some possible sintering temperatures

Temperature (°C)	Thermal diffusivity (cm <sup>2</sup> /s)	Specific heat capacity (J/cm <sup>3</sup> K)	Thermal conductivity (W/cm K)	Thermal effusivity (Ws <sup>1/2</sup> /cm <sup>2</sup> k)
900	0.008 ± 0.0001	0.98 ± 0.00	<b>0.007 ± 0.00</b>	0.088 ± 0.0011
950	0.004 ± 0.0005	1.12 ± 0.15	<b>0.005 ± 0.11</b>	0.072 ± 0.0008
1000	0.009 ± 0.0008	1.57 ± 0.04	<b>0.014 ± 0.08</b>	0.148 ± 0.0005
1050	0.006 ± 0.0004	1.43 ± 0.17	<b>0.008 ± 0.06</b>	0.111 ± 0.0010
1100	0.004 ± 0.0009	1.25 ± 0.02	<b>0.005 ± 0.09</b>	0.082 ± 0.0009

Table 7. Thermal properties of the J clay with 30% sanitary ware mass residues as in function of some possible sintering temperatures

Tables 6 and 7 show the thermal properties of the J clay and J clay with 30% residue, respectively.

Regarding to the ceramic thermal properties, the CG clay ceramic sample presented much higher values than the J clay ceramic. Thus, depending on the application, considering thermal properties we can use a kaolinite raw material if we need ceramics with fast thermalization or illitic clays for a better thermal isolation. We noted that the aggregation of 30% of sanitary ware mass residue in the J clay matrix generates higher values of the ceramic thermal properties.

## 6. Pollutant gases from the firing of clay ceramic added with residues

The gas emission concentrations during the CG and J clays firing process were measured. The figures were displayed in such way that it is possible to compare the whole samples for each gas, obeying the CG clay samples and the J clay samples.

### 6.1 Experimental procedure

The following materials were studied in this present research: **a)** the CG clay and steel slag considered as a waste by the National Steel Plant (CSN) located at the south of the state. This slag was generated during the conventional oxygen blowing, LD (Linz Donawitz) process, of steel refining; **b)** The J clay and the sanitary ware mass rejects from a ceramic industry of São Paulo state.

The emitted gases from the firing process were quantitatively measured by means of a photothermal technique.

The gas released from the furnace was directly connected to an infrared model URAS 14, ABB gas analyser under a suction flux of 0.3 L/min. This gas analyser detected and quantified simultaneously CO, CO<sub>2</sub>, CH<sub>4</sub>, NO, N<sub>2</sub>O, NH<sub>3</sub> e SO<sub>2</sub>. Gas samples were collected 20 min. after settled temperature stages of respectively, 150, 300, 450, 550, 650, 800, 950, 1050 and 1100 °C. The samples were brought to room temperature following the inertial cooling of the resistive furnace.

The gas analyser measurement process is based on resonance absorption at the characteristic vibrational rotation spectrum bands of non-elemental gases in the middle infrared range between 2 µm and 12 µm. Because of their bipolar moment, the gas molecules interact with infrared emissions. For selectivity, the receiver is filled with the applicable sample components to establish reference and sensitivity to these components (~1 ppm). It consists of the cell divided into two identical compartments: one in the measuring cell, through which the sampled gas is flowed, and the other acts as reference, filled with nitrogen. The light emitted from a hot filament is modulated by a mechanical chopper and divided by a beam splitter. Each beam goes simultaneously through the measuring cell and the reference cell. The detector consists of two sealed chambers separated by a diaphragm capacitor. Both chambers are filled with pure gas of the chemical species under study. The light beams emerged from the sample and reference cells reach independently the two detector chambers, causing a differential pressure that is proportional to the light absorption by the sample. The pressure difference is converted by the diaphragm capacitor into an electrical signal. A detailed description of the Uras performance can be found in the literature (11). Before each sample analyses the cells were calibrated using pure standard N<sub>2</sub>.

## 6.2 Results and discussion

Figures 14 and 15 show the released CO<sub>2</sub> and CO gases as in function of the temperature from the CG clay with (5%, 10%) and without (0%) steel slag residue in different concentrations in weight. The other gases had not presented significant values.

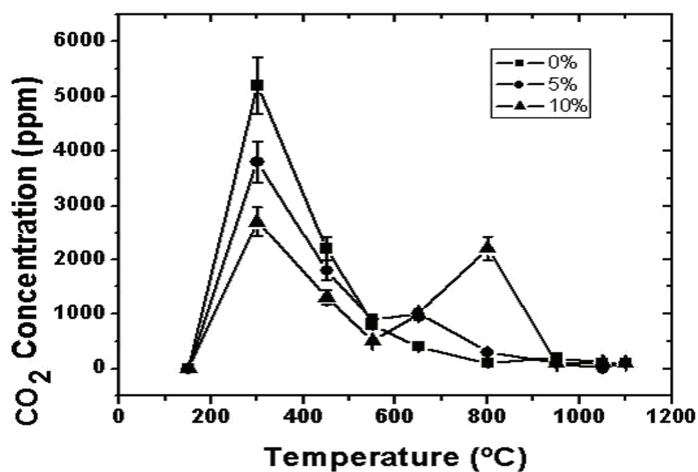


Fig. 14. CO<sub>2</sub> profiles as in function of the firing temperature for the samples with 0 %, 5 %, and 10 %

CO<sub>2</sub> concentration values were emitted more significantly in the presence of the residue. Generally, carbon composites, as CO<sub>2</sub>, in the range of 300 °C to 500 °C are emitted due to the organic matter oxidation. Moreover, the reaction of the kaolinite and goethite dehydroxilation deals to a metakaolinite, that is, an amorphous phase.

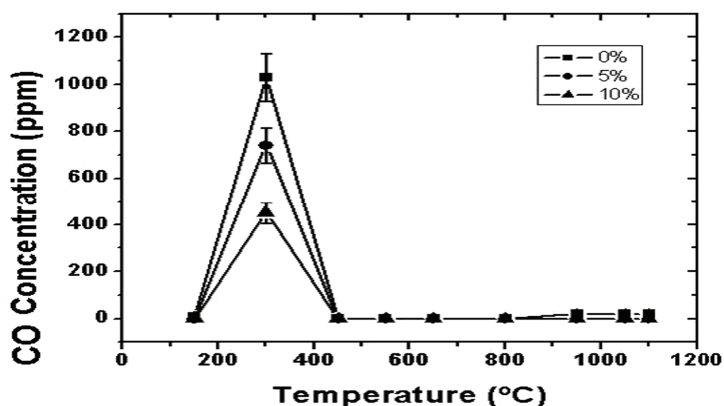


Fig. 15. CO profiles as in function of the firing temperature for the samples with 0 %, 5 %, and 10 %

The CO<sub>2</sub> emission in temperatures higher than 850 °C, is possibly due to: the hydroxyl (OH) release, proceeding from the gases that were locked up in the pores, which are set free later when the pores begin processes of volumetric reduction, due to the high temperature; the chemical dehydration of minerals that contains mica (muscovite); and the calcite decomposition ( $\text{CaCO}_3 = \text{CaO} + \text{CO}_2$ ). Values reached in this section were just proportional to a laboratory furnace.

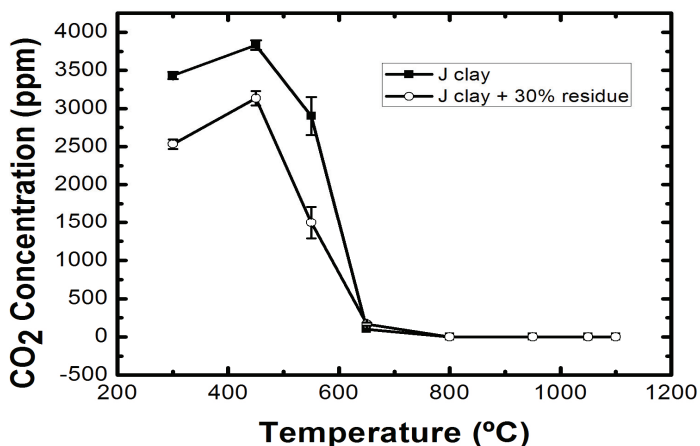


Fig. 16. CO<sub>2</sub> emitted during the ceramic firing process as in function of the firing temperature

Figures 16 and 17 show the CO<sub>2</sub> and CO emissions as in function of firing temperature from the J clay without and with 30% in weight of sanitary ware mass residue. Firstly, we observed that the addition of the residue diminishes the amount of CO<sub>2</sub> emission. The amount of CO<sub>2</sub> emitted between 300 and 550 °C has the same explanation previously cited, that is, due to organic matter oxidation and the dehydroxilation of clay minerals.

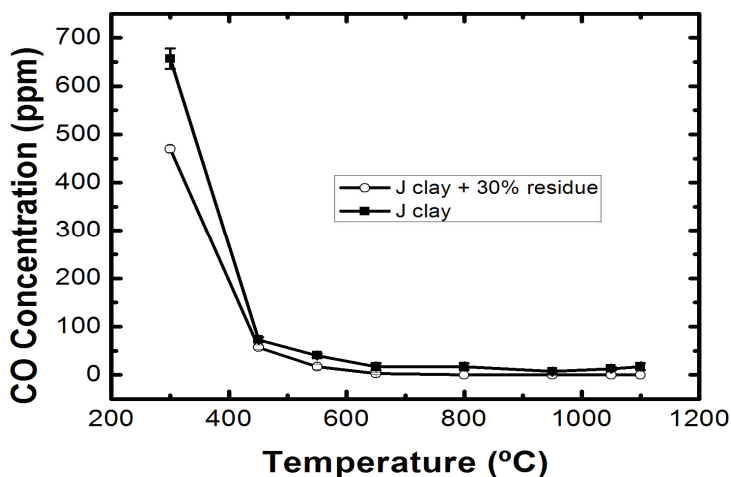


Fig. 17. CO emitted during the ceramic firing process as in function of the firing temperature

## 7. Conclusions

Here, red ceramic samples from Rio de Janeiro state and from São Paulo state were analysed as in function of firing temperature. In order to study the ceramics quality, technological essays were prepared. Comparisons between the Kaolinite CG clay and the illitic J clay were made, indicating the advantages and disadvantages of each specimen.

The thermal property of red ceramic samples as well as their crystalline phases were analysed as a function of sintering temperature. Photothermal techniques were used to measure the thermal properties and the microstructures were identified by x-ray diffraction, in order to compare structural and thermal features of the samples. It was shown that there is an intrinsic relationship between the structure and the thermal diffusivity. When the crystalline structure undergoes strong perturbations the thermal diffusivity values decrease and vice-versa. When liquid phases achieve the highest concentration at around 1060 °C (CG clay) and 1000 °C (J clay), the thermal diffusivity shows its maximum peak. Afterwards, there is a decrease, although the thermal diffusivity maintains high values, due to mullite enhancement and vitreous phase consolidation in the red ceramics. The J clay sintering temperature is lower than to the CG clay, due to a larger amount of flux material.

Thermal property values are consistent with the literature. As the specific heat capacity has values of approximately unity, thermal conductivity and effusivity follow that of thermal diffusivity. Considering thermal properties, it was shown that red ceramic sintering temperatures should be greater than 950 °C, but below 1060 °C from both clays.

The steel slag investigated, considered as a steelmaking waste, has an elevated amount of Ca, Fe, Mg and Si. The main crystalline phases identified were magnetite,  $\text{Fe}_3\text{O}_4$ , calcite,  $\text{CaCO}_3$ , magnesium manganese oxide,  $\text{Mg}_6\text{MnO}_8$  and calcium silicate,  $\text{Ca}_2\text{SiO}_4$ ,  $\text{CaSiO}_3$ . The incorporation of steel slag into clayey ceramics, must be done in amounts of up to 10 wt.%. In relation to the steel slag incorporation, it had been mainly detected CO and  $\text{CO}_2$ . Comparing the diverse percentages of residues into the ceramic mass, it observed that the  $\text{CO}_2$  concentrations decrease in the range of 300 °C to 500 °C, when increased the percentage of residue to the mass. On the other side, between 500 °C and 950 °C, there was a reasonable increase of the concentration (in relation to the pure clay), when the residues percentage was enlarged. The calcite starts to decompose around 675 °C and its complete decomposition occurs up to 950 °C. When mixed to another minerals, the calcite presents lower temperature of decomposition (880 °C, approximately).

It is possible that sanitary ware residues can attenuate the pollutant gas release from the ceramic firing. We concentrate in this chapter the CO and  $\text{CO}_2$  gases, in order to facilitate the point of view of our study. It will appear elsewhere the complete set of measured gases from this research.

## 8. Acknowledgment

The authors thank the Brazilian agencies FAPERJ, CNPq and CAPES for the financial support.

## 9. References

- Alexandre, J.; Saboya, F.; Marques, B. C.; Ribeiro, M. L. P.; Salles, C., da Silva, M. G.; Sthel, M. S., Auler, L. T. & Vargas, H. (1999). Photoacoustic thermal characterization of kaolinite clays. *The Analyst*, vol. 124, pp. 1209–1214.
- Almond, D.P., & Patel, P.M. (1996). *Photothermal Science and Techniques*. Chapman & Hall, London.
- Dubois, J.; Murat, M.; Amroune, A.; Carbonneau, X. & Gardon, R. (1995). High-temperature transformation in kaolinite: the role of the crystallinity and of the firing atmosphere. *Appl. Clay Science*, vol. 10, pp. 187–198.
- Faria Jr., R.T.; Filgueira, M.; Esquef, I.A.; Machado, F.A.; Rodrigues, M.F.; Bobrovitchii, G.S. & Vargas, H. (2005). Thermal characterization of sintered hardmetal. *Journal de Physique. IV*, vol. 125, pp. 237–239.
- García, E., Osendi, M.I., Miranzo, P., 2002. Thermal diffusivity of porous cordierite ceramic burners. *Journal of Applied Physics* 92, 2346–2349.
- Heydorn, K. & Thuesen, I. (1989). Classification of ancient Mesopotamian ceramics and clay using SIMCA for supervised pattern recognition. *Chemometrics and Intelligent Laboratory Systems*, vol.7, pp. 181–188.
- Manhães, R. S. T.; Auler, L. T.; Sthel, M. S.; Alexandre, J.; Massunaga, M. S. O.; Carrió, J. G.; dos Santos, D. R.; da Silva, E. C.; Garcia-Quiroz, A. & Vargas, H. (2002). Soil characterisation using X-ray diffraction, photoacoustic spectroscopy and electron paramagnetic resonance. *Appl. Clay Science*, vol. 21, pp. 303.
- Mansanares, A.M.; Bento, A.C.; Vargas, H., Leite, N.F. & Miranda, L.C.M. (1990). Photoacoustic measurement of the thermal properties of two-layer systems. *Physical Review B*, vol. 42, pp. 4477–4486.

- Marín, E.; Marín-Antuna, J. & Díaz-Arencibia, P. (2002). On the wave treatment of the conduction of heat in photothermal experiments with solids. *European Journal of Physics*, vol. 23, pp. 523-532.
- Morgan, D. J. (1993). Thermal analysis including evolved gas analysis of clay raw materials, *Applied Clay Science*, vol. 8, pp. 81.
- Mota, L.; Toledo, R. ; Machado, F.A.L.; Holanda, J.N.F.; Vargas, H. & Faria Jr., R.T. (2008). Thermal characterization of red clay from the Northern Region of Rio de Janeiro State, Brazil using an open photoacoustic cell, in relation to structural changes on firing. *Appl. Clay Science*, vol. 42, pp. 168-174.
- Nastro, V.; Vuono, D.; Guzzo, M.; Niceforo, G.; Bruno, I. & de Luca, P. (2006). Characterisation of raw materials for production of ceramics. *Journal of Thermal Analysis Calorimetry*, vol. 84, pp. 181-184.
- Okada, K.; Otsuka, N. & Ossaka, J. (1986). Characterization of spinel phase formed in the kaolin-mullite thermal sequence. *J. Am. Ceram. Soc.*, vol. 69, pp. C251-C253.
- Oliveira, G.E., & Holanda, J.N.F., (2004). Utilization of solid waste from siderurgical industry in red ceramic, *Cerâmica*, vol. 50, pp. 75-80.
- Parsons, A. J.; Inglethorpe, S. D. J.; Morgan, D. J. & Dunham, A. C. (1997). Evolved gas analysis (EGA) of bricks clays. *J. Therm. Analysis*, vol. 48, pp.49.
- Perondi, L.F. & Miranda, L.C.M. (1987). Minimal volume photoacoustic cell measurement of thermal diffusivity: effect of the thermoelastic sample bending. *Journal of Applied Physics* , vol. 62, pp. 2955-2959.
- Reed J.S. (1976). *Principles of the Ceramics Processing*. John Wiley and Sons, New York.
- Rice, R.W. & Dekker, M. (1998). *Porosity of Ceramics*, Elsevier, New York
- Rosencwaig, A. & Gersho, A. (1976). Theory of the photoacoustic effect with solids. *Journal of Applied Physics*, vol. 47, pp. 64-69
- Souza, V.P.; Toledo, R.; Holanda, J.N.F.; Vargas, H. & Faria Jr, R.T. (2008). Pollutant gas analysis evolved during firing of red ceramic incorporated with water treatment plant sludge. *Cerâmica*, vol. 54, pp. 351-355.
- Vargas, H. & Miranda, L.C.M. (1988). Photoacoustic and related photothermal techniques. *Physics Reports*, vol. 161, pp. 43-101.
- Vieira, C.M.F. & Monteiro, S.N. (2009). Incorporation of solid wastes in red ceramics: an updated review. *Matéria (Rio J.)*, vol.14, nº .3, pp. 881-905. ISSN 1517-7076.
- Yunus, W.M.M.; Fanny, C.Y.J.; Phing, T.E.; Mohamed, S.B.; Halim, S.A. & Moskin, M.M. (2002). Thermal diffusivity measurement of Zn, Ba, V, Yand Sn doped Bi-Pb-Sr-Ca-Cu-O ceramics superconductors by photoacoustic technique. *Journal of Material Science*, vol. 37, pp. 1055-1060.

# Mechanical Properties of Kaolin-Base Ceramics During Firing

Igor Štubňa<sup>1</sup>, Anton Trník<sup>1,2</sup>, František Chmelík<sup>3</sup> and Libor Vozár<sup>1</sup>

<sup>1</sup>*Department of Physics, Constantine the Philosopher University, Nitra,*

<sup>2</sup>*Department of Materials Engineering and Chemistry,  
Czech Technical University, Prague,*

<sup>3</sup>*Department of Physics of Materials, Charles University Prague, Prague*  
<sup>1</sup>*Slovakia*

<sup>2,3</sup>*Czech Republic*

## 1. Introduction

Firing of silicate ceramics, which are made of clays with high contents of kaolinite, transforms a green body into a ceramic product [1, 2]. The green body exhibits significant changes of its properties resulting from dehydration at low temperatures, phase changes during dehydroxylation and high-temperature reactions, and densification during sintering [3, 4]. All these changes significantly influence mechanical properties of the fired body as well as its other physical properties.

To save time and energy, it is desirable to conduct the firing in the shortest time possible without damage to the fired ceramic body. Calculating the safe upper limit of the heating or cooling rate of the large ceramic bodies (e.g. high-voltage insulators) is a complex task that requires knowing five material quantities: mechanical strength (MOR), Young's modulus (YM), Poisson's ratio, thermal conductivity, and coefficient of the linear thermal expansion (CLTE). All of these quantities must have to be known as functions of the actual temperature at the firing. The upper limit of the heating rate according to [2] is

$$v_{\max} = \frac{\sigma_f(1-\mu)\lambda}{A\alpha E r^2 c \rho} \quad (1)$$

where  $\sigma_f$  is MOR,  $\mu$  is Poisson's ratio,  $\lambda$  is thermal conductivity,  $A$  is the shape factor of the ceramic body,  $\alpha$  is CLTE,  $E$  is YM,  $r$  is the characteristic dimension of the body,  $c$  is volumetric heat capacity and  $\rho$  is the volume mass density.

The relationships between the temperature and these qualities (MOR, YM, CLTE,  $\mu$  and  $\lambda$ ) can be identified only using experimental approach despite of some theoretical connection between YM and CLTE or between YM and MOR. These theoretical relationships were derived for simple materials and they are only very approximately applicable to complex multiphase material as kaolin-base ceramics. For thin-wall ceramic bodies such as whiteware, a more simple method based on thermilatometric results can be used for control of the firing [5].

This chapter is devoted to the development of the two most important mechanical parameters, MOR and YM of the green ceramic material during heating and cooling stages of the firing, with the exception of the highest temperature region where the body becomes partially plastic. Poisson's ratio  $\mu = (E / 2G) - 1$ , where  $E$  is YM and  $G$  is the elastic shear modulus, can be easily calculated if  $\mu$  at the room temperature is known. The relationships between YM or shear modulus and the temperature during firing can be assumed as qualitatively identical, i.e.  $\mu \approx \text{const}$  during the all firing.

## 2. Experimental

### 2.1 Samples

Samples from quartz porcelain mixture for the modulated-force thermomechanical analysis (mf-TMA) and measuring MOR were made from 50 % kaolin and clay, 25% quartz and 25% feldspar. The mixture was ground and sieved on a 100 mesh/mm<sup>2</sup> sieve and turned into a plastic material. Then cylindrical samples (diameter 11 mm) were made with the laboratory vacuum extruder. The samples were dried in the open air and finally content ~1 wt.% of the physically bounded water.

### 2.2 Modulated force thermomechanical analysis (mf-TMA)

The mf-TMA is an effective experimental method to determine temperature dependence of YM of ceramics [6]. Most of the technical solutions of the method are based on continual measuring the resonant frequency of the sample during a defined temperature regime. The resonant frequency  $f$ , the volume mass density  $\rho$ , and the sample dimensions (length  $l$  and diameter  $d$ ) serve for the calculation of YM [7, 8]

$$E = 1.12336 \left( \frac{l^2 f}{d} \right)^2 \rho T \quad (2)$$

Here,  $T$  is a correction coefficient, which should be used if  $l/d < 20$ . Since the ratio for the used samples  $l/d = 15 < 20$ , and assuming Poisson's ratio  $\mu = 0.2$ , the coefficient  $T = 1.06821$  can be determined from the table given in [9].

Since the mass and the dimensions of the green sample are not constant during firing, to obtain the correct value of Young's modulus at the actual temperature  $t$ , the mass and the dimensions at the actual temperature  $t$  should be substituted into Eq. (2). Then we obtain

$$E(t) = 1.52782 \frac{m_0 \left( 1 + \frac{\Delta m(t)}{m_0} \right) l_0^3 f^2(t)}{d_0^4 \left( 1 + \frac{\Delta l(t)}{l_0} \right)} \quad (3)$$

Relative changes in the mass  $\Delta m(t) / m_0$  and dimensions  $\Delta l(t) / l_0$  must be determined from the results of thermogravimetric (TGA) and thermogravimetric (TGA) analyses. The values  $m_0$  and  $l_0$  are the initial mass and length of the sample at room temperature. If Eq. (3) is used, simply considering  $\Delta m(t) = 0$  and  $\Delta l(t) = 0$ , a certain error arises. Its relative value for measuring the green sample is shown in Fig. 1.



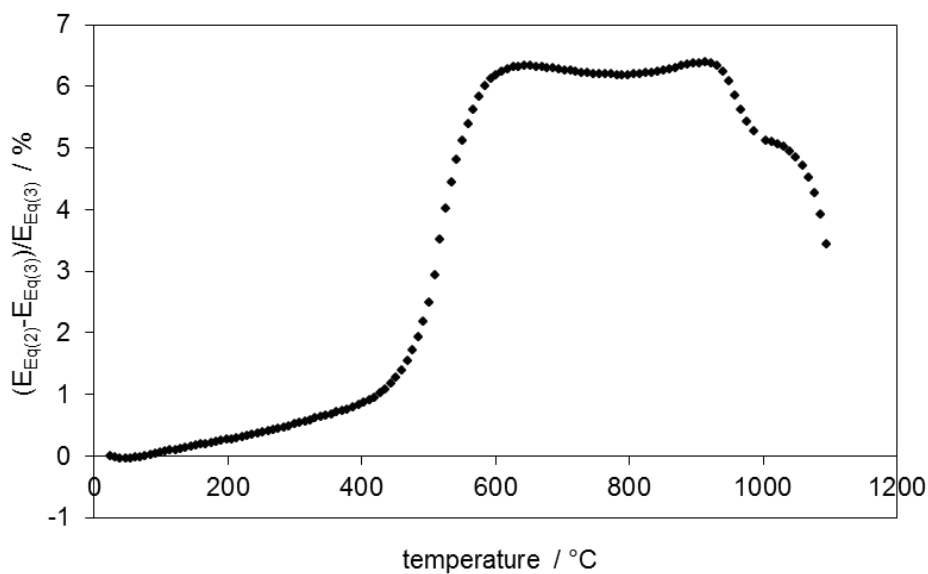


Fig. 1. Relative error  $(E_{Eq(2)} - E_{Eq(3)}) / E_{Eq(3)}$  originated from neglecting the mass and dimensions changes of the sample

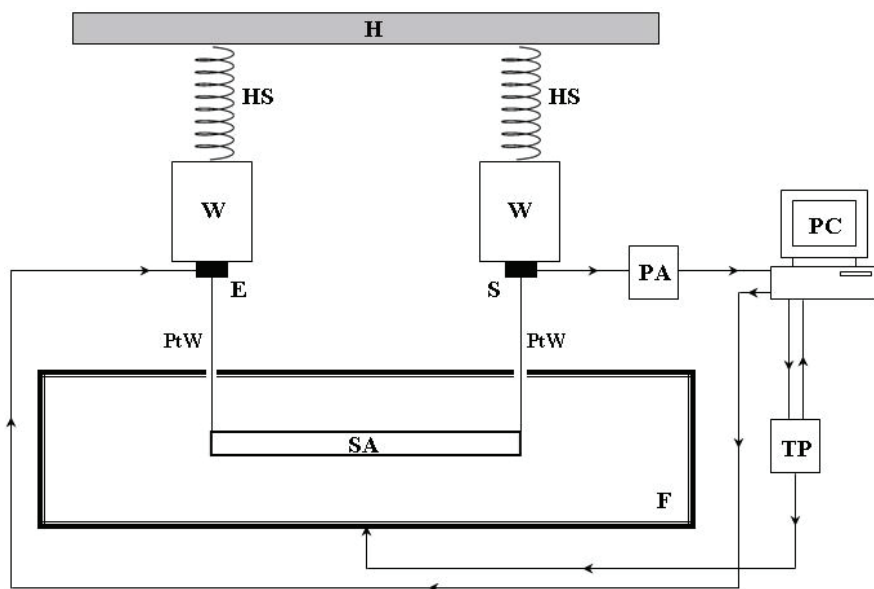


Fig. 2. A scheme of the apparatus for measuring YM.

H - frame, HS - helical spring, W - weight, E - exciter, PtW - platinum wire, S - sensor, PA - preamplifier, SA - sample, F - furnace, PC - computer, TP - temperature programmer

The apparatus for measuring Young's modulus of ceramics at higher temperatures has to satisfy several requirements: a) the sample must be adequately large because some ceramic materials are inhomogeneous and contain crystals of different minerals, glassy phase, and pores; b) green ceramic material is brittle and soft and its mechanical strength is low, and c) the dimensions of the sample contract by up to 8 – 12 % during sintering. We designed an apparatus that satisfies these requirements, see Fig. 2 [10]. It is based on the chart showed in [7, 8] and, in more detail, in [11]. A sample placed horizontally in a furnace is suspended on thin platinum wires ( $\varnothing 0.15$  mm) which connect the sample with exciter and sensor located outside the furnace. For the measurement of the sample temperature we use the thermocouple Pt-PtRh10. Its hot ending is in the vicinity of the sample and the cold endings are connected to the temperature programmer.

### 2.3 Measurement of MOR

Measurements at high temperatures are energy and time-consuming. To make a measurement of MOR more effective, a new apparatus with a heated magazine for 10 samples was designed (Fig. 3). It allows testing of these samples in one heating cycle from 20 to 900 °C using the three-point-bending method.

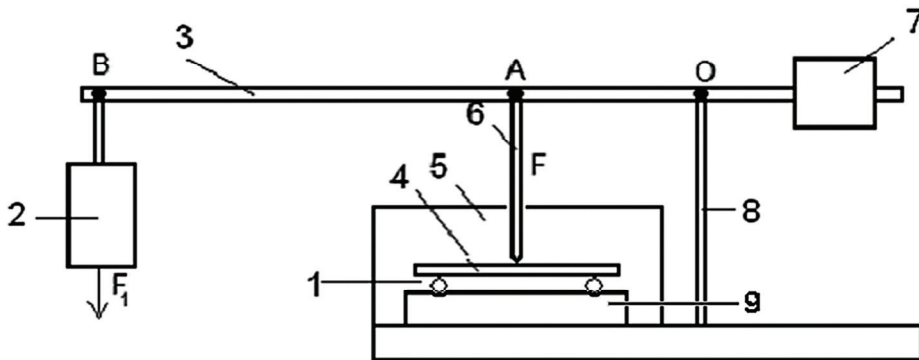


Fig. 3. Apparatus for measuring MOR.

1- supports, 2 - dynamometer, 3 - lever, 4 - sample, 5 - furnace, 6 - alumina rod, 7 - counterweight, 8 - frame, 9 - alumina brick

Temperature of the samples changed linearly at the rate of 5 °C/min. When the temperature reached a chosen value, one sample was broken. The next sample was broken at the next chosen temperature, etc. The loading force increased linearly with a rate of 2 N/s. If the three-point-bending is used, MOR can be calculated from a formula [12]

$$\sigma_f = \frac{8lF_f}{\pi d^3} \quad (4)$$

where  $d$  is the diameter of the sample,  $l$  is the span between the supports and  $F_f$  is the force at the moment of the rupture. However, thermal expansion of the sample diameter  $\Delta d(t)$  and the span between supports  $\Delta l(t)$  must be taken into account at elevated temperatures. Then Eq. (4) obtains the form

$$\sigma_f(t) = \frac{8[l_0 + \Delta l(t)]}{\pi[d_0 + \Delta d(t)]^3} [aF_{1f}(t) + F_2] , \quad (5)$$

Where  $d_0$  and  $l_0$  are the diameter and the span at room temperature,  $a$  is a constant of the lever mechanism,  $F_{1f}(t)$  is the force registered at the moment of the rupture and  $F_2$  is a small known initial pre-loading force.

### 3. Heating stage of firing

During heating, several important processes take place in ceramic material. To understand them in more detail it is useful to perform thermal analyses, mainly TGA, DTA and TDA. Their results are shown in Fig. 4 and Fig. 5. Both curves depicted in Fig. 4, TGA and DTA, are of a typical shape for kaolin base ceramics. Since the sample was not fully dried, some physically bounded water was present at the surface defects on walls of kaolinite crystals [13] and in micropores, which caused a subsequent loss of the sample mass at the lowest temperatures. This process is endothermic as confirmed by DTA.

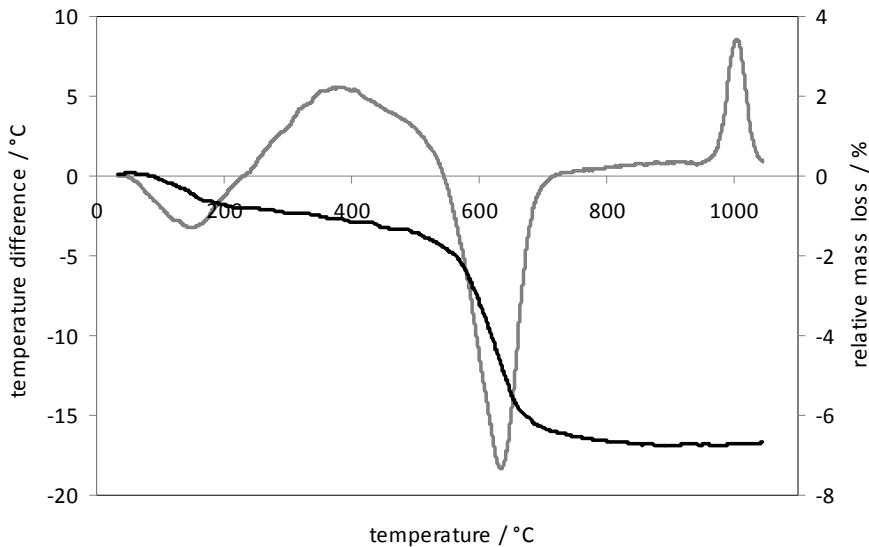


Fig. 4. Relative mass loss (black line) and DTA (gray line)

Fig. 5 and Fig. 6 show the results of TDA and mf-TMA of the green porcelain sample reflecting the same processes as Fig. 4. Comparing Fig. 5 to Fig. 6, the rule “the higher thermal expansion, the lesser YM” is not fulfilled in the temperature range of 20 – 200 °C. Here, two concurrent mechanisms appear. The first is the escaping of the physically bound water from the finest pores and the surface of crystals. This leads to a) a closer contact between crystals and, thereby, to an increasing YM and b) to a small contraction of the sample. Simultaneously, thermal expansion makes YM lower and the dimensions of the sample larger. The net effect of these phenomena demonstrates itself as a steep growth of YM and as a very moderate deceleration of the thermal expansion up to 120 °C.

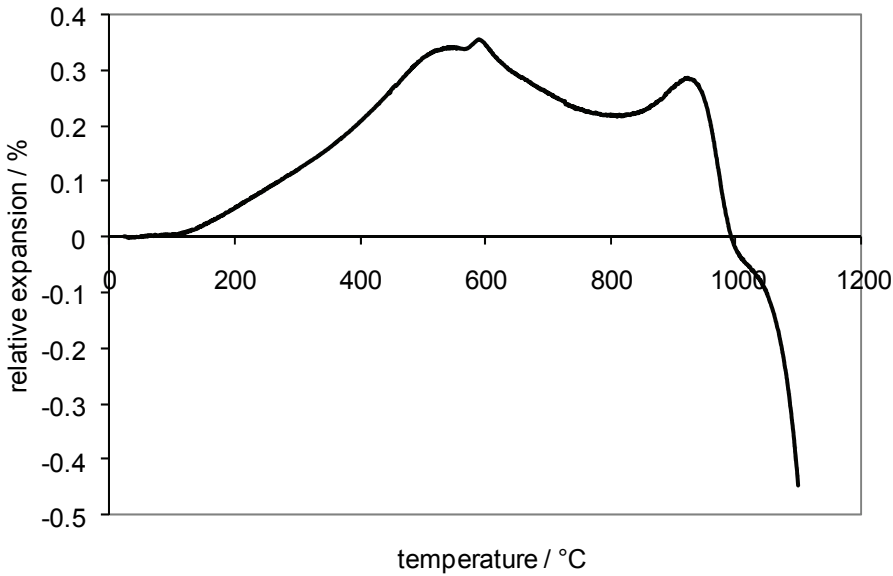


Fig. 5. Thermodilatometric curve of the green sample during heating

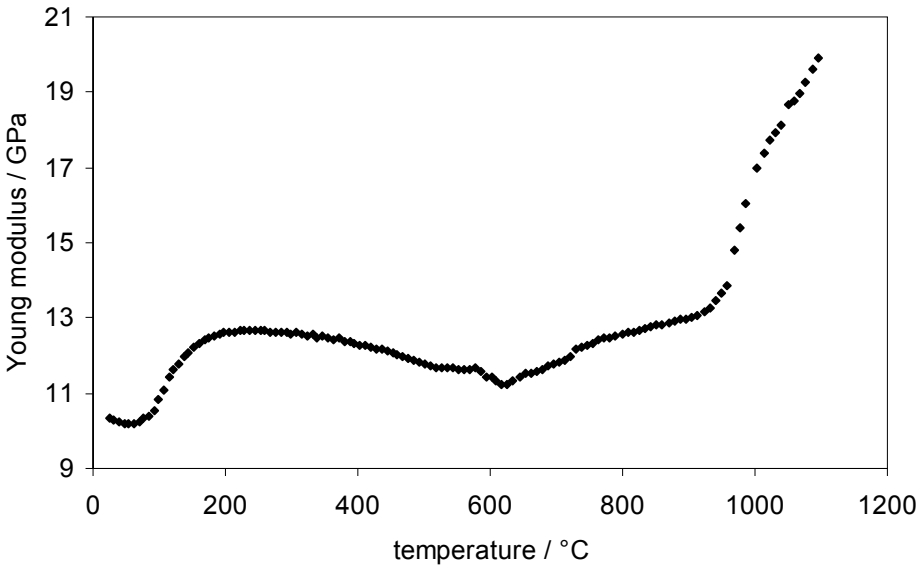


Fig. 6. The results of mf-TMA - Young modulus (calculated according to Eq. (3)) versus temperature

After removing the weakly bound physically water, the sample loses the rest of this water and a very small amount of the organic material, see TGA in Fig. 4. The course of the dilatometric curve represents a simple thermal expansion, as shown in Fig. 5. The values of the thermal expansion increase up to ~500 °C when dehydroxylation occurs, which leads to a contraction of the sample and dropping of its mass. Following the escape of the physically bound water, there is no further change in the structure and composition. Hence, above 200 °C both TDA and mf-TMA results approximately satisfy the rule “the higher thermal expansion, the lesser YM” as long as dehydroxylation emerges at ~450 °C. This process is exhibited in different ways for mf-TMA and TDA. The TDA reflects a) shrinkage of the kaolinite crystals as the result of escaping the crystalline water from their octahedral sheets and b) thermal expansion of the feldspar and quartz.

The mf-TMA is a complex result of four phenomena: a) creation of defects in the kaolinite crystals interiors (which makes YM lower), b) probably the beginning of the solid phase sintering (which makes YM higher), c) loss of the sample mass (which makes YM lower) and d) shrinkage of the sample dimensions (which makes YM higher).

We can conclude that the thermodilatometric behavior of the sample during dehydroxylation is determined primarily by the dehydroxylation process in the kaolinite crystals. The elastic behavior is determined mainly by improving the contacts between the crystals as a consequence of the solid phase sintering. Dehydroxylation plays a minor role in the mf-TMA results (except at a short temperature interval 550 – 620 °C). The temperature interval of dehydroxylation is considered a critical stage of the firing process. It is known that an inadequately high rate of heating or cooling leads to cracking of the ceramic body. This was studied in detail on large cylindrical samples in the dehydroxylation region [14].

The  $\alpha \rightarrow \beta$  transition of quartz takes place in the dehydroxylation background, and in spite of a relatively large content of quartz in the sample (25 wt.%), the transition proves only with a small peak at ~570 °C on both curves, TDA and mf-TMA.

Thermal expansion after the completion of dehydroxylation ends at temperature ~950 °C when the collapse of the metakaolinite lattice accompanied by a rapid shrinkage appears. Identically, there is a steep increase in YM in response to a faster solid state sintering and the new structure. A typical exothermic peak on the DTA curve at 1000 °C is characteristic for this process.

Mechanical strength (Fig. 7) approximately follows the course of mf-TMA in Fig. 6. As our preliminary (not yet published) results show, MOR slightly increases in the interval 20 – 200 °C. However, MOR is much more sensitive to defects created by dehydroxylation. Its values run through a clear minimum at ~450 °C. Very similar results were published in [15]. An increase of MOR during the continuing dehydroxylation (above 450 °C) as well as insignificant decrease of YM (Fig. 6) and of the sound velocity (Fig. 8) during dehydroxylation are not easy to explain. Other constituents (quartz and feldspar) do not lose their mechanical properties, and metakaolinite must be considered a mechanically weak material because of the high concentration of defects [16]. The structure of metakaolinite does not change until ~950 °C, so the effect of the MOR increase should be attributed to improving the interfaces between metakaolinite crystals. Solid phase sintering could be a possible relevant mechanism.

It is interesting to compare the results of mf-TMA of the green porcelain sample (Fig. 6) to mf-TMA of kaolin (Fig. 8) [17]. Sound velocity  $c$  is related to YM by formula  $c^2 = E / \rho$ ; therefore the temperature dependence of YM and the sound velocity are similar. Comparing

Fig. 6 with Fig. 8 we can conclude that the changes of YM in the three-axial porcelain mixture are predominantly caused by the changes in the kaolin phase and the kaolin crystals interfaces. The same can be stated about MOR. We also made some trial measurements of the acoustic emission during heating. Weak signals were monitored at the temperature range of 250 – 650 °C, which is in accordance with the results of mf-TMA.

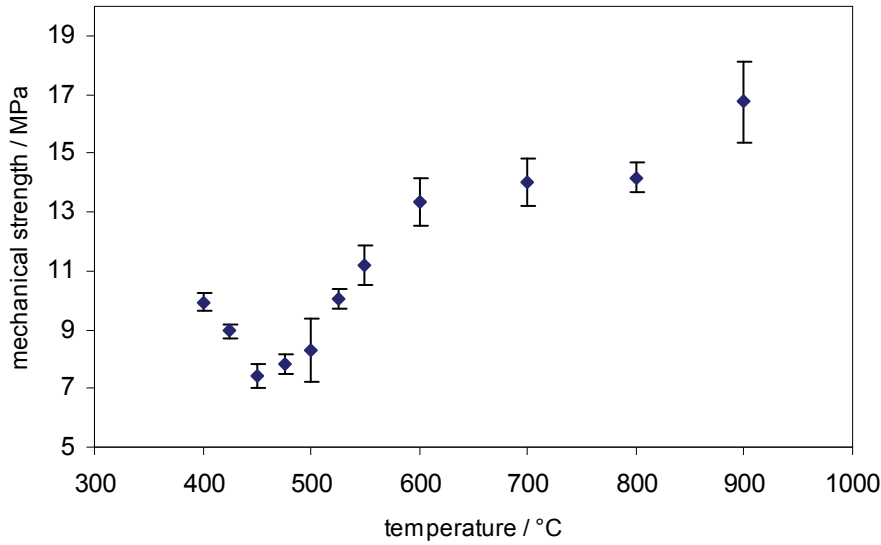


Fig. 7. Mechanical flexural strength measured during heating stage of the firing

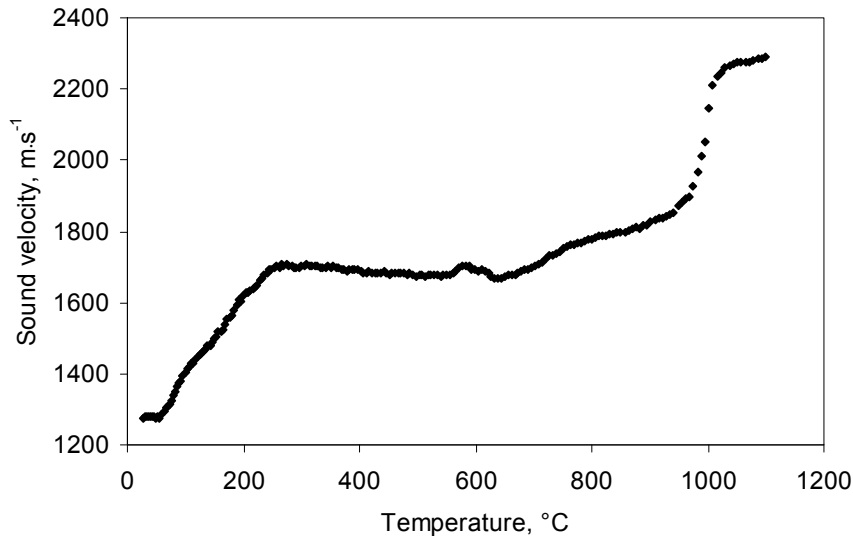


Fig. 8. Sound velocity of kaolin vs. temperature

In theory, the direct implication of Hooke's law is that the relationship between MOR and YM is linear. As can be seen in Fig. 6 and Fig. 7, the courses of YM and MOR are similar, which confirms this theoretical assumption. But there is a considerable scatter of points in this relationship, see Fig. 9, which allows only for a rough estimation of MOR from YM [18].

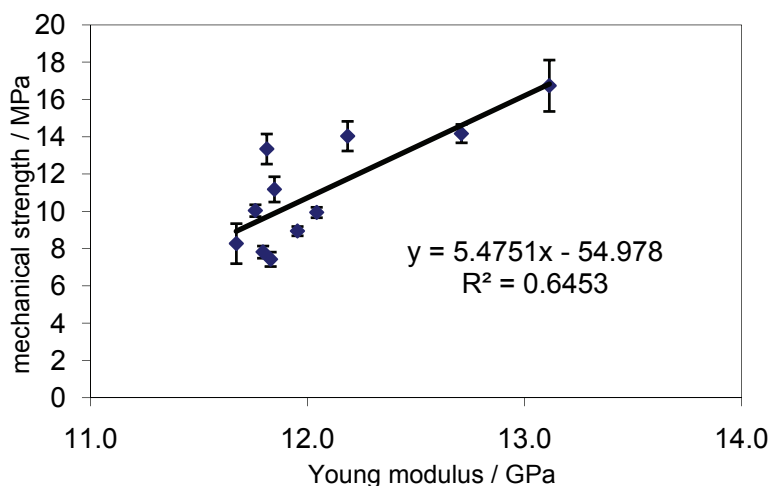


Fig. 9. Relationship between mechanical strength and Young modulus measured at the actual temperature

#### 4. Cooling stage of firing

During heating of the ceramic body from ~1150 °C up to the maximum firing temperature, mullite is created, feldspar melts, the glassy phase occurs and the liquid phase sintering runs. The ceramic body losses elastic properties and becomes plastic. Shrinkage of the sample volume is significant, porosity decreases to a low value [3, 4, 19]. When the body cools down, a viscosity of the glassy phase increases and elastic properties progressively restore. The ceramic material becomes a porcelain.

Numerous studies deal with the influence of the unsolved quartz grains in the porcelain structure. It is recognized that residual quartz grains have a negative influence on the strength of the porcelain. The primary problems associated with quartz in electroporcelain and the ways to decrease the negative effects of quartz were recently described by J. Liebermann [20, 21, 22]. It is commonly believed that the relatively large volume change accompanying the  $\beta \rightarrow \alpha$  transformation of the unsolved quartz grains ( $\Delta V/V = -0.68\%$  for free quartz grain) is the basic source of microcracking. Investigations performed at room temperature with the help of the electron or light microscopy show circumferential microcracks and (less often) microcracks in quartz grains, see Fig. 10. Based on the model of quartz grain with glassy cladding and the thermodilatometric results (as depicted in Fig. 11), the cooling interval can be divided in two parts. Above 570 °C, the volume of the quartz grain remains approximately constant, and the glassy cladding tends to contract its volume.

The grain is under the compressive stress and no circumferential cracks can arise. But in the narrow temperature interval around the  $\beta \rightarrow \alpha$  transition of quartz, the quartz grain volume rapidly contracts and the circumferential microcracks can appear around the grain. The microcracks are the result of the release of the mechanical stress caused by the difference in the thermal expansion between the quartz grains and the glass matrix [21, 23, 24, 25].

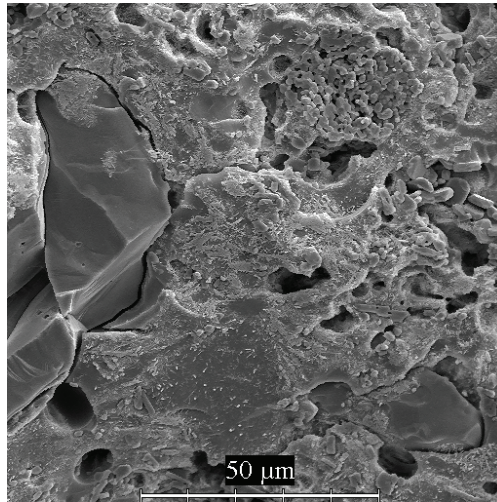


Fig. 10. Fracture surface with quartz grains and circumferential cracks around them. SEM after etching with 2.5 % HF for 15 s. Courtesy of PPC Čab

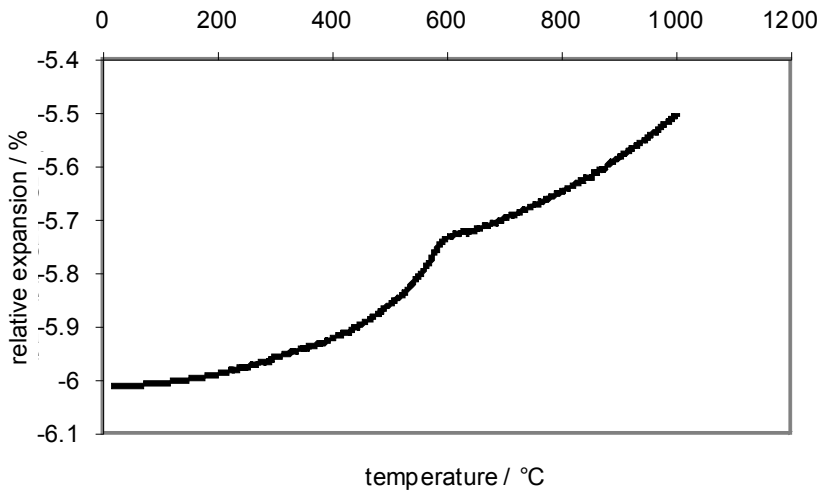


Fig. 11. Thermodilatometric curve of porcelain during cooling stage of firing



Results obtained using the real time non-destructive methods applied during the cooling stage of firing offer another view on the cracking process. An acoustic emission measurement directly registers the formation of the microcracks, and mf-TMA, which measures YM (or sound velocity), is sensitive to the concentration of the microcracks. The acoustic emission was employed in [26] to examine spontaneous cracking in porcelain samples during cooling. Acoustic emission signals were detected in the temperature range of 900 – 800 °C and never at temperatures less than 600 °C. These results were indirectly confirmed in [27] through measuring the sound velocity. Beside that, a decrease in the sound velocity below 570 °C was observed and assigned to the microcracks.

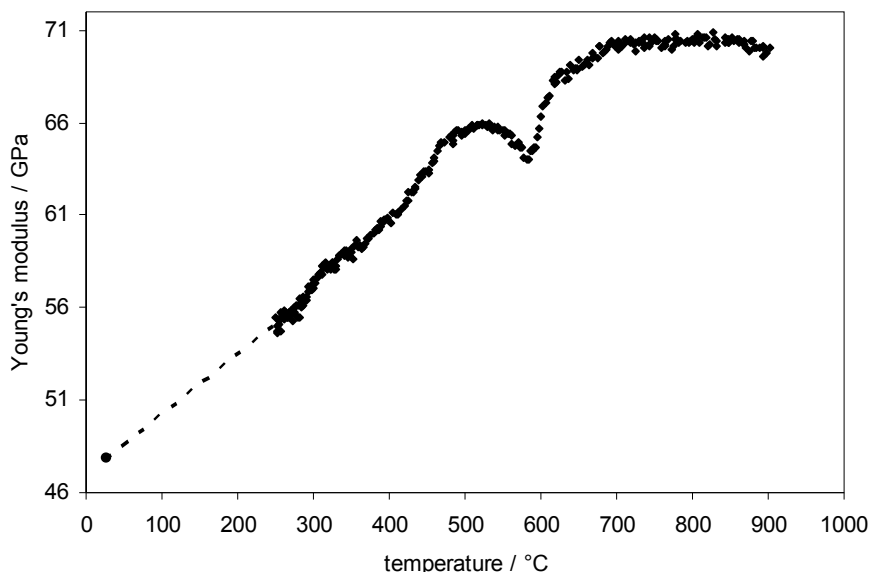


Fig. 12. Relationship between Young's modulus and temperature of green quartz sample during cooling stage of firing from max. temperature 1250 °C

A resonant flexural vibration develops in the sample if viscosity of the glassy phase is high enough for propagation of the mechanical flexural wave. This condition appears during cooling at the temperature of ~1000 °C. The relationship between YM and the temperature during cooling is depicted in Fig. 12. Values of YM increase with a decreasing temperature as long as the viscosity of the glassy phase is low enough to accommodate the mechanical stress generated during cooling. Subsequently, creation of microcracks may begin as a consequence of releasing the stress between phases with different thermal expansion coefficients. This process is demonstrated through descending values of YM below ~750 °C. Then there is a rapid decrease in the values with a sharp minimum at ~580 °C, which belongs to the  $\beta \rightarrow \alpha$  quartz transition. During the further temperature decrease, there is a moderate and temporary recovery of Young's modulus values, followed by their restored drop from 500 °C to room temperature. This behavior supports results from the acoustic emission measurement. Intense acoustic signals, connected with the crack creation, were observed from ~800 °C to ~650 °C, then no signals appeared between 600 °C – 500 °C and

weak signals appeared again below 500 °C [28]. Consequently, most of the cracks in the vicinity of the quartz grains are created before the  $\beta \rightarrow \alpha$  transition and not during this transition as commonly believed.

Crack creation around the unsolved quartz grain can be caused by mechanical stress. According to [19], the total stress  $\sigma$  acting on the quartz particle may be calculated as

$$\sigma = \frac{\Delta\alpha\Delta T}{\frac{1+\mu_g}{2E_g} + \frac{1-2\mu_q}{E_q}} \quad (6)$$

where  $\Delta\alpha = \alpha_g - \alpha_q$  is the difference between the thermal expansion coefficients of the glassy matrix and the quartz grain, and  $\Delta T$  is the temperature range of the cooling process.  $E_g$  and  $E_q$  are Young's moduli of the glassy matrix and the quartz grain, respectively, and  $\mu_g$  and  $\mu_q$  are their Poisson's ratios. The thermodilatometric curves of the quartz and glassy phase and mullite (the last two curves are approximately identical according [26]) are depicted in Fig. 13. As can be deduced from Fig. 13, the quartz grain volume is almost constant and its glassy surrounding contracts its volume during cooling from 1000 °C to 570 °C. The stress applied on the grain according to Eq. (6) is positive (i.e. compressive stress). The glassy phase is under the tensile stress. Below the glass transformation temperature, the glassy matrix becomes brittle, which could result in formation of radial cracks nucleating at the quartz particles [19]. The nucleation and the growth of cracks are demonstrated by the decreasing values of Young's modulus (Fig. 12) below 800 °C. This process is finished by the  $\beta \rightarrow \alpha$  transition accompanied by a fast decrease in the thermal expansion of the quartz grains.

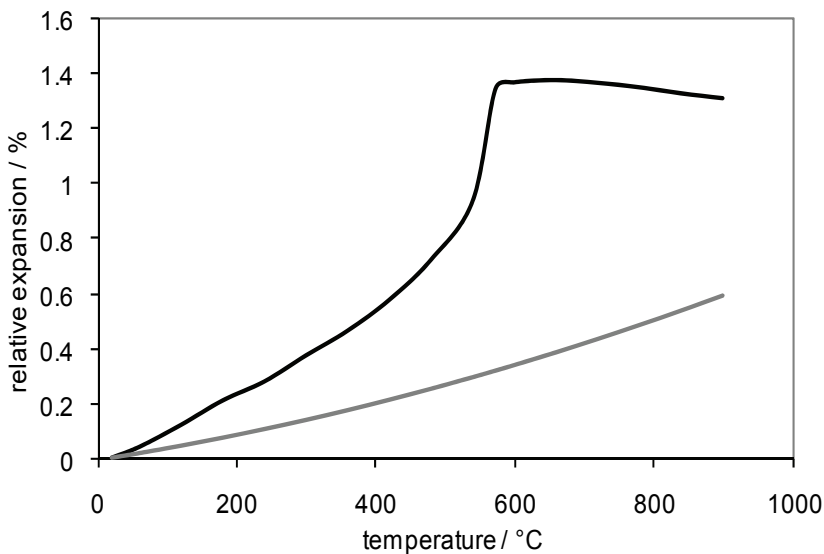


Fig. 13. Thermodilatometric curves of quartz (black line, main values from the curves for c-axis and a-axis [29]) and mullite [30] or glassy phase (gray line)

During the  $\beta \rightarrow \alpha$  transition of quartz, the contraction of the quartz phase volume proceeds faster than the contraction of the glassy phase, i.e.  $\alpha_q > \alpha_g$  and the stress applied on the quartz grains becomes negative according to Eq. (6). During this fast process the tensile stress applied on the glassy matrix was rapidly relaxed, and upon further cooling, the compressive stress built up. This process took place between 573 and 500 °C, demonstrating itself by vanishing of acoustic signals (no new cracks nucleated) and a partial recovery of Young's modulus, likely due to the shrinkage of voids caused by previous cracking.

Below 500 °C, the relation  $\alpha_q > \alpha_g$  continues to be valid until the room temperature is reached. After a short interval between 600 °C and 500 °C where no acoustic signals were detected [26, 28] and YM passed over a small maximum, YM continued to decrease its values and weak acoustic signals appeared again [28]. This can be explained by the newly built compressive stresses which induce an interface decohesion that takes the form of cracks around the quartz grains. The acoustic signals disappear at temperatures below 300 °C, which indicates that no further cracking occurs and the ongoing decrease of Young's modulus is caused by the accretion of already existing cracks [28].

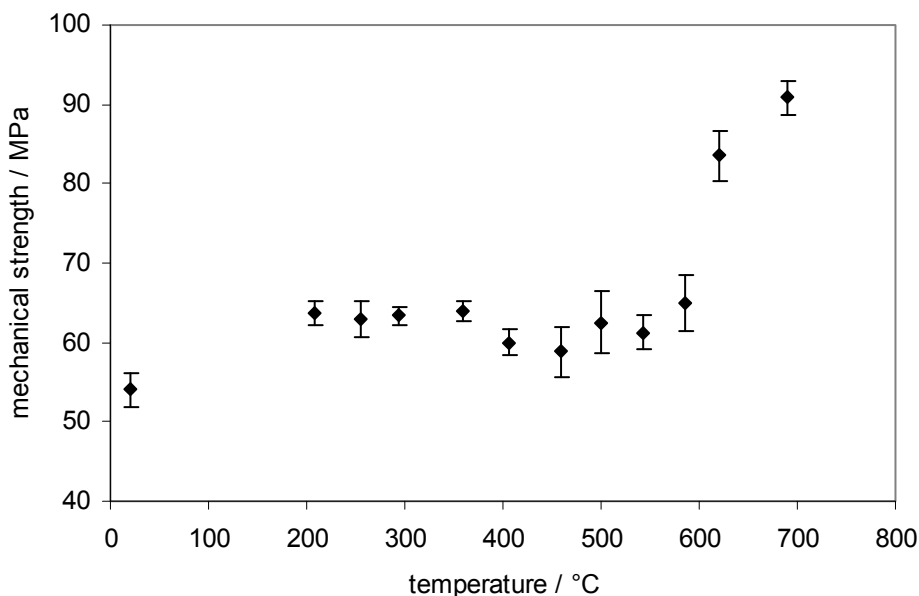


Fig. 14. Mechanical strength measured during cooling stage of the firing

The values of MOR measured in the cooling stage of firing, see Fig. 14, approximately confirm the conclusions shown above. MOR decreases before the  $\beta \rightarrow \alpha$  transition occurs, which is in agreement with the decreasing YM, and reaches the minimum at ~550 °C. A slightly higher value of MOR at 500 °C can be hardly considered a maximum, although it could correspond to the maximum of YM. Because of a few measured points in this region (450, 500, 550, 600 °C) and relatively large standard deviations of MOR, it is questionable to unambiguously relate the small increase in MOR at ~550 °C to a temporary recovery of YM.

The behavior of MOR and YM below 450 °C differs from the theoretical requirement of the direct proportion between these two quantities. The values of MOR initially increase (between 450 and 350 °C) and then remain constant up to 200 °C. On the other hand, YM decreases its values permanently. Both quantities, MOR and YM, reach their lowest values at room temperature.

## 5. Conclusions

Elastic properties (Young's modulus, sound velocity and mechanical strength) of the green quartz porcelain body reflect the changes in the structure of the body and the processes in it. They are linked to

- a. escape of the physically bound water, dehydroxylation, the  $\alpha \rightarrow \beta$  quartz transition, high-temperature reactions and solid-phase sintering during the heating stage of firing,
- b. solidifying of the glassy phase, differences between the thermal expansion coefficients of the glassy phase, mullite and quartz grains, and the  $\beta \rightarrow \alpha$  transition of quartz during the cooling stage of firing.

Results obtained by mf-TMA during heating showed a direct relationship between the elastic properties of kaolin and green porcelain samples. Young's modulus and the mechanical strength of the green porcelain sample seem to be determined by the properties of the interfaces between kaolinite crystals. Mechanical properties improve between 50 – 250 °C and then between 650 – 1100 °C, which can be explained by solid-phase sintering.

Young's modulus and the mechanical strength in the cooling stage of firing are predominantly determined by the stresses created and relaxed between the glassy phase and the quartz grains. They are a source of microcracks that are mostly located in the vicinity of the quartz grains. As a consequence, Young's modulus and the mechanical strength decrease.

Results obtained using the AE technique reveal several stages of microcracking. This process begins at the temperature of the glass transition. At the temperature of the  $\beta \rightarrow \alpha$  transition, cracking is temporarily interrupted and a partial recovery of the structure occurs. Below this temperature circumferential cracks around the particles appear with less intensity, especially when the temperature is decreased below 300 °C.

## 6. Acknowledgment

This work was supported by the grant VEGA 1/0216/09, Ministry of Education of Slovakia. One of the authors (F.C.) gratefully acknowledges a financial support from the Research Goal MSM0021620834 that is financed by the Ministry of Education, Youth and Sports of the Czech Republic and from the research Grant 108/11/1267 financed by the Czech Science Foundation.

## 7. References

- [1] Pospíšil, Z. – Koller, A.: *Fine Ceramics, Basics of Technology*. SNTL/ALFA, Praha 1981 (in Czech)
- [2] Pytlík, P. – Sokolář, R.: *Building ceramics – technology, properties, applications*. Akad. nakladatelství CERM, Brno 2002 (in Czech)

- [3] Norton, F.H.: *Fine ceramics – Technology and Application*. McGraw-Hill Book Co., New York 1970
- [4] Hanykýř, V. – Kutzendorfer, J.: *Technology of Ceramics*. Silis Praha a Vega Hradec králové, Praha 2000 (in Czech)
- [5] Palmour III, H.: Rate-controlled sintering of a whiteware porcelain. *Ceramic Engineering and Science Proceedings*, 7, 1986, 1203-1212
- [6] Štubňa, I. – Trník, A. – Vozár, L.: Thermomechanical and thermodilatometric analysis of green alumina porcelain. *Ceramics International*, 35, 2009, 1181-1185
- [7] ASTM C 848-88: Standard test method for dynamic Young's modulus, shear modulus and Poisson's ratio for ceramic whiteware by sonic resonance. (published in 1999, Standard Documents, Philadelphia USA)
- [8] ASTM C 1198-01: Standard test method for dynamic Young's modulus, shear modulus and Poisson's ratio for advanced ceramics by sonic resonance. (published in 2001, Standard Documents, Philadelphia USA)
- [9] Schreiber, E. – Anderson, O. – Soga, N.: *Elastic constants and their measurement*. McGraw-Hill Book Co., New York 1973
- [10] Štubňa, I. – Trník, A. – Vozár, L.: Determination of Young's modulus of ceramics from flexural vibration at elevated temperatures. *Acta Acustica + Acustica*, 97, 2011, 1-7
- [11] Kashtaljan, J.A.: Elastic properties of materials at high temperatures. *Naukova dumka*, Kiev 1970 (in Russian)
- [12] Rath, J. et al.: *Fine ceramics – measurement methods and testing*. SNTL/ALFA Praha, 1988 (in Czech)
- [13] Polakovič, J. – Polakovičová, J. – Sokoly, J.: Interaction between kaolinite surface and hematoxyline. In: *Proc. 5th Meeting of European Clay Groups*, Prague, 1983, 279-282
- [14] Kozík, T. – Rakovský, O. – Ondrejko, E.: Resistivity of ceramic material to thermal shock in dehydroxylation region. *Sklár a keramik*, 28, 1978, 176-180 (in Slovakian)
- [15] Kozík, T. – Štubňa, I.: Mechanical strength of ceramic material in dehydroxylation region. *Silikáty*, 25, 1981, 237-241 (in Slovakian)
- [16] Freund, F.: Kaolinite-metakaolinite, a model of a solid with extremely high lattice defect concentration. *Ber. Deutsche Keram. Ges.*, 44, 1967, 5-13
- [17] Trník, A. – Štubňa, I. – Moravčíková, J.: Sound velocity of kaolin in the temperature range from 20 °C to 1100 °C. *International Journal of Thermophysics*, 30, 2009, 1323-1328
- [18] Štubňa, I. – Trník, A. – Šín, P. – Sokolář, R.: Relationship between mechanical strength and Young's modulus in traditional ceramics. *Materiali in Tehnologije*, submitted article
- [19] Carty, W.M. – Senapati, U.: Porcelain – raw materials, phase evolution, and mechanical behavior. *J. Amer. Ceram. Soc.*, 81, 1998, 3-20
- [20] Liebermann, J.: About the important correlation between microstructure properties and product quality of strength-stressed high-voltage insulators. *Interceram*, 53, 2003, 238-241
- [21] Liebermann, J.: Avoiding quartz in alumina porcelain for high-voltage insulators. *Keramische Zeitschrift*, 53, 2001, 683-686
- [22] Liebermann, J.: Reliability of materials for high-voltage insulators. *www.ceramicbulletin.org*, (Amer. Ceram. Soc. Bulletin, May 2000)

- [23] Porte, F. - Brydson, R. - Rand, B. - Riley, F.L.: Creep viscosity of vitreous china. *J. Amer. Ceram. Soc.*, 87, 2004, 923-928
- [24] Carty, W.M. - Pinto, B.M.: Effect of filler size on the strength of porcelain bodies. *Ceram. Engineering and Science Proceedings*, 23, 2002, 95-105
- [25] Braganca, S.R. - Bergman, C.P.: Porcelain microstructure and technical properties. *Cerâmica*, 50, 2004, 291-299
- [26] Ohya, Y. - Takahashi, Y.: Acoustic emission from a porcelain body during cooling. *J. Amer. Ceram. Soc.*, 82, 1999, 445-448
- [27] Štubňa, I. - Trník, A. - Vozár, L.: Thermomechanical analysis of quartz porcelain in temperature cycles. *Ceramics International*, 33, 2007, 1287-1291
- [28] Chmelík, F. - Trník, A. - Pešička, J. - Štubňa, I.: Creation of microcracks in porcelain during firing. *J. of the European Ceramic Society* (accepted article)
- [29] Prjanishnikov, V.P.: *Sistema kremnezema*. Izd. lit. po stroitelstvu, Leningrad 1971 (in Russian)
- [30] Pena, B. - Bartolomé, J. - Requena, J. - Moya, J.S.: Mullite-alumina functionally gradient ceramics, *J. Physique IV*, 1993, 3, 1261-1266

# Mechanical Properties of New Ceramic Materials Obtained from Granular Solid Residuals Coming from Mines and Diatomaceous Earth

Jaime Vite-Torres, María del Carmen Carreño de León,  
Manuel Vite-Torres and Juan Rodrigo Laguna-Camacho  
*Instituto Nacional de Investigaciones Nucleares (ININ),  
SEPI-ESIME-Campus Zacatenco-IPN,  
Universidad Veracruzana, Campus Poza Rica, Veracruz  
México*

## 1. Introduction

Granular solid residuals are produced by different industries in Mexico. Some of these are considered dangerous because they are stored in open areas contaminating and affecting the flora, fauna, and aquifers, and occasionally to the human being. These solid residuals coming from mines and diatomaceous earth are known as “jales” (náhuatl derived from xalli, it means sand). The “jales” have a high content of cyanide and heavy metals. These high contents are commonly out of the limits permitted by the Mexican standards. On the other hand, the “diatomita” (diatomaceous earth) is not as dangerous as the “jales”, however, this needs a treatment to eliminate the occluded organic material. This is normally used by producers of gelatin, antibiotics, industrial grease and oil, sugar refining, etc.

The leaching process of metals using the sodium cyanide was introduced in 1887 (Li, 1993). This revolutionizes the techniques to obtain gold and silver. This is a method usually employed in the world to recover metals. Two international patents were obtained by developing equipment and also a process to extract toxic metals and wastes from foundry sands (Vite, 1994a, 1994b). In addition, a national patent was achieved by the leaching of heavy metals from foundry sands (Vite, 1997).

Approximately, 330,000 tons of these solid residuals are generated daily in Mexico. In some states, such as Guanajuato, Zacatecas and cities as Pachuca in the state of Hidalgo, the waste deposits are found in open areas. The chemical composition of these solid residuals is varied. Figure 1 shows a photograph of the pipe used to transport the solid residuals until a “jales” dam.

An important case is related to “jales” when they have high pyrite content ( $\text{FeS}_2$ ). This affects considerably the chemical composition due to their weathering. Due to this fact, it is necessary to process the “jales” before being used at applications such as the construction of landfills in the leveling of roads, additives for asphalt mixtures or dam construction (Botz & Stevenson, 1995, Orozco & Orozco, 1992, Sengupta, 1993, Vite et al., 2003, Wills, 1994).

In this study, a multidisciplinary work combining different mechanical, chemical and physical aspects was conducted. Industrial solid residuals coming from mines were leached to eliminate the toxic metals present in their chemical matrix. This process was carried out by using special equipment as mentioned and described above. It was developed and patented in Mexico and United States of America. The resultant solid material was mixed with solid residuals coming from diatomaceous earth and mines, and binders were employed to obtain new compact ceramic materials.



Fig. 1. Pipe used to transport the solid residuals until the jales dam

The mechanical properties of these ceramic materials, such as the compressive strength were determined in accordance to ASTM C170-50 and ASTM C-36 standard. The final results showed that these ceramic materials are lighter and exhibit higher compression strength than conventional materials such as bricks.

### 1.1 Background of the invention

The invention refers to an apparatus and process for extracting metals from foundry sands and, more specifically, to an apparatus and process for extracting these metals by making use of a thermostated column.

In the field of metal extraction based on foundry sands, the extraction techniques most utilized to date in a liquid-solid system involve mechanically-stirred leaching tanks, the Pachuca (State of Mexico) tank and Bonotto, Kennedy or Rotocel extractors. None of this equipment however has been specifically designed to extract small quantities of metals from foundry sands, which represents a problem not, so far, resolved.

Of the conventional apparatus mentioned above, the Pachuca tank is that which most resembles the apparatus object of the present application. However, the thermostated column of the new apparatus differs from the Pachuca tank insofar as regards its air dispersion system, the use of decarbonated and humidified air, because it consists of a heating jacket and because temperature control of the heating fluid is by means of a thermostat. These features of an apparatus which is desired to protect, allow a suitable pulp suspension, prevent the formation of a silicate and carbonate layer at the bottom of the



column, permit better temperature control and a finer control of the process variables, such as the pH, the air flow and the solution's oxidation-reduction potential.

### 1.2 Summary of the apparatus

The apparatus and the process of the present invention allow low concentrations of the metals contained in the mining tailings to be simultaneously extracted, thus achieving two main goals which are 1) the recovery of metal values which can be recycled and 2) An important reduction in the toxicity of the industrial solid wastes ( Mining Tailings) which once treated, can be handled as normal industrial waste, which can be used to make ceramic materials or construction materials, with important savings. From among the metals which are possible to recover, one can mention, among others platinum, gold, cobalt, germanium, zinc, manganese, silver and cooper, metals with many industrial uses, and some others such as chromium, vanadium and arsenic, which are highly toxic. Figure 2 shows a schematic diagram of the patented equipment ((Vite, 1994a, 1994b).

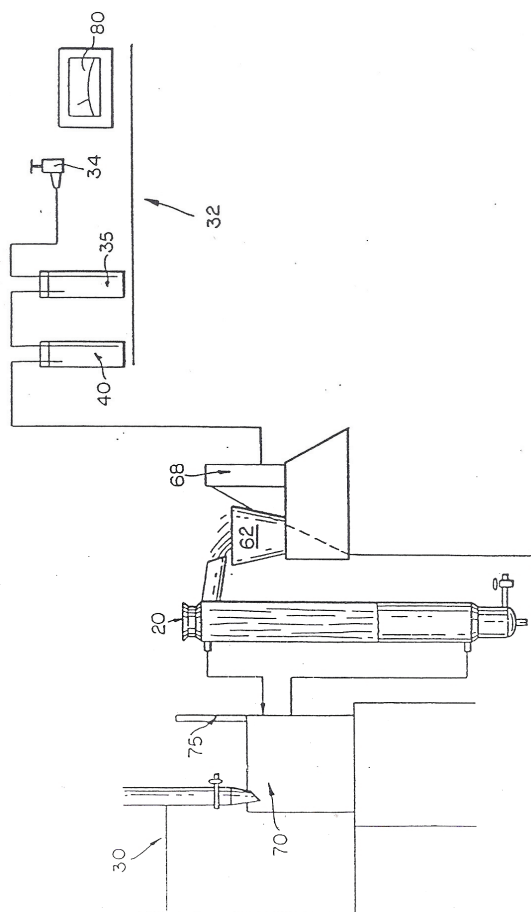


Fig. 2. Schematic diagram of the patented equipment (Vite, 1994a, 1994b)

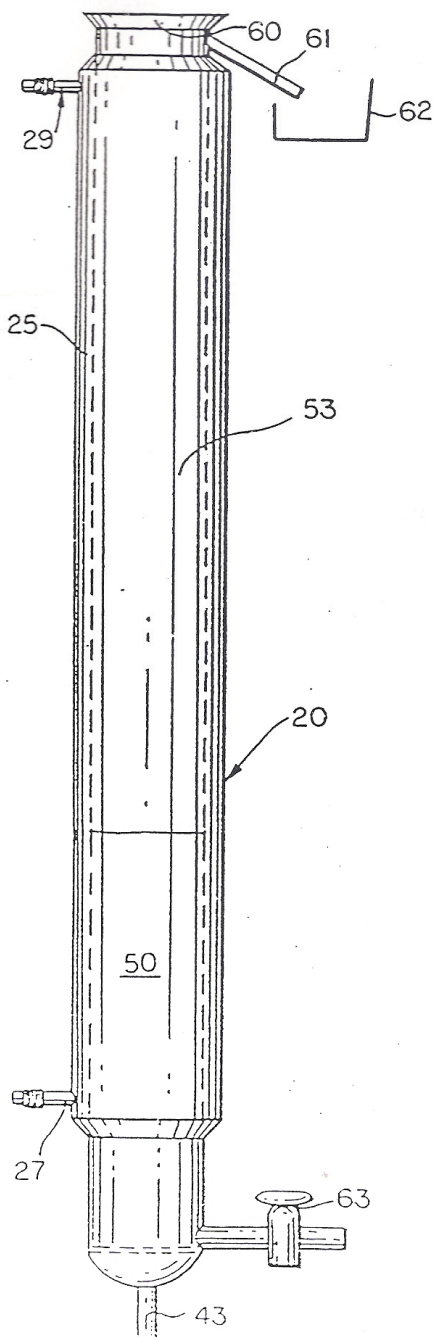


Fig. 3. Side view of the thermostated column (Vite, 1994a, 1994b)

In order to achieve its purpose, the apparatus consists of a thermostatic includes column which is connected to a decarbonated and humidified air supply source, and with a controlled heating system. This column includes an inlet for introduction of the components to form an aqueous pulp, and device for sparging, it in such away that a suitable suspension and homogenization of same is obtained. For it's part , the process is characterized by the introduction into the column of some reagents, distilled water and industrial solid wastes (mining tailings) in order to form an aqueous pulp which is processed in same for 2 hours under controlled temperature , air flow and pH conditions. Upon termination of the above mentioned period, the pulp in the column is extracted and once again heated for 20 minutes, after which it is filtered in order to obtain liquor with the metals in solution.

Another distinctive characteristic of this process is that, as distinguished from the existing system, it permits the extraction of metals from metallic alloys; the thermodynamic stability is higher than covalent bonds.

### 1.3 Detailed description of the invention

In the structural aspect of the invention (Figure 2, 3, 4 and 5) this consists of an apparatus comprising a thermostated column 20 having a double wall defining a heating jacket 25 through which a heating fluid circulates coming from a heating system 30 which is in flow communications with said jacket by means of the heating fluid inlet and outlet means 27, 29 disposed in element 25 for connection with said system 30. The purpose of said heating system is to maintain the interior of the column 20 at an approximate temperature of 60° C., in accordance with one of the variables of the process for extracting metals from foundry sands. To this end, the heating system 30 includes thermal control devices such as a thermostat 70 and thermometer 75 to control the temperature of the heating fluid.

The apparatus also includes a source 32 of supply of air to the column, where said source comprises a valve 34 for the admission of air and a carbonating device 35 and humidifier 40, the latter two placed in the path which communicates said source with de column. The air is passed through the device 35 and humidifier 40 before it reach the column, to which it is introduced by an inlet 43 and crosses to a sparging device 45 placed next to said inlet which server to finely divide the air in order to foster suitable suspension and homogenization of the pulp. Device 45 consist of a membrane with multiple orifices 46 of a diameter such as not to allow the pulp to pass through same towards the airflow inlet 43. The upper end of the column 20 includes an opening 48 through which the different components forming the aqueous pulp 50 are introduced, said pulp containing the metals which it is desired to extract in accordance with the aim of the apparatus and process invented. Pulp 50 is placed in the inner chamber 53 of the column, which has been previously heated by the heating system 30 and supplied with air from supply source 32, with the characteristics mentioned hereinabove, wherein said pulp is sparged by the air flow crossing device 45 in order to provide it with the suspension and homogenization properties required for the process. A frosted glass cap 60 is placed in opening 48 in order to avoid the escape of air and foam. However, the column is provided with means 61 through which the foam may leave into a reservoir 62. For extracting samples from the pulp during the process, the column has a valve 63, through which the necessary samples are taken to verify that the pulp being processed retains the ideal conditions for obtaining the desired results. In addition, a device 68 for controlling and measuring the airflow supplied to the column is located at a point

before the air inlet 43. With regard to the process the tailings are analyzed in order to verify their compatibility with said process and in order to subsequently carry out the corresponding metallurgic balances. Once analyzed the tailings are finely ground and suspended in an aqueous pulp with a solid-liquid ratio of 1 to 4 and the necessary reagents added; that from 10 to 40 g, of a mineral acid in order to reach a pH of 2, from 4 to 15 of a compound of the family of the bisulphites and from 0.3 to 1.5 g of mono and dialkylamines amineoxides and ethoxylated alkyl amines, all these reagents being of analytical grade. The addition of surfactant is preferred because it is a cationic surfactant which reduces the surface tension and promotes foam formation, thus obtaining a greater efficiency in the leaching process.

Figure 3 and 4 displayed a side view of the thermostated column and the membrane device of the column, respectively. Additionally, Figure 5 shows a design of diagram of a preliminary pilot plant for leaching metal values and toxic metals from industrial solid wastes. Finally, Figure 6 presents a block diagram of the process for the extraction of metal values from foundry sands.

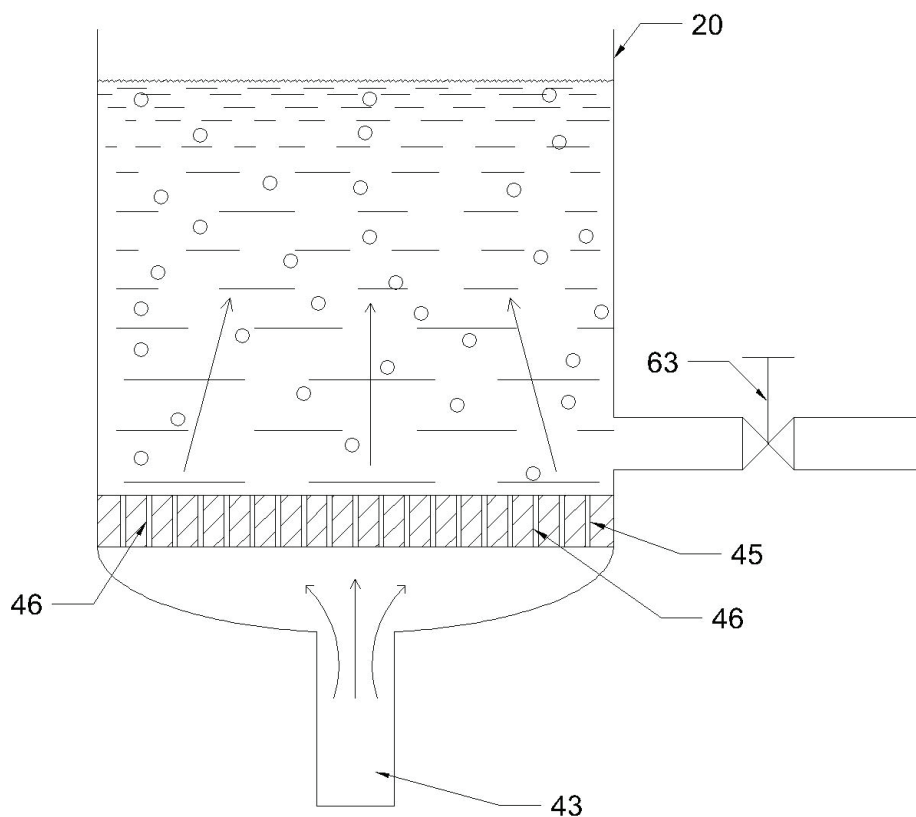


Fig. 4. Membrane device of the column (Vite, 1994a, 1994b)

## 2. Experimental details

### 2.1 Preparation of granular solid industrial residuals

#### 2.1.1 Treatment of granular solid industrial residuals coming from diatomaceous earth

The diatomite (diatomaceous earth) is a marine sedimentary rock. This can be found in lake deposits and consist mainly of the accumulation of shells or hydrated silica secreted by diatoms which are microscopic organisms. Chemically consists of silicon dioxide ( $\text{SiO}_2$ ), which is essentially inert; is attacked only by strong alkalis and hydrofluoric acid. Other components of the diatomite are: Sand, clay, volcanic ashes, magnesium carbonate, soluble salts and organic matter. The types and amounts of impurities are highly variable and depend on the conditions of sedimentation and deposition time of the diatomite. Diatomite is used primarily as filters, insulation or filler material. In the first case, the substance is used to filter sludge. Another application is in sugar refining and industrial plants in various solvents antibiotics, grass and oils. In many other cases diatomaceous earth are used for separation process. The diatomite is contaminated with organic material, after being used in the processes described above.

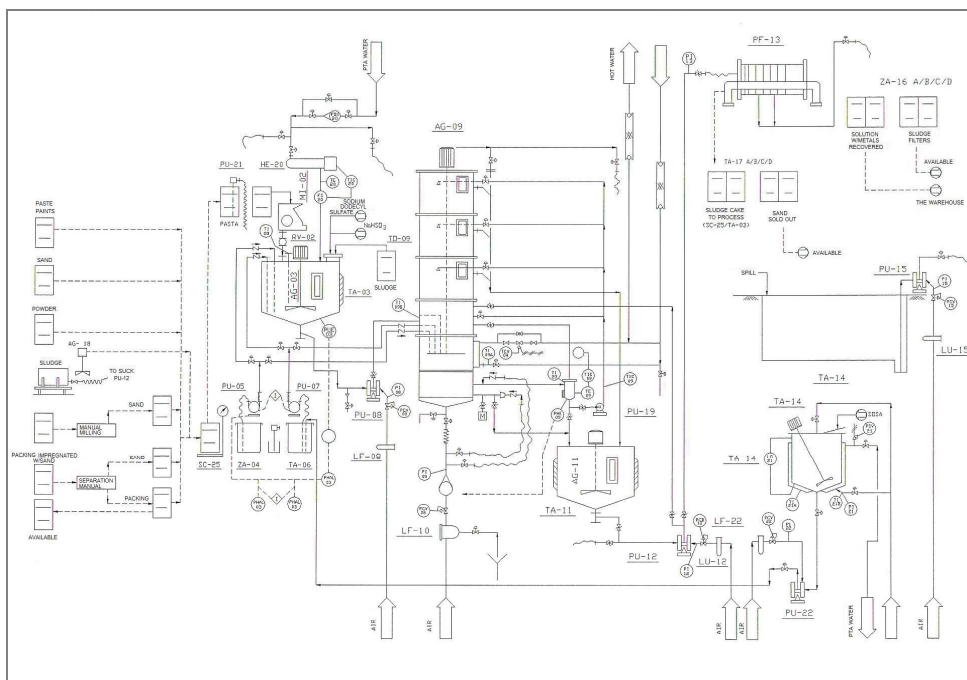


Fig. 5. Design plant for leaching of metal for values and toxic metals from industrial solidwastes (Vite, 1994a, 1994b)

In the laboratory, the organic material adhered to the diatomaceous earth was removed by a physical-chemical process developed here, thus obtaining innocuous material. Subsequently, the sample was sieved to achieve a grain size between 100-200  $\mu\text{m}$ , likewise, a representative sample was taken, using the counting method and quartering, to analyze

qualitatively and quantitatively. Figure 7 shows the morphology of one of the samples obtained from granular solid industrial wastes coming from diatomaceous earth.

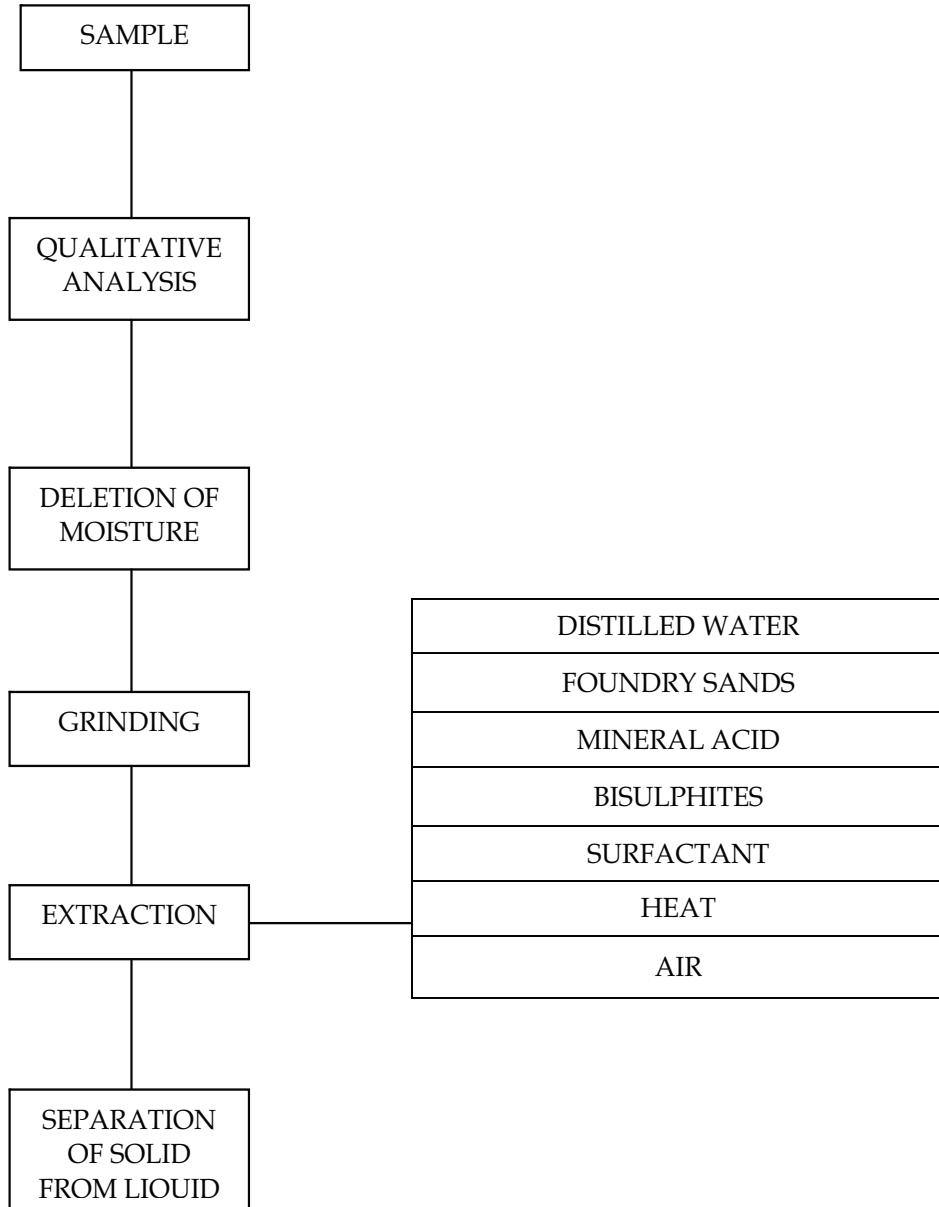


Fig. 6. Block diagram of the process for the extraction of metal values from foundry sands (Vite, 1994a, 1994b)

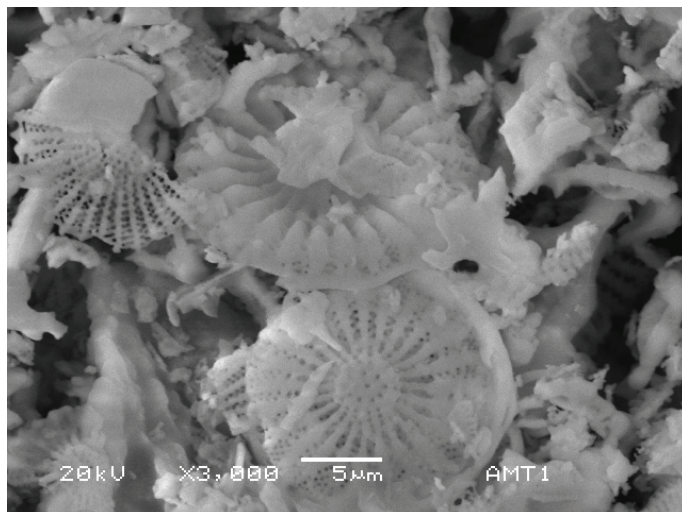


Fig. 7. Morphology characteristics of industrial residual coming from diatomaceous earth

### 2.1.2 Treatment of the mining industrial residuals samples (MIR)

To determine the presence and concentration of cyanide and heavy metals, representative samples were analyzed qualitative and quantitatively using conventional and nuclear techniques. Then, the content of cyanide was removed using thermostated coupled columns. This process and the equipment was developed and patented in the United States and Mexico (Vite, 1994a, 1994b). Samples are placed into the equipment, where sodium hypochlorite is added, the temperature in the columns is set at 28 ° C, during 20 min. Once the process is completed, the separation solid-liquid is performed. Then, the solid sample is dried and placed back in the thermostated coupled columns in order to leach heavy metals. The sample of “jales” is mixed with reducers, surfactants and complexing agents to perform the leaching process at different pH. Then, an acid or a base is added, la pulp is stirred by injecting air and each sample is processed for 120 min. at 60 ° C. After all this process, the solid-liquid separation is made. The solid was sieved to obtain a grain size between 100-200 µm and was analyzed qualitative and quantitatively, in order to verify the decrease in the concentration of cyanide and heavy metals content in the samples, if there is any evidence of a toxic component, the operation is repeated until obtain innocuous samples. The treatment of solid residuals to leach cyanide and heavy metals was successful, as it eliminates 100% of the cyanide content, as well as 80-100% of the heavy metals content occluded in the chemical matrix of the sample.

### 2.2 Specimens

The materials used to conduct the tests were ceramic materials identified as “JADIAR” due to a mixture of Jale-Diatomaceous earth-Clay. The samples were named as 1A, 1B and 1C. In the sample 1A, 50% was material coming from diatomaceous earth, 40% of mining industrial residual (Jale) and 10% clay. In sample 1B, was used 50% of diatomaceous earth, 30% solid residual (jale) and 20% clay. Finally, in sample 1C, the contents were 50% diatomaceous earth, 20% mining industrial residuals and 30% clay. Table 1 presents the

material contents. Each sample was mixed separately and was heat- treated first to remove moisture in an oven at a temperature of 100°C for 120 min., then the sample was treated in an oven at 950 °C for 180 min. The diagram shown in Figure 8, presents a flow chart of processing of materials coming from mining industrial residuals and diatomaceous earth.

Sample	Diatomaceous earth (%)	Mining industrial residuals (jales) (%)	Clay (%)
1A	50	40	10
1B	50	30	20
1C	50	20	30

Table 1. Material contents

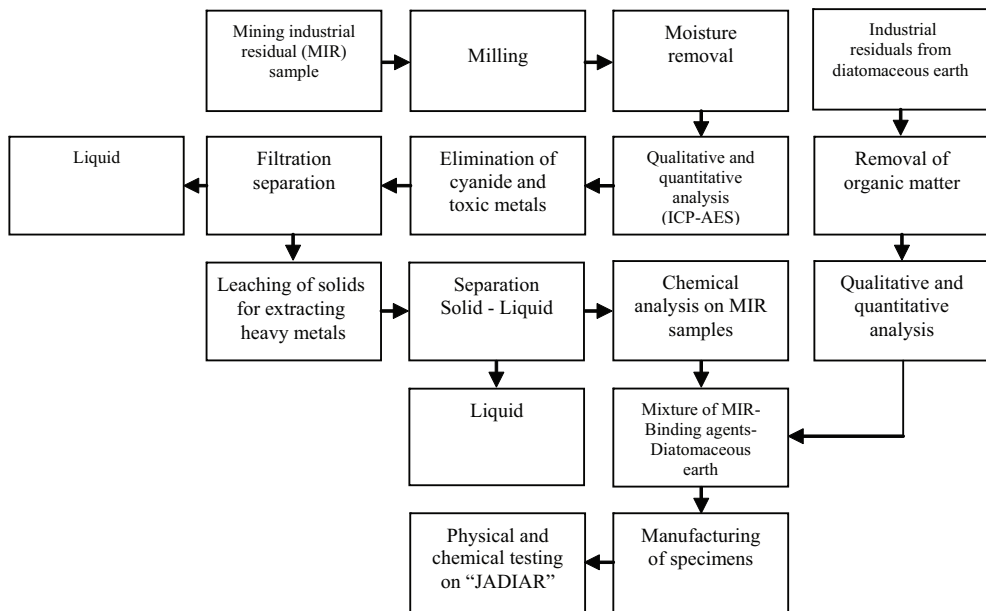


Fig. 8. Flowchart of processing of materials

### 3. Results and discussion

#### 3.1 Methodology for the production of construction materials (lattice and bricks)

The main objectives pursued with these building blocks are: Ease of construction, increased insulation and ease of operation. Light inert materials are generally chosen. The manufacture may be carried out by mortars and concretes conveniently dispensed with fluid consistencies, paste or dried, depending on the system followed and the shape of the final piece.



### 3.1.1 Pasta preparation

Pastas are prepared from the mixture of granular solid industrial residuals coming from mines and diatomaceous earth with binding agents such as cement or clay mixed with water conveniently without exceeding their plasticity.

### 3.1.2 Molding

The molding is made by direct compression or by vibration, with mortar or concrete, the materials has to be practically dry, if the process is done by casting, the material must be more or less fluid. The procedures may be manual or mechanical, depending on the production, cost and product quality.

In this particular case, the manual procedure was used because the pieces were made solely for laboratory analysis. Metallic and Wood molds were used for the lattices. The results of the materials obtained using the methodology mentioned above, can be seen in the bricks and lattices in Figure 9 and Figure 10 where it is possible to observe the manufactured samples for tribological tests.

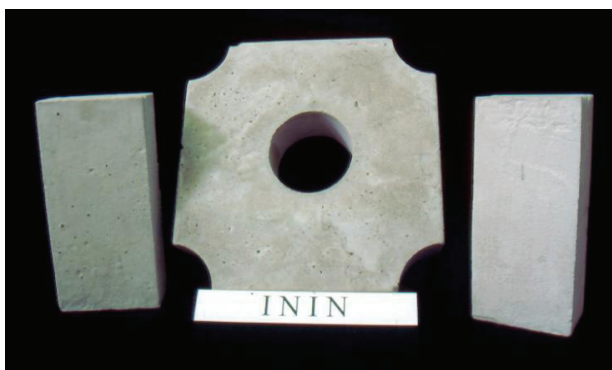


Fig. 9. Bricks and lattices obtained from granular solid residuals coming from diatomaceous, mining industrial residuals and binders

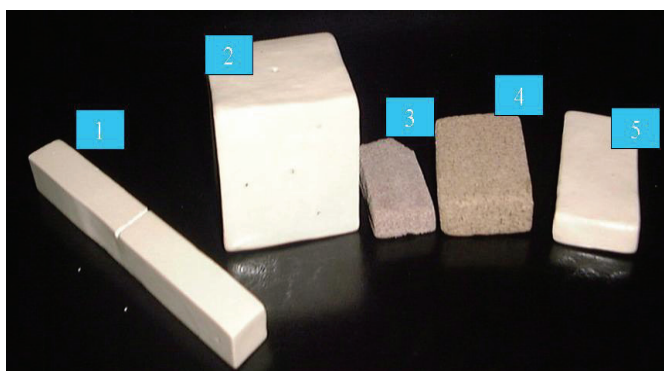


Fig. 10. Manufactured samples with clay and materials coming from mines and diatomaceous earth, 1) Impact and flexion testing, 2) Compression testing, 3) Erosive wear tests (Vite et al., 2010) 4) wet abrasion tests, 5) dry abrasion tests (Vite et al., 2011)

These bricks and lattices were obtained from solid industrial residuals coming from diatomaceous earth, which were mixed with mining industrial residuals and clay. These materials duplicate in tensile strength compared to conventional bricks, according to NOM-C-101, also, the percentage of absorption in the material obtained is smaller (about 17.1%) than required by the NOM-C-101, whose maximum value is 25%.

Note: It should be mentioned in the case of the lattice there are no regulations that specify the quality requirements to be met. The procedure for manufacturing was based on the proportions of the materials that give to a brick, the optimal resistance conditions.

### 3.2 Mechanical testing

#### 3.2.1 Compressive strength according to ASTM C-170-50 and ASTM C-36

Compression tests are required to subject the sample to a compressive load, until it breaks or fractures. These can be made on most materials according to ASTM C-170-50 standard. The compression tests are conducted on materials such as cement, concrete, rubber, wood, plastic and clay (ceramics). This test consists of applying a variable vertical load to the material, in order to determine whether it complies or not the preset compressive load according to the type of the material studied. The manufacture of these materials can be carried out by mortars and concretes conveniently dispensed. The samples tested were named as 1A, 1B and 1C as mentioned previously. The dimensions of the test samples were 50.8 X 50.8 mm (a 2 inch cube). Figure 11 shows that the compressive strength of the samples analyzed had a maximum when the content of the binder agent was 30% in volume and such resistance was 160.3 kg/cm<sup>2</sup> and a minimum of 119.7 kg/cm<sup>2</sup> was obtained when the binder content was 10%. In both cases, the resistance was higher than that of a conventional brick whose resistance varies between 80-100 Kg/cm<sup>2</sup>, also, the weight of the material obtained was 20-25% lower than the weight of conventional bricks, had less porosity and for this reason these materials were considered as a sustainable because the costs of processing were 25% lower, that the materials available on the market. Table 2 presents the compressive strength results for each testing sample.

The parameters obtained were:

- $\sigma_{\max}$  - Maximum stress
- $\sigma_{\text{yield}}$  - Yield stress
- E - Young Modulus
- $\epsilon_{\max}$  - Maximum strain

Sample	Binder agent (%)	$\sigma_{\max}$ (Kg/cm <sup>2</sup> )	$\sigma_{\text{yield}}$	E	$\epsilon_{\max}$ (%)
1A	10	119.7	-----	-----	2.7
1B	20	151.9	-----	-----	2.5
1C	30	160.3	-----	-----	3.0

Table 2. Mechanical test results

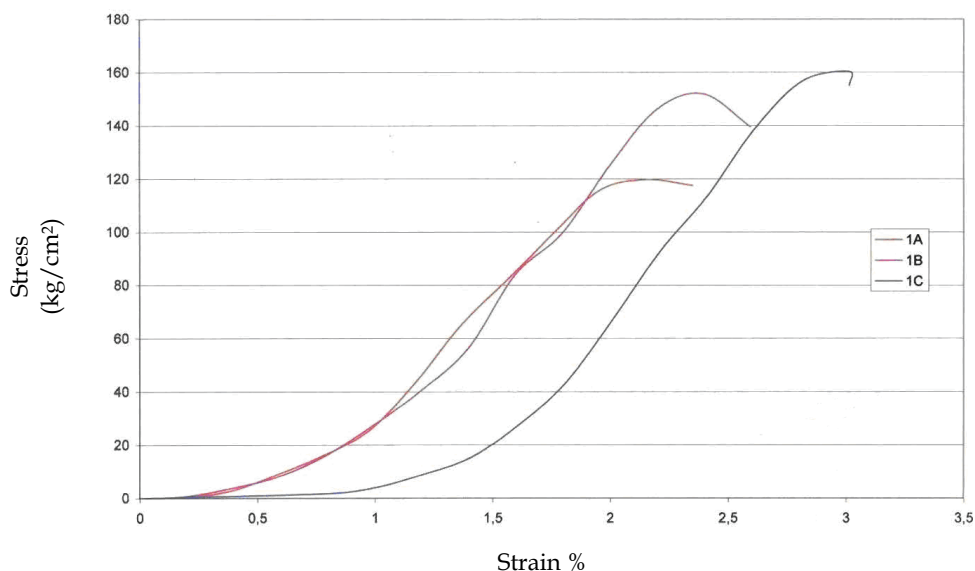


Fig. 11. Graph of the compressive resistance of test samples 1A, 1B and 1C

There are a variety of granular solid industrial residuals in all industrial countries, of anthropogenic origin and produced by nature, with which it is possible to generate proposals based on technical feasibility, economic and social development for the implementation of processes that help to the production of ceramic materials [10] or inputs for the construction industry. Due to this fact, the use of the patented equipment and the process employed in this work can provide sustainable economic and environmental benefits.

The management and implementation of solid and semisolid industrial residuals coming from different industrial sectors is important because it is possible to recover its usability by incorporating the production cycle as materials applicable to the construction industry. In addition, the impact to the environment and health of the population caused by proper handling of industrial solid residuals, which are often stored in open areas and dispersed by wind and rainwater.

#### 4. Conclusions

Using thermostated columns can completely remove the cyanide content of “Jales” present in a recent process. After this treatment, the solid material is dried, characterized and processed with a binder agent, the final result provides a material with excellent mechanical properties for application in construction industries.

The bricks obtained had excellent physical and mechanical properties, such as greater resistance to compression than conventional bricks.

The materials obtained are 20-25% lighter than conventional materials, are also less porous and are sustainable, because development costs are 25% lower compared to other materials used in the construction industry.

There is a wide variety of possibilities of using solid residuals coming from mining and granular residuals from diatomaceous earth to be applied in the construction industry or to the development of ceramic materials.

## 5. References

- Botz, M., Stevenson, J. (1995). Cyanide Recovery and Destruction. *Engineering and Mining Journal.*, Vol.196, pp. 44-47, ISSN 0095-8948.
- Li, J., Wadsworth, E.M. (1993). Indirect Manipulation of a Sphere on a Flat Disk Using Force Information. *J. Electrochemical Soc.*, Vol.140, No.7, pp. 1921-1927, ISSN 0013-4651.
- Orozco, R.V., Orozco, Y.Y. (1992). Las Presas de Jales en México, Criterios Básicos para su Proyecto, Construcción y Operación, XVI Reunión Nacional de Mecánica de Suelos, México, 1992.
- Sengupta, M. (1993). *Environmental Impacts of Mining: Monitoring, Restoration and Control*, Lewis Publishers, ISBN 0873714415, United States of America.
- Vite, J. (1994a). Apparatus for Extracting Metal Values from Foundry Sands. U.S. Patent 5376000.
- Vite, J. (1994b). Process for Extracting Metal Values from Foundry Sands. U.S. Patent 5376001.
- Vite, J. (1997). Aparato para extraer Metales Valiosos de Arenas de Fundición. Mexican Patent 186702.
- Vite, J., Vite, M., Castillo, M., Laguna-Camacho, J.R., Soto, J., Susarrey, O. (2010). Erosive wear on ceramic materials obtained from solid residuals and volcanic ashes. *Tribology International*, Vol.43, pp. 1943-1950, ISSN 0301-679X.
- Vite, M., Vite, J., Laguna-Camacho, J.R., Castillo, M., Marquina-Chávez, A. (2011). Abrasive wear on ceramic materials obtained from solid residuals coming from mines. *Wear*, Article in press, ISSN 0043-1648.
- Vite-Torres, J., Díaz-Calva, A., Vite-Torres, M., Carreño de León, C. (2003). Application of Coupled Thermostated Columns in Civil Engineering and for Leaching Heavy Metals of Wastes from Foundry Sands and Mining. *International Journal of Environment and Pollution*, Vol.19, No. 1, pp. 46-65, ISSN 0957-4352.
- Wills, B. (1994). *Tecnología del Procesamiento de Minerales*, Editorial Limusa, México.

# Strength of a New All-Ceramic Restorative Material “Turkom-Cera” Compared to Two Other Alumina-Based All-Ceramic Systems

Bandar M. A. AL-Makramani<sup>1</sup>, Abdul A. A. Razak<sup>2</sup>  
and Mohamed I. Abu-Hassan<sup>3</sup>

<sup>1</sup>*Department of Conservative Dentistry, Faculty of Dentistry, Sana'a University,*

<sup>2</sup>*Department of Conservative Dentistry, Faculty of Dentistry,  
University of Malaya, Kuala Lumpur,*

<sup>3</sup>*Department of Restorative Dentistry, Faculty of Dentistry,  
University Teknologi MARA, Selangor,*

<sup>1</sup>*Yemen*

<sup>2,3</sup>*Malaysia*

## 1. Introduction

Early types of metal-free ceramics did not enjoy success in dentistry, especially in the posterior region (Shimada et al., 2002). The high crystalline content ceramic systems have been developed in an attempt to improve the strength of metal-free restorations as well as deliver more esthetic results than conventional metal-fused-to-ceramic restorations (Ozcan et al., 2001; Valandro et al., 2006). Glass infiltrated alumina ceramic (eg. In-Ceram Alumina, Vita Zahnfabrik, Bad Sackingen, Germany), densely sintered aluminum oxide ceramic (eg, Procera AllCeram, Nobel Biocare AB, Gothenburg, Sweden) and zirconium oxide ceramic (eg, Lava 3M ESPE, St. Paul, MN, USA) are popular oxide-based high-strength ceramic materials that offer favorable esthetic characteristics, mechanical properties and biocompatibility (Blatz et al., 2004; Della Bona et al., 2007).

It is obvious from the different studies in relation to the occlusal fracture resistance of all-ceramic systems that the values reported are highly variable. This is because the testing of the occlusal fracture resistance of crowns is not a standard procedure like a bending test for a geometrically well-defined bar. As reported by some researchers (Webber et al., 2003; AL-Makramani et al., 2008a; Di Iorio et al., 2008), the results of the fracture load of all-ceramic crowns may be influenced by different factors. These include the microstructure of the ceramic material, preparation design, shape and thickness of the restoration, size and distribution of surface flaws, the magnitude, direction and location of the applied load, luting methods, the elastic modulus of the restoration components and storage conditions before loading to fracture.

Regarding the effect of finish line on the occlusal fracture resistance of all-ceramic crowns, it was shown that preparation with a 1.2 mm shoulder finish line and sharp axiogingival line

angle produced the strongest Dicor crowns, while crowns prepared with a chamfer finish line produced the weakest restoration when cemented to metal dies (Doyle et al., 1990a; Doyle et al., 1990b). A similar in-vitro study on Procera AllCeram crowns found that the shoulder finish line showed significantly higher fracture resistance than chamfer finish line (Di Iorio et al., 2008). In contrast, some authors reported that the fracture resistance of Dicor crowns luted with a resin luting cement was unaffected by the type of finish line used (Bernal et al., 1993; Malament and Socransky, 1999).

The present study investigated the effect of three variables on the occlusal fracture resistance of all-ceramic crowns. Attempts were made to standardize the other variables that may have an influence on the results of the fracture load. The studies concerning the effect of ceramic material and margin design on the occlusal fracture resistance of Turkom-Cera restorations are limited. Therefore, the objectives of this study were to:-

1. Determine the occlusal fracture resistance of Turkom-Cera copings compared to In-Ceram and Procera All-Ceram copings cemented to extracted teeth.
2. Examine the effect of finish line design on the occlusal fracture resistance of Turkom-Cera copings.

#### **Null hypotheses**

1. There is no difference in the occlusal fracture resistance of Turkom-Cera, In-Ceram and Procera AllCeram copings when cemented to natural teeth.
2. There is no effect of finish line design on the occlusal fracture resistance of Turkom-Cera copings.

## **2. Materials and methods**

### **2.1 Materials used**

40 sound and crack-free maxillary premolar teeth, extracted for orthodontic reasons (the patient's ages ranged from 15-20 years), were used for this study. In addition, three types of all-ceramic systems were used for coping production namely, Turkom-Cera™ (Turkom-Ceramic (M), Puchong, Malaysia), In-Ceram (Vita Zahnfabrik, Bad Sackingen, Germany) and Procera AllCeram (Nobel Biocare, Goteborg, Sweden), and one type of resin luting cement (Panavia-F, Kuraray Medical Inc., Okayama, Japan) with its silane coupling agent (Clearfil Silane Kit, Kuraray), were used in this study.

### **2.2 Methods**

#### **2.2.1 Specimen collection and storage**

Based on criteria, the selected teeth were free of cracks and fractures, had no evidence of caries or restorations and had no previous endodontic treatment. The average bucco-lingual, mesio-distal crowns width and teeth length were 9.1 mm, 7.3 mm and 22.3 mm, respectively. The teeth were obtained directly after extraction and stored in 0.5% Chloramine-T trihydrate solution for one week (ISO/TS 11405/2003). Both calculus deposits and residual periodontal tissues were removed by Ultrasonic Scaler (Peizon® Master 400, EMS, Nyon, Switzerland). All teeth were examined under stereo microscope (Olympus SZ61, Olympus Corp., Tokyo, Japan) at 30x to detect cracks before including them in the study. Throughout this study, the teeth were kept hydrated in distilled water as this storage solution does not seem to alter dentine permeability (Goodis et al., 1993). The storage solution was changed every one week and the teeth were stored at 4 degrees Celsius (ISO/TS 11405/2003).

### 2.2.2 Preparation of teeth

The teeth were embedded in epoxy resin 2.0 mm below the cemento-enamel junction using a plastic mould with 30 mm diameter and 30 mm height (Fig. 1). Two layers of nail polish were applied to the external surface of the entire roots. A dental surveyor was used to position the long axis of the teeth vertically.



Fig. 1. The tooth embedded in the epoxy resin

The preparation of the teeth was carried out using high-speed handpiece attached to a paralleling apparatus (Fig. 2), which allowed standardized preparations. The apparatus consists of a specimen fixture as well as vertical and horizontal arms. The specimen fixture holds the specimen and designed in a way that the fixture can rotate the specimen against a diamond bur (Fig. 3a & b). The vertical arm of the apparatus which holds the handpiece permits vertical as well as rotational movement around the tooth. The high-speed handpiece was attached to the vertical arm of the paralleling apparatus using a custom made jig (Fig. 4). This jig secures the handpiece to the vertical arm in such a manner that the attached bur can be fixed at a set angle to that of the tooth during preparation.





Fig. 2. The paralleling apparatus used

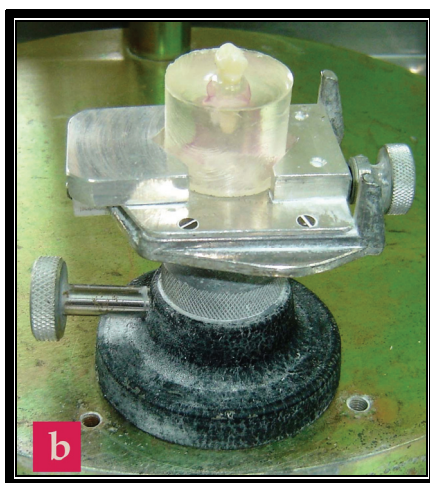


Fig. 3a & b. Two views of the specimen fixture



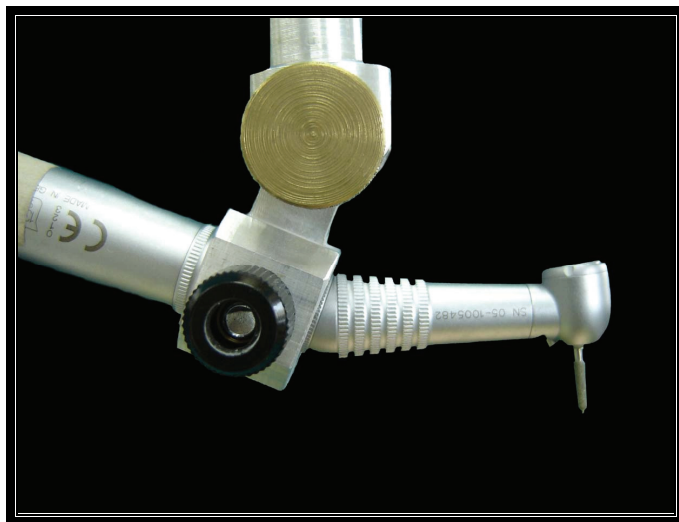


Fig. 4. The jig used to fix the handpiece to the vertical arm of the apparatus

The axial taper angle used in the present study was  $6^\circ$ . According to Shillingburg et al., (1997) a tapered bur will impart an inclination of 2-3 degrees to any surface it cuts if the shank of the instrument is held parallel to the intended path of insertion of the preparation. A specially designed jig which consists of a semi-circular transparent Perspex block with a protractor fixed to its side was used to set the degree of taper (Fig. 5). A hole was drilled along the outer side of the perspex block corresponding to a taper angle of  $3^\circ$ .

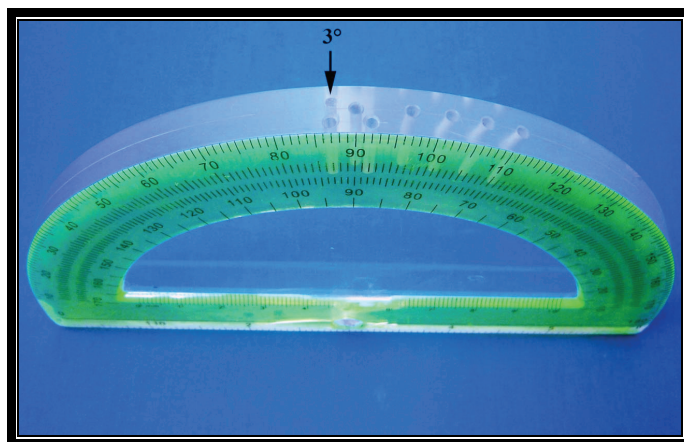


Fig. 5. The jig used to set the degree of taper

Therefore, to achieve a  $6^\circ$  axial taper preparation, the handpiece was secured to the apparatus so that the attached tapered diamond bur was oriented at a  $3^\circ$  angle to the vertical axis of the tooth. This, in addition to the  $3^\circ$  taper of the tapered bur, resulted in a total axial taper angle of  $6^\circ$  corresponding to a convergence angle of  $12^\circ$ .

The axial reduction was performed by rotating the specimen in the fixture against a coarse rotating tapered diamond burs (5856.314.018, chamfer; and 8847KR.314.018, shoulder, Komet GmbH, Lemgo, Germany) as shown in Fig. 6. After that, the preparation surfaces were finished with a fine grit diamond burs (No. 5856.314.018, chamfer; and 8847KR.314.018, shoulder).

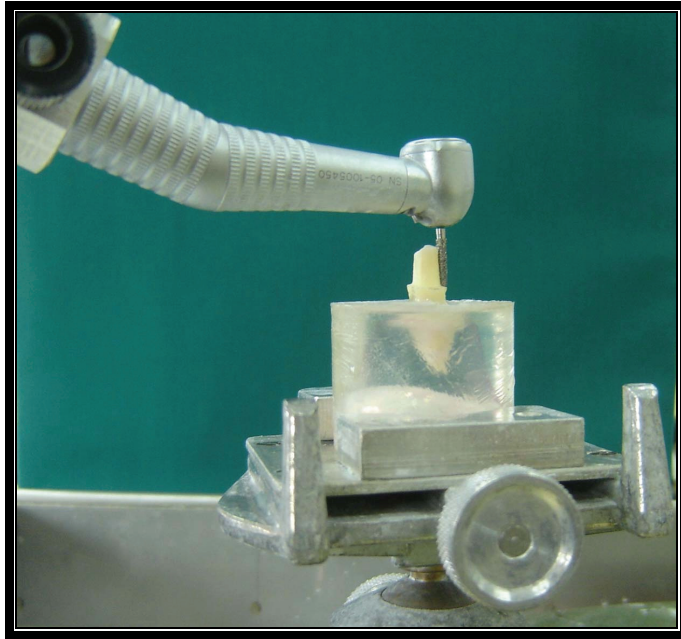


Fig. 6. The tooth during axial preparation

After the completion of axial preparation, the occlusal surface of the teeth was cut flat. A pencil was used to mark the prepared tooth 4 mm above the margin and the occlusal surface was flattened with a diamond wheel (Komet No. 909.204.055) to the marked line (Fig. 7a), which resulted in a preparation with 4.0 mm height (Fig. 7b).

The preparation was smoothed and all sharp angles or internal line angles were rounded with a fine abrasive disk (Sof-Lex Discs, 3 M Corp., St. Paul, Minn.) connected to a micromotor handpiece. All preparations were made under copious water irrigation by the same investigator.

These series of reductions resulted in a standardized teeth preparation with 6° axial taper, a 1.2 mm circumferential chamfer/shoulder margin, placed 0.5 mm occlusal to the cemento-enamel junction, and total preparation height of 4.0 mm. The finished preparation is illustrated in Fig. 8a &b.

In summary, 30 premolar teeth were prepared with chamfer margin and divided randomly into 3 groups (n=10) for each of the three ceramic systems used (In-Ceram, Procera and Turkom-Cera). In addition, 10 premolars were prepared with round shoulder margin and used to study the effect of finish line design on the fracture resistance of Turkom-Cera all-ceramic copings.

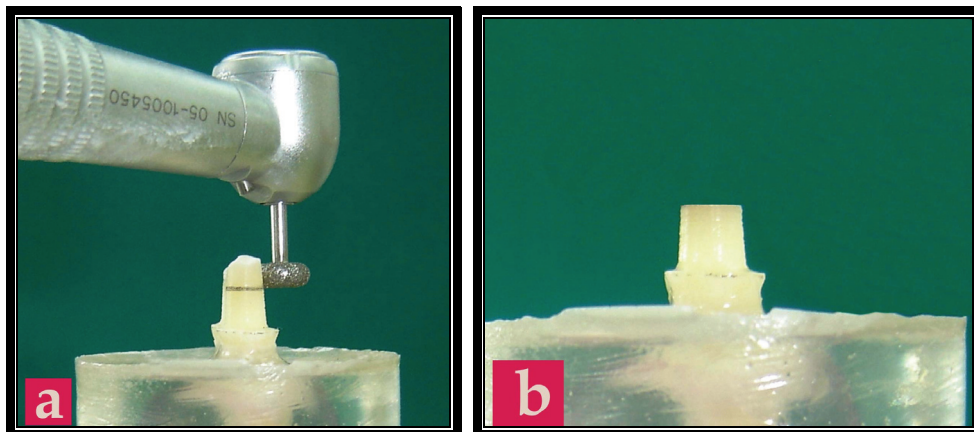


Fig. 7a & b. The tooth before (a) and after (b) occlusal reduction

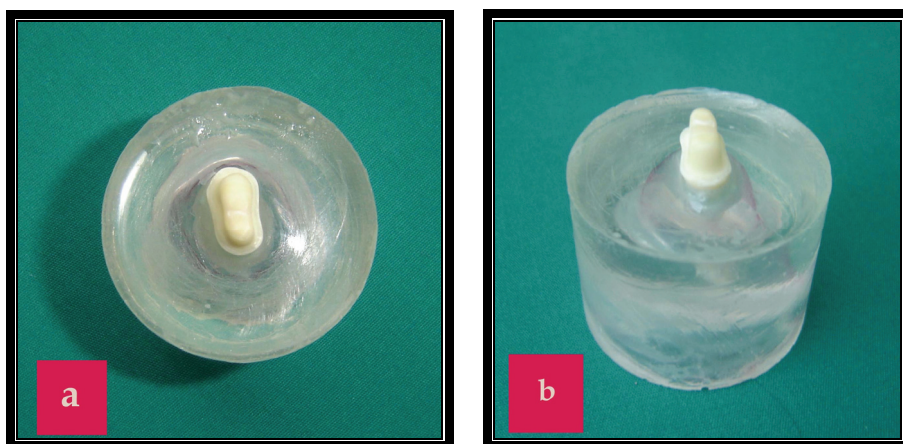


Fig. 8a & b. Occlusal (a) and buccal views (b) of the finished preparation

### 2.2.3 Impression and die preparation

The teeth were dried with an air/water syringe and impression was taken for each tooth using a bottle cap with pipette which act as an impression tray and silicone impression material (Aquasil Monophase Ultra; Dentsply Caulk, Dentsply International Inc., Milford, Germany) (Fig. 9a & b). The impression material was injected into the cap and placed on the tooth while maintaining finger pressure until setting.

Then, the impressions were boxed (Fig. 10a) using boxing wax (Boxing In Wax, Metrodent Ltd., Huddersfield, Enland). The impressions were then vaporized with a wetting agent and poured in die stone (Densite, Shufo, Kyoto, Japan) (Fig. 10b). The stone was mixed with distilled water in a 20cc liquid to 100 grams of stone ratio as recommended by the manufacturer. After a 4 hours setting time, the dies were trimmed and numbered according to their respective teeth (Fig. 11).

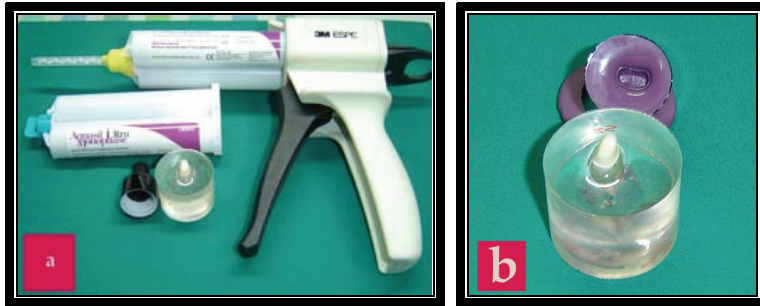


Fig. 9a & b. The impression material, tooth model and plastic cap (a); and impression of the prepared tooth (b)

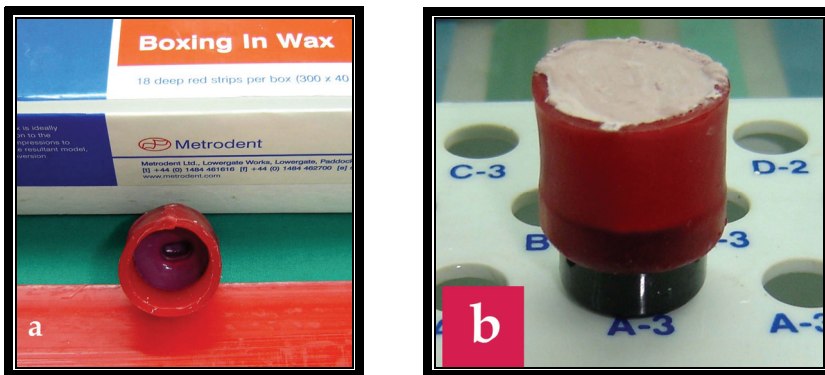


Fig. 10a & b. Boxing of the impression (a) and pouring with die stone (b)

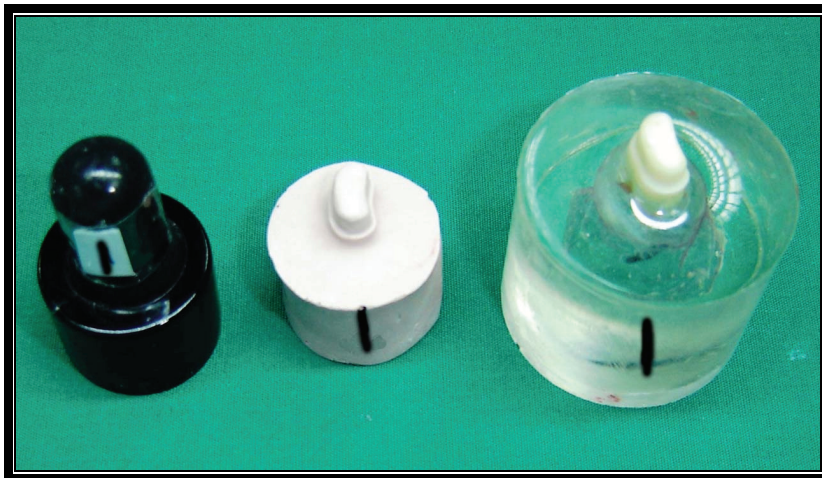


Fig. 11. The die numbered according to its respective tooth



#### **2.2.4 Fabrication of all-ceramic copings**

Ten randomly selected stone dies with chamfer margin and the 10 stone dies with shoulder margin were sent to Turkom-Cera dental laboratory and 20 Turkom-Cera copings were fabricated with a thickness of 0.6 mm. The remaining 20 stone dies with chamfer margin were randomly divided into two groups of 10 specimens for In-Ceram (n=10) and Procera (n=10) and sent to other dental laboratories. 10 In-Ceram and 10 Procera copings were fabricated with a thickness of 0.6 mm.

The macroscopic fit of all copings on the corresponding stone dies, and finally on the specimens were visually assessed. Copings that were found to rock or did not seat on the finish line were rejected and refabricated to ensure 10 copings per group.

#### **2.2.5 Cementation**

The specimens were identified by their numbers. The teeth were pumiced with a prophylaxis cup mounted on a slow speed handpiece and rinsed with an air/water syringe prior to cementation. The copings were then internally sandblasted with 50 µm aluminium oxide (Al<sub>2</sub>O<sub>3</sub>) particles at an air pressure of 2.5 bars for 13s from a distance of 10 mm. After that, the copings were steam cleaned and air dried.

All copings were cemented to their respective teeth using Panavia F resin luting cement. The ED primer was applied to the entire surface of the tooth and allowed to set for 60s before air drying with gentle air flow. The fit surfaces of all copings were silanated with a mixture of Clearfil Porcelain Bond Activator and Clearfil SE Bond Primer. The mixture was applied to the internal surface of the coping and left for 5s before air drying with gentle air flow. Sufficient amount of the Panavia F (one complete turn from each cartridge A & B) were dispensed, mixed for 20s and applied to the internal surface of each coping.

Finger pressure was applied to initially seat each coping on its respective tooth, and each coping was held in place while any excess paste remaining at the margins was removed with a disposable brush. A layer of Oxyguard II (Kuraray) was applied for three minutes around the margins of each specimen. The specimens were then placed in a custom-made vertical loading apparatus (Makramani Load) (AL-Makramani et al., 2008a), for 10 minutes under a 5 kg load. Following cementation, the 30 specimens with chamfer margin and the 10 specimens with shoulder margin were placed in a sealed container of distilled water and left in an incubator at a constant temperature of 37°C for 24 hours.

#### **2.2.6 Testing procedure**

The tooth with cemented coping was removed from the storage container, secured in a mounting jig and subjected to testing in a universal testing machine (Shimadzu, Shimadzu Corp., Tokyo, Japan) (Fig. 12). A 3 mm stainless steel bar, mounted on the crosshead of the Shimadzu testing machine was used and applied a compressive load at the centre of the occlusal surface, along the long axis of the cemented copings, at a crosshead speed of 1mm/min until failure occurred (Fig. 13). A piece of tin foil 0.7 mm thick was placed between the loading piston and the specimen to distribute the force over a larger area and to avoid loading stress peaks on the coping surface. The maximum force to produce fracture was recorded in Newtons. The failed copings were examined in order to determine the mode of fracture. The mode of fracture was classified using categories as described by Burke & Watts (1994) (Table 1).

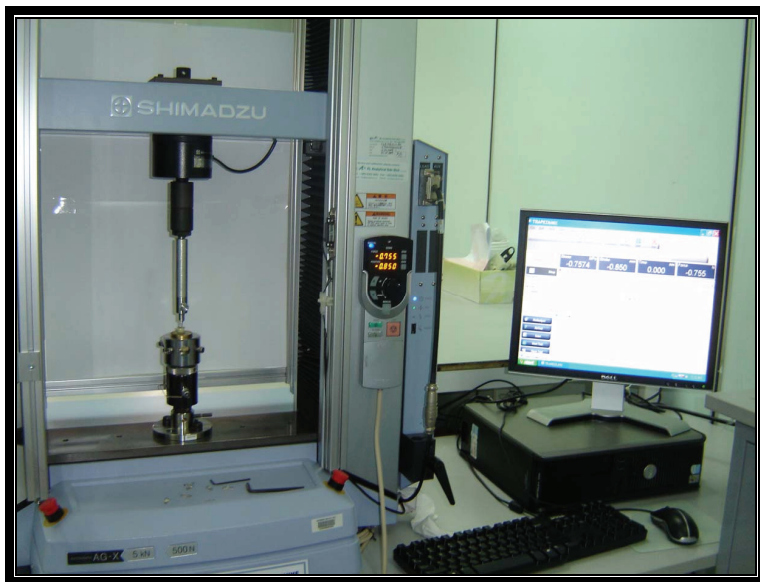


Fig. 12. The universal testing machine used



Fig. 13. The specimen during testing

Mode of fracture	Description
I	Minimal fracture or crack in coping.
II	Less than half of coping lost.
III	Coping fracture through midline (half of coping displaced or lost).
IV	More than half of coping lost.
V	Severe fracture of coping and/or die.

Table 1. Modes of fracture (After Burke and Watts, 1994)

### 2.2.7 Statistical analysis

The first objective was to determine the occlusal fracture resistance of Turkom-Cera copings compared to In-Ceram and Procera AllCeram copings. Descriptive statistics will be recorded for load at fracture of the three groups. The normally distributed data of load at fracture (histogram and Shapiro-Wilk test) will be analyzed by One Way ANOVA to achieve the objective, provided that equal variances will be assumed (Levene's test). Then, Tukey's HSD test will be carried out for post-hoc comparisons.

Whenever assumptions of normal distribution and equal variances of load at fracture between the three groups will not be met, an equivalent nonparametric Kruskal-Wallis test will be conducted. Subsequently, a post hoc test using Mann-Whitney tests with Bonferroni correction will be performed to test which pair of groups differ from each other significantly.

Regarding the second objective, effect of finish line design on load at fracture of Turkom-Cera copings, descriptive statistics will be recorded for load at fracture of each group. Then, independent samples t-test should be used to determine the significant differences in load at fracture between the two groups of Turkom-Cera copings with chamfer and shoulder finish lines. However, this is dependent on the assumptions of normal distribution and equal variances of load at fracture between each two groups to be met.

Whenever assumptions of normal distribution and equal variances of load at fracture between the two groups will not be met, an equivalent nonparametric Mann-Whitney tests will be performed.

In addition, descriptive statistics for modes of fracture and load at fracture will be recorded and the result will be descriptively analyzed. Statistical analysis will be carried out using a computer program (SPSS, SPSS Inc., Chicago, IL). Statistical significance will be set at  $\alpha=0.05$ .

## 3. Results

### 3.1 Effect of ceramic material on the fracture resistance

The objective is to test if the mean load at fracture of Procera AllCeram, Turkom-Cera, and In-Ceram all-ceramic copings differ from each other. Descriptive analysis was performed

and the mean load at fracture and standard deviation for the three groups are recorded in Table 2.

Ceramic	n	Mean	SD	95% Confidence Interval	
				Lower Bound	Upper Bound
<b>Procera AllCeram</b>	10	975.0	112.7	894.3	1055.6
<b>Turkom-Cera</b>	10	1341.9	216.5	1187.0	1496.8
<b>In-Ceram</b>	10	1151.6	180.1	1022.7	1280.4

Table 2. The mean load at fracture (N) and standard deviation for Procera AllCeram, Turkom-Cera, and In-Ceram copings

Since the assumption of normal distribution was met, the equality of variances (homogeneity) was tested using the Levene's test and showed that there was no significant deviation from homogeneity ( $p=0.163$ ). Therefore, the parametric One Way ANOVA procedure was used to achieve objective. The results were recorded in Table 3. There was a significant difference in load at fracture between the three groups ( $p<0.001$ ).

Ceramic	n	Mean (N)	SD	F Statistics (df)	P value <sup>a</sup>
Procera AllCeram	10	975.0	112.7	10.98 (2,27)	<0.001
Turkom-Cera	10	1341.9	216.5		
In-Ceram	10	1151.6	180.1		
<sup>a</sup> One Way ANOVA was used.					
Significant level was set at 0.05.					

Table 3. Comparison of load at fracture between Procera AllCeram, Turkom-Cera and In-Ceram copings by One Way ANOVA

Further analysis using Tukey HSD Post Hoc Test was done to determine the pair of means that differ significantly. Based on Tukey HSD Post Hoc Test (Table 4), the mean load at fracture of Turkom-Cera ( $1341.9 \pm 216.5$  N) was significantly more than Procera AllCeram ( $975.0 \pm 112.7$  N) ( $p<0.001$ ). There were no significant differences between the mean load at fracture of In-Ceram ( $1151.6 \pm 180.1$  N) and Procera AllCeram ( $p=0.080$ ) and also between the mean load at fracture of Turkom-Cera and In-Ceram ( $p=0.056$ ).



Pairewise comparison	Mean (SD)	Mean Difference	P value
<b>Procera AllCeram vs Turkom-Cera</b>	975.0 (112.7) 1341.9 (216.5)	-366.93 366.93	<0.001*
<b>Procera AllCeram vs In-Ceram</b>	975.0 (112.7) 1151.6 (180.1)	-176.60 176.60	0.080
<b>Turkom-Cera vs In-Ceram</b>	1341.9 (216.5) 1151.6 (180.1)	190.33 -190.33	0.056
* 2 pairs of means are significantly different by Tukey HSD Test			

Table 4. Multiple pairwise comparisons of fracture load (N) using Tukey HSD Test

### 3.1.1 Mode of fracture

A cross-tabulation between treatment groups and modes of fracture was obtained (Table 5). The Chi-square test was used to test if there is any association between treatment groups (Procera, Turkom-Cera and In-Ceram) and modes of fracture. Due to unmet assumption of Chi-Square test and non-meaningful combination of different modes the result can be only descriptively analyzed.

Examination of the mode of fracture of specimens revealed that (70 %) of Turkom-Cera and (80 %) Procera AllCeram copings exhibited minimal fracture. Whereas, only 40 % of In-Ceram copings exhibited minimal fracture.

Ceramic	Mode of Fracture				Total
	Minimal Fracture n (%)	Less than half of coping lost n (%)	More than half of coping lost n (%)	Severe fracture of die and/or coping n (%)	
<b>Procera All-ceram</b>	8 (80%)	1 (10%)	1 (10%)	0 (0%)	10
<b>Turkom-ceram</b>	7 (70%)	2 (20%)	1 (10%)	0 (0%)	10
<b>In-ceram</b>	4 (40%)	1 (10%)	2 (20%)	3 (30%)	10

Table 5. Distribution of modes of fracture in each treatment group (Procera, Turkom-Cera and In-Ceram)

Descriptive summary for modes of fracture and mean load at fracture was recorded (Table 6). The identified modes of fracture were: minimal fracture, less than half of coping lost, more than half of coping lost and severe fracture of die and/or coping.

Mode of Fracture	Procera		Turkom-Ceram		In-Ceram	
	n	Mean LAF (SD)	n	Mean LAF (SD)	n	Mean LAF (SD)
Minimal fracture	8	999.72 (102.67)	7	1344.09 (194.26)	4	1158.32 (245.54)
Less than half of coping lost	1	965.36	2	1233.47 (362.48)	1	1077.61
More than half of coping lost	1	786.51	1	1543.40	2	1159.21 (139.41)
Severe fracture of die and/or coping	0	0	0	0	3	1162.12 (206.71)

(LAF: load at fracture)

Table 6. Descriptive summary for modes of fracture and mean load at fracture (N)

As shown in Table 6, the severe fracture mode was not seen within Procera and Turkom-Cera groups. The minimal fracture mode occurred at a higher load with Turkom-Cera group (1344.09 N) followed by In-Ceram (1158.32 N) and Procera AllCeram (999.72 N) groups.

Furthermore, the minimal fracture mode occurred at a higher load than other modes of fracture in the Procera group. Whereas, in the Turkom-Cera group the minimal fracture mode occurred at a lower load than the more than half of coping lost mode, and at a lower load than the more than half of coping lost mode. Regarding In-Ceram group, the minimal fracture mode occurred at almost similar load to the other modes of fracture.

### 3.2 Effect of finish line on the fracture resistance of Turkom-Cera

Specimens were divided into two groups according to finish line used; Group 1 (Turkom-Cera with chamfer finish line) and Group 2 (Turkom-Cera with shoulder finish line). The mean and median load at fracture of the two groups are shown in Table 7.

Finish line	n	Mean (SD) (n=10)	Median (IQR) (n=10)	95% CI	
				Lower Bound	Upper Bound
Turkom-Cera (Chamfer)	10	1341.9 (216.5)	1407.38 (343.99)	1187.0	1496.8
Turkom-Cera (Shoulder)	10	1545.2 (186.6)	1549.35 (318.38)	1411.8	1678.7

Table 7. The mean and median load at fracture (N) of Turkom-Cera (Chamfer) and Turkom-Cera (Shoulder) groups

For testing normality, the histogram and Shapiro-Wilk test were used and showed no normal distribution of the mean load at fracture of the two groups. Since the assumption of

normal distribution was not met, comparison of the load at fracture between the two groups was performed using the nonparametric Mann-Whitney U Test (Table 8). There was no significant difference in the load at fracture between the two groups ( $p=0.059$ ). Therefore, there was no influence of the finish line on the load at fracture of Turkom-Cera all-ceramic copings.

Variable	Turkom-Cera (Chamfer) (n=10)		Turkom-Cera (Shoulder) (n=10)		P value
	Mean (SD)	Median (IQR)	Mean (SD)	Median (IQR)	
Load at fracture (N)	1341.9 (216.5)	1407.38 (343.99)	1545.2 (186.6)	1549.35 (318.38)	0.059*
* 2 pairs of medians are not significantly different by Mann-Whitney Test.					

Table 8. Comparison of load at fracture (N) between Turkom-Cera (Chamfer) and Turkom-Cera (Shoulder) groups by Mann-Whitney Test

## 4. Discussion

### 4.1 Methodology

An ideal experimental model of an in-vivo situation to determine the occlusal fracture resistance of all-ceramic crowns is difficult to achieve. The occlusal fracture resistance of a clinical ceramic crown is influenced by several factors, such as method of luting, loading condition and the elastic modulus of the supporting die (Scherrer and de Rijk, 1993, Webber et al., 2003; AL-Makramani et al., 2008a). However, the so called "crunch-the-crown" mechanical test had been widely used to examine the occlusal fracture resistance of sound and restored teeth (Al-Wahadni et al., 2009).

Mechanical tests on ceramic materials are difficult to carry out because of the presence of several limitations related to specimen preparation (Di Iorio et al., 2008). The present study attempted to isolate the ceramic material, artificial ageing and the finish line as the only variables. Natural teeth with comparable size and length were selected for this study to eliminate a possible effect of variations. In addition, a paralleling apparatus was used to prepare the teeth which allowed standardized preparations for all teeth.

In vivo, the teeth are supported by a visco-elastic periodontal ligament, which was not duplicated in the mounting of the specimens in the current study. The ability of the artificial ligament to reproduce the complex visco-elastic properties exhibited by ligament in vivo is limited (King and Setchell, 1990; Gu and Kern, 2006). In the clinical situation, the periodontal ligament may help to dissipate some of the applied load but at high loads simulation of a periodontal ligament in vitro is not useful as previous work has indicated that the root compresses the simulated ligament and impacts against the rigid mounting system and this might not reflect the clinical reality (Fokkinga et al., 2006; Gu and Kern, 2006; Good et al., 2008).

In the current study, two layers of nail varnish were therefore used for coating the root surfaces prior to embedding them in epoxy resin, which helped to avoid external reinforcement of the root by resin (Gu and Kern, 2006).

In the present study, the ceramic copings were cemented to natural teeth to replicate fracture load results more related to clinical situations than using ceramic discs (Wakabayashi and Anusavice, 2000; Ku et al., 2002) or crowns cemented to resin or metal die replicas (Neiva et al., 1998; AL-Makramani et al., 2009). Die replicas made of steel or resin fail to reproduce the actual force distribution at the inner surface of the crown or to reliably produce the characteristics of bonding between crowns and prepared teeth (Kelly, 1999; AL-Makramani et al., 2008a). However, die replicas provide a standardized preparation and identical physical qualities of materials used in comparison with natural teeth (Potiket et al., 2004; AL-Makramani et al., 2008b). Natural teeth show a large variation depending on their age, individual structure, and storage time after extraction, thus, causing difficulties in standardization (Strub and Beschnidt, 1998; Potiket et al., 2004).

Since the effect of the veneering porcelain on the load at fracture of high-strength all-ceramic restorations is still debatable, the copings were not veneered with porcelain (Webber et al., 2003; Beuer et al., 2008). In fact, fracturing of multilayer crowns starts at their weakest part. In the case when a stronger and stiffer core substructure is veneered with weaker porcelain, the failure usually occurs in the weak veneering porcelain or at the bond between the core and veneer (Aboushelib et al., 2006; Zahran et al., 2008). In addition, the veneering procedures could actually introduce factors (such as: flaws, cracks, voids, or internal stresses) that influence the results of mechanical tests (Vult von Steyern et al., 2006; Di Iorio et al., 2008). As stated by Miranda et al., (2001) flaws play a crucial role in the fracture resistance of brittle materials. Therefore, all-ceramic copings without porcelain veneering were loaded until fracture in this study.

The most commonly used artificial ageing technique is long-term water storage. Another widely used ageing technique is thermocycling (De Munck et al., 2005). The ISO/TS 11405 standard (2003) indicates that a thermocycling regimen comprised of 500 cycles in water between 5°C and 55°C is an appropriate artificial ageing test. In order to evaluate the effect of water storage and thermocycling on the fracture resistance of Turkom-Cera copings, 10 Turkom-Cera specimens were stored in distilled water for 30 days and subjected to 500 cycles in water between 5°C and 55°C before testing their fracture resistance.

The present study was conducted to evaluate the occlusal fracture resistance of copings fabricated using three ceramic systems and bonded to prepared teeth using resin luting cement. Such an *in vitro* study does not require natural teeth as a control group for comparison of results (Al-Wahadni et al., 2009; Komine et al., 2004; Potiket et al., 2004) since the stress distribution in restored teeth is different than in unrestored teeth (Arola et al., 2001). Furthermore, studies have found a large variability in the occlusal fracture resistance of extracted unprepared natural teeth (Attia et al., 2004; Attia et al., 2006).

#### 4.2 Discussion of results

In the present study, the load at fracture of Turkom-Cera, In-Ceram and Procera AllCeram all-ceramic copings cemented to extracted teeth using resin luting cement was evaluated. The data showed that the mean load at fracture for Turkom-Cera, In-Ceram and Procera AllCeram were: 1341.9 N, 1151.6 N and 975.0 N, respectively. Statistical analysis showed that the differences were significant between Turkom-Cera and Procera AllCeram ( $p < 0.001$ ).

However, no significant differences were detected between Turkom-Cera and In-Ceram ( $p=0.056$ ) and also between In-Ceram and Procera AllCeram ( $p=0.080$ ).

The results of this study for Turkom-Cera and In-Ceram copings were in agreement with those obtained in a previous study (AL-Makramani et al., 2009), which found that Turkom-Cera had a significantly higher load at fracture than Procera AllCeram. Furthermore, the results of this study for In-Ceram and Procera AllCeram copings were in agreement with those obtained in previous studies (Webber et al., 2003; Neiva et al., 1998; Harrington et al., 2003; AL-Makramani et al., 2009), which found no significant differences in load at fracture between Procera AllCeram and In-Ceram copings that were resin cemented.

An in vitro study (AL-Makramani et al., 2009), which evaluated the fracture resistance of Turkom-Cera, In-Ceram and Procera AllCeram copings cemented on a metal master die using resin luting cement, shows that the load necessary to fracture the Turkom-Cera, In-Ceram and Procera AllCeram copings in the current study was less than that reported in that study. In this study, extracted natural teeth were used as abutments. However, metal dies are very rigid and have a higher modulus of elasticity than dentine so that metal dies deform less which results in a lower shear stress at the inner crown surface (Scherrer & de Rijk, 1993). Therefore, the fracture load of all-ceramic restorations may be greater if crowns are supported by dies with a high modulus of elasticity (Scherrer & de Rijk, 1993). This factor should also be considered when interpreting the results of the studies utilizing different die materials.

The results of the present study show that there is no influence of the finish line design on the load at fracture of Turkom-Cera all-ceramic copings. Statistical analysis revealed no significant difference between shoulder (1545.2 N) and chamfer (1341.9 N) margins used in this study ( $p=0.059$ ). In this study only Turkom-Cera copings were evaluated. Due to this limitation, the load at fracture values obtained in this study should be compared with caution with results obtained in the studies where copings were veneered with feldspathic porcelain.

Results of the present study concurred with other studies on glass-ceramic crowns (Dicor) which did not demonstrate any differences in the loading capacity in relation to the type of finish lines used (Bernal et al., 1993; Malament and Socransky, 1999).

Di Iorio et al., (2008) found that the load at fracture for Procera (alumina-based) crowns with shoulder preparation was significantly higher than the chamfer preparation. In the current study, the load at fracture of Turkom-Cera copings with shoulder margin (1545.2 N) was higher than chamfer margin (1341.9 N), however, statistical analysis revealed no significant difference between them ( $p=0.059$ ). A possible reason for this may be that the occlusal forces were also borne by the circumferential shoulder margin, and there was less stress concentration on the axial walls compared to chamfer margin (Beuer et al., 2008).

Conversely, a study on ceramic optimized polymer (Ceromer) crowns demonstrated that the fracture resistance of the chamfer finish line specimens was greater than that of the shoulder finish line (Cho et al., 2004).

The classification description of mode of failure by Burke & Watts (1994) was useful in distinguishing between minimal loss of crown material and catastrophic damage (mode II-IV). Examination of the mode of failure of specimens in the current study revealed that Procera AllCeram, Turkom-Cera and In-Ceram copings exhibited (80%), (70%) and (20%) of minimal fracture, respectively. The copings made from Turkom-Cera with shoulder margin and Turkom-Cera with artificial ageing exhibited 50% and 60% of minimal fracture, respectively.

Clinically, dental restorations are subjected to cyclic forces ranging from 60 N to 250 N during normal function and up to 500 N to 800 N for short periods (Zahran et al., 2008; Waltimo and Könönen, 1993; Waltimo and Könönen, 1995). Waltimo & Könönen (1993), reported that the maximum biting force in the molar region was 847 N for men and 597 N for women. The maximum biting force in the premolar region has been reported to be between 181 and 608 N (Widmalm and Ericsson, 1982). However, the normal masticatory forces in human beings have been reported to range from 37% to 40% of the maximum biting force (Lundgren and Laurell, 1986; Gibbs et al., 1981).

Although the results of the present study cannot be directly compared with the in vivo situation, the mean loads at fracture for all groups (ranging from 975.0 to 1545.2 N) exceed the clinically anticipated loads in the molar and premolar regions. However, clinical trials are necessary to validate the results.

Clinically, crown failure usually occurs under a complex type of stresses. However, all specimens in the current study were tested using vertical loads which appear to be appropriate for posterior teeth (Probster, 1992). Therefore, clinical implications of the current study must be limited to that application.

In this study, the specimens were loaded until failure in a single cycle, even though restorations may fail clinically through slow crack growth caused by cyclic fatigue loading (Baran et al., 2001). Subjecting the specimens to cycling fatigue loading could be considered in further investigation to give more information about the longevity and performance of Turkom-Cera crowns in condition relatively resemble the clinical situation.

## 5. Conclusions

Under the conditions of this study, it was found that:

1. Turkom-Cera copings cemented to extracted teeth using the resin luting cement (Panavia F) provided load at fracture (1341.9 N) that was significantly higher to that obtained by Procera AllCeram (975.0 N) copings tested under the same conditions. However, there was no significant difference between the mean load at fracture of Turkom-Cera and In-Ceram (1151.6 N) and also between In-Ceram and Procera AllCeram copings tested under the same conditions. Thus, the null hypothesis was rejected.
2. There is no influence of the finish line on the load at fracture of Turkom-Cera all-ceramic copings. Thus, the null hypothesis was accepted.

## 6. Acknowledgment

This study was supported by a grant (P019/2006C); University of Malaya, Kuala Lumpur, Malaysia.

## 7. References

- Aboushelib, M.N.; Kleverlaan, C.J. & Feilzer, A.J. (2006). Microtensile bond strength of different components of core veneered all-ceramic restorations. Part II: zirconia veneering ceramics. *Dental Materials*; Vol. 22, No. 9, (September 2006) 857-863, ISSN 0109-564.

- AL-Makramani , B.M.A.; Razak, A.A.A. & Abu-Hassan, M.I. (2008a). Evaluation of Load at Fracture of Procera AllCeram Copings Using Different Luting Cements. *Journal of Prosthodontics*, Vol. 17, No. 2, (February 2008) 120-124, ISSN 1532-849X.
- AL-Makramani, B.M.A.; Razak, A.A.A. & Abu-Hassan, M.I. (2008b). Effect of luting cements on the compressive strength of Turkom-Cera all-ceramic copings. *The Journal of Contemporary Dental Practice*, Vol. 9, No. 2, (February 2008), 33-40, ISSN 1526-3711.
- AL-Makramani, B.M.A.; Razak, A.A.A. & Abu-Hassan, M.I. (2009). Comparison of the load at fracture of Turkom-Cera to Procera AllCeram and In-Ceram all-Ceramic restorations. *Journal of Prosthodontics*, Vol. 18, No. 6, (August 2009) 484-488, ISSN 1532-849X.
- Al-Wahadni, A.M.; Hussey, D.L.; Grey, N. & Hatamleh, M.M. (2009). Fracture Resistance of Aluminium Oxide and Lithium Disilicate-based Crowns using Different Luting Cements: An in vitro Study. *J Contemp Dent Pract*, Vol. 10, No. 2, (March 2009) 051-058, ISSN 1526-3711.
- Arola, D.; Galles, L.A. & Sarubin, M.F. (2001). A comparison of the mechanical behavior of posterior teeth with amalgam and composite MOD restorations. *Journal of Dentistry*, Vol. 29, No. 1, (January 2001) 63-73, ISSN 0300-5712.
- Attia, A. & Kern, M. (2004). Fracture strength of all-ceramic crowns luted using two bonding methods. *The Journal of Prosthetic Dentistry*, Vol. 91, No. 3, (March 2004) 247-252, ISSN 0022-3913.
- Attia, A.; Abdelaziz, K.M.; Freitag, S. & Kern, M. (2006). Fracture load of composite resin and feldspathic all-ceramic CAD/CAM crowns. *The Journal of Prosthetic Dentistry*, Vol. 95, No. 2, (February 2006) 117-123, ISSN 0022-3913.
- Baran, G.; Boberick, K. & McCool, J. (2001). Fatigue of restorative materials. *Critical Reviews in Oral Biology & Medicine*, Vol. 12, No. 4, (July 2001) 350-360, ISSN 1544-1113.
- Bernal, G.; Jones, R.M.; Brown, D.T.; Munoz, C.A. & Goodacre, C.J. (1993). The effect of finish line form and luting agent on the breaking strength of Dicor crowns. *The International Journal of Prosthodontics*, Vol. 6, No. 3, (May-June 1993) 286-290, ISSN 0893-2174.
- Beuer, F.; Aggstaller, H.; Edelhoff, D. & Gernet, W. (2008). Effect of Preparation Design on the Fracture Resistance of Zirconia Crown copings. *Dental Materials Journal*, Vol. 27, No. 3, (May 2008) 362-367, ISSN 0287-4547.
- Blatz, M.B.; Richter, C.; Sadan, A. & Chiche, G.J. (2004). Critical appraisal. Resin bond to dental ceramics, Part II: high-strength ceramics. *Journal of Esthetic and Restorative Dentistry*, Vol. 16, No. 5, (September 2004), 324-328, ISSN 1708-8240.
- Burke, F.J.T. & Watts, D.C. (1994). Fracture resistance of teeth restored with dentin-bonded crowns. *Quintessence International*, Vol. 25, No. 5, (May 1994) 335-340, ISSN 0033-6572.
- Cho, L.; Choi, J.; Yi, Y.J.; Park, C.J. (2004). Effect of finish line variants on marginal accuracy and fracture strength of ceramic optimized polymer/fiber-reinforced composite crowns. *The Journal of Prosthetic Dentistry*, Vol. 91, No. 6, (June 2004) 554-560, ISSN 0022-3913.
- De Munck, J.; Van Landuyt, K.; Peumans, M.; Poitevin, A.; Lambrechts, P.; Braem, M. & Van Meerbeek, B. (2005). A critical review of the durability of adhesion to tooth tissue: methods and results. *Journal of Dental Research*, Vol. 84, No. 2, (February 2005) 118-132, ISSN 1544-0591.

- Della Bona, A.; Borba, M.; Benetti, P. & Cecchetti, D. (2007). Effect of surface treatments on the bond strength of a zirconia-reinforced ceramic to composite resin. *Brazilian Oral Research*, Vol. 21, No. 1, (January-March 2007) 10-15, ISSN 1806-8324.
- Di Iorio, D.; Murmura, G.; Orsini, G.; Scarano, A. & Caputi, S. (2008). Effect of Margin Design on the Fracture Resistance of Procera® All Ceram Cores: An in vitro Study. *The Journal of Contemporary Dental Practice*, Vol. 9, No. 2, (February 2008), 001-008, ISSN 1526-3711.
- Doyle, M.G.; Goodacre, C.J.; Munoz, C.A. & Andres, C.J. (1990a). The effect of tooth preparation design on the breaking strength of Dicor crowns: 3. *The International Journal of Prosthodontics*, Vol. 3, No. 4, (July-August 1990) 327-340, ISSN 0893-2174.
- Doyle, M.G.; Munoz, C.A.; Goodacre, C.J.; Friedlander, L.D. & Moore, B.K. (1990b). The effect of tooth preparation design on the breaking strength of Dicor crowns: 2. *The International Journal of Prosthodontics*, Vol. 3, No. 3, (May-June 1990) 241-248, ISSN 0893-2174.
- Fokkinga, W.A.; Kreulen, C.M.; Le Bell-Rönnlöf, A.M.; Lassila, L.V.; Vallittu, P.K. & Creugers, N.H. (2006). In vitro fracture behavior of maxillary premolars with metal crowns and several post-and-core systems. *European Journal of Oral Sciences*, Vol. 114, No. 3, (June 2006) 250-256, ISSN 0909-8836.
- Gibbs, C.H.; Mahan, P.E.; Lundeen, H.C.; Brehnan, K.; Walsh, E.K. and Holbrook, W.B. (1981). Occlusal forces during chewing and swallowing as measured by sound transmission. *The Journal of Prosthetic Dentistry*, Vol. 46, No. 4, (October 1981) 443-449, ISSN 0022-3913.
- Good, M.L.; Orr, J.F. & Mitchell, C.A. (2008). In vitro study of mean loads and modes of failure of all-ceramic crowns cemented with light-cured or dual-cured luting cement, after 1 and 30 d of storage. *European Journal of Oral Sciences*, Vol. 116, No. 1, (February 2008) 83-88, ISSN 0909-8836.
- Goodis, H.E.; Marshall, G.W. Jr.; White, J.M.; Gee, L.; Hornberger, B. & Marshall, S.J. (1993). Storage effects on deitin permeability and shear bond strengths. *Dental Materials*; Vol. 9, No. 2, (March 1993) 79-84, ISSN 0109-564.
- Gu, X.H. & Kern, M. (2006). Fracture resistance of crowned incisors with different post systems and luting agents. *Journal of Oral Rehabilitation*, Vol. 33, No. 12, (December 2006) 918-923, ISSN 13652842.
- Harrington, Z.; McDonald, A. & Knowles, J. (2003). An in vitro study to investigate the load at fracture of Procera Allceram crowns with various thickness of occlusal veneer porcelain. *The International Journal of Prosthodontics*, Vol. 16, No. 1, (January-February 2003) 54-58, ISSN 0893-2174.
- International Organization for Standardization. ISO/TS 11405:2003. *Dental materials-testing of adhesion to tooth structure*, 2nd ed. Geneva, Switzerland: ISO; 2003.
- Kelly, J.R. (1999). Clinically relevant approach to failure testing of all-ceramic restorations. *The Journal of Prosthetic Dentistry*, Vol. 81, No. 6, (June 1999) 652-661, ISSN 0022-3913.
- King, P.A. & Setchell, D.J. (1990). An in vitro evaluation of a prototype CFRC prefabricated post developed for the restoration of pulpless teeth. *Journal of Oral Rehabilitation*, Vol. 17, No. 6, (November 1990) 599-609, ISSN 13652842.



- Komine, F.; Tomic, M.; Gerds, T. & Strub, J.R. (2004). Influence of different adhesive resin cements on the fracture strength of aluminum oxide ceramic posterior crowns. *The Journal of Prosthetic Dentistry*, Vol. 92, No. 4, (October 2004) 359-364, ISSN 0022-3913.
- Ku, C.W.; Park, S.W. & Yang, H.S. (2002). Comparison of the fracture strengths of metal-ceramic crowns and three ceromer crowns. *The Journal of Prosthetic Dentistry*, Vol. 88, No. 2, (August 2002) 170-175, ISSN 0022-3913.
- Lundgren, D. & Laurell, L. (1986). Occlusal force pattern during chewing and biting in dentitions restored with fixed bridges of cross-arch extension. I. Bilateral end abutments. *Journal of Oral Rehabilitation*, Vol. 13, No. 1, (January 1986) 57-71, ISSN 13652842.
- Malament, K. & Socransky, S. (1999). Survival of Dicor glassceramic dental restorations over 14 years. Part II: Effect of thickness of Dicor material and design of tooth preparation. *The Journal of Prosthetic Dentistry*, Vol. 81, No. 6, (June 1999) 662-667, ISSN 0022-3913.
- Miranda, P.; Pajares, A.; Guiberteau, F.; Cumbrera, F.L. & Lawn, B.R. (2001). Role of flaw statistics in contact fracture of brittle coatings. *Acta Materialia*, Vol. 49, No. 18, (October 2001) 3719-3726, ISSN 1359-6454.
- Neiva, G.; Yaman, P.; Dennison, J.B.; Razzoog, M.E. & Lang, B.R. (1998). Resistance to fracture of three all-ceramic systems. *Journal of Esthetic and Restorative Dentistry*, Vol. 10, No. 2, (March 1998) 60-66, ISSN 1708-8240.
- Ozcan, M.; Alkumru, H.N. & Gemalmaz, D. (2001). The effect of surface treatment on the shear bond strength of luting cement to a glass-infiltrated alumina ceramic. *The International Journal of Prosthodontics*, Vol. 14, No. 4, (July-August 2001) 335-339, ISSN 0893-2174.
- Potiket, N.; Chiche, G. & Finger, I.M. (2004). In vitro fracture strength of teeth restored with different all-ceramic crown systems. *The Journal of Prosthetic Dentistry*, Vol. 92, No. 5, (November 2004) 491-495, ISSN 0022-3913.
- Probster L. (1992). Compressive strength of two modern all-ceramic crowns. *The International Journal of Prosthodontics*, Vol. 5, No. 5, (September-October 1992) 409-414, ISSN 0893-2174.
- Scherrer, S.S. & de Rijk, W.G. (1993). The fracture resistance of all-ceramic crowns on supporting structures with different elastic moduli. *The International Journal of Prosthodontics*, Vol. 6, No. 5, (September-October 1993) 462-467, ISSN 0893-2174.
- Shillingburg, H.T.; Hobo, S.; Whitsett, L.D.; Jacobi, R. & Brackett, S.E. (1997). *Fundamentals of fixed prosthodontics*. 3rd ed., Quintessence Publishing Co, Inc, 0-86715-201-X, Chicago.
- Shimada, Y.; Yamaguchi, S. & Tagami, J. (2002). Micro-shear bond strength of dual-cured resin cement to glass ceramics. *Dental Materials*; Vol. 18, No. 5, (July 2002) 380-388, ISSN 0109-564.
- Strub, J.R. & Beschnidt, S.M. (1998). Fracture strength of five different all-ceramic crown systems. *The International Journal of Prosthodontics*, Vol. 11, No. 6, (November-December 1998) 602-609, ISSN 0893-2174.
- Valandro, L.F.; Ozcan, M.; Bottino, M.C.; Bottino, M.A.; Scotti, R. & Della Bona, A. (2006). Bond strength of a resin cement to high-alumina and zirconia-reinforced ceramics: the effect of surface conditioning. *The Journal of Adhesive Dentistry*, Vol. 8, No. 3, (June 2006) 175-181, ISSN 1461-5185.

- Vult von Steyern, P.; Ebbesson, S.; Holmgren, J.; Haag, P. & Nilner, K. (2006). Fracture strength of two oxide ceramic crown systems after cyclic pre-loading and thermocycling. *Journal of Oral Rehabilitation*, Vol. 33, No. 9, (September 2006) 682-689, ISSN 13652842.
- Wakabayashi, N. & Anusavice, K. (2000). Crack initiation modes in bilayered alumina/porcelain disks as a function of core/veneer thickness ratio and supporting substrate stiffness. *Journal of Dental Research*, Vol. 79, No. 6), (June 2006) 1398-1404, ISSN 1544-0591.
- Waltimo, A. & Könönen, M. (1993). A novel bite force recorder and maximal isometric bite force values for healthy young adults. *Scandinavian Journal of Dental Research*, Vol. 101, No. 3, (June 1993) 171-175, ISSN 0029-845X.
- Waltimo, A. & Könönen, M. (1995). Maximal bite force and its association with signs and symptoms of craniomandibular disorders in young Finnish non-patients. *Acta Odontologica Scandinavica*, Vol. 53, No. 4, (August 1995) 254-258, ISSN 1502-3850.
- Webber, B.; McDonald, A. & Knowles, J. (2003). An in vitro study of the compressive load at fracture of procera allceram crowns with varying thickness of veneer porcelain. *The Journal of Prosthetic Dentistry*, Vol. 89, No. 2, (February 2003) 154-160, ISSN 0022-3913.
- Widmalm, S.E. & Ericsson, S.G. (1982). Maximal bite force with centric and eccentric load. *Journal of Oral Rehabilitation*, Vol. 9, No. 5, (September 1982) 445-450, ISSN 13652842.
- Zahran, M.; El-Mowafy, O.; Tam, L.; Watson, P.A. & Finer, Y. (2008). Fracture strength and fatigue resistance of all-ceramic molar crowns manufactured with CAD/CAM technology. *Journal of Prosthodontics*, Vol. 17, No. 5, (July 2008) 370-377, ISSN 1532-849X.

# Physical and Metallurgical Characteristics of Fiber Reinforced Ceramic Matrix Composites

Zdeněk Jonšta, Evelyn A. Bolaños C., Monika Hrabalová and Petr Jonšta  
*VŠB-Technical University of Ostrava  
Czech Republic*

## 1. Introduction

Ceramics represent a very wide range of materials, which differ from each other by their chemical composition, structure and properties. These materials can be defined as predominantly crystalline materials, formed mainly by inorganic compounds of non-metallic character, which are bound particularly by ionic and ion-covalent bonds.

Ceramics are most frequently divided by the purpose of its use into **traditional** and **structural ceramics**. Traditional ceramics are produced entirely from natural raw materials (such as kaolin, clays, quartz, feldspar), which are formed and fired.

These ceramic materials can also be designated as vitreous or porous due to the fact that they contain a considerable portion of vitreous phase, pores and crystals of various compositions. Traditional ceramics can be further divided into constructional, artistic, utility and refractory.

Structural ceramics are produced only from synthetic raw materials. It is a newer type of ceramic, which has a considerable development from the seventies of the 20th century. It is used in numerous technical applications, especially under extreme conditions where, thanks to its properties, completely replaces the traditional ceramics. These ceramic materials include also functional and bio-ceramic materials.

Structural ceramics represent a fine-grained, poly-crystalline material, usually with grains smaller than 1  $\mu\text{m}$ . It contains random technological defects and micro-structural heterogeneities. The structure of ceramic materials can be characterized as **heterogeneous, poly-crystalline and poly-phased**.

## 2. Classification of structural ceramics

### 2.1 Oxidic ceramics

The ceramics based on aluminium oxide ( $\text{Al}_2\text{O}_3$ ) called also sintered alumina ( $\text{Al}_2\text{O}_3$  with addition of  $\text{ZrO}_2$ ) has the biggest significance for structural applications. Thanks to the zirconium oxide this ceramics has better mechanical properties. Increasing the  $\text{Al}_2\text{O}_3$  content increases its mechanical strength and hardness, as well as thermal expansion coefficient.

Oxidic ceramics have high strength, hardness, corrosion resistance, and they are very good electric insulators. They are used mainly at the machining of cast iron, as a structural material for components of high-temperature devices, melting crucibles, cutting plates for metals machining, spark plug insulators for engines, etc.

## 2.2 Non-oxidic ceramics

This group includes mainly nitrides, carbides and borides. Non-oxidic ceramic materials have higher strength at high temperatures in comparison with oxidic ceramics. They have higher heat conductivity and lower thermal expansion coefficient than oxides, which means they have a better resistance to thermal shocks. For this reason they are in practice used mainly as high-temperature structural materials. Their disadvantage consists in lower resistance to oxidation. In non-oxidic compounds covalent bond prevails (for example SiC, B<sub>4</sub>C, Si<sub>3</sub>N<sub>4</sub>, BN) or metallic bond (for example TiC, UC, WC, TaC, TiN). Carbides and nitrides have the broadest use of non-oxidic ceramics, mainly in special fields of mechanical and electrical engineering.

## 2.3 Mixed ceramics

It is formed by a combination of structural oxidic and non-oxidic ceramics. Composite cutting tools based on Al<sub>2</sub>O<sub>3</sub>+ZrO<sub>2</sub>+SiC are used for the lathe work of quenched steels and hardened cast irons, at the end of the machining process, such as milling. Except SiC, the most frequently used non-oxide additives are TiC or TiN.

## 3. Ceramic properties

The physical, mechanical and chemical properties of ceramic materials depend on their chemical composition and micro-structure.

### 3.1 The positive properties of ceramic materials are the following:

- low density
- low thermal expansion coefficient
- high hardness
- high temperature and corrosion resistance
- high wear resistance
- high melting temperature
- stability of mechanical properties in a wide temperature interval

### 3.2 Main disadvantages of ceramic materials are the following:

- brittleness
- difficult reproducibility of complex shapes
- highly demanding processing
- difficult joining of different ceramic components or between ceramic components and other materials

### 3.3 Causes of brittleness

Brittleness is the main problem of structural ceramics. It expresses itself by:

- the creation of brittle failure
- static fatigue
- the degradation of properties at mechanical and thermal shocks

It results from the constitution of ceramic materials, that it is suppressed in them the development of plastic deformation under conventional conditions.

The causes of brittleness are divided into:

- Fundamental
- Secondary

FUNDAMENTAL CAUSES result from the type of inter-atomic bond (physical cause), but also from the type of crystalline lattice (geometric cause).

Fundamental causes of brittleness are essentially caused by **low mobility of dislocations** and by **bad manoeuvrability**.

Low mobility of dislocations is related to the high level of the Peierls–Nabarro stress in materials with an ionic and covalent bond. Bad manoeuvrability is connected with non-fulfilment of the requirement of five independent slip systems in single crystals – so called von Mises criteria.

The fundamental causes of ceramic brittleness as a result of ionic and covalent bonds comprise also a less perfect connection of the lattices along the grain boundaries, than with metallic bonds which manifest itself by a lower cohesion strength on the grain boundaries.

Brittleness transition temperature  $T_P$  exists in ceramic materials. Below this temperature the materials suffer brittle failure – they are unable to deform plastically. The brittleness is caused by the fact that a plastic zone is not formed in front of initiated cracks and the crack propagates by cleavage along the grain boundaries or through the extend of the grains.

Fundamental causes do not lead to absolute suppression of macroscopic plastic deformation below the transition temperature  $T_P$ . For example, BeO, AlN,  $Al_2O_3$  in a poly-crystalline state at superimposed multiple pressures are capable even at room temperature of a plastic deformation up to 10% - easier formability of ceramics while loading with a big hydrostatic pressure. The strength of the boundaries is sufficient for the movement of dislocations and the activation of additional slip planes while realizing shear stress.

SECONDARY CAUSES include the heterogeneity of the structure and properties, as well as the significant weakening of the grain boundaries due to an imperfect sintering and to the presence of pores, cracks and vitreous phases along grain boundaries. The characteristic defects of ceramics include cracks and other defects caused by incorrect technological process at forming, drying or sintering.

The level of mutual contact of crystalline grains or of their contact with vitreous or binding phase is of great importance. The pores significantly influence the strength of ceramics by reducing the carrying section, as well as by the fact that they act as stress concentrators.

The mentioned secondary causes of brittleness are usual sources of failure of traditional ceramics already at low stresses. They are partly suppressed at structural ceramics.

These secondary causes are strongly applied at high temperatures, when the softening of the vitreous phase occurs and there is an easy slip along the grain boundaries, which cannot be compensated by the plastic deformation of the grain. It leads to the initiation of cracks and to their brittle inter-crystalline propagation above the transition temperature  $T_P$ .

#### 4. Possibilities to enhance the mechanical properties by toughening the ceramics

Minimum capability of plastic deformation has an essential influence on the achieved level of mechanical properties of structural ceramics. The enhancement of the level of the mechanical properties can be therefore achieved by increasing the toughness of the ceramic materials, i.e. by the achievement of a certain level of development of the process zone for

the cracks under limited conditions. The increase of the fracture toughness can be achieved by several ways as follows.

#### 4.1 Structure optimization

In this possibility to increase the toughness we talk about the so-called engineering of the grain boundaries. It consists in the reduction of porosity, the removal or reduction of the volumetric part of the vitreous phase on grain boundaries. This reduction requires highly pure initial powders and the perfection of all of the production of ceramics in sintering and pre-sintering processes.

If the ceramic contains a large portion of the vitreous phase, the crack propagates mainly through this phase and other phases have very little influence on this propagation. Ceramics with increased fracture toughness should contain only a very small part of the vitreous phase.

Another condition is a homogenous fine-grained material, a grain size from tenths of micrometers to units of micrometers. The pores of spherical shape, occurring for example in the vitreous phase, can even have a favourable influence, since they obstruct the front of the crack.

The shape of the grains and their way of strengthening is of great importance. For example  $\text{Si}_3\text{N}_4$  with **acicular grains** has even **4-times higher** fracture toughness -  $K_{IC}$  - than in the case of **uniform equi-axial grains** (Jonšta, 1998).

Increase the strength (toughening), i.e. to increase of resistance to crack propagation, can be achieved with the effect of dispersive particles. At the use of these particles the solid grains of the dispersed phase cause a deviation of the crack from its direct course, and this results in an extension of the fracture area. Except that the particles take over a greater part of the load and they thus reduce the stress on the matrix. This final result leads to a reduction of the stress factor on the front of the crack.

#### 4.2 Phase transformation

It is based on an induced phase transformation of the dispersed particles in the matrix of a ceramic material. It is used mainly in the area in front of the crack, where the effectuation of a **martensitic phase transformation** contributes to energy absorption. A pre-requisite for using this type of strengthening is the requirement that the transforming material must have a greater volume of its low-temperature modification than it has in the high-temperature structural modification.

The considered process must therefore lead to the creation of a phase with bigger volume, where the phase transformation should be made with a martensitic mechanism. It may also be assumed that the strains are not relaxed, since the relaxation process proceeds very slowly. Among the materials that have this behaviour, zirconium dioxide ( $\text{ZrO}_2$ ) seems to be the most advantageous technical ceramic.

$\text{ZrO}_2$  crystallizes in three modifications:

- \* *cubic* - stable up to 2680°C
- \* *tetragonal* - stable up to 2370°C
- \* *monoclinic* - stable up to 950°C

A big volumetric change at the transition of tetragonal modification to a monoclinic one, when relaxation by diffusion or relaxation mechanisms is impossible, is the cause of the fact that pure  $\text{ZrO}_2$  cannot be used as ceramic. That is because at cooling from the sintering temperature it could crack along the grain boundaries, at the modification change temperature, due to big internal strains.

If we stabilize this modification till room temperature (so called complete stabilization) by the addition of various oxides that are soluble in cubic modification of  $\text{ZrO}_2$ , such as for example  $\text{Y}_2\text{O}_3$ , in such case the detrimental transition from tetragonal to monoclinic modification cannot occur in whole volume.

The transformation of tetragonal modification to a monoclinic one occurs only at the places of high tensile stresses, i.e. in the front of the crack. Due to the fact that the monoclinic phase has a volume approximately by 4% bigger than the tetragonal phase, the development of pressure strains occurs at these places, which modify the state of stress on the crack and thus slows a further development of cracks.

The following three mechanisms participate in a decisive way on energy dissipation at a material failure, initiated by strengthening at phase transformation:

- stress induced transformation in the course of load
- initiation of fine cracks
- deviation of cracks from their initial direction of growth

The stress induced martensitic phase transformation of tetragonal  $\text{ZrO}_2$  to monoclinic is significantly manifested by a *protective effect of the crack*, which is accompanied by the above mentioned *volume changes*. The dissipation of fracture energy occurs by the energy consumed for the nucleation of phase transformation and the energy consumed for the creation of a new volume originated by transformation. As a result of the already mentioned increase of volume, the tensile stresses are also eliminated (Pokluda et al., 1994).

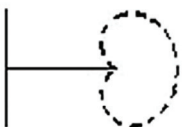

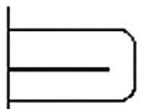
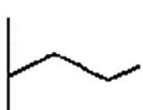
			<b>FRACTURE TOUGHNESS [MPa m<sup>1/2</sup>]</b>
Metals		Mechanisms Process zones Movement of dislocations	20 - infinity 150 - steel
Ceramics			2 - 3
Ceramics strengthened by transformation		Transformation zone (~20 mikrometer)	5 - 15
Ceramics strengthened at breakaway of cracks		Breakaway effects	2 - 20

Fig. 1. Schematic representation of the effects related to the dissipation of energy at crack growth in metallic and ceramic matrices

The creation of fine micro-cracks in the regions of dispersed particles, in which the tetragonal phase has transformed into a monoclinic phase, has a favourable effect on the increase of the fracture toughness. These cracks have usually lengths of 10 to 100 nm. They are initiated around the front of the crack in the process zones. Their frequency in the matrix

can be quite high and at the increase of the load there can be appropriately oriented micro-cracks expanded by a certain part of their original length, which is also connected with their ramification.

As a result we have the reduction or elimination of local stress peaks. It is possible to imagine this process as the distribution of stresses induced on the front of the crack onto a large number of small cracks. The material behaves under these conditions in an elastic-plastic manner, because the opening of micro-cracks is at the unstressing, partly reversible.

#### 4.3 Formation of composite materials

The biggest increase of the resistance to crack propagation, i.e. the increase of the level of ceramic's fracture toughness, promises the use of compound ceramic materials - composites. This means using the strengthening effect of ceramics thin fibres or whiskers in the ceramic matrix. The diameter of the used fibres is usually several  $\mu\text{m}$  and their length is of several millimetres, while the whiskers' dimensions are smaller almost by one order. Optimum properties are achieved, if the cracks do not propagate through the fibres, and a considerable part of energy is consumed on extraction of the fibres and at the failure of the fibre interface - matrix.

### 5. Evaluation of mechanical properties of structural ceramics

The basic characteristics of structural ceramics are the fracture toughness, tensile and bending strength, compressive strength, elastic constants, the parameters of the statistical distribution of strength and parameters of growth curves of the statistical or dynamic fatigue. The evaluation of these parameters is often difficult, because there are a number of empirical relationships for the characterization of ceramic materials.

Right now, the attention is devoted mainly to the determination of the fracture toughness by the use of the indentation technique. This technique, usually used to measure hardness, finds its application in the evaluation of these important material characteristics. In our case it was used the Vickers indenter. In the use of these techniques there are measured the length of the cracks initiated at the corners of the indentation print when it is exceeded the critical value of the loading force, which involves the initiation of cracks and their subsequent development as shown in Fig. 2.

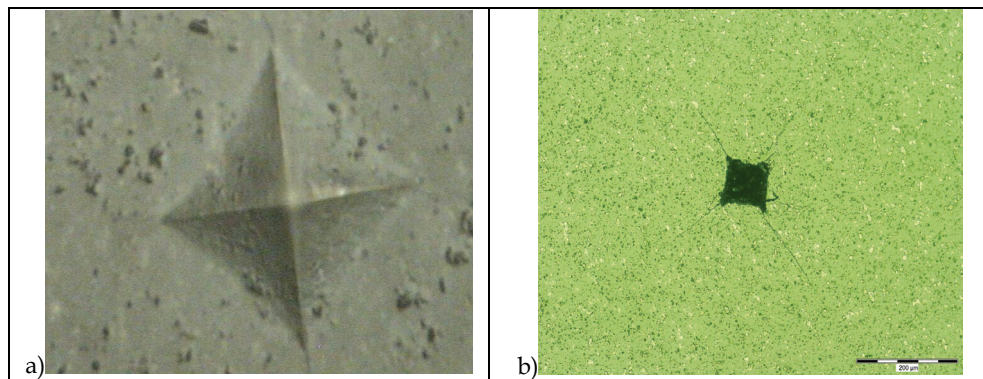


Fig. 2. Vickers' print with a load of 10 N, for a sample material a) zoom 1000x b) zoom 100x



This approach, however, requires overcoming some limiting characteristics which are related to the type of the initiated cracks. Preferential incidence of one type or another is related to the type of materials and the intensity of load on the print. On Fig. 3 are schematically illustrated the cross-section variations of the initiated cracks by Vickers indentation.

This is known as radial / median crack (see Fig. 3a), where  $m_t$  corresponds to the median crack and  $l_t$  to the side (lateral) crack. The figure 3b shows the radial or Palmquist cracks  $r_t$  and  $l_t$  shows the side (lateral) cracks. The Palmquist cracks type can be observed at lower levels of indenter loads and on the contrary the radial / median cracks are initiated at higher levels.

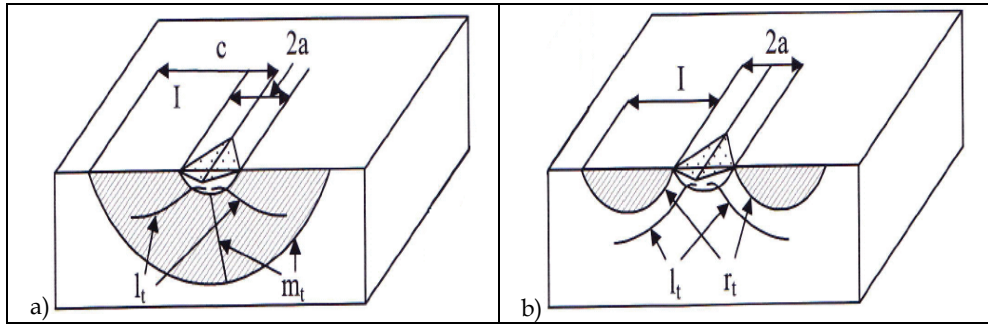


Fig. 3. a) median crack, b) lateral crack

This evaluation technique requires the preparation of a relatively small area of the material sample for the indentation prints. Of course, there are a number of restrictive conditions in its application related both to the level of surface preparation, and to the conditions for the initiation and propagation of the cracks. We could also consider a risk on the evaluation associated with the use of small areas and the fact that the measurement is performed on the material surface (assuming that the homogeneity and the volume of the tested material is maintained).

Matzke pointed out these limiting factors, on behalf of his special attention to the study of this kind of situation (Matzke, 1980, 1990, 1991). It should also be taken into account the possible presence of discontinuities by major or minor deviations in the width of cracks. It cannot be excluded in some cases the possibility to initiate more than one indentation crack in the corners of the print.

According to Matzke this leads to a possibility of underestimation of the crack length, but in macroscopic terms the fracture toughness values would be realistic data (Matzke, 1991). The processes of uneven development of cracks are an integral part of a complete evaluation of the parameter of resistance to brittle fracture.

In our works we have used, for determining the values of fracture toughness, a relationship that is independent of the crack profile and allows you to evaluate different types of materials or a type of material in a wide range of applied loads. This relationship was presented by Liang et al. (in 1990) and is expressed as follows:

$$K_{IC} = \frac{\left[ \frac{2I}{u} \right]^{\left( \frac{1}{9u} - 1,51 \right)} \cdot HV \left( \frac{u}{2} \right)^{\frac{1}{2}}}{\left( \frac{HV}{E \cdot \Phi} \right)^{0,4} \cdot \alpha \cdot \Phi} \quad [\text{MPa m}^{1/2}] \quad (1)$$

with:

$$\alpha = 14 \left[ 1 - 8 \left( \frac{4\nu - 0,5}{1 + \nu} \right)^4 \right] \quad (2)$$

and the length of the crack is:

$$l = \frac{\sum_{i=1}^n l_i}{4} \quad [\text{m}] \quad (3)$$

Where:

HV - hardness by Vickers,

u - diagonal length,

l - crack length,

$\alpha$  - dimensionless constant dependent on the order of the Poisson's number of a particular type of ceramic material - 9.3,

$\Phi$  - limiting factor - 3,

E - Young's module of elasticity.

With the indentation technique we can make an evaluation of structural ceramics response to repeated loadings. Here, we also have similar limitations as in the previous case. Informatively it may be noted that in the evaluation of the kinetics the advances of the fatigue cracks in structural ceramics the obtained and modified characteristics are compared with the results obtained at structural steels. Although this technique does not allow to establish an analogical relation with Paris' kinetic equation, it allows to determine the response of a certain type of ceramic to repeated loading based on the dependence between the number of burdened cycles and the length of the induced cracks, or in that case based on a defined number of burdened cycles leading to the chip of the evaluated material around the indentation print.

## 6. Indentation model of the origin of cracks

At the formation of a Vickers' indentation print an elastic-plastic stress fields in the material are originated, which affects the subsequent expansion of cracks. The period of the cracks derivation is an important factor that determines the fracture threshold value and could be the control parameter for determining the dominant influence of the surface radial cracks or of the subsurface median cracks in the first stage of propagation.

According to the model of Marshall and Lawn, the fully loaded indenter with an elastic / plastic field is considered as a superposition of a residual field of an unloaded material and as an ideal plastic contact field. The essence of the mentioned model is the assumption that during the unloading operation of the indenter does not appears the action of a reverse plasticity. (Marshall & Lawn, 1979)

During the indenter loading, in the material the origin of elastic deformation zones occur with the subsequent development of the radial / median cracks. The growing tensions cause the subsequent stable growth of median cracks. During the subsequent unloading the closure of median cracks occurs, while the lateral cracks grow until the indenter load is completely removed, and there is when the subsequent chipping can occur (Cook & Pharr,

1990). The initiation and propagation of the radial/median and lateral cracks leads, in brittle materials, to a subsequent chipping formation. On Fig.4 a schematic representation of the cracks system under Vickers' indentation print is shown.

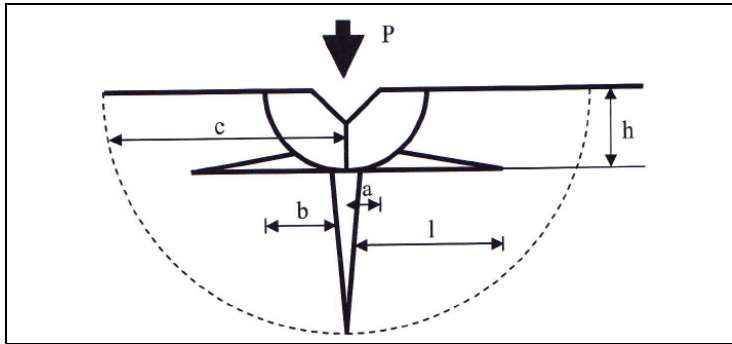


Fig. 4. Schematic representation of the crack system under Vickers' print

On the presented picture -  $P$  - is the index load at which the origin of median cracks with a length of -  $c$  - occurs. The plastic zone is formed during the application of the Vickers' load of the indenter with an appropriate angle  $2\psi$ , where -  $a$  - is half the diagonal of the Vickers' print and -  $b$  - is the plastic deformation zone accommodated under the print in the plastic zones. The critical stress for the formation of radial/median crack is given by (Evans & Marshall, 1981; Kumar & Khamba, 2006):

$$P = \alpha \cdot \frac{K_{IC}^4}{HV^3} \quad [N] \quad (4)$$

where:

$\alpha$  - dimensionless constant

$K_{IC}$  - fracture toughness

$HV$  - hardness by Vickers

At the Vickers indenter loading, just below the indentation print in the material, the formation of irreversible strains occurs. From the schematic view of the cracks resulting in a material when exposed to Vickers indentation, we have that  $\delta V$  is the printed volume,  $V$  is the volume of the deformed zone and  $\psi$  is half the size of the Vickers' indentation print. Then the next equation applies:

$$\frac{\delta V}{V} = \left(\frac{a}{b}\right)^3 \cdot \cot g\psi \quad (5)$$

This zone is to maintain its constant volume elastically compressed with the surrounding material. The result is the formation of a residual force  $F_r$  on the surface of the indentation print, which then acts on the axis of the indenter in the opposite load direction. At the same time the formation of the residual forces  $F_m$  occurs, which are located in close proximity to the plastic zone. These residual forces cause on their surroundings the creation of tensile stresses and with the absence of a reverse plasticity they achieve, at full loading of the indenter, the maximum levels of the force  $F$  ( $F_{r0}$  and  $F_{m0}$ ).

This level is maintained even after the subsequent unload of the indenter, if during the loading there are no material cracks. At a sufficient level of strength of  $F_{r0}$  occurs after unloading the indenter the formation of lateral cracks at the depth  $h$ , while the power  $F_{m0}$  is associated with the formation of radial/median cracks. The lateral crack grows up to the equilibrium length  $l$  and the residual strength, leading to the formation of these cracks, is reduced from the maximum level  $F_{r0}$  to the level equilibrium value  $F_r$  (Evans & Marshall, 1981). Marshall et al. (in 1982) derived an equation from an elastic-plastic analysis that expresses the relationship between the so-called equilibrium length of the lateral cracks  $l$  and the index load:

$$l = l_0 \cdot \left[ 1 - \left( \frac{F_0}{F} \right)^{\frac{1}{4}} \right]^{\frac{1}{2}} \quad [\text{mm}] \quad (6)$$

where  $F_0$  is the apparent threshold value, which can be expressed with the use of the fracture toughness:

$$F_0 = \frac{\zeta_0 \cdot \frac{E}{H} \cdot K_C^4}{A^2 \cdot (\cot g\psi)^{\frac{2}{3}} \cdot HV^3} \quad [\text{N}] \quad (7)$$

where  $l_0$  corresponds to the length of the crack limits defined by the following equation:

$$l_0 = \left[ \frac{\zeta_l \cdot (\cot g\psi)^{\frac{5}{6}} \cdot \left( \frac{E}{H} \right)^{\frac{3}{4}}}{A^{\frac{1}{2}} \cdot K_C \cdot HV^{\frac{1}{4}}} \right] \cdot F^{\frac{5}{8}} \quad [\text{mm}] \quad (8)$$

In this equation  $\zeta_0$  and  $\zeta_L$  are dimensionless constants independent of the system material - indenter. These constants determined Marshall et.al. (in 1982), based on the measurements of ceramic materials. The constant  $\zeta_0$  corresponds to the value  $1,2 \cdot 10^3$  and the constant  $\zeta_L$  to the value  $25 \cdot 10^{-3}$ . The magnitude  $A$  on the previous equations is a dimensionless geometric constant. Using the previous relationships it can be predicted the dependence between the equilibrium length of lateral cracks and indenter's load.

## 7. Crack propagation and chipping formation

During the loading, in the material occurs the crack propagation and may subsequently also occur the chipping formation. The formation of cracks in the index corresponds to the time of contact of the indenter with the surface of the evaluated material and its subsequent entry into the volume of the material.

This process can be simply described as a penetrating process that leads to plastically deformed zones surrounding the Vickers' indentation prints. There also occurs the formation of the surface tension zones which are adjacent to the contact places between the indenter and the material and occurs the emergence of a field for tensile stresses in the front of the indenter (Antis et al., 1981).

The perforation of the indenter into the sample surface leads to the initiation of subsurface cracks at the indentation's front. At this place the subsurface tensile stress levels reach their maximum. A bigger load leads to the development of already initiated median type cracks, in both directions: towards the material and towards the surface of the sample - radial/median crack- (see Fig.5).

The median crack remains, in the case of a no sufficient load during the loaded cycle, under the surface of the evaluated material, which means that it is primarily propagated into the volume of the material and only a minority to its surface.

The subsequent intersection of the cracks with the surface of the sample can be detected only after unloading, when the active surface compressive stresses are sufficiently reduced (Sglavo & Green, 1995).

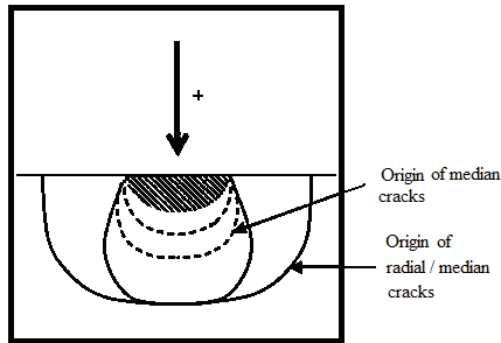


Fig. 5. Schematic representation of the origin of median and radial/median cracks under load

The median crack has a tendency to close during the subsequent unload if the indenter. The full closure will not result because of the action of the fields of internal stresses, which is related to the execution of the elastic-plastic state. Such induced residual stress fields cause the formation of lateral (side) cracks that are initiated at the plastic zone and then propagated in a parallel to the sample surface plane. The development of lateral cracks continues during the indenter's unloading.

The initiated induced internal stresses affect the next development of subsurface median or eventually radial/median cracks. Dissemination of lateral cracks increases proportionally with increasing the load of the indenter. Their intersection with the surface of the material leads to the chipping formation.

## 8. Composite materials based on ceramics

As previously mentioned, composite (compound) materials present due to their high resistance to brittle crack propagation, that is because of their high fracture toughness, promising materials for technical applications. Particularly, ceramic nanocomposites meet the demands of modern technologies.

Micro / nanocomposites based on nitride and silicon carbide are a new generation of the ceramic materials developed in the last decade. The range of materials based on  $\text{Si}_3\text{N}_4$  is recently widely used in the manufacture of cutting tools, for components exposed to friction, combustion engine components, water pumps, industrial pumps, piston engines, gas turbines etc. This type of ceramic material is characterized mainly by the high strength

at normal and elevated temperatures, chemical stability, good hardness, wear resistance, low coefficients of friction and low density.

Ceramics and ceramic composites are nowadays used in various technological fields. The ceramic composites are classified according to their particles size into microcomposites where the secondary phase particle size is measured in microns, and nanocomposites where there is a nanometric size of the secondary phase particles.

In addition to improved mechanical properties of ceramic nanocomposites there were observed new features such as machinability and superplasticity. The aim of the preparation of ceramic composites is to improve not only the "traditional" mechanical properties such as hardness, strength and reliability at room temperature, but mainly to improve the mechanical properties at high temperatures, such as creep resistance to high temperature, strength and corrosion resistance.

As a disadvantage we can see quite a significant financial demand of the preparation of nanocomposites because of the high prices of the nanopowders and the expensive furnace equipment, because the compaction of the nanocomposite requires special methods of sintering with rapid heating and short holding time at high temperature.

The ceramic nanocomposites can be divided into four categories (Fig. 6): *intragranular nanocomposites*, *intergranular nanocomposites*, *intra-intergranular nanocomposites* and *nano/nano composites*. Intra and intergranular nanocomposites have a two to five times higher toughness and strength at room temperature than the monolithic materials.

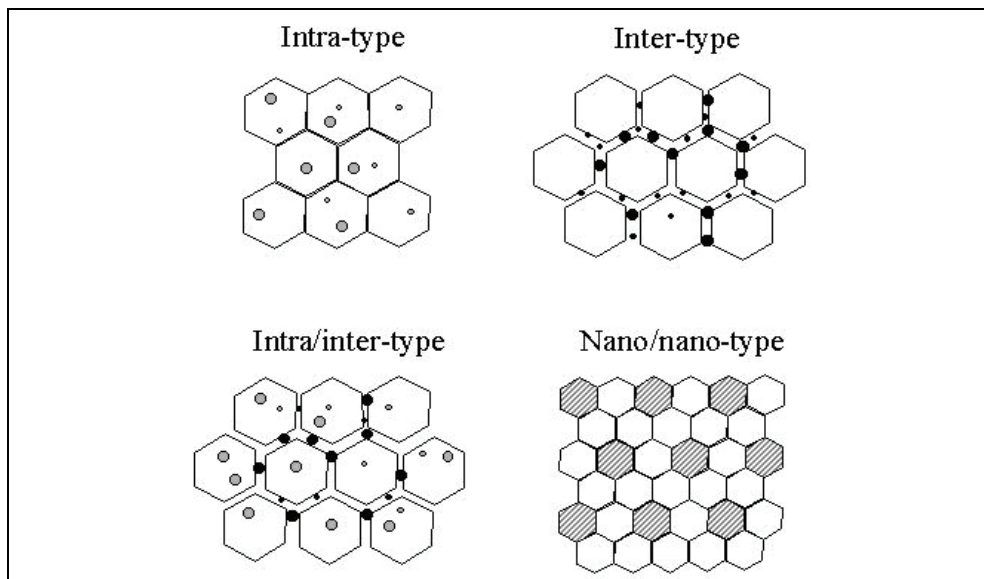


Fig. 6. Types of ceramic nanocomposites (Jonšta et al., 2010)

## 9. Nanocomposites based on $\text{Si}_3\text{N}_4/\text{SiC}$

Ceramic materials on the base of  $\text{Si}_3\text{N}_4$  are recently one of the best candidates for tribological application due to the combination of their good thermal and mechanical properties, chemical resistance and high hardness.

On recent investigations (Bolaños et al., 2010) it was studied the preparation of  $\text{Si}_3\text{N}_4/\text{SiC}$  nanocomposites with different rare earth oxide sintering aids ( $\text{La}_2\text{O}_3$ ,  $\text{Sm}_2\text{O}_3$ ,  $\text{Yb}_2\text{O}_3$  a  $\text{Lu}_2\text{O}_3$ ) and the evaluation of their hardness, indentation fracture toughness and wear resistance at room temperature.

## 9.1 Analyzed results of the investigation

### 9.1.1 Density

The density of the samples after the hot pressing process amounted to 99%, so it is considered that the sintering conditions were chosen properly. At temperatures above  $1510^\circ\text{C}$ , there was a decrease in the vacuum, ie. CO gas was liberated proving the formation of SiC with the carbothermic reduction. After this reaction and the subsequent increase on the temperature to  $1650^\circ\text{C}$  occurred the formation of the liquid phase in the system  $\text{RE}_2\text{O}_3 - \text{SiO}_2$ . In the presence of  $\text{Si}_3\text{N}_4$ , the ternary eutectic point is lower, as for binary systems.

The formation of liquid phase allowed the compaction of the ceramic composite. The densities of the sintered samples prepared by hot pressing are shown in table 1.

Sample	Density $\rho$ [ $\text{g}\cdot\text{cm}^{-3}$ ]
K3Lu-2	3,378
K3Yb-2	3,348
K3Sm-2	3,322
K3La -2	3,289

Table 1. Densities of the K3Re-2 nanocomposite materials

### 9.1.2 Microstructure

The microstructure of the hot-pressed composite materials denominated as K3La, K3Sm, K3Yb and K3Lu are shown in Fig. 7 and Fig. 8. According to the observed microstructures, we can conclude that the samples are slightly over etched ( $\text{Si}_3\text{N}_4$  fine particles below 300 nm are not visible), so visually it appears that glass phase is more than 10% by volume. In all samples the microstructure contains large elongated particles of  $\beta\text{-Si}_3\text{N}_4$  (whiskers) which are surrounded by finer particles of  $\beta\text{-Si}_3\text{N}_4$  with needle shapes. We call this fine fraction the matrix and we call the larger  $\beta\text{-Si}_3\text{N}_4$  whiskers the tougher particles.

It was expected a different evolution of the microstructures because of the used oxide  $\text{RE}_2\text{O}_3$ . A more detailed study of the Fig. 7 and Fig. 8, shows that the microstructure of the sample matrix of K3Yb and K3Lu is fine-grained. The large extended  $\beta\text{-Si}_3\text{N}_4$  grains are comparable in thickness with the sample K3La, which has lower viscosity of the glass phase. In the process of sintering of  $\text{Si}_3\text{N}_4$ , some  $\alpha\text{-Si}_3\text{N}_4$  grains of the primary powder dissolved in the liquid phase and then precipitated, and grew in the form of  $\beta\text{-Si}_3\text{N}_4$  needles.

Their growth was mainly controlled by diffusion, and that is why, in systems with a higher viscosity of the liquid phase (system containing Yb and Lu) the transport of material from the melting  $\alpha\text{-Si}_3\text{N}_4$  grains to the growing  $\beta\text{-Si}_3\text{N}_4$  grains was slower, and that means that the microstructure of the matrix of these materials has then finer grains.

Another possible reason for the fine-grained microstructure of the systems with higher viscosity, is the slower dissolution of the original  $\beta\text{-Si}_3\text{N}_4$  grains (about 5 wt.% on the



starting  $\text{Si}_3\text{N}_4$  powder SN-E10) with small diameter so-called critical diameter (0,1 to 0,2 $\mu\text{m}$ ). On the systems with the addition of  $\text{La}_2\text{O}_3$  and  $\text{Sm}_2\text{O}_3$  the dissolving speed of the  $\text{Si}_3\text{N}_4$  is slightly higher, and therefore the matrix of these systems is slightly coarse-grained.

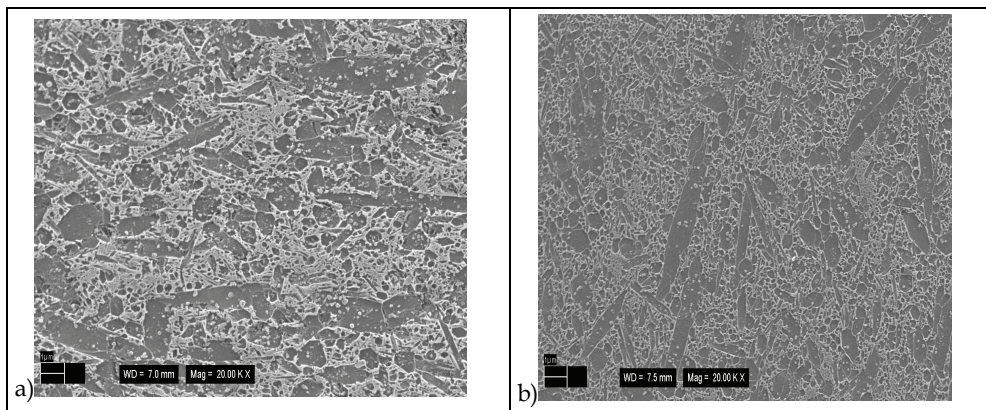


Fig. 7. Microstructure of samples a) K3La, b) K3Sm obtained by SEM at 20000<sup>th</sup> magn

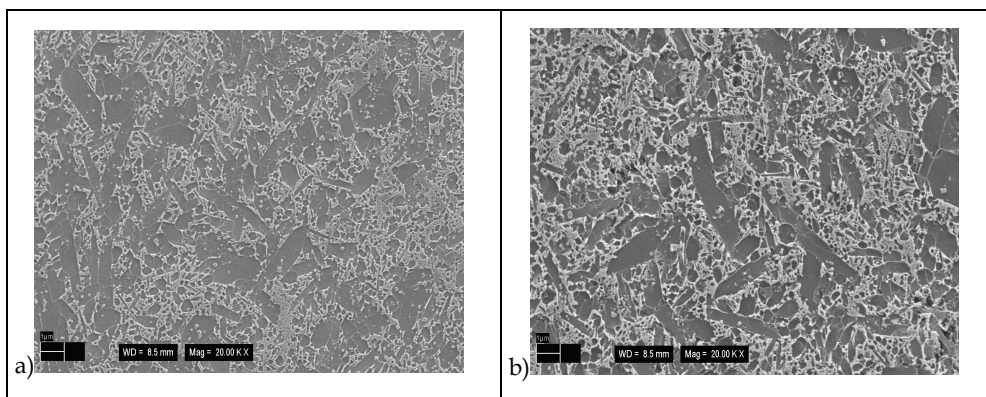


Fig. 8. Microstructure of samples a) K3Yb, b) K3Lu obtained by SEM at 20000<sup>th</sup> magn

The rare earth metal oxides also affect the thinness of the  $\beta\text{-Si}_3\text{N}_4$  particles. The average value of slenderness decreases with the growing ionic radius of the rare earth metals, or with the decrease of the viscosity of the liquid phase.

The growth of elongated  $\beta\text{-Si}_3\text{N}_4$  grains is affected not only by the viscosity of the liquid phase, but also by the ability of rare earth elements to adsorb itselfs on the surface of  $\text{Si}_3\text{N}_4$  crystals. It was observed, with a transmission electron microscopy, that Lu has a higher stability in an oxy-nitride glass (stronger bond with O), while La adsorbs preferentially on the prismatic surface of the  $\text{Si}_3\text{N}_4$  grains (binding with N), thereby preventing the further build up of dissolved Si in the surface of N, and thus growing on the thickness of the  $\beta\text{-Si}_3\text{N}_4$  grains.

From the observation of 15 photomicrographs of each sample of K3RE-2, was showed that with the decrease of the ionic radius of the rare earth elements ( $\text{La} \rightarrow \text{Sm} \rightarrow \text{Yb} \rightarrow \text{Lu}$ ) the structure is more bimodal, the matrix is finer and therefore has more elongated particles of



$\beta$ - $\text{Si}_3\text{N}_4$ . From La to Lu their thickness slightly increases. For a more detailed statistical analysis it is necessary to measure the slenderness of at least 2000 grains of each microstructure of each ceramic material containing K3RE.

The microstructure of the samples contains, together with elongated  $\text{Si}_3\text{N}_4$  grains, irregularly distributed SiC particles, which are located both at grain boundaries and inside the  $\text{Si}_3\text{N}_4$  grains. The larger SiC particles are mainly located at the grain boundaries (inter SiC grains), and the finer SiC particles (<50 nm) were observed within the  $\text{Si}_3\text{N}_4$  grains (intra SiC grains). The SiC nanoparticles can slow up, or may completely stop the abnormal growth of the  $\beta$ - $\text{Si}_3\text{N}_4$  grains. Therefore, the overall microstructure of the composites with K3RE was finer compared with the reference samples.

### 9.1.3 Abrasion resistance

The abrasion resistance tests were performed using the "ball-on-disc" method. The friction curve had a similar pattern for all the tested samples (K3RE-1). At the beginning, the friction coefficient was low, but then increased to a maximum value and then stabilized at a relatively constant value during the test.

The Fig.9 shows the friction coefficients of reference (monolith:  $\text{Si}_3\text{N}_4 + 3 \text{ mol. \% RE}_2\text{O}_3$ ) and composite samples with K3RE ( $\text{Si}_3\text{N}_4 + \text{SiC} + 3 \text{ mol. \% RE}_2\text{O}_3$ ). The friction coefficient of the monolithic samples was higher compared with the composite samples with the same additive  $\text{RE}_2\text{O}_3$  (RE = La, Sm, Yb, Lu). The lower friction coefficient of composite materials is attributable to their higher hardness compared to the reference monoliths and the presence of SiC nanoparticles. From the figure 3 it is also clear, that the friction coefficient slightly decreases with decreasing the ionic radius of  $\text{RE}^{3+}$ . The better sliding properties of the composites with K3Lu and K3Yb compared with K3Sm and K3La may be due to a finer microstructure of the matrix (Fig. 7-8) and to a higher rigidity of the glassy phase at the grain boundaries, because the glass with a smaller radius of the  $\text{RE}^{3+}$  ion has a higher hardness, fracture toughness and Young's modulus.

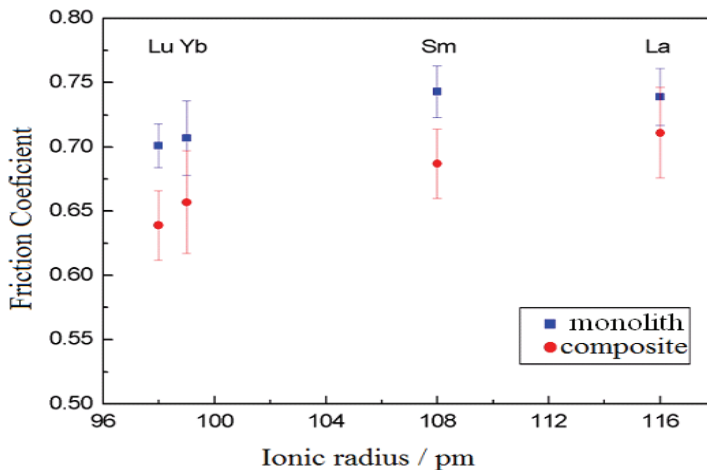


Fig. 9. Effect of ionic radius of  $\text{RE}^{3+}$  sintering additives on the friction coefficients of the reference monoliths ( $\text{Si}_3\text{N}_4 + 3 \text{ mol. \% RE}_2\text{O}_3$ ) and composite materials K3RE ( $\text{Si}_3\text{N}_4 + \text{SiC} + 3 \text{ mol. \% RE}_2\text{O}_3$ )

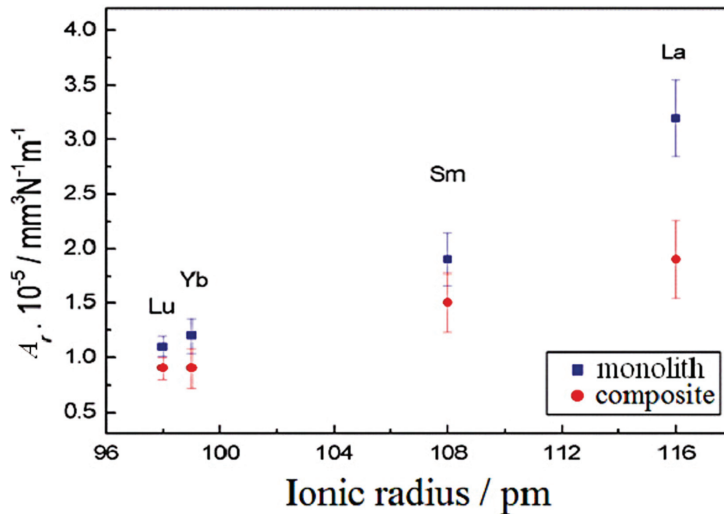


Fig. 10. Effect of ionic radius of RE<sup>3+</sup> sintering additives on the abrasion rate (Ar) of the reference monoliths (Si<sub>3</sub>N<sub>4</sub>+ 3 mol. % RE<sub>2</sub>O<sub>3</sub>) and composite materials K3RE (Si<sub>3</sub>N<sub>4</sub>+ SiC + 3 mol.% RE<sub>2</sub>O<sub>3</sub>)

The Fig. 10 shows the relationship of the abrasion rate (Ar) of the reference monoliths (Si<sub>3</sub>N<sub>4</sub>+ 3 mol.% RE<sub>2</sub>O<sub>3</sub>) and the composite materials K3RE (Si<sub>3</sub>N<sub>4</sub>+ SiC + 3 mol.% RE<sub>2</sub>O<sub>3</sub>) with the ionic radius of the RE<sup>3+</sup> sintering additives. The difference in the abrasion rates is more pronounced than the difference in the friction coefficients; however, the tendency is maintained. The samples with the addition of smaller RE<sup>3+</sup> ionic radius (K3Lu and K3Yb) exhibit less abrasion in comparison with the samples containing additives with larger ionic radius (K3Sm and K3La). This is expected to be due to a higher rigidity of the glassy phase of the samples K3Lu and K3Yb because, in general, the abrasion rate of the ceramic materials based on Si<sub>3</sub>N<sub>4</sub> with lower strength on the grain boundaries is higher.

Moreover, the Si<sub>3</sub>N<sub>4</sub> materials with the addition of Lu<sub>2</sub>O<sub>3</sub> and Yb<sub>2</sub>O<sub>3</sub> have better high-temperature properties compared with ceramics containing Sm<sub>2</sub>O<sub>3</sub> or La<sub>2</sub>O<sub>3</sub>. Then, during the “ball-on-disc” tests, the tested sample or the standard Si<sub>3</sub>N<sub>4</sub> ball could get heated to higher temperatures, because of the lack of lubricant, and this exhibits the high-temperature characteristics of the material.

## 10. Use of carbon nanotubes as reinforcement material

Recently, CNTs are considered for use as reinforcements in advanced composite materials in view of their high elastic modulus and strength compared to existing fibers. In that respect, being rolled up graphite sheets, their mechanical properties are expected to be equal to or greater than the value for a graphene sheet. Qualitative and quantitative TEM and AFM studies have been performed on individual tubes and have confirmed their superior strength and stiffness. The Young's modulus of a CNT is over 1 TPa and its estimated tensile strength is over 150 GPa, i.e. they are a hundred times stronger than steel, though three to five times lighter.

The properties of carbon nanotubes are a mix of diamond and graphite: strong, thermally conductive like diamond; electrically conductive like graphite; and are light and flexible. Many potential applications have been proposed for carbon nanotubes like: conductive polymers; energy storage and energy conversion devices; sensors; field emission displays; replacing silicon in microcircuits; multilevel chips; probes for SPM (scanning probe microscopy).

The objective of current investigations is to prepare, by sintering in the presence of liquid phase, a dense ceramic material based on SiC with sintering additives, with the addition of CNTs, resulting in a composite with high electrical conductivity, while maintaining its good mechanical properties.

### **10.1 Sintering in the presence of liquid phase**

This type of sintering is one of the used techniques to accelerate the process, while maintaining the mechanical properties of the material. The liquid phase is understood as an additive which is liquid at the sintering temperature. This liquid phase must fulfill two basic conditions: first, it has to drench all of the areas of the solid phase, and second, the sintered material has to have the liquid phase grains partly dissolved.

Sintering in the presence of liquid phase consists in three processes. First, we have the formation of the liquid phase and its flow, which causes changes in the spatial organization of the grains at the solid formation. This process is called relocation and it often leads to a sharp increase on the density of the sintered material. The relocation, which is due to the capillary forces of the liquid phase wetting the solid grains, is dependent on the amount of liquid phase, its viscosity, and the grain size and solubility of the solids in the liquid. The next and most important process for sintering in the presence of liquid phase is the process of increasing the density by dissolving the solid grains in the liquid phase and then the process of the subsequent elimination.

It is thus clear, that the melt should have the lowest possible viscosity at the sintering temperature and the highest possible at the application temperatures. These are conflicting requirements, and are very difficult to joint. The chemical composition of the phases at the grain boundaries is the subject of study of many authors, because grain boundaries have a significant effect on the mechanical and functional properties of the material.

### **10.2 Formation of the CNTs by CCVD**

The CNTs can be added by a method called catalytical chemical vapor deposition (CCVD), where tubular carbon nanofibers are formed on a support by a catalytical deposition of carbon out of the vapor phase. This method is characterized by a catalyst layer, which is deposited without current, and is applied to the support at least in places. Said catalyst layer is thermally activated before depositing carbon out of the vapor phase in a reducing atmosphere. Since it was discovered, that the elements of the iron group, Fe, Co and Ni, are catalytically active, these elements are used as catalytics.

## **11. Conclusion**

In the present paper are discussed issues of ceramic materials as basic elements of composite materials, which present advanced technical materials for a wide practical use. The attention was focused mainly on the causes of brittleness on ceramics and the possibilities of its

elimination. There were also discussed issues of composite materials based on ceramics considering their preparation and evaluation of selected properties. The results obtained extend the knowledge about the preparation of the above mentioned advanced materials with the addition of rare earth metals and their selected mechanical properties.

## 12. Acknowledgment

This paper was created in the project No Cz.1.05/2.1.00/01.0040 "Regional Materials Science and Technology Centre" within the frame of the operation programme "Research and Development for Innovations" financed by the Structural Funds and from the state budget of the Czech Republic. The authors gratefully acknowledge the Ministry of Education, Youth and Sports of the Czech Republic for the financial support of the project MSM 6198910013.

## 13. References

- Anstis, G.R., et al. (1981). A critical evaluation of indentation techniques for measuring fracture toughness: I direct crack measurements, *J.Am.Ceram.Soc.*, vol.64, No 9, pp.533-538
- Bolaños, A., E., Mores, M., Hrabalová, M., Jonšta, Z (2010): Vztah mikrostruktury a otěruvzdornosti nanokompozitu  $\text{Si}_3\text{N}_4/\text{SiC}$  s přidavkem oxidu vzácných zemin. *Zeszyty Naukowe Pol.Opolskiey, Mechanika*, z. 97, Nr 337/2010, red. Prazmowskiego, pp. 15-23. ISSN 1429-6055, Opole, Poland, October, 2010.
- Cook,R.F.,Pharr,G.M.: Direct observation and analysis of indentation cracking in glasses and ceramics. *J.Am. Ceram.Soc.*, 1990, 73, pp.787-817
- Evans, A.G., Marshall,D.B. (1981): Fundamentals of friction and wear of materials, ASME, 439-442.
- Jonšta, Z., Bolanos, A., E., Hrabalová, M. (2010): Influence Of Metallic Oxides of Rare earth on the Abrasion Resistance and Microstructure of  $\text{Si}_3\text{N}_4/\text{SiC}$  Nanocomposites. *Hutnické listy* č.6/2010, roč.LXIII, pp.72-76. ISSN 0018-8069
- Jonšta, Z. (1998): Vlastnosti technické keramiky a metody jejich hodnocení. Vyd.Kovosil, Ostrava
- Kumar, V., Khamba, J.S. (2006): Experimental investigation of ultrasonic machining of an alumina-based ceramic composite. *J.Am.Ceram.Soc.*, pp.2413-2417
- Liang, K.M., Orange, G., Fantozzi, G. (1990): *Jnl. Mat. Sci.*, 25, 207
- Marshall, D.B., Lawn, B.R.: Residual stress effecting sharp contact cracking. *Jnl. of Mat.Sci.*, 1979, 14, 8, pp.2001-2012
- Marshall, D.B., Lawn,B.R., Evans,A.G. (1982): *J.Am.Ceram.Soc.*, 65, pp.561-566
- Matzke, H. (1980): *Jnl. Mat. Sci.*, 15, 739
- Matzke, H., Toscono, E.H. (1990): Indent. Techniques, EUR-Rep. 12799 EN
- Matzke, H. (1991): *Key Engineering Materials*, 56-57, 365
- Pokluda, J., Kroupa, F., Obdržálek, L. (1994): Mechanické vlastnosti a struktura pevných látek. Vyd. PC-DIR spol. S r.o., Brno.
- Sglavo, V.M., Green, D.J. (1995): Subcritical growth of indentation median crack in soda-lime-silica glass. *J.Am.Ceram.Soc.*, 78, 3, pp.650-665

## **Part 3**

### **Topics in Degradation, Aging and Healing of Ceramic Materials**



# Considerations about Degradation of the Red Ceramic Material Manufactured with Granite Waste

Xavier Gustavo de Castro, Saboya Fernando,  
Maia Paulo Cesar de Almeida and Alexandre Jonas  
*State University of Norte Fluminense Darcy Ribeiro – UENF, Department of Civil  
Engineering, Campos, Rio de Janeiro  
Brazil*

## 1. Introduction

Ceramics are used as construction materials since the earliest days of civilization, around 5,000 B.C. Manufactured fired earth bricks had firstly been used as protection walls against invaders and fierce animals. However, during the industrial revolution on century XIX, the steam machines allowed a marked development of the ceramic industry.

The term “Ceramic” is originated from *Keramikos*”, which, in Greek, means fired raw material. The most important materials used in the composition of the red ceramic bodies are clayey soils. Chemically the clay mineral is composed basically by hydrous aluminum, iron and magnesium silicates, which can be dispersed in fine particles. Presence of impurities such as ferric oxides, quartz among others plays an important role on the characteristics of the final product.

Despite its great technological advances, some industries in the developing countries have not invested in high technology in order to manufacture bricks with high durability and acceptable mechanical properties.

Therefore, for the achievement of the better quality of the ceramic bricks and in accordance with the environmental appeal, some industrial by-products have been used in the raw material in ceramic industries.

In the case presented herein, by-products from decorative stone industry have been used aiming to improve the durability of the ceramic bricks as well as their mechanical properties.

In this particular perspective, the ceramic industry emerges as a great attractive to promote the use of industrial by-products. Moreover, the use of industrial by-products, as being granulated materials, does not affect the path normally followed during ceramic processing. As a secondary effect, but not less important, the insertion of industrial by-products can also help to save noble materials in the pit borrow, avoiding, thus, the increasing on the rate of exploration works.

## 2. Red ceramic materials

Red ceramic raw materials are generally taken from natural deposits of clayey soils composed by clay minerals and others organic and/or inorganic particles that are very

“reactive” in the presence of water. This property is known as plasticity, which is very dependent on chemical interaction among particles and the liquid, which percolates through the pores.

Most of ceramic materials are fragile and stiff, with very low tenacity. They have high fusion/sintering temperature and good chemical stability specially, in hostile environment, due to their strong chemical bonding between structural units.

### 2.1 Durability of the red ceramic materials

Despite its stable mechanical behavior, it is not rare to observe problems in ceramic bodies regarding its durability, i.e., strength against weathering.

This is commonly observed in artifacts that are fired at temperature below its sintering point. Cracks and weathering signs are well developed inside the ceramic body, with time, due to work done by external agents like temperature, humidity and insulation. The main problem found in construction materials regarding their durability are:

1. Deterioration in brick wall and tiles resulting in cracks and infiltration (Fig. 1);
2. Degradation of the first lines of masonry due to capillarity effect of sulphate water ( $\text{Na}_2\text{SO}_4$ ) (Fig. 1)
3. Rapid degradation due sudden changes in temperature (Fig. 2)
4. Quickly degradation in coastal environment resulting in complete deterioration of the ceramic brick (Fig. 4)
5. Mechanical and abrasive deterioration of the floor (Fig. 4)



Fig. 1. Fast degradation of masonry and tiles



Fig. 2. Fast degradation of masonry due to sulfate water and temperature change

White stain on masonry surface (effluorescence) appears as shown in Figure 3. This is consequential from a chemical process where the cement reacts with water resulting, thus, in a soluble binder, calcium hidroxile ( $\text{Ca}(\text{OH})_2$ ) that adheres on the ceramic brick. As long as the mortar layer contains cement and this layer has high porosity, the free calcium



hydroxile found in its composition reacts with air (carbonic anidre). This reaction between these two components results in calcium carbonate, non-soluble white salt, which leads to the expansion of the brick (Fig. 3).

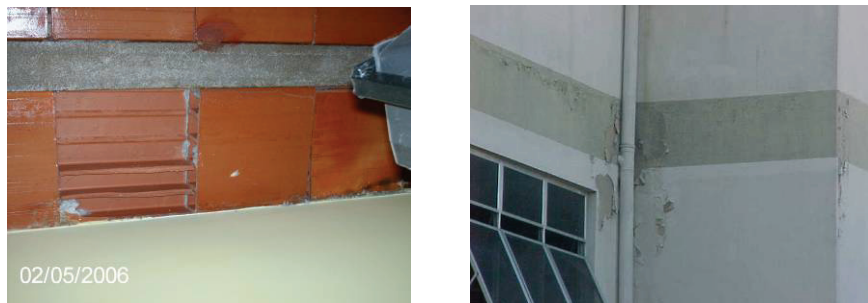


Fig. 3. Detachment of the floor brick and walls



Fig. 4. Fast degradation in masonry due to saline spray and abrasion

The process of degradation takes place when the body gets in contact with atmospheric conditions. Therefore, degradation can be understood as the effect of atmospheric agents on the ceramic bodies without crystallographic modification.

Alterability is defined as the susceptibility of a ceramic body to suffer degradation. Durability, on the other hand, means the capacity in keeping its structural stability, as well as the appearance with time. Therefore, alterability and durability will be closely dependent on the material and environmental characteristics and the exposure time, as well.

In tropical regions a wide range of temperature and humidity variation is commonly observed. The weathering agents that act directly on ceramic bodies are:

- Rain and air humidity
- Periodic insulation and drop of temperature in a short period of time, causing contraction and dilation, respectively.
- Air temperature favoring chemical reactions
- Wind and kinetic energy favoring abrasive deterioration.

Mechanisms that act on degradation process are the same as those that act on weathering. Dilation and contraction resulting from temperature and humidity changes can give rise to cracks that commonly leading the ceramic body to undermine.

Chemical agents can flow into these cracks and pores, reducing, thus, the bond between grains, making easier the erosion process and leaching the constituent materials. These transported constituents can induce the formation of new crystals resulting from chemical reactions, mainly when soluble salts are present in the mortar. When the air humidity

penetrates into the structure, these crystals are generally dissolved and carried to the surface, provoking thus, stains on the ceramic artifact. If these salts remain inside the ceramic body, they will re-crystallize causing expansion, favoring thus, degradation of the material.

These alterations can be very harmful in particular in coastal zones and industrial areas due to the saline sprays and acid rain, respectively.

The intensity of the effects of these degradation processes is closely dependent on the environmental conditions and also on the level of the thermal treatment specified to the ceramic material.

### 3. Characterization of the materials and evaluation of the alterability and durability of ceramic mass with addition of granite waste

This chapter presents the adopted methodology in order to evaluate the durability of ceramic bricks when granite waste by-product is incorporated in the raw material. Figure 5 shows the flow chart for complete characterization of the materials used in the confection of brick ceramic.

It is presented here the test sequence for the identification of the studied raw material: the clay mass and the granite by-product.

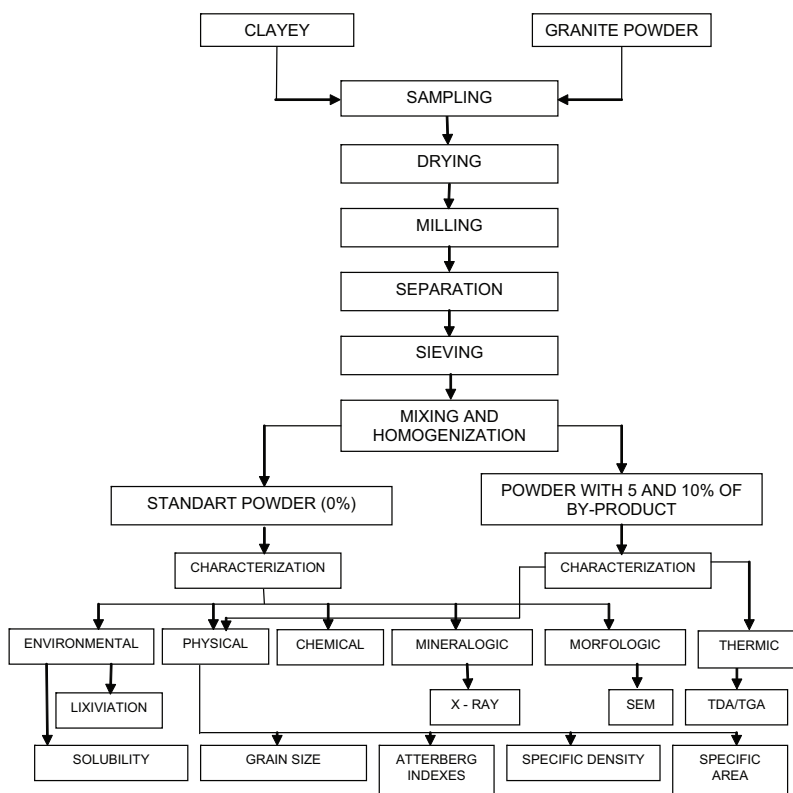


Fig. 5. Flow chart for complete characterization of the raw material with different content of granite powder

Further results and information can be reached in Saboya *et al* (2006), Xavier (2006), Xavier (2001) and Alexandre (2000).

### 3.1 Environmental characterization of the granite waste

The description of the results obtained from leaching test is shown in Table 1 and Table 2 where some results obtained from literature are shown in order to make the reader familiar with characteristic values and allow a direct comparison. Maximum allowed values for each chemical element are also presented aiming the classification of the material harmfulness.

Chemical Element	Waste Granite (mg/l)	Waste Silva (1998) (mg/l)	Waste Neves (2002) (mg/l)	Maximum limits (leaching test lab) NBR- 10005 (mg/l)
Ag	<0.005	< 0.010	<0.010	5.000
Cd	<0.002	< 0.010	<0.047	0.500
Cr	0.020	< 0.020	<0.010	5.000
Pb	0.030	< 0.050	2.120	5.000
Ba	0.110	1.160	N.S.	100.000

Legend: N.E.: Not Specified.

Table 1. Results of the leaching test and presented in literature

Condition test lab	Granite Waste (mg/l)	Waste (Silva,1998) (mg/l)	Waste (Neves, 2002) (mg/l)	Maximum limits (Leaching test in laboratory) NBR- 10005 (mg/l)
pH Begin	9.400	10.300	9.400	N.S.
pH final	5.150	6.500	5.500	N.S.
Vol. Acid (ml)	80	130	400	N.S.
Time (h)	28	28	28	N.S.

Legend: N.S.: Not Specified.

Table 2. Conditions of the leaching test

Evaluating the results obtained in the leaching test and comparing them with the maximum limits established by the norm ABNT 10004 (1987), it is observed that none of its chemical elements of the gross mass presented superior concentrations than permitted, being the sample considered non toxic.

The pH of the leached extract from the gross mass (Table 2) falls in the interval between 5.15 and 9.4, being, thus, characterized as not corrosive (ABNT 10004, 1987).

The results of the leaching tests together with the results obtained in the literature are shown in the Table 3.

Evaluating the results obtained in Table 3 and comparing them with the maximum limits established by the norm ABNT 10004 (1987), the chemical element Pb (lead) of the mass gross has presented concentration slightly superior to the established as the maximum limit. Therefore, the residue is classified as class II, not inert.

Chemical Element	Granite Waste (mg/l)	Granite Waste (Silva, 1998) (mg/l)	Granite Waste (Neves, 2002) (mg/l)	Maximum limits solubilized NBR - 10.004 (mg/l)
Ag	<0.005	<0.010	0.070	0.050
Cd	<0.002	<0.001	<0.001	0.005
Cr	<0.020	<0.020	<0.001	0.050
Pb	<0.060	<0.050	0.001	0.050
Ba	<0.020	0.120	0.230	1.000
Al	0.150	1.080	2.990	0.200
Cu	<0.010	<0.010	<0.040	1.000
Fe	0.030	0.4000	0.010	0.300
Mn	<0.010	<0.010	<0.010	0.100
Zn	<0.003	<0.010	0.005	5.000
Na	33.800	134.000	24.000	200.000
NaCl	9.440	78.000	35.500	250.00
Ca <sup>+</sup>	19.900	3.700	19.000	500.000
Sulfate	11.170	<10.000	44.000	400.000

Table 3. Results of the leaching test and some values reported in literature

The results obtained in this work are similar to those obtained by Silva (1998) and Neves (2002), which can be conclude that the granite waste is a non toxicant material, not corrosive, not inert of class II.

### 3.2 Chemical characterization

Following, the Table 4 depicts semi-quantitative chemical compositions of the standard clayey raw material granite waste.

Raw Materials	L.O.I. (%)	SiO <sub>2</sub> (%)	Al <sub>2</sub> O <sub>3</sub> (%)	Fe <sub>2</sub> O <sub>3</sub> (%)	CaO (%)	MgO (%)	Na <sub>2</sub> O (%)	K <sub>2</sub> O (%)	TiO <sub>2</sub> (%)
Clay	15.40	42.30	32.00	6.87	0.20	0.70	0.04	0.94	1.24
Granite Waste	1.55	69.20	14.60	3.49	3.21	0.032	3.13	4.49	0.16

Table 4. Chemical Components of the clayey and granite waste materials

Observing the values obtained in Table 4, it is verified that for the standard clay sample, the amount of SiO<sub>2</sub> (42.3%) indicates the probable presence of kaolinite (Al<sub>2</sub>O<sub>3</sub> · 2SiO<sub>2</sub> · 2H<sub>2</sub>O) and illite, as well as the probable presence of free quartz in the total sample. The amount of Al<sub>2</sub>O<sub>3</sub> (32.0%) almost totally is responsible for forming clay minerals, but it can also be credited to the presence of hydroxides as gibbsite (Al(OH)<sub>3</sub>). The total value of 64.3% (SiO<sub>2</sub> + Al<sub>2</sub>O<sub>3</sub>) indicates the refractory character of the raw material.

The high amount of coloring oxide Fe<sub>2</sub>O<sub>3</sub> (6.87%) characterizes it as fondant agent and also indicates the prone for the red color achieved after burning. It can also indicate the goethite presence (FeO.OH). The oxides of calcium and magnesium (CaO + MgO) corresponds a

total of 1%. They are fondant agents and, as consequence, they lower the refractory properties of the clay. The presence of alkalis ( $\text{Na}_2\text{O} + \text{K}_2\text{O}$ ) in the amount of 0.98% indicates also fondants forming liquid phase during firing, reducing, thus, the porosities of the material.

The coloring oxide  $\text{Ti}_2\text{O}$  in the amount of 1.24% can be credited due to the presence of rutile or anatase (Toledo, 2003) and it contributes to the yellow color of the raw material. The loss of ignition (LOI) of 15.40% indicates the loss of free, adsorbed and constitution water of the raw material and, also, the degradation of the organic content of the sample.

It is noticed in the chemical analysis carried out on granite waste, that the amount of silica is higher than 69% and the amount of  $\text{Al}_2\text{O}_3$  can reach values higher than 14%, indicating chemical compositions of primary minerals (quartz, feldspar and minerals of the group of the mica). The traces of  $\text{CaO}$  (3.21%) and  $\text{Fe}_2\text{O}_3$  (3.49%) come mainly from the whitewash and from the metallic particle used as lubricant and abrasive, respectively.

The oxides of sodium and of potassium ( $\text{Na}_2\text{O} + \text{K}_2\text{O}$ ) in the amount of 7.62% presented by the by-product, are almost totally originated from the feldspar and mica and they are considered as fondant agents that could fill the voids. The loss of ignition (LOI) of 1.55% of the by-product is considered small indicating structural stability of the waste. However, this loss can also be credited to the degradation of the mica.

Comparison the results of the chemical analysis shown on Table 4 between the standard clay mass and that of red ceramic reported by Souza Santos (1989), Alexandre (2000) and Vieira (2001), there is a clear indication that this material is quite suitable to be used in the Brazilian industry of red ceramic.

In the same way, comparison the results of the chemical analysis shown in Table 4 for the granite waste with the chemical analyses for granite waste carried out by Neves (2002), Mothé Filho (2003) and Vieira *et al.* (2003), it can be shown that the incorporation of the by-product in ceramic mass can be used in the process of production of red ceramic goods without any special measure.

### 3.3 Thermal characterization from Differential Thermal Analysis

Observing the thermal curves of the ceramic mass and the mass with addition of waste with 5R (5%) and 10R (10%) in Figure 6, it can be detached, for each curve, two endothermic events of medium intensity very close to each other.

In this figure it is verified that the clay samples 0R, 5R and 10R present endothermic events of medium intensity between 258,50°C and 260,90°C, indicating a shift to the left of the peak values (in relation to the sample 0R) due to the presence of waste in the ceramic mass. These peaks are mainly due to the loss of  $\text{OH}^-$  of the hydroxides of aluminum ( $\text{Al}(\text{OH})_3$ ) and iron ( $\text{FeO}(\text{OH})$ ) probably credited by the presence of gibbsite and goethite.

There are also endothermic events of medium intensity between 448.50°C and 499.84°C due to the beginning of the reaction of loss of hydroxyls of the kaolinite creating, thus, an amorphous phase (metakaolinite). Endothermic bands are observed starting from 900°C. It could indicate the transformation of the metakaolinite ( $\text{Al}_2\text{O}_3 \cdot 2\text{SiO}_2 \cdot \text{H}_2\text{O}$ ) amorphous in spinally ( $2\text{Al}_2\text{O}_3 \cdot 3\text{SiO}_2$ ) forming a stable crystalline structure.

The corresponding curve of the granite waste in the Figure 6 shows an endodermic event of small intensity for 570°C, indicating the transformation of the quartz for generating expansion. At 663.18°C an endothermic peak of small intensity corresponding to the beginning of loss of  $\text{OH}^-$  of the mica is verified in the sample.

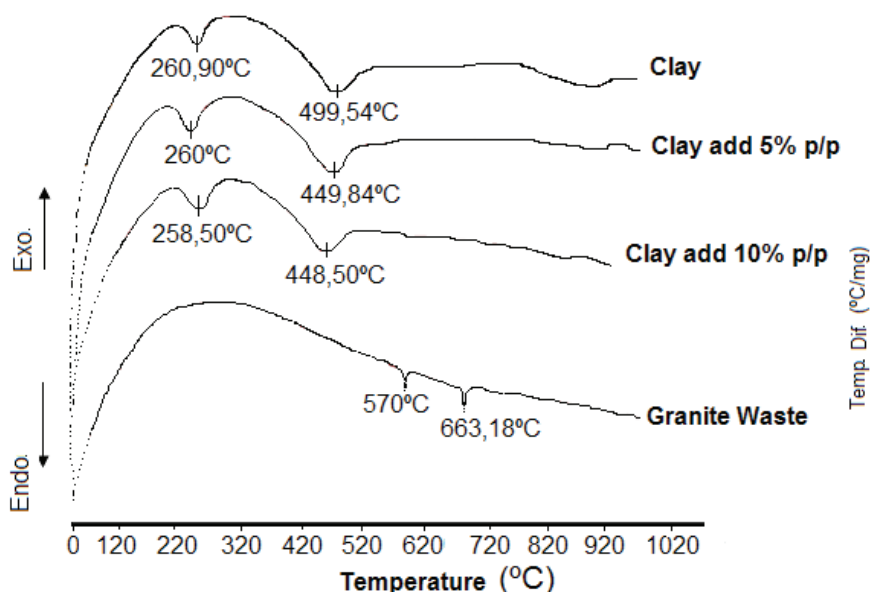


Fig. 6. Curves of the Thermal Analysis Differential (ATD) of the ceramic samples 0R, 5R and 10R

#### 4. Experimental program for natural and accelerated degradation of samples 0R, 5R and 10R

The condition of alteration of a ceramic piece depends primarily on their physical-chemical, mechanic properties and also on the characteristics that are correlated with the time of alteration. Another important features is the degradation potential caused by the aggression of the environment, affecting the durability of the material, especially, the red ceramic in tropical countries.

For the evaluation of durability of the red ceramic materials incorporated with granite waste in the proportions of 0%, 5% and 10% known herein as 0R, 5R and 10R respectively, fired at temperatures of 500°C, 700°C and 900°C, it was used the methodology presented in the Figure 7, in the form of illustrative organization chart.

For the evaluation of the changes experienced by the red ceramic materials, it should be considered the following aspects (adapted from Maia, 2001):

- The characteristic of the change processes of the ceramic material used in the civil construction;
- The methodology adopted for the evaluation of the technological properties after alteration tests carried out in laboratory and in the field;
- The representatively of the considered intact and naturally altered samples,
- Correlation of the properties with the time of natural alteration, for the prediction of the potential of the damage caused by this alteration, i.e., long time prediction.

To evaluate the changes in the red ceramic materials it should identify the mechanisms that influence the natural alteration, whose processes of the evolution of the degradation are visually accompanied.

For the determination of the characteristics of the alteration of the red ceramic pieces incorporated with granite residue in the field and in the laboratory in an induced and accelerated way, it was used some procedures considered essential, as follows:

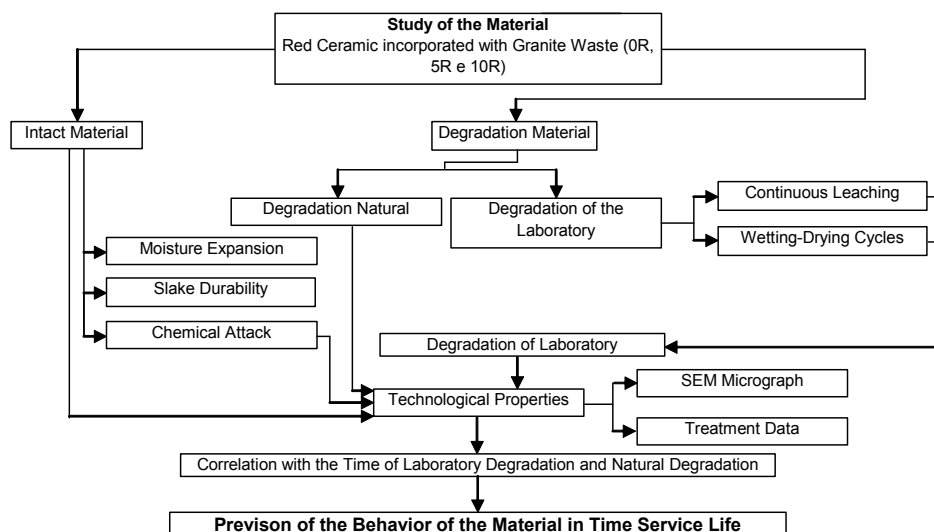


Fig. 7. Methodology for evaluation of the degradation of red ceramic samples incorporated with 0R, 5R and 10R of granite waste

#### 4.1 Test of continuous leaching in laboratory

This particular laboratory test is considered to mimic the climatic conditions that degrade the red ceramic artifacts. When it is intended to determine the state of alteration of a rock or other natural material, the extractor Soxhlet is most suitable because the samples are submitted to leaching in distilled hot and cold water. The extractor Soxhlet allows the samples to be submitted to temperature variation in controlled periods of precipitation and water level variation.

Farjallat (1971) used the extractor Soxhlet to evaluate changes in rocks specimens using correlation with Los Angeles abrasion test.

After associating the characteristics of the rock with the quality indexes, this author compared these characteristics in different alteration stages. The quality indexes are applied in the specific quantification of measurable properties as strength, porosity, water absorption and others (Maia, 2001).

Maia (2001) has used an extractor Soxhlet of great dimensions to evaluate the alteration of rocks used in rockfill. Based on this author's work, it was manufactured in LECIV/CCT/UENF in Campos/RJ a degradation equipment (Figure 8) similar to that extractor Soxhlet.

The Equipment of Degradation developed at LECIV was designed to make possible to control periods of temperature variation and of precipitation of the solution. Distilled water is used as leaching solution. During the leaching, this solution can be monitored and, if necessary, changed.

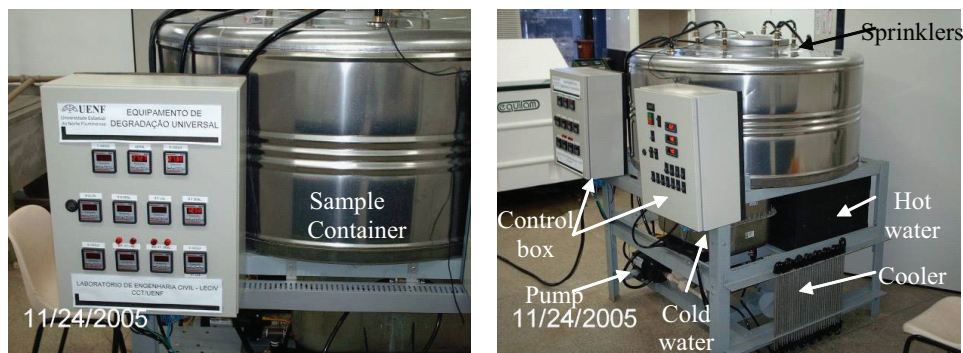


Fig. 8. LECIV/CCT/UENF Laboratory Degradation Equipment

Inside the tank, samples are subjected to environment similar to atmospheric conditions, where the material is placed on shelves of stainless-steel and submitted the temperature variations. At the same time, the samples are washed periodically with hot and cold water, simulating the natural precipitation. The wash is made by the leaching solution, coming from the pumps of hot or cold water that goes through the sprinkles placed at the top of the tank creating a saturated vapor atmosphere (this phase is only when there is the circulation of hot water).

The vapor condensation also takes place when the cycle of hot water is in operation. The equipment was programmed to work for 1 hour for each cycle of hot or cold water, meaning that when the leaching for hot water is in operation, the cold water system keeps turned off. During the cycle (hot or cold water), the water is pumped every each 15 minutes.

The hot water is controlled to be kept at approximately 70°C and the cold water around 35°C. The time periods of 300 hours, 658 hours and 1500 hours were used to submit to the samples to this complete process. The equipment possesses an electronic system of operation (I-square of command) which ignores manual control of the time and water cycles.

It also allows the verification of the temperature of the hot and cold water and the tank of samples as well (Figure 9). To avoiding shortage of water in the system, a device of production of distilled water is connected directly to a column of water. It is linked to the equipment and it monitors the level of the water tanks by means a level buoy, renewing the solution constantly allowing monitoring the pH of the solution.

To guarantee the required temperature of the cold water, it was installed a cooling system that starts operation when it reaches a pre-established temperature. The pumping system is constituted of three pumps. The 1st and 2nd are responsible for the suction and hot and cold water pressure toward the sample tank. The third pump, besides the cold water suction, direct it to the coolers and is also responsible to guide the water back to the cold water tank.

The pump of hot water possesses a system to support high temperatures. The tanks of hot and cold water possess a capacity of approximately 200 liters (each) and the container of samples possess 500 liters of volumetric capacity. The equipment is constantly monitored by a computer and by a camera installed in the laboratory to notice possible defects during the night and weekends when the same is in operation.

Curves shown in Figure 9 depict the temperature balance inside the sample tank (500 liters) and also the temperature balance inside the hot and cold water tanks. It can be noticed that



at around 100 minutes from the beginning of the operation the balance is reached. This means that the electronic circuits work with synchrony and precision and that the samples are always under the same conditions inside the equipment.

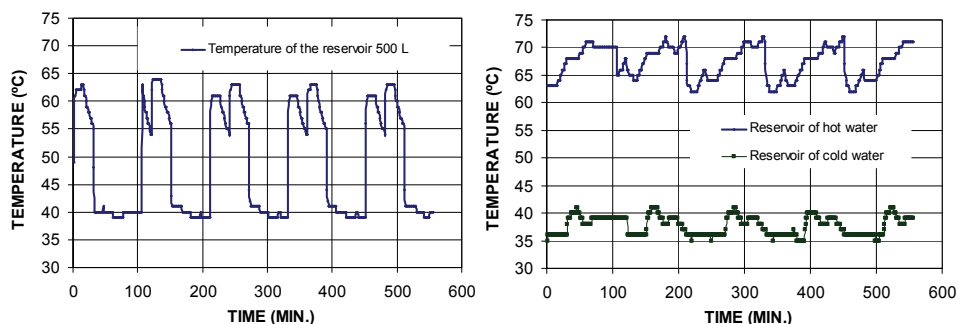


Fig. 9. Temperature of the sample container, hot and cold water tanks with time

In the change of cycle of hot and cold water inside of the samples tank, it is noticed the continuous fall in temperature, simulating in an accelerated way the climatic conditions of temperature variation between the days and the nights, provoking dilation and retraction in the samples due to thermal gradients.

#### 4.2 Laboratory test of wetting and drying cycles

This particular test intends to simulate, in laboratory, the aggression suffered by the ceramic when subject to environmental natural conditions. It is known that the laboratory conditions are not the same that of the field. However, the results can be somewhat representative (Maia, 2001; Cunha, 2006).



Fig. 10. Laboratory tank for wetting and drying cycling test

The washing water was monitored periodically every 15 days through pH meter aiming to assure keeping the solution as basic acid. The environment temperature inside the room

was controlled to keep it about  $21 \pm 1^\circ\text{C}$  and relative humidity of the about  $64 \pm 5\%$ . Cycling was composed of 50 and 150 cycles, representing respectively 1.200 hours and 3.600 hours of soaking and drying steps.

#### 4.2.1 Field natural degradation

This procedure has as the objective comparison of the degradation accelerated in laboratory to the alteration of the material under local environmental conditions. Samples were exposed to periods of 6, 8 and 10 months where variables like air temperature, relative humidity, wind speed, precipitation and the solar radiation, were recorded.

The natural degradation of the samples was carried out at the Campus of the State University of the Norte Fluminense Darcy Ribeiro - UENF, Campos of Goytacazes/RJ, with latitude of  $21^\circ 45'$  South, longitude of  $41^\circ 18'$  West and altitude of 11 m. This kind of degradation is used for the long time prediction which will serve as a base to obtain the information about the effects of the degradation of a specific material (Cunha, 2006).

The samples were fastened in a special support made of wood placed on the roof of a UENF building, according to the Illustration 11. It was placed in such way to guarantee ideal incidence and absorption of solar radiation, facilitating, thus, the effective degradation process during the research period. The supports for samples were designed to guarantee free air circulation.



Fig. 11. Samples on terrace exposed on the roof directed to the best insulation direction according to the local coordinates

The climatic conditions define the processes of degradation of ceramic materials exposed to the environment. It is naturally believed that those ceramics material that have been under more severe conditions of temperature variation and humidity are more susceptible to damage.

### 5. Evaluation of the alterability and durability of incorporated red ceramic pieces with granite waste

#### 5.1 Technological properties of the intact material

The curves related to the technological properties of the standard clay for 0R, 5R and 10R after firing are presented. These curves were obtained from laboratory tests carried out on

the so-called intact samples. These curves considered as standard are compared to the results obtained from laboratory and natural degradation process.

Figure 12 presents the curves corresponding of the mean results of five determinations of the technological properties after firing. Results of the diametrical compression test are presented in Table 1.

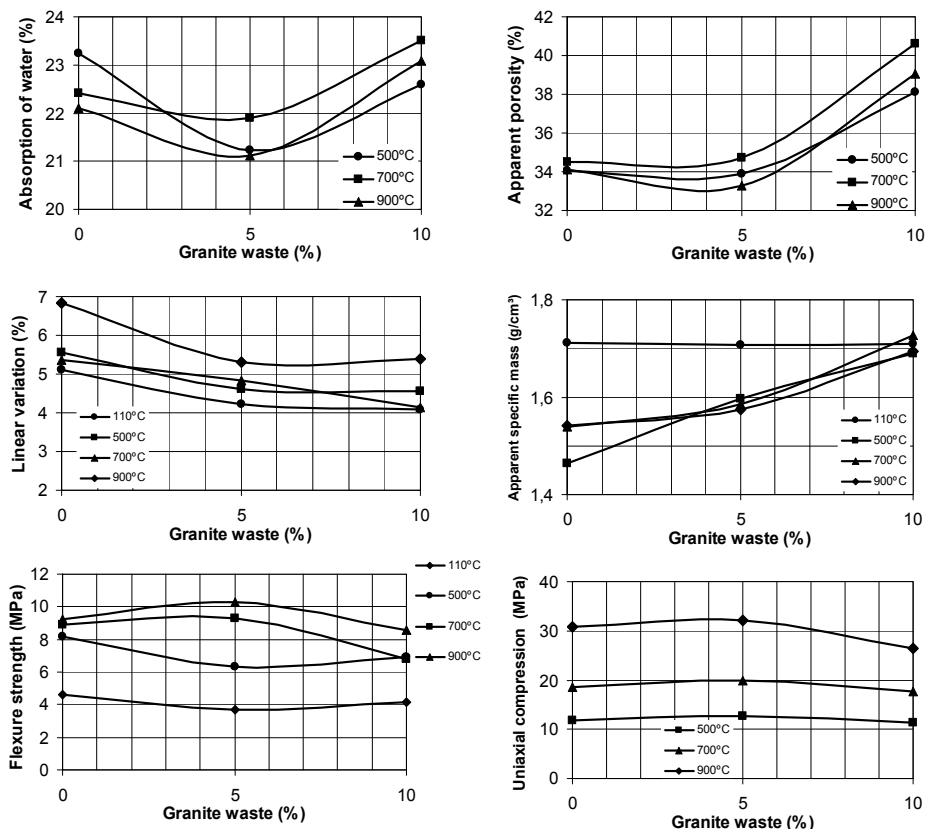


Fig. 12. Technological Properties of the samples 0R, 5R and 10R after firing

Values of the Diametrical compression (MPa) of the intact samples						
Temp. (°C)	Mix (%)					
	0R	$\sigma$ (SD)	5R	$\sigma$ (SD)	10R	$\sigma$ (SD.)
500	1.06	$\pm 0.5$	1.99	$\pm 0.03$	0.60	$\pm 0.09$
700	1.69	$\pm 0.01$	0.85	$\pm 0.10$	1.97	$\pm 0.62$
900	1.74	$\pm 0.16$	1.21	$\pm 0.20$	3.02	$\pm 0.12$

Table 5. Values of the diametrical test on so-called intact samples

The Figure 12 also shows the tendency of the absorption of water and apparent porosities of the samples 0R, 5R and 10R after firing. It is observed that the results indicate reductions in the mean values when added 5R in the sample for all firing temperatures, however, for 700°C and 900°C this effect is accentuated indicated by smaller peak.

This behavior is closely linked to the formation of liquid phase during the thermal treatment due to presence of alkaline ( $\text{Na}_2\text{O}+\text{K}_2\text{O}>7\%$ ) and earthy alkaline ( $\text{CaO}+\text{MgO}>3\%$ ), according to the Table 4, provoking, thus, a reduction in the mean values of the absorption of water and apparent porosities, as expected.

In this case, the amount of 5% of granite waste can be used in massive bricks and ceramic blocks because of the obtained absorption lower than 25% (ABC, 2000). This represents the formation of rigid vitreous phase during cooling filling voids of the ceramic pieces.

In general, it is observed a new increase in the curves starting from the addition of 10R, revealed by the higher values of absorption of water and porosities. Extrapolating the mean values, it seems that when the amount of waste is increased, the water absorption is also increased, which means that it may not be attractive for practical use.

However, the curves of the open porosities of the green samples converge for very close values (between 33 and 35%), showing that when rising the temperature, it does not provoke significant densification of the pieces, being close to that range shown for values of open porosities.

It is observed in the Figure 12(c), that the linear retraction of the ceramic mass with 5R at 900°C, presents tendency of stabilization, being the largest values found for the samples with 0R. As expected, the higher the firing temperature, the higher the sample retraction is.

The Figure 12(d) indicates a tendency of increase of the apparent specific mass with the increase of the waste percentage, independently of the firing temperature. That increasing tendency can be justified for the granolas presence in the waste.

The convergence of the mean points for the samples is verified with 5R of addition, characterizing the densification of the ceramic pieces (Figure 12d). It is observed in the Figure 12(b) the same convergence tendency in the curves for open porosities. The tendency of these curves is to show opposite behavior, because when the open porosities are reduced the volumetric density is increased.

In Figure 12(e) and (f) it is noticed higher values for the curves of simple compression and flexural strength for sample 5R, regardless the firing temperature. The differences obtained from both tests are solely in the failure stress level. Higher mechanical strengths are achieved for sample 5R fired at 900°C.

When the thermal curves (Figure 6) are observed, it can be observed transformations in the solid state of the particles increasing, thus, stiffness and strength of ceramic bodies. Consequently, the increase of the mechanical strength with the increase of the firing temperature is independent of the addition waste amount (Figure 12e).

It is noticed that when passing from 0R to 5R of addition of granite waste for samples fired above 700°C, the strength increases considerably, which indicates that the addition of 5R for process of ceramic production can be a very acceptable value.

Observing the Table 5, it is noticed that the results of the diametrical compression strength for standard clay, show themselves varied and dispersed when compared to those obtained for incorporated samples which also depend on firing temperature, indicating that this test cannot bet conclusive, not being indicated to evaluate the material behavior. This can be explained by the presence of cracks randomly distributed in all samples provoked by air drying process.

## 5.2 Technological properties of the natural and accelerated altered material

### 5.2.1 Physical properties: Water Absorption (WA) and Apparent Porosity (AP)

Figures 13 and 14 present the variations of the absorption of water and apparent porosities with the time for both natural and laboratory degradation of the samples fired at temperatures of 500°C, 700°C and 900°C and with 0, 5 and 10% of waste content in the ceramic mass. It should be stood out that the absorption of water and apparent porosities are inter-correlated properties, presenting the same pattern of variation of the degradation.

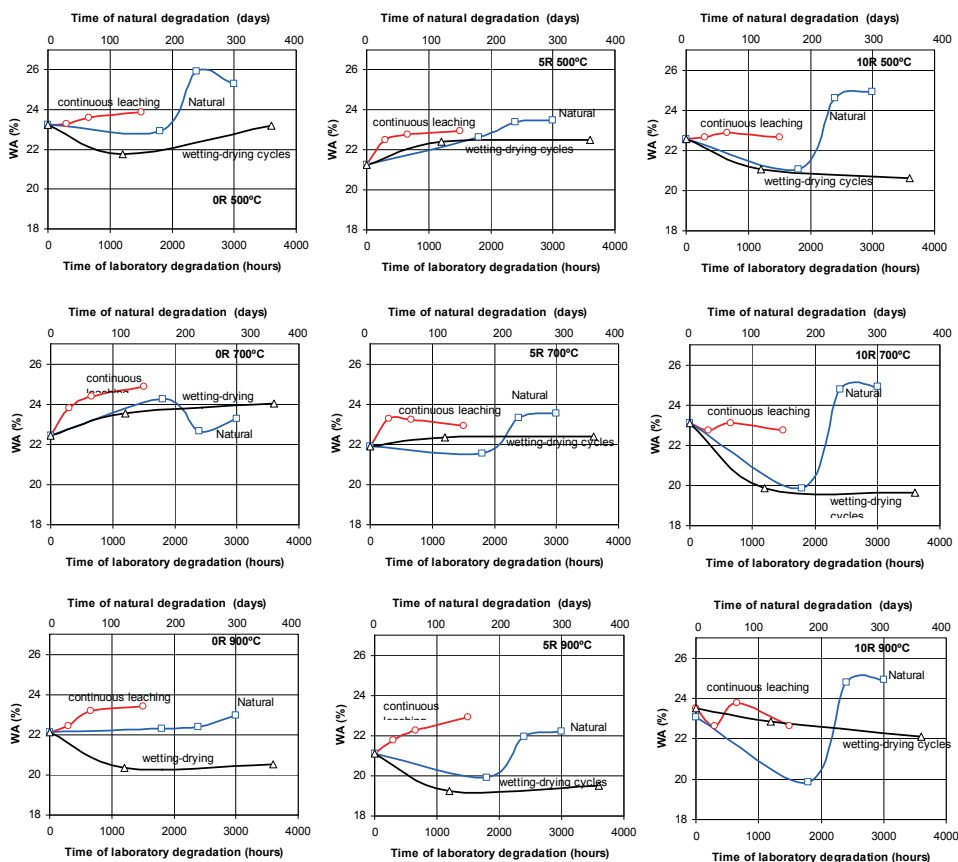


Fig. 13. Effect of the degradation type in the absorption of water for the samples with addition of granite waste for firing temperatures of 500°C, 700°C and 900°C

The variation in the magnitude of the absorption of water with the degradation time observed in the Figure 13 is, in general, not much affected by the firing temperature. It is noticed in the last alteration stages a variation of the absorption of water about 2% in relation to that of intact material. Variations of the order of 3% were noticed in the naturally degraded material with 10R.

It is observed in Figure 14 that the variation of the range of the apparent porosities with the time of degradation was not very much affected by the firing temperature. It is also observed in the last alteration stages, a variation of the open porosities about 4% in relation to that of intact material. Variations of the order of 5% were noticed in the naturally degraded material with 10R.

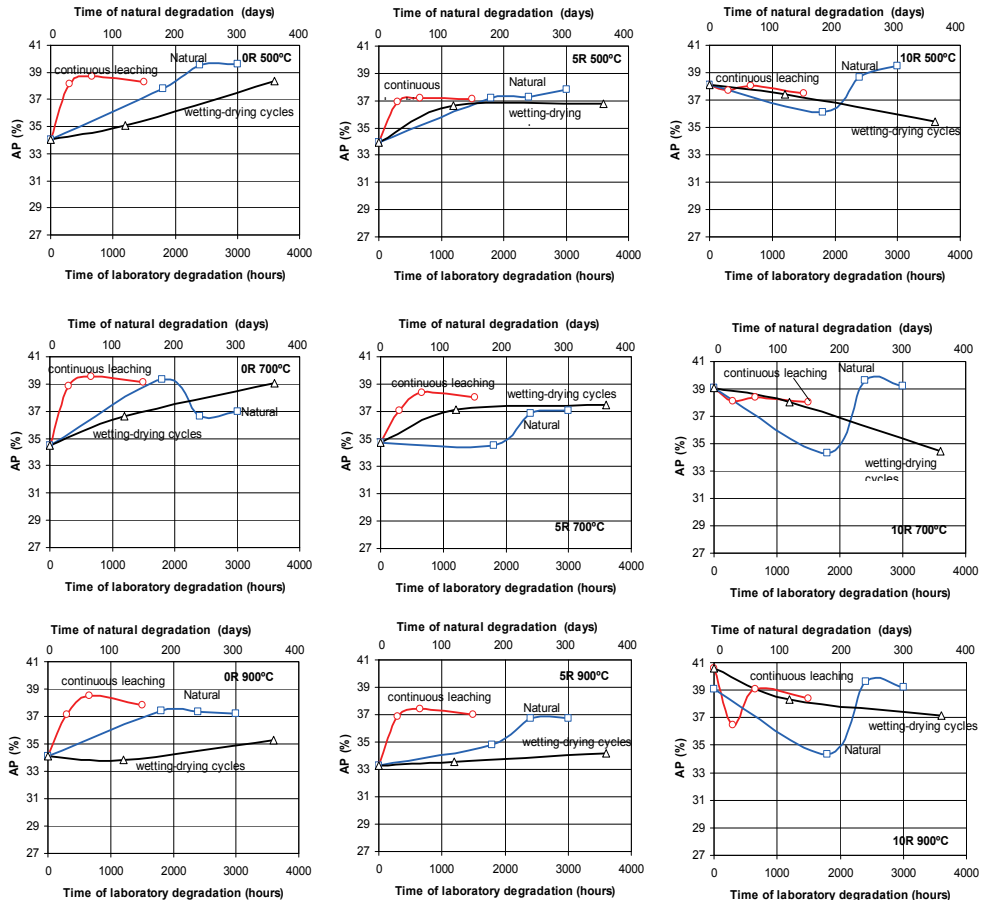


Fig. 14. Effect of the degradation type in the apparent porosities for samples with granite waste for firing temperatures of 500°C, 700°C and 900°C

### 5.2.1.1 Continuous leaching

For the leaching conditions also shown in Figures 13 and 14, the largest effect of the degradation was noticed in the samples with 0R at 700°C, which can evidence the loss of cohesion among particles due to the increase of the water absorption.

In the samples fired at 900°C under continuous leaching, the variation of the absorption of water is small due to the great influence of vitreous phase and larger changes in the present

crystalline phases of the samples maintaining it, therefore, more resistant against leaching effects. It should be stood out that the elevation of the firing temperature is also responsible for the densification of the ceramic material due to the fondant properties of some existing oxides.

The vitreous phase is characterized by the presence of alkaline ( $\text{Na}_2\text{O} + \text{K}_2\text{O}$ ) and earthy alkaline ( $\text{CaO} + \text{MgO}$ ), that are fondant oxides, mainly when granite waste is added, as observed in the Table 4. When the temperature increases, a eutectic formation takes place. During cooling a plug partially or totally seals the pores, making difficult the effect of the continuous percolation of distilled water through voids of the ceramic sample.

The results of the apparent porosities are similar to the absorption of water for the inter-correlation among these properties. In general, the increments of open porosities observed in all cases provoked by the field and laboratory degradation facilitates the displacement of the particles welded by firing before submitting them to the continuous leaching. It has been observed reductions on the values obtained in the samples with 10R.

Open porosity decreasing in these samples reflects on the reduction of the absorption of water of the ceramic piece, when compared to the intact samples. This is accredited to the presence of the  $\text{CaO}$  and  $\text{MgO}$  (Table 4) in the granite waste, corroborating, thus, for plugging openings.

The largest increments of the porosities opened after the continuous leaching, were observed in the samples with 0R in all range of the thermal treatment. That indicates the susceptibilities of the samples to the degradation conditions imposed by the laboratory tests and calls for the attention for the suitability of waste use, aiming to assess more durability of red ceramic goods.

#### 5.2.1.2 Cycles of drying and wetting

It is verified in the Figures of 13 and 14 that the values of the water absorption are similar to those of open porosity for 0R, 5R and 10R, as expected. It can be noticed in the curves of 500°C after 50 cycles a quite similar behavior of that observed for 150 cycles with reductions of the water absorption. The samples 5R at 500°C depict significant increase in water absorption for 50 (and after) cycles.

On the other hand, the curves of the samples fired at 900°C have shown reduction in water absorption after 50 and 150 cycles when compared to those values of the intact samples. This can be credited to the severity of the tests in laboratory, mainly if the stove is used to dry samples causing increase in volumetric density, as shown later.

The largest effect of the degradation given by larger water absorption was noticed for the samples with 0R at 700°C in all conditions of wetting and drying cycles due to the loss of mass induced by these cycles which favors the cohesion reduction among particles.

The samples fired at 900°C show the reduction of the water absorption after cycling, due to the great influence of the vitreous phase and also due to the crystalline phases presented in the sample at this temperature, increasing, thus, the volumetric density as a result of pore plugging.

The tendency of increasing the open porosity is verified for 50 wetting-drying cycles for sample 5R. On the other hand, small reductions are observed for the samples 10R under same conditions. This applies for all firing temperature.

After 150 wetting-drying cycles, the sample 10R has its porosity reduced for all tested firing temperature.

The open porosity values after degradation tests for each waste addition (0R, 5R and 10R), suffered alteration in the wetting-drying cycles. The samples 0R and 10R presented higher increase in porosity, and the samples 5R did not show any change in their initial porosity.

### 5.2.1.3 Natural alteration (Field)

The Figures 13 and 14 show that after 8 and 10 months of field alteration the values of the absorption of water and apparent porosities are quite similar. The values for the samples molded with standard clay at 500°C after 6 months of natural degradation, are kept unchanged. For samples 5R Increasing in water absorption can be observed. On the other hand, for samples 10R this values decreases.

The largest variation took place for samples 0R after 8 months of natural degradation. However, the samples 10R tend to converge to the same point of water absorption, slightly below 25% after 8 months. For these same samples, after 10 months of natural degradation, the mean values of water absorption rise above 25%.

The smallest values are still observed for samples 5R for all firing temperatures, revealing, thus, their stability against natural degradation. The samples 0R are more inclined to suffer natural degradation as a consequence of high values of water absorption.

It is also noticed the similarity between natural degradation and wetting-drying cycles test regarding water absorption values obtained for the two groups. These results indicate that 6 months of natural degradation can be replicated by around 50 to 150 wetting and drying cycles, revealing that such laboratory test may, somehow, represent field effects acting on degradation process.

The largest variation of open porosity is shown for samples 0R after 8 months of natural degradation. Samples 10R, after 8 months of natural degradation, tend to converge to the same values of open porosity at values slightly below 40%, staying stable after further 10 months of natural degradation.

The smallest value of apparent porosities is observed in the samples with 10R to 900°C, revealing the stability to the natural degradation of the samples with addition of waste.

## 5.2.2 Mechanical properties

### 5.2.2.1 Index of Flexural Strength (FS)

Variation of the index of the Flexural strength ( $I_{FS}$ ) with time for natural and laboratory degradation is shown in Figure 15.

This index expresses a correlation between a given material property for both intact and degraded states. The index  $I_{FS}$  which uses the flexural strength (FS) to define de degradation index is defined as follows:

$$I_{FS} = \left( \frac{ES_D - ES_I}{ES_D} \right) \times 100$$

Where, subscripts "D" and "I" mean "degraded" and intact, respectively.

It can be observed that the tendency of the curve of the index Flexural strength ( $I_{Flexure\ Strength}$  (%)) with firing temperature follows the same pattern regardless the kind of degradation. These curves present similar pattern of those obtained for water absorption and open



porosity, as expected. This indicates that the firing temperature has little or no influence on  $I_{FS}$ .

The variation of the  $I_{FS}$  with degradation time is significantly affected by the degradation process regardless the firing temperature and waste content, as well.

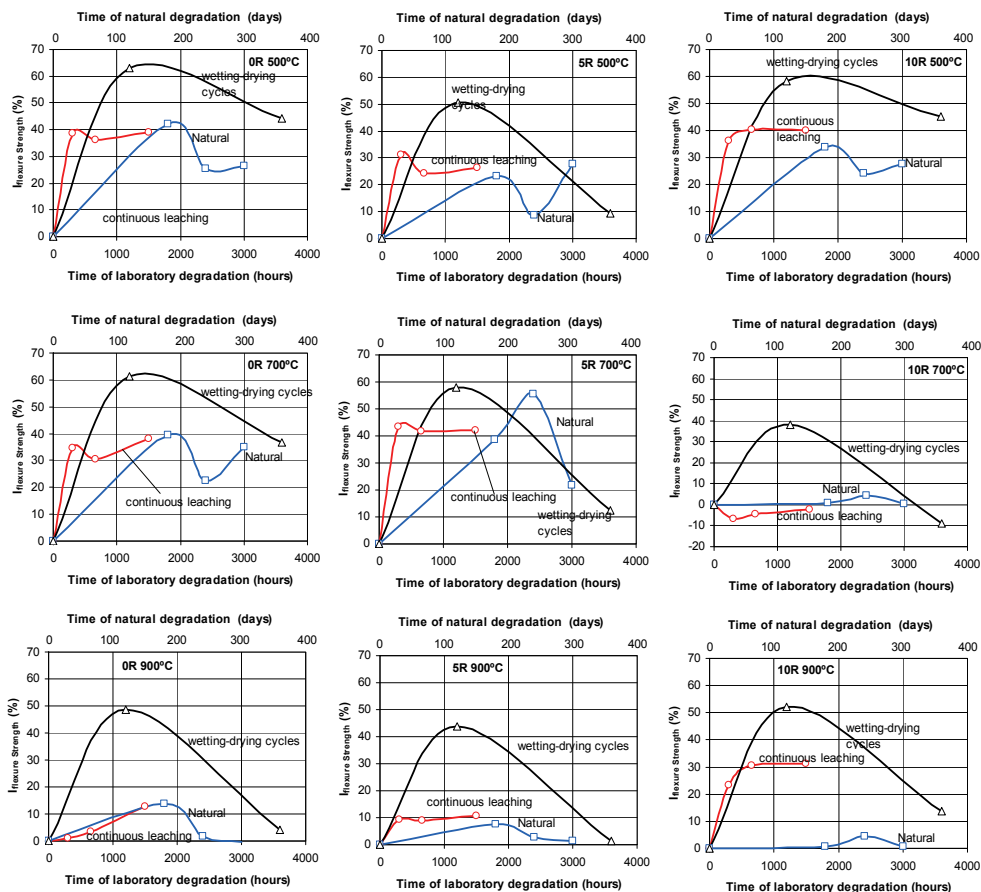


Fig. 15. Effects of the degradation process in the index of FS for samples with addition of granite waste fired at temperatures of 500°C, 700°C and 900°C

#### 5.2.2.2 Continuous leaching

The effect of the reduction of mechanical strength of the ceramic pieces after the continuous leaching is shown in Figure 15. It can be observed that this reduction on mechanical strength is accentuated at 500°C and 700°C, which can be explained by the low firing temperatures that are suitable for promoting coalescences among particles.

Flexural strength is reduced with leaching time for those standard clay samples (without waste content) when fired at 900°C, (300 hours). After 1500 hours of leaching, samples with

waste content (5R and 10R) did not show any loss of strength which indicates that the granite waste content is a very suitable mechanical stabilizer.

In the leaching test, the samples are submitted to the cycles of hot ( $\approx 70^{\circ}\text{C}$ ) and cold water ( $\approx 35^{\circ}\text{C}$ ). These conditions intend to simulate the temperature variations and humidity of the environment and can be efficient when it is compared to those results from natural degradation.

#### 5.2.2.3 Wetting – drying cycles

The loss of mechanical strength is verified for the samples after 50 cycles. For 150 cycles there is a significant gain of strength of  $I_{FS}$ . The samples 5R show higher mechanical strength, once they present smaller strength indexes for all firing temperature.

Some degradation mechanisms may occur contributing for the increase of the  $I_{FS}$ : Formation of new clay minerals, restructuring, suction, arrangement of glass phase and pores clogging. It is believed that, amongst these mechanisms involved in this process, suction and pores clogging are most presented.

#### 5.2.2.4 Field or natural degradation

The Figure 15 depicts the values of  $I_{FS}$  for the samples 0R, 5R and 10R for firing temperatures of  $500^{\circ}\text{C}$  to  $900^{\circ}\text{C}$ . It is observed that the samples, in these conditions, show higher increase in  $I_{FS}$  after 6 months of natural degradation. After 8 months of natural degradation, the  $I_{FS}$  decreases slightly and are kept stabilized thereafter, except sample 5R which shows increase in  $I_{FS}$  after 10 months of leaching.

No significant degradation is verified for samples fired at  $900^{\circ}\text{C}$  for all waste content. This suggests high cohesion amongst the flat particles guaranteeing, thus, larger mechanical strength under the natural degradation. For samples 5R higher strength are obtained, showing, thus, that the firing temperature of  $900^{\circ}\text{C}$  or higher is suitable when waste is used.

### 6. Scanning electronic microscopy of the intact and degraded samples

For the evaluation of the surface morphology and texture of the intact and degraded samples, the Scanning Electronic Microscopy (SEM) was used. Images of the ceramic samples 0R, 5R and 10R, fired at  $700^{\circ}\text{C}$  in intact and degrades samples (wetting-drying cycling) were obtained and presented in Figure 16.

The Figure 16 (a, b and c) shows the evolution of the densification of the ceramic mass with and without addition of waste. It can be noticed that the absence of granite waste makes easy micro-cracks to occur and also to avoid small diameter pores clogging, characterizing the coarse texture of the sample

The Figure 16 (b) also shows some defects associated to the pores of wide range of magnitude for samples 5R. It is observed that the texture is finer than of 0R and 10R, for the same firing temperature, indicating that 5R may be considered an optimum waste content for achieving higher densities.

The Illustration 16 (c) presents the image of the intact sample 10R, evidencing a coarse texture with pores of large diameters. It is noticed an intrusion of waste particles into the larger pores which can be attributed to waste that did not reacted to firing.

Figure 17 (a, b and c) shows SEM images from samples 0R, 5R and 10R fired at  $700^{\circ}\text{C}$  after 150 wetting – drying cycles.

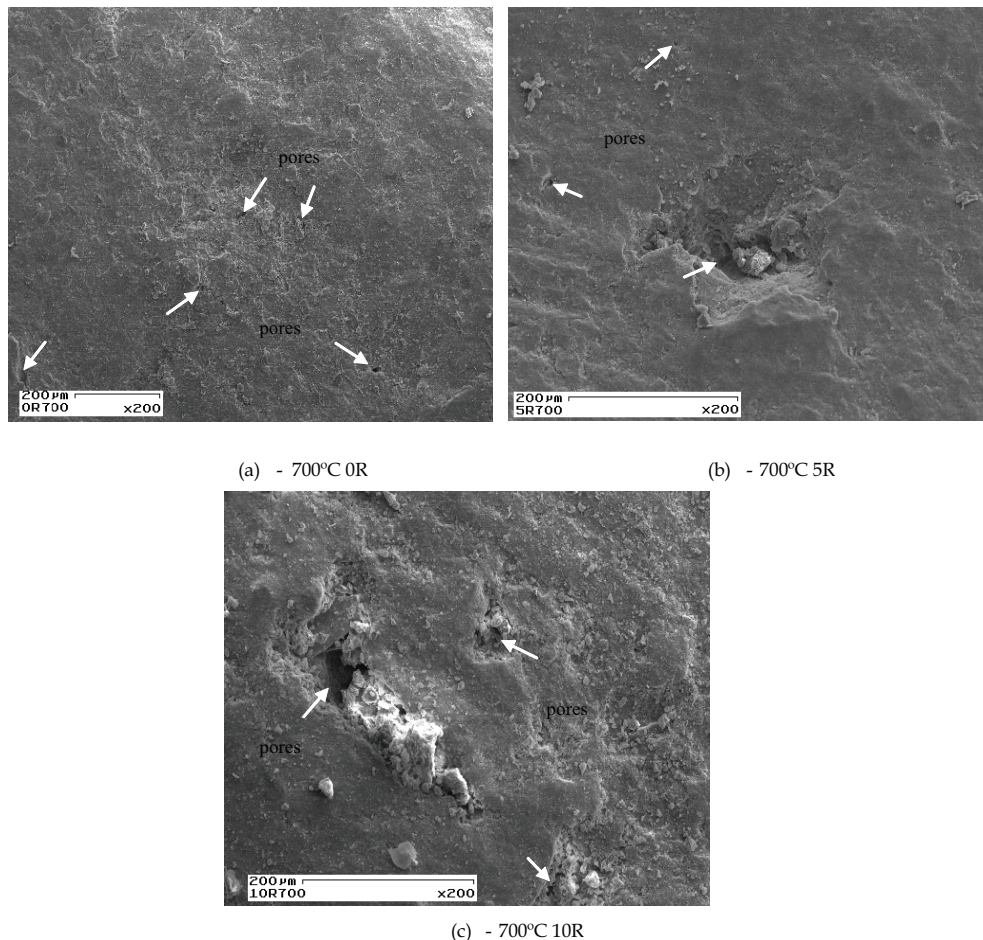


Fig. 16. SEM micrograph of the intact samples (0R, 5R, 10R) fired at 700°C

It is observed in the Illustration 17 (a) an agglomeration of free flat particles on the surface along with a micro-crack and a considerable concentration of shallow pores which are believed to be created by the wetting-drying cycles. This pore size distribution and their characteristics are strongly linked to high values of water absorption shown by these samples.

The effect of the wetting-drying cycles was more intense than that of samples 5R and 10R, causing higher strength decrease (Figure 15).

In the Figure 17 (b) sample 5R presents a smoother surface texture and very few loose particles. This sample has, as expected, less porosity and less surface degradation when compared to sample 0R. This can be a clear indicative of pores clogging caused by thermal movement hysteresis and humidity variation imposed during the test.

It is also verified in the Illustration 17 (c), free particles, pores and defects on the whole surface area, aggravated by the degradation after 150 cycles.

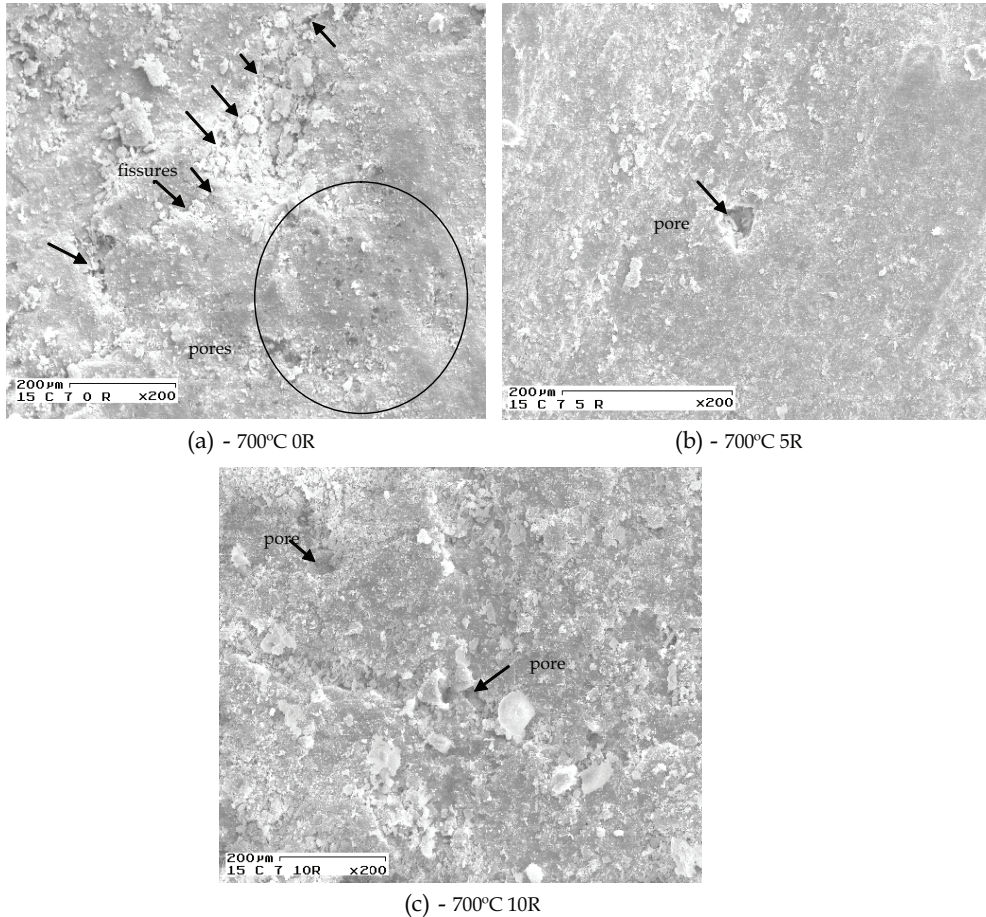


Fig. 17. (a, b e c) SEM micrograph of the samples 0R, 5R and 10R fired at 700°C degraded after 150 wetting - drying cycles

## 7. Remarks

In this chapter, it was studied the behavior of the ceramic material with additions of granite waste (0R, 5R and 10R) fired at 500°C, 700°C and 900°C. The samples were submitted to artificial and natural degradation. Through these tests it was possible to obtain some response that can help the understanding the physical mechanisms associated to the mechanical behavior of the ceramic-based material used in civil construction industry.

The laboratory tests, in special that of wetting and drying cycles tests showed themselves suitable for testing samples fired at 500°C and 700°C. However, for 900°C the results did not matched well with those obtained from natural degradation test, indicating that, for this temperature, the samples seemed to be somewhat stronger than those submitted to natural degradation process.

When technological properties of intact and degraded ceramic are evaluated in laboratory, it is possible to assess the mechanisms involved in this process based on changes in porosity, volumetric density, shrinkage and dilation amongst other parameters.

The images obtained in SEM allowed the analysis of the so called intact and degraded ceramic material surface, reflecting the effects suffered by the ceramic pieces, in accordance with the evolution of the degradation process imposed in laboratory and natural environment.

It was also observed that the natural and laboratory degradation causes heterogeneity on the mechanical behavior of the materials without following a pre-defined pattern.

It is verified that the granite waste addition influences in the degradation of the red ceramic materials, for propitiating them better durability characteristics, mainly for high firing temperature that, based on the results obtained herein, is the most important variable governing the ceramic materials behavior against degradation

## 8. References

- ABNT (Associação Brasileira de Normas Técnicas) (1987). Resíduos Sólidos – Classificação. NBR 10004.
- ABNT (Associação Brasileira de Normas Técnicas) (2004). Procedimentos para Obtenção de Extratos Solubilizados de Resíduos Sólidos. MB 2616 (1987\_Lixiviação de Resíduos - Procedimento. NBR 10005).
- ABNT (Associação Brasileira de Normas Técnicas) (2004). Procedimentos para Obtenção de Extratos Solubilizados de Resíduos Sólidos. NB 1067 (Solubilização de resíduos - Procedimento: antiga NBR 10006\_1987).
- ABNT (Associação Brasileira de Normas Técnicas) (2004). Amostragem de Resíduos Sólidos. NB 1068 (1987 NBR 10007).
- ALEXANDRE, J. (1997). Caracterização das Argilas do Município de Campos dos Goytacazes para Utilização em Cerâmica Vermelha. Tese (Mestrado em Ciências de Engenharia com ênfase em Geotecnia) – Campos dos Goytacazes – RJ. Universidade Estadual do Norte Fluminense – UENF. 164p.
- ALEXANDRE, J. (2000). Análise de Matéria-Prima e Composições de Massa Utilizada em Cerâmica Vermelha. Tese de Doutorado em Ciências de Engenharia – Campos dos Goytacazes – RJ. Universidade Estadual do Norte Fluminense – UENF. 174p.
- ALGRANTI, E.; HANDAR, Z.; RIBEIRO, F.S.N.; BOM, A.M.T.; SANTOS, A.M. BEDRIKOW, B. (2004). Exposición a Sílice y Silicosis em Brasil (PNES). *Ciência do Trabalho*. Capítulo 6 (11) págs 1-13.
- ASSOCIAÇÃO BRASILEIRA DE CERÂMICA (2005). Panorama Nacional da Indústria Cerâmica. Disponível: [www.abceram.org.br/asp/abc\\_21.asp](http://www.abceram.org.br/asp/abc_21.asp) [capturado em 05 de novembro de 2005].
- ASTM C 373 (American Society Tecnology Materials) (1977a). Standard Test Method for Water Absorption, Bulk Density, Apparent Porosity and Apparent Specific Gravity of Fired Whiteware Products.
- ASTM C 674 (American Society Tecnology Materials) (1977b). Standard Test Method for Flexural Properties of Ceramic Whiteware Materials.
- ÁVILA JÚNIOR, M. M.; Ferreira, H. S.; Menezes, R. R.; Neves, G. A.; Lira, H. L.; Ferreira, H. C. (2002). Expansão por Umidade (EPU) de Blocos Alternativos Utilizando Rejeitos de Granito. *Anais do 46º Congresso Brasileiro de Cerâmica*. São Paulo – SP. 12p.

- BERNETT, F.E. (1976). Effects of Moisture of Installed Quarry Tile. *Ceramic Bulletin*. Vol.55, nº12.
- BIZERRIL, C.R.S.F.; ARAÚJO, L.M.N.; TOSIN, P.C. (1998). Contribuição ao Conhecimento do Rio Paraíba do Sul – Coletânea de Estudos. *ANEEL/CPRM*. Rio de Janeiro-RJ. 128p.
- BUSTAMANTE, G.M.; BRESSIANI, J.C. (2000). A Indústria Cerâmica Brasileira. *Revista Cerâmica Industrial*. Vol. 5 (3). Maio/junho.
- CABRAL, G. L.L. (2005). Metodologia de Produção e Emprego de Agregados de Argila Calcinada para Pavimentação. Dissertação de Mestrado. Rio de Janeiro-RJ. IME – Instituto Militar de Engenharia. 358p.
- CASTRO, E.M. (2005a). O que esperar para o setor em 2006? Editorial. *Revista Rochas de Qualidade*. Edição 185: pág. 06.
- CASTRO, E.M. (2005b). Um ano bom que poderia ser melhor. Editorial. *Revista Rochas de Qualidade*. Edição 180: pág. 07.
- CALLISTER, W. D. J. (2000). *Materials Science and Engineering*, 5ª Edição, New York-USA, Editora John Wiley & Sons, Inc. 852p.
- CEN (Comité Européen de Normalisation). (1995) – Methods of Testing Cement – Part X: Determination of the Resistance of Cements to Attack by Sulphate Solution and by Seawater, PR ENV 196-X.
- CHIODI FILHO, C. (2001). Situação brasileira do setor de rochas ornamentais. *Revista Rochas de Qualidade*, Edição 158: págs. 87-106.
- CUNHA, V. P. (2006). Estudo da Degradação de Geotêxteis Tecidos. Dissertação de Mestrado em Engenharia Civil - Campos dos Goytacazes - RJ. Universidade Estadual do Norte Fluminense – UENF. 151p.
- FALCÃO BAUER, R.; RAGO, F. (2000). Expansão por Umidade em Placas Cerâmicas para Revestimento. *Revista Cerâmica Industrial*. São Paulo-SP. 5(3), maio/junho. 5p.
- FARJALLAT, J. E. S.; DE BARROS, F.P. YOSHIDA, R.; DE OLIVEIRA, J. A. N. 1972. Alguns Problemas de Desagregação dos Basaltos da Barragem de Capivara, Rio Paranapanema. 4ª *Semana Paulista de Geologia Aplicada*, São Paulo, vol. II A, pp. 73-102.
- FRASCA, M.H.B.O. (2005). Durabilidade e Alterabilidade em Rochas Ornamentais e para Revestimento. *Revista Rochas de Qualidade*. Edição 180: pág. 178-188.
- GUIMARÃES, J. E. P. (1998). A Cal. São Paulo. Editora PINI. 285p.
- ISRM – International Society for Rock Mechanics. (1981). *Rock Characterization Testing and Monitoring*. – ISRM Suggested Methods, Ed. E. T. Brow, Pergamon Press, Oxford, pp. 51-60.
- JOHN, V.M. (2000). Reciclagem de Resíduos na Construção Civil: Contribuição à metodologia de Pesquisa e Desenvolvimento. Tese (Livro Docente) de Doutorado – São Paulo – SP. Universidade de São Paulo. 102p.
- JOHN, V.M.; Zordan, S.E. (2001). *Waste Management* 21. 213-219.
- LUZ, A. B. (2005). O setor de rochas ornamentais. *Revista Rochas de Qualidade*, Edição 180: pág. 129.
- MACHADO, M. A. (2002). “O Setor de Rochas Ornamentais”. “Rejeitos”. Palestra apresentada no CREA/ES sobre rejeitos da Indústria de Rochas Ornamentais. Cachoeiro de Itapemirim-ES.



- MAIA, P. C. A. (2001). Avaliação do Comportamento Geomecânico e de Alterabilidade de Enrocamentos. Tese de Doutorado – Rio de Janeiro-RJ. Pontifícia Universidade Católica do Rio de Janeiro. 351p.
- MOTHÉ FILHO, H.F.; POLIVANOV, H.; MOTHÉ, C.G. (2002). O Uso do Resíduo do Mármore e Granito para Indústria da Cerâmica Vermelha. *Anais do 46º Congresso Brasileiro de Cerâmica*. São Paulo – SP. 8p.
- MOTHÉ FILHO, H.F. (2003). Caracterização e Aplicação Tecnológica do Rejeito da Indústria do Mármore e Granito. Tese de Doutorado em Geologia – Rio de Janeiro – RJ. Universidade Federal do Rio de Janeiro – UFRJ. 137p.
- MOTTA, J.F.M.; ZANARDO, A.; CABRAL, M.J. (2001). As Matérias-primas Cerâmicas. Parte I: O Perfil das principais Indústrias Cerâmicas e seus Produtos. *Revista Cerâmica Industrial*. Vol. 6 (2). Março/Abril.
- NEVES, G.A. (2002). Reciclagem de Resíduos da Serragem de Granitos para Uso como Matéria-Prima Cerâmica. Tese de Doutorado em Engenharia de Processos – Campina Grande – PB. Universidade Federal de Campina Grande – UFCG. 242p.
- NITES – Núcleo Regional de Informação Tecnológica do Espírito Santo. (1994). Desperdício na Indústria de Mármore e Granito. *Rochas de Qualidade*. São Paulo. Ed. 118, p. 27-32.
- PEITER, C.C.; CARANASSOIS, A.; VIDAL, F.W.H.; ALBUQUERQUE, G.S.C.; FERREIRA, G.E.; FILHO, C.C.; CALAES, G.; VALE, E. (2001). Rochas ornamentais no século XXI. CETEM, ABIROCHAS. (Relatório Técnico sobre o Setor de Rochas Ornamentais do Brasil, TR – 30/07). 113p.
- PESAGRO/RIO (2005). Boletim de Dados Climatológicos da Região de Campos dos Goytacazes-RJ. *Estação Automática Thies-Clima*.
- ROC MAQUINA. (1989). Referências arqueológicas sobre la explotación de piedras naturales em época romana de España. Cuarto trimestre.
- SABOYA, F.A.J., XAVIER, G. C., ALEXANDRE, J. (2006). The Use of the Powder Marble By-Product to Enhance the Properties of Brick Ceramic. In: *Construction and Building Materials*, Vol. 20, pág. 1-8.
- SILVA, S.A.C. (1998). Caracterização de Resíduo da Serragem de Blocos de Granito. Estudo Potencial de Aplicação na fabricação de Argamassas de Assentamento e de Tijolos de Solo-Cimento. Tese (Mestrado em Engenharia Ambiental) – Vitória – ES. Universidade Federal do Espírito Santo – UFES. 159p.
- SMITH, W.F. (1998). *Princípios de Ciência e Engenharia dos Materiais*. 3ª Edição, Lisboa-Pt, Ed. McGRAW-HILL, 892p.
- SOUZA SANTOS, P. (1989). Ciência e Tecnologia das Argilas. 2ª Ed. São Paulo: Editora Edgard Blucher Ltda. Vol. 1, 499p.
- TOLEDO, R. (2003). Técnicas Fototérmicas e de Raios-X para o Monitoramento de Sólidos e Gases em Materiais Cerâmicos. Tese (Doutorado em Engenharia e Ciência dos Materiais) – Campos dos Goytacazes – RJ. Universidade Estadual do Norte Fluminense – UENF. 315p.
- VIEIRA, C.M.F. (2001). Caracterização de Argilas de Campos dos Goytacazes Visando à Fabricação de Revestimento Cerâmico Semiporoso. Tese de Doutorado em Engenharia de Materiais – Campos dos Goytacazes – RJ. Universidade Estadual do Norte Fluminense – UENF. 118p.

- VIEIRA, C.M.F.; SOARES, T.M.; SÁNCHEZ, R.; MONTEIRO, S.N. (2003). Incorporation of Granite Waste in Red Ceramics. Materials Science & Engineering. Campos dos Goytacazes - Brazil. 7p.
- WARREN, J. (1999). Conservation of Brick. New York, Oxford University.
- WIKPEDIA, (2005). História da Cerâmica. Disponível:  
<http://www.en.wikipedia.org/wiki/brick>. [capturado em 20 de março de 2005].
- WINGER, R.J.J. (1965). In place permeability tests use for subsurface Drainage investigation. Division of Drainage and Groundwater EGINEERING. Denve, Colorado-USA. 9p.
- XAVIER, G.C. (2001). Utilização de Resíduos de Mármore e Granito na Massa de Conformação de Cerâmica Vermelha. Dissertação de Mestrado em Ciências de Engenharia - Campos dos Goytacazes - RJ. Universidade Estadual do Norte Fluminense - UENF. 285 p.
- XAVIER, G.C. (2006). Resistência, Alterabilidade e Durabilidade de Peças Cerâmicas Vermelhas Incorporadas com Resíduo de Granito. Tese de Doutorado em Engenharia Civil - Campos dos Goytacazes - RJ. Universidade Estadual do Norte Fluminense - UENF. 201 p.



# Behavior of Aging, Micro-Void, and Self-Healing of Glass/Ceramic Materials and Its Effect on Mechanical Properties

Wenning Liu, Xin Sun and Moe Khaleel  
*Pacific Northwest National Laboratory, Richland  
USA*

## 1. Introduction

Among the high-efficiency energy conversion devices that are environmentally friendly with little or no toxic emissions, the solid oxide fuel cell (SOFC) continues to show great promise as a future power source. It has potential applications in stationary power generation and as auxiliary power units. Among various SOFC designs under development, anode-supported planar cells have shown great potential in delivering high performance at reasonable costs (Teagan et al., 2000; Chung et al. 2005). Planar SOFCs offer a significant advantage of a compact design along with higher power densities. In the meantime, they require that hermetic gas seals be incorporated for efficient and effective channeling of fuel and oxygen.

Seals are the most critical components in commercializing the planar SOFC technology (Nielsen et al., 2007; Choi & Bansal, 2005; Smeacetto et al., 2008). They must adequately prevent air and fuel from leaking, effectively isolate the fuel from the oxidant, and insulate the cell from short circuit. Essentially, there are two standard methods for sealing: compressive sealing and rigid bonding (Singh, 2007; Fergus, 2005; Chou et al., 2003). In compressive sealing, a compliant, high-temperature material is captured between the two sealing surfaces and compressed with a load frame external to the stack to deliver hermetic sealing. The sealing surfaces can slide with respect to one another without disrupting the hermeticity of the seal. This technology, however, remains incomplete due to the lack of a reliable, high-temperature, sealing material (Simner & Stevenson, 2001) and the difficulty of designing the appropriate load frame under high-operating temperatures. Rigid seals rely on effective bonding of the seal material to the sealing surfaces. They offer significant advantages over compressive seals that suffer from problems of oxide scaling and chemical stability under highly reactive environments in addition to the disadvantages of incorporating an externally applied load (Singh, 2007).

As a rigid seal, glass joining provides a cost-effective and relatively simple method for bonding ceramic and metal parts. However, the softening point of the glass component typically limits the maximum operating temperature to which the joint may be exposed. As discussed by Weil et al. (2004), there are a number of other key materials and processing variables that can influence the performance of glass seals, including the composition of the metal substrate against which the seal is made, the operating parameters, such as the

expected lifetime of the device (and therefore the seals), and the degree of thermal cycling to which the seals will be exposed during system operation. In addition, a glass seal in room temperature is brittle, non-yielding, and particularly susceptible to fracture when exposed to tensile stresses. Because of these complications, much of the development effort for SOFC seal materials has been focused on developing materials that have compatible, temperature-dependent, coefficients of thermal expansion (CTEs) for each of the components being joined, i.e., the ceramic cell, the seal, and the metal separator, to minimize the buildup of residual stresses within the joint. Only a handful of high-temperature glass compositions in the borate- or phosphate-doped aluminosilicate families satisfy these requirements (Lahl et al., 1999). The glass seal composition used in this study, designated as G18 (Meinhardt et al., 2002), was developed by Pacific Northwest National Laboratory (PNNL) for planar-type SOFC applications. G18 is a barium-calcium-aluminosilicate (BCAS)-based glass with boron oxide added. Silicon-based glasses provide a better combination of chemical compatibility and stability properties than phosphate- or borate-based glasses, although this material is susceptible to chromium migration when used with ferritic stainless steels (Yang et al., 2003; Yang et al. 2004). For rigid bonds as such, stress levels in the glass seal and its mechanical properties, such as Young's modulus and interfacial strength between different interfaces, become critical for long-term reliability of the seal and therefore the stacks.

To obtain a reliable SOFC design in the complex operating environments, the stress level in the glass seal materials as well as at the various interfaces must be carefully examined and managed. To accurately predict these stresses, accurate material models that consider the various aspects of the seal materials under different operating conditions, including aging and cooling, become critical for long-term performance of the sealing system and SOFC stacks.

This chapter first describes tests to investigate the temporal evolution of the volume fraction of ceramic phases, the evolution of micro-damage, and the self-healing behavior of the glass ceramic sealant used in SOFCs. Then a phenomenological model based on mechanical analogs is developed to describe the temperature-dependent Young's modulus of glass ceramic seal materials. It was found that after the initial sintering process, further crystallization of the glass ceramic sealant does not stop, but slows down and reduces the residual glass content while boosting the ceramic crystalline content. Under a long-term operating environment, distinct fibrous and needle-like crystals in the amorphous phase disappeared, and smeared/diffused phase boundaries between the glass phase and ceramic phase were observed. Meanwhile, the micro-damage was induced by the cooling-down process from the operating temperature to the room temperature, which can potentially degrade the mechanical properties of the glass/ceramic sealant. The glass/ceramic sealant self-healed upon reheating to the SOFC operating temperature, which can restore the mechanical performance of the glass/ceramic sealant. The phenomenological model developed here includes the effects of continuing aging and devitrification on the ceramic phase volume fraction, and the resulting mechanical properties of glass ceramic seal material are considered. The effects of micro-voids and self-healing are also considered using a continuum damage mechanics (CDM) model. This formulation is for glass/ceramic seals in general, and it can be further developed to account for effects of various processing parameters. This model was applied to G18, and the temperature-dependent experimental measurements were used to calibrate the modeling parameters and to validate the model prediction.

## 2. Material and experimental

In planar-type SOFCs, different components need to be hermetically sealed to make certain that the SOFC system functions properly. The seals prevent mixing of the fuel and oxidant and also keep the fuel from leaking out of the stack. Thus, seal integrity is essential to stack performance and operation. The glass ceramic sealant material, named G18, which was developed at PNNL, was a BCAS-based glass designed in-house. It was originally melted from the following mixture of oxides (by weight percent): 56.4% BaO, 22.1% SiO<sub>2</sub>, 5.4% Al<sub>2</sub>O<sub>3</sub>, 8.8% CaO, and 7.3% B<sub>2</sub>O<sub>3</sub> (Meinhardt et al., 2002). The G-18 powder was milled to an average particle size of 20 μm and mixed with a proprietary binder system to form a paste that could be dispensed onto the substrate surfaces at a uniform rate of 0.075 g/linear cm with an automated syringe dispenser. The glass paste may be dispensed onto the YSZ side of the bilayer discs of the Ni-YSZ anode and the YSZ electrolyte, which are 25 mm in diameter. Each disk was then concentrically positioned on a washer specimen, loaded with a 100-g weight, and heated in air under the following sealing schedule: heat from room temperature to 850°C at 10°C/min, hold at 850°C for 1 hour, cool to 750°C at 5°C/min, hold at 750°C for 4 hours, and cool to room temperature at 5°C/min (Weil et al., 2004).

The hermetic seal is easily formed by dispensing a paste or tape casting followed by heating. The glass wets the surfaces to be bonded at the joining temperature, and partial crystallization then provides mechanical stiffness and strength at operating temperatures.

### 2.1 Temporal evolution of volume fraction of ceramic (crystalline) phase

The volume fraction of the ceramic (crystalline) phase varies with aging or operating time under SOFC operating temperatures. To evaluate the temporal evolution of the ceramic phase, the phase structure of the glass-ceramic sealant was determined by X-ray diffraction (XRD). XRD finds the geometry or shape of a molecule using X-rays, based on the elastic scattering of X-rays from structures that have a long-range order. XRD relies on the dual wave/particle nature of X-rays to obtain information about the structure of crystalline materials. The dominant effect that occurs when an incident beam of monochromatic X-rays interacts with a target material is scattering of those X-rays from atoms within the target material. In materials with a regular structure (i.e., crystalline), the scattered X-rays undergo constructive and destructive interference. This is the process of diffraction. The diffraction of X-rays by crystals is described by Bragg's Law as

$$n\lambda = 2d \sin\theta \quad (1)$$

The directions of possible diffractions depend on the size and shape of the unit cell of the material. The most comprehensive description of scattering from crystals is given by the dynamical theory of diffraction (Azároff et al., 1974).

Specimens used for the XRD test were prepared according the aforementioned procedure with dimensions of 3 mm × 4 mm × 45 mm. They were heated in air under the following sealing schedule: heat from room temperature to 850°C at 10°C/min, hold at 850°C for 1 hour, cool to 750°C at 5°C/min, hold at 750°C for 4 hours, and cool to room temperature at 5°C/min. The specimen's surfaces were ground to a 600-grit finish and then ultrasonically cleaned with distilled water and acetone.

Figure 1 shows the evolution of the volume fraction of crystalline phases that form within the devitrifying glass as a function of time held at 750°C (Weil et al., 2004). This graph was

constructed from a series of quantitative XRD measurements conducted on the aged glass-ceramic samples. For glass/ceramic sealing materials, the volume fraction of the ceramic crystalline is time dependent under the SOFC operating temperature. Some volume of the ceramic crystalline is formed at the end of the initial sealing process at 850°C. The crystallization process slows down but does not stop when it is subjected to the typical operating environment of 750°C. The volume fraction of the ceramic crystalline in the sealant material is increased with the holding time in the air at the operating temperature.

After 1 hour of the initial sealing process at 850°C, the crystalline contents of  $\text{BaSiO}_3$ ,  $(\text{Ba}_{1.5}\text{Ca}_{0.5})\text{SiO}_4$ , and Hexa- $\text{BaAl}_2\text{Si}_2\text{O}_8$  were observed in the glass/ceramic seal.  $\text{BaSiO}_3$  is the main crystalline phase composition, taking up approximately 40% of the volume fraction. After the first 20 hours under the SOFC working temperature of 750°C, the volume fractions of both  $\text{BaSiO}_3$  and  $(\text{Ba}_{1.5}\text{Ca}_{0.5})\text{SiO}_4$  remained relatively unchanged, and the volume fraction of hexa- $\text{BaAl}_2\text{Si}_2\text{O}_8$  doubled from 7% to 15%. With a longer working time, the content of  $(\text{Ba}_{1.5}\text{Ca}_{0.5})\text{SiO}_4$  and the hexa- $\text{BaAl}_2\text{Si}_2\text{O}_8$  began to decrease, and the content of  $\text{BaSiO}_3$  started to increase. A new phase of mono- $\text{BaAl}_2\text{Si}_2\text{O}_8$  started to appear at about 150 hours of working time and continued to increase because  $(\text{Ba}_{1.5}\text{Ca}_{0.5})\text{SiO}_4$  and Hexa- $\text{BaAl}_2\text{Si}_2\text{O}_8$  were both transformed into this phase. The overall crystalline phase increased almost linearly with  $\log(\text{time}[\text{h}])$  in the first 300 hours of aging. After that, the crystallization process gradually stopped, and the crystalline content in the material remained relatively unchanged.

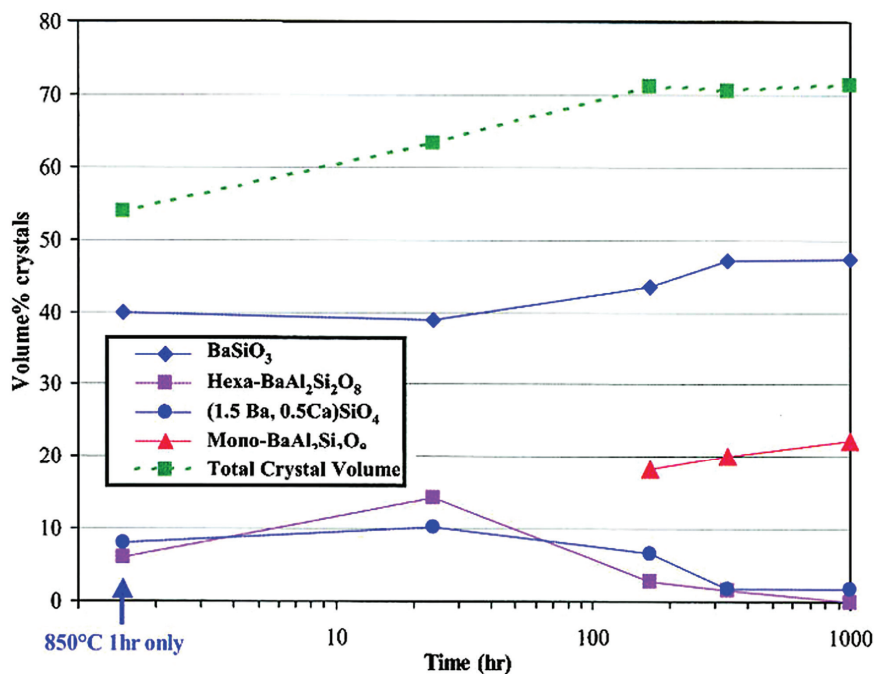


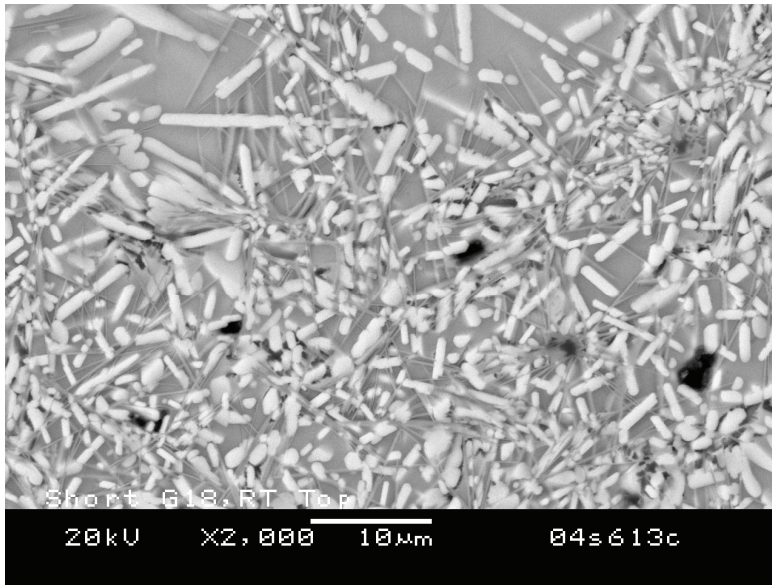
Fig. 1. Quantity of crystalline phase formed in glass-ceramic sealant (G18) as a function of time held in air at 750°C

In general, ceramic crystalline possesses more stable mechanical properties under high temperature than pure amorphous glass. The glass transition temperature of the amorphous glass is about 500°C to 600°C; therefore, the mechanical modulus of the amorphous glass will degrade dramatically over the glass-transition temperature. This causes the pure amorphous glass to overflow during the operation. An aging dependent increase of the volume fraction of the ceramic crystalline in the glass ceramic sealant enhances the mechanical modulus of the sealant at high temperatures to prevent the sealant from overflowing during the operation under stack clamping loads. This will greatly benefit the long-term reliability and performance of SOFCs.

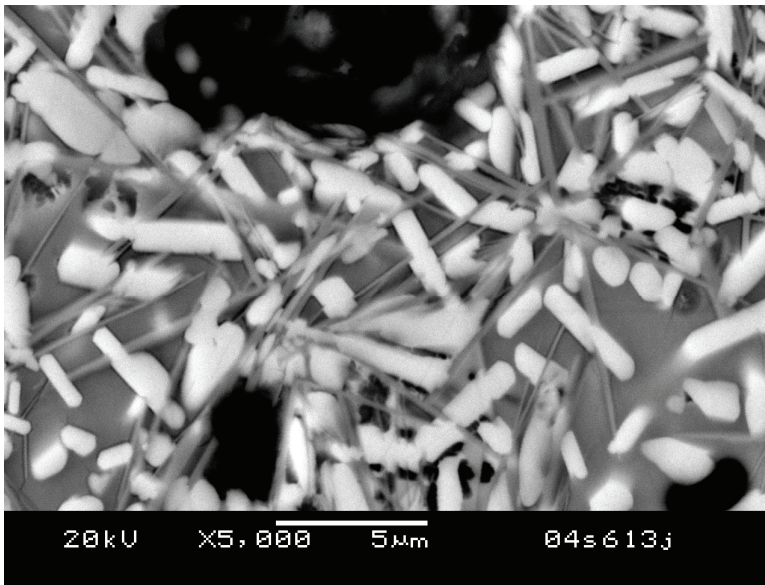
## 2.2 Evolution of micro-damage of glass-ceramic sealant

During further devitrification of glass under the operating temperatures of SOFCs, not only does the volume fraction of the crystalline phases increase, but also the morphology of the crystalline phases changes. Samples used here for the evolution of micro-damage of glass-ceramic sealant were 3 mm × 4 mm × 45 mm. Ten samples were prepared. They were placed into the furnace and heat treated at 850°C for 1 hour and then aged at 750°C. Five samples were aged for 4 hours, and another five samples were aged for 1,000 hours. To look inside of the glass-ceramic sealant materials, these specimens were cross-sectioned along the central line. The top surface and the cross-section of the specimens were ground to a 600-grit finish and then ultrasonically cleaned with distilled water and acetone like the XRD experiments. Scanning electron microscopy (SEM) was adopted to probe the microstructure of the glass-ceramic sealant material. SEM images of the microstructure of the glass ceramic sealant materials were taken by JEOL JSM-840 with an LaB6 emitter.

Figures 2 and 3 show the typical microstructure of the top and cross-section of the glass ceramic sealant, respectively, after glass paste is spread and is sintered initially. At the end of the initial sintering process, no matter where it is (the surface or the interior of the glass-ceramic sealant), distinct boundaries between the glass (amorphous) phase and the ceramic (crystalline) phase can be observed, and the fibrous and needle-like crystalline structures can be seen clearly in the amorphous glass phase. Some small voids and flaws are also illustrated in the microstructures. The structure of the two phases is relatively intact even with some voids and flaws. The microstructures of the glass ceramic sealant after aging for 1,000 hours at 750°C are depicted in Figures 4 and 5 for the top surface and the cross-section, respectively. Obviously, many more small voids were now present, particularly in the amorphous phase. This occurred not only on the surface, but also the interior of the material. The overall void volume fraction also increased from the volume observed after the initial sintering process shown in Figures 2 and 3. Compared with Figures 2 and 3, the distinct fibrous and needle-like crystals in the amorphous phase disappeared, and smeared/diffused phase boundaries between the glass phase and ceramic phase were observed after aging for 1,000 hours. The CTE of the ceramic phase, in general, was higher than that of the amorphous glass phase (Roos et al., 2007; Brochu et al., 2006; Fei, 1995). The mismatch of the CTE of the ceramic and glass phases will cause different shrinkages of the ceramic phase and glass phase during cooling. The shrinkage of the ceramic phase is much larger than that of the glass phase; therefore, a crack will be created along the weak boundary between the glass phase and the ceramic phase; furthermore, this will possibly create micro-voids, particularly in the glass phase.



a)



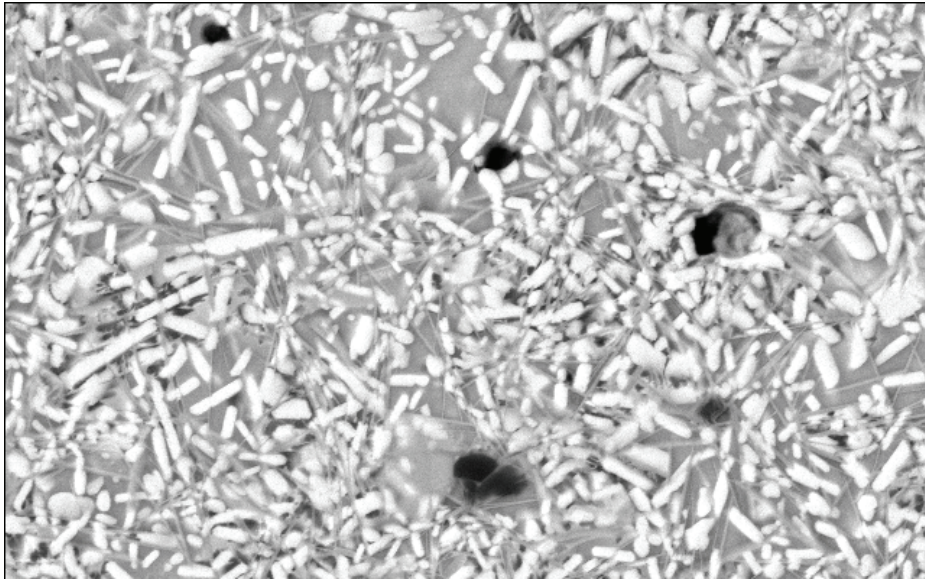
b)

Fig. 2. SEM image of microstructure of top surface of glass-ceramic sealant after initial sintering process: a) magnification: 2000×; b) magnification: 5000×

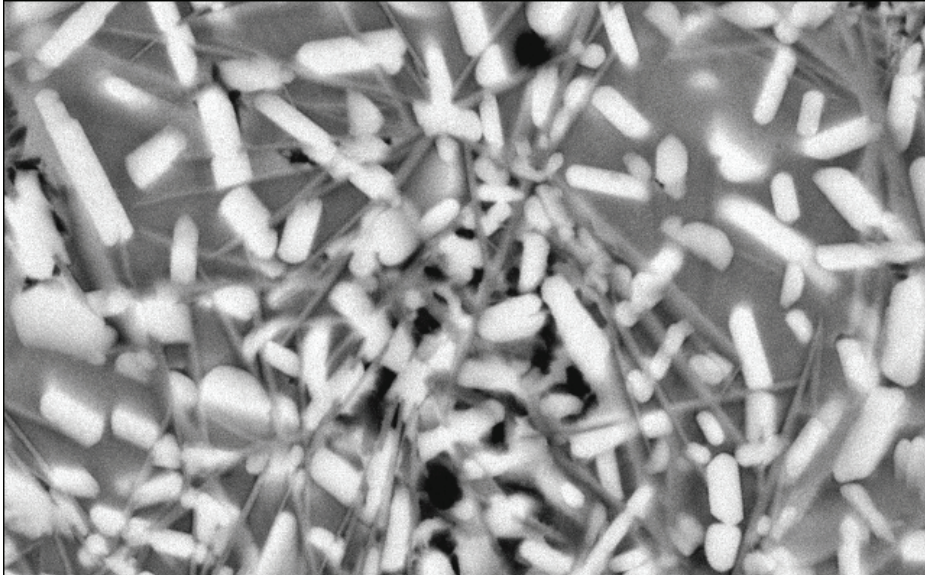
At room temperature, the glass/ceramic sealant is characterized by brittle material. Small crack and flaw in the brittle materials is dreadful to cause the propagation of the small crack



and flaw under residual tensile stresses induced by the mismatch of CTE of various components, and to lead to failure of the sealant in SOFC.



a)



b)

Fig. 3. SEM image of microstructure of cross-section of glass-ceramic sealant after initial sintering process a) magnification: 2000 $\times$ ; b) magnification: 5000 $\times$

### 2.3 Possible self-healing of glass-ceramic sealant

Even though G18 exhibits creep/flow behavior under operating temperatures, its behavior at room temperature can be characterized as being brittle. During thermal cycling, the tensile residual stresses caused by the mismatch of CTEs of various cell components can potentially generate many small cracks and voids in the brittle seal material after cooling down. If left untreated/unhealed, these small cracks in the seal could be detrimental to the overall stack reliability for the next operating cycle.

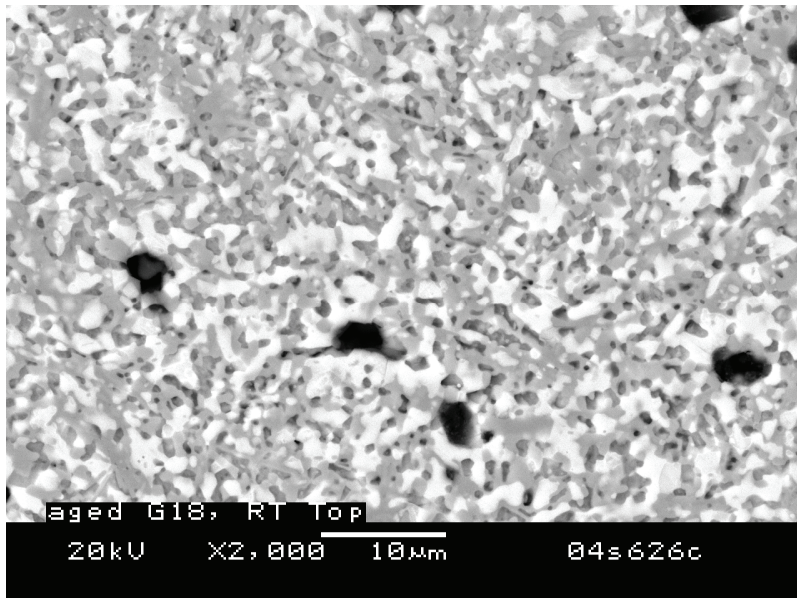
To gain a deep insight into the behavior of damaged glass ceramic sealant under high temperatures, indentation and four-point bend tests were used on the short crystallized glass ceramic sealant. The short crystallized bend bar was polished to a diamond finish of 3 microns, and its edge was rounded. The polished bend bar was then indented with a Vickers diamond at 2 kg. Five indentations were made within the inner span of the bend bar with the objective to drive the crack under slow crosshead (0.025 mm/min) and stop the crack propagation to observe the damage ahead of the crack tip. As shown in Figure 6, the typical Vickers impressions with perfectly symmetrical, four radial cracks emanating from the four corners were created on the surface of the short crystallized glass ceramic sealant by the Vickers indentation. Under higher magnification for one of the radial cracks (Figure 7), it was observed that crack propagation followed a less tortuous path as compared to typical structural ceramics (Fang et al., 2002; Marliere et al., 2003). The white crystallite in rod shape (likely  $\text{BaSiO}_3$ ) appears to be stronger than the featureless glass (gray area) because some crack deflection and bridging were observed as compared to the straight crack path through the gray area (likely the un-crystallized residual glasses). Nevertheless, the glass ceramic sealant used here showed typical brittleness with a single crack at room temperature.

After indentation, the bend bar was placed in a four-point fixture and tested at a slow cross speed of 0.025 mm/min (as compared to the normal speed of 0.5 mm/min) at 750°C. The sample was loaded up to ~20 N and held for a half hour at 750°C, and then was stopped for damage characterization under SEM. It may be seen that all the radial cracks were healed. Figures 8 and 9 show the typical SEM images of the example at low and high magnifications. It is evident that all of the four radial cracks healed completely. One would expect the Vickers impression to tend to smooth (rounding at four sharp corners) slightly during the half hour of soaking at 750°C such that the two radial cracks at N and S directions would be experiencing compressive stress (just like a circular hole) when the bend bar was loaded, and these two radial cracks could heal; however, this was not the case for the other two radial cracks (E and W directions) because they are under tensile stresses upon loading. These experimental observations can serve as evidence that the glass/ceramic sealant material exhibits some degree of self-healing: when reheated again to a high operating temperature, the damage in the glass ceramic sealant may disappear because of the flow of the glass phase, potentially restoring its mechanical property to its undamaged level. Other possible physical explanations for this healing behavior may be the capillary force of the residual glass phase as well as the residual stresses caused by the Vickers indentation.

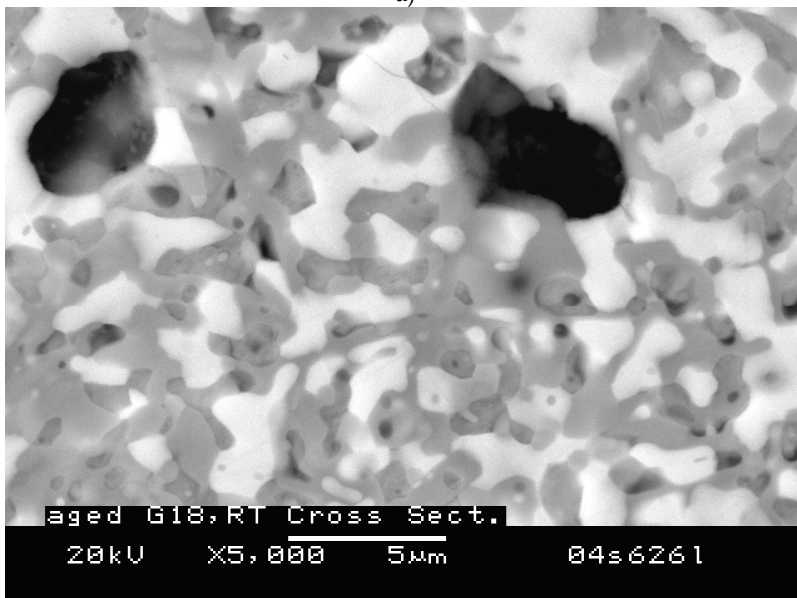
The advantage of this self-healing behavior of the glass ceramic sealants is that materials with a dramatically different expansion can potentially be used for seals because at the cell operating temperatures, CTE mismatch-induced damage, like micro-voids, can be healed automatically. Then the mechanical performance of the glass ceramic sealant can be restored as undamaged. For SOFC stacks during the operating thermal cycles, the micro-damage in the glass ceramic sealant may be formed when cooling down from the operating



temperature to room temperature. Then the micro-damage may be healed at some threshold temperature.

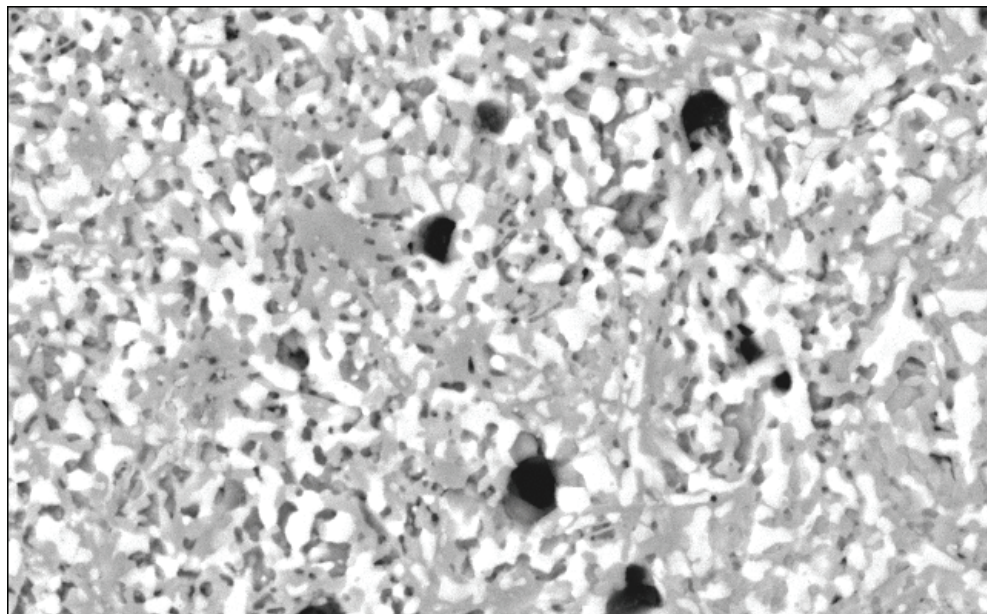


a)

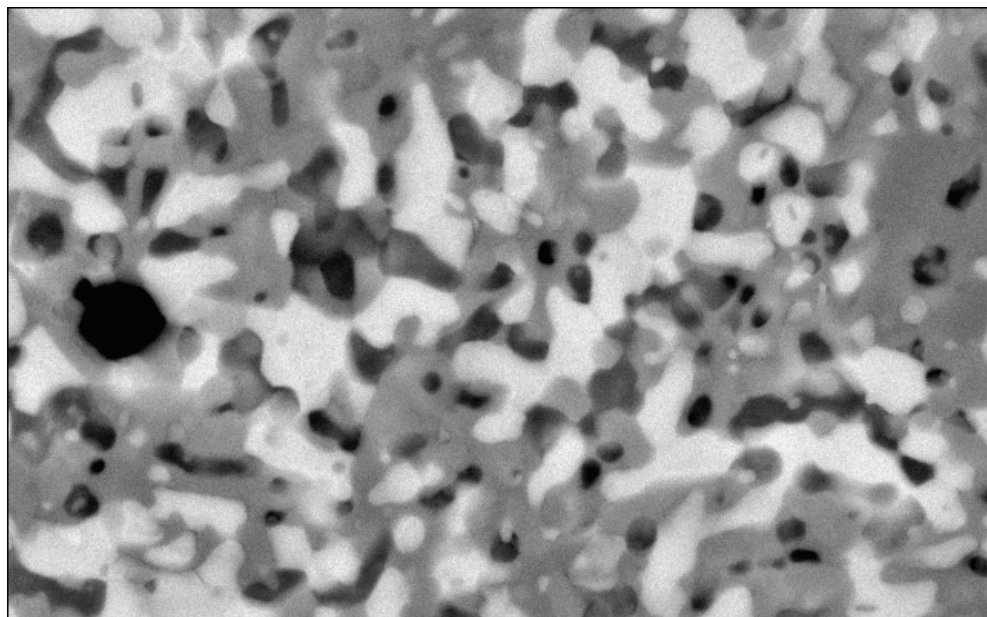


b)

Fig. 4. SEM image of microstructure of top surface of glass-ceramic sealant after 1000 hours of aging at 750°C: a) magnification: 2000×; b) magnification: 5000×



a)



b)

Fig. 5. SEM image of microstructure of cross-section of glass-ceramic sealant after 1000 hours of aging at 750°C: a) magnification: 2000×; b) magnification: 5000×

### 3. Degradation of mechanical properties of glass-ceramic sealants

The dynamic resonance technique (ASTM C1198) was used to measure the elastic moduli of the specimens of both non-aged and 1000-h aged short crystallized G18 at room and elevated temperatures.<sup>1</sup> The instrument used to measure the resonant frequencies was constructed following ASTM C1198. The specimen was suspended within a resistance-heated furnace using single-crystal, sapphire fibers with beaded ends. Small, narrow notches were cut into the corners of the specimen to accept the fibers. The fibers coupled the specimen to two piezoelectric transducers mounted above the furnace. One transducer was used as a driver, and the other as a receiver. A computer-controlled system was used to send frequency signals sweeping from 20 Hz to 20 kHz through the driver transducer. The signal from the receiving transducer was fed back into the computer, and the resonant frequencies were identified and recorded. Both the transverse and longitudinal resonant frequencies could be reliably detected at the corners of the specimen. Resonant frequency data were then used in calculating the elastic moduli with the following equations (ASTM, 2008):

$$E = 0.9465 \frac{mf_f^2}{b} \frac{L^3}{h^3} T_1 \quad (2)$$

$$G = \frac{4Lmf_f}{bh} \frac{B}{1+A} \quad (3)$$

where  $E$  and  $G$  are the Young's modulus and shear modulus, respectively;  $m$  is the mass of the bar;  $b$ ,  $h$ , and  $L$  are the width, thickness, and length of the bar, respectively;  $f_f$  represents the fundamental resonant frequency of the bar in flexure; and  $T_1$  denotes the correction factor for the fundamental flexural mode to account for the finite thickness of the bar and Poisson's ratio, etc. The Young's and shear moduli were then used to calculate Poisson's ratio:

$$\mu = (E / 2G) - 1 \quad (4)$$

The precisions of the  $E$ ,  $G$ , and  $\mu$  values were calculated by propagating the uncertainty of each term through the equations.

The test specimen was a right parallelepiped measuring 50.75 x 25.34 x 5.96 mm. All surfaces were ground smooth. Resonant frequencies were measured at room temperature and in 100°C intervals from 200–800°C. The furnace was heated at a rate of approximately 12°C/min and was held for 15 minutes at each temperature for equilibration.

The measured Young's modulus for the non-aged and 1000-h aged G18 at room and elevated temperature is tabulated in Table 1. Both of the measured Young's modulus and shear modulus for the non-aged and 1000-h aged G18 at room and elevated temperature are shown in Figure 10. For non-aged short crystallized glass/ceramic sealant (G18), both the Young's modulus and shear modulus decrease with an increasing test temperature. The resonant peaks became very broad at about 700°C, making it impossible to differentiate between the longitudinal and transverse peaks with any certainty. This may have been

<sup>1</sup> Shelleman, D. L., & Green, D. J. (2006). *Measurement of Elastic Constants on Sample Supplied by PNNL*, Internal Technical Report, Pacific Northwest National Laboratory, Richland, Washington.



caused by the softening of the glass phase present in these specimens. Additional measurements were taken again at room temperature (30°C) after the high-temperature tests achieved the same moduli as the pre-test values.

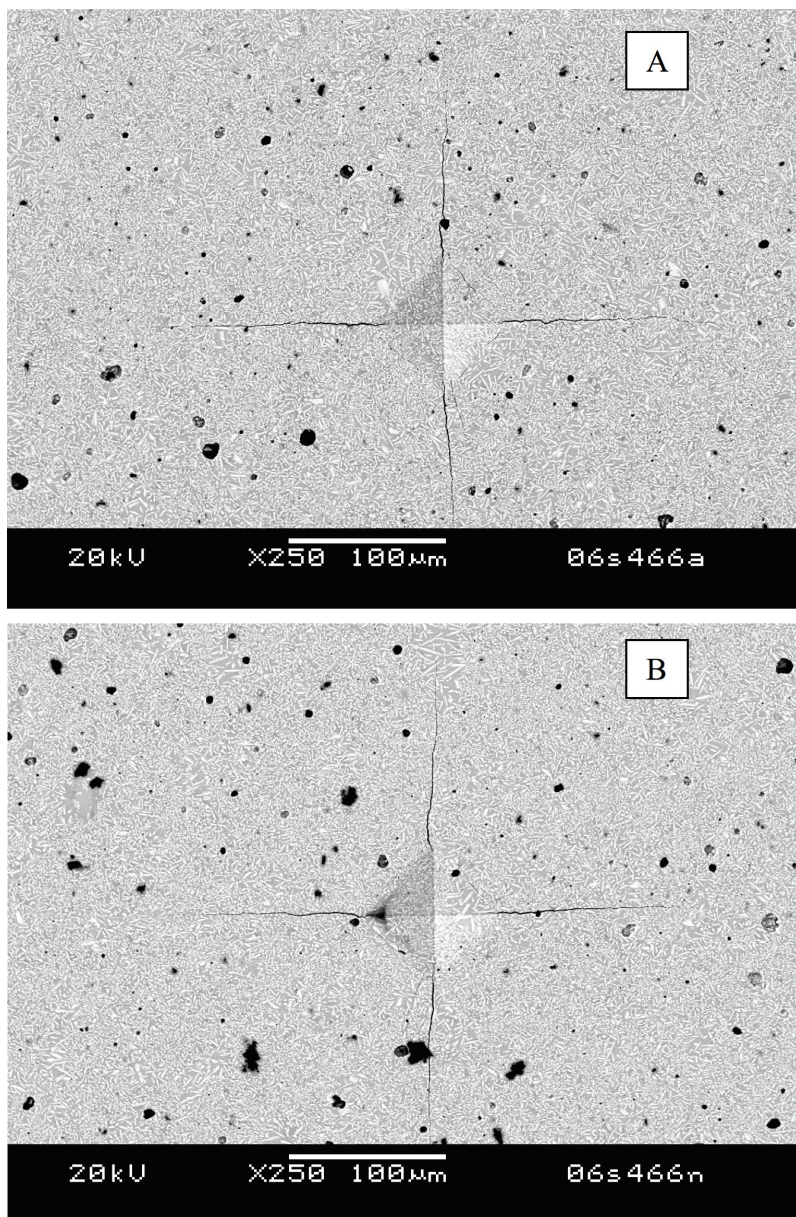


Fig. 6. Typical impression of indentation with Vickers indenter at 2 kg indentation load on polished, short crystallized, glass-ceramic specimen

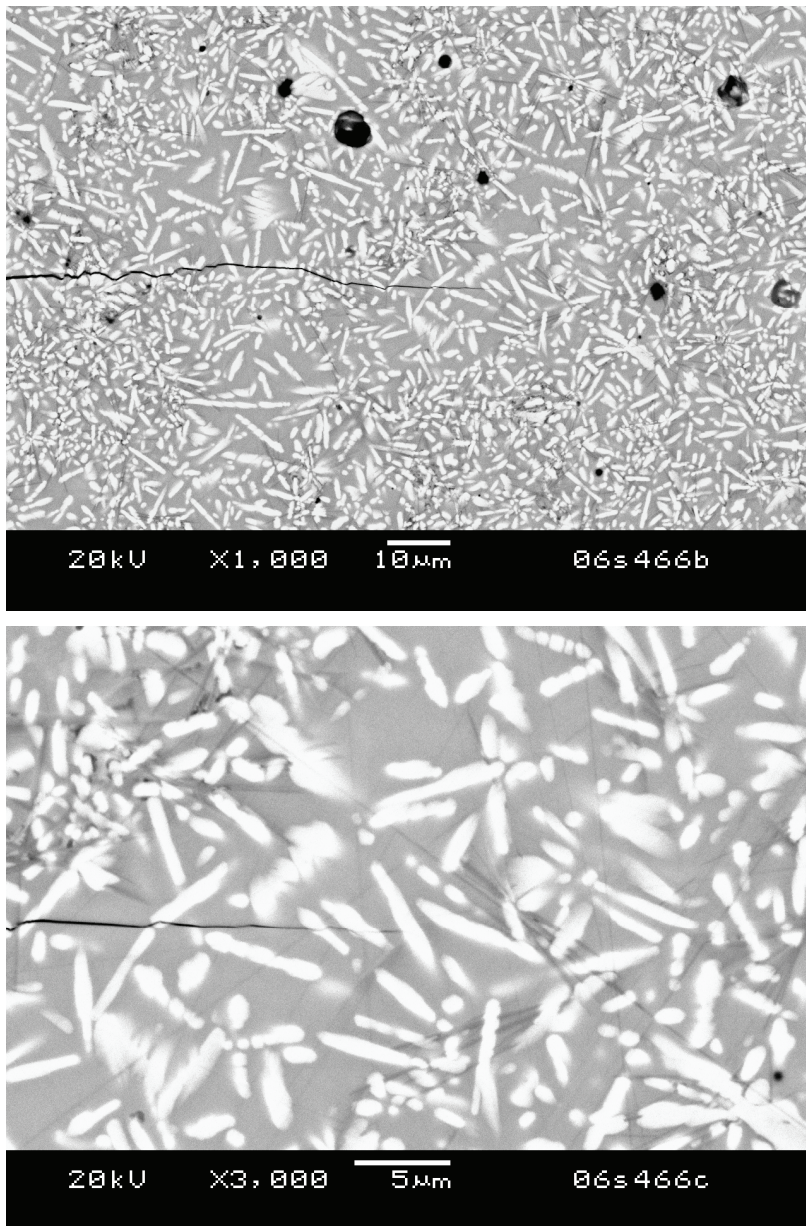
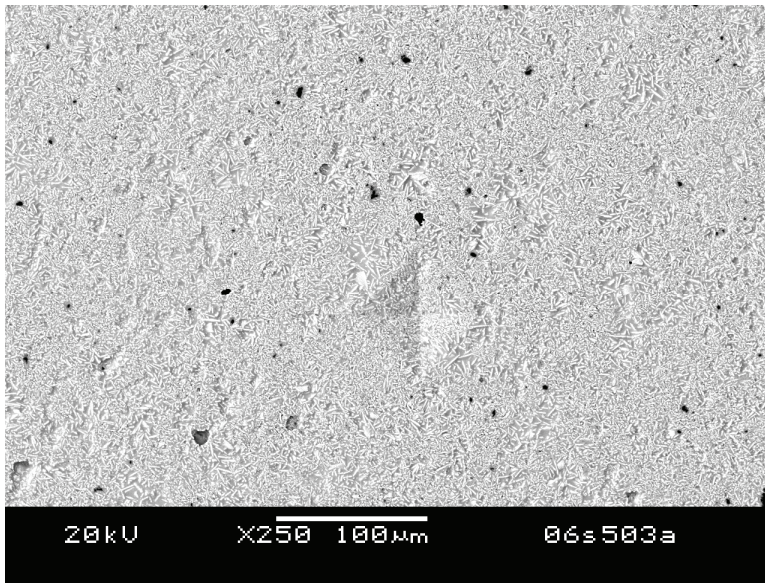


Fig. 7. SEM pictures of indentation impression at the crack tip on polished, short crystallized, glass-ceramic specimen with higher magnification

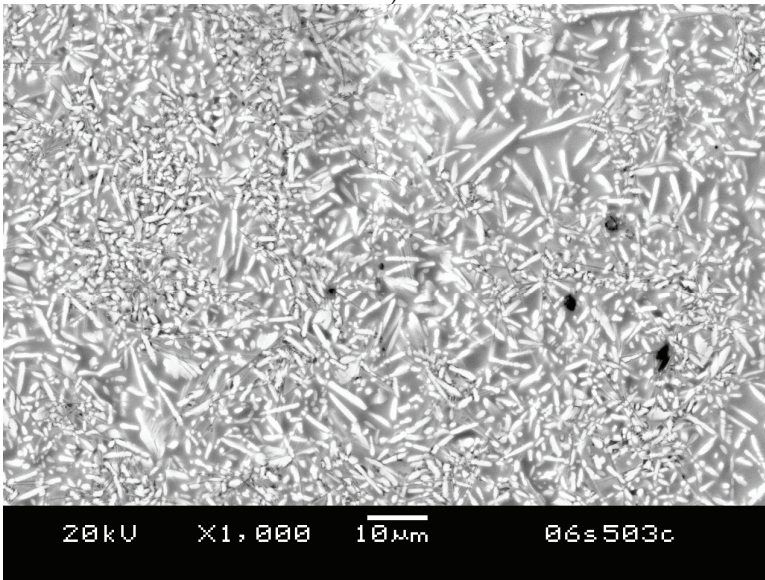
The measured Young's modulus and shear modulus for the 1000-h aged G18 show some very distinct and interesting features. For temperatures lower than 400°C, both Young's modulus and the shear modulus increase with increasing test temperature. The moduli



exhibit somewhat temperature-independent behaviors from 400°C to 600°C. Above 600°C, the moduli start to decrease with increasing temperature.

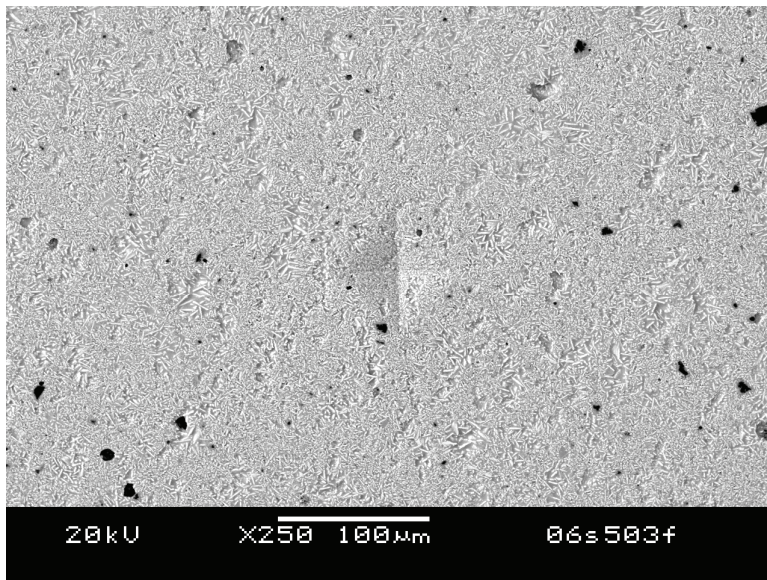


a)

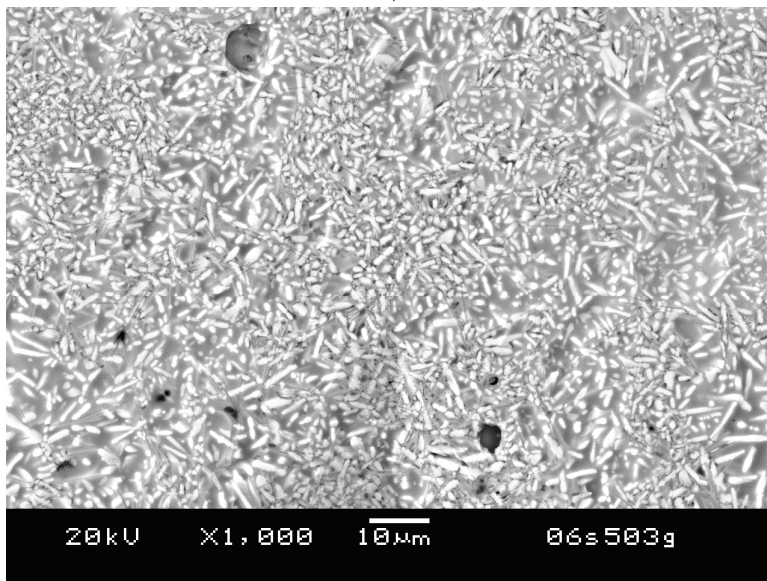


b)

Fig. 8. SEM pictures of the indentation impression on polished, short crystallized, glass-ceramic specimen after it was reheated and loaded to ~20 N at 750°C: a) overview with low magnification, and b) crack tip with high magnification



a)



b)

Fig. 9. SEM pictures of the indentation impression on polished, short crystallized, glass-ceramic specimen after it was reheated and loaded to ~20 N at 750°C: a) overview with low magnification, and b) crack tip with high magnification

For temperatures lower than 400°C, the measured modulus for the aged glass ceramic sealant is consistently less than that of the non-aged (short-term aged) glass ceramic. At

about 500°C, the moduli for the aged and non-aged samples cross over. For temperatures above 600°C, the moduli trend reverses itself: the modulus for 1000-h aged G18 is higher than that of the non-aged G18.

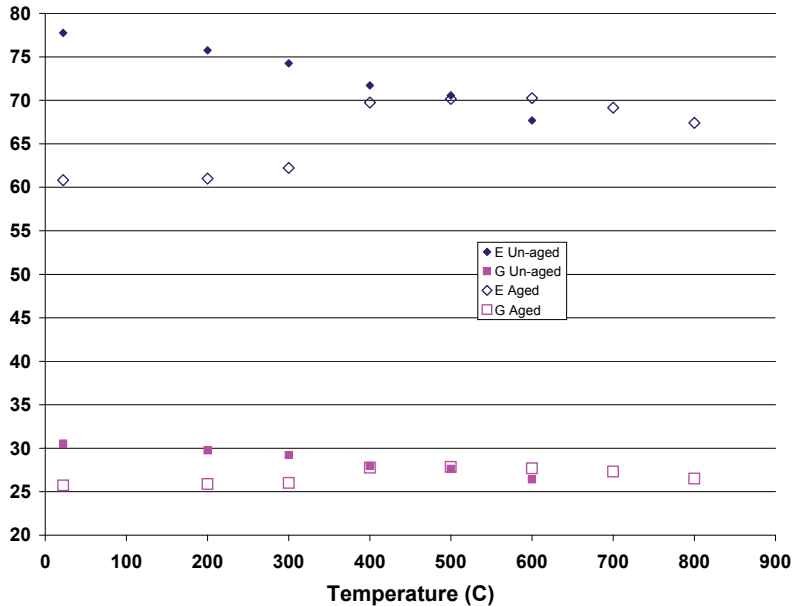


Fig. 10. Young's and shear moduli for aged and un-aged G18 at room and elevated temperatures. The furnace was heated at a rate of approximately 12°C/min, and was held for 15 minutes at each temperature for equilibration

This distinct temperature-dependent modulus behavior for the aged G18 is another motivation for our current work. Our goal is to see whether this unique behavior can be predicted by coupling the various phenomena such as aging, cooling, and reheating-induced self-healing. The eventual goal is to develop a predictive capability for glass ceramic seals such that better seal materials can be developed for improved reliability and durability.

Temperature (°C)	1000-h Aged (GPa)	Un-aged (GPa)
22	60.8 ± 0.3	77.7 ± 0.4
200	61.0 ± 0.3	75.8 ± 0.4
300	62.2 ± 0.3	74.3 ± 0.4
400	69.7 ± 0.3	71.7 ± 0.3
500	70.2 ± 0.3	70.6 ± 0.3
600	70.3 ± 0.3	67.7 ± 0.3
700	69.2 ± 0.3	-----
800	67.4 ± 0.3	-----
30	53.2 ± 0.3	78.1 ± 0.4

Table 1. Young's modulus aged and un-aged G18 at room and elevated temperatures



#### 4. Predicting Young's modulus of glass-ceramic sealant with consideration of aging, micro-damage, and self-healing

##### 4.1 Aging time-dependent volume fraction evolution of crystalline phase

Aging changes the volume fraction of the ceramic phase in the glass ceramic microstructure, hence influencing seal mechanical properties such as Young's modulus, strength, fracture toughness and durability (Han & Tomozawa, 1989; Bhathena et al. 1984; Bentur et al., 1985; Schwarz et al., 2001; Baudin & Villar, 1998). For glass/ceramic sealing materials, the volume fraction of the ceramic crystalline is aging-time dependent under the SOFC operating temperature. At the end of the initial sealing process at 850°C, some volume fraction of the ceramic crystalline is formed. Subjected to the typical operating environment of 750°C, the crystallization process slows down but does not stop. This continuing devitrification causes the volume fraction of the ceramic crystalline in the sealant material to increase with the holding time at the operating temperature.

Assuming that the devitrification of glass/ceramic can reach an asymptotic level after 300 hours of aging/working time at 750°C, the evolution of the volume fraction of the crystalline phases with respect of time  $t$  may be expressed as

$$f_c(t) = f_c^\infty - (f_c^\infty - f_c^0)e^{(-t/A_t)} \quad (5)$$

where  $f_c^\infty$  and  $f_c^0$  represent the volume fractions of the ceramic phase in the stable stage and the initial stage of the sealing process, respectively.  $A_t$  represents the characteristic aging time. Note that various crystalline phases are lumped into one term,  $f_c$ , in this work.

According to the experimental data shown in Figure 1, the parameters in Eq. (5) can be determined for G18 as:

$$f_c^\infty = 72.0, \quad f_c^0 = 54.0, \quad A_t = 40.0(\text{hour}) \quad (6)$$

These are material-specific parameters that are closely dependent on the glass composition and associated heat treatment processes.

##### 4.2 Aging induced micro-voids in glass-ceramic

Aging at high temperature often leads to material property degradations (Nam & Seferis, 1991; Nam & Seferis 1992). One possible degradation mechanism is the appearance of the voids and cracks (Kim et al., 2002).

To capture the effect of aging and cooling-induced microstructure changes on the mechanical properties of the glass ceramic sealant, a continuum damage mechanics model (Jessen & Plumtree, 1991; Jeong & Adib, 2005; Lemaitre, 2002; Sun et al., in press) is used here as a phenomenological approach to the constitutive modeling of the glass/ceramic seal. The microstructure-level heterogeneous G18 is represented by an equivalent homogeneous material with effective properties. The model accounts for the material damage because of various mechanisms (i.e., void growth, void nucleation and coalescence, decohesion between different phases, etc.) in a phenomenological way through a scalar damage variable,  $D$ , that governs the reduction of the homogenized elastic modulus (Sun et al., 2009):

$$E^D(t, T, D) = E(t, T)(1 - D) \quad (7)$$

where  $E^D$  and  $E$  represent the Young's modulus with and without damage,  $t$  is time, and  $T$  is temperature.  $D$  is the quantitative measure of the void volume fraction in comparison with the virgin microstructure.

### 4.3 Possible self-healing of glass-ceramic seals

It should be mentioned that the concept of self-healing glass seals was first reported by Singh (Singh 2006). The rationale behind this concept is that at the SOFC operating temperature, a sealing glass with appropriate properties can heal cracks created during thermal transients. The advantage of this approach is that materials with dramatically different expansions can potentially be used for seals because at the cell operating temperatures, the CTE mismatch-induced, thermo-mechanical stresses can be relaxed out. If proven feasible, this type of seal can tolerate some of the thermal expansion mismatch and still form a functioning seal between materials with a significant expansion mismatch. However, there are still a number of challenges in making a functioning seal with self-healing glasses. The first challenge is that the glass seal must maintain contact with all the components to be sealed without excess creep/flow at a cell operating temperature of 750°C. Concepts involving various ceramic phase stoppers have been proposed to address this. In addition, the self-healing glass seal must be capable of remaining chemically stable under SOFC operating temperatures for the designed stack operating time.

For SOFC stacks under deep thermal cycles, cracking and micro-voids may occur in the glass ceramic sealant because of the tensile residual stress caused by a CTE mismatch of different components during cooling. However, upon reheating, the damage/crack may be healed at temperatures above some threshold temperature because of the flow behavior of the glass phase. Therefore, the scalar damage  $D$  defined in Eq. (7) is temperature and aging-time dependent, which may be simplified as the product of the following uncoupled factors:

$$D = A_D D_T \quad (8)$$

Here  $A_D$  is the aging influence function, representing the increase of the micro-void volume fraction with aging time:

$$A_D = 1 - e^{-t/t_c} \quad (9)$$

where  $t$  is the aging time, and  $t_c$  represents the characteristic time.

$D_T$  in Eq. (8) represents the temperature-dependence of damage, reflecting the possible self-healing behavior of G18 above the threshold temperature,  $T_{th}$ :

$$D_T = D_0 \frac{\pi / 2.0 - \arctan[(T - T_{th}) / R]}{\pi} \quad (10)$$

where  $D_0$  is the damage parameter at room temperature, and  $T_{th}$  is the threshold temperature above which damage to the glass ceramic composite starts to heal,  $T$  is operating temperature and  $R$  is a constant.

### 4.4 Assembly of the phenomenological model

Various formulations and frameworks have been developed to model the mechanical behaviour of composite materials (Bigaud & Hamelin, 1997; Annapragada et al., 2007; Chen

& Argon, 1979; Leble et al., 1999; Ahzi et al., 2003; Makradi et al., 2005). For simplicity, we adopt here the simple Rule of Mixture approach. In general, the Young's modulus of the multi-phase composite materials can be expressed as (Gibson, 2007):

$$E = \sum_{i=1}^m f_i E_i \quad (11)$$

where  $f_i$  and  $E_i$  represent the volume fraction and modulus of the  $i$ th phase, and  $m$  is the number of the phases in the composite material. The volume fractions of all the phases should satisfy

$$\sum_{i=1}^m f_i = 1 \quad (12)$$

In the case of the two phase glass/ceramic sealant composite material, the above equation can be rewritten as

$$E = f_C E_C + (1 - f_C) E_G \quad (13)$$

or

$$E = f_C (E_C - E_G) + E_G \quad (14)$$

where the subscripts "C" and "G" refer to the glass phase and the ceramic phase, respectively. In general, the modulus of the glass phase is temperature dependent, and the modulus of the ceramic crystalline is independent of temperature.

Substituting the aging-time-dependent volume fraction of the ceramic phase, i.e., Eq. (5), into Eq. (14) leads to

$$E(t, T) = (f_C^\infty - f_C^0 e^{(-t/A_t)})(E_C - E_G(T)) + E_G(T) \quad (15)$$

Incorporating the effects of micro-damage and self-healing described in Eq. (7-9) into Eq. (15) yields the following phenomenological model describing the elastic modulus of the glass ceramic materials:

$$E^D(t, T, D) = \left[ (f_C^\infty - f_C^0 e^{(-t/A_t)})(E_C - E_G(T)) + E_G(T) \right] * \left\{ 1 - \frac{D_0}{\pi} (1 - e^{-t/t_c}) \left[ \pi / 2.0 - \arctan \left( \frac{T - T_{th}}{R} \right) \right] \right\} \quad (16)$$

Again,  $f_C^\infty$  and  $f_C^0$  represent the volume fractions of the ceramic phase in the stable stage and at the initial stage of the sealing process, respectively.  $A_t$  represents the characteristic aging time.  $D_0$  is the damage parameter at room temperature, and  $T_{th}$  refers to the threshold temperature above which damage to the glass ceramic composite starts to heal.  $R$  is a material constant,  $t$  is the aging time, and  $t_c$  represents the characteristic time for aging-induced micro-damage.

## 5. Comparison between experimental measurements and predictions

For the phenomenological model described in Eq. (16), the modulus of the ceramic phase is considered to be temperature independent, and the modulus for the glass phase is

considered to be temperature dependent. In general, the Young's modulus of glass drops dramatically over the glass transition temperature,  $T_g$  (McGraw, 1952).

The input Young's moduli used for the glass and crystalline phases are shown in Figure 11 in dashed lines (McGraw, 1952). The predicted Young's moduli of G18 under different aging times are shown in solid lines in Figure 11. The following parameters for Eq. (16) are calibrated based on the experimental data:

$$D_0=0.24, \quad T_{th}=375^\circ\text{C}, \quad R=50^\circ\text{C}, \quad t_c=100 \text{ h}$$

With the proposed phenomenological model, reasonably good comparisons between the predicted and measured Young's modulus have been achieved for both the aged and un-aged G18. This is particularly true for temperatures lower than  $600^\circ\text{C}$ . Above  $600^\circ\text{C}$ , the predicted modulus decreases more rapidly with temperature than the measured data. This is because the predicted modulus is very sensitive to the input temperature-dependent modulus for the glass phase. For temperatures above  $600^\circ\text{C}$ , the Young's modulus for glass may vary dramatically (Bourhis et al., 2001; Andrews, 1924). The exact high-temperature Young's modulus for regular glass is rarely reported, and the high-temperature Young's modulus for the glass phase in G18 has not yet been separately determined. Therefore, for temperatures above  $600^\circ\text{C}$ , the glass moduli used in Figure 10 could have been much lower than the actual values.

It is interesting to note that, by considering the combined effects of aging, micro-voids, and self-healing, the distinct feature of the moduli "cross-over" can be predicted by the the following simple phenomenological model: below  $500^\circ\text{C}$ , the 1000-h aged sample has a lower Young's modulus compared to the 4-h aged sample; above  $500^\circ\text{C}$ , the trend reverses itself when considering self-healing of the glassy phase.

## 6. Conclusions

We have investigated experimentally the effects of aging time, micro-damage induced by cooling down from the operating temperature to room temperature, and self-healing when reheating to operating temperatures on the microstructure and mechanical properties of a glass ceramic sealant. This sealant, a glass ceramic material for SOFC sealing applications, was developed at PNNL. The combined effects of aging, cooling-induced micro-voids, and possible reheating-related self-healing were examined and modeled with some simple, phenomenological models. After the initial sealing process, the crystallization process of G18 slows down but does not stop, and the volume fraction of the crystalline phase increases with aging/working time. In addition, aging causes the diffusion/smearing of the boundaries between the crystalline and the amorphous phases and potentially changes the mechanical properties of the amorphous phase.

Upon cooling to room temperature, shrinkage micro-voids form because of the CTE differences between the crystalline and the amorphous phases. On the stack level, cooling-induced micro-cracks are also likely to occur because of the CTE mismatch between different stack components. These micro-voids and micro-cracks can noticeably degrade the Young's modulus of the glass ceramic seal at room temperature. However, when reheated back to SOFC working temperatures, this study shows that G18 does exhibit some degree of self-healing behaviors because of the flow characteristics of the glass phase at high temperatures. Therefore, the mechanical properties, i.e., the Young's modulus of the glass/ceramic seal material, can be potentially restored to an undamaged level at high temperatures.

The phenomenological model based on some simple mechanical analogs has been developed to capture the above-described mechanical behaviors of glass ceramic seal materials. The aging-time-dependent, crystalline phase evolution model was first developed to describe the increase of crystalline content due to the continuing devitrification during operation. A continuum damage mechanics model was adapted to model the effects of micro-voids and self-healing. Reasonably good comparisons between the measured and the predicted temperature-dependent Young's modulus have been obtained. The modeling parameters presented here were calibrated with the experimental data for G18, and yet the modeling framework should be applicable to glass/ceramic seals in general. The model can be further developed to account for the effects of various processing parameters on the mechanical properties of glass/ceramic seal materials.

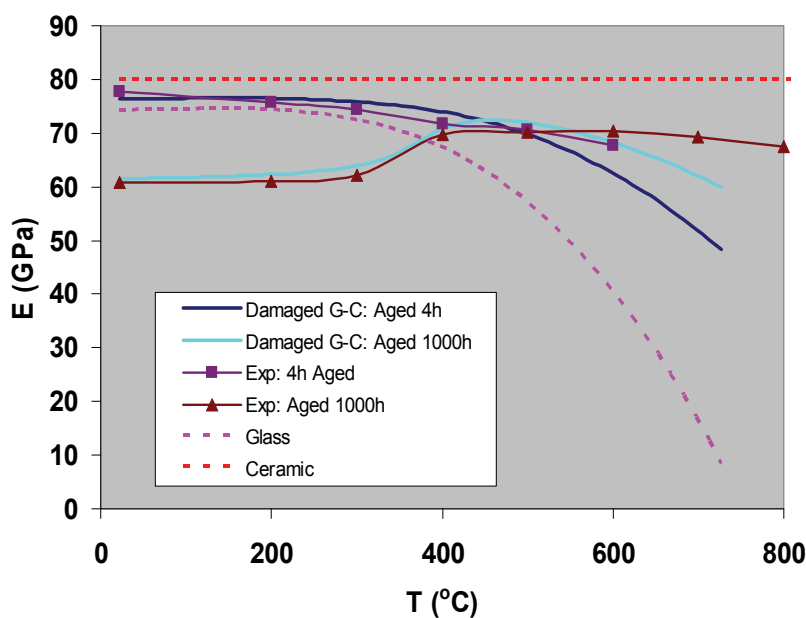


Fig. 11. Predicted and measured Young's modulus versus temperature

## 7. Acknowledgments

Pacific Northwest National Laboratory is operated by Battelle for the U.S. Department of Energy under Contract DE-AC05-76RL01830. The work was funded as part of the Solid-State Energy Conversion Alliance Core Technology Program by the U.S. Department of Energy's National Energy Technology Laboratory.

## 8. References

- Ahzi, S., Makradi, A., Gregory, R., & Edie, D. (2003). Modeling of deformation behavior and strain-induced crystallization in poly(ethylene terephthalate) above the glass transition temperature. *Mechanics of Materials*, Vol. 35, pp. 1139-1148.

- Andrews, J. P. (1924). The Variation of Young's Modulus at High Temperatures. *Proc. Phys. Soc.*, Vol. 36, pp. 169–177.
- Annappagada, S. R., Sun, D., & Garimella, S. V. (2007). Prediction of Effective Thermo-Mechanical Properties of Particulate Composites. *Computational Materials Science*, Vol. 40, No. 2, pp. 255–266.
- ASTM. (2008). Standard Test Method for Dynamic Young's Modulus, Shear Modulus, and Poisson's Ratio for Advanced Ceramics by Sonic Resonance, ASTM, C1198, *American Society for Testing and Materials*.
- Azároff, L. V., Kaplow, R., Kato, N., Weiss, R. J., Wilson, A. J. C., & Young, R. A. (1974). *X-Ray Diffraction*. McGraw-Hill, Columbus, Ohio.
- Baudin, C., & Villar, M. P. (1998). Structural and Morphological Transformations of the (NH<sub>4</sub>, Na)-exchanged Zeolites 4A, 13X and Synthetic Mordenite by Thermal Treatment. *Journal of the American Ceramic Society*, Vol. 81, No. 10, pp. 2741–45.
- Bentur, A., Ben-Bassat, M., Schneider, D. (1985). Durability of glass fibre reinforced cerents with different alkali resistant fibres. *Journal of the American Ceramic Society*, Vol. 68, No. 4, pp. 203–208.
- Bhathena, N., Hoagland, R. G., & Meyrick, G. (1984). Effects of Particle Distribution on Transformation-Induced Toughening in an MgO-PSZ. *Journal of the American Ceramic Society*, Vol. 67, No. 12, pp. 799–805.
- Bigaud, D., & Hamelin, P. (1997). Mechanical properties prediction of textile-reinforced composite materials using a multiscale energetic approach. *Composite Structures*, Vol. 38, No. 1-4, pp. 361–71.
- Bourhis, E. L., Gadaud, P., Guin, J. P., Tournier, N., Zhang, X. H., Lucas, J., & Rouxel, T. (2001). Temperature dependence of the mechanical behaviour of a GeAsSe glass. *Scripta Materialia*, Vol. 45, pp. 317–323.
- Brochu, M., Gauntt, B. D., Shah, R., Miyake, G., & Loehman, R. E. (2006). Comparison between barium and strontium-glass composites for sealing SOFCs. *Journal of the European Ceramic Society*, Vol. 26, No. 15, pp. 3307–3313.
- Chen, I. W., & Argon, A. S. (1979). Steady-State Power-Law Creep in Heterogeneous Alloys with Coarse Microstructures. *Acta Metallurgica*, Vol. 27, pp. 785–791.
- Choi, S. R., & Bansal, N. P. (2005). Mechanical properties of SOFC seal glass composites. *Mechanical, Ceramic Engineering and Science Proceedings*, Vol. 26, No.4, pp. 275–283.
- Chou, Y. S., Stevenson, J. W., & Chick, L. A. (2003). Novel compressive mica seals with metallic interlayers for solid oxide fuel cell applications. *Journal of the American Ceramic Society*, Vol. 86, No. 6, pp. 1003–1007.
- Chung, B. W., Chervin, C. N., Haslam, J. J., Pham, A., Glass, R. S. (2005). Development and characterization of a high performance thin-film planar SOFC stack. *Journal of the Electrochemical Society*, Vol. 152, No. 2, pp. A265–A269.
- Fang, Y., Ravi-Chandar, K., & White, K. W. (2002). Influence of surface residual stress state on crack path evolution in polycrystalline alumina. *Journal of the American Ceramic Society*, Vol. 85, No. 7, pp. 1783–87.
- Fei, Y. (1995). *Mineral Physics and Crystallography, A Handbook of Physical Constants*, AGU Reference Shelf 2, the American Geophysical Union, Washington, D.C.
- Fergus, J. W. (2005). Sealants for solid oxide fuel cells. *Journal of Power Sources*, Vol. 147, pp. 46–47.

- Gibson, R. F. (2007). *Principles of Composite Material Mechanics*, pp. 91–101, CRC Press, Boca Raton, Florida.
- Han, W. T., & Tomozawa, M. (1989). Mechanism of mechanical strength increase of soda-lime glass by aging. *Journal of American Ceramic Society*, Vol. 72, No. 10, pp. 1837–1843.
- Jeong, J., Adib, H., & Pluvinae, V. (2005). Proposal of new damage model for thermal shock based on dynamic fracture on the brittle materials. *Journal of Non-Crystalline Solids*, Vol. 351, No. 24–26, pp. 2065–75
- Jessen, S. M., & Plumtree, A. (1991). Continuum damage mechanics applied to cyclic behaviour of a glass fibre composite pultrusion. *Composites*, Vol. 22, No. 3, pp. 181–190.
- Kim, J., Lee, W., Tsai, S. W. (2002). Modeling of mechanical property degradation by short-term aging at high temperatures. *Composites: Part B*, Vol. 33, pp. 531–543.
- Lahl, N., Singheiser, L., Hilpert, K., Singh, K., & Bahadur, D. (1999). In: Aluminosilicate glass ceramics as sealant in SOFC stacks, pp. 1057–65, *Proceedings of the Sixth International Symposium on Solid Oxide Fuel Cells*, The Electrochemical Society, Pennington, New Jersey, 1999.
- Leble, P., Dong, M., & Schmauder, S. (1999). Self-consistent matrixity model to simulate the mechanical behavior of interpenetrating microstructures. *Computational Materials Science*, Vol. 15, pp. 455–465.
- Lemaitre, J. (2002). Introduction to Continuum Damage Mechanics. In: *Continuum Damage Mechanics of Materials and Structures*, Edited by O. Allix, & F. Hild, pp. 235–238, Elsevier Science Ltd, Amsterdam.
- Makradi, A., Ahzi, S., Gregory, R. V. & Edie, D. D. (2005). A two-phase self-consistent model for the deformation and phase transformation behavior of polymers above the glass transition temperature: Application to PET. *International Journal of Plasticity*, Vol. 21, No. 4, pp. 741–758.
- Marliere, C., Despetis, F., & Phalippou, J. (2003). Crack path instabilities in DCDC experiments in the low speed regime. *Journal of Non-Crystalline Solids*, Vol. 316, No. 1, pp. 21–27.
- McGraw, D. A. (1952). Method for determining Young's modulus of glass at elevated temperatures. *Journal of the American Ceramic Society*, Vol. 35, No. 1, pp. 22–27.
- Meinhardt, K. D., Vienna, J. D., Armstrong, T. R., & Pederson, L. R. (2002). Glass-Ceramic Material and Method of Making. U. S. Patent 6 430 966.
- Nam, J., & Seferis, J. C. (1992). Generalized composite degradation kinetics for polymeric systems under isothermal and nonisothermal conditions. *Journal of Polymer Science, Part B: Polymer Physics*, Vol. 30, pp. 455–63.
- Nam, J., Seferis, J. C. (1991). A composite methodology for multistage degradation of polymers. *Journal of Polymer Science, Part B: Polymer Physics*, Vol. 29, pp. 601–608.
- Nielsen, K. A., Solvang, M., Nielsen, S. B. L., Dinesen, A. R., Beeaff, D., Larsen, P. H. (2007). Glass composite seals for SOFC application. *Journal of the European Ceramic Society*, Vol. 27, No. 2–3, pp. 1817–22.
- Roos, C., Becker, O., & Siebers, F. (2007). Microstructure and stresses in a keatite solid-solution glass-ceramic. *Journal of Materials Science*, Vol. 42. pp. 50–58.

- Schwarz, I., Stranz, M., Bonnet, & M., Petermann, J. (2001). Changes of mechanical properties in cold-crystallized syndiotactic polypropylene during aging. *Colloid Polymer Science*, Vol. 279, pp. 506–512.
- Simner, S. P., & Stevenson, J. W. (2001). Compressive mica seals for SOFC applications. *Journal of Power Sources*, Vol. 102, pp. 310–316.
- Singh, R. N. (2007). Sealing Technology for Solid Oxide Fuel Cells (SOFC). *International Journal of Applied Ceramic Technology*, Vol. 4, No. 2, pp. 134–144.
- Singh, R. N. (2006). High-Temperature Seals for Solid Oxide Fuel Cells (SOFC). *Journal of Materials Engineering and Performance*, Vol. 15, No. 4, pp. 422–426.
- Smeacetto, F., Salvo, M., Ferraris, M., Cho, J., Boccaccini, A. R. (2008). Glass-ceramic seal to join Crofer 22 APU alloy to YSZ ceramic in planar SOFCs. *Journal of the European Ceramic Society*, Vol. 28, No. 1, pp. 61–68.
- Sun, X., Liu, W. N., Chen, W. N., & Templeton, D. (2009). Modeling and Characterization of Dynamic Failure of Soda-lime Glass Under High Speed Impact. *Journal of Impact Engineering*, Vol. 36, No. 2, pp. 226–234.
- Teagan, W. P., Thijssen, J. H. J. S., Carlson, E. J., & Read, C. J. (2000). Current and Future Cost Structures of Fuel Cell Technology Alternatives. In: *Procedures of the 4<sup>th</sup> European Solid Oxide Fuel Cell Forum*, A. J. McEvoy (Ed.), Lucerne, Switzerland, Vol. 2, pp. 969–980.
- Weil, K. S., Deibler, J. E., Hardy, J. S., Kim, D. S., Xia, G. G., Chick, L. A., & Coyle, C. A. (2004). Rupture testing as a tool for developing planar solid oxide fuel cell seals. *Journal of Materials Engineering and Performance*, Vol. 13, No. 3, pp. 316–326.
- Yang, Z., Meinhardt, K. D., Stevenson, J. F. (2003). Chemical compatibility of barium-calcium-aluminosilicate-based sealing glasses with the ferritic stainless steel interconnect in SOFCs. *Journal of the Electrochemical Society*, Vol. 150, No. 8, A1095–A1101.
- Yang, Z., Xia, G., Meinhardt, K. D., Weil, K. S., & Stevenson, J. W. (2004). Chemical stability of glass seal interfaces in intermediate temperature solid oxide fuel cells. *Journal of Materials Engineering and Performance*, Vol. 13, No. 3, pp. 327–334.



# Crack-Healing Ability of Structural Ceramics and Methodology to Guarantee the Reliability of Ceramic Components

Koji Takahashi, Kotoji Ando and Wataru Nakao  
*Yokohama National University, Yokohama  
 Japan*

## 1. Introduction

The heat-resistant limit of structural ceramics is 1273K ~ 1773K, which is greatly superior to that of metallic material. Structural ceramics are a candidate element for high-temperature apparatuses such as gas-turbines and fusion reactors. However, the fracture toughness of ceramics is fairly low compared with metallic material, and the following problems have occurred. (1) Cracks occur by the usual machining process (grinding, polish, etc.), lowering the reliability. In order to prevent this, precise polishing is required in the final stage, which is time-consuming, and there are also problems with fabrication efficiency and fabrication cost (2) Crack sizes of about 10 ~ 30  $\mu\text{m}$  in depth affect the reliability. The nondestructive-inspection technology for detecting cracks of 10 ~ 30  $\mu\text{m}$  is underdeveloped. Therefore, the reliability of major parts is low. (3) There is a possibility that a crack will occur in the components while they are being used at higher temperatures, by whatever cause. When a crack occurs, the reliability is greatly lowered.

The options for resolving these problems are as follows. (a) Improve the fracture toughness of the material by such means as microstructure control and fiber reinforcement. (b) Conduct a nondestructive inspection before use, and detect and repair any dangerous cracks found. (c) Conduct a proof test to prevent use of a low reliability member. (d) Induce a self-crack-healing ability, so that all dangerous cracks can be healed. There are world-wide active investigations of options (a) to (c). In this chapter, special attention is paid to method (d), the self-crack-healing ability of structural ceramics.

There are three advantages to using a material that can heal surface cracks. (A) If the self-healing of the surface crack which exists is carried out after an efficient machine operation is performed, then there is a great advantage in fabrication efficiency and fabrication cost. (B) Since all surface cracks are healed, reliability improves greatly. (C) It is advantageous if a crack which occurs while in service can be healed and full recovery of strength achieved.

From the above ideas, the self-crack-healing behaviors of ceramics were investigated by Ando and co-worker. Silicon nitride (Ando et al., 1998; Yao et al., 2001), alumina (Takahashi et al., 2003; Ando et al., 2004; Nakao et al., 2005a), and mullite (Chu et al., 1995; Nakao et al., 2006), SiC (Kim Y.W. et al., 2003; Lee et al., 2005a) and  $\text{ZrO}_2$  (Houjou et al., 2010), with the self-crack-healing ability have been developed. In the following section, an outline is given of the crack-healing behavior of ceramics.

## 2. Nano-composite and multi-composite

The nano-composite material has the following specificity (Niihara, 1991; Ando et al., 2004) .

1. SiC particles of nano size are added to the material, preventing grain growth of the matrix in the sintering process, and improving the bending strength through grain refinement: For example, in the case of an alumina, bending strength can be increased from about 400 MPa to 700 ~ 1000 MPa (Ando et al., 2004).
2. SiC particles of nano size 15 to 30 vol% added to the material, and induce a self-crack-healing ability.
3. SiC particles of nano size are distributed not only in the grain boundaries of an alumina, but in individual grains and increases the heat-resistant limit by 300 K.

The fracture-surface photography of the  $\text{Al}_2\text{O}_3$  nano-composite material is shown in Fig 1. Most of the SiC particles were distributed uniformly in the grain boundaries; however, several nanosized SiC particles were distributed in the  $\text{Al}_2\text{O}_3$  grain, as shown in Fig. 1 (Ando et al., 2004).

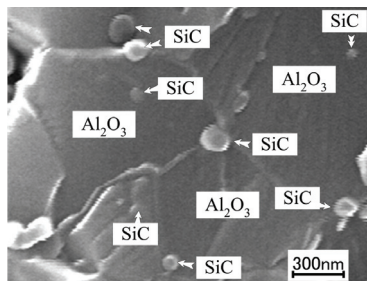


Fig. 1. Microstructure of  $\text{Al}_2\text{O}_3$ / 15 vol% SiC particles nanocomposite

A multi-composite material is a material which combines nanosized SiC particles and SiC whiskers in the proportion of 25 to 30%, and has excellent self-crack-healing ability, fracture toughness, strength (Nakao et al., 2006, Takahashi et al., 2007). The proportion fraction of SiC particles to SiC whiskers is determined by taking into consideration the self-crack-healing ability and fracture toughness requirements. If the proportion fraction of SiC particles is increased, then the crack healing rate will be increased. If the proportion fraction of SiC whiskers is increased, then the fracture toughness will be improved (Nakao et al, 2005a).

The composition system of the ceramics used in this paper and the effective temperature ranges in which crack-healing is possible are shown in Table 1. The room-temperature bending strength and fracture toughness of the multi-composite ceramics are shown in Table 2.

It has been common knowledge for many years that the strength of ceramics is improved by heat-treatment in air. This occurs by three mechanisms, as follows.

- i. The crack-healing phenomena, which is explained in this paper.
- ii. Re-sintering.
- iii. Release of tensile residual-stress.

In case ii), the material must be heated to a nearly sintering temperature, which is a higher temperature than it is heated in the crack-healing phenomena (Lange et al., 1970; Kim et al., 2003). In case iii), the strength recovery rate is small and the crack still remains (Thompson et al., 1995).

The material with a self-crack-healing ability described in this paper has all of the following attributes.

1. The material itself detects an occurrence of a crack and begins crack-healing activities.
2. A crack causes a 50 ~ 90 % reduction in the strength of a material, but in material with a self-crack healing ability, the material heals the crack completely, and the strength of the material is completely recovered.
3. The strength of a crack-healed area is equivalent to or higher than that of a matrix area up to about 1673 K.

Materials	Effective Temperature Range for crack-healing			
Si <sub>3</sub> N <sub>4</sub> / 20 vol% SiC particles composite (8 wt% Y <sub>2</sub> O <sub>3</sub> )	1073	—	1573	K
Al <sub>2</sub> O <sub>3</sub> / 15 vol% SiC particles composite	1173	—	1573	K
Mullite/ 15 vol% SiC particles composite	1273	—	1473	K
SiC sintered with Sc <sub>2</sub> O <sub>3</sub> and AlN	1473	—	1673	K

Table 1. Effective temperature range of self-crack-healing for several ceramics

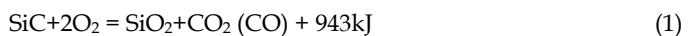
Sample name	Content			Strength (MPa)	Fracture Toughness (MPam <sup>1/2</sup> )
	Alumina	Mullite	SiC Particle (Diameter:0.27 μm) SiC Whisker (Diameter:0.8-1.0 μm, Length:30-100 μm)		
AS15P	85		15	850	3.2
AS30P	75		30	1050	3.6
AS20W	80		20	970	4.8
AS30W	70		30	830	5.8
AS20W10P	70		10	980	5
MS15P		85	25	470	2.2
MS15W		85	15	710	2.8
MS20W		80	20	840	3.6
MS25W		75	25	820	4.2
MS15W5P		80	5	750	3.2
MS15W10P		75	10	740	3.5

Table 2. Strength and fracture toughness of Al<sub>2</sub>O<sub>3</sub> and Mullite reinforced by SiC particles and Whiskers

### 3. Nano-composite and multi-composite

#### 3.1 Mechanism of crack healing

The crack healing of ceramics developed by the authors is caused by the following oxidation reaction of SiC.



From Eq.(1), it can easily be understood that a monolithic mullite or a monolithic alumina does not reveal a crack healing ability, since oxidation is saturated in these materials. A schematic diagram of the crack healing mechanism is shown in Fig 2. The following three conditions must be met for a crack-healed area to recover completely.

- i. The volume between the crack walls must be completely filled with the products formed by the crack-healing reaction:
- ii. The strength of the crack-healing substance must be equivalent to or higher than that of the matrix:

There is a glass phase and a crystalline phase in  $\text{SiO}_2$  in Eq.(1). If the crack-healing material was crystal  $\text{SiO}_2$ , then the crack-healed sample would exhibit high bending strength even at an elevated temperature. However, if the crack-healing material was glassy  $\text{SiO}_2$ , then the crack-healed sample would exhibit low bending strength at an elevated temperature. A key point of crack-healing technology is how many crystalline phases are deposited in a crack-healing substance. The large exothermic heat of 943 kJ in Eq. (1) seems to satisfy this condition.

- iii. The crack healing substance must be strongly bonded to a matrix.

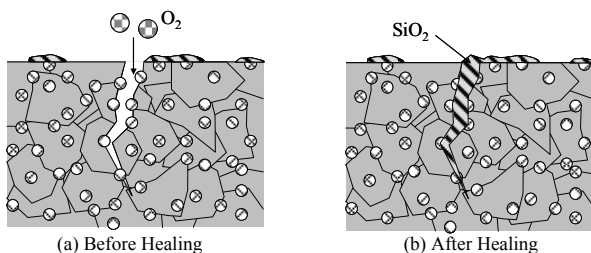


Fig. 2. Schematic illustration of crack-healing mechanism

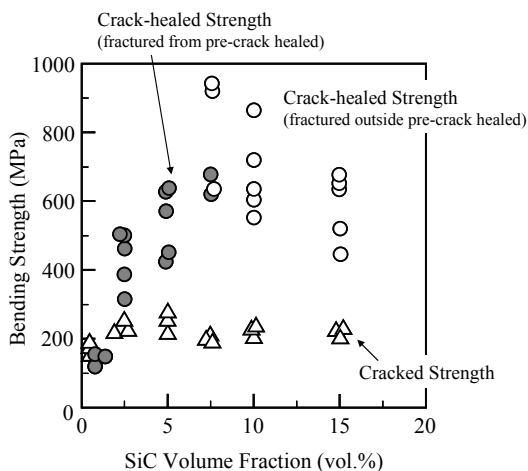


Fig. 3. Crack-healed and cracked strength of a  $\text{Al}_2\text{O}_3/\text{SiC}$  composites as a function of SiC volume fraction

Bonding to a matrix is attained by the huge exothermic heat of 943 kJ by fusion and mixture of a matrix and a healing substance. How much nano size SiC should be added to the  $\text{Al}_2\text{O}_3$  matrix in order to satisfy the three crack-healing conditions? We investigated the effect of the volume fraction of SiC on the crack-healing behavior of an  $\text{Al}_2\text{O}_3/\text{SiC}$  composite.

Figure 3 shows the experimental results. The crack introduced on the test specimen is a semi-elliptical crack 100  $\mu\text{m}$  in surface length and 45  $\mu\text{m}$  in depth (hereafter called a standard crack). The open circles show the fracture of the specimens initiated from outside the crack-healed zone, indicating that complete crack healing occurred. With respect to strength, the optimal volume fraction of SiC is 7.5 to 10 %. However, with respect to crack-healing ability, a volume fraction of SiC larger than 10 % is recommended. However, when the SiC additive rate exceeds 30%, the strength begins to vary greatly, since a SiC agglomeration is formed. On the other hand, a large crack can be healed with an increased SiC volume fraction. The authors recommend a standard SiC volume fraction of 15 ~ 30 %.

### 3.2 Oxygen partial pressure and temperature dependency of crack-healing behavior

We used three-point bending-test specimens as shown in Fig 4 to evaluate the bending strength ( $\sigma_B$ ) of a crack-healed specimen. We introduced the standard crack into the central part of the test specimen. The decreasing rate of the strength by this crack was 50 to 85%, although it was greatly dependent on the fracture toughness of the material.

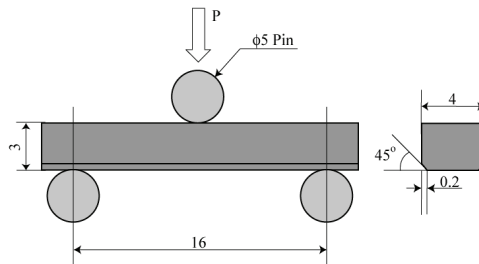


Fig. 4. Dimensions of three point bending specimens

The influence of atmosphere on the crack-healing behavior of  $\text{Al}_2\text{O}_3/15 \text{ vol\% SiC}$  is shown in Fig 5 (Kim B.S. et al., 2003). The bending strengths ( $\sigma_B$ ) of a as-received test specimen are about 650 MPa. When a standard crack was introduced into this specimen, the  $\sigma_B$  was reduced to 180MPa and the decreasing rate of  $\sigma_B$  was about 73 %. However, when the crack healing of this pre-cracked specimen was carried out in air at 1573K for 1 h, the bending strength ( $\sigma_B$ ) was improved up to about 800 MPa. The  $\sigma_B$  of a crack-healed specimen is larger than the  $\sigma_B$  of a as-received specimen. The reason for this is because even minute cracks on the surface of the as-received specimens recovered completely. However, when the pre-cracked specimens were heated in a vacuum,  $\text{N}_2$  gas, and argon gas, the  $\sigma_B$  recovered to at most 350 MPa. The recovery of  $\sigma_B$  is insufficient. The slight increase of  $\sigma_B$  by this heat-treatment occurred because the tensile residual-stress of the crack tip was removed. Similar crack healing and strength recovery behaviors were reported in mullite (Chu et al., 1995),  $\text{Al}_2\text{O}_3$  (Chou et al., 1998) and  $\text{Si}_3\text{N}_4$  (Ando et al., 1998; Jung et al., 2008a). Figure 6 shows a specimen after the bending test. Fig 6 (a) shows the case of a pre-cracked specimen. The pre-cracked specimens fractured from the pre-crack division. In the case of Fig 6 (b), because a crack was healed completely, the crack was initiated from matrix division.

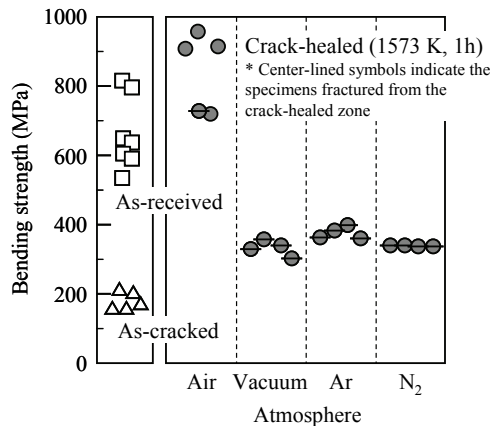


Fig. 5. Crack-healing behavior of alumina / 15 vol% 0.27  $\mu\text{m}$  SiC particles composite under several atmospheres

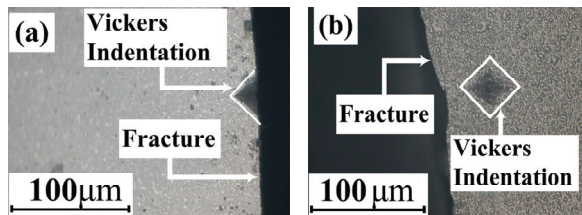


Fig. 6. Fracture initiation of  $\text{Al}_2\text{O}_3$  / 15 vol% SiC particles composite (a) as-cracked (b) crack-healed at 1573 K for 1 h in air, from that one can find that pre-crack healed is stronger than the other part

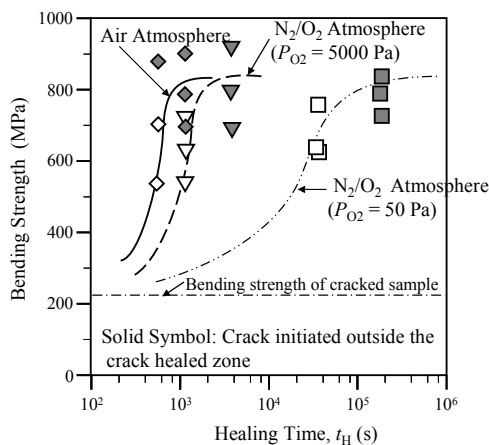


Fig. 7. Effect of partial oxygen pressure on crack healing behavior at 1673K

As described in section 3.1, crack healing is dependent on an oxidation reaction. Therefore, it is assumed that crack-healing behavior is greatly dependent on oxygen partial pressure. The influence of oxygen partial pressure on crack-healing behavior is shown in Fig 7, in  $\text{Al}_2\text{O}_3/\text{SiC}$  composite materials (Osada et al., 2009). When crack-healing was carried out at 1673K, in air (oxygen partial pressure: 21kPa), the crack healed completely in about 20 minutes. When the oxygen partial pressures were 5000 and 50 Pa, the crack healed completely in about 1 h and 70 h, respectively. Moreover, the test specimen which healed in thin oxygen showed a bending strength equivalent to a matrix division to 1673K. It is said that the oxygen partial pressure in the exhaust gas of a gas-turbine or a vehicle is about 8kPa-10kPa, which is approximately half in an atmosphere. So it is anticipated that the surface crack can be healed in oxygen partial pressure in the exhaust gas of a gas-turbine or a vehicle.

The influence of temperature on crack-healing behavior is shown in Fig 8 (Ando et al., 2009; Nakao et al., 2009). When the crack-healing times were 10 h and 300 h, the temperatures in which a crack was healed completely were about 1473 K and 1273 K, respectively. By conducting an experiment as shown in Fig 8 on various materials, we found the shortest time  $t_{\text{HM}}$  which can heal a crack completely from a certain temperature  $T_{\text{HL}}$ . Fig 9 shows the Arrhenius plot of the experimental result. The relationship between  $1/t_{\text{HM}}$  and  $1/T_{\text{HL}}$  can be shown by the Arrhenius equation as follows (Ando et al., 2002a).

$$\frac{1}{t_{\text{HM}}} = Q_0 \exp\left(\frac{-Q_{\text{H}}}{RT_{\text{HL}}}\right) \quad (2)$$

The activation-energy ( $Q_{\text{H}}$ ) and proportional moduli ( $Q_0$ ) of each material were calculated from Fig. 9. The result is shown in Table 3. By using Table 3, the relationship between the time ( $t_{\text{HM}}$ ) required to heal a standard crack completely and the crack-healing temperature can be estimated. However, Eq. (2) is applicable in  $t_{\text{HM}} = 1 \text{ h} \sim 300 \text{ h}$ .

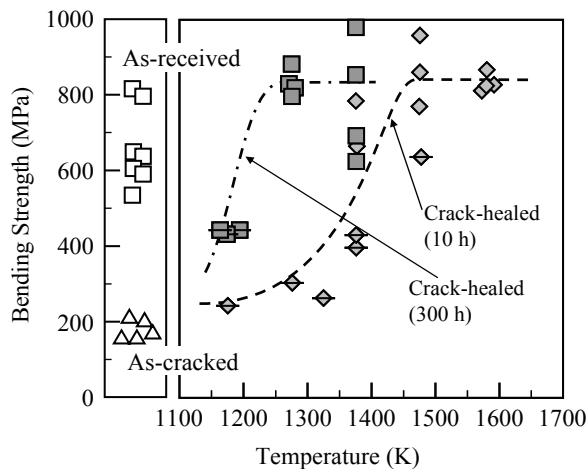


Fig. 8. Relationship between crack-healing temperature and strength recovery for  $\text{Al}_2\text{O}_3/15 \text{ vol\% SiC}$  particles composite

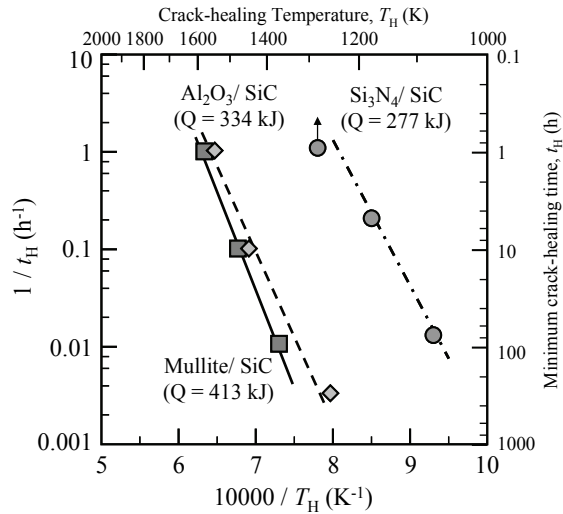


Fig. 9. Arrhenius plots on the crack-healing of several ceramics having crack-healing ability

Material	Activation Energy $Q_H$ (Kj/mol)	Proportional Coefficient $Q_0$ (1/hour)
$Si_3N_4/SiC$	277	$4.2 \times 10^{11}$
$Si_3N_4$	150	$5.3 \times 10^4$
$Al_2O_3/SiC$	334	$1.7 \times 10^{11}$
Mullite/SiC	413	$4.7 \times 10^{23}$

Table 3. Active energy and proportional coefficient for crack-healing

### 3.3 Crack-length dependency of crack-healing behavior and strength

The crack-length dependency of a fracture stress or a crack-healing behavior is important. The crack-length dependency of a fracture stress or a crack-healing behavior obtained with  $Al_2O_3$  strengthened with SiC whiskers is shown in Fig 10 (Nakao et al., 2005a). The crack-healing conditions are 1673K and 1h in air. The  $2c$  in Fig. 10 is the surface length of a semi-elliptical crack. The aspect ratio of a crack is about 0.9. The open triangles are the bending strength ( $\sigma_B$ ) of a pre-cracked specimen, and the solid circles are the bending strength of a crack-healed specimen. When the pre-crack length was less than 250  $\mu m$ , the specimens recovered bending strength nearly completely and fractured from the matrix division except for one example. This result showed that the pre-crack length in which crack healing is possible is about 250  $\mu m$ . In addition, with the material shown in Table 1 and Table 2, the pre-crack length in which crack healing is possible is about 250  $\mu m$ , as in the case of Fig 10.



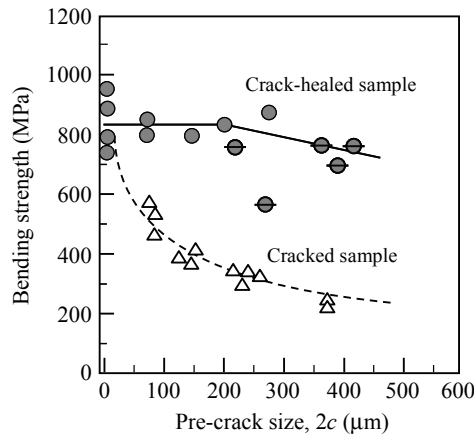


Fig. 10. Bending strength of the crack-healed  $\text{Al}_2\text{O}_3$  / 30 vol% SiC whiskers composite as a function of surface length of a semi-elliptical crack

#### 4. High-temperature strength characteristic of crack-healed specimen

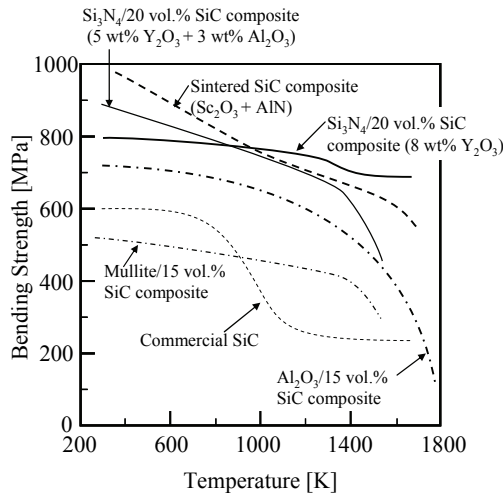


Fig. 11. Temperature dependences of the bending strength of the typical several ceramics crack-healed

The temperature dependency of the bending strength ( $\sigma_B$ ) of a crack-healed specimen is shown in Fig. 11. Each test specimen was crack healed by an optimum condition after a standard crack was introduced. The heat resistance limit for the bending strength of  $\text{Al}_2\text{O}_3/\text{SiC}$  is about 300 K higher than that of monolithic  $\text{Al}_2\text{O}_3$ ; this excellent increase in the heat resistance limit was attained by a nano-composite, as mentioned in section 2. The heat-resistant limit at the crack-healed division of the commercial SiC was 873K, much lower than that of the matrix division (Lee et al., 2005b). As shown in the figure, a new SiC, which

has a heat-resistant limit of a crack-healed division of about 1673K, has been developed, and we examined its usage (Lee et al., 2005a). The heat-resistant limit of the silicon-nitride with  $\text{Al}_2\text{O}_3$  added to it was about 1273K. The heat-resistant limit of the new silicon nitride which improves the composition system is about 1673K, which is higher than the heat-resistant limit of the silicon nitride with  $\text{Al}_2\text{O}_3$  added. The large improvement in such a heat-resistant limit was attained by the crystallization of a grain boundary or a crack-healing substance. In addition, most test specimens fractured from the matrix division below to the heat-resistant limit temperature among the materials of Fig. 11, except the commercial SiC. This implied that the crack-healing division had sufficient bending strength.

## 5. Crack-healing behavior of machined specimens

In general, final machining processes such as polishing and lapping are performed to remove non-acceptable flaws. Although these processes are generally very costly, they cannot eliminate minute cracks. Moreover, even if final machining is adopted, a minute crack may remain, causing a reliability problem. It is anticipated that substituting the crack-healing process for the final machining processes leads to economical manufacturing of ceramic components with high reliability. The crack-healing behavior of machined specimens was investigated by several researchers (Lee et al., 2005c; Osada et al., 2007; Jung et al., 2008b). The experimental results showing the effects of crack-healing on increasing the reliability of machined components will be explained (Osada et al., 2007).

Machined  $\text{Al}_2\text{O}_3/20$  vol.% SiC whiskers having a semicircular groove were used. The sintered plates were cut into 3 mm × 4 mm × 22 mm rectangular bar specimens. A semicircular groove was made at the center of the smooth specimens by using a diamond-coated ball-drill as shown in Fig. 12. The cut depth by one pass ( $d_c$ ) during machining of the semicircular groove was  $d_c = 5 \sim 15$   $\mu\text{m}$ .

All fracture tests were performed on a three-point bending system with a span of 16 mm, as shown in Fig. 12. The crosshead speed was 0.5 mm/min. The tests were conducted at room temperature. The local fracture stresses ( $\sigma_{\text{LF}}$ ) considering the stress concentration factor of the semicircular groove ( $\alpha = 1.2$ ) were evaluated.

Figure 13 shows the strength of the machined specimens with a semicircular groove as a function of the cut depth by one pass ( $d_c$ ). The open triangle symbols show the local fracture stress ( $\sigma_{\text{LF}}$ ) of the as-machined specimen. The  $\sigma_{\text{LF}}$  of the as-machined specimens decreased with increasing  $d_c$ . This behavior was caused by the fact that the crack depth caused by machining increased with increasing  $d_c$ . The as-machined specimens always fractured from the surface cracks caused by machining, as shown in Fig. 14. Figure 14 shows the scanning electron microscope (SEM) images of the fracture surface of the as-machined specimen. The dashed lines in Fig. 14 indicate the crack front. As shown in this figure, these surface cracks acted as the fracture initiation. Thus, the  $\sigma_{\text{LF}}$  of the as-machined specimens decreased compared with the healed smooth specimens. The open square symbols in Fig. 13 show the  $\sigma_{\text{LF}}$  of the machined specimen healed at 1673 K for 10 h in air. The  $\sigma_{\text{LF}}$  of these specimens increased significantly by crack healing. The  $\sigma_{\text{LF}}$  of the machined specimens was almost equal to the fracture stress of the healed smooth specimens (solid circles). Thus, the surface cracks introduced by the machining process were healed.

Therefore, it was concluded that crack healing could be an effective method for improving the structural integrity of machined alumina and reducing machining costs.

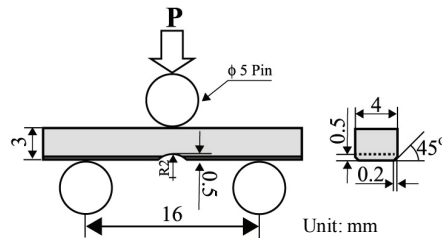


Fig. 12. Schematics of machined specimen

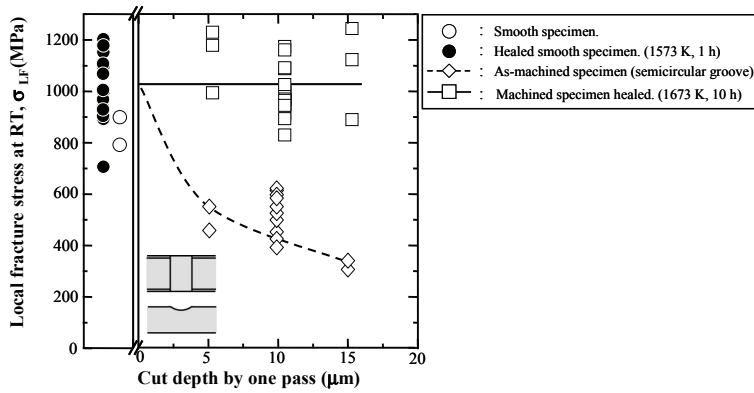


Fig. 13. Effect of depths of cut by one pass on the local fracture stress at room temperature of the machined specimens healed

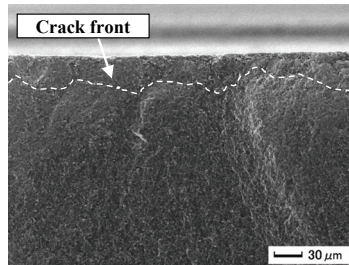


Fig. 14. SEM images of fracture surface of as-machined specimen

## 6. Crack-healing behavior during service

Ceramic components are often operated continuously under constant or cyclic loading at elevated temperatures under lower oxygen partial pressure. If a crack initiates during service, the component's reliability will be considerably reduced. If the crack could be healed under even service conditions, and the healed zone had sufficient strength, the reliability and lifetime of ceramic components could be increased. The crack-healing behaviors under constant or cyclic stress have been systematically studied for  $\text{Si}_3\text{N}_4/\text{SiC}$

(Ando et al, 2002b; Takahashi et al., 2005), Mullite/SiC (Ando et al., 2001; Takahashi et al. 2007),  $\text{Al}_2\text{O}_3/\text{SiC}$  (Nakao et al., 2005b), and SiC (Lee et al., 2005a). Pre-cracks of 100  $\mu\text{m}$  can be healed completely, even under constant or cyclic stress.

To take advantage of the crack-healing ability during service, it is essential to determine the threshold stress for crack-healing below which a crack can be completely healed. In this section, the critical stress condition for crack healing in  $\text{Si}_3\text{N}_4/\text{SiC}$  and other ceramics are shown.

### 6.1 Crack-healing behavior of $\text{Si}_3\text{N}_4/\text{SiC}$ under stress and low oxygen pressure

The material studied was a hot-pressed SiC-particle reinforced  $\text{Si}_3\text{N}_4$  that contained 20 wt% SiC particles and 8 wt%  $\text{Y}_2\text{O}_3$  as a sintering additive. Semi-circular surface cracks of 100  $\mu\text{m}$  in surface length were introduced at the center of the tensile surface of the bending test specimens using a Vickers indenter. After introduction of the pre-cracks, crack-healing tests under cyclic or constant stress were carried out. Figure 15 shows the crack-healing process. Crack-healing was carried out under cyclic ( $\sigma_{\text{max, ap}}$ ) or constant ( $\sigma_{\text{ap}}$ ) bending stresses at a healing temperature ( $T_h$ ) for a prescribed healing time ( $t_h$ ). After the crack-healing process, the bending strengths of the specimens were measured at room temperature in air.

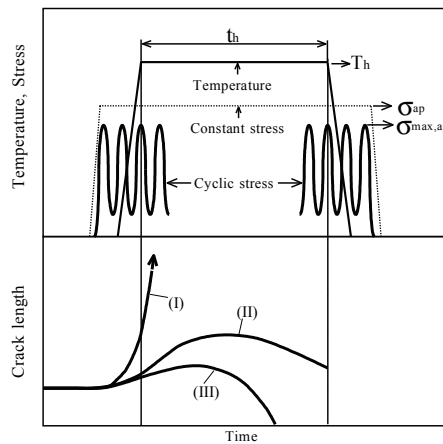


Fig. 15. Schematic illustration of crack-healing under stress and crack growth behaviors

Figure 16 shows the results of the bending tests on specimens crack-healed at 1473K for 5h under constant stress in  $P_{\text{O}_2}=500$  Pa (Takahashi et al., 2010). The solid triangles represent the bending strengths of the crack-healed specimens. Open triangle symbols indicate the bending strengths of the pre-cracked specimens. The asterisks indicate specimens that fractured outside the crack-healed zone, suggesting that the pre-cracks were healed completely. The threshold stresses for crack-healing were defined as the maximum stresses below which the crack-healed specimens recovered their bending strengths and below which most specimens fractured outside the crack-healed zone. The specimens crack-healed under a constant stress of 200 MPa showed quite high bending strength, comparable to that of the specimens crack-healed under no stress. Most of the specimens crack-healed under 200 MPa fractured outside the crack-healed zone. However, the specimens crack-healed under a constant stress of 250 MPa showed low bending strength and fractured from the

crack-healed zone. Therefore, the threshold stress for crack-healing in air was determined to be 200 MPa. These results indicate that complete strength recovery could be achieved by crack-healing even under service conditions, i.e., with an applied stress below  $\sigma_{app.}=200$  MPa and an oxygen partial pressure over  $P_{O_2} = 500$  Pa.

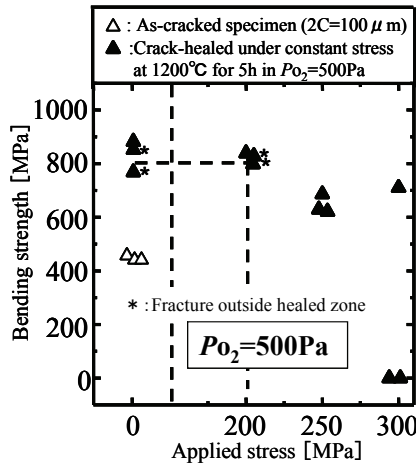


Fig. 16. Room temperature bending strength of crack-healed specimen as a function of applied stress during crack-healing in  $P_{O_2}=500$ Pa at 1473K. ( $Si_3N_4/SiC$ )

Figure 17 shows the bending strength ( $\sigma_B$ ) and cyclic fatigue limit ( $\sigma_{f0}$ ) at the healing temperatures between 1173 K and 1473 K. The ratio of  $\sigma_{f0}/\sigma_B$  was 0.67 ~ 0.86 at each healing temperature (Takahashi et al., 2005). Therefore, it can be concluded that the cyclic fatigue limit was sufficiently high even at the healing temperature.

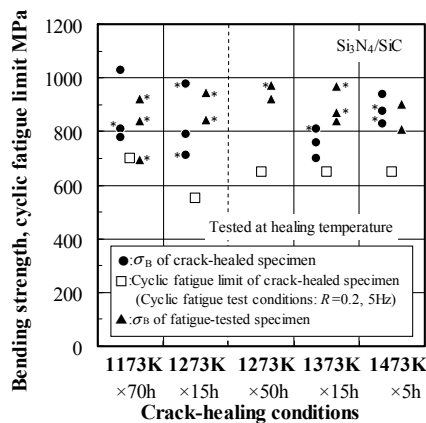


Fig. 17. Results of bending tests and cyclic fatigue tests of  $Si_3N_4/SiC$  at healing temperatures between 1173 K and 1473 K. Cyclic stress during crack-healing:  $\sigma_{max} = 210$  MPa,  $R = 0.2$  and  $f = 5$ Hz. Asterisk indicate that fracture occurred outside of the crack-healed zone

On the bottom of Fig. 15, the crack-healing behaviors under stress are indicated schematically (Takahashi et al., 2005). The change in the crack-length during crack-healing is divided into three cases, (I), (II) and (III). In process (I), slow crack growth from the pre-crack tip occurs and the cracks lead the specimen to failure because the crack growth rate is higher than the crack-healing process. In process (II), slow crack growth from the pre-crack tip also occurs. The crack-healing process starts at high temperature, the crack growth rate decreases due to crack-healing and finally the cracks are healed. In process (III), slow crack growth from the pre-crack does not occur, and thus the pre-cracks are easily healed.

In the case of crack-healing under the constant bending stress ( $\sigma_{ap}$ ) of 250 MPa and 300 MPa, the crack-healing behavior is classified into process (I) or (II). However, in the case of  $\sigma_{ap}$  = 200 MPa, the crack-healing behavior is classified into process (III). The applied stresses are lower than the threshold stress for crack-healing and the pre-cracks were healed easily.

## 6.2 Threshold stress for crack-healing for $\text{Al}_2\text{O}_3/\text{SiC}$ and Mullite/ $\text{SiC}$

Figure 18 shows the threshold constant or cyclic stress for crack healing as a function of the bending strength of pre-cracked specimens (Nakao et al., 2007).  $\text{Al}_2\text{O}_3/15 \text{ vol}\% \text{ SiC}$  particles (AS15P),  $\text{Al}_2\text{O}_3/15 \text{ vol}\% \text{ SiC}$  whiskers (AS15W), mullite/15 vol% SiC particles (MS15P), and mullite/15 vol% SiC whiskers (MS15W) were tested. The closed and open symbols indicate the threshold constant and cyclic stresses, respectively. All data except that of MS15W are satisfied by the proportional relation in spite of the different crack-healing conditions. The proportional constants for the relationship between the threshold stress and bending strength of pre-cracked specimens is 64 % for constant stress and 76 % for cyclic stress.

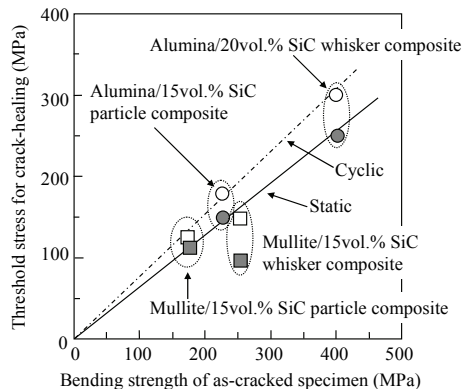


Fig. 18. Relation between threshold stress during crack-healing and the fracture strength for the corresponding as-cracked specimens

## 7. A methodology to increase the structural integrity against embedded flaws

Oxygen is necessary for crack-healing, and thus embedded flaws such as pores and abnormally large grains cannot be healed. These facts suggest the importance of a proof test for higher reliability. However, engineering ceramics show nonlinear fracture behavior as shown in Fig. 19, and ceramics components are not used only at the proof-tested temperatures. Ando et al. have proposed a theory to evaluate the temperature dependence of a guaranteed

(minimum) fracture stress of a proof-tested sample based on nonlinear fracture mechanics (Ando et al., 2002c). In this section, the theory and its application are explained.

The nonlinear fracture behavior is expressed very well by the process zone size failure criterion, as shown in Fig. 19 proposed by Ando et al (Ando et al., 1993). The criterion is expressed by eq. (3) as follows:

$$D_C = \frac{\pi}{8} \left( \frac{K_{IC}}{\sigma_0} \right)^2 = a_e \left\{ \sec \left( \frac{\pi \sigma_C}{2 \sigma_0} \right) - 1 \right\} \quad (3)$$

where  $D_C$  is the critical process zone size,  $\sigma_C$  and  $\sigma_0$  are the fracture stress of the as-cracked specimen and the plain specimen (intrinsic bending strength), respectively,  $K_{IC}$  is the plane strain fracture toughness and  $a_e$  is the equivalent crack length.

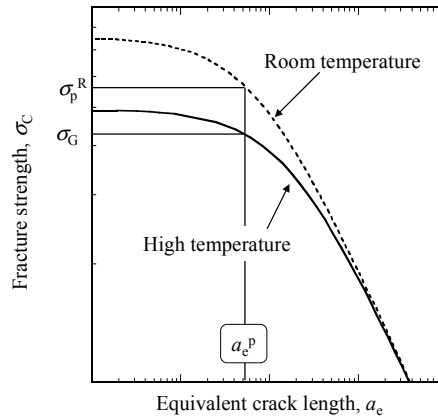


Fig. 19. Schematic illustration of proof-test theory and the effect of equivalent crack on fracture strength at room temperature and high temperature

Figure 19 shows a schematic relationship between  $\sigma_C$  and  $a_e$ . The dotted line and solid line show the relationship between  $\sigma_C$  and  $a_e$  at room temperature and high temperature, respectively. If the proof test is carried out at room temperature, the maximum residual equivalent crack size,  $a_e^P$ , can be expressed by eq. (4):

$$a_e^P = \frac{\pi}{8} \left( \frac{K_{IC}^R}{\sigma_0^R} \right)^2 \left\{ \sec \left( \frac{\pi \sigma_p^R}{2 \sigma_0^R} \right) - 1 \right\}^{-1} \quad (4)$$

where  $\sigma_p^R$  is the proof test stress at room temperature, and the superscript  $R$  indicates the value at room temperature. Since embedded flaws cannot be healed, the value of  $a_e^R$  is not changed in spite of the crack-healing treatment. Thus, the  $\sigma_G$  can be expressed as follows by expanding eq. (5) with regard to room temperature and high temperature:

$$\sigma_G = \frac{2 \sigma_0^T}{\pi} \arccos \left\{ \left( \frac{K_{IC}^T}{K_{IC}^R} \right)^2 \left( \frac{\sigma_0^R}{\sigma_0^T} \right)^2 \left\{ \sec \left( \frac{\pi \sigma_p^R}{2 \sigma_0^R} \right) - 1 \right\} + 1 \right\}^{-1} \quad (5)$$

where the superscript  $T$  indicates the value at elevated temperature  $T$ . By obtaining the temperature dependence of  $K_{IC}$  and  $\sigma_0$ , one can estimate  $\sigma_G$ .

Figure 20 shows the data on the fracture stress of the crack-healed and the proof-tested specimens as a function of temperature with the evaluated  $\sigma_G$  for the crack-healed alumina/20 vol% SiC particles composite when  $\sigma_p = 435$  MPa (Ono et al., 2007). Except the data at 1373 K, all specimens have higher strength than the  $\sigma_G$  at all temperatures. Also, the minimum values of the experimental fracture stress are almost equal to the  $\sigma_G$  at all temperatures. At 1373 K, the  $\sigma_{Fmin}$  is 6.8 % less than  $\sigma_G$ , but the value exists in the dispersion evaluated from the  $K_{IC}$  and the  $\sigma_0$  that have large scatters.

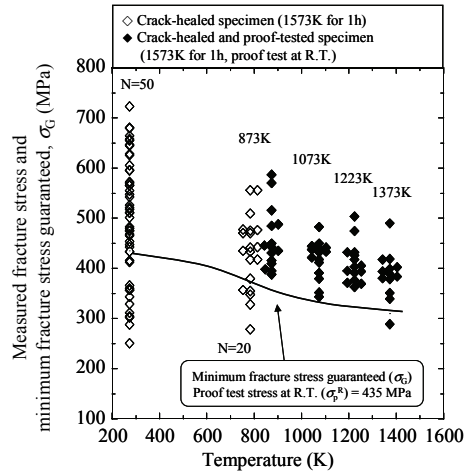


Fig. 20. Fracture stress of the crack-healed and proof tested specimens as a function of temperature with the evaluated minimum fracture stress guaranteed of the crack-healed  $Al_2O_3$ / 20 vol.% SiC particles composite proof tested under 435 MPa

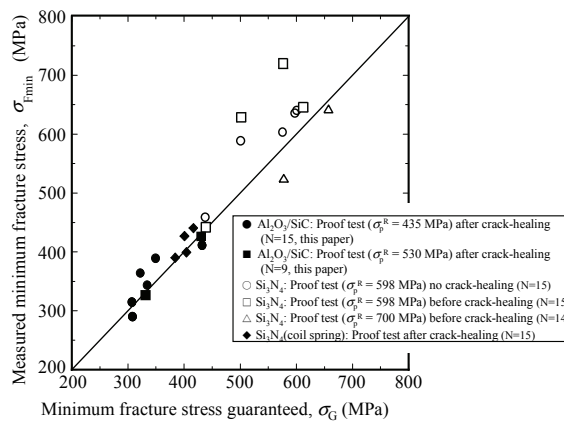


Fig. 21. Comparison between minimum fracture stresses guaranteed and measured minimum fracture stress



Moreover, the guaranteed theory can be applied to  $\text{Si}_3\text{N}_4$  (Ando et al., 2002b; Ando et al., 2005) and coil spring made of  $\text{Si}_3\text{N}_4$  (Nakatani et al., 2005). The results obtained can be seen in Fig. 21, where the measured  $\sigma_{\text{Fmin}}$  is plotted as a function of the evaluated  $\sigma_{\text{G}}$ .  $N$  in the figure denotes the number of samples used to obtain  $\sigma_{\text{Fmin}}$ . Four solid diamonds indicate the data on the ceramic coil spring made of silicon nitride. All  $\sigma_{\text{Fmin}}$  showed good agreement with  $\sigma_{\text{G}}$ . From this figure, it can be concluded that eq. (5) can be applied to  $\text{Al}_2\text{O}_3/\text{SiC}$ ,  $\text{Si}_3\text{N}_4$ , and even to a coil spring.

## 8. Through life reliability of ceramic components

The flow chart of a new methodology to guarantee the structural integrity of a ceramic component is shown in Fig. 22. This new concept consisted of the following three stages: (a) crack-healing under optimized conditions, (b) proof testing, and (c) in-situ (in-service) crack-healing.

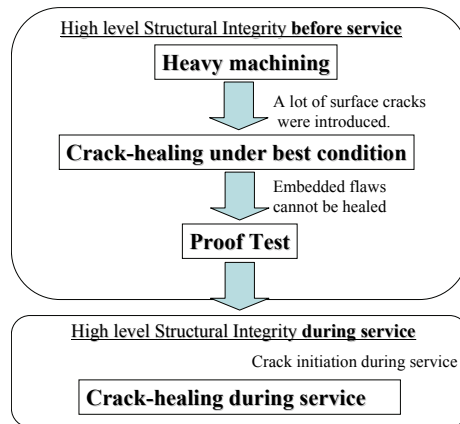


Fig. 22. Through life reliability management of ceramic component using crack-healing and proof test

By machining, many surface cracks will be induced and reliability will decrease considerably. However, by crack-healing under optimized conditions, surface cracks can be healed completely and reliability will be increased.

However, for the crack-healing of the above ceramics, oxygen is necessary. Consequently an embedded flaw cannot be healed. This means that the structural integrity of ceramic components before service cannot be guaranteed only by crack-healing technology. A new theory to explain the temperature dependence of minimum fracture stress guaranteed based on non-linear fracture mechanics was proposed as mentioned in section 7. Thus, before service, the structural integrity of ceramic components can be confidently guaranteed using the concept: crack-healing + proof test.

After service, if a crack is initiated, structural integrity will decrease considerably depending on the crack size. However, if a material can heal a crack in service, it would be very desirable for structural integrity. As mentioned in section 6, several materials developed by the present authors can heal a crack during service. Thus, a new concept shown in Fig. 22 is effective to increase the through life reliability of ceramic components.

## 9. Conclusion

Structural ceramics are generally brittle, which seriously affects the reliability of ceramic components. Four methods are used to resolve this weakness: (a) the ceramic is toughened by fiber reinforcement or microstructural control, (b) high level non-destructive inspection and repair of the unacceptable flaws, (c) using the proof test and then only using the components that have high reliability, and (d) making use of the self-crack-healing ability. In this chapter, special attention was paid to method (d), the self-crack-healing ability of structural ceramics.

In Section 1, the advantages of using the crack-healing ability of ceramics are outlined. In Section 2, nano-composite and multi-composite materials having crack-healing ability are presented. In Section 3, basic crack-healing ability is introduced in detail. In Section 4, the high-temperature strength characteristics of crack-healed specimens are explained. Machining is a necessary process for ceramic machine components, but machining can cause many cracks in the components. In Section 5, it is explained in detail how the many cracks introduced by machining can be healed and strength recovered completely. If a material were able to heal a crack that initiated during its service, it would be extremely beneficial for the structural integrity of a ceramic component. Thus, in Section 6, crack-healing behavior under stress and the resultant strength at the temperature of the crack healing are introduced in detail. Even if all surface cracks were healed completely, embedded flaws such as cracks and pores cannot be healed, because oxygen is necessary for crack healing. Thus, a proof test is necessary for the higher reliability. In Section 7, a detailed explanation of the proof test theory and its usefulness is given. In Section 8, a methodology to increase the through life reliability of ceramic components is explained.

In conclusion, the crack-healing ability of structural ceramics is a very useful technology for higher structural integrity and for reducing the machining and non-destructive inspection costs.

## 10. References

- Ando, K.; Iwasa, M.; Kim, B.A.; Chu, M.C. & Sato, S. (1993). Effects of crack length, notch root radius and grain size on fracture toughness of fine ceramics. *Fatigue & Fracture of Engineering Materials & Structures*, 16, pp. 995-1006.
- Ando, K.; Ikeda, T.; Sato, S.; Yao, F. & Kobayashi, Y. (1998). A preliminary study on crack healing behaviour of  $\text{Si}_3\text{N}_4/\text{SiC}$  composite ceramics. *Fatigue & Fracture of Engineering Materials & Structures*, 21,1,pp.119-122.
- Ando, K.; Furusawa, K.; Chu, M.C.; Hanagata, T.; Tuji, K. & Sato, S. (2001). Crack-healing behavior under stress of mullite/silicon carbide ceramics and the resultant fatigue strength. *Journal of the American Ceramic Society*, 84, 9, pp.2073-2078.
- Ando, K.; Furusawa, K.; Takahashi, K.; Chu, M.C. & Sato, S. (2002a). Crack-healing behavior of structural ceramics under constant and cyclic stress at elevated temperature. *Journal of the Ceramic Society of Japan*, 110, 8, pp.741-747.
- Ando, K., Takahashi, K., Nakayama, S. & Saito, S. (2002b). Crack-Healing Behavior of  $\text{Si}_3\text{N}_4/\text{SiC}$  Ceramics under Cyclic Stress and Resultant Fatigue Strength at the Healing Temperature. *Journal of the American Ceramic Society*, 85, 9, pp.2268-2272.
- Ando, K.; Shirai, Y.; Nakatani, M.; Kobayashi, Y. & Sato, S. (2002c). (Crack-healing + proof test): a new methodology to guarantee the structural integrity of a ceramics component. *Journal of the European Ceramic Society*. 22, 1, pp.121-128.

- Ando, K.; Kim, B.S.; Chu, M.C.; Saito, S. & Takahashi, K. (2004). Crack-healing and mechanical behaviour of  $\text{Al}_2\text{O}_3/\text{SiC}$  composites at elevated temperature. *Fatigue & Fracture of Engineering Materials & Structures*, 27, 7, pp.533-541.
- Ando, K.; Furusawa, K.; Takahashi, K. & Sato, S. (2005). Crack-healing ability of structural ceramics and a new methodology to guarantee the structural integrity using the ability and proof-test. *Journal of the European Ceramic Society*. 25, 5, pp. 549-558.
- Ando, K.; Takahashi, K.; & Nakao, W. (2009). Self-crack-healing behavior of structural ceramics, In: *Handbook of Nanoceramics and Their Based Nanodevices*, T.Y. Tseng and H.S. Nalwa (Eds.), Vol.1, Chapter 3, 1-26, American Scientific Publishers, Valencia, USA.
- Chou, I. A., Chan, H. M. and Harmer, M. P. (1998), Effect of annealing environment on the crack healing and mechanical behavior of silicon carbide-reinforced alumina nanocomposites. *Journal of the American Ceramic Society*, 81, pp.1203-1208.
- Chu, M.C.; Sato, S.; Kobayashi Y. & Ando, K. (1995). Damage Healing and Strengthening Behavior in Intelligent Mullite/SiC Ceramics. *Fatigue & Fracture of Engineering Materials & Structures*, 18, 9, pp. 1019-1029.
- Houjou, K.; Ando, K. & Takahashi, K. (2010). Crack-healing behaviour of  $\text{ZrO}_2/\text{SiC}$  composite ceramics, *International Journal of Structural Integrity*, 1, 1, pp.73-84.
- Jung, Y.S.; Nakao, W.; Takahashi, K.; Ando, K. & Saito, S. (2008a). Crack-Healing Behavior of  $\text{Si}_3\text{N}_4/\text{SiC}$  Composite under Low Oxygen Partial Pressure. *Journal of the Society of Materials Science, Japan*, 57, 11, pp.1132-1137.
- Jung, Y.S.; Guo, Y.; Nakao, W.; Takahashi, K.; Ando, K. & Saito, S. (2008b). Crack-healing behaviour and resultant high-temperature fatigue strength of machined  $\text{Si}_3\text{N}_4/\text{SiC}$  composite ceramic. *Fatigue & Fracture of Engineering Materials & Structures*, 31, 1, pp. 2-11.
- Kim, B.S.; Ando, K.; Chu, M.C. & Saito, S. (2003). Crack-healing behavior of monolithic alumina and strength of crack-healed member. *Journal of the Society of Materials Science, Japan*, 52, 6, pp.667-673.
- Kim, Y.W.; Ando, K. & Chu, M.C. (2003). Crack-healing behavior of liquid-phase-sintered silicon carbide ceramics. *Journal of the American Ceramic Society*, 86, 3, pp.465-470.
- Lange, F.F. & Gupta, T.K. (1970). Crack healing by heat treatment. *Journal of the American Ceramic Society*, 53, 1, pp. 54-55.
- Lee, S.K.; Ando, K. & Kim, Y.W. (2005a). Effect of heat treatments on the crack-healing and static fatigue behavior of silicon carbide sintered with  $\text{Sc}_2\text{O}_3$  and AlN. *Journal of the American Ceramic Society*, 88, 12, pp.3478-3482.
- Lee, S.K.; Ishida, W; Lee, S.Y.; Nam, K.W. & Ando, K. (2005b). Crack-healing behavior and resultant strength properties of silicon carbide ceramic. *Journal of the European Ceramic Society*, 25, 5, pp.569-576.
- Lee, S.K.; Ono, M.; Nakao, W.; Takahashi, K. & Ando, K. (2005c). Crack-healing behaviour of mullite/SiC/ $\text{Y}_2\text{O}_3$  composites and its application to the structural integrity of machined components, *Journal of the European Ceramic Society*. 25, 15, pp.3495-3502.
- Nakao, W.; Osada, T.; Yamane, K.; Takahashi, K. & Ando, K. (2005a). Crack-healing mechanism by alumina/SiC particles/SiC whiskers multi-composite, *Journal of The Japan Institute of Metals*, 69, 8, pp.663-666.

- Nakao, W.; Ono, M.; Lee, S.K.; Takahashi, K. & Ando, K. (2005b). Critical crack-healing condition for SiC whisker reinforced alumina under stress. *Journal of the European Ceramic Society*, 25, 16, pp.3649-3655.
- Nakao, W.; Mori, S.; Nakamura, J.; Takahashi, K.; Ando, K. & Yokouchi, M. (2006). Self-crack-healing behavior of mullite/SiC particle/SiC whisker multi-composites and potential use for ceramic springs. *Journal of the American Ceramic Society*, 89, 4, pp.1352-1357.
- Nakao, W.; Takahashi, K. & Ando, K. (2007). Threshold stress during crack-healing treatment of structural ceramics having the crack-healing ability. *Material Letters*, 61, 13, pp.2711-2713.
- Nakao, W.; Takahashi, K. & Ando, K. (2009). Self-healing of surface cracks in structural ceramics, In: *Self-healing Materials*, S.K. Ghosh (Ed.), Chapter 6, 183-217, WILEY-VCH, Weinheim, Germany.
- Nakatani, M.; Sato, S.; Kobayashi, Y. & Ando, K. (2005). A study on crack-healing + proof test to guarantee the structural integrity of ceramic coil springs, *Journal of High Pressure Institute of Japan*, 43, 2, pp.85-91.
- Niihara, K. (1991). New design concept of structural ceramics. *Journal of the Ceramic Society of Japan*, 99, 10, pp.974-982.
- Ono, M.; Nakao, W.; Takahashi, K.; Nakatani, M. & Ando, K. (2007). A new methodology to guarantee the structural integrity of  $\text{Al}_2\text{O}_3/\text{SiC}$  composite using crack healing and a proof test, *Fatigue & Fracture of Engineering Materials & Structures*, 30, 7, pp.599-607.
- Osada, T.; Nakao, W.; Takahashi, K.; Ando, K. & Saito, S. (2007). Strength recovery behavior of machined alumina/SiC whisker composite by crack-healing, *Journal of the Ceramic Society of Japan*, 115, 1340, pp.278-284.
- Osada, T.; Nakao, W.; Takahashi, K. & Ando, K. (2009). Kinetics of self-crack-healing of alumina/silicon carbide composite including oxygen partial pressure effect, *Journal of the American Ceramic Society*, 92, 4, pp.864-869.
- Takahashi, K.; Yokouchi, M.; Lee, S.K. & Ando, K. (2003). Crack-healing behavior of  $\text{Al}_2\text{O}_3$  toughened by SiC whiskers, *Journal of the American Ceramic Society*, 86, 12, pp.2143-2147.
- Takahashi, K.; Ando, K.; Murase, H.; Nakayama, S.; & Saito, S. (2005). Threshold stress for crack-healing of  $\text{Si}_3\text{N}_4/\text{SiC}$  and resultant cyclic fatigue strength at the healing temperature. *Journal of the American Ceramic Society*, 88, 3, pp.645-651.
- Takahashi, K.; Uchiide, K.; Kimura, Y.; Nakao, W.; Ando, K. & Yokouchi, M. (2007). Threshold stress for crack healing of mullite reinforced by SiC whiskers and SiC particles and resultant fatigue strength at the healing temperature. *Journal of the American Ceramic Society*, 90, 7, pp.2159-2164.
- Takahashi, K.; Jung, Y.S.; Nagoshi, Y. & Ando, K. (2010). Crack-healing behavior of  $\text{Si}_3\text{N}_4/\text{SiC}$  composite under stress and low oxygen pressure, *Materials Science and Engineering A*, 527, 15, pp.3343-3348.
- Thompson, A. M., Chan, H. M., Harmer, M. P. and Cook, R. E. (1995), Crack healing and stress relaxation in  $\text{Al}_2\text{O}_3$  / SiC "nanocomposites". *Journal of the American Ceramic Society*, 78, pp.567-571.
- Yao, F.; Ando, K.; Chu, M.C. & Sato, S. (2001). Static and cyclic fatigue behaviour of crack-healed  $\text{Si}_3\text{N}_4/\text{SiC}$  composite ceramics. *Journal of the European Ceramic Society*, 21, 7, pp.991-997.